Seismic analysis of red giants on the asymptotic giant branch

Guillaume Dréau

PSL UNIVERSITÉ PARIS

THÈSE DE DOCTORAT
DE L'UNIVERSITÉ PSL

Préparée à l'Observatoire de Paris

Analyse sismique des géantes rouges sur la branche asymptotique

Soutenue par
Guillaume DRÉAU
Le 19 septembre 2022

Ecole doctorale n° 127
École doctorale Astronomie et Astrophysique d'Île de France

Spécialité
Astronomie et Astrophysique

Composition du jury :

Patrick, FRANÇOIS GEPI, Observatoire de Paris	*Président*
Stéphane, CHARPINET IRAP, Université de Toulouse	*Rapporteur*
Valérie, VAN GROOTEL STAR, Université de Liège	*Rapporteure*
Margarida, CUNHA IA, Universidade do Porto	*Examinatrice*
Yveline, LEBRETON LESIA, Observatoire de Paris	*Directrice de thèse*
Benoît, MOSSER LESIA, Observatoire de Paris	*Directeur de thèse*
João, MARQUES IAS, Université Paris-Saclay	*Invité*

l'Observatoire de Paris | PSL

UNIVERSITÉ PARIS SCIENCES & LETTRES

DOCTORAL THESIS

AT

OBSERVATOIRE DE PARIS

Seismic analysis of red giants on the asymptotic giant branch

---

Author:
Guillaume Dréau

Supervisors:
Yveline Lebreton
Benoît Mosser

Doctoral school:

ED127 École doctorale Astronomie et Astrophysique d'Île de France

Research unit:

Laboratoire d'Études Spatiales et d'Instrumentation en Astrophysique (LESIA)

Scientific team:

Sismologie pour l'Etude des Intérieurs Stellaires et leur Modélisation (SEISM)

December 15, 2022

Abstract

The success of the CoRoT, *Kepler* and TESS space-borne missions has opened a new era for stellar physics. Asteroseismology provides unique information on stars, which is crucial for probing their structure and evolution, but also for understanding the Galaxy evolution and for assessing the physical properties of the exoplanets they host. To this end, studying the global seismic parameters of an ensemble of stars gives us the opportunity to analyse the variation of stellar internal properties along stellar evolution.

Among the diverse evolutionary stages of stars, the Asymptotic-Giant Branch (AGB) stage is important in many aspects. On the one hand, AGB stars provide unique constraints for the mixing processes in all previous burning stages, which modify their core and surface composition. On the other hand, AGB stars are important contributors to Galactic enrichment. Indeed, their circumstellar envelopes supplied by mass loss have a complex chemical composition. Nevertheless, performing a seismic study of these stars is demanding since it requires long observation periods for the seismic signal to be exploitable. Hopefully, the four-year time series of *Kepler* allow us to decipher in detail the oscillation spectrum of AGB stars, based on the pressure-mode pattern. Moreover, *Kepler* data clearly exhibit an excess of AGB stars that can be identified as the AGB bump (AGBb). The AGBb not only provides constraints for stellar physics but it could also be taken as a standard candle if its luminosity is independent of metallicity, which has to be confirmed.

First, this thesis focuses on a thorough analysis of the oscillation spectrum of evolved red giants, including Red-Giant Branch (RGB) and AGB stars. I show how the typical signature of the helium second-ionisation zone in mode frequencies makes a seismic classification between RGB and AGB stars possible. I discuss the extent to which an asymptotic pattern is valid for interpreting the oscillation spectrum of high-luminosity red giants. Besides, I examine potential additional damping contributions to the non-radial modes. These modes probe the innermost layers of stars during the early-AGB, which brings valuable constraints to the damping mechanisms on the AGB. Finally, I investigate the main structural differences between RGB and AGB stars by complementing this seismic study with stellar models and their oscillation frequencies calculated with the codes MESA and ADIPLS, respectively.

Second, this thesis is dedicated to assessing the potential of the AGBb to be a suitable standard candle as well as to constraining mixing processes in stellar interiors. To this end, I characterise the AGBb position in the seismic Hertzsprung-Russell diagram as a function of stellar mass and metallicity by combining *Kepler* and TESS data. Then, I compute a grid of stellar models with MESA, considering a sample of input physics including convective core and envelope overshooting, thermohaline mixing, and rotation. Accordingly, I evaluate the needs for these mixing mechanisms to reproduce the AGBb location according to the stellar mass. At last, I discuss the implications of this work on astrometry and Galactic archaeology.

Résumé

Le succès des missions spatiales CoRoT, *Kepler* et TESS a mené à de nouvelles opportunités pour la physique stellaire. L'astérosismologie fournit des informations uniques sur les étoiles qui sont non seulement essentielles pour sonder leur intérieur et leur évolution, mais aussi pour suivre l'évolution de la Galaxie et pour estimer les propriétés physiques des exoplanètes qu'elles abritent. Pour cela, l'étude des paramètres sismiques globaux d'un ensemble d'étoiles donne accès aux variations de leurs propriétés internes au fil de leur évolution.

Parmi les différents stades évolutifs que les étoiles entreprennent, la branche des géantes asymptotique (AGB) est importante par plusieurs aspects. D'une part, les étoiles AGB fournissent des contraintes uniques sur les processus de mélange qui modifient la composition de leur cœur et de leur enveloppe, en passant de la séquence principale aux phases de brûlage d'hélium. D'autre part, les étoiles AGB contribuent significativement à l'enrichissement Galactique. En effet, leur enveloppe circumstellaire alimentée par la perte de masse renferme une composition chimique complexe. Néanmoins, l'étude sismique de ces étoiles est exigeante puisqu'il est nécessaire de les observer suffisamment longtemps afin que leur signal sismique soit exploitable. Heureusement, les séries temporelles collectées par *Kepler* pendant quatre ans nous permettent de déchiffrer en détail le signal sismique des étoiles AGB en se basant sur le spectre d'oscillation des modes de pression. De plus, les données de *Kepler* montrent nettement la présence d'une accumulation d'étoiles AGB assimilable au bump de l'AGB. Non seulement, ce dernier apporte des contraintes pour la physique stellaire, mais il pourrait aussi être utilisé comme chandelle standard si la luminosité à ce stade est indépendante de la métallicité, ce qui reste à confirmer.

L'un des objectifs principaux de ma thèse concerne l'analyse complète du spectre d'oscillation des géantes évoluées, qui inclut les étoiles de la branche des géantes rouges (RGB) et de l'AGB. A partir de cette analyse, j'expose en quoi la signature caractéristique de la zone de seconde ionisation de l'hélium dans la fréquence des modes d'oscillation permet la classification des étoiles RGB et AGB. Ensuite, j'explore dans quelle mesure l'approche asymptotique est valide pour interpréter le spectre d'oscillation des géantes rouges lumineuses. Par ailleurs, j'examine les traces éventuelles de contributions supplémentaires à l'amortissement des modes non radiaux. Ces derniers sondent les couches les plus profondes des étoiles pendant le début de l'AGB, apportant des contraintes inestimables sur les mécanismes d'amortissement pendant l'AGB. Finalement, j'investigue les principales différences de structure entre les étoiles RGB et AGB en couplant cette analyse sismique avec des modèles stellaires et leurs fréquences d'oscillation associées calculées à partir des codes MESA et ADIPLS, respectivement.

La seconde facette importante de ma thèse consiste à évaluer la pertinence d'utiliser le bump de l'AGB comme chandelle standard ainsi que comme contrainte pour les processus de mélange dans les intérieurs stellaires. Pour y arriver, je caractérise la position du bump de l'AGB dans le diagramme Hertzsprung-Russell sismique en fonction de la masse et de la métallicité, tout cela en combinant les données de *Kepler* et TESS. Puis, je calcule une grille de modèles stellaires avec MESA, en considérant un ensemble de mécanismes physiques tels que l'extension de la zone convective du cœur et de l'enveloppe, la convection thermohaline et la rotation. Ainsi, nous évaluons le besoin de ces processus physiques pour reproduire la position du bump de l'AGB en fonction de la masse. Enfin, je passe en revue les implications de ce travail sur les domaines de l'astrométrie et de l'archéologie Galactique.

Remerciements

C'est avec passion que j'ai réalisé cette grande étape dans la réalisation de mon projet professionnel. La thèse a été non seulement une expérience professionnelle unique dans le monde de la recherche, dans lequel j'ai interagi avec des personnes passionnantes, mais aussi un défi de longue date. Cette aventure n'aurait donc pas pu aboutir en l'état sans le soutien d'un nombre de personnes, auxquelles je suis reconnaissant et que je souhaite exprimer ma gratitude dans ce court paragraphe.

Tout d'abord, j'adresse mes remerciements à Benoît et Yveline pour m'avoir donné l'opportunité de vivre cette expérience. Je vous suis très reconnaissant d'avoir associé vos compétences complémentaires en traitement de données et modélisation pour établir la ligne directrice de la thèse. Il n'y a rien de plus épanouissant que de découler ses propres résultats observationnels et de chercher à comprendre la physique sous-jacente par l'intermédiaire de modèles théoriques ! A ce sujet, je vous exprime toute ma gratitude pour le temps que vous m'avez accordé pendant les moments difficiles auxquels j'ai été confronté durant ces trois années, y compris pendant les différentes périodes de confinement et pendant la relecture du manuscript. Vous avez su vous tenir à l'écoute aux moments cruciaux, et ce malgré vos agendas bien remplis. En particulier, je remercie infiniment Yveline de m'avoir accompagné dans les méandres du code d'évolution MESA, qui nous a joué des tours bien plus d'une fois ! Sans ton aide, je n'aurais pas pu atteindre ma compréhension actuelle des différentes options de MESA qui régissent l'évolution d'une étoile jusqu'à ses derniers instants. Et enfin, je vous remercie, Benoît et Yveline, de votre bienveillance et de m'avoir introduit dans le cercle international de la recherche en astérosismologie. Ceci a participé aux différentes collaborations que j'ai pu entretenir au cours de ma thèse, sans compter les projets en cours et futurs dont je ne vois pas le bout ! Benoît, ne te décourage pas, je resterai toujours parmi ton grand public pour apprécier tes blagues classieuses !

J'aimerais remercier les membres du pôle Étoile du LESIA pour les échanges que j'ai pu entretenir avec eux, aussi bien professionnels que divertissants. J'ai pu y trouver rapidement ma place grâce à l'environnement jovial qui y règne. Tout particulièrement, je suis reconnaissant envers Caroline pour m'avoir accompagné dans l'organisation de mes tâches d'enseignement; Daniel pour m'avoir introduit à l'utilisation de son code d'inversion InversionKit; Kévin pour m'avoir aiguillé sur l'interprétation de mes résultats sur l'amortissement des modes; Réza pour avoir partagé avec moi son expertise sur les techniques d'ajustement des modes d'oscillation stellaire; Rhita et Coralie pour m'avoir assisté dans la recherche de post-docs. Je remercie également Réza et Benoît, ancien et nouveau coordinateurs de pôle, respectivement, qui m'ont permis de présenter mes travaux lors des réunions d'équipe mensuelles. J'exprime ma gratitude envers Benoît, Yveline, Rhita et Daniel qui ont pris le temps d'assister à mes répétitions. Que ce soit pour ma soutenance de thèse ou mes présentations via divers workshops/conférences, vos commentaires et corrections m'ont aidé à améliorer la qualité et la clarté de mes exposés oraux. Je tiens aussi à remercier les jeunes du pôle Étoile pour les bons moments qu'on a pu passer. Particulièrement, je suis reconnaissant envers David, Fernando, Keegan et Mina pour avoir ranimé la cohésion de l'équipe en organisant des soirées escape game, jeux de rôle et de société. Enfin, j'aimerais remercier toute l'équipe une seconde fois pour leur patience infaillible au restaurant, où j'ai facilement fait perdre une trentaine de minutes à tout le monde chaque midi !

Ensuite, je tiens à remercier vivement les membres de mon jury de thèse, le président Patrick François, les rapporteurs Stéphane Charpinet et Valérie Van Grootel, l'examinatrice Margarida Cunha et le membre invité João Marques d'avoir accepté d'en faire partie et de s'être déplacés jusqu'à Meudon pour le bon déroulé de la soutenance. En particulier, je suis reconnaissant envers les rapporteurs pour leur lecture attentive de mon manuscript, et pour leurs commentaires constructifs facilitant la lecture de ce dernier et enrichissant son contenu et les perspectives de mon travail.

J'exprime ma gratitude envers mes collaborateurs, sans qui mes travaux n'auraient pas pu atteindre la qualité que j'espérais. Spécifiquement, je remercie Charlotte Gehan de son accompagnement lors de mes travaux introductifs à la thèse effectués pendant mon stage de Master 2; Diego Bossini d'avoir

partagé son expertise sur la semiconvection dans les intérieurs stellaires qui s'est révélée capitale pour la modélisation des étoiles AGB; Jie Yu et Thomas Kallinger d'avoir partagé un point de comparaison sur la détection bump de l'AGB et l'ajustement du glitch d'hélium dans les géantes rouges, respectivement. Je remercie chalheureusement Pierre Houdayer pour les discussions riches et instructives que nous avons pu avoir et qui m'ont permis d'approfondir ma compréhension du glitch d'hélium d'un point de vue théorique. Je te remercie aussi pour ton enthousiasme dans le projet collaboratif que nous avons débuté lors du workshop ibérique de 2021, et qui va se poursuivre dans les mois à venir.

Enfin et surtout, j'aimerais exprimer toute ma reconnaissance envers les personnes qui ont suscité mon intérêt pour la sismologie stellaire, et qui m'ont donné la possibilité d'en arriver où j'en suis actuellement. Parmi ces personnes, je compte mon enseignant de physique stellaire de Master 1 João Marques, qui m'a introduit à l'astérosismologie et m'a ouvert la voie dans ce domaine grâce à ses recommandations de stage à l'étranger. Mes superviseurs de stage de Master 1, à savoir Margarida Cunha, Mathieu Vrard, ainsi que Pedro Avelino, y sont pour beaucoup également, en m'ayant proposé un sujet de stage passionant sur le sondage de la structure interne des géantes rouges et un cadre de travail immersif dans le monde de la recherche. Je remercie chalheureusement Annie pour avoir éveillé en moi l'intérêt pour les sciences et tous mes amis qui se sont tenus à mes côtés pendant cette aventure et qui n'ont cessé de m'encourager, de façon non exhaustive Théo, Quentin, Thomas, Jean-Baptiste, Marc, Alexandre, Jérémie, Noémie. Et enfin, je remercie infiniment ma famille pour le soutien qu'elle m'a apporté pendant toutes mes années d'études supérieures, en particulier ma mère et mon père pour toute l'aide financière qui m'a été attribuée lorsque j'en avais le plus besoin. Je vous rassure que les efforts qui ont été faits lors de mes années de licence et master en valaient la peine !

Contents

List of Figures

List of Tables

Chapter 1

Introduction

1.1 What is asteroseismology?

1.1.1 The needs for stellar constraints

Stars, approximated by self-gravitating spheroids composed of plasma, provide essential information through electromagnetic radiations they emit. This radiative energy is mainly produced by thermonuclear reactions in the core and because of the strong interaction between photons and matter, photons reach the stellar surface several million years after being produced. These radiations are well known for providing constraints on the stellar surface composition through the analysis of absorption lines in the electromagnetic spectrum. Not only analysing the light is essential for the understanding of stellar evolution and classification, but also for other fields of astrophysics such as the characterisation of exoplanets and galactic archaeology. In other words, we are able to give a global picture of stars simply by examining their light emission. However, the information carried by the light is limited to integrated quantities or reduced to the stellar surface, which is not sufficient to understand stellar evolution and structure. Further measurements are needed to probe the deepest layers of stars, this is exactly where asteroseismology comes into play.

1.1.2 Behind the scene

Below the slowly changing surface, stellar interiors are far from being quiet. Stars periodically swell and contract, get cooler and hotter due to the propagation of waves in their interiors, which justifies the designation of pulsating stars and pulsation cycle. Asteroseismology is dedicated to the probing of stellar interiors through the study of their pulsations, as indicated by the Greek etymology "seiein" and "logos", which stands for "shake" and "study", respectively. At first glance, those waves are out of reach due to their inability to travel in the vacuum. In other words, unlike photons they cannot be directly observed. Nevertheless, they can be detected by our telescopes thanks to the periodic changes in the star's brightness and surface velocity that they cause. More exactly, it is the superposition of waves that propagate in the stellar cavity that can be detected. Due to the finite size of stars, waves are trapped and propagate in well-defined regions. This allows waves to constructively interfere at specific frequencies in stellar interiors, giving rise to stationary waves: the so-called stellar oscillation modes. Assuming spherical symmetry, these constructive interferences lead to the existence of only a discrete set of solutions that in the most general case are characterised by three quantum numbers: the radial order n, the mode degree ℓ, and the azimuthal order m. A given set $\{n, \ell, m\}$ defines a mode that is susceptible to develop in stellar interiors. The stellar modes can be approached as those of an organ pipe in 1-D with one end closed and the other opened, as illustrated in Fig. 1.2. A powerful tool to highlight the periodicity of the star's brightness is the Fourier's transform applied to the time series. Those periodicities in temporal space are translated into spectral responses at specific frequencies: the stellar oscillation mode frequencies $\nu_{n,\ell,m}$.

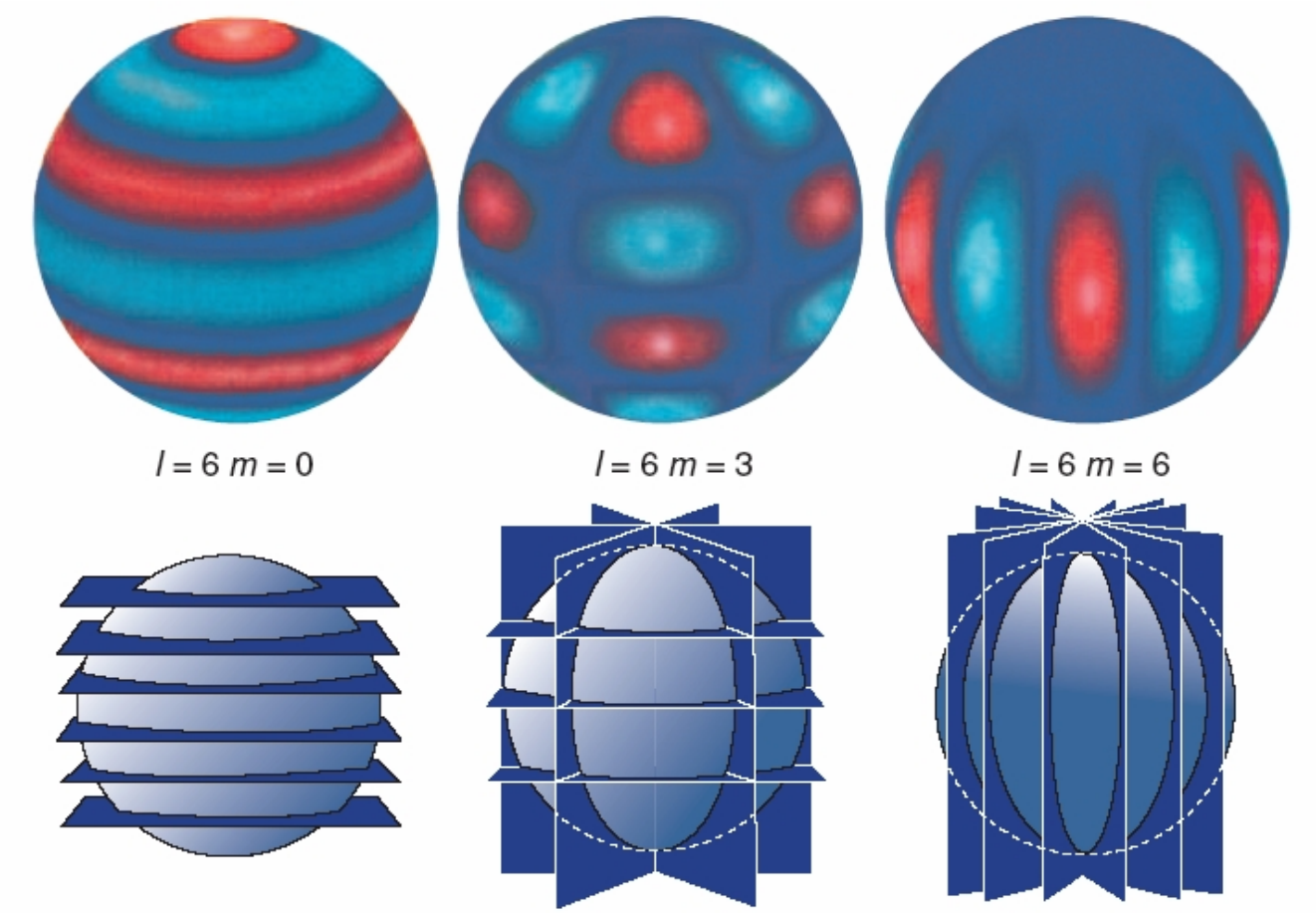

FIGURE 1.1: Three examples of oscillation modes in stars. The red regions correspond to the swelling up and heating up zones while the blue regions correspond to the contracting and cooling zones. Credit: CEA/Irfu

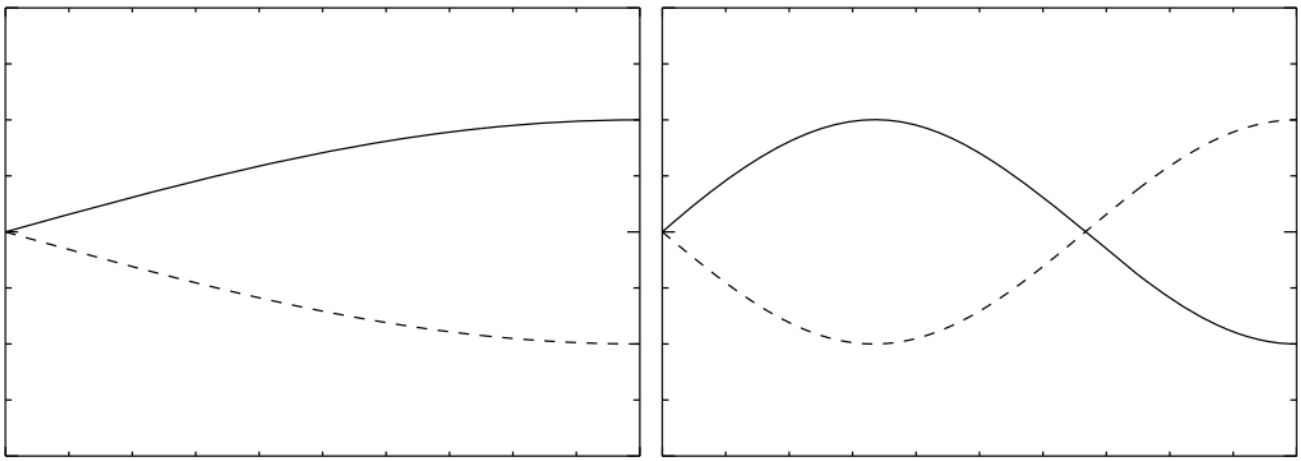

FIGURE 1.2: Organ pipe with one end closed and one end opened. The solid line indicates the motion along the pipe and the dashed lines is its antiphase counterpart. On the left is the fundamental mode with a node at the closed end and on the right is the first overtone, which has two nodes. Credit: Aerts, Christensen-Dalsgaard, and Kurtz (2010)

1.2 Asteroseismology, for what purpose?

Asteroseismology has made a breakthrough in our understanding of stellar structure. The waves carry signatures of some localised structures, for instance the base of convective envelopes, the boundary of convective cores, and ionisation zones of hydrogen and helium (Monteiro, Christensen-Dalsgaard, and Thompson, 1994; Monteiro and Thompson, 2005; Deheuvels et al., 2016). The valuable information brought on stellar interiors by asteroseismology is studied all along this manuscript, and a specific attention is paid on the second helium ionisation zone in Chapter 4.

The study of stellar pulsations not only has implications in our understanding of stellar structure and evolution, but also in many other fields of astrophysics. Probably one of the most dynamic association with asteroseismology currently is Galactic archaeology. On the one hand, the determination of mode frequencies in stars leads to estimates of global asteroseismic parameters that can be used as proxies for stellar age, as illustrated in Fig. 1.3. On the other hand, physical mechanisms considered in stellar models such as mixing processes can be calibrated to reproduce the observed asteroseismic parameters (Bossini et al., 2015). These calibrations impact the surface abundance of stars, hence the enrichment of the stellar environment through mass loss mechanisms. Precise stellar ages and chemical abundances are crucial for the study of different stellar populations in the Galactic disc, in particular to trace the history of the Galaxy formation and evolution (Borre et al., 2022).

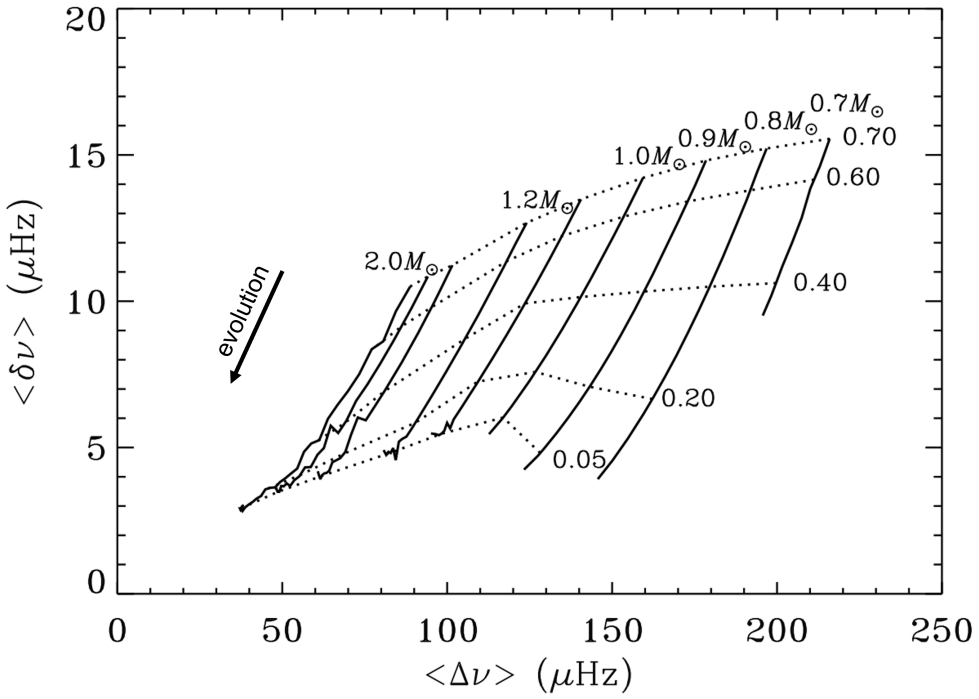

FIGURE 1.3: An asteroseismic HR diagram showing several evolutionary tracks with different masses (black solid lines). In this diagram, two combinations of mode frequencies are used: the large separation $\Delta\nu$ and the small separation $\delta\nu$. The large separation $\Delta\nu$ is mostly sensitive to mass while the small separation $\delta\nu$ is rather sensitive to stellar age. The dashed lines are plotted at constant hydrogen mass fraction in the core, and the associated values are indicated in the figure. The full knowledge of $\Delta\nu$ and $\delta\nu$ allows us to determine stellar ages and masses in case of well separated tracks. Credit: Aerts, Christensen-Dalsgaard, and Kurtz (2010)

The other major active field taking advantage of asteroseismology is exoplanetology. Several techniques allows for determining the parameters of companions orbiting around their host stars in exoplanetary systems. For instance, the transit method is a photometric method that consists of regularly measuring the stellar luminosity in order to detect a decrease of luminosity associated to the passing of

the exoplanet in front of the host star. Then, the amplitude and the period of the luminosity variation can be used to infer the companion's radius and revolution period, respectively. Nevertheless, the estimate of stellar parameters plays a non-negligible role in the inference of orbiting companion's parameters. The radial velocity method is a spectroscopic method that consists in measuring the shift of the host star's spectrum due to its radial velocity induced by the presence of the companion. The radial velocity data, *i.e.* the amplitude of the velocity variation and the orbital period can be used to derive the mass of the orbiting companion. However, a precise estimate of the host star's mass is necessary to derive the orbiting companion's mass (Perryman, 2011). Precise mass of the companion is crucial for determining its nature, which can be a hot Jupiter, hot Neptune, a terrestrial planet, brown dwarf. Finally, precise ages of the host stars can be derived from stellar models based on asteroseismic parameters (Lebreton and Goupil, 2014). These age estimates are crucial for the understanding of planet formation and evolution (Havel et al., 2011).

In the following, we focus on the inputs brought by asteroseismology of red giants, which are one of the stellar pulsators known up to date.

1.3 Categories of stellar pulsators

We focus on stars whose pulsations have been detected with an amplitude above some $\sim 1\,\mu$mag in photometry and $\sim 10\,\mathrm{cm.s^{-1}}$ in radial velocity. These limits correspond to the precision level of observations. The diversity of pulsating stars is rich across the Hertzsprung-Russell (HR) diagram: the period of the oscillations spans few minutes up to several years. So far, two driving mechanisms are known for the origin of stellar pulsations:

- The κ mechanism, which is a thermal instability caused by rapid variations in the opacity, called bumps, in the ionisation layers of H and He. This mechanism drives the oscillations in the so-called classical pulsators.
- The stochastic driving, which results from the turbulent motion of convection cells at the sound speed near the stellar surface. The excitation is caused by a large number of convective elements, causing the random aspect of the driving. Since the stochastic movements drives the Sun's oscillations, stars exhibiting stochastically excited oscillations are called solar-like pulsators.

An overview of stellar pulsators across the HR diagram is shown in Fig. 1.4.

1.3.1 Classical pulsators

The most abundant oscillators covering the HR diagram are the classical pulsators, as depicted by Fig. 1.4. Their pulsations are driven by the κ mechanism at specific layers that gain heat during the contracting part of the pulsation cycle in stellar interiors. As a global picture, they behave as heat engines, converting thermal energy into mechanical energy so that this type of driving is referred to as *heat-engine mechanism*. The latter creates intrinsically unstable oscillations, which grow until some amplitude-limiting mechanism emerges. As a result, those pulsators exhibit oscillations with large amplitudes that can reach a few $\mathrm{km.s^{-1}}$ in radial velocity, which makes them easier to observe and justifies their 'classical' designation. The characteristic time determining if the modes can be excited is the local thermal timescale of the driving zone, which is the time this region can radiate with the gravitational energy as the only source of energy (Aerts, Christensen-Dalsgaard, and Kurtz, 2010):

$$\tau_{\mathrm{th}} = \int_{r_d}^{R} \frac{c_p(r)T(r)\mathrm{d}m}{L(R)}, \tag{1.1}$$

where r_d is the distance from the stellar centre of the driving zone, R is the stellar radius, $c_p(r)$ is the heat capacity of the gas at constant pressure, $\mathrm{d}m$ is the infinitesimal mass of a thin layer at radius r, $T(r)$ is the temperature at radius r and $L(R)$ is the luminosity at the stellar surface. If this thermal timescale

is lower than the oscillation period, the driving zone remains in thermal equilibrium and modes cannot be excited. The oscillation period depends on the type of classical pulsators, it can be several minutes up to several days (see Table. 1.1).

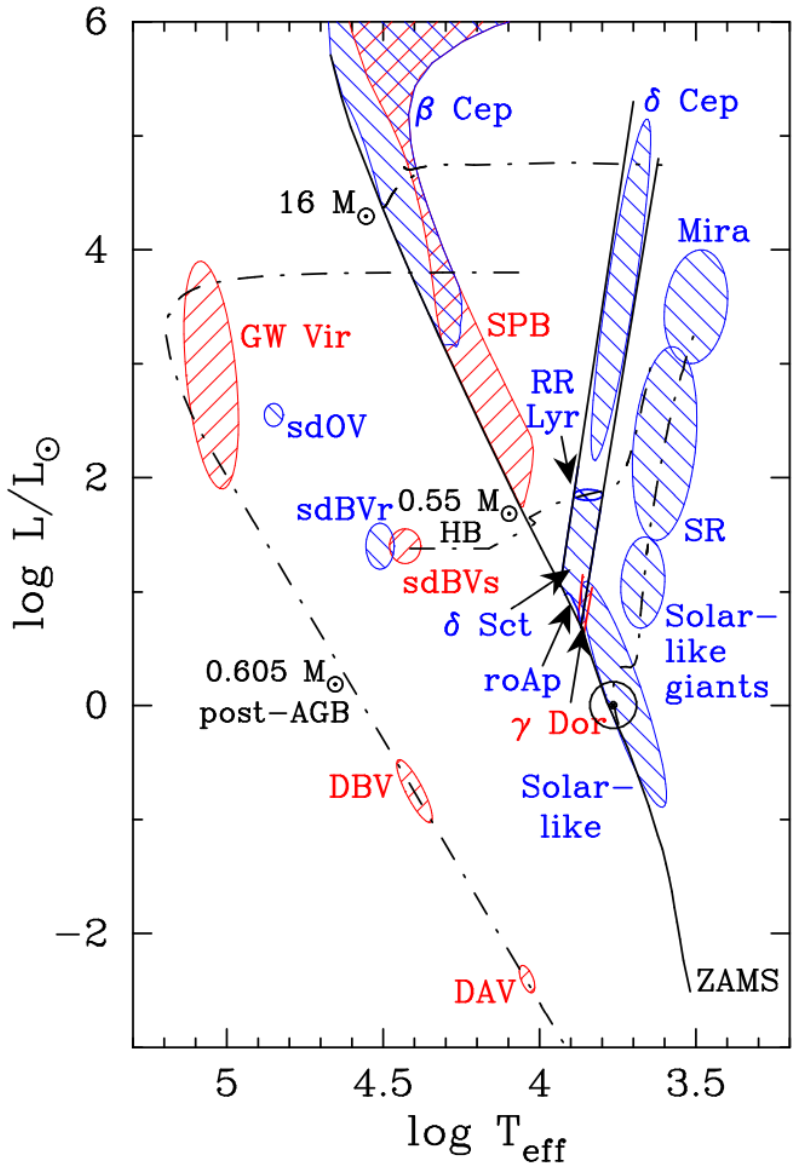

FIGURE 1.4: Hertzsprung-Russell diagram with different types of pulsators. Solar-like pulsators are indicated in the low-temperature part, they are low-mass main-sequence stars and red giants. The remaining pulsators spread in the HR diagram are classical pulsators. Type of oscillations are indicated in color, in blue for pressure modes and red for gravity modes (further details of these types of modes are presented in Sec. 3.3). Credit: Aerts, Christensen-Dalsgaard, and Kurtz (2010)

1.3.2 Solar-like pulsators

Solar-like pulsators have an outer convective envelope, in which oscillations can be excited. Near-surface convective motions with near-sonic speed are an efficient source of acoustic noise. Large number of uncorrelated convective cells, which play the role of the external forcing, cause the mode excitation. Then, a fraction of the stochastic noise is transferred to energy of global oscillation, and the star resonates in some of its natural oscillation frequencies (Aerts, Christensen-Dalsgaard, and Kurtz, 2010). The resulting oscillations have their period close to the characteristic timescale of vigorous convective motions in the near-surface layers: few minutes (typically for Sun-like stars) to several years (typically

Name Approx.	Periods	Discovery/Definition
Mira variables	100 - 1000 d	Fabricius (1596)
Semiregular (SR) variables 2	0 - 2000 d	Herschel (1782)
δ Cephei stars	1 - 100 d	1784, Pigott, Goodricke (1786)
RR Lyrae stars	0.3 - 3 d	Fleming (1899)
δ Scuti stars	0.3 - 6 h	Campbell & Wright (1900)
β Cephei stars	2 - 7 h	Frost (1902)
ZZ Ceti stars (DAV)	2 - 20 min	1964, Landolt (1968)
GW Virginis stars (DOV)	5 - 25 min	McGraw et al. (1979)
Rapidly oscillating Ap (roAp) stars	5 - 25 min	1978, Kurtz (1982)
V777 Herculis stars (DBV)	5 - 20 min	Winget et al. (1982)
Slowly Pulsating B (SPB) stars	0.5 - 3 d	Waelkens & Rufener (1985)
V361 Hydrae stars (sdBVr)	2 - 10 min	1994, Kilkenny et al. (1997)
γ Doradus stars	0.3 - 1.5 d	1995, Kaye et al. (1999)
V1093 Herculis stars (sdBVs)	1 - 2 hr	Green et al. (2003)
Pulsating subdwarf O star (sdOV)	1 - 2 min	Woudt et al. (2006)
Solar-like oscillators	3 - 15 min	Kjeldsen et al. (1995)
Semiregular variables seen as solar-like oscillators	200 - 2000 d	Christensen-Dalsgaard et al. (2001)
Early RGB oscillators	1 - 18 hr	Frandsen et al. (2002)
Intermediate RGB and He-core burning oscillators	30 - 150 d	De Ridder et al. (2009)

TABLE 1.1: Classes of pulsating star. Credit: Handler (2013)

for high-luminosity red giants). Given the turbulent convection in the envelope, solar-like pulsations are stochastically excited and intrinsically stable. The resulting amplitude depends on the balance between the energy input from the forcing and the damping. In terms of radial velocity, the amplitudes can fall to a few cm.s^{-1} and reach a few m.s^{-1}. Among stellar pulsators, red giants were found to exhibit clear stochastically excited modes. They will be the central objects in this thesis.

1.4 From the beginning of helioseismology to the emergence of asteroseismology

1.4.1 The discovery of pulsating stars

Periodic variable stars have been discovered in the 17th century, when Jan Fokkens Holwarda realised that the star Mira (also called "*o* Ceti" and discovered 40 years earlier by David Fabricius) disappears from the visible sky every $\sim$ 11 months due to a brightness drop. The cause of this variability due to intrinsic pulsations came almost three centuries later. Until 1914 enough evidence has been collected to make the connection between variability and radial pulsations (Shapley, 1914). In the meantime, Leavitt and Pickering (1912) pointed out that the Cepheids in the Small Magellanic Clouds follow a period-luminosity relation, which paved the way for the determination of distances in the visible Universe. Since then, this period-luminosity relation is one of the major astrophysical applications of pulsating stars, and also marked the beginning of stellar seismology.

1.4.2 The birth of helioseismology

During the decades following the discovery by Henrietta Leavitt, theoretical studies were conducted to formalise the mathematical framework of stellar pulsators and understand the driving mechanism behind their oscillations (*e.g.* Pekeris, 1938; Cowling, 1941). In the early 1960s, solar oscillations have been highlighted by the Doppler shift of spectroscopic lines (Evans and Michard, 1962; Leighton, Noyes, and Simon, 1962). These authors measured that the solar pulsations were periodic, with a period of 5 minutes. At this stage, the cause of this periodicity, namely the existence of acoustic modes in the Sun's

interior, was not known. In the next decade, additional works reached that conclusion, and revealed that the signature of oscillations in timeseries could be used to probe the Sun's interior (Ulrich, 1970; Leibacher and Stein, 1971).
Nevertheless, astronomers were confronted to a major complication while extracting the solar oscillation mode properties: the Sun needs to be observed as long as possible to bring the oscillation modes out of the oscillation spectrum. On the one hand, the signal-to-noise ratio must be high enough to observe a large number of modes. On the other hand those modes can only be resolved with a sufficiently long observation time, which is essential to reach precise mode characterisation. To this end, several networks of ground-based telescopes have been deployed to overcome these difficulties such as the International Research on the Interior of the Sun (IRIS) (Fossat, 1991), the Global Oscillation Network Group (GONG) (Hill et al., 1994a; Hill et al., 1994b) and the Birmingham Solar-Oscillations Network (BiSON) (Chaplin et al., 1996). Then, helioseismology has been marked by the launch of space borne telescopes enabling to bypass the limitations of ground-based observations, particularly since 1995 with the instrument Global Oscillations at Low Frequencies (GOLF) of the Solar and Heliospheric Observatory (SoHO) telescope (Gabriel et al., 1995). Accordingly, more than a thousand of Solar oscillation modes with different degree ℓ have been detected (see Fig. 1.5), making a breakthrough on our understanding of stellar interiors such as the internal rotation profile of the Sun (Schou et al., 1998; Di Mauro and Dziembowski, 1998).

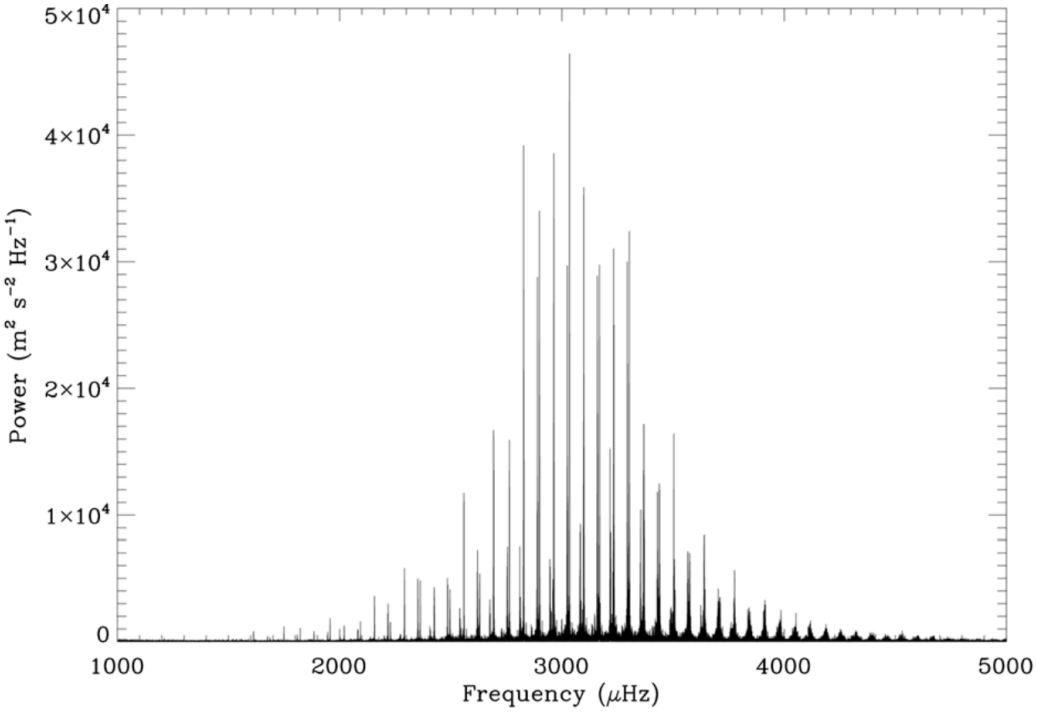

FIGURE 1.5: Oscillation power spectrum of the Sun, obtained by the network of ground-based telescopes BiSON. Credit: Elsworth et al. (2015)

1.4.3 From helioseismology to asteroseismology

After the detection of solar oscillation modes, a serious challenge was to extend the helioseismology techniques to stars. This was not expected to be an easy task because of their faint apparent magnitude. Finally, the first evidence of solar-like oscillations in stars has been found in 1998 by the 10 days observing runs of Procyon (Martić et al., 1999; Barban et al., 1999): asteroseismology was born.
In the meantime, the first exoplanet has been discovered by Mayor and Queloz in 1995 (Mayor and Queloz, 1995). This exoplanet (referred as hot jupiter) being massive and orbiting very close to its host star unlike in the Solar system, it raised many questions about planetary system formation. As a consequence, exoplanetologists needed to evaluate the recurrence of those hot jupiters in the Galaxy. They needed higher precision photometric observations to detect the luminosity drop caused by the transit of the planet in front of its host star. Given their shared needs, exoplanetologists and asteroseismologists

collaborated and planned incoming space missions together. Since then, several space missions have made asteroseismology one of the most active field in stellar physics. Among them, the Convection, Rotation and planetary Transits (CoRoT) satellite launched by CNES observed more than 160,000 stars with a visual magnitude $m_V \in [5.4, 9.5]$ between January 2007 and November 2012. Those stars have been observed for six months, leading to a frequency resolution of ~ 0.1 μHz and allowing us to explore the oscillation spectrum of main-sequence stars and red giants. This was the first opportunity to perform ensemble asteroseismology, which consists in highlighting solar-like oscillations in a large sample of stars and use the global seismic properties to constrain stellar evolution.
In the same period, the *Kepler* mission was launched in 2009 by NASA to monitor more than 170,000 stars with a visual magnitude $m_V \in [9, 15]$ over a period of four years, providing the best frequency resolution up to date, of ~ 8 nHz. Not only it enabled us to improve the precision on the seismic constraints used in stellar models, but it also permitted us to probe the internal structure of high-luminosity red giants. In the next section, we will see that this mission has revolutionised red-giant seismology.
Presently, the Transiting Exoplanet Survey Satellite (TESS) by NASA is at work since April 2018, but it mainly focuses on the detection of exoplanets (Ricker et al., 2015). It is expected to monitor more than 200,000 main-sequence dwarf stars showing planetary transits and 6,000 solar-like pulsators mainly composed of main-sequence stars and subgiants with a visible magnitude $m_V \leq 7.5$. Each star will be observed between 1 month to 1 year, providing a frequency resolution of ~ 0.05 μHz. The next high-precision photometric data will be collected by the PLAnetary Transits and Oscillations of stars (PLATO) space mission to be launched in 2026 by ESA, whose goal is to derive precise stellar ages, masses, and radii.

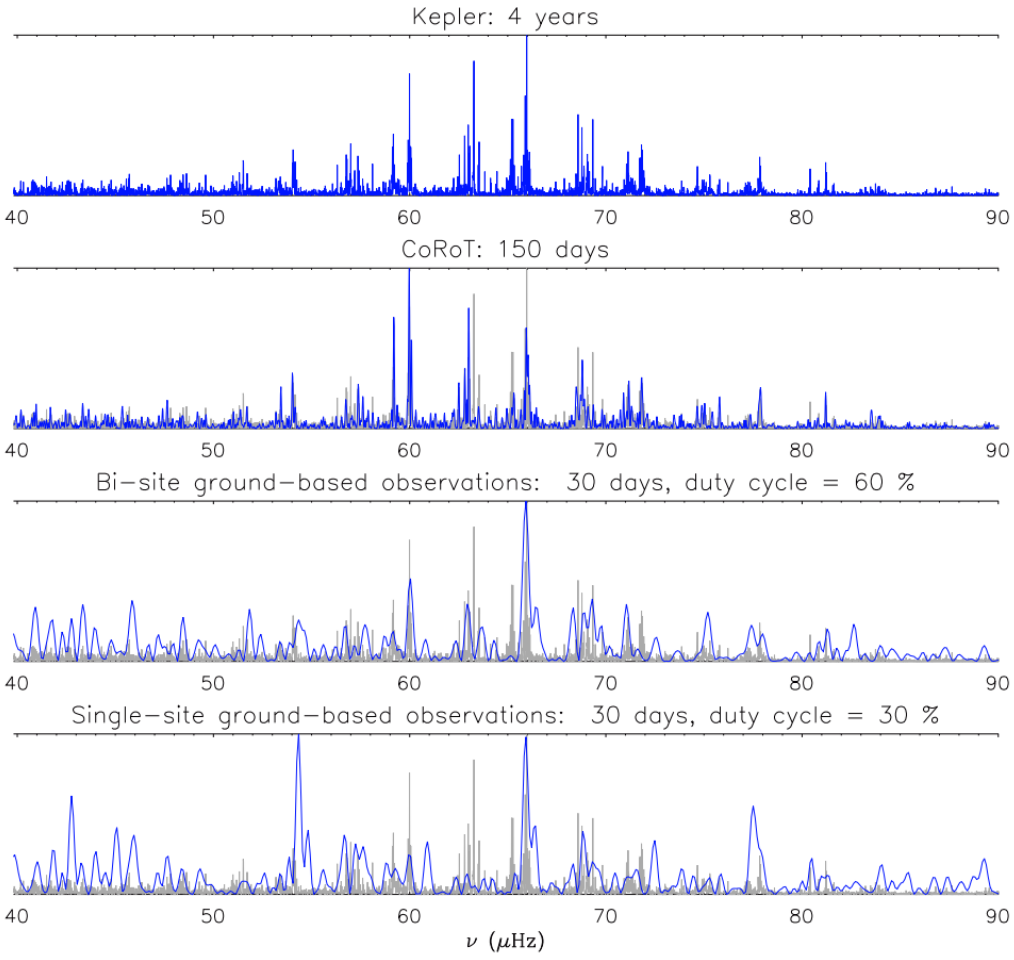

FIGURE 1.6: Simulation of the oscillation spectrum of a 1.3-$M_\odot$ star on the RGB, with different observation durations and telescopes. In all panels, the 4-year long spectrum obtained with *Kepler* is indicated in grey as a reference. Credit: Mosser, Miglio, and CoRot Team (2016)

1.5 The emergence of red-giant seismology

The success of solar-like star seismology has motivated attempts for detecting solar-like oscillations in red giants. The first detections were reported with the ground-based Swiss Euler telescope for the red giants ξ Hya, ε Oph, and η Ser (Frandsen et al., 2002; Barban et al., 2004). However, the mode identification remained under debate because of the unexpected presence of short-lived modes in the oscillation spectrum. Theoretical works could neither solve if radial and non-radial modes were equally excited, nor provide reliable information on the damping mechanisms that could justify these short mode lifetimes. Since those objects have large radius, hence low mean density, the period of oscillations are long and reach several days. Accordingly, one necessary ingredient is a long observation time to fully resolve red-giant oscillation modes (see Fig. 1.6).

Ground-based observations could fulfil this requirement but were affected by day/night aliases. High-quality photometry of red giants could be achieved with the successful space-borne telescopes CoRoT and *Kepler*. They could prove the presence of non-radial modes in the oscillation spectrum of red giants, which was controversial before the launch of the associated space missions (see e.g. Dziembowski et al., 2001; Christensen-Dalsgaard, 2004).
CoRoT and *Kepler* not only allowed us to lift the uncertainties on the structure of red-giant oscillation spectrum, but also revealed the presence of modes that have a non negligible amplitude both in the envelope and the core: the so-called mixed modes. The particularity of the mixed modes is that they are able to develop both in the stellar envelope and core cavities, then they carry precious information on the deepest layers of stars. They were not expected to be detectable because of their strong damping and the closeness between consecutive modes, forming a very dense oscillation spectrum. But finally, the high precision and long time series collected by those telescopes were so excellent that they could be detected without ambiguity. They revolutionised red-giant seismology notably through the elaboration of a classification method of red giants, including H-shell burning stars and He-burning stars (Bedding et al., 2011; Stello et al., 2013; Mosser et al., 2014), as well as the study of the internal rotation profile of red giants (Beck et al., 2012; Mosser et al., 2012c; Gehan et al., 2018).

1.6 Contextualisation of my Ph.D.

The AGB is a key stage of stellar evolution in many aspects. First, it is the last phase of stellar evolution before the envelope is ejected through stellar winds, forming a planetary nebula and a remnant compact object. The seismic study of AGB stars provides information not only on their structure, but also on the physical mechanisms they experienced to reach their current state. On the other hand, AGB stars play a major role in Galactic archaeology: they allows for inferring the activity of star formation in the past 0.5-1.0 Gyr. Finally, they are fundamental contributors to the chemical enrichment of the galaxy through stellar nucleosysthesis.

The characterisation of AGB oscillation spectrum provides valuable information on regions characterised by strong gradients of the sound speed such as helium ionisation zones. In case of resolved modes, i.e. when the oscillation period is lower than the observation duration, the mode width can be measured, then used to infer the physical mechanisms behind mode damping at evolved stages of stellar evolution. In this part, we present a global picture of high-luminosity red-giant seismology, unveiling our current progress of their oscillation spectrum analysis and structure modelling.

1.6.1 Overview of evolved red giants

Oscillation spectrum

The nature of the variability of high-luminosity red giants has been first investigated in ground-based observations with the microlensing surveys MACHO (Massive Compact Halo Objects Wood et al., 1999) and OGLE (Optical Gravitational Lensing Experiment Wray, Eyer, and Paczyński, 2004; Soszyński

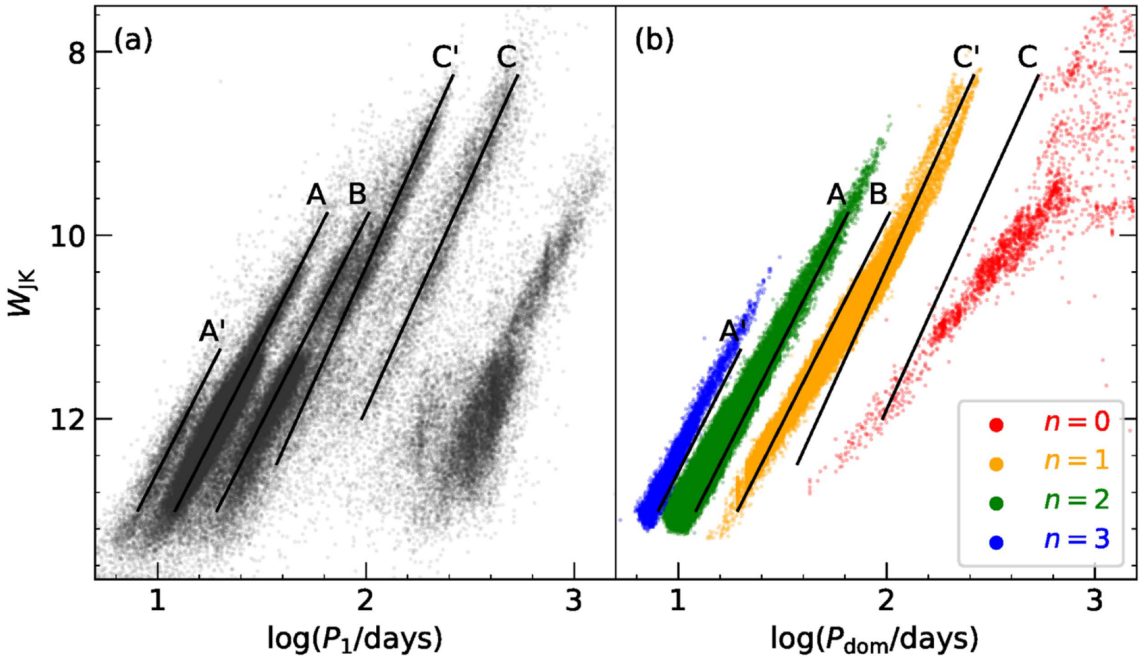

FIGURE 1.7: Period-Luminosity Sequences of Long-period Variables. **Left:** Reddening-free magnitude W_{JK} as a function of the primary oscillation period from observations. **Right:** same figure but the periods are derived from linear, radial, nonadiabatic pulsation models. Those periods are associated to the highest peak in the power spectrum. Different colours represent periods of different modes, red points contain Mira variables while other markers are associated to semi-regular variables including RGB and AGB stars. Solid lines help to identify the approximate location and slope of observed sequences. Credit: Trabucchi et al. (2017)

and Wood, 2013). Given their proximity with both Mira variables and solar-like giants, those high-luminosity red giants, also called semi-regular variables (SRs, see Fig. 1.4), were tested to be either classical pulsators with self-excited pulsations or solar-like pulsators with stochastically excited pulsators (Dziembowski et al., 2001; Christensen-Dalsgaard, Kjeldsen, and Mattei, 2001). Finally, by using the OGLE-III Catalog of Variable Stars based on photometric data collected during 8 years (2001-2009), Dziembowski and Soszyński (2010) found that high-luminosity red giants were solar-like pulsators, showing modes in the frequency range that is consistent with solar-like oscillations. These modes correspond to pressure modes that are excited by the turbulent motions of convection near the stellar surface (Goldreich and Keeley, 1977; Belkacem et al., 2006). Those modes revealed to be crucial for the interpretation of the period-luminosity diagram. Indeed, different branches as represented in Fig. 1.7 are associated to different radial orders n, which helps to distinguish Mira variables, semi-regular variables, and less evolved RGB stars. Both radial ($\ell = 0$) and non-radial ($\ell = 1, 2$) modes could be detected in evolved red giants at low radial order $n \leq 5$ (Mosser et al., 2013b; Yu et al., 2020). This gives us the opportunity to test the validity of the asymptotic relation (presented in Chapter 3) that provides an analytical expression for the mode frequencies in the limit $n \gg \ell$. Accordingly, models have been computed to follow the evolution of the frequency pattern near the luminosity-tip of the RGB (Stello et al., 2014), showing that departure from the asymptotic regime are expected at the RGB tip. On the other hand, global seismic parameters could be estimated such as the frequency at maximum oscillation power $\nu_{\max}$ and the frequency spacing $\Delta\nu$ (also called large separation) between modes of consecutive radial order n at fixed degree ℓ (see Fig. 1.8). Those parameters have been used to test the validity of the scaling relations (Kjeldsen and Bedding, 1995) at evolved stages that provide estimates of stellar parameters such as mass and radius (Yu et al., 2020).

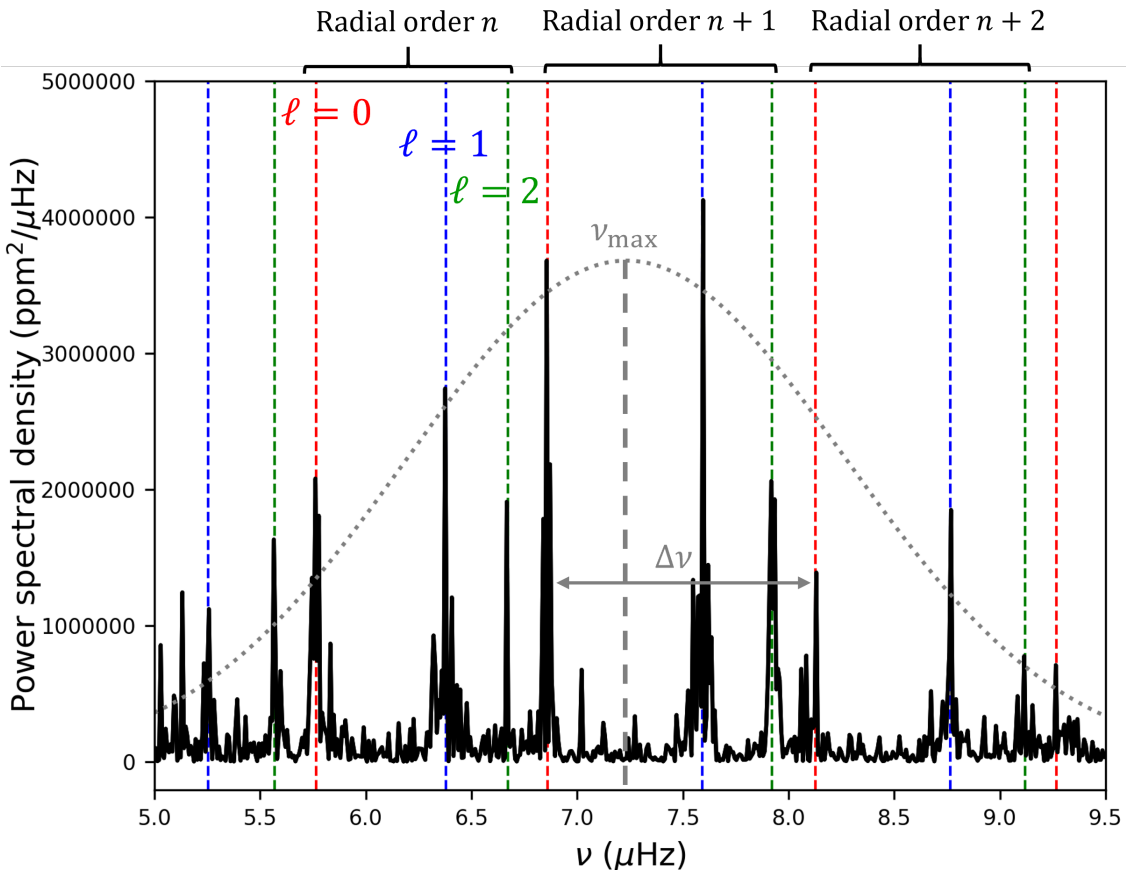

FIGURE 1.8: Oscillation spectrum of the RGB star KIC 1719297 observed by *Kepler* with $\Delta\nu = 1.22$ μHz. The red dashed lines indicates the location of the radial modes ($\ell = 0$) while the blue and green dashed lines locate the non-radial modes, i.e. dipole ($\ell = 1$) and quadrupole modes ($\ell = 2$), respectively. The grey dotted line represents the underlying Gaussian envelope of the observable modes, where the maximum reached at ν_{max} marks the maximum oscillation power. The mode identification is based on the method described in Chapter 7.

Internal structure

Evolved RGB and AGB stars have similar luminosity, effective temperature and radius. These global similarities are caused by similar dynamics of the core and the envelope: while the core contracts because the temperature is too low to continue the nuclear-chain burning reactions, the envelope dilates. This makes the classification of H-shell burning stars and He-shell burning stars challenging due to the lack of observables that differentiate one star from another. Despite these similarities, RGB and AGB have clear structure differences (see Fig. 1.10). Indeed, AGB stars exhibit an additional He-shell burning compared with their RGB counterparts. Moreover, AGB stars suffered from significant mass loss as they passed the RGB luminosity tip. Such important mass loss is expected at the luminosity tip where the envelope expands up to the point that it is weakly bound by gravitational interaction. Accordingly, the extent of the convective envelope differs before and after the He-core burning phase.

The seismic study of RGB and clump stars has brought valuable parameters for the investigation of structure differences between RGB and AGB stars. The detection of mixed modes that probe the deepest layers of stars have been found to be sensitive to the growing convective core that settles during the He-core burning phase (Bedding et al., 2011). Their signature in seismic parameters, particularly in the gravity-mode period spacing $\Delta\Pi_1$ between modes of consecutive radial order n at degree $\ell = 1$, is so strong that an unambiguous classification of H-shell burning stars and He-core burning stars is possible (see Fig. 1.9). Another classification method exists, which is based on the impact of ionisation zones on

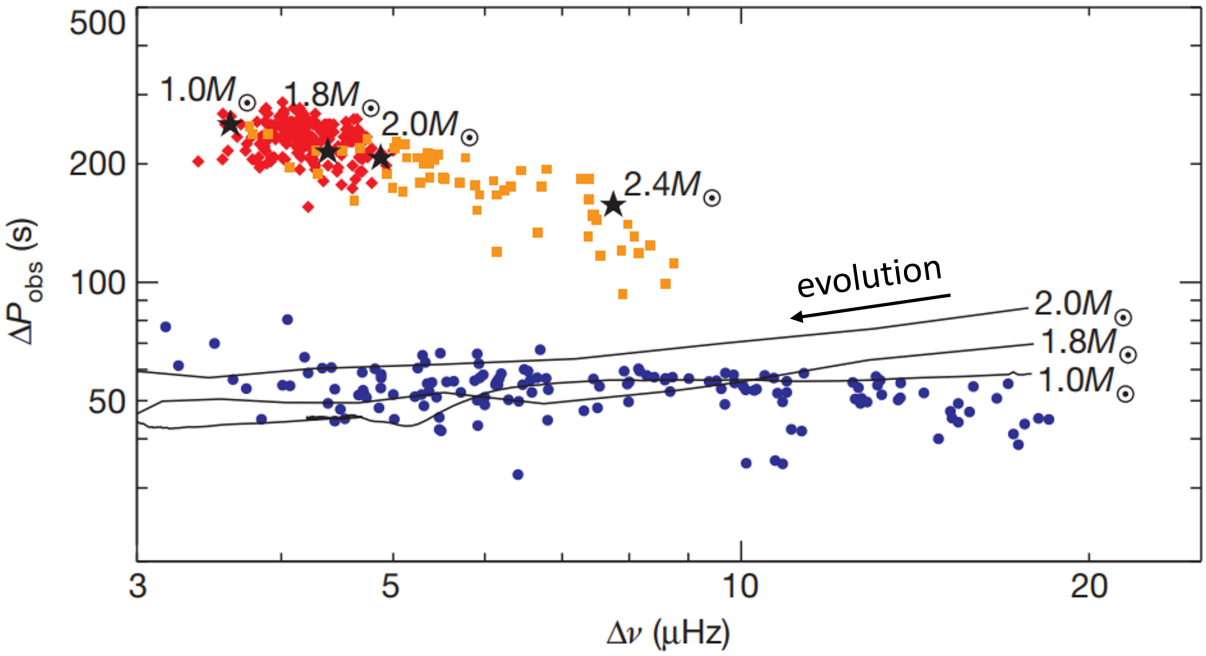

FIGURE 1.9: Spacing in period ΔP_{obs} between gravity modes of consecutive radial order n at degree $\ell = 1$ as a function of spacing in frequency $\Delta\nu$ between pressure modes of consecutive radial order n at degree $\ell = 0$. H-shell burning stars are indicated in blue while He-core burning stars are represented in red for primary clump stars with $M \leq 2\,M_\odot$ and orange for secondary clump stars with $M \geq 2\,M_\odot$. Three evolutionary tracks with different initial mass are represented on the RGB. Credit: Bedding et al. (2011)

pressure modes in the stellar envelope. The variations of the sound speed caused by the ionisation of helium introduce a signature in mode frequencies, whose characteristics are linked to the properties of the envelope and the helium ionisation region (Kallinger et al., 2012; Vrard et al., 2015). These classification methods help to understand the structure changes that stars undergo between H-shell burning and He-burning phases, providing clear seismic constraints for stellar models. For instance, they offered the possibility to track the evolution of rotation from the early-RGB up to the He-core burning phase, showing a clear slowing down of the core rotation rate (Mosser et al., 2012c; Deheuvels et al., 2014). Even now, the study of stellar structure signature in $\Delta\Pi_1$ still leads to fruitful results, such as the discovery of intermediate-mass red giants with degenerate cores induced by a substantial mass transfer from a close companion (Rui and Fuller, 2021; Deheuvels et al., 2021), and the investigation of lithium depletion in red giants (Deepak and Lambert, 2021).

The AGB bump

One of the key event in the early-AGB that can strongly constrain physical mechanisms in stellar interiors is the luminosity bump. The AGB bump (AGBb) manifests as a drop of luminosity as a star evolves on the AGB after the He-core burning phase (see Fig. 1.11) and is associated with the ignition of the He-burning shell source (further details in Sect. 2.5.1). Due to the additional time spent in the luminosity range of the AGBb, a local excess of stars can be observed in the luminosity distribution of stellar population. Such overdensity of stars has been first predicted by stellar evolutionary models (Caputo, Castellani, and Wood, 1978), then identified in the colour-magnitude diagram (CMD) of a few Galactic globular clusters (Ferraro, 1992) and of the Large Magellanic Cloud (Gallart, 1998) as illustrated in Fig. 1.12.

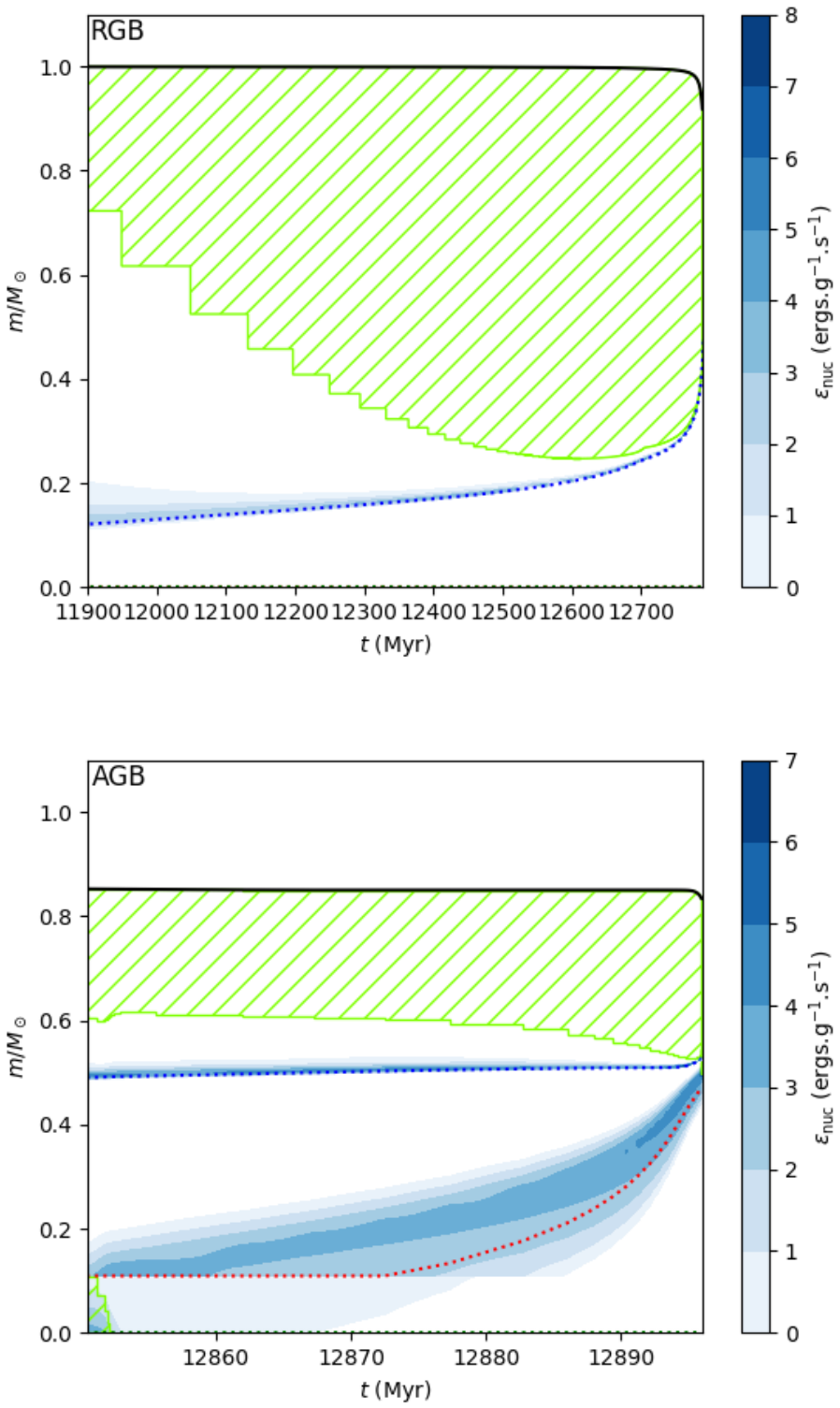

FIGURE 1.10: Kippenhahn diagrams that represent the mass coordinate in star interiors ($m/M_\odot = 0$ is the centre and $m/M_\odot = 1$ is the surface) as a function of the stellar age. These diagrams are computed with the MESA models described in Chapter 6. **Left** panel (respectively, **right** panel) is from the early-RGB (respectively, early-AGB) up to the luminosity tip of the RGB (respectively, high-luminosity AGB). Green-shaded area correspond to convective zones while blank ones are radiative zones. The thick black line marks the limit of the stellar surface and dotted lines locate the burning shells: in blue the H-burning shell and red the He-burning shell. The colourbar indicates the energy produced by nuclear reactions.

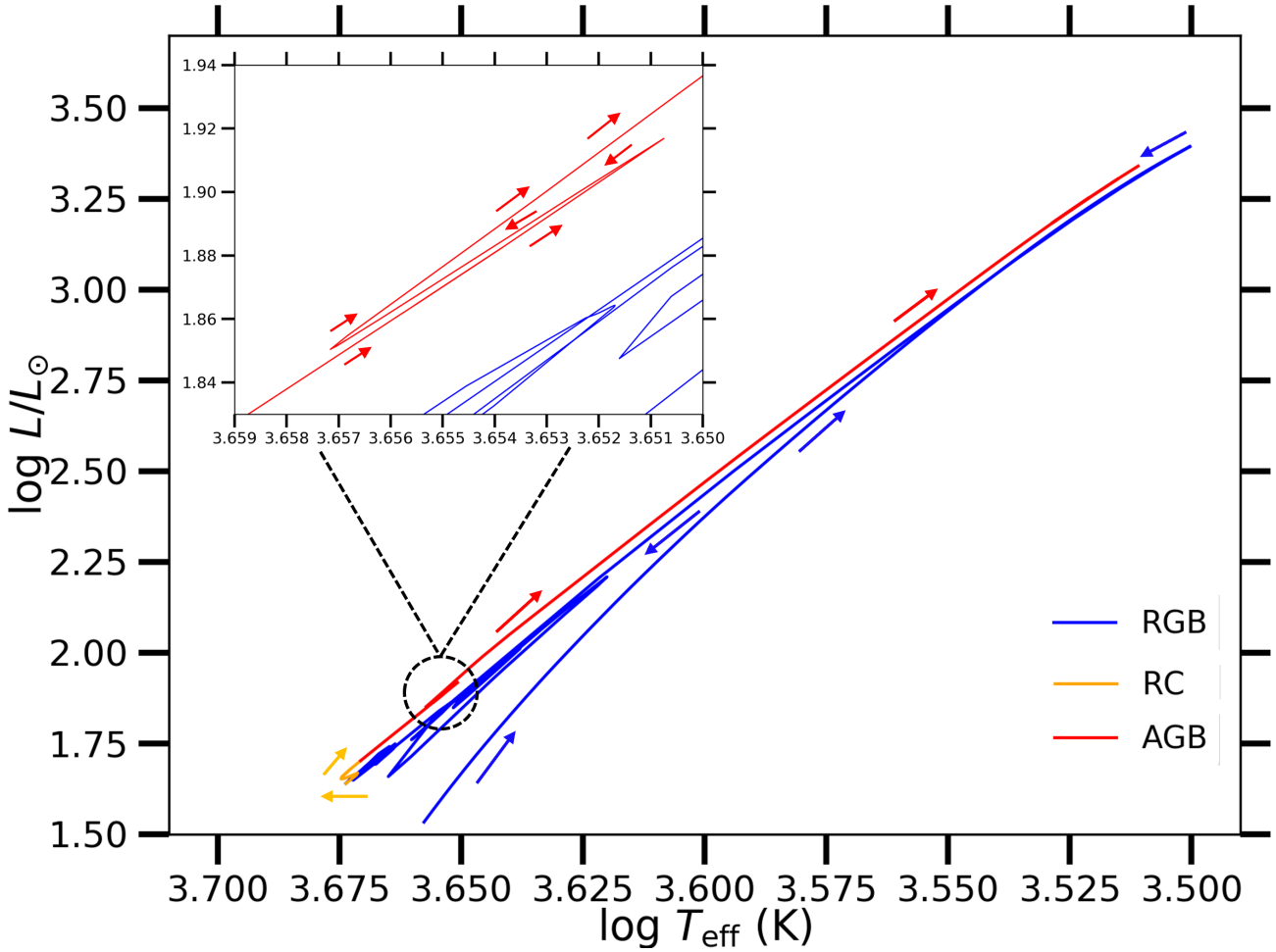

FIGURE 1.11: Evolutionary track computed with MESA of a $1M_\odot$-mass star in the Hertzsprung-Russell Diagram (HRD). The track is represented in blue for the RGB, in orange for the Red Clump (RC), and in red for the AGB. The arrows indicate the evolution direction along the evolutionary track. The inset is a zoom-in portion of the large panel at the AGBb location. The numerous turning-backs in blue located before the red clump correspond to the He burning phases in unstable conditions (also called subflashes), which are so rapid that they are hardly visible in observations.

According to theoretical work, the AGBb luminosity is expected to vary with stellar parameters: the higher the mass, the higher the luminosity at the AGBb (Alves and Sarajedini, 1999). On the other hand, the metallicity dependence of the AGBb luminosity is still under debate. The AGBb luminosity may be independent of the metallicity (Pulone, 1992; Ferraro, 1992) or slightly increasing when the metallicity decreases (Alves and Sarajedini, 1999). Shedding light on the metallicity dependence would have important implications for astrometry and the study of stellar populations. Indeed, AGBb stars with identical mass formed in the same cluster could be suitable candidate for standard candles if their luminosity is independent of metallicity (Pulone, 1992; Ferraro, 1992).
Finally, the AGBb revealed to be an ideal constraint for stellar models, in particular for mixing processes. Indeed, Bossini et al. (2015) could extract the AGBb luminosity in a sample of *Kepler* stars of mass $M \in [1.3, 1.7]M_\odot$ and metallicity $[\mathrm{Fe/H}] \in [-0.4, 0.4]$dex. They showed that an additional mixing region above the convective core during the He-core burning phase is necessary to reproduce both the AGBb luminosity and the distribution of seismic parameters. This way, by improving our understanding of convection, we can predict not only the properties of the deep layers of He-core burning stars but also the chemical composition of stellar envelopes, which has implications on the evolution of the stellar environment.

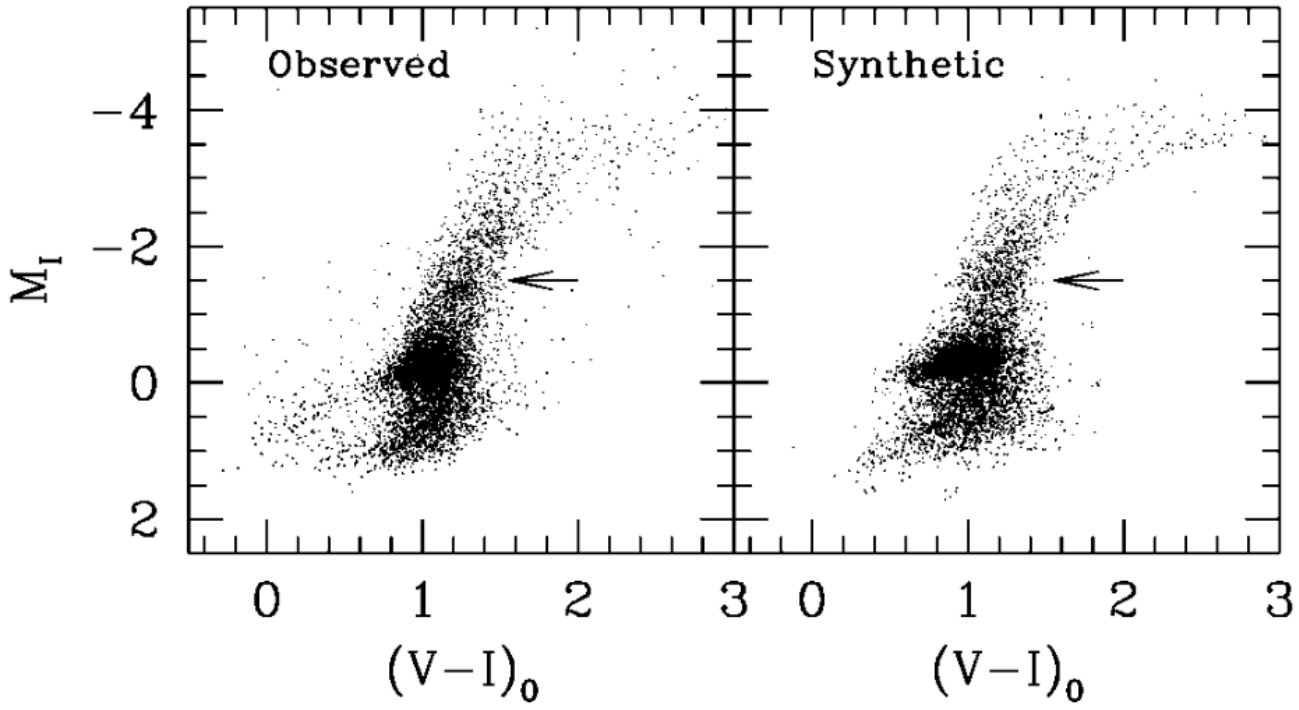

FIGURE 1.12: M31 halo field CMD (**left**) and the corresponding synthetic CMD (**right**). In this CMD, the magnitude in the I-band is represented as a function of the colour index V − I. The arrow indicates the AGBb location. Credit: Gallart (1998)

1.6.2 Goals of the thesis

Each of the topics approached in this section unveiled the potential of the seismic analysis of evolved red giants to constrain stellar models and open new prospects for other fields of astrophysics. Currently, such studies have been so far approached for low- and intermediate-luminosity red giants only, but need to be extended to high-luminosity red giants. As described in Sect. 1.6, the oscillation spectrum of evolved giants including high-luminosity RGB and AGB stars has been described through their global seismic parameters (Mosser et al., 2013b). Nevertheless, an individual analysis of oscillation modes of those stars still needs to be performed, particularly to study the mode damping and the second helium ionisation zone. In low- and intermediate-luminosity red giants, Vrard et al. (2018) identified a clear mass and temperature dependence of the radial ($\ell = 0$) mode damping and a clear distinction between H-shell burning stars and He-core burning stars. Our aim is to perform a similar analysis but for high-luminosity red giants, including RGB and AGB stars. On the other hand, the classification method illustrated in Fig. 1.9 is the most powerful to distinguish H-shell burning stars and He-core burning stars as it relies on modes that are able to probe the deepest stellar layers. However, the former is no longer applicable for evolved RGB and AGB stars since the seismic coupling between the core and the envelope is weaker, which makes the extraction of core properties out of reach. Still, other stellar identification methods are available for those evolved red giants. Vrard et al. (2015) have shown that the classification method proposed by Kallinger et al. (2012) and based on the radial mode pattern between RGB and clump stars in fact relies on a difference in the second helium ionisation zone. This suggests that RGB and AGB can be disentangled with the signature of the second helium ionisation in mode frequencies, but this needs to be confirmed. Accordingly, the first part of my thesis is dedicated to the seismic analysis of the evolved RGB and AGB stars. With a sample of thousands of stars observed by the *Kepler* telescope, we aim at extending the previous works to evolved RGB and AGB stars. We want to carry out an exhaustive characterisation of their oscillation spectrum to inspect the similarities and differences between those stars, and discuss the physical mechanisms on the line.

Such seismic analysis provides us new sets of constraints for stellar models. Stellar models are computed with the stellar evolution code MESA (Paxton et al., 2011; Paxton et al., 2013; Paxton et al., 2015; Paxton et al., 2018; Paxton et al., 2019) to make stellar models evolve from the pre-main sequence phase up to the luminosity tip of the AGB. Physical ingredients are updated in MESA such as mass loss on the RGB and AGB, convective core overshooting, and rotation. In parallel, we calculate the mode frequencies associated to MESA models with the stellar oscillation code ADIPLS (Christensen-Dalsgaard, 2008). This gives us the opportunity to compare seismic parameters from observations to those from models, and test the effects of the physical ingredients on stellar oscillations. Computing the p-mode frequencies near the luminosity tip of the RGB also allows us to test the relevance of the asymptotic framework ($n \gg \ell$), which is not expected to be valid for those low-frequency p-mode pulsators.

Finally, the study led by Bossini et al. (2015) opened new prospects for the AGBb to be a calibrator of mixing processes in the He-core burning phase. Nevertheless, they could not explore the mass and metallicity dependence of the AGBb occurrence due to the small number of stars simultaneously observed by *Kepler* and subject to a spectrometric study with available effective temperature and metallicity. This is important since theoretical models predict the AGBb luminosity to be sensitive to stellar parameters, as summarised in Sect. 1.6. With the increasing number of stars observed by TESS, we are now able to detect the AGBb in several bins of mass and metallicity. Subsequently, we intend to investigate the mass and metallicity dependence of the AGBb location in luminosity and effective temperature, and discuss the possibility of the AGBb to be a suitable standard candle. In possession of these AGBb locations, we would like to explore how the mass and metallicity dependences impact the calibration of the He-core overshooting, and quantify the uncertainty of this calibration regarding other physical ingredients. In a perspective view, the study of the AGBb brings valuable information for the study of stellar populations and Galaxy evolution. They will be discussed by way of opening.

Chapter 2

Evolution of low-mass stars ($M \leq 2.5 M_{\odot}$)

Studying stellar interiors of RGB and AGB stars obviously implies the understanding of physical mechanisms taking place during their respective branches. Nevertheless, those stars are the results of stellar evolution from the beginning of their formation, going through the main sequence up to their current state. They experienced many structure changes associated to nuclear reaction burning phases, core contraction and envelope expansion. Then, an accurate understanding of their interiors not only relies on the knowledge of the current physical mechanisms they experience, but also of the earlier steps they went through. Accordingly, this chapter is devoted to summarise the different steps stars undergo throughout their evolution up to the AGB. In the meantime, we introduce the physical ingredients of stellar models that play a role in the structure changes experienced by the star during its evolution. To this end, we illustrate stellar evolution with two different diagrams: the Hertzsprung-Russell diagram (HRD), which describes how the luminosity L and the effective temperature $T_{\rm eff}$ vary with stellar age (see Fig. 2.1), and the Kippenhahn diagram, which schematically shows the evolution of the internal structure with age.

2.1 Main sequence

2.1.1 Reaching the H-core burning phase

Stars are formed by the gravitational collapse of interstellar gas clouds. This collapse is caused by several mechanisms such as the passing of a shock wave produced by a supernova, or the collision with another interstellar gas cloud. Those perturbations create local overdensities, where the hydrodynamic stability breaks. Under the assumption of a spheroid isothermal ideal gas cloud, a fraction of this interstellar cloud collapses under gravitational instability if its mass exceeds the critical mass named the Jeans mass (Kippenhahn, Weigert, and Weiss, 2012)

$$M_{\rm J} = 1.1 M_{\odot} \left(\frac{T}{10\rm K}\right)^{3/2} \left(\frac{\rho}{10^{-19}\rm g.cm^{-3}}\right)^{-1/2} \left(\frac{\mu}{2.3}\right)^{-3/2}, \tag{2.1}$$

where μ is the mean molecular weight, i.e. the average number of atomic mass units per particle. The typical values in molecular clouds where stellar formation is active are $\rho = 10^{-19}$ g.cm^{-3}, $T = 10$ K, and $\mu = 2.3$. Once the collapse begins, the density increases and the Jeans mass decreases following Eq. 2.1. Eventually, local regions become more massive than the Jeans mass and local collapses begin. Then, the interstellar cloud breaks up to form several stars in a cluster.
A few steps after the fragmentation, the new born star is fully convective and reaches the pre-main sequence (PMS). Pre-main sequence stars evolve on a characteristic Kelvin-Helmoltz timescale $t_{\rm KH}$, which is the time necessary for a thermal fluctuation to propagate from the centre to the surface. It reads

$$t_{\rm KH} = \frac{|E_g|}{L} = \frac{GM^2}{RL}, \tag{2.2}$$

where E_g is the gravitational energy released by the star contraction. Next, the star adiabatically contracts and the density becomes high enough for the infrared radiations to be trapped in the central

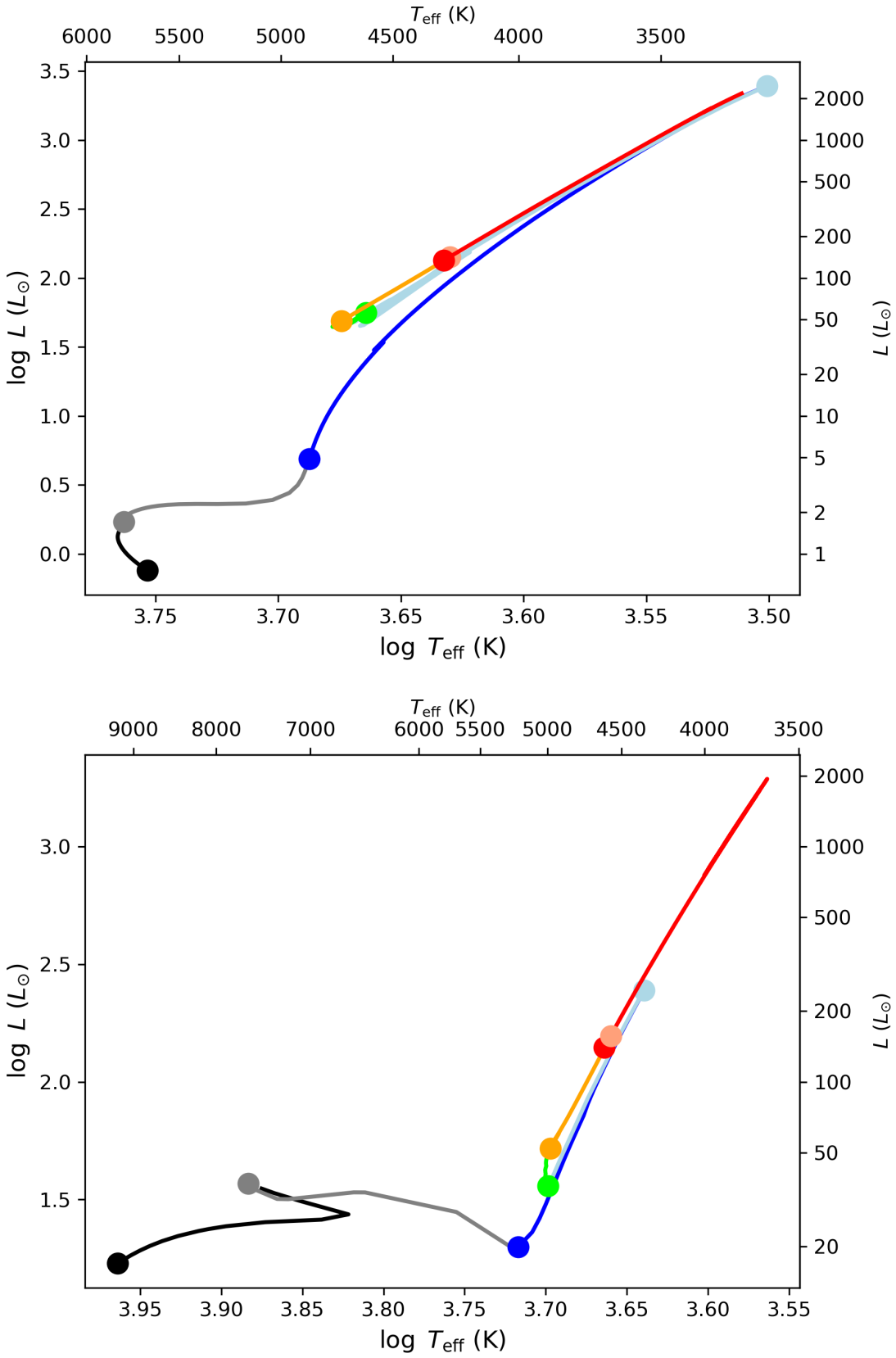

FIGURE 2.1: Evolutionary tracks of stellar models computed with MESA. **Top:** models of initial mass 1 $M_{\odot}$. **Bottom:** models of initial mass 2 $M_{\odot}$. Different evolutionary stages are colour-coded: the main sequence in black, the subgiant phase in grey, the RGB in blue, from the luminosity tip of the RGB up to the start of He-core burning in light blue, the He-core burning phase in green, from the end of the He-core burning phase up to the early AGBb in orange, and toward high-luminosity phases of the AGB in red. The thick dots correspond to the beginning of each evolutionary stage with the associated colour code. The light red thick dot marks the beginning of the AGBb.

layers: the star becomes opaque to its own radiations. In these conditions, the core temperature increases to such an extent that the radiative gradient $\nabla_{\rm rad}$ becomes lower than the adiabatic gradient $\nabla_{\rm ad}$. Consequently, central layers become convectively stable and a radiative core in hydrostatic equilibrium grows (Lamers and Levesque, 2017). Moreover, thermonuclear reactions are triggered when the core temperature reaches $\sim 10^6$ K, starting with deuterium burning. The initial carbon that was present in the interstellar cloud is consumed in an incomplete Carbon Nitrogen Oxygen (CNO) chain-reaction processing, releasing an important flux of energy and stopping the star contraction. When the temperature reaches $\sim 10^7$ K, the burning of hydrogen into helium starts and the star enters the main sequence.

2.1.2 During the main sequence

The hydrogen main sequence is a stable phase of H-core burning where the nuclear-chain reactions provide sufficient energy to the gas to counterbalance the gravitational collapse. The Zero Age Main-Sequence (ZAMS) is reached when the luminosity $L_{\rm nuc}$ generated by nuclear reactions is dominant compared to that released by the star contraction $L_{\rm g}$, typically when $L_{\rm g}/L_{\rm nuc} \leq 1\%$. Contrary to the core where nuclear reactions modify the composition, the composition of the envelope does not change except under the influence of mixing processes such as rotational mixing, overshooting, and atomic diffusion. In the following, we do not consider very low-mass stars ($M \leq 0.5\,M_\odot$) as these fully convective stars do not reach the helium burning phases (including the AGB phase).
For higher mass stars ($0.5\,M_\odot \leq M \leq 2.5\,M_\odot$), the hydrogen burning in the central layers makes the mean molecular weight μ increase and the structure evolve slowly. Namely, the radius and effective temperature weakly vary and the evolutionary track is almost stationary below the characteristic nuclear-reaction time for a star to burn 10% of its hydrogen supply (Maeder, 2009)

$$\tau_{\rm nuc} = \frac{E_{\rm nuc}}{L} = 0.1\frac{\eta M c^2}{L}, \tag{2.3}$$

where $E_{\rm nuc}$ is the energy released by nuclear-chain reactions, c is the light speed, and $\eta = 0.7\%$ represents the efficiency of energy production by the nuclear-chain reactions of hydrogen into helium relatively to the total rest energy. This is the timescale for the energy loss by radiation to be counterbalanced by the energy supplied by nuclear-chain reactions. Although stars spend most of their life in the MS, their lifetime on the MS strongly depends on the mass. For instance, the $1M_\odot$ model spends roughly 9.8 Gyrs in the MS while the $2M_\odot$ leaves the MS after 1.2 Gyrs since the hydrogen ignition (see Fig. 2.2).

Low-mass stars $M \leq 1.2M_\odot$

The convective core developed during the PMS vanishes due to the weak central temperature that prevents CNO nuclear-chain reactions from setting up. Accordingly, the energy is transported by photons in the core and the proton-proton (PP) nuclear-chain reactions are dominant. Eventually, these stars have a convective envelope and a radiative core, as illustrated in Fig. 2.2. In the envelope, the energy is transported by convection since the opacity is so high that chemical elements are partially ionised, which makes the radiative gradient higher than the adiabatic gradient and fulfils the convection instability criterion $\nabla_{\rm rad} > \nabla_{\rm ad}$. Given the absence of a mixing process (equivalently absence of convection), the core of low-mass stars are more heterogeneous while helium is produced through hydrogen burning.

Intermediate-mass stars $M \geq 1.2M_\odot$

The major part of the nuclear energy is no longer produced by the PP chain as the central temperature is higher than the threshold $T_{\rm PP-CNO} = 1.7\ 10^7$ K above which the CNO cycle dominantly produces energy. This nuclear energy is produced following the CNO cycle in the most central layers due to the intense sensitivity of the energy production rate with the central temperature $\varepsilon_{\rm nuc} \propto T_c^{16-20}$ (Maeder, 2009).

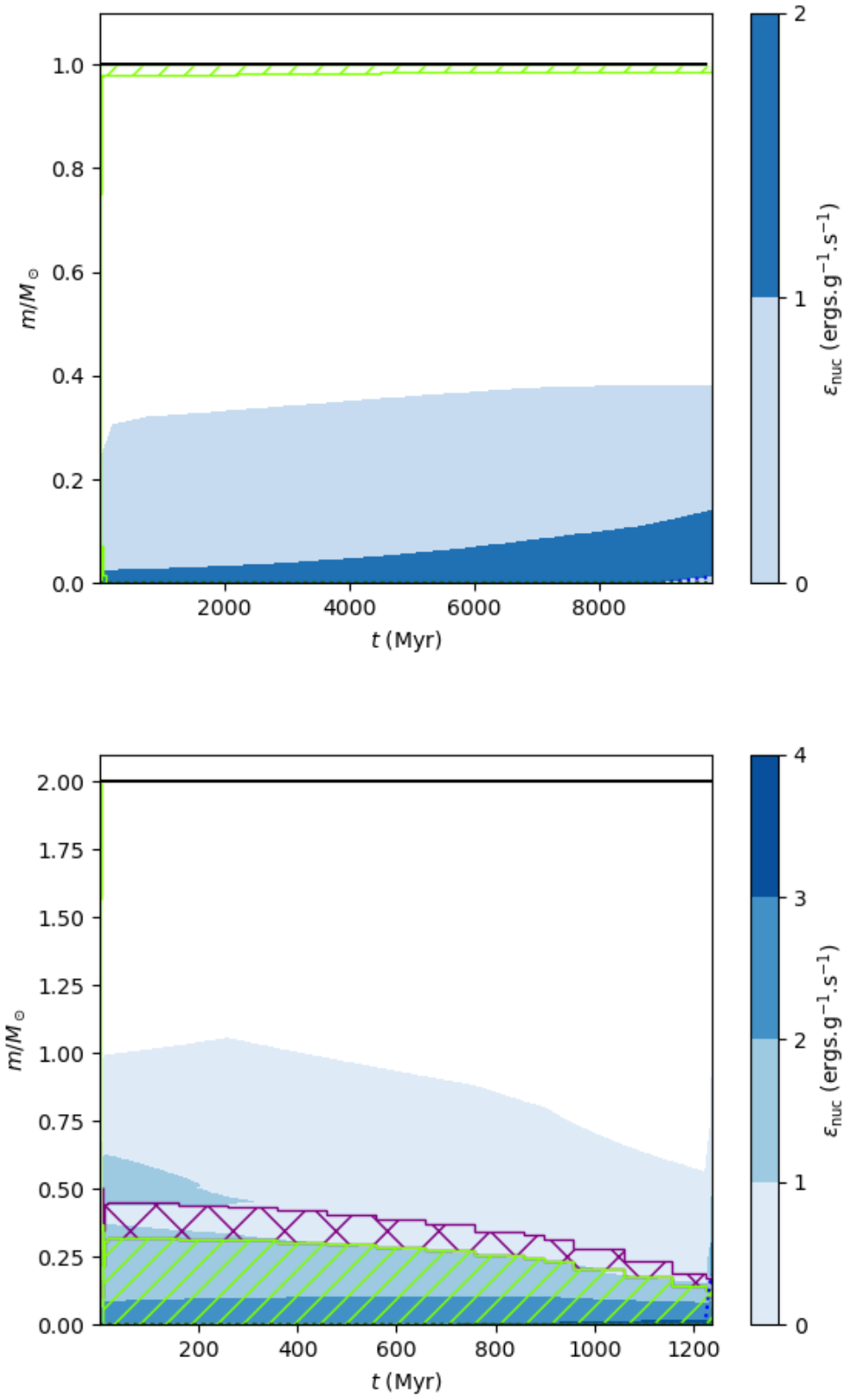

FIGURE 2.2: Kippenhahn diagrams representing the mass coordinate in star interiors ($m/M = 0$ is the centre and $m/M = 1$ is the surface) as a function of the stellar age. Both panels show the structure evolution during the main sequence for a $1\,M_{\odot}$ model (**top**) and a $2\,M_{\odot}$ model (**bottom**). The green-shaded area corresponds to convective zones while blank ones are radiative zones. The colorbar indicates the energy produced by nuclear reactions. An additional core-overshooting region above the convective core is present in the purple hatched area for the $2\,M_{\odot}$ star. The black solid line shows the stellar surface. These models are computed with the stellar evolution code MESA, as described in Chapter 6.

Consequently, the energy transport is efficient and the convective core continues to grow. Convection induces instantaneous mixing and homogenises the composition in the core, which causes a composition discontinuity between the convective core and the radiative envelope. Eventually, these intermediate-mass stars have a convective core, surrounded by a radiative zone and a convective envelope as illustrated in Fig. 2.2. At the end of the hydrogen burning phase, the central convective zone starts to vanish as the nuclear energy production rate gradually decreases.

On top of the spontaneous mixing in the core, extra mixing region can be induced in the radiative zone due to the momentum of the convecting materials that carries the material beyond the convective core. This additional mixing from the core into the envelope is named core overshooting (Kippenhahn, Weigert, and Weiss, 2012). Its extent is usually expressed in fraction of the pressure scale height $H_P = -(\mathrm{d}\log P/\mathrm{d}r)^{-1}$ evaluated at the boundary of convective instability in the core where the Schwarzschild condition $\nabla_{\rm rad} > \nabla_{\rm ad}$ is fulfilled. The amount of H-core overshooting $\alpha_{\rm ov,H}$ has been calibrated to reproduce observed properties of eclipsing binaries (*e.g.* Claret and Torres, 2016; Claret and Torres, 2017; Claret and Torres, 2018; Claret and Torres, 2019). Similarly, values of $\alpha_{\rm ov,H}$ lower than 0.2 have been derived from the calibration of $\ell = 1$ modes in low-mass stars by Deheuvels et al. (2016). Finally, recent theoretical predictions based on 3D numerical hydrodynamics simulations of penetrative convection also give $\alpha_{\rm ov,H} < 0.2$ for masses $M < 3\ M_\odot$ (Anders et al., 2022; Jermyn et al., 2022). It has been shown that the calibration of H-core overshooting depends on the stellar mass, as illustrated in Fig. 2.3. This mixing process has significant impact on the core mass as it brings additional hydrogen that can participate to nuclear reactions, then can increase the lifetime on the MS. In Chapter 10, we highlight that the physical ingredients taking place in the H-core burning phase also impact the structure of He-burning stars. Particularly, we investigate how H-core overshooting modifies the luminosity of clump and AGBb stars.

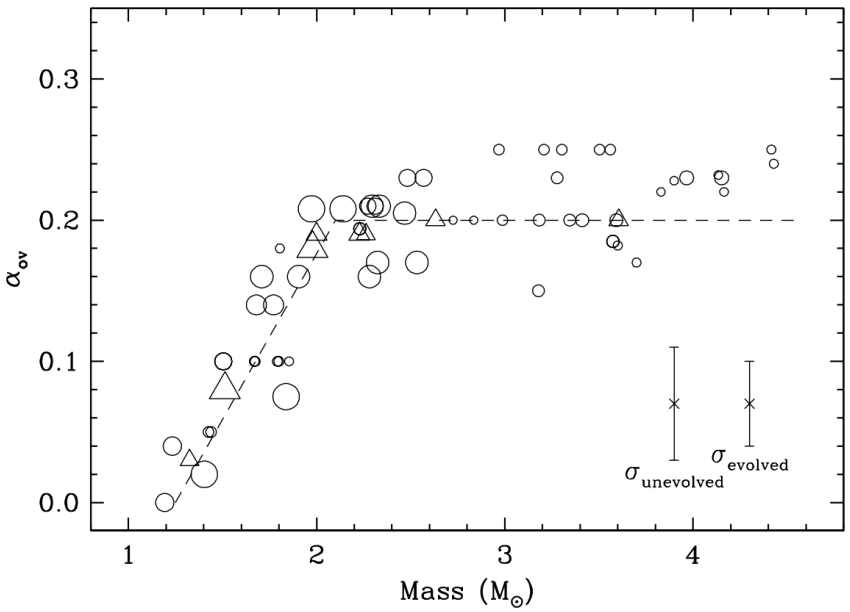

FIGURE 2.3: H-core overshooting distance in units of the pressure scale height H_P above the edge of the convective core as a function of the stellar mass M. The size of the points is proportional to the metallicity [Fe/H], which varies between -1.01 dex and +0.01 dex (metal-poor stars have smaller symbols). Typical error bars for dwarfs and giants are shown on the bottom right. Stars for which the inferred age difference between observations and models exceed 5% are represented by triangles. Credit: Claret and Torres (2016)

For both low-mass and intermediate-mass stars, the Terminal Age Main Sequence (TAMS) is reached when the central hydrogen mass fraction is lower than $X_c \approx 10^{-4}$. Namely, stars leave the main sequence when their central hydrogen supply through nuclear-chain reactions is not abundant enough

to counterbalance gravitation. Then, their envelope expands, their effective temperature $T_{\rm eff}$ decreases, and the hydrogen burning gradually takes place in a shell around the inert helium core. At this moment, they enter the Subgiant phase.

2.2 The subgiant phase

Because hydrogen is depleted in their core, subgiant stars can no longer generate nuclear energy in their cores. As a result, the layers where $T \geq 10^7$ K, which include the core and H-burning shell, contract and release gravitational energy. The H-burning shell plays a crucial role in the core and envelope dynamics as it acts like a mirror. In that sense, the region within the burning shell (i.e. the core) contracts while the region outside the shell (i.e. the envelope) expands. This observation supported by the results of numerical simulations is known as the mirror principle (*e.g.* Hekker et al., 2020). Although this mechanism is empirical, it can be approached in a simple way as follows. By considering that the Virial theorem[1] and the conservation of the total stellar energy are valid, both gravitational and thermal energy are conserved. Since most of the stellar mass is concentrated in the core, we can consider that $M_c \gg M_{\rm env}$, where M_c and $M_{\rm env}$ are the core and envelope masses, respectively. Then, the total gravitational energy E_g can be decomposed as the sum of the contribution of the core $E_{g,c}$ and that of the envelope $E_{g,{\rm env}}$. If we assumed that the binding energy of the envelope is dominated by the gravity of the core, we have

$$\left|E_g\right| = \left|E_{g,c} + E_{g,{\rm env}}\right| \approx \frac{GM_c^2}{R_c} + \frac{GM_c M_{\rm env}}{R}, \tag{2.4}$$

where R_c is the core radius and R is the stellar radius. Finally, under the assumption that the masses M_c and $M_{\rm env}$ remain constant but the radii R_c and R vary with time, it yields

$$\frac{{\rm d}R}{{\rm d}R_c} = -\left(\frac{M_c}{M_{\rm env}}\right)\left(\frac{R}{R_c}\right)^2. \tag{2.5}$$

From Eq. 2.5, the core contraction leads to the envelope dilatation. As a consequence, the stellar radius increases and the boundary between the convective envelope and radiative core sinks in the deep layers. The H^- ions contribute to increase the opacity and the convective envelope develops. Despite these important structure changes, the stellar luminosity remains constant as the effective temperature decrease is counterbalanced by the radius increase (see Fig. 2.1).

At this stage, subgiant stars have an isothermal core, surrounded by an hydrogen-burning shell (see Fig. 2.4). The ashes of hydrogen-shell burning are deposited on the helium inert core, then the core mass increases (Catelan, 2007). Nevertheless, there is a maximum relative core mass that an isothermal and non-degenerate core can have. Indeed, the core mass cannot indefinitely increase while maintaining hydrostatic and thermal equilibrium when the star derives all its energy from a nuclear shell burning source. This threshold is called the Schönberg-Chandrasekhar limit and reads (Schönberg and Chandrasekhar, 1942)

$$\frac{M_c}{M} = 0.37\left(\frac{\mu_{\rm env}}{\mu_c}\right)^2, \tag{2.6}$$

where $\mu_{\rm env}$ is the mean molecular weight in the envelope. For instance, this limit is $M_c \sim 0.08M$ for a pure helium core surrounded by an envelope with solar-like abundances. Without additional pressure support such as electron degeneracy to counterbalance gravitation, contraction takes place on a Kelvin-Helmoltz timescale once the core mass exceeds this Schönberg-Chandrasekhar limit. Such a restructuring is necessary for the star to maintain equilibrium between energy generation and losses at the surface. Given the short timescales, stars do not spend a lot of time in this evolutionary phase. As

[1] In a system dominated by gravitation, $\langle E_g \rangle + 2\langle E_c \rangle = 0$, where E_c and E_g are the total thermal energy and gravitational energy of the star, respectively.

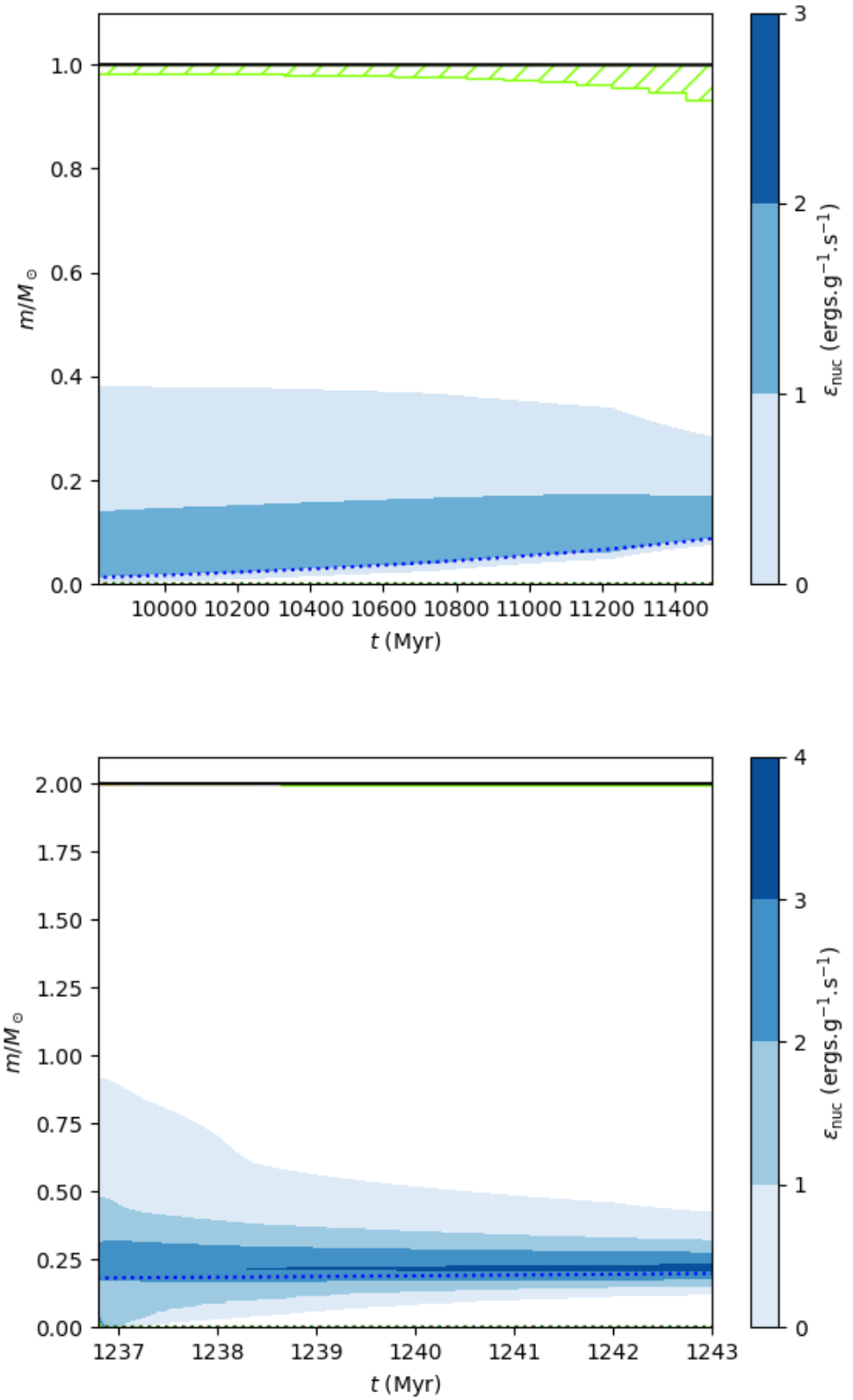

FIGURE 2.4: Same label as in Fig. 2.2, but during the subgiant phase for a $1M_{\odot}$ model (**top**) and a $2M_{\odot}$ model (**bottom**). The dotted blue line locates the H-burning shell.

a result, this region of the HR diagram is devoid of stars, and referred to as the Hertzsprung gap. The envelope continues expanding and cooling until the star reaches the Hayashi line, which is the location in the HR diagram where fully convective stars cannot decrease their temperature further otherwise they cannot maintain hydrostatic equilibrium. The position of the Hayashi line mainly depends on the stellar mass and chemical composition. Once subgiants reach the Hayashi line, their envelope continues to expand while their effective temperature hardly decreases. The star is now on the Red-Giant Branch, with a large convection envelope on top of a small radiative core.

2.3 The ascent on the Red-Giant Branch

In alignment with the subgiant phase, the mirror principle continues to apply on the RGB because of the H-burning shell. While the RGB star evolves alongside the Hayashi line, the base of the convective zone still sinks towards deep interiors. The core contracts, which leads to a core temperature increase. Meanwhile, the envelope dilates, the radius significantly increases and the envelope temperature slowly decreases without passing the limit fixed by the Hayashi line (Fig. 2.1). Then, the convective envelope represents a major part in the star. Given the proximity of the core, the hydrogen burning shell is carried at sufficiently high temperature so that the hydrogen dominantly burns following the CNO cycle. While ascending the RGB, the hydrogen burning shell becomes thinner as hydrogen is gradually transformed into helium through nuclear reactions (see Fig. 2.5). Again, the way stars ascent the RGB noticeably depends on the stellar mass as the core and envelope properties differ.

Mass lower than $M \leq 2M_\odot$

The core of low-mass stars is sufficiently cool and dense so that the electron degeneracy is important (Kippenhahn, Weigert, and Weiss, 2012). The latter can be so high that the main source to oppose gravitation is the electron degeneracy pressure. This pressure results from the Pauli exclusion principle stating that two identical fermions cannot simultaneously occupy the same quantum state. As a result, the electrons occupy different quantum states associated to the lowest accessible energy levels, defining the minimal total energy the electron gas in the core can have. Then, the electron gas cannot reorganise itself and the latter efficiently opposes the effect of gravitational collapse. Nevertheless, this only concerns the innermost parts of the core and the superficial layers of the core continue to contract. Consequently, the pressure in the central parts of the core only varies with the density since the equation of state is that of a degenerate electron gas. The former is no longer linked to the temperature, so the temperature is no longer self-regulated as the core evolves. Owing to the core contraction and the efficient energy transport by electronic conduction, the core temperature increases and the temperature gradient is weak. The core is therefore isothermal. The density contrast between the degenerate core and the envelope is so large that the envelope has very limited influence on the core properties. The properties of the hydrogen burning shell are then determined by those of the inert helium core. Being the main source of energy produced in the star, the luminosity provided by the hydrogen burning shell depends on the core mass and radius as follows (Refsdal and Weigert, 1970; Kippenhahn, Weigert, and Weiss, 2012)

$$L \propto M_c^7 R_c^{-16/3}. \tag{2.7}$$

All in all, the ascent on the RGB is gently achieved in hydrostatic and thermal equilibrium.

Mass higher than $M \geq 2M_\odot$

Similarly to their low-mass counterparts, stars of mass $M \geq 2M_\odot$ develop a deep convective envelope, which prevents the star from cooling beyond the Hayashi line. In the same time, core and envelope are still coupled. The core contracts and heats, the envelope dilates and cools. Contrary to their low-mass counterparts, the core of high-mass stars is not degenerate and the evolution on the RGB is faster. In that sense, the core temperature reaches more rapidly the ignition temperature of helium ($\sim 10^8$ K). So the

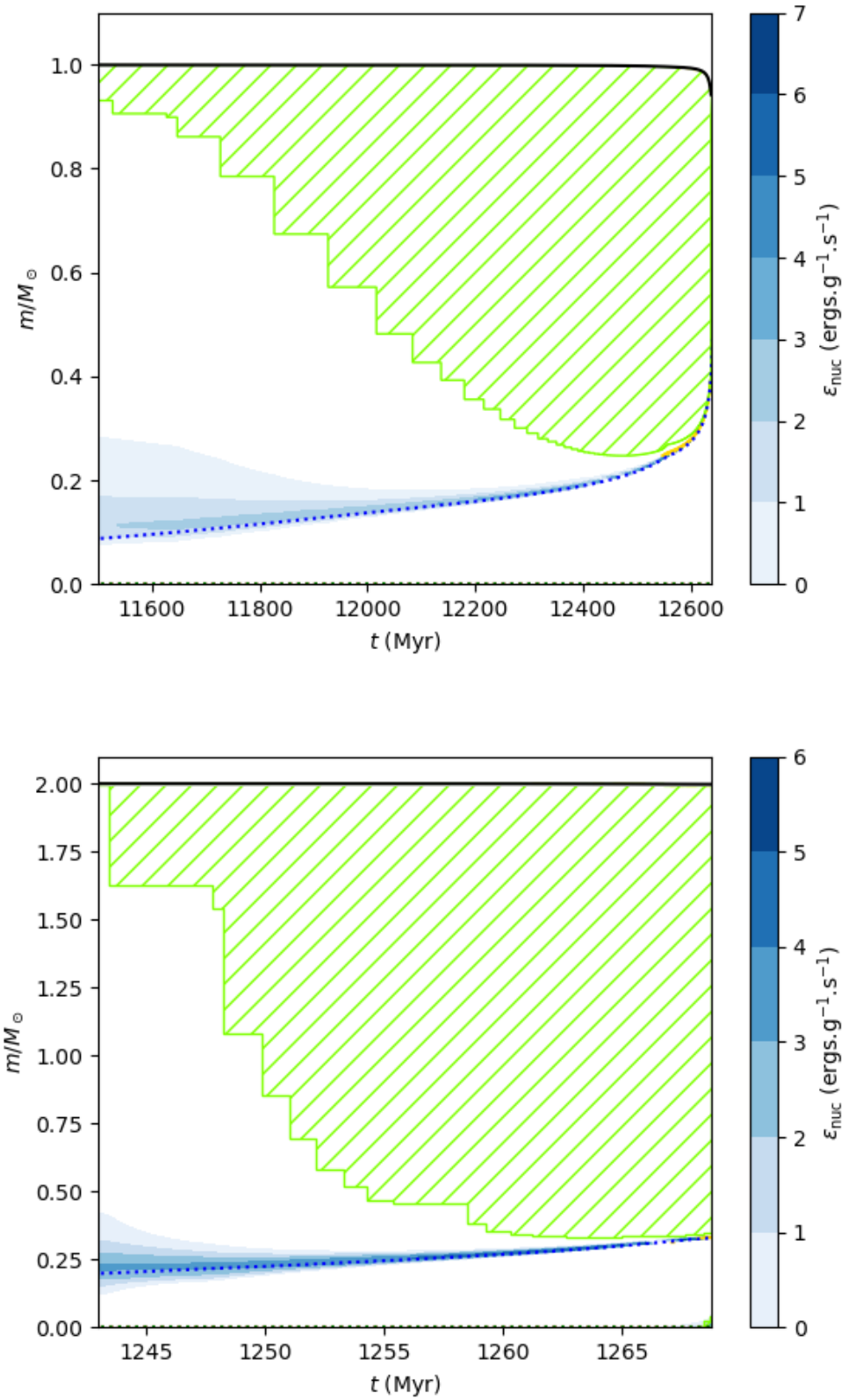

FIGURE 2.5: Same label as in Fig. 2.2, but during the RGB phase for a $1M_{\odot}$ model (**top**) and a $2M_{\odot}$ model (**bottom**).

star does not experience key events such as the Red-Giant Branch bump that highly impact the structure evolution and the composition of the envelope (further details are given in Sect. 2.3.2). Since the core is not degenerate, the core pressure and temperature are related through the ideal gas equation of state, which guarantees the self-regulation of the temperature and the helium gently ignites in the core.

2.3.1 The first dredge-up

While the base of the convective zone keeps moving towards the deep interior in an environment made of the same composition as the stellar surface, there is a point where the former reaches helium-rich regions that have been subject to nuclear reactions during the main sequence. Then, convection efficiently brings materials produced by nuclear reactions. The initial surface composition is mixed with chemicals produced by the hydrogen burning, which marks the first dredge-up event (Kippenhahn, Weigert, and Weiss, 2012). This event affects the element abundances of the stellar surface, essentially those of C, N, Li, and He. Both abundances of N and He elements increase, but those of C and Li decrease. This is caused by the mixing of the envelope composition with inner layers where the CN-cycle produced N elements but consumed C and Li elements. The study of these compositions along evolution is meaningful as they can be used as an age indicator and track the chemical properties of stars across different Galactic stellar populations, particularly the ratio [C/N] (Salaris et al., 2015; Lagarde et al., 2017). The first dredge-up also marks the maximum inward penetration of the convective envelope, which begins to retreat because of the rising of the hydrogen burning shell to upper layers. This leaves a chemical discontinuity between the fully mixed envelope and the helium-rich regions formed by nuclear reactions.

2.3.2 The Red-Giant Branch bump (RGBb)

The H-burning shell continues to progress outward in mass, making the size of the inert helium core grow. At some point, the former encounters the chemical discontinuity left by the maximum inward penetration of the convective envelope during the first dredge-up (*e.g.* Iben, 1968). Namely, the H-burning shell switches from a region where H is already being consumed to a region that presents an extra H supply coming from the stellar envelope, making the mean molecular weight decrease in that shell. This event has crucial impacts on the structure as it suddenly readjusts to this new environment. The whole stellar structure is affected as it evolves in the reversed direction that it used to since the beginning of the ascent on the RGB. The core swells and cools, the envelope contracts and heats up. As a results, it causes a temporary drop in luminosity as a star evolves on the RGB. This event announces the beginning of the RGBb (Catelan, 2007). Once the excess of hydrogen brought by the envelope is burnt, the star goes back to its ascent on the RGB as it was before the RGBb, with a contracting core and an expanding envelope. Stars that experience the RGBb spend additional time in the evolutionary track as they cross three times the luminosity bin where the RGBb occurs. This produces an excess of stars in that specific luminosity bin, which can be detected in the observed CMD of stellar populations (King, Da Costa, and Demarque, 1985). The RGBb could be identified in stellar clusters that include low- and intermediate-mass stars with a maximum mass roughly about $M \leq 2.2 M_{\odot}$. Higher-mass stars with $M \geq 2.2 M_{\odot}$ burn their helium in the core before the H-burning shell could reach the composition discontinuity left by the first dredge-up, which explains the absence of such a luminosity drop in stellar models and the associated excess of stars in observations.

The specific conditions for the RGBb to occur essentially depend on the precise abundance profile in the H-burning shell. As illustrated in Fig. 2.6, the adding of diffusive processes changes the profile of the RGBb and the location in luminosity at which the RGBb occurs. In this respect, it offers the possibility to calibrate mixing processes such as envelope overshooting for stellar populations with different masses and metallicities, as could be done with *Kepler* observations (Khan et al., 2018). The sensitivity of the RGBb to diffusive processes is related to the strong change of the mean molecular weight μ at the chemical discontinuity left by the base of the convective zone during the first dredge-up, and to the dependence of the H-burning on μ. Strong discontinuity profiles significantly affect H-burning efficiency, then the surface luminosity. To sum up, the RGBb is a key observable to investigate the chemical profile in star interiors, and a powerful diagnostic of the maximum depth reached by the

base of the convective zone during the first dredge-up. In Chapter 10, we emphasise that the calibration of envelope overshooting by the RGBb does not impact the AGBb luminosity.

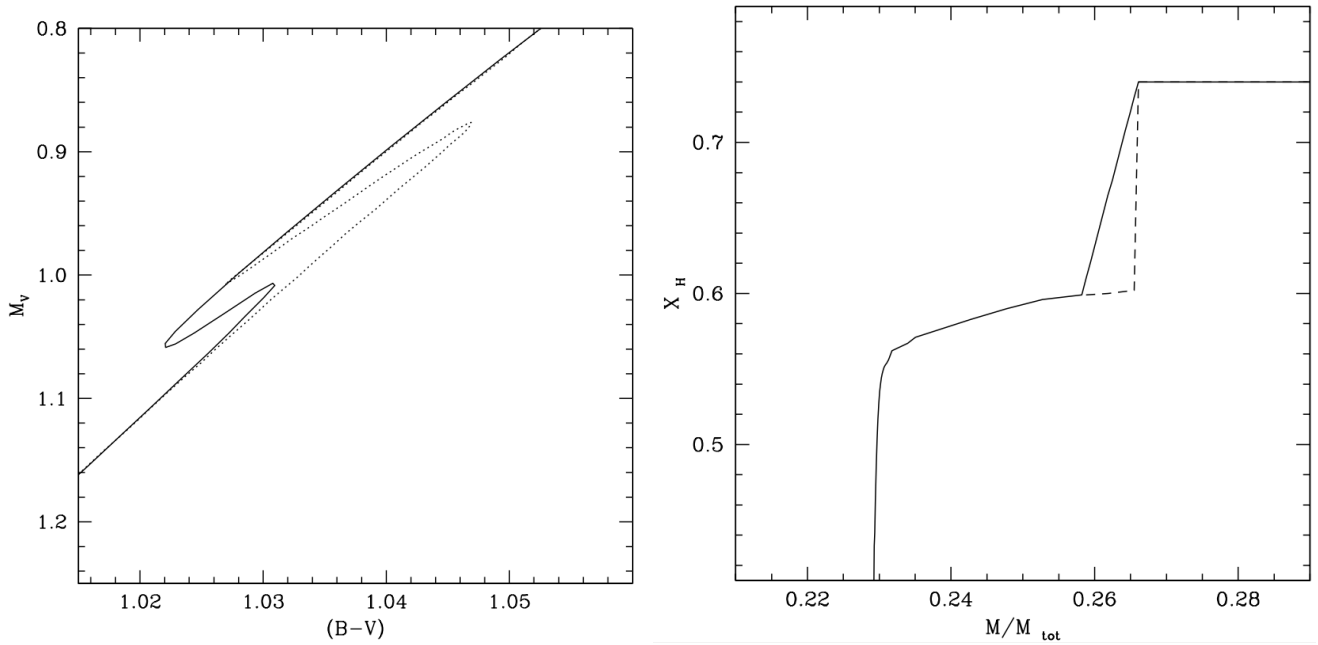

FIGURE 2.6: Left: Evolutionary track in the CMD at the RGBb phase. The dashed line refers to a standard model ($M/M_\odot = 1.0$, $Y = 0.23$, $Z = 0.006$) that does not include diffusive processes at the H-discontinuity (neither atomic diffusion nor envelope overshooting). The solid line refers to models computed with the same input parameters but the H-discontinuity is smoothed out over a region of 0.5 H_p, where H_p is the pressure scale height. Right: Hydrogen abundance profile (in mass fraction) as a function of the stellar mass fraction around the lower edge of the convective zone at its maximum extent for both models (same label). Credit: Cassisi, Salaris, and Bono (2002)

2.3.3 Thermohaline instability

Not only the first dredge-up but also other mixing processes govern the photospheric chemical composition by bringing materials produced in the deep interiors to the surface. Among them, the thermohaline instability significantly modifies the surface composition of red giants after the first dredge-up when they pass the RGBb (Charbonnel and Zahn, 2007). Thermohaline convection develops in regions that are stable against convection (according to the Ledoux criterion) and where the molecular weight gradient becomes negative, *i.e.* when $\nabla_\mu = \mathrm{d}\ln\mu/\mathrm{d}\ln P < 0$ (Ulrich, 1972). The thermohaline mixing effects are noticeable notably after the first dredge-up as a molecular weight inversion is created by the reaction ^{3}He(^{3}He,2p)^{4}He in the external wing of the H-burning shell when the latter enters the chemically homogeneous part of the envelope (see Fig. 2.7). This mixing process affects the surface composition only if the additional mixing region induced by thermohaline convection connects the H-burning shell and the convective envelope. Otherwise thermohaline instability is not efficient. This condition is fulfilled during the He-core burning phase for low-mass stars ($M \leq 1.5M_\odot$), but it does not happen for higher-mass stars ($M > 1.5M_\odot$) because of the lower ^{3}He abundance that results in a smaller μ-inversion then a slower thermohaline mixing (Cantiello and Langer, 2010). When the additional mixing region connects the H-burning shell to the stellar surface, the latter undergoes a decrease of ^{3}He, the chemical elements ^{13}C and ^{14}N diffuse outwards while ^{12}C diffuse inwards, hence the ratio [C/N] decreases (Charbonnel and Lagarde, 2010). As a result, thermohaline instability has non negligible effect on the surface composition, but marginally shifts the clump and AGBb location (see Chapter 10).

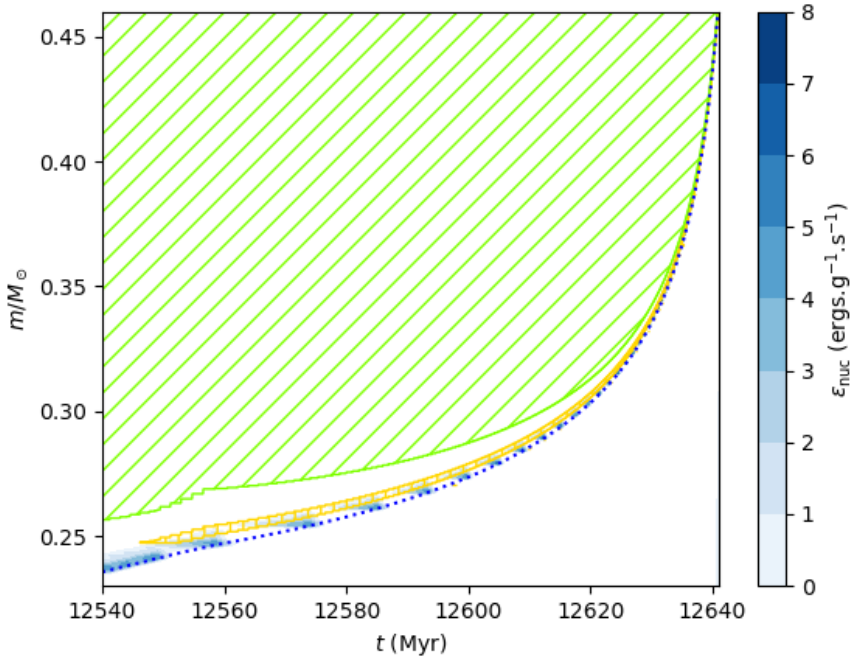

FIGURE 2.7: Zoom-in portion of the left panel of Fig. 2.5 during the RGB, when thermohaline mixing is present in the $1 M_{\odot}$ model. The dotted blue line locates the H-burning shell. The orange hatched area correspond to the thermohaline mixing.

2.3.4 High-luminosity RGB stars

After all these episodic phases at intermediate luminosity, stars continue their ascent on the RGB while their core contracts and their envelope dilates. Accordingly, the radius increases, as does the luminosity, up to the point where the surface gravity becomes weak (see Fig. 2.1). In Chapters 6−10, we perform a full seismic analysis of those stars that reached high-luminosity stages on the RGB and beyond, including He-core and He-shell burning phases. We study their oscillation mode pattern in order to learn more about the origin of mode damping in those stars and the behaviour of the He-second ionisation zone with stellar evolution. For those high-luminosity RGB stars, the envelope is weakly bound to the star. As a consequence, the star loses mass due to the radiative pressure exerced by the photon flux, pushing the envelope outwards. Mass loss is an essential parameter for the understanding of stellar evolution as it induces restructuring of the star interiors. More importantly, it directly affects the fate of stars as their mass is the main parameter that determines the evolutionary track they follow all along their evolution. Presently, the physical mechanisms behind mass loss are not fully understood, so theoretical models suffer from this lack of knowledge. Most of the information we have come from observational constraints, which allow us to calibrate empirical relations to quantify the mass loss in RGB models. RGB mass-loss is generally parameterised by simple relations. One of the most commonly used is that of Reimers (1975), which is based on Population I giants. It reads

$$\dot{M}_R = -4 \times 10^{-13}\, \eta_R \frac{L}{L_{\odot}} \frac{R}{R_{\odot}} \left(\frac{M}{M_{\odot}} \right)^{-1} M_{\odot}.\mathrm{yr}^{-1} \tag{2.8}$$

where η_R is a scaling factor that determines the mass loss efficiency on the RGB. Typical integrated mass loss estimates in old-open clusters NGC 6791, NGC 6819 and M67 suggest a Reimers parameter $\eta_R \leq 0.25$ (Miglio et al., 2012; Stello et al., 2016b; Handberg et al., 2017; Miglio et al., 2021a). From Eq. 2.8, it is clear that mass loss is important at the luminosity tip of the RGB, where the luminosity and radius are maximum (see the evolution of the surface limit in Fig. 2.5). We also notice that the lower the mass, the higher the mass loss. With this mass dependence, we would expect to find very

low-mass stars in the He-core burning phase that suffered strong mass loss at the RGB tip. This is in agreement with observations that report stars having a mass $M = 0.6 - 0.7 M_{\odot}$ at this stage. Indeed, stars with initial mass $M = 0.6\, M_{\odot}$ do not reach the clump phase since the core temperature does not attain the temperature threshold for He burning. Then, He-core burning stars of mass $M = 0.6 - 0.7 M_{\odot}$ necessarily are stars whose initial mass is larger than their current mass but suffered high mass loss. Notwithstanding the mass loss they endure, RGB stars are getting closer to the luminosity tip, where the central temperature attains the ignition threshold of helium and marks the beginning of helium burning phases.

2.4 All the way through the He-core burning phase

2.4.1 From the RGB tip to the He-core burning phase

Once the core temperature is close to 10^8 K, helium starts to burn in a triple-α process, which consists in consuming 3 atoms of ^{4}He and 2 atoms of ^{8}Be to form an atom of ^{12}C. However, this nuclear-chain reaction cannot be fully completed since ^{8}Be is an unstable element that fast decays into 2 atoms of ^{4}He (with a half-life on the order of 8.19 10^{-17} seconds). For the triple-α nuclear-chain reaction to be complete, the temperature must be high enough to maintain a sufficient supply of ^{8}Be. The energy released by nuclear reactions is too weak to yield major structure changes and the star continues getting closer to the RGB tip. Eventually, once at the RGB tip the core temperature reaches 10^8 K and allows a large number of ^{8}Be to be present. Again, two scenarios are possible depending on the stellar mass.

Mass lower than $M \leq 2M_{\odot}$

The full triple-α nuclear-chain reaction can now be completed. However, at this stage the helium burning takes place in a degenerate core, where the pressure is not related to the temperature. The helium burning releases energy that leads to a temperature increase. Consequently, the latter cannot be regulated via a potential pressure increase that would make the core expand, that would lead to a cooling. The temperature cannot stop increasing and a thermal runaway process is created for a short time where the helium burns in unstable conditions (Catelan, 2007). This is the helium flash, which starts when the core mass is $M_c \simeq 0.45 - 0.47\, M_{\odot}$ in degenerate conditions, regardless the stellar mass (Sweigart and Gross, 1978).
Because of energy loss caused by neutrino emissions in the innermost layers near the RGB tip, the central temperature does not reach the threshold of helium burning and nuclear reactions do not take place in the centre of the star (Kippenhahn, Weigert, and Weiss, 2012). They develop in a shell where the core degeneracy is partially lift. In those regions, the pressure becomes again related to the temperature and the nuclear energy production now leads to the expansion and the cooling of the core, hence a decrease of energy production: the temperature evolution is now regulated. Next, the temperature gradually increases towards the centre, and the core degeneracy is completely lifted. This temperature increase may be caused by follow-up subflashes (Fig. 2.8), but they have not been confirmed by observations. Nevertheless, few *Kepler* targets have been suspected to be in the He-flash stage (Mosser et al., 2014), and about 30 He-flash stars are expected to be present in the sample of $\sim$ 6,000 stars studied by Vrard, Mosser, and Samadi (2016) according to theoretical predictions (Deheuvels and Belkacem, 2018). In this thesis, we do not focus on these stars, but they will be part of an exhaustive study by extending the methods developed in Chapter 7. Finally, the helium burning settles in the whole stellar core, which expands in response of the additional heat brought by nuclear reactions. By the mirror principle, the envelope contracts and cools, with a remarkable luminosity decrease. Given the strong restructuring the star undergoes, the evolutionary track is not as smooth as it has ever been.

Mass higher than $M \geq 2M_{\odot}$

The ignition of helium is by far smoother for high mass stars as is reflected by the continuous evolutionary track (Fig. 2.1). The stellar core is not degenerate, so the nuclear reactions are stable. The energy

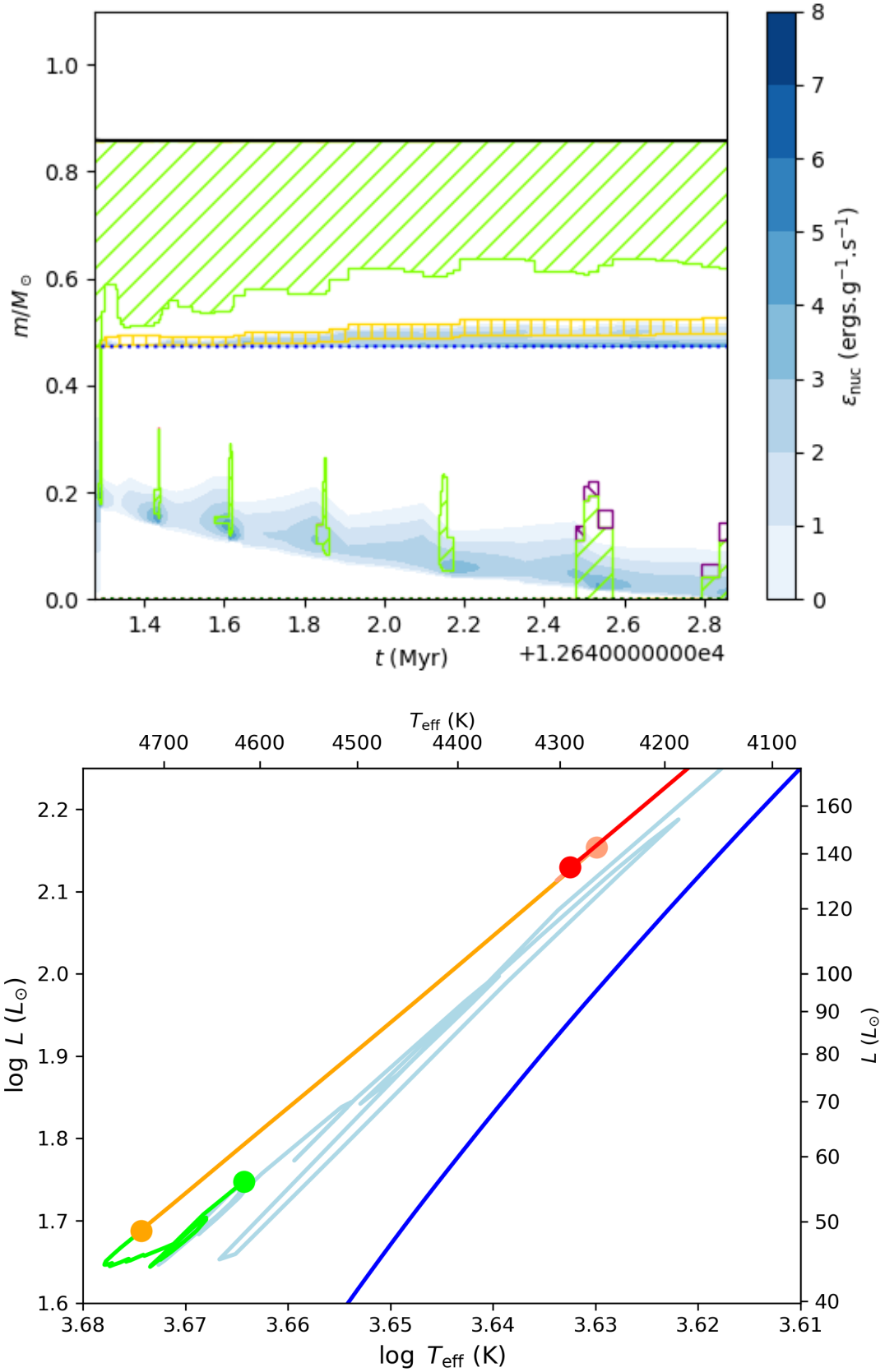

FIGURE 2.8: **Top:** same label as in Fig. 2.2, but during the He-flash phase for a $1 M_{\odot}$ model. The dotted blue line locates the H-burning shell. The orange and purple hatched area correspond to the thermohaline mixing and He-core overshooting regions, respectively. **Bottom:** zoom-in portion in the He-burning phases of the evolutionary track with initial mass 1 $M_{\odot}$ (left panel of Fig. 2.1). The numerous light blue turning-backs are associated to the He subflashes.

released by nuclear reactions is followed by an expansion of the core, and a contraction of the envelope by the mirror principle. No thermal runaway process occurs and helium is gently burnt in the whole core.

2.4.2 The He-core burning phase

While He-core burning settles, the H-burning shell shifts outwards as the core expands. Therefore, the temperature and density in the shell decreases and less energy is generated. Nevertheless, the H burning shell remains the main source of energy generation in the star, and participates to the star restructuring. Once the helium burning takes place in stable conditions in the core, the star enters the clump phase.

Mass lower than $M \leq 2M_{\odot}$

For these stars, helium burning started in degenerate conditions, where the pressure and temperature are independent. Consequently, the physical conditions in which helium is ignited regardless the stellar mass are quite similar in degenerate conditions (when the core mass is $M_c \simeq 0.45 - 0.47\,M_{\odot}$). Those stars evolve towards a specific region in the HR diagram, called the Red Clump (RC) or equivalently the Horizontal Branch (HB). The latter manifests as an overdensity of stars at fixed luminosity that is clearly identifiable in the CMD, and can be used to constrain stellar models. However, the amount of mass lost during the ascent of the RGB tip depends on the stellar mass (see Eq. 2.8), which implies that low-mass stars suffer a stronger mass loss than their high-mass counterparts. As a result, low-mass stars have the same luminosity, but smaller radius and higher effective temperature than high-mass stars The former are shifted toward high effective temperature, which justifies the designation horizontal branch.

Mass higher than $M \geq 2M_{\odot}$

These stars did not ignite helium in degenerate conditions, meaning that pressure and temperature are related. As the core properties can be different depending on the stellar mass at helium ignition, high-mass stars do not get in the same group as red-clump stars. Instead, they form another group of stars at lower luminosities and effective temperature, designated as secondary clump (Girardi, 1999).

For both stellar populations, the He-core burning is performed in conditions of thermal and hydrodynamical equilibrium, which induces minor structure changes and makes the evolutionary track smooth as depicted by Fig. 2.9) (Lamers and Levesque, 2017). At this stage, there are two main sources of energy: the H-shell burning and the He-core burning (see Fig. 2.9). Due to the core expansion, the hydrogen burning shell is expelled outwards.
Stars spend less time in the clump phase than in the stable H-core burning phase. Indeed, the lifetime of stars on the clump phase relies on the central helium supply to burn and the characteristic timescale for the star to evolve on the clump phase is that of the nuclear timescale given in Eq. 2.3. He-core burning stars have higher luminosities than H-core burning stars, so their evolution is shorter. Stellar models indicate that the evolution speed before and after the clump phase is faster for low-mass stars, as suggested by Eq. 2.3. We have confirmed it in *Kepler* observations, where a clear depletion of low-mass stars is present between the He-core and He-shell burning phases (Dréau et al., 2021). This is discussed in Chapter 10.

The energy production rate of helium burning is highly sensitive to the temperature, then the main source of nuclear energy is located in the innermost layers where the temperature is maximum. The opacity is dominated by free-free interactions, i.e. free electrons both before and after the interactions with ions, and increases as the core enhances its C and O reservoirs. This opacity increase makes the radiative gradient larger in the core, which finally gives rise to a convective core (see Fig. 2.9) as the region is no longer convectively stable following the Schwarzschild criterion (Kippenhahn, Weigert, and Weiss, 2012). Similarly, as in the H-core burning phase, extra mixing processes are induced by the convecting materials from the convective core into the radiative envelope. This phenomenon is referred to as He-core overshooting and its extent is usually expressed in units of pressure scale height

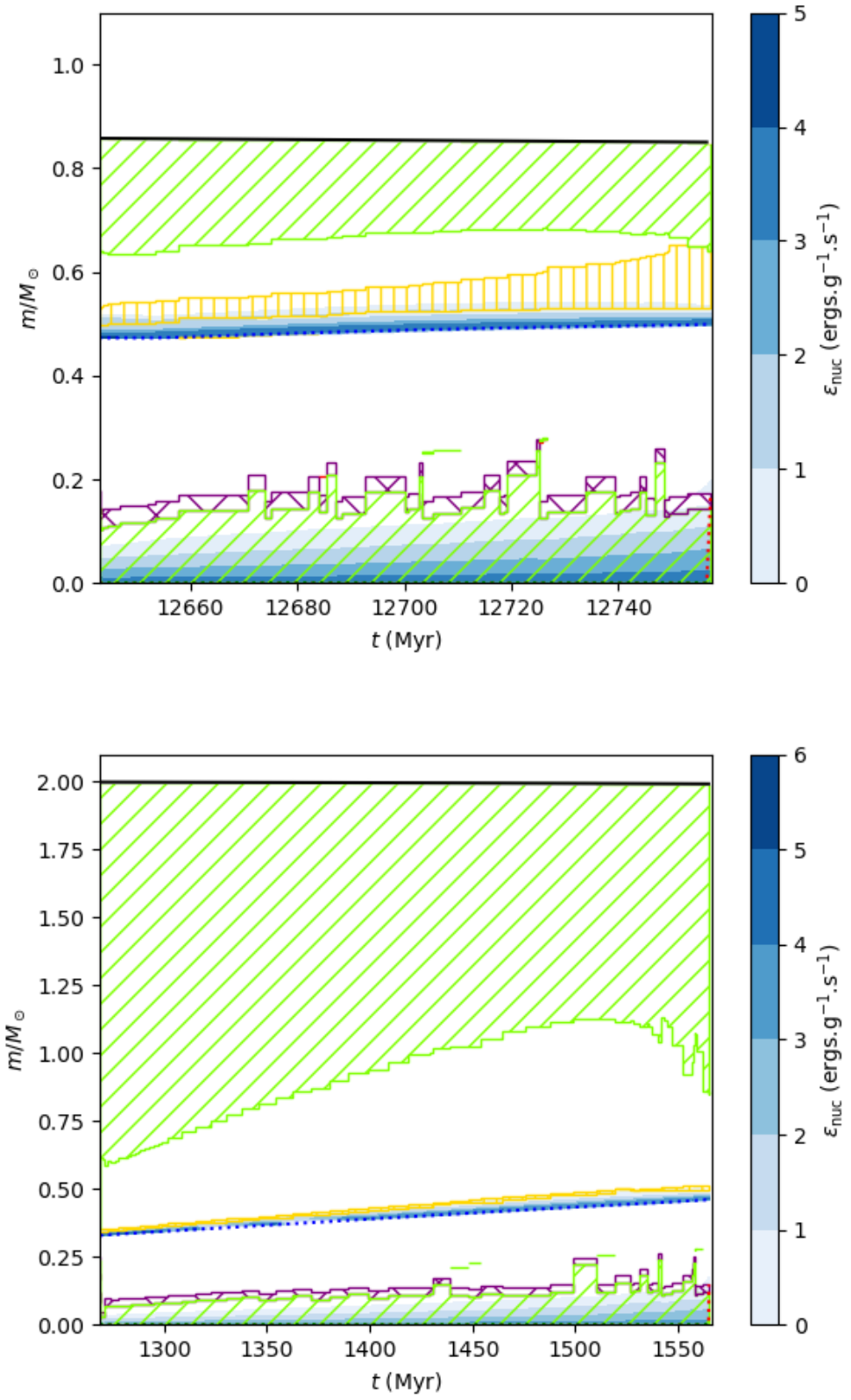

FIGURE 2.9: Same label as in Fig. 2.2, but during the He-core burning phase for a $1 M_{\odot}$ model (**top**) and a $2 M_{\odot}$ model (**bottom**). The dotted blue line locates the H-burning shell. The orange and purple hatched areas correspond to the thermohaline mixing and He-core overshooting regions, respectively. In the presence of a He-core overshooting, an incomplete treatment of the He-semiconvection may induce artificial small convection layers above the convective core, as we can see in these figures. These physical effects are discussed in Chapter 6.

$H_P = -(\mathrm{d}\log P/\mathrm{d}r)^{-1}$ (isothermal atmosphere scenario) at the boundary between the convective part and the radiative part. The efficiency of this overshooting can be calibrated with specific events of stellar evolution that occurs during He burning phases such as the AGB bump (Bossini et al., 2015). In Chapter 10, we show that this calibration by the AGBb depends on the stellar mass and metallicity, and the He-core overshooting alone cannot reproduce the observations at high mass $M \geq 1.5\,M_{\odot}$. Additional mixing may be caused by the presence of a gradient of mean molecular weight in convectively unstable regions according to the Schwarzschild criterion. These semi-convection regions are typically created by the advance of the shell sources or by the presence of He-core overshooting during the clump phase (e.g. Castellani, Giannone, and Renzini, 1971a; Robertson and Faulkner, 1972; Sweigart and Gross, 1973; Salaris and Cassisi, 2017). Since a molecular weight gradient tends to slow down convection, these unstable regions are slowly mixed, which leads to a readjustment of the chemical composition by moving light elements downward and heavy elements upward.

The end of the clump phase is attained when the nuclear production rate is no longer able to provide sufficient energy to the core to counterbalance gravitation, i.e. when helium is sufficiently depleted (typically $Y_c \simeq 10^{-4}$). At this moment, the inert core composed of C and O is under the influence of contraction and by the mirror principle, the envelope dilates. The effective temperature decreases and the luminosity increases in a similar way as in the early ascent of the RGB. The star is entering the Asymptotic-Giant Branch (AGB).

2.5 The prelude of the final stage: The Asymptotic-Giant Branch

With core contraction, the central pressure increases, as does the central temperature and the core becomes more and more degenerate. Like RGB stars, the mirror effect rules the evolution of the core and envelope dynamics in the AGB phase. Due to the cooling of the envelope, the opacity increases and the envelope spreads deeper in the interior. As a result, the envelope represents a large fraction of the star's extent (see Fig. 2.10) and the evolutionary track closely follows the Hayashi line (see Fig. 2.1)). Because stars suffer important mass loss at the RGB tip, the radius of AGB stars is smaller than that of RGB stars at fixed luminosity. Then the evolutionary track on the AGB is shifted towards high effective $T_{\rm eff}$ relatively to that on the RGB. Similarly as for RGB stars, AGB stars experience several events that result from the structure changes and impact the stellar properties.

2.5.1 The AGB bump

The layers above the core are also affected by core contraction, and these regions reach the temperature threshold to ignite helium in a shell. Then, the star has two sources of nuclear energy: the hydrogen and helium burning shells. In the early AGB, the He-burning shell is thermally unstable and the onset of He burning in a shell causes the H-burning shell to expand and cool (Catelan, 2007). As a consequence, the H-burning shell only supplies a small fraction of energy and most of the stellar luminosity is produced by the He-burning shell. This allows the base of the convective zone to penetrate inward. As a result, the onset of the He-shell burning induces a temporary reversal of the star's evolutionary direction (see Fig. 1.11) as the core briefly swells and cools and the envelope contracts and heats. This produces a drop of luminosity as the star evolves on the AGB (Castellani, Chieffi, and Pulone, 1991). Meanwhile, the matter at the base of the convective zone heats up, until the H-shell burning reignites and makes the convective envelope move outward in mass above the H-shell burning. The luminosity increases again and the star resumes its ascent on the AGB. This event is called the AGB bump or AGB clump. Like the RGBb, the AGBb causes an excess of stars due to the additional time spent in the luminosity bin where the AGBb occurs. This local excess of stars can be identified in the CMD of stellar populations, as illustrated in Fig. 1.12 (Ferraro, 1992; Pulone, 1992). The specific conditions for the AGBb to occur depend on the chemical composition of the radiative zone below the convective envelope. Indeed, the adding of mixing processes such as He-core overshooting brings products of He-burning reactions in the radiative zone where the He-shell burning takes place. These changes in the chemical composition shift the luminosity and effective temperature at which the AGBb occurs (Bossini et al., 2015). Chapter 10 is

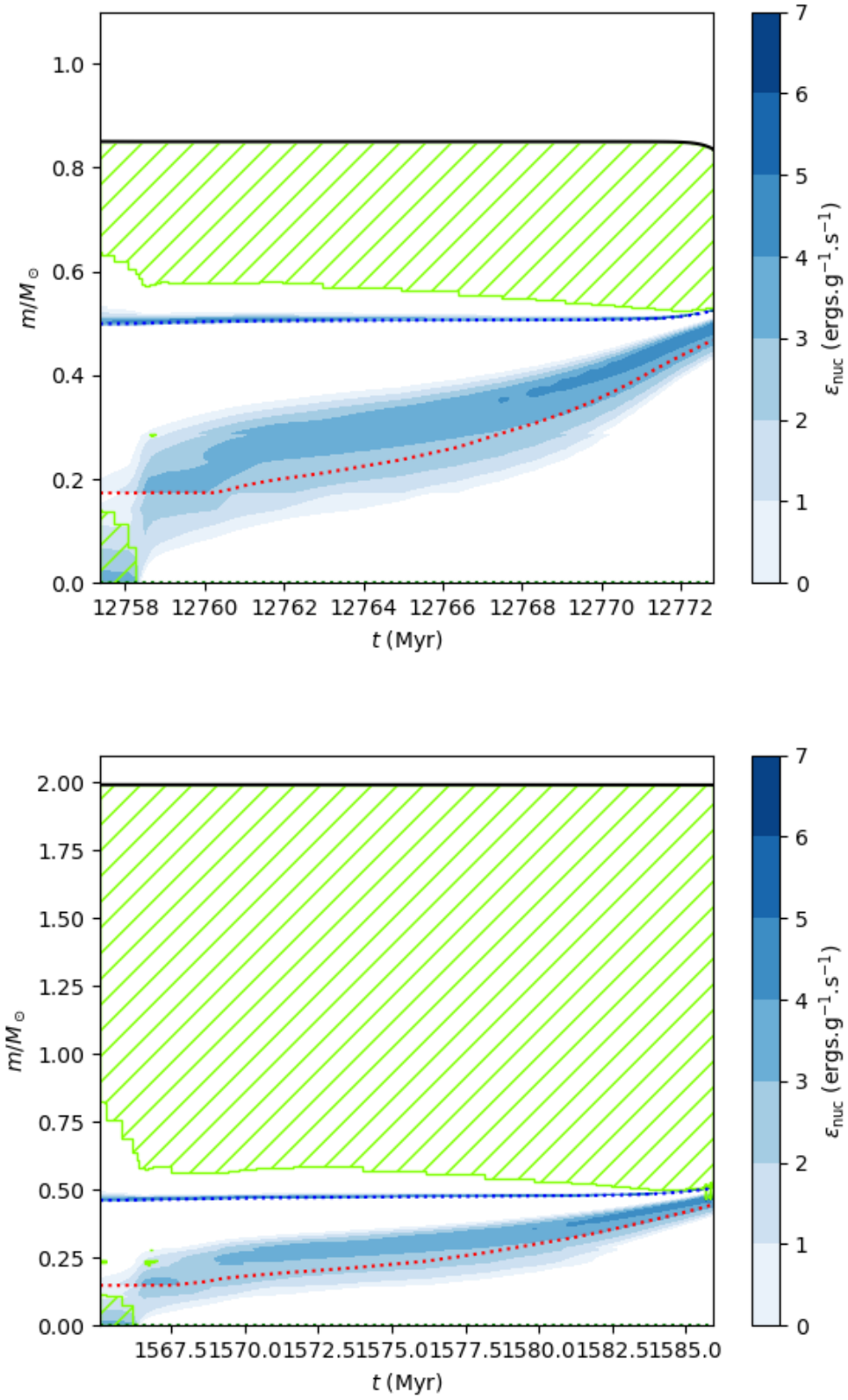

FIGURE 2.10: Same label as in Fig. 2.2, but during the He-shell burning phase for a $1M_{\odot}$ model (**top**) and a $2M_{\odot}$ model (**bottom**). The dotted blue and red lines locate the H-burning and He-burning shells, respectively. Here, the evolution is stopped before the TP-AGB phase.

specifically dedicated to the dependence of the AGBb location on the stellar mass and metallicity. We highlight that the AGBb occurs at higher luminosity and lower effective temperature for high-mass and metal-poor stars.

2.5.2 The Thermally Pulsing (TP) AGB phase

After the AGBb occurrence, the He-shell burning still provides most of the energy to the stellar surface. This shell advances towards the H-burning shell until they become close to each other. At a given point, the He-burning shell reaches the chemical composition discontinuity near the H-burning shell and helium ceases to burn. The H-burning shell is no longer pushed away by the He-burning shell, contracts and reignites. The latter yields a deposition of He ashes that are compressed and heated, then ignited in a thermal runaway process once they reach a critical value (Salaris and Cassisi, 2005). The latter event is called thermal pulse and marks the beginning of the Thermal Pulsing AGB (TP-AGB) phase. The TP-AGB phase is composed of long periods of quiescent hydrogen burning in a shell followed by instabilities of the helium-burning shell. This phase can be summarised by a cycle that is repeated several times when a thermal pulse occurs. This cycle is composed of four distinct phases (Hekker and Christensen-Dalsgaard, 2017):

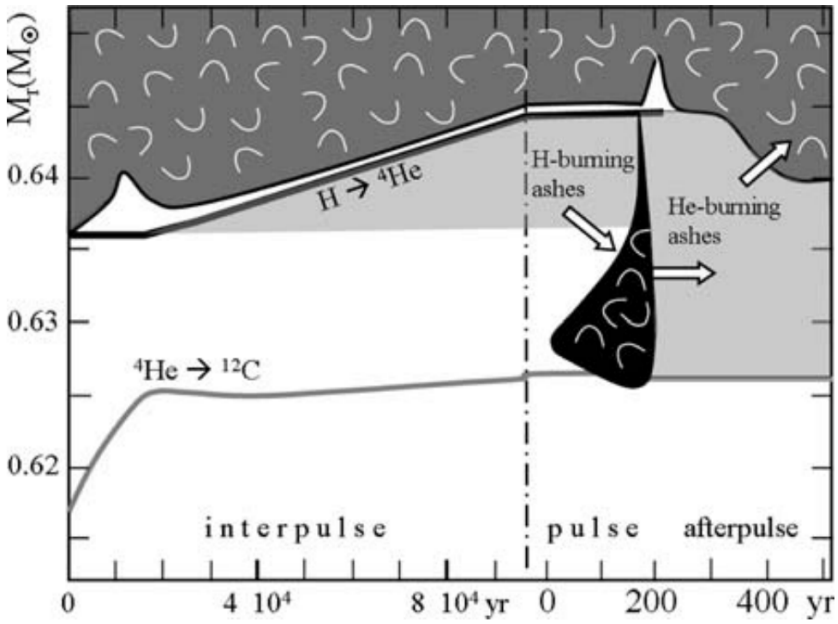

FIGURE 2.11: Kippenhahn diagram of a star of mass $M = 2.5\,M_\odot$ centred in a thermal pulse during the TP-AGB phase. The H-burning and He-burning shells are labelled by H $\rightarrow$ ^{4}He and ^{4}He $\rightarrow$ ^{12}C, respectively. The dark grey areas with wavelets refer to the convective envelope while black areas with wavelets show the intershell convection zone, respectively. The blank and light grey areas correspond to the radiative zones and regions containing H/He-burning ashes, respectively. The left side shows an interpulse with H-shell burning and the right side is associated to the pulse phase. In the afterpulse, the nucleosynthesis products are brought to the surface as indicated by the arrows. Credit: Maeder (2009)

- A pulse-driven intershell convection zone grows and the products of the triple-α process occurring in the He-burning shell are driven into the region below the H-burning shell (see Fig. 2.11). The entire matter between the two shells is mixed into the He-burning shell.
- The flash instability in the He shell occurs in a non-degenerate region of the stellar interior. Then, the energy generated by the flash helps drive expansion of the star, extinguishing the H-burning shell. Also, the expansion lowers the rate at which He is burning since the He-burning region expands and cools down. This leads to a phase of quiescent He burning.

- The intershell convection zone may attain the He/H discontinuity, dredge hydrogen into the intershell region, and enrich the outer layers with products of the helium-burning reactions such as carbon. As the star expands and cools, the convective envelope penetrates the former location of the He/H discontinuity into inter-shell region between the H- and He- burning shells. Then, the products of He burning are brought back to the envelope where they can be observed at the surface. The occurrence of this mixing process not only depends on the core mass, but also on the total mass and metallicity (Iben and Renzini, 1983). This mixing process plays an important role in the chemical enrichment of galaxies since the additional amount of carbon raises the C/O abundance ratio at the stellar surface.
- During the quiescent He-burning phase, the He that has been created by the previous H-burning shell is consumed by the advancing He-burning shell. This process continues until the He-burning shell encounters a He/H discontinuity region again. H-shell burning resumes and a thermal pulse is engaged.

This thermal pulse loops until the envelope mass is insufficient to allow thermal pulses to continue. Mass loss is then one of the major factor that determines the fate of AGB stars. The TP-AGB phase occurs at so high luminosities, for stars with a so large radius that they oscillate at frequency too low to be monitored by *Kepler*. Then, we do not study TP-AGB stars in this work.

2.5.3 Nucleosynthesis on the AGB

The mixing induced by the intershell convection zone leads to regions that both contain the products of the nuclear-chain reactions of H and He burning. At high temperatures of several 10^7K to 10^8K, the simultaneous presence of protons and α-particles leads to a complex nucleosynthesis network on the AGB, producing and consuming elements from C to Ne (Kippenhahn, Weigert, and Weiss, 2012). First, the He-shell converts ^{4}He into ^{12}C and ^{16}O. Thanks to the mixing induced in the intershell region, these elements can be brought to the hydrogen shell source, where they react with protons to give ^{14}N. When the H-shell expands and burns outwards between two consecutive thermal pulses, the previously formed ^{14}N is left behind and the next intershell convective zone takes the ^{14}N nuclei to the helium shell source. In this place, ^{14}N can interact with α-particles to form ^{18}O and ^{22}Ne. Moreover, if the hydrogen-rich material from the bottom of the convective envelope is mixed into the ^{12}C-rich region, the protons can be captured by the ^{12}C nuclei to produce ^{13}C. When the H-burning shell is inactive, the formation of ^{13}C is possible and the ^{13}C supply can be transported to the helium shell source. Here, the ^{13}C can interact with α-particles to form ^{16}O and neutrons through a slow s-process. All in all, the presence of the H- and He- burning shells and the details of mixing episodes in the intershell convective zone participate to the unique complexity of nucleosynthesis on the AGB.

2.5.4 Mass loss

Mass loss is believed to be caused by the combination of atmospheric levitation by long-period stellar pulsations and the radiation pressure on dust forming in the star's environment. This coupling creates a strong wind, also known as superwind that is correlated with the increasing luminosity and decreasing effective temperature. The stellar winds are so intense that a dusty circumstellar envelope is formed (e.g. Iben and Renzini, 1983). This dusty envelope has the potential to absorb the radiations in the visible electromagnetic spectrum and mostly emits infrared radiations. The observations of circumstellar CO line emission and stellar light scattered by dust in circumstellar envelopes can then be used to quantify the mass loss rate on the AGB (e.g. Knapp et al., 1998; Mauron and Huggins, 2006; Ramstedt et al., 2008). The superwind causes a mass loss rate that typically ranges from $10^{-7} M_{\odot}$/yr to $10^{-4} M_{\odot}$/yr. As a consequence, the envelope is gradually blown away and participates to the interstellar medium enrichment with the products of stellar nucleosynthesis. As already stated for the mass loss on the RGB, there is no up-to-date theoretical model that allows us to carefully describe mass loss on the AGB by stellar wind. Most of the information come from observations that can be used to derive empirical scaling relation to quantify mass loss as a function of stellar parameters. The Blöcker's prescription that

is based on dynamical calculations of the atmosphere of Mira-like stars is often used to quantify the mass loss on the AGB (Blocker, 1995). It reads

$$\dot{M}_B = -1.93 \times 10^{-21} \eta_B \left(\frac{M}{M_\odot}\right)^{-3.1} \frac{R}{R_\odot} \left(\frac{L}{L_\odot}\right)^{3.7} M_\odot.\mathrm{yr}^{-1}, \tag{2.9}$$

where η_B is the Blöcker's scaling factor of the order of 0.1 (Choi et al., 2016) that sets the mass loss efficiency on the AGB. This prescription is similar to the Reimers' prescription but with a revised dependence on luminosity and mass. The Blöcker's prescription was developed to consider the strong increase in mass loss for AGB stars at high luminosity (Bowen, 1988).

2.6 On the way to the final stage: from the post-AGB to the white dwarf phase

As the star climbs up the AGB, the envelope decouples from the core and the envelope mass significantly decreases when it approaches the high-luminosity stages of the AGB. The outer layers of the AGB star are ejected by the superwind and when the envelope mass drops below few percent of the total mass ($\sim 5\%$), the remaining envelope contracts and the burning shell extinguishes. This forms the post-AGB star, surrounded by a circumstellar shell created by the ejected gas. The resulting star mainly composed of C and O is in equilibrium while its radius decreases, its effective temperature increases at constant luminosity. With the increasing $T_{\rm eff}$, a high number of UV photons emerge from the star and can ionise the circumtellar matter, this leads to the formation of a planetary nebula. The star horizontally moves toward high effective temperature in the HR diagram until the envelope totally vanishes. Eventually, the remaining core enters the white dwarf cooling sequence that is the final stage of low-mass stars.

At this moment, white dwarfs are compact objects composed of C and O[2] in which the gravitational collapse is counterbalanced by the electron degeneracy pressure. The stratified layers of these stars cause a strong mode trapping and allow them to pulsate. Then, multiperiodic variations can be seen in the light curve of white dwarfs. These variations are induced by low degree ℓ and high order n gravity modes, which originate from the balance between the gravity force and the buoyancy force after a perturbation of the stellar structure (see Sect. 3.3). These modes especially bear the signature of core chemical stratification in white dwarf stars (Córsico et al., 2002; Giammichele et al., 2017). Indeed, the regions that contribute to the period of the modes depend on the degree ℓ and radial order n, to such an extent that modes with different degrees ℓ and radial orders n are differently impacted by the inner chemical profile. Not only these modes can be used to constrain the deep chemical structure of white dwarf stars, but also physical processes that these stars experienced in previous evolutionary stages (Giammichele et al., 2017; Charpinet et al., 2021). On the one hand, the overshooting during the He-core burning phase inevitably affects the stratification of white dwarfs, and its effects can be measured in the period spectrum of white dwarfs (Córsico and Althaus, 2005; Charpinet et al., 2021). On the other hand, mixing events during the TP-AGB phase such as overshooting change the chemical structure of the helium-rich progenitors of white dwarfs, altering their cooling track (Althaus et al., 2015; Miller Bertolami, 2016; Althaus et al., 2017). As a result, the study of white dwarf stars not only allows us to understand the final stage of stellar evolution, but also the prior evolutionary stages the star went through, including the clump and AGB phases.

[2]This is particularly true for stars having been through the AGB, as described above. Low-mass stars may reach the white dwarf stage following other evolutionary paths. For instance, RGB stars may circumvent the He burning phases if the He core does not fulfil the conditions for He ignition, in which case a He white dwarf is formed. Stars may also attain the white dwarf stage by skipping the AGB if they arrive on the horizontal branch at high effective temperature (see Fig. 1.4) or by ignoring the thermal pulsing phase on the early AGB (Greggio and Renzini, 1990; Brocato et al., 1990).

Chapter 3

Mode properties in solar-like stars

The goal of this chapter is to recall the mode properties of solar-like stars. To make the most of the potential diagnostic of stellar oscillations, we need to understand the links between the oscillation modes and the properties of stellar interiors. We first define the theoretical framework to derive the local and global mode parameters that can be extracted from the oscillation spectrum of solar-like stars.

3.1 Equations and approximations

The plasma in stellar interiors can be treated as a fluid, whose properties is described as a function of the position $\vec{r}$ and time t. The theory of stellar oscillations relies on the hydrodynamic equations where the physical properties are perturbed by the propagation of the seismic waves. The relevant set of physical parameters is: local pressure p, local density ρ, the local velocity field v, the gravitational potential Φ, the internal energy E, and the heat q supplied to the system per unit mass. The conservation laws require that in a non-rotating, inviscid and non-magnetic fluid, the set of variables is bound by the following set of equations (Cunha, 2018):

$$\begin{cases} \frac{\partial \rho}{\partial t} + \rho \overrightarrow{\nabla} . \overrightarrow{v} = 0 & \text{Continuity equation} \\ \rho \frac{\partial \overrightarrow{v}}{\partial t} + \rho [\overrightarrow{v} . \overrightarrow{\nabla} v] = - \overrightarrow{\nabla} p - \rho \overrightarrow{\nabla} \Phi & \text{Equation of motion} \\ \nabla^2 \Phi = 4 \pi G \rho & \text{Poisson equation} \\ \frac{\mathrm{d}q}{\mathrm{d}t} = \frac{\mathrm{d}E}{\mathrm{d}t} + p \frac{\mathrm{d}(1/\rho)}{\mathrm{d}t} & \text{Energy conservation} \end{cases} \tag{3.1}$$

The energy conservation can also be expressed in terms of temperature T, specific entropy s per unit mass, rate of energy generation per unit mass ε_n and the flux of energy $\vec{F}$. It reads

$$\rho T \frac{\partial s}{\partial t} + \rho T \left[\vec{v} . \vec{\nabla} s \right] = \rho \varepsilon_n - \vec{\nabla} . \vec{F} \tag{3.2}$$

In the framework of solar-like oscillations, we adopt the following approximations and simplifications perturbations that vary on relatively short scales (much smaller than the radius of the star)

- Effects of rotation, magnetic fields, turbulent pressure, and diffusive processes are ignored.
- *Cowling approximation*. We neglect the perturbation to the gravitational potential. This largely simplifies the complexity of the system of equations as it reduces the general equations from fourth order to second order, with a reduction in the number of boundary conditions. The Cowling approximation (Cowling, 1941) reveals to be adequate for perturbations that vary on scales much smaller than the stellar radius, when the mode degree ℓ and the radial order n are large. In case of red giants where the mode degree ℓ and the radial order n are close to unity, the Cowling approximation may be too crude (Takata, 2006).
- *Adiabatic approximation*. We neglect the energy exchanged between the seismic wave and the fluid. This approximation is justified when the temporal evolution of the seismic wave is much rapid than the characteristic time of any mechanism transferring energy between the different fluid elements. Therefore, the heating term in the energy equation can be neglected. Near the surface, the

density is so low that it exists a region called the super-adiabatic region, where the thermal and convective time scales are of the order of the oscillation period. For those regions, the full energy equation must be taken into account.

- *JWKB approximation*. The Jeffreys, Wentzel, Kramers and Brillouin (JWKB) method is commonly used to approach the Schrödinger equation in quantum mechanics, but can be generalised to any quasi-harmonic equations. This method consists in finding a quasi-harmonic solution under the assumption that the wavelength of the oscillation is larger than the scale heights of the parameters describing the equilibrium structure in the environment.

3.2 Derivation of the dispersion equation

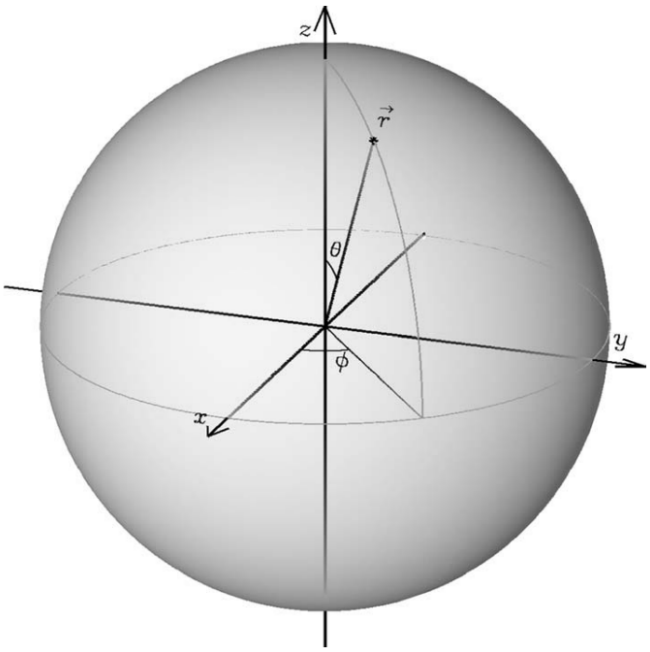

FIGURE 3.1: The spherical polar coordinate system. Credit: Aerts, Christensen-Dalsgaard, and Kurtz (2010)

The linear theory of stellar oscillations describes the oscillations as the result of small perturbations to the stellar structure initially at hydrostatic equilibrium. The equilibrium structure is assumed to be static and all time derivatives are neglected. The perturbations to the physical parameters can be treated in the *Eulerian* description, in which the observer focuses on specific locations in the space, through which the fluid flows as time elapses. For any physical parameter X at a given position $\vec{r}$ and time t, we have in the Eulerian description

$$X(\vec{r},t) = X_0(\vec{r}) + X'(\vec{r},t) \qquad \text{with } \frac{X'}{X_0} \ll 1, \tag{3.3}$$

where the subscript "0" refers to the value taken at equilibrium and the prime corresponds to the Eulerian perturbation to the parameter X associated to the oscillation. The stellar properties at equilibrium are considered to be static on the relevant time scale of the oscillations, which justifies the independence of X_0 on t. Equivalently, the physical properties of the star can be treated in the *Lagrangian* description, which is that of an observer who follows the motion of the gas. In such conditions, the physical parameters can be expressed as follows

$$X(\vec{r_0},t) = X_0(\vec{r_0}) + \delta X(\vec{r_0},t) \qquad \text{with } \frac{\delta X}{X_0} \ll 1, \tag{3.4}$$

where δX is the Lagrangian perturbation associated to the oscillation and $\vec{r_0}$ is the position at equilibrium of the tracked fluid element. The two descriptions are linked by the relation

$$\delta X(\vec{r},t) = X'(\vec{r},t) + \vec{\xi}.\vec{\nabla}X_0, \tag{3.5}$$

where $\vec{\xi} = \vec{r} - \vec{r_0}$ is the displacement vector provoked by the perturbation associated to the oscillation. Based on the absence of any mechanism that would break the spherical symmetry, the equilibrium model is spherically symmetric. Then, we describe the star in spherical polar coordinates (r, θ, ϕ), where r is the distance to the centre, θ is the angle from the polar axis, and ϕ is the longitude (see Fig. 3.1). Since the equilibrium is independent of the coordinates θ and ϕ, the solution can be separated in these coordinates. Accordingly, we decompose the displacement vector on this spherical basis as follows

$$\vec{\xi} = \vec{\xi}_r + \vec{\xi}_h, \tag{3.6}$$

where $\vec{\xi}_r$ and $\vec{\xi}_h$ are the radial and horizontal displacement vectors, respectively. On the other hand, the spherical symmetry allows us to decompose the oscillation modes following the spherical harmonics basis Y_ℓ^m that reads

$$Y_\ell^m(\theta,\phi) = (-1)^m \sqrt{\frac{(2\ell+1)}{4\pi}\frac{(\ell-m)!}{(\ell+m)!}} P_\ell^m(\cos\theta) e^{im\phi}. \tag{3.7}$$

$P_{\ell,m}$ are the Legendre polynomials, the angular degree ℓ corresponds to the number of nodal lines at the stellar surface while the azimuthal order m is the number of those nodal lines that go through the stellar poles (see Fig. 1.1). By injecting the perturbed physical parameters into Eq. 3.1 and keeping the linear terms of the perturbation, we have

$$\begin{cases} \rho' + \vec{\nabla}.\left(\rho_0\vec{\xi}\right) = 0 & \text{Continuity equation} \\ \rho_0 \frac{\partial^2\vec{\xi}}{\partial t^2} = -\vec{\nabla}p' - \rho'\vec{\nabla}\Phi_0 - \rho_0\vec{\nabla}\Phi' & \text{Equation of motion} \\ \nabla^2\Phi' = 4\pi G\rho' & \text{Poisson equation} \\ \rho_0 T_0\left(\frac{\partial s'}{\partial t} + \frac{\partial\vec{\xi}}{\partial t}\cdot\vec{\nabla}s_0\right) = \rho_0\varepsilon_n' + \frac{\rho'}{\rho_0}(\vec{\nabla}\cdot\vec{F}_0) - \vec{\nabla}\cdot\vec{F}' & \text{Energy conservation} \end{cases} \tag{3.8}$$

Then, we are looking for the oscillation modes of a spherical star where the spatial and temporal coordinates are separable. The perturbations to physical parameters have an harmonic form

$$\text{Eulerian} : X'(\vec{r}) = \overline{X'}(\vec{r})e^{i\omega t} \qquad \text{Lagrangian} : \delta X(\vec{r}) = \overline{\delta X}(\vec{r})e^{i\omega t}, \tag{3.9}$$

where $\overline{X'}$ and $\overline{\delta X}$ are the complex amplitude of the Eulerian and Lagrangian perturbations, respectively, and ω is the pulsation frequency of the mode.

By developing the system of equations 3.8 under the assumptions presented in Sect. 3.1, the radial part of this system of four equations simplifies in a system of two equations. Moreover, for large radial orders n, the mode wavelength in the radial direction is small relatively to the pressure scale height $H_p = -(\mathrm{d}\log p_0/\mathrm{d}r)^{-1}$ (isothermal atmosphere scenario), except in the central and superficial layers. In the following, we neglect the derivative of physical parameters at equilibrium to simplify the understanding of the behaviour of oscillation modes and the propagation of seismic waves in stellar interiors. The set of Eqs. 3.8 leads to (Mosser, 2015)

$$\begin{cases} \frac{\mathrm{d}\xi_r}{\mathrm{d}r} = \frac{1}{\rho_0 c_0^2}\left(\frac{S_\ell^2}{\omega^2} - 1\right)p' \\ \frac{\mathrm{d}p'}{\mathrm{d}r} = \rho_0\left(\omega^2 - N_{\mathrm{BV}}^2\right)\xi_r, \end{cases} \tag{3.10}$$

where $c_0 = \sqrt{(\partial P_0/\partial\rho_0)_s}$ is the sound speed at equilibrium and constant entropy. The Lamb frequency S_ℓ and the Brunt-Väisälä frequency N_{BV} are two characteristic frequencies that limit the propagation of the seismic waves, they are defined by

$$\begin{cases} S_\ell^2 = \frac{\ell(\ell+1)c_0^2}{r^2} \\ N_{\rm BV}^2 = g_0 \left(\frac{1}{\Gamma_1} \frac{{\rm d}\ln p_0}{{\rm d}r} - \frac{{\rm d}\ln \rho_0}{{\rm d}r} \right), \end{cases} \tag{3.11}$$

where $\Gamma_1 = \left({\rm d}\ln p_0 / \ln \rho_0\right)_s$ is the first adiabatic exponent and the subscript s indicates that the derivative is taken at constant specific entropy. In a regularly stratified region, the Brunt-Väisälä frequency $N_{\rm BV}$ represents the frequency at which a fluid element oscillates around its equilibrium position. By using the ideal gas law for a fully ionised gas, which is valid for the interiors of not too cool stars, the Brunt-Väisälä frequency $N_{\rm BV}$ can be alternatively written

$$N_{\rm BV}^2 = \frac{g_0 \rho_0}{p_0} \left(\nabla_{\rm ad} - \nabla_T + \nabla_\mu \right), \tag{3.12}$$

where T is the temperature, μ is the mean molecular weight, and

$$\nabla_{\rm ad} = \left(\frac{\partial \ln T_0}{\partial \ln p_0} \right)_{\rm ad} \qquad \nabla_T = \frac{{\rm d}\ln T_0}{{\rm d}\ln p_0} \qquad \nabla_\mu = \frac{{\rm d}\ln \mu_0}{{\rm d}\ln p_0}. \tag{3.13}$$

Finally, the two equations in Eq. 3.10 can be combined to form a single second-order differential equation in ξ_r. By neglecting the derivative of the physical parameters at equilibrium, we have

$$\frac{{\rm d}\xi_r}{{\rm d}r^2} = \frac{\omega^2}{c_0^2} \left(1 - \frac{N_{\rm BV}^2}{\omega^2} \right) \left(\frac{S_\ell^2}{\omega^2} - 1 \right) \xi_r. \tag{3.14}$$

The previous equation leads to the dispersion equation

$$c_0^2 k_r^2 = \omega^2 \left(1 - \frac{N_{\rm BV}^2}{\omega^2} \right) \left(\frac{S_\ell^2}{\omega^2} - 1 \right), \tag{3.15}$$

from which we can infer the fundamental properties of the waves.

3.3 Propagation diagram

The equation 3.15 shows that the propagation condition ($k_r^2 > 0$) implies

$$\begin{cases} \omega^2 > S_\ell^2 \text{ and } \omega^2 > N_{\rm BV}^2 \\ \text{or} \\ \omega^2 < S_\ell^2 \text{ and } \omega^2 < N_{\rm BV}^2 \end{cases} \tag{3.16}$$

From these conditions, we can define the nature and the propagation region of two types of seismic waves, as illustrated in Fig. 3.2.

3.3.1 Acoustic waves

The first condition of Eq. 3.16 defines the acoustic waves. The same condition tells us that acoustic waves can propagate both in radiative zones and in convective zones. They are generated by the turbulent flux at the near-surface convection zone. In that case, local pressure perturbations are induced and the main restoring force of acoustic waves is linked to the pressure gradient.

3.3.2 Gravity waves

The second condition of Eq. 3.16 defines the gravity waves. When a blob of fluid is perturbed away from its equilibrium position, its density is different from the one of the stratified environment. The restoring force, which is the buoyancy force, tends to take the fragment of fluid back to its equilibrium position. This requires that the region is convectively stable, *i.e* $N_{\rm BV}^2 > 0$. Otherwise, convection takes the fragment of fluid away from its equilibrium position and the oscillation vanishes, as reflected by the

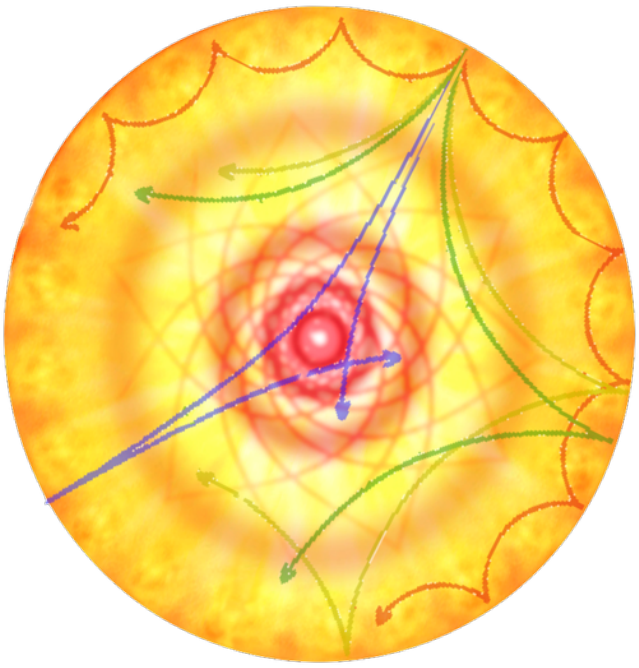

FIGURE 3.2: Simplified picture of the interior of a Sun-like star, with a large radiative core surrounded by a convective envelope. Gravity waves are represented by the orange solid lines in the radiative zone while pressure waves are represented by blue, green and brown solid lines throughout the star. Credit: IAC

second condition of Eq. 3.16. Consequently, gravity waves result from the balance between the gravity force and the buoyancy force, the inertia of the neighbouring fluid make the fragment of fluid oscillate around its equilibrium position. Contrary to acoustic waves, gravity waves cannot propagate everywhere: Eq. 3.16 tells us that they can only propagate in regularly stratified regions in density where $N^2_{\rm BV} > 0$, corresponding to radiative zones.

In the context of a finite cavity with specific boundary conditions, the waves can interfere. At specific frequencies, these interferences are constructive, forming standing waves, also called stellar modes. These modes develop both in the p- and g-wave cavities, and are referred to as p and g modes, respectively (*e.g.*, Unno et al., 1989; Mosser, Belkacem, and Vrard, 2013). Radial modes, defined with the degree $\ell = 0$ are pure pressure modes. P- and g-wave cavities do not interact if their resonant frequencies are different. In this case, they can be studied separately. Fig. 3.2 enables us to visualise where p and g waves propagate in the Sun. In solar-like stars, g waves are trapped in the radiative zone and they have an evanescent behaviour outside this zone. Therefore, it is very difficult to detect them at the stellar surface. As illustrated in Fig. 3.3, the typical frequency of p modes is relatively large compared to that of g modes in Sun-like stars. Luckily, g waves can couple with p waves in red giants, giving rise to the so-called mixed modes, which can be detected at the surface.

3.3.3 Mixed modes

A sharp gradient of chemical composition at the base of the convective zone is formed after the H-core burning phase, which increases the Brunt-Väisälä frequency $N_{\rm BV}$ according to Eq. 3.12. Then, the frequency of g modes increases (see right panel of Fig. 3.3). In parallel, the convective envelope dilates and its density decreases. The frequency range of the excited p modes is shifted towards low frequency, up to a point where it overlaps that of the excited g modes. Gravity waves propagating in the stellar core can couple with pressure waves propagating in the envelope if their frequencies are close to each other and the evanescent region between the two cavities is not important. Such coupling gives rise

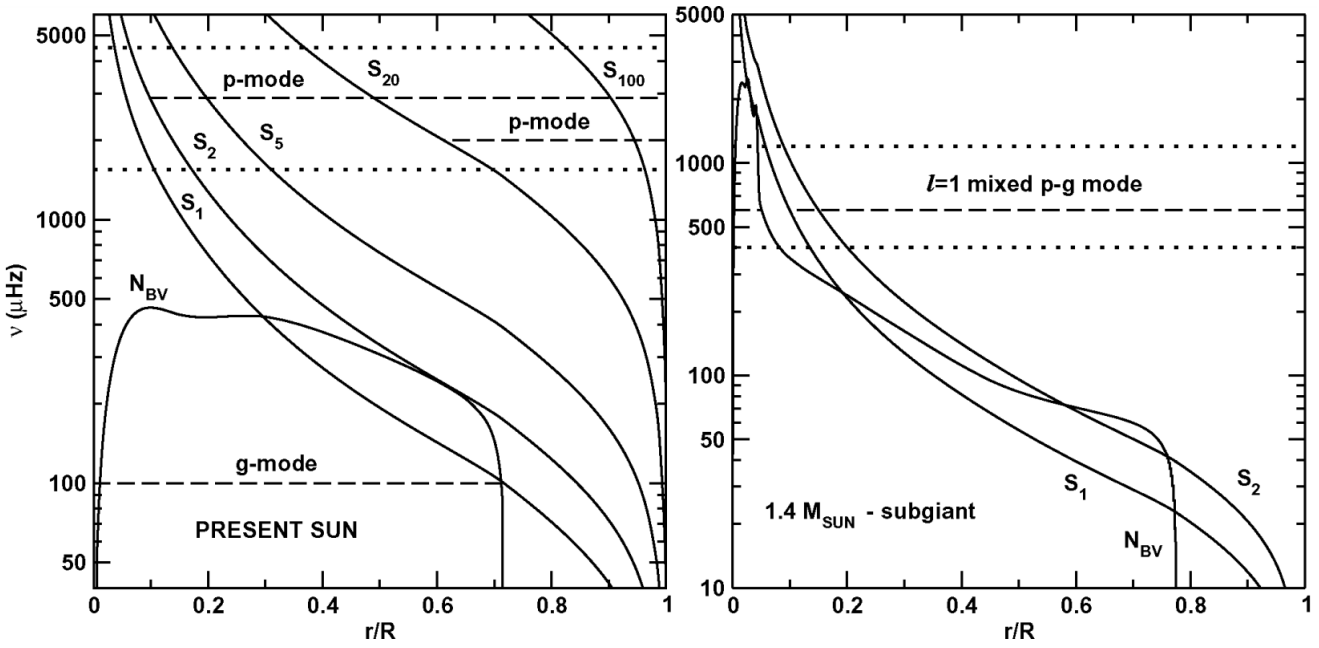

FIGURE 3.3: Propagation diagrams for a solar model (**left**) and a $1.4\,M_\odot$ model on the subgiant branch (**right**). The solid lines correspond to the Brunt-Väisälä frequency $N_{\rm BV}$ and the Lamb frequencies S_ℓ at different angular degree ℓ. The dashed lines delimit the regions where p and g modes can develop (p modes of degree $\ell = 2$, 20 are represented on the left panel). The frequency domains of solar-like oscillations is located in-between the dotted lines. Credit: Lebreton and Montalbán (2009)

to the so-called mixed modes, behaving as gravity modes in the core and as pressure modes in the envelope. A simple mechanical model can be used to understand the presence of mixed modes (Mosser, Belkacem, and Vrard, 2013). This toy model contains a chain of two masses $m_{\rm g}$ and $m_{\rm p}$ that represent the gravity and pressure mode inertia, respectively, linked by three springs (see Fig. 3.4). The stiffness of the coupling spring between $m_{\rm g}$ and $m_{\rm p}$ represents the coupling between the p- and g-wave cavities. In case of a moderate coupling, the energy input from the oscillation is not highly perturbed by the leak through the coupling between $m_{\rm p}$ and $m_{\rm p}$. Then, pressure waves are efficiently excited and have enough energy to excite gravity waves, and mixed modes can be observed. In the absence of coupling between $m_{\rm g}$ and $m_{\rm p}$, the excitation mechanisms at the stellar surface are able to move $m_{\rm p}$ without impacting $m_{\rm g}$, and no mixed modes are observed. Frequencies of mixed modes are shifted relatively to pure pressure or gravity modes by an amount that depends on the coupling strength between the gravity and pressure oscillation cavities (Unno et al., 1989). In red giants, modes with a degree $\ell \geq 1$ are mixed, only radial modes are pure p modes. In the upper RGB and Asymptotic Giant Branch (AGB), the conditions for the p- and g-mode cavities to couple are no longer met and mainly pressure-dominated modes are observable (Mosser et al., 2019).

The propagation conditions presented in Eq. 3.16 precisely delimit the cavity in which modes can develop. This is illustrated in Fig. 3.3 for the Sun where the p- and g-mode cavities are uncoupled, and for a subgiant branch star where these cavities are coupled and give rise to mixed modes. Nevertheless, Eq. 3.16 does not provide an upper limit restraining the propagation of acoustic waves in case of a convective envelope. Near the surface, acoustic waves are unable to propagate when their vertical wavelength is too long compared to the density scale height $H_\rho = -(\mathrm{d}\ln\rho_0/\mathrm{d}r)^{-1}$ in the equilibrium structure. This defines a frequency called cut-off frequency $\nu_c = c_0/H_\rho$ below which waves are evanescent. The highest value of ν_c is reached at the level where the density scale height is minimum (Cunha, 2018), close to the level where the temperature is minimum. This defines the 'seismic surface', and implies that waves are reflected there. The cut-off frequency shows large values and a steep profile at the surface. This ensures that all waves are approximately reflected at the same location.

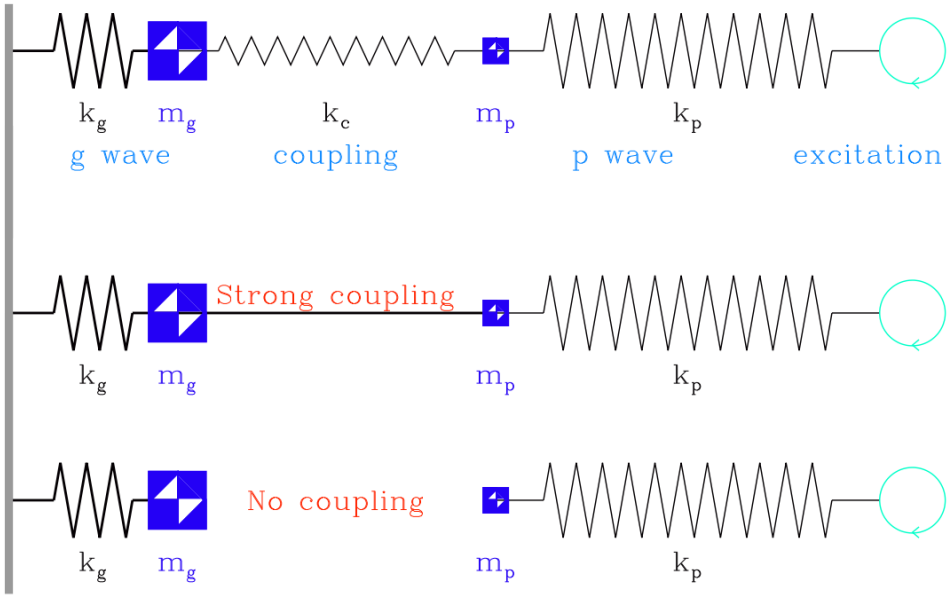

FIGURE 3.4: Toy model to represent the coupling of gravity and pressure waves, with two masses and three coils. **Top:** the intermediate-case coupling, which explains most of the observed gravity-dominated mixed modes in red giants. **Middle:** very strong coupling case, which can explain the presence of mixed modes with weak amplitude. **Bottom:** very weak coupling case, only pressure modes are observed, for example in high-luminosity red giants. Credit: Mosser, Belkacem, and Vrard (2013)

3.4 Properties of p modes

3.4.1 Asymptotic relation of p-mode pulsators

For a mode to resonate, specific boundary conditions must be fulfilled at the edges of the resonant cavity (i.e. the turning points). In the JWKB approximation, the eigenfunctions are developed around the turning points of the cavity. Then, these solutions are asymptotically connected to form the eigenfunction in the whole cavity. In order to form a standing wave, the change in phase of the eigenfunction in the radial direction must fulfil the condition (Shibahashi, 1979)

$$\int_{r_{\mathrm{p,int}}}^{r_{\mathrm{p,ext}}} k_r \mathrm{d}r = \pi(n + \alpha(\omega)), \tag{3.17}$$

where $r_{\mathrm{p,int}}$ and $r_{\mathrm{p,ext}}$ are the inner and outer turning points of the propagation cavity, respectively, n is an integer, and $\alpha(\omega)$ is a frequency-dependent parameter that captures the phase changes the wave experience at the internal turning point and at the surface.

Eq. 3.17 leads to the relation for frequencies of low-degree p modes ($n \gg \ell$). The development performed in this chapter is led at first order and does not consider that the properties of the equilibrium state of the star may vary on a scale that is smaller than the radial wavelength of the modes. Particularly, the latter assumption is not verified near the stellar surface, where the density significantly varies. By carrying the asymptotic expansion further, which is valid for $\ell \ll n$, it can be shown that the p-mode frequencies are given by the asymptotic pattern (Tassoul, 1980; Scherrer et al., 1983)

$$\nu_{n,\ell} \simeq (n + \varepsilon_{\mathrm{as}} + \ell/2)\Delta\nu_{\mathrm{as}} - \frac{\ell(\ell+1) + \delta}{n + \ell/2 + \epsilon_{\mathrm{as}}} A, \tag{3.18}$$

where $\Delta\nu_{\mathrm{as}}$ is the asymptotic large separation, namely the asymptotic frequency spacing between consecutive radial modes, ϵ_{as} is the asymptotic acoustic offset that allows us to locate the radial modes, δ is a small correction term predominantly related to the near-surface regions, and A is a second-order term

accounting for the fact that non-radial modes do not probe the innermost regions, contrary to radial modes. It can be expressed by

$$A = \frac{1}{4\pi^2}\left(\frac{c(R)}{R} - \int_0^R \frac{\mathrm{d}c}{\mathrm{d}r}\frac{\mathrm{d}r}{r}\right). \tag{3.19}$$

The universal oscillation pattern enables us to identify the mode frequency at a given radial order n and degree ℓ, $\ell = 0$ corresponding to a pure pressure mode while $\ell \geq 1$ corresponds to a pressure-dominated mode.

Typically, in red-giants, the radial order is $n \leq 15$ and it becomes even smaller when the star ascends the RGB. Consequently, the asymptotic condition $\ell \ll n$ is no longer satisfied and the observed large separation differs from its asymptotic value $\Delta\nu_{\rm as}$. The p-mode oscillation pattern of red giants no longer matches the asymptotic pattern, but rather follows the pattern (Mosser et al., 2011)

$$\nu_{n,\ell} = \left(n + \frac{\ell}{2} + \varepsilon - d_{0\ell} + \frac{\alpha_{\rm curv}}{2}\left[n - n_{\rm max}\right]^2\right)\Delta\nu, \tag{3.20}$$

where ε is the observed acoustic offset, $d_{0\ell}$ is a reduced small separation defined as $d_{0\ell} = \delta\nu_{0\ell}/\Delta\nu$ where $\delta\nu_{0\ell}$ is the small frequency separation between a mode of degree ℓ and its neighbouring radial mode. These parameters are interesting because they are sensitive to the stellar structure, hence to the evolutionary stage of a star. The radial order[1] $n_{\rm max} = \nu_{\rm max}/\Delta\nu - \varepsilon$ corresponds to the equivalent radial order where the oscillation power is maximum. The curvature of the radial mode pattern noted $\alpha_{\rm curv}$ corresponds to the signature of the non-negligible second-order asymptotic terms, which induces a significant gradient in the frequency spacing between consecutive radial modes. Eq. 3.20 correctly describes the observed oscillation spectrum of red giants, in particular the large separation $\Delta\nu$ and the acoustic offset ε. The deviations from the asymptotic relation (Eq. 3.18) are quantified following the relations (Mosser et al., 2013a)

$$\begin{cases} \Delta\nu_{\rm as} = \Delta\nu\left(1 + \frac{n_{\rm max}\alpha_{\rm curv}}{2}\right) \\ \varepsilon_{\rm as} = \frac{\varepsilon - n_{\rm max}^2\alpha_{\rm curv}}{1 + n_{\rm max}\frac{\alpha_{\rm curv}}{2}}. \end{cases} \tag{3.21}$$

We remind that the p-mode oscillation pattern of red giants Eq. 3.20 has been calibrated for low- and intermediate-luminosity red giants (*i.e.* $\Delta\nu \in [2, 10]$ μHz). Accordingly, some deviations may be visible for more evolved red giants.

3.4.2 The large separation $\Delta\nu$

As illustrated in Fig. 1.8, the oscillation spectrum of p-mode pulsators is regularly spaced. At a given radial order n, radial ($\ell = 0$), dipole ($\ell = 1$), and quadrupole ($\ell = 2$) modes are observed in the oscillation spectrum of evolved red giants. They form a pattern of three modes that recreate every $\Delta\nu$ intervals. The asymptotic value of the large separation $\Delta\nu_{\rm as}$ is related to the inverse of the time for a pressure wave to travel from one turning point of the cavity to the other. The former is defined by

$$\Delta\nu_{\rm as} = \left(2\int_0^R \frac{\mathrm{d}r}{c_0(r)}\right)^{-1}, \tag{3.22}$$

where R is the stellar radius. The large separation can also be related to the frequency difference between pressure modes of consecutive radial order at the same degree ℓ

$$\Delta\nu \simeq \langle\Delta\nu_{n,\ell}\rangle = \langle\nu_{n+1,\ell} - \nu_{n,\ell}\rangle. \tag{3.23}$$

The large separation $\Delta\nu$ is a crucial parameter in asteroseismology as it is a direct probe of the sound speed, hence of the mean density as (Ulrich, 1986)

[1] Note that n_{max} is not an integer

$$\Delta\nu_{\rm as} \propto \sqrt{\rho} \propto \sqrt{\frac{GM}{R^3}}. \tag{3.24}$$

3.4.3 The frequency at maximum oscillation power $\nu_{\rm max}$

The oscillation power spectrum of p-mode pulsators is modulated by an envelope whose shape and maximum are determined by the balance between the driving and damping of oscillations. The modes that are efficiently excited lies in this power excess envelope, which is centred around the frequency at maximum oscillation power $\nu_{\rm max}$. This frequency is set by resonance between the local thermal time-scale $\tau_{\rm th}$ in the super-adiabatic region and the period of oscillations (Belkacem et al., 2011)

$$\nu_{\rm max} = \frac{1}{2\pi\tau_{\rm th}}. \tag{3.25}$$

The local thermal time scale $\tau_{\rm th}$ depends on the time scale of energy transport processes in the super-adiabatic region, *i.e.* radiative and convective thermal time scales. This relation implies that the frequency at maximum oscillation power $\nu_{\rm max}$ scales as the cut-off frequency $\nu_c = c_0/H_P$ (Brown et al., 1991; Belkacem et al., 2011). Since the pressure scale height at the surface is related to the effective temperature $T_{\rm eff}$ and the gravitational acceleration g_0 by $H_P \propto T/g_0$, the frequency $\nu_{\rm max}$ scales as (Kjeldsen and Bedding, 1995)

$$\nu_{\rm max} \propto \frac{g_0}{\sqrt{T_{\rm eff}}} \propto \frac{M}{R^2\sqrt{T_{\rm eff}}}. \tag{3.26}$$

3.4.4 Ensemble asteroseismology: a key diagnostic

Ensemble asteroseismology turned out to be of major interest when highlighting the evolutionary stages of a star. The former consists in studying the correlation between seismic parameters in an ensemble of stars, allowing us to build scaling relations between these parameters. With a large set of stars, we are able to deliver key information on the stellar interior structure, even restricted to global seismic parameters.

Among the scaling relations derived with ensemble asteroseismology, the $\Delta\nu - \nu_{\rm max}$ relation is interesting to infer stellar parameters such as the stellar mass and radius. Indeed, we can extract the stellar mass and radius thanks to a seismic diagnostic, combining Eqs. 3.24, 3.26 with spectroscopic estimates of $T_{\rm eff}$:

$$\begin{cases} \frac{M}{M_\odot} = \left(\frac{\nu_{\rm max}}{\nu_{\rm max,\odot}}\right)^3 \left(\frac{\Delta\nu}{\Delta\nu_\odot}\right)^{-4} \left(\frac{T_{\rm eff}}{T_{\rm eff,\odot}}\right)^{3/2} \\ \frac{R}{R_\odot} = \left(\frac{\nu_{\rm max}}{\nu_{\rm max,\odot}}\right) \left(\frac{\Delta\nu}{\Delta\nu_\odot}\right)^{-2} \left(\frac{T_{\rm eff}}{T_{\rm eff,\odot}}\right)^{1/2}. \end{cases} \tag{3.27}$$

Here, the scaling relations are normalised by the Sun's parameters. The former have provided relevant estimates of the stellar mass and radius of main sequence stars, subgiants and red giants, reaching the precision of interferometry (Kallinger et al., 2010; Huber et al., 2012). While $\Delta\nu$ can be extracted with high precision using the autocorrelation of stellar oscillation time series (*e.g.* Mosser and Appourchaux, 2009), the inference of $\nu_{\rm max}$ is not as precise as $\Delta\nu$. This is mainly due to the way to extract $\nu_{\rm max}$, which is not based on a physical definition of this parameter. These scaling relations must be calibrated to the evolutionary stage of a star, because they may change accordingly (Mosser et al., 2013b; Coelho et al., 2015; Sharma et al., 2016; Zinn et al., 2019).

3.4.5 The acoustic offset ε

The acoustic offset ε is a parameter that is sensitive to the structure changes of a star, just as in the core as in superficial layers. Indeed, the eigenfrequency Eq. 3.18 can also read (Roxburgh and Vorontsov, 2000; Roxburgh and Vorontsov, 2003)

$$\frac{\nu_{n,\ell}}{\Delta\nu_{as}} \simeq \left(n + \frac{\ell}{2}\right) + \frac{\alpha_\ell(\nu_{n,\ell}) - \delta_\ell(\nu_{n,\ell})}{\pi}, \tag{3.28}$$

where α_ℓ is an outer phase shift primarily determined by the mode propagation in the outer layers (including the atmosphere) of the star and δ_ℓ is an inner phase shift determined by the structure of the inner regions. For radial modes (with $\ell = 0$), equations (3.18) and (3.28) are equivalent, adopting

$$\varepsilon_{\rm as} = \frac{1}{\pi}\left(\alpha_0 - \delta_0\right). \tag{3.29}$$

Hence, $\epsilon_{\rm as}$ is clearly sensitive to the inner structure, the site of the most fundamental differences between evolutionary stages. However, the envelope contribution is dominant, by more than a factor of 6 in the RGB and clump phases (Christensen-Dalsgaard et al., 2014). Although $\varepsilon_{\rm as}$ is predominantly determined by the surface layers, it has been shown that the acoustic offset ε in the asymptotic pattern of red giants (Eq. 3.20) could be used to distinguish He-core burning stars and AGB stars from RGB stars. This classification method is presented in Sect. 5. Despite its clear dependence with stellar structure, the acoustic offset ε is a phase term that is not only marked by signature of internal structures but also by the upper layers of the surface, which are poorly understood. Consequently, the acoustic offset ε defined in Eq. 3.20 is not suited to constrain physical mechanisms in stellar interiors.

3.4.6 The reduced small separation $d_{0\ell}$

One can highlight a characteristic frequency separation between modes of different degree ℓ. The so called small frequency separation between radial and dipole modes; between radial and quadrupole modes are defined by

$$\begin{cases} \delta\nu_{01}(n) = \frac{1}{2}\left(\nu_{n,0} - 2\,\nu_{n,1} + \nu_{n+1,0}\right) \\ \delta\nu_{02}(n) = \nu_{n,0} - \nu_{n-1,2} \end{cases} \tag{3.30}$$

These small separations are defined by frequency differences, which makes them even more sensitive to sharp variation region of the sound speed according to Eq. 3.18. Indeed, the small separation $\delta\nu_{\ell\,\ell+2}$ between modes of degree ℓ and $\ell+2$ is related to the integral of the sound speed gradient as follows (Gough, 1986)

$$\delta\nu_{\ell\,\ell+2}(n) = \nu_{n,\ell} - \nu_{n-1,\ell+2} \simeq -(4\ell+6)\frac{\Delta\nu_{\rm as}}{4\pi^2\nu_{n,\ell}}\int_0^R \frac{{\rm d}c}{{\rm d}r}\frac{{\rm d}r}{r}. \tag{3.31}$$

We also define dimensionless parameters, based on the ratio between small frequency separations and $\Delta\nu$

$$d_{0\ell}(n) = \frac{\delta\nu_{0\ell}(n)}{\Delta\nu_n}. \tag{3.32}$$

Both reduced small separations can be used as a powerful diagnostic to probe stellar interiors. Indeed, these dimensionless small separations are less sensitive to gradients in the frequency differences and are less perturbed by poorly modelled features such as the surface effects (Roxburgh and Vorontsov, 2003). By relating equations (3.18) and (3.28), one can find

$$d_{0\ell} = \frac{\Delta\nu_{\rm as}}{\pi}\left(\alpha_0 - \alpha_\ell + \delta_\ell - \delta_0\right). \tag{3.33}$$

Reduced small separation d_{01}

In a Fourier spectrum, dipole modes are located approximately mid-way between consecutive radial modes, as illustrated in Eq. 3.30. Conventionally, the small separation $\delta\nu_{01}$ locates the acoustic $\ell = 1$ mode in comparison of the middle point between two consecutive radial ($\ell = 0$) modes.

Reduced small separation d_{02}

Conventionally, $\delta\nu_{02}$ locates the acoustic $\ell = 2$ mode in comparison to the closest radial mode. The asymptotic approximation of $\delta\nu_{02}$ (see Eq. 3.31) shows that the small separation between $\ell = 0$ and $\ell = 2$ modes depends on the sound-speed gradient. Being sensitive to any change of slope of the sound-speed in the deep interiors, d_{02} can be used as an age indicator (Christensen-Dalsgaard, 1988). Particularly, the cores of RGB and clump stars, being slightly different, affect d_{02} differently as illustrated in Fig. 3.5.

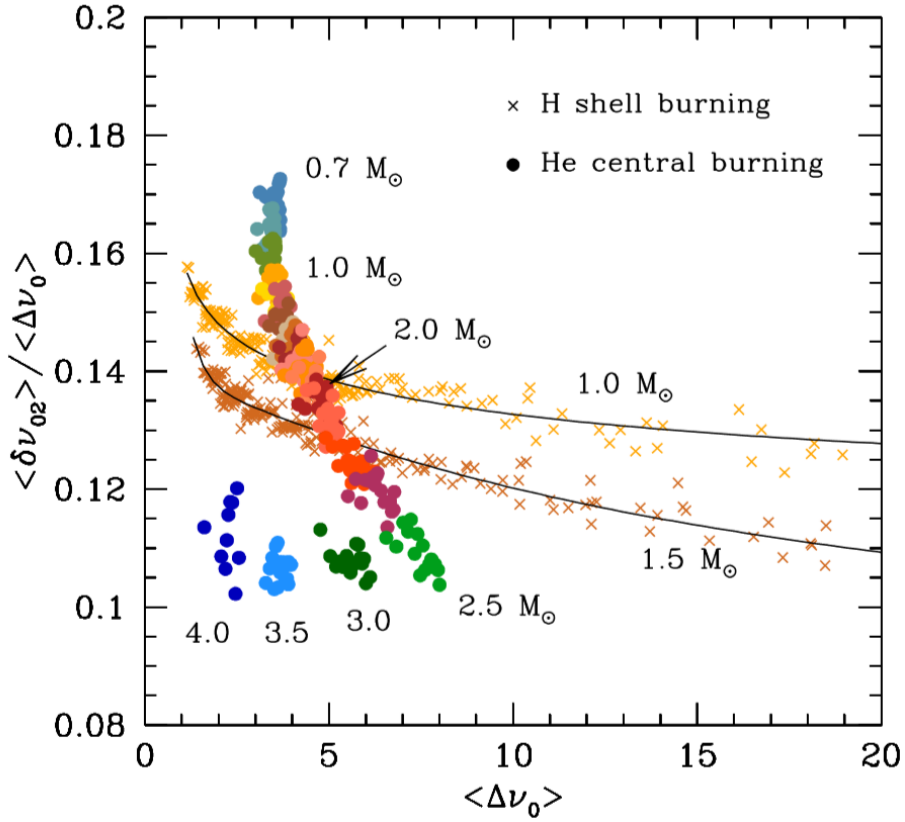

FIGURE 3.5: Reduced small separation d_{02} as a function of the large separation of radial modes $\Delta\nu$ for the RGB phase (cross) with masses 1.0 and 1.5 $M_\odot$; metallicity Z = 0.006, 0.01, 0.02,0.03; fractional helium abundance Y = 0.25 and 0.278. Dots correspond to models burning He in the centre, with masses between 0.7 and 2.3 $M_\odot$ and between 2.5 and 4.0 $M_\odot$ and chemical composition Z = 0.02, Y = 0.278. Credit: Montalbán et al. (2012)

3.5 Properties of g modes

3.5.1 Asymptotic relation of g-mode pulsators

The turning points of the g-mode cavities are determined by the condition $N_{\rm BV} = \omega$. Still in the JWKB approximation, the trapping condition for the g waves to form a standing wave is (Shibahashi, 1979)

$$\int_{r_{\rm g,in}}^{r_{\rm g,out}} k_r {\rm d}r = \left(n - \frac{1}{2} + \alpha_{{\rm g},\ell}\right)\pi, \tag{3.34}$$

where $r_{\rm g,in}$ and $r_{\rm g,out}$ are the inner and outer turning points of the g-mode cavity, and $\alpha_{{\rm g},\ell}$ is a phase term that captures the details of the boundaries of the g-mode cavity. Similarly as p modes, a proper analysis for g modes leads to the dispersion relation

$$k_r = \frac{\ell(\ell+1)}{r}\left(\frac{N_{\rm BV}^2}{\omega^2} - 1\right)^{1/2}. \tag{3.35}$$

We can also highlight a characteristic pattern for gravity waves. In the asymptotic approximation, gravity modes of degree ℓ appear with near constant separation in period. In case of a radiative core surrounded by a convective envelope, the g-mode periods $\Pi_{n,\ell}$ are given at first order by the asymptotic pattern (Tassoul, 1980; Provost and Berthomieu, 1986)

$$\Pi_{n,\ell} = \frac{\Pi_0}{\sqrt{\ell(\ell+1)}} \left(|n_g| + \frac{\ell}{2} - \frac{1}{2} - \epsilon_g \right), \tag{3.36}$$

where n_g is the radial order of gravity modes[2], ϵ_g is a term sensitive to the behaviour near the turning points of the cavity (Pinçon, Takata, and Mosser, 2019) and

$$\Pi_0 = 2\pi^2 \left(\int_{r_{in}}^{r_{out}} N_{BV} \frac{dr}{r} \right)^{-1}. \tag{3.37}$$

3.5.2 The period spacing $\Delta\Pi_\ell$

By analogy with the large separation $\Delta\nu$ of p modes, the period spacing is the period difference between modes of consecutive radial order at the same degree ℓ

$$\Delta\Pi_{n\ell} = \Pi_{n+1,\ell} - \Pi_{n,\ell}, \qquad \text{where } \Pi_{n,\ell} = 1/\nu_{n,\ell}. \tag{3.38}$$

With the asymptotic period of g modes (Eq. 3.36), we can extract the asymptotic period spacing at degree ℓ

$$\Delta\Pi_{\ell,as} = \frac{\Pi_0}{\sqrt{\ell(\ell+1)}}. \tag{3.39}$$

The asymptotic period spacing $\Delta\Pi_{\ell,as}$ is a constant parameter at a given degree ℓ for gravity modes. Then, gravity modes are evenly spaced at a given degree ℓ. In case of a radiative core, the period spacing is a direct probe of the deepest layer of stars as it expresses as an integral of the Brunt-Väisälä frequency N_{BV} over the whole g-mode cavity. This is how H-shell burning stars and He-core burning stars can be disentangled as their core have different properties and different sizes (Bedding et al., 2011; Stello et al., 2013; Mosser et al., 2014). Moreover, period spacings carry the signature of sharp variation regions of chemical composition. In red giants, these signatures can be extracted from the mode frequencies, providing valuable information of these regions (Cunha et al., 2015; Vrard and Cunha, 2019). However, in solar-like oscillators, no pure gravity modes can be observed. In red giants, only mixed-modes can be observed, hence the spacing in period deviates from the asymptotically predicted value for pure gravity modes.

3.6 Properties of mixed modes

In red giants, the asymptotic analysis must take the coupling between the acoustic and buoyancy cavities into consideration. In the JWKB approximation, the matching of the solution between the two cavities leads to the resonance condition (Shibahashi, 1979; Unno et al., 1989)

$$\tan\theta_p \cot\theta_g = q, \tag{3.40}$$

where q is an estimate of the coupling strength between the two cavities (*i.e.* $q = 0$ if the seismic waves strongly decay in the region between the cavities, $q = 1$ otherwise), θ_p and θ_g are the phase terms that depend on the properties of the p- and g-mode cavities, respectively. These phase terms quantify the closeness of the mixed modes with the associated pure p and g modes following (Mosser et al., 2012b; Deheuvels et al., 2015; Mosser et al., 2015)

[2]The radial order of gravity modes is defined by a negative integer while that of p modes is defined by a positive integer

$$\begin{cases} \theta_{\rm p} = \int_{r_{\rm p,in}}^{r_{\rm p,out}} k_r {\rm d}r = \frac{\pi}{\Delta\nu}\left[\nu - \nu_{\rm p}\right] \\ \theta_{\rm g} = \int_{r_{\rm g,in}}^{r_{\rm g,out}} k_r {\rm d}r = \frac{\pi}{\Delta\Pi_1}\left(\frac{1}{\nu} - \frac{1}{\nu_{\rm g}}\right), \end{cases} \tag{3.41}$$

where $\nu_{\rm p}$ and $\nu_{\rm g}$ are the expected frequencies of the pure p and g modes, respectively. By injecting the expressions of $\theta_{\rm p}$ and $\theta_{\rm g}$ in Eq. 3.40, we recover the asymptotic pattern of mixed modes in red giants

$$\nu = \nu_{\rm p} + \frac{\Delta\nu}{\pi}\arctan\left[q\tan\left(\pi\left[\frac{1}{\nu\Delta\Pi_1} - \frac{1}{\nu_{\rm g}\Delta\Pi_1}\right]\right)\right] \tag{3.42}$$

The previous equation is an implicit equation for ν that can be computed by iteration.

3.6.1 The mode inertia $\mathcal{I}$

The capability of a mode to be excited depends on how the mode displacement vector $\vec{\xi}$ is able to put the environment into motion. This can be quantified by the mode inertia $\mathcal{I}$, which is defined by

$$\mathcal{I} = \int_{m_{\rm in}}^{m_{\rm out}} \left|\vec{\xi}\right|^2 {\rm d}m. \tag{3.43}$$

In the previous equation, $m_{\rm in}$ and $m_{\rm out}$ are the inner and outer mass coordinates that delimit the extent of the mode cavity. Mode inertia are useful to compare the mode amplitudes. Indeed, two modes with similar degree ℓ and close frequencies show similar amplitudes only if they have close inertia, which is not the case for dipole mixed modes in red giants (Dupret et al., 2009; Grosjean et al., 2014). In fact, the coupling between the acoustic and buoyancy cavities in red giants gives rise to several modes. They can be either g-dominated or p-dominated modes depending on the difference between their frequency and the expected p- mode frequency. Due to their low inertia, the amplitude of p-dominated modes is more intense than that of g-dominated modes, p-dominated modes easily resonate relatively to g-dominated modes. Then, we can define the fraction ζ of the mode inertia that comes from the innermost layers $\mathcal{I}_{\rm g}$ relatively to the total mode inertia $\mathcal{I}_{\rm tot}$ in the star. It reads

$$\zeta = \frac{\mathcal{I}_{\rm g}}{\mathcal{I}_{\rm tot}} = \frac{\int_{m_{\rm g,in}}^{m_{\rm g,out}} \left|\vec{\xi}\right|^2 {\rm d}m}{\int_0^M \left|\vec{\xi}\right|^2 {\rm d}m}, \tag{3.44}$$

where $m_{\rm g,in}$ and $m_{\rm g,out}$ are the mass coordinates of the inner and outer turning points of the g-mode cavity, respectively. In the asymptotic analysis, it can be shown that the ratio between the mode inertia coming from the envelope $\mathcal{I}_{\rm p,as}$ and that coming from the core $\mathcal{I}_{\rm g,as}$ is (Shibahashi, 1979; Goupil et al., 2013; Deheuvels et al., 2015)

$$\frac{\mathcal{I}_{\rm p,as}}{\mathcal{I}_{\rm g,as}} = q^{-1}\frac{\cos^2\theta_{\rm g}}{\cos^2\theta_{\rm p}}\frac{\Delta\Pi_1\nu^2}{\Delta\nu}. \tag{3.45}$$

Knowing that the total inertia is the sum of the inertia coming from the core and that coming from the envelope $\mathcal{I}_{\rm tot} = \mathcal{I}_{\rm g} + \mathcal{I}_{\rm p}$, by injecting Eq. 3.45 into Eq. 3.44 we get the first-order asymptotic mode inertia fraction

$$\zeta_{\rm as} = \left(1 + \frac{\mathcal{I}_{\rm p,as}}{\mathcal{I}_{\rm g,as}}\right)^{-1} = \left[1 + \frac{1}{q}\frac{\nu^2\Delta\Pi_1}{\Delta\nu}\frac{\cos^2\left(\pi\frac{1}{\Delta\Pi_1}\left(\frac{1}{\nu} - \frac{1}{\nu_{\rm g}}\right)\right)}{\cos^2\left(\pi\frac{\nu-\nu_{\rm p}}{\Delta\nu}\right)}\right]^{-1}. \tag{3.46}$$

or equivalently (Hekker and Christensen-Dalsgaard, 2017)

$$\zeta_{\rm as} = \left[1 + \frac{q\Delta\Pi_1\nu_{\rm p}^2}{\Delta\nu}\frac{1}{q^2\cos^2\left(\pi\frac{\nu-\nu_{\rm p}}{\Delta\nu}\right) + \sin^2\left(\pi\frac{\nu-\nu_{\rm p}}{\Delta\nu}\right)}\right]^{-1}, \tag{3.47}$$

The asymptotic $\zeta_{\rm as}$ is a powerful tool to analyse the period spacings of mixed modes. Indeed, the period spacing is linked to the asymptotic mode inertia fraction via the relation

$$\Pi_{n,1} - \Pi_{n+1,1} = \zeta_{\rm as}\Delta\Pi_1. \tag{3.48}$$

The previous equation has been verified with the $\zeta_{\rm as}$ and period spacings estimates of red-giant models (see Fig. 3.6). The relative contributions of mode inertia in the core and in the envelope of the star is also linked to the mode splitting caused by rotation, providing valuable information on the core rotation rate (Mosser et al., 2015). Nevertheless, the asymptotic derivation of $\zeta_{\rm as}$ requires a slow variation of the equilibrium quantities in the JWKB method. Some sharp variation regions in the Brunt-Väisälä frequency $N_{\rm BV}$ can invalidate the hypothesis of slowly varying equilibrium quantities. In these cases, the asymptotic expression Eq. 3.46 is no longer appropriate and a more complex analysis is required (Cunha et al., 2015; Cunha et al., 2019).

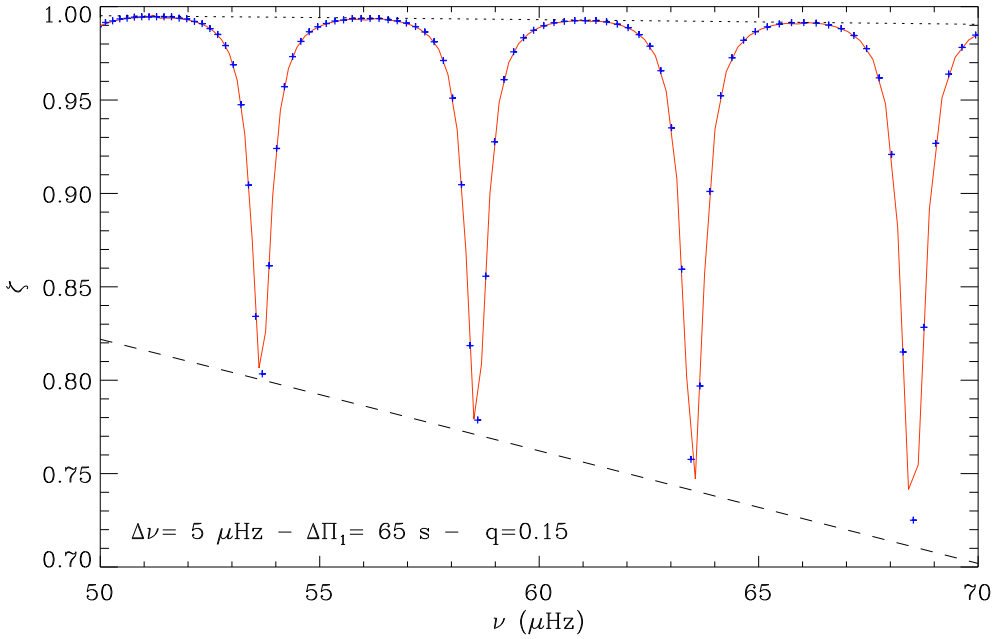

FIGURE 3.6: Ratio ζ of mode inertia in the core and that in the envelope as a function of frequency for a synthetic RGB mixed-mode spectrum. The red line shows the asymptotic value $\zeta_{\rm as}$ while the blue crosses correspond to the period spacings $\Delta\Pi_{n\ell}$ scaled to $\Delta\Pi_1$. The dashed line shows the maximum value of ζ reached by p-dominated modes while the dotted line shows the maximum value of ζ reached by g-dominated modes. Credit: Mosser et al. (2015)

3.6.2 g-dominated versus p-dominated modes

A mode is p-dominated when its frequency is close to that of an expected pure p mode while a g-dominated mode has its frequency far from a pure p-mode frequency. The number $\mathcal{N}$ of g-dominated modes associated with a given acoustic resonance at frequency $\nu_{\rm p}$ is defined by

$$\mathcal{N} = \frac{\Delta\nu}{\nu_{\rm p}^2\Delta\Pi_1}. \tag{3.49}$$

For example, the typical number of mixed modes that can be observed in a $\Delta\nu$-frequency range for a red clump star with $\Delta\nu = 3.5\,\mu$Hz and $\Delta\Pi_1 = 300\,$s at the frequency of its maximum oscillation power $\nu_{\rm max} = 28\,\mu$Hz is $\mathcal{N} = 15$. Nevertheless, the observability of gravity-dominated mixed modes is limited by the frequency resolution in the oscillation spectrum. Indeed, if these mixed modes are too close, *i.e.* the spacing between consecutive mixed modes is of the order of the frequency resolution, they overlap.

In this case, instead of forming several distinct mixed modes, they appear as a jumble of several mixed modes. Gravity-dominated mixed modes can only be observed if the condition

$$\mathcal{N} \leq \frac{1}{4q}\left(\frac{\pi}{2}\frac{\Gamma_0}{\delta\nu_{\rm res}} - 5\right) \tag{3.50}$$

is satisfied (Mosser et al., 2018), where Γ_0 is the radial mode width and $\delta\nu_{\rm res}$ is the frequency resolution.

3.7 Stochastic excitation of oscillations

3.7.1 Derivation of the stochastic and damped nature of modes

In low-mass stars with a convective envelope, near-sonic speed convective motions reach the near-surface layers. A large number of those convective cells creates an efficient source of acoustic radiation, which can transfer part of the stochastic energy to stellar modes, then excite the acoustic modes of the star. Due to the large number of convective cells, the driving is random. The mechanism of acoustic noise generation by turbulence has already been studied in fluid mechanics (*e.g.*, Lighthill, 1962). A simple analysis can be led to approach the stochastic excitation in solar-like stars (Aerts, Christensen-Dalsgaard, and Kurtz, 2010). We consider a damped linear oscillator model $\mathcal{O}(t)$ driven by a random forcing function $f(t)$ that satisfies the equation

$$\frac{\mathrm{d}^2\mathcal{O}}{\mathrm{d}t^2} + 2\eta_{n,\ell}\frac{\mathrm{d}\mathcal{O}}{\mathrm{d}t} + \omega_{n,\ell}^2\mathcal{O}(t) = f(t), \tag{3.51}$$

where $\eta_{n,\ell}$ is the damping rate and $\omega_{n,\ell} = 2\pi\nu_{n,\ell}$ is the pulsation frequency at degree ℓ and radial order n. By introducing the Fourier transforms of $\mathcal{O}$ and f

$$\tilde{\mathcal{O}}(\omega) = \int \mathcal{O}(t)\mathrm{e}^{-i\omega t}\mathrm{d}t, \qquad \tilde{f}(\omega) = \int f(t)\mathrm{e}^{-i\omega t}\mathrm{d}t, \tag{3.52}$$

we get

$$-\omega^2\tilde{\mathcal{O}}(\omega) + 2i\omega\eta_{n,\ell}\tilde{\mathcal{O}}(\omega) + \omega_{n,\ell}^2\tilde{\mathcal{O}}(\omega) = \tilde{f}(\omega). \tag{3.53}$$

In Eq. 3.52, we do not take initial transients into account in the solution so we omit the limits of integration. The power spectrum $P(\omega)$ is simply defined as the squared modulus of $\tilde{\mathcal{O}}(\omega)$, giving

$$P(\omega) = \left|\tilde{\mathcal{O}}(\omega)\right|^2 = \frac{\tilde{f}(\omega)}{(\omega_{n,\ell}^2 - \omega^2)^2 + 4\eta_{n,\ell}^2\omega^2}. \tag{3.54}$$

Eq. 3.54 represents the power spectrum that we would have from one realisation of the forcing. In fact, several realisations for the forcing of a single mode occur in a long observation window. Then, Eq. 3.51 must be averaged over several such realisations. By assuming that the damping rate $\eta_{n,\ell}$ is small relatively to the pulsation frequency $\omega_{n,\ell}$, which is valid for most solar-like oscillators including red giants, we have

$$\langle P(\omega)\rangle = \frac{1}{\omega_{n,\ell}^2}\frac{\langle\left|\tilde{f}(\omega)\right|^2\rangle}{\left(\omega - \omega_{n,\ell}\right)^2 + \eta_{n,\ell}^2}. \tag{3.55}$$

If the power spectrum of the forcing function $\langle P_f\rangle = \langle\left|\tilde{f}(\omega)\right|^2\rangle$ is a slowly varying function of frequency, then Eq. 3.55 shows that a mode can be modelled by a Lorentzian-shape function located at frequency $\nu_{n,\ell}$, of height $\mathcal{H}_{n,\ell}$, and width $\Gamma_{n,\ell}$. It reads

$$\langle P(\nu)\rangle = \frac{\mathcal{H}_{n,\ell}}{1 + 4\left(\frac{\nu-\nu_{n,\ell}}{\Gamma_{n,\ell}}\right)^2}, \tag{3.56}$$

where

$$\nu_{n,\ell} = \frac{\omega_{n,\ell}}{2\pi}, \qquad \mathcal{H}_{n,\ell} = \frac{\langle P_f(\omega)\rangle}{4\omega_{n,\ell}^2 \eta_{n,\ell}^2}, \qquad \Gamma_{n,\ell} = \frac{\eta_{n,\ell}}{\pi}. \tag{3.57}$$

In the oscillation spectrum, Eq. 3.56 tells us that the stellar modes have a mean Lorentzian profile. This is a major characteristic of solar-like modes, contrary to unstable modes observed for classical pulsators that have a square sinus cardinal shape. Owing to the stochastic excitation, modes do not show the characteristic Lorentzian profile, but a scattered profile similar to speckles of width $\delta\nu_{\rm res}$[3] randomly distributed in the mean Lorentzian profile. Nevertheless, the Lorentzian profile presented in Eq. 3.56 can be used to fit observations, then derive the mode properties as illustrated in Fig. 3.7.

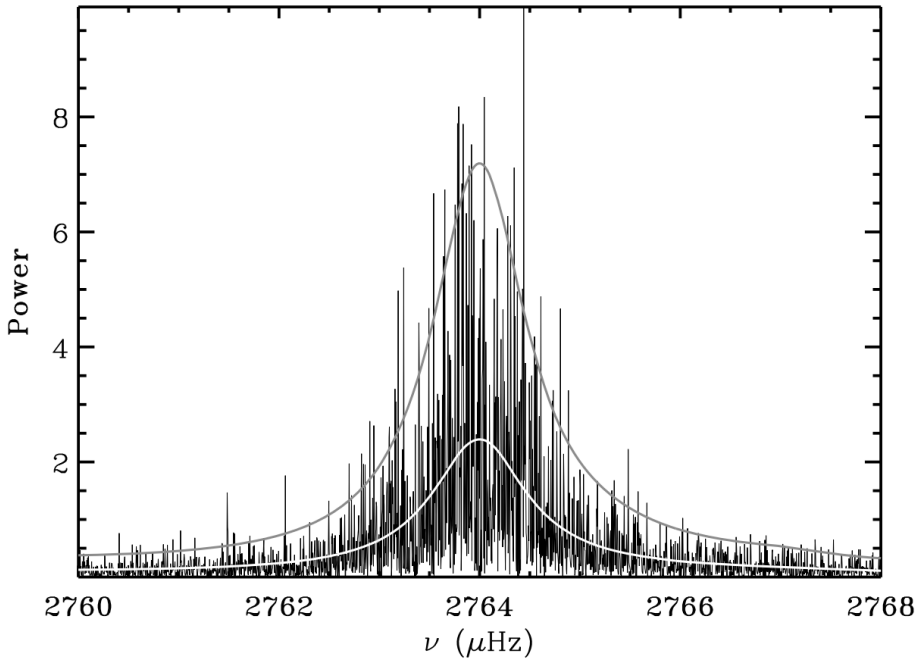

FIGURE 3.7: Solar radial mode in the oscillation spectrum from Doppler observations extending over 8 yr with BiSON (Birmingham Solar Oscillations Network). The white curve shows the fitted Lorentzian profile, and the grey curve shows the same fit multiplied by three for clarity. Data courtesy of W. J. Chaplin.

3.7.2 The mode damping

While the physical mechanism causing pressure mode excitation is identified as the Reynolds stresses (equivalently additional momentum fluxes) induced by turbulent convection (Goldreich and Keeley, 1977; Belkacem et al., 2006), the physical mechanisms behind the mode damping are not fully understood. The difficulty of identifying the main contributors to the mode damping can be illustrated by analysing the expression of the mode-damping rate. The analytic expression of the mode damping can be extracted from the perturbed system of equations 3.8, but adding the damping rate η in the perturbed physical parameters as follows

$$\delta X(\vec{r}, t) = \overline{\delta X}(\vec{r})\, \mathrm{e}^{i\omega t - \eta}, \tag{3.58}$$

where $\overline{\delta X}$ is the complex amplitude of the Lagrangian perturbation. By following the developments adopted in, Samadi, Belkacem, and Sonoi (2015), the mode-damping rate can be expressed as an integral over the mass

$$\eta = \frac{1}{2\omega \mathcal{I}} \int_0^M \mathrm{Im}\left[\frac{\delta\rho^*}{\rho}\frac{\delta P}{\rho}\right] \mathrm{d}m, \tag{3.59}$$

[3] the spectral resolution $\delta\nu_{\rm res}$ is linked to the duration of the time series T through $\delta\nu_{\rm res} = 1/T$

where Im denotes the imaginary part, the exponent '*' refers to the complex conjugate, $\delta\rho$ and δP are the Lagrangian perturbations of the density and the pressure, respectively. Equation 3.59 can be developed further to emphasise four main contributors as follows

$$\eta = \eta_{\rm turb} + \eta_{\rm conv} + \eta_{\rm rad} - \eta_{\rm diss}. \tag{3.60}$$

The first term $\eta_{\rm turb}$ corresponds to the turbulent pressure, created by the perturbation of the Reynolds stress tensor[4] and induced by the turbulent convection. The second term $\eta_{\rm conv}$ is the damping associated to the perturbation of the convective heat flux. This contribution depends on the coupling between the oscillation and convection, *i.e.* the perturbation induced by the oscillations on convection and consequent feedback of perturbed convection on oscillations. The third contribution $\eta_{\rm rad}$ comes from the perturbation of the radiative flux caused by the temperature fluctuations δT. Finally, the fourth term $\eta_{\rm diss}$ is associated to the perturbation of the dissipation rate of turbulent kinetic energy into heat that acts to compensate the perturbation of the turbulent pressure.
Eq. 3.60 contains what are considered as the main contributors to mode damping in solar-like pulsators. Their weights have been investigated in several studies (see *e.g.*, Gough, 1980; Goldreich and Kumar, 1991; Balmforth, 1992; Dupret et al., 2006; Belkacem et al., 2012), but their relative contributions and possible cancellations are still under debate. Moreover, additional possible sources of damping have been investigated (*e.g.*, Houdek et al., 1999). Accordingly, mode properties need to be extracted from observations to constrain stellar models and help to identify the relevant contributors in mode damping.

3.7.3 The mode energy

In the following, we admit that the conservation equation for the mean mode energy $E_{n,\ell}$ is ruled by the driving $\mathcal{P}$ and the damping $\mathcal{D}$ following (Samadi, Belkacem, and Sonoi, 2015)

$$\frac{{\rm d}E_{n,\ell}}{{\rm d}t} = \mathcal{P} + \mathcal{D}, \tag{3.61}$$

where the mode energy is defined by

$$E_{n,\ell} = \int \rho_0 \vec{v_{n,\ell}}^2(\vec{r},t){\rm d}^3\vec{r}, \tag{3.62}$$

and $\vec{v_{n,\ell}}$ is the mode velocity. The driving $\mathcal{P}$ is the energy that a given source provides to a mode by unit of time while the damping $\mathcal{D}$ is the energy lost by the mode per unit of time. Damping and driving occur on two different time scales, so they can be studied separately in time. By assuming a constant and linear damping on a time scale much larger than the characteristic time of mode driving, we have (Samadi, Belkacem, and Sonoi, 2015)

$$\frac{{\rm d}\vec{v_{n,\ell}}(t)}{{\rm d}t} = -\eta_{n,\ell}\vec{v_{n,\ell}}(t), \tag{3.63}$$

where the time derivative is performed over a time scale much larger than the characteristic time over which the driving occurs. We can infer that the mode damping term $\mathcal{D}$ is obtained by combining the time derivative of Eq. 3.62 with Eq. 3.63:

$$\frac{{\rm d}E_{n,\ell}}{{\rm d}t}(t) = \mathcal{P} - 2\eta_{n,\ell}E_{n,\ell}(t). \tag{3.64}$$

Unlike classical pulsators, solar-like pulsators show stable oscillations over time. This implies that the mean mode energy cannot grow on time scales that are much larger than the characteristic times of the driving and damping processes, *i.e.* ${\rm d}E_{n,\ell}/{\rm d}t = 0$ for any t longer than the two time scales. Finally, the

[4]The Reynolds stresses are the second terms of the total turbulent stress tensor given by $\sigma^*_{ij} = \overline{\sigma_{ij}} - \rho\overline{u'_i u'_j}$, where i, j refer to the spatial coordinates, $\overline{\sigma_{ij}}$ are the mean components of the stress tensor, the terms u'_i are the unsteady components of the velocity field with zero time average, and the overline indicates that the parameters are averaged over a period more larger than that of the turbulent fluctuations.

steady state implies that the mean mode energy is determined by the balance between the driving and the damping following

$$E_{n,\ell} = \frac{\mathcal{P}}{2\eta_{n,\ell}}. \tag{3.65}$$

In parallel, it can be shown that the mean mode energy can be related to the mode amplitude following

$$E_{n,\ell} = \frac{1}{2} A^2_{n,\ell} \mathcal{I}_{n,\ell} \omega^2_{n,\ell}, \tag{3.66}$$

where $A^2_{n,\ell}$ is the mean squared amplitude of the mode and $\mathcal{I}$ is the mode inertia (see Sect. 3.6.1). By injecting Eq. 3.66 in Eq. 3.65, we see that the driving term is related to the mean mode amplitude following

$$A^2_{n,\ell} = \frac{\mathcal{P}}{\eta_{n,\ell} \mathcal{I}_{n,\ell} \omega^2_{n,\ell}}. \tag{3.67}$$

Accordingly, the mode amplitude is a valuable information to constrain the driving mechanism. However, the former also depends on the mode damping $\eta_{n,\ell}$, the mode inertia $\mathcal{I}$, and the pulsation frequency $\omega_{n,\ell}$: the higher those parameters, the smaller the mode amplitude. When the frequency resolution and the signal-to-noise ratio are satisfactory, the oscillation modes can be meticulously characterised through their frequency $\nu_{n,\ell}$, height $\mathcal{H}_{n,\ell}$, and width $\Gamma_{n,\ell}$. Also, the mean squared mode amplitude can be measured on the oscillation spectrum as it corresponds to the value of the integral along the mode profile. In the case of a Lorentzian profile with the notation introduced in Eq. 3.56, we have

$$A^2_{n,\ell} = \pi \mathcal{H}_{n,\ell} \Gamma_{n,\ell}. \tag{3.68}$$

In practice, the mode profile is modified by several factors such as the observational technique and geometrical effects. When measuring the mode amplitude in observation data, a multiplicative factor $\mathcal{C}_{\text{obs}}$ is necessary to quantify these effects.

3.7.4 Mode visibility

In observations, the energy is not equally distributed between modes of different degree ℓ. This implies that in an observation time series, modes of different degree ℓ do not have the same amplitude, noted A_ℓ. Consequently, at a given observation duration some modes may be visible while others are not intense enough to be detected. This leads us to define visibility factors, noted V^2_ℓ, as the ratio between the mode amplitude of degree ℓ and that of the radial mode $\ell = 0$,

$$V^2_\ell = \frac{A^2_\ell}{A^2_0}. \tag{3.69}$$

The visibility factor depends on geometrical factors, particularly the angle $\widehat{MCO}$, where M is the considered point at the stellar surface, C is the stellar centre, and O is the observer (Gizon and Solanki, 2003). The higher the amplitude of the radial displacement vector relatively to that of the horizontal displacement vector, the higher the visibility factor. Typically, in red giants we have $V^2_0 = 1$ by definition, $V^2_1 \simeq 1.5$, $V^2_2 \simeq 0.6$, and $V^2_3 \simeq 0.1$ (Ballot, Barban, and van't Veer-Menneret, 2011). Despite the unequal energy distribution in modes of different degree ℓ, because of the symmetry of a star in spherical equilibrium without rotation and magnetic field the energy equipartition should be satisfied between modes of even and odd degrees. Since mainly radial, dipole, quadrupole, and octupole modes are visible in the oscillation spectrum of red giants, the energy equipartition reads

$$V^2_0 + V^2_2 = V^2_1 + V^2_3. \tag{3.70}$$

Any departure from this equality suggests that non-symmetric mechanisms are present, differently affecting the mode visibility depending on the degree ℓ. For instance, in red giants the presence of a strong magnetic field can cause an additional dissipation of dipole modes in the core, which leads to lower dipole mode visibility and breaks the energy equipartition (*e.g.*, Fuller et al., 2015; Stello et al., 2016a; Cantiello, Fuller, and Bildsten, 2016; Bugnet et al., 2021).

3.7.5 Relation between properties of pure pressure and gravity-dominated modes

Due to the high mode inertia of g-dominated modes in the core (see Fig. 3.6), the g-mode amplitude and width are weaker than those of the pure pressure modes. However, the properties of the pure p and g-dominated modes can be related thanks to the ζ factor. By labelling the properties of the pure p modes with a 'p' and those of g-dominated modes with 'g', we extract the ratio between the amplitudes of pure p- and g-dominated dipole ($\ell = 1$) modes using Eq. 3.67. This relation reads (Benomar et al., 2014)

$$\frac{A_{1,g}^2}{A_{1,p}^2} = \frac{\mathcal{P}_{1,g}}{\mathcal{P}_{1,p}} \frac{\Gamma_{1,p}}{\Gamma_{1,g}} \frac{\mathcal{I}_{1,p}}{\mathcal{I}_{1,g}}, \tag{3.71}$$

where we assume that the frequencies $\nu_{1,p}$ and $\nu_{1,g}$ are very close to each other (typically $\left|\nu_{1,p} - \nu_{1,g}\right| \leq \Delta\nu/2$). In this case, the shape of the eigenfunctions in the upper layers are very similar (*i.e.* $|\vec{\xi_{1,p}}(R)| = |\vec{\xi_{1,g}}(R)|$). This implies that (Dupret et al., 2009)

$$\mathcal{P}_{1,p}\mathcal{M}_{1,p} = \mathcal{P}_{1,g}\mathcal{M}_{1,g}, \tag{3.72}$$

where we introduced the mode mass $\mathcal{M} = \mathcal{I}/|\vec{\xi}(R)|^2$. Eq 3.72 shows that at similar frequencies the work done by the driving source on the modes is the same. Since $|\vec{\xi_{1,p}}(R)| = |\vec{\xi_{1,g}}(R)|$, the mode inertia is proportional to the mode mass and Eq. 3.71 leads to

$$\frac{\mathcal{M}_{1,g}}{\mathcal{M}_{1,p}} \simeq \frac{\mathcal{I}_{1,g}}{\mathcal{I}_{1,p}} = \frac{A_{1,p}}{A_{1,g}} \sqrt{\frac{\Gamma_{1,p}}{\Gamma_{1,g}}}. \tag{3.73}$$

The previous equation shows that the ratio of mode inertia can be extracted from the properties of the pure pressure mode and its neighbouring g-dominated mixed mode. In red giants where the mode is either evanescent or of acoustic type in the envelope above the core, the mode inertia ratio $\mathcal{I}_{1,g}/\mathcal{I}_{1,p}$ can be related to the ζ factor following Goupil et al. (2013) and Benomar et al. (2014)

$$\frac{\mathcal{I}_{1,g}}{\mathcal{I}_{1,p}} = \frac{1}{1-\zeta}. \tag{3.74}$$

Finally, Eq. 3.73 allows us to directly relate the width and amplitude of pure pressure and g-dominated modes. Those properties are related following

$$\Gamma_{1,p} = \frac{\Gamma_{1,g}}{1-\zeta}, \qquad A_{1,p} = \frac{A_{1,g}}{\sqrt{1-\zeta}}. \tag{3.75}$$

By measuring the mixed mode properties, *i.e.* the ζ factor, the width $\Gamma_{1,g}$ and amplitude $A_{1,g}$, we can infer the properties a mode would have in the hypothesis that it was a pure pressure mode.

3.8 Overview of stellar oscillation through evolution

3.8.1 During the main sequence

The nature of oscillations observed in main-sequence stars depends on their mass. Indeed, stars with a mass $M \leq 1.2\,M_\odot$ have a radiative core surrounded by a convective envelope while stars with a mass $M \geq 1.2\,M_\odot$ possess a convective core surrounded by a radiative envelope and a near-surface

convective layer. As a consequence, we can define three type of pulsators for stars with a mass $M \leq 2.5\,M_\odot$: solar-like stars, γ Doradus stars, and δ Scuti stars. Solar-like pulsators exhibit stable oscillations with a clear p-mode pattern, which are predicted for the lowest mass main-sequence stars up to stars situated near the cool edge of the classical instability strip (see Fig. 1.4) with masses near about $1.6\,M_\odot$ (Christensen-Dalsgaard, 1982; Houdek et al., 1999). As for γ Doradus stars that have a mass $M \in [1.5, 1.8]\,M_\odot$, they show stable oscillations associated to high order non-radial g modes. Finally, oscillations in δ Scuti stars are unstable as they are situated in the instability region of stellar oscillation where the classical instability strip crosses the main sequence (see Fig. 1.4). Their class members with masses in the range $1.5 - 2.5\,M_\odot$ exhibit p modes in their oscillation spectrum, both radial and non radial. Their oscillation pattern is complex as their modes have variable amplitudes from non-linear resonant mode coupling, making their identification challenging (*e.g.*, Breger et al., 1999; Arentoft et al., 2001; Breger and Pamyatnykh, 2006). As illustrated in Fig. 3.3, the inner cavity is uncoupled to the outer cavity in the frequency range of observable modes since the modes that develop in those cavities have different frequencies.

3.8.2 After the main sequence

When stars with a mass $M \geq 1.2\,M_\odot$ leave the main sequence and reach the RGB, the radiative envelope gradually fades to give rise to a convective envelope. As a consequence, the p-mode cavity extends up to the stellar surface while the g-mode cavity is confined to the deep layers. At this stage, g modes are no longer visible in the oscillation spectrum. Nevertheless, as the base of the convective zone recedes and the envelope expands, the frequency range of observable modes decreases up to a point where it corresponds to the frequency range of high order g modes in the g-mode cavity (see right panel of 3.3). Then, the waves that propagate in both cavities can couple and give rise to mixed modes. Both radial modes and mixed non-radial modes are visible in the oscillation spectrum of red giants, as depicted by Fig. 3.8. In this figure, we notice that the higher the star on the RGB, the less visible the mixed modes are. The disappearance of mixed modes is due to the combination of two factors. First, the radiative contribution to the damping (see Eq. 3.60) increases through evolution, so the modes in the g-mode cavity are efficiently damped and the gravity-dominated mixed modes cannot reach the stellar surface with a sufficiently high amplitude to be detected. Second, the coupling between the two cavities decreases due to the core contraction and the envelope expansion. Consequently, non-radial modes visible in the oscillation spectrum are pressure-dominated modes for high-luminosity RGB stars.

Once helium burning sets on, the coupling between the p- and g-mode cavities gets stronger, the core expands and the envelope dilates to such an extent that the evanescent region between the g- and p-mode cavities gets thinner. As a result, mixed modes become detectable again during the He-core burning phase. These mixed modes bring crucial information since they allow for an effective classification between He-burning stars (including clump and AGB stars) and H-shell burning stars (further details in Chapter 5). Finally, when the helium supply is exhausted, the star enters the AGB phase, the core contracts and the envelope dilates. The coupling between the inner and outer cavities decreases and mixed modes slowly disappear in the oscillation spectrum, leaving solely the p-dominated non radial modes detectable. Then, distinguishing RGB and AGB stars is challenging. In my thesis, we intend to identify the physical basis on which RGB and AGB stars can be disentangled (see Chapters 5, 8). To this end, I perform a comprehensive analysis of the oscillation spectrum of RGB and AGB stars. I extract the seismic parameters that characterise the p-mode pattern in Chapters 6, 7 and look for signatures of stellar evolution in Chapter 8. Besides, part of my work is dedicated to the study of the mode damping on the AGB in Chapter 9. I aim at measuring the mode properties of radial and p-dominated non-radial modes that would help to identify the main contributors to mode damping on the AGB, in analogy with the analysis performed on the RGB (Vrard et al., 2018).

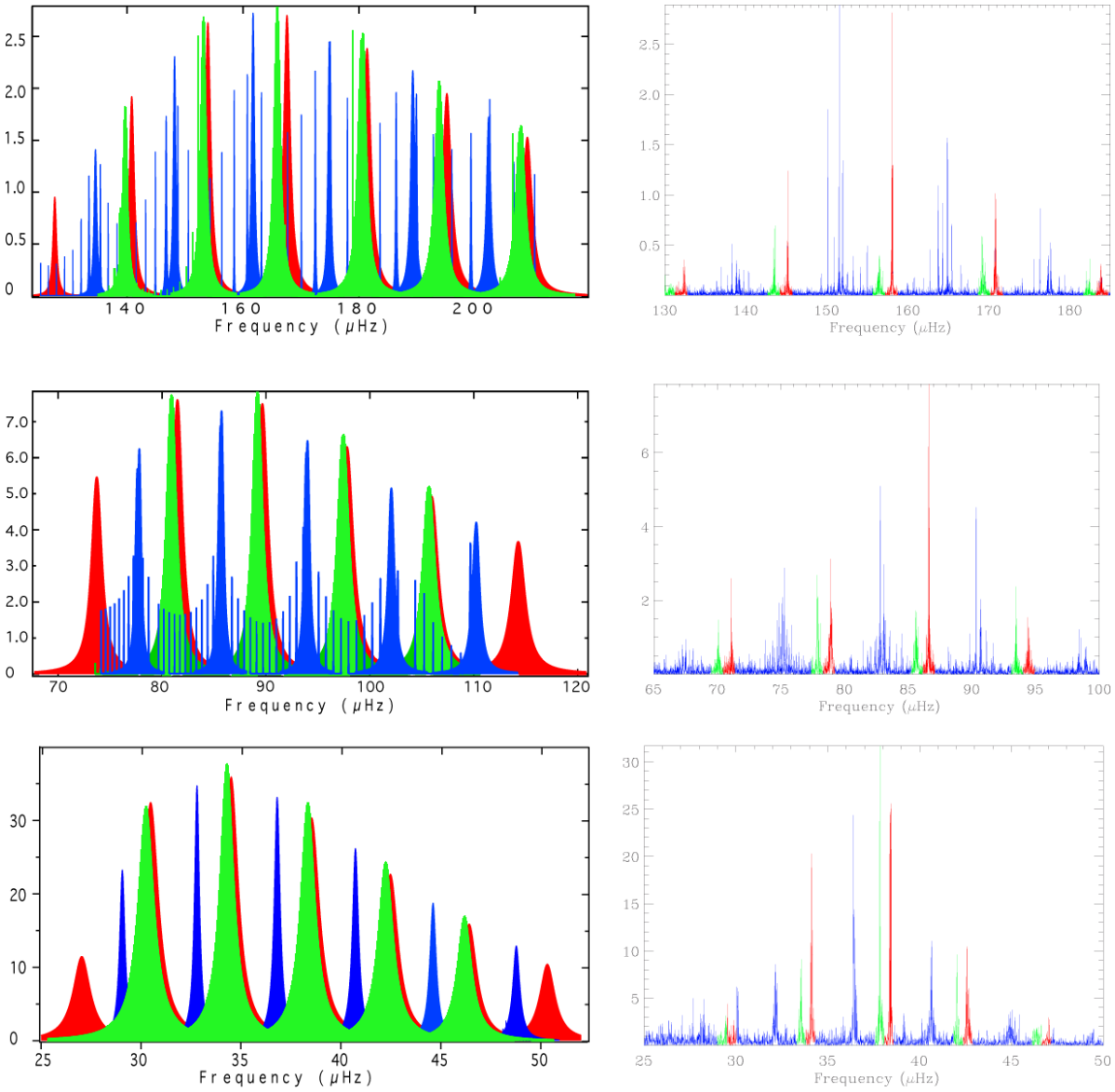

FIGURE 3.8: Theoretical (**left**) and observed (**right**) power spectra of *Kepler* RGB stars. Radial, dipole, and quadrupole modes are indicated in red, blue, and green, respectively. The width of pressure-dominated dipole modes is large relatively to that of mixed dipole modes. The theoretical models are computed for RGB stars of mass 1.5 $M_{\odot}$, the panels are ordered in increasing age from top to bottom. At a given row, the theoretical and observed power spectral density have similar $\Delta\nu$, $\nu_{\rm max}$, and M. The heights in the theoretical power spectral density are given in $\mathrm{m}^2.\mathrm{s}^{-2}.\mu\mathrm{Hz}^{-1}$ while those in the observed spectra are given in $\mathrm{ppm}^2.\mu\mathrm{Hz}^{-1}$ divided by a factor 6000 to have similar scales with the theoretical spectra. **Top:** $\Delta\nu = 14.1\,\mu$Hz, $\nu_{\rm max} = 190\,\mu$Hz, **Middle:** $\Delta\nu = 8.4\,\mu$Hz, $\nu_{\rm max} = 97\,\mu$Hz, **Bottom:** $\Delta\nu = 4\,\mu$Hz, $\nu_{\rm max} = 37\,\mu$Hz. Credit: Grosjean et al. (2014)

Chapter 4

Structural discontinuities in stellar interiors

As presented in Chapter 3, the asymptotic analysis provides valuable tools to decipher the oscillation spectrum of solar-like oscillations. Since seismic parameters depend on the radial profile of physical parameters such as the sound speed, density, and temperature, they offer the possibility to probe the stellar structure. Nevertheless, the asymptotic analysis assumes that the gradients of these physical parameters are not important, *i.e.* these parameters do not change on a scale substantially smaller than the wavelength of the oscillations. Yet, sharp variations of physical quantities are clearly present and their effects are detectable in the oscillation spectrum of solar-like stars. In this chapter, we consider the deviations to the asymptotic analysis induced by such strong gradients in stellar interiors.

4.1 What is a glitch?

Specific localised events in stellar interiors can generate sharp variations in the radial profile of physical parameters, especially the first adiabatic exponent Γ_1 (equivalently the sound speed c_s)

$$\Gamma_1 = \left(\frac{\partial \log P}{\partial \log \rho}\right)_{\rm ad} = c_s^2 \frac{\rho}{P}, \tag{4.1}$$

where $c_s = \sqrt{(\partial P/\partial \rho)_{\rm ad}}$. These sharp variations take place on a scale that is smaller than the local wavelength of the seismic oscillations (Gough, 1990), to the extent that the seismic wave"see" the environment changes while propagating. These sharp features are called *glitches* (Gough, 2002; Cunha et al., 2015) and cause a shift in the mode frequencies with respect to the asymptotic pattern of p modes (Eq. 3.18), g modes (Eq. 3.36), or mixed modes (Eq. 3.42). This shift is a frequency-dependent modulation so the mode frequencies are not equally affected, as illustrated in Fig. 4.1. Characterising this modulation allows for obtaining information on the glitch characteristics. The period of the modulation depends on the location of the feature, while its amplitude depends on the amplitude of the structural glitch (Gough, 1990; Monteiro, Christensen-Dalsgaard, and Thompson, 1994; Basu et al., 2004; Houdek and Gough, 2007; Cunha et al., 2015). Glitches can be efficiently probed by combination of frequencies that are sensitive to gradients of composition or sound speed like the large frequency separation $\Delta\nu$ (Eq. 3.23) or the reduced small frequency separations (Eq. 3.30).

4.2 Measuring the glitch effects

4.2.1 The observation of glitch signatures

The existence of such sharp variation regions has been first predicted (Vorontsov, 1988; Gough, 1990). Theoretical studies showed that the signature of glitches provides valuable information on the region where they lie. Some of them started to investigate the existence of an overshooting region in the Sun through the signature of the base of the convective envelope, where a strong composition gradient hence sound speed gradient is expected (Christensen-Dalsgaard, Gough, and Thompson, 1991; Monteiro, Christensen-Dalsgaard, and Thompson, 1994). In parallel, other theoretical studies explored the potential of the helium ionisation zone signature to constrain the helium abundance in the envelope (Dziembowski, Pamiatnykh, and Sienkiewicz, 1991; Perez Hernandez and Christensen-Dalsgaard,

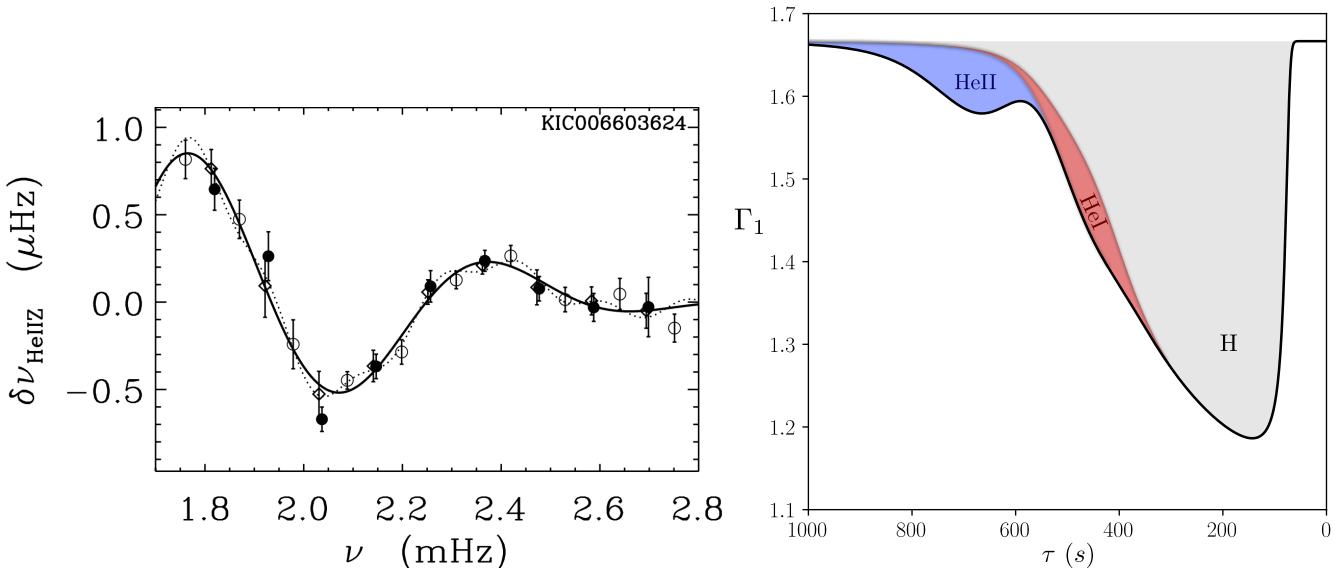

FIGURE 4.1: **Left:** Modulation in frequency induced by the helium second-ionisation zone. The points correspond to $\ell = 0$ (black circles), $\ell = 1$ (open circles), $\ell = 2$ (diamonds). The solid line shows a fit to the modulation induced by the helium second-ionisation zone and the dotted line is the same fit but including the effects of the base of the convective zone. Credit: Mazumdar et al. (2014). **Right:** Typical Γ_1 profile in the ionisation region as a function of the acoustic depth τ relatively to the surface ($\tau = 0$ is the surface). The contributions of the three main ionisation zones are shown, *i.e.* , the hydrogen (H), the first (HeI), and helium second ionisation (HeII) zones. They cause a deviation from the standard value 5/3. Credit: Houdayer et al. (2021)

1994; Monteiro and Thompson, 2005). The signatures of these sharp variation regions have been first confirmed for the Sun (Ballot, Turck-Chièze, and García, 2004; Houdek and Gough, 2007), then for main-sequence stars (Lebreton and Goupil, 2012; Mazumdar et al., 2012; Mazumdar et al., 2014; Verma et al., 2014; Deheuvels et al., 2016), and for red giants (Miglio et al., 2010; Broomhall et al., 2014; Vrard et al., 2015; Corsaro, De Ridder, and García, 2015). In the case of red giants, the dominant glitch has its origin in the helium second-ionisation zone. As the base of the convective zone sinks toward the deep interior in red giants, the effects of this sharp feature is no longer visible in the mode frequencies. Instead, effects of buoyancy glitches have been highlighted near the core of red giants both with theoretical models and *Kepler* observations (Cunha et al., 2015; Vrard and Cunha, 2019). In this chapter, we focus on the helium second ionisation (HeII) zone located in the envelope. This sharp feature in the sound speed profile impacts the stellar modes that develop in the envelope, *i.e.* p modes, which justifies their designation as acoustic glitches.

4.2.2 Probing the properties of the helium second-ionisation zone

Theoretical studies aimed at finding links between the helium second-ionisation zone signature and the properties of the stellar envelope, where the helium ionisation zone lies. Indeed, the signature of the HeII zone can be exploited to extract the helium abundance of the envelope of low-mass stars (Basu et al., 2004; Houdek and Gough, 2007). The amplitude of the glitch signature has been tested as an indirect way to estimate the helium abundance in main-sequence stars (Verma et al., 2014; Verma et al., 2019) and in red giants (Broomhall et al., 2014; Dréau et al., 2020). The asteroseismic estimates of helium abundance are valuable since the spectroscopic determination of this quantity is not possible for low-mass stars. Their effective temperature is not high enough for the helium to be excited, and He-absorption lines cannot be detected. Nonetheless, expressing the signature of the HeII zone in terms of helium abundance is not an easy task since the theoretical connection between these quantities is not straightforward, *i.e.* other parameters influence the signature of the HeII zone. Houdayer et al. (2021) could derive an analytical expression of Γ_1 from thermodynamic relations, including chemical

equilibrium between ionised species of hydrogen and helium in stellar interiors. They showed that the profile of Γ_1 can be expressed in the presence of the hydrogen and helium ionisation zones as

$$\Gamma_1 = \frac{5}{3} - \frac{2}{3}\gamma_1\left(Y_s, \psi_{CZ}, \varepsilon_H\right), \tag{4.2}$$

where γ_1 is a term with a complex expression depending on several parameters. Among them, there are the helium mass fraction at the surface Y_s, the electron degeneracy parameter ψ_{CZ} [1] from the centre up to the ionisation region, and the parameter ε_H that is the ratio between the ionisation energy for the hydrogen (13.6 eV) and the thermal energy at the centre. The effects of those physical parameters on the Γ_1 profile are shown in Fig. 4.2.

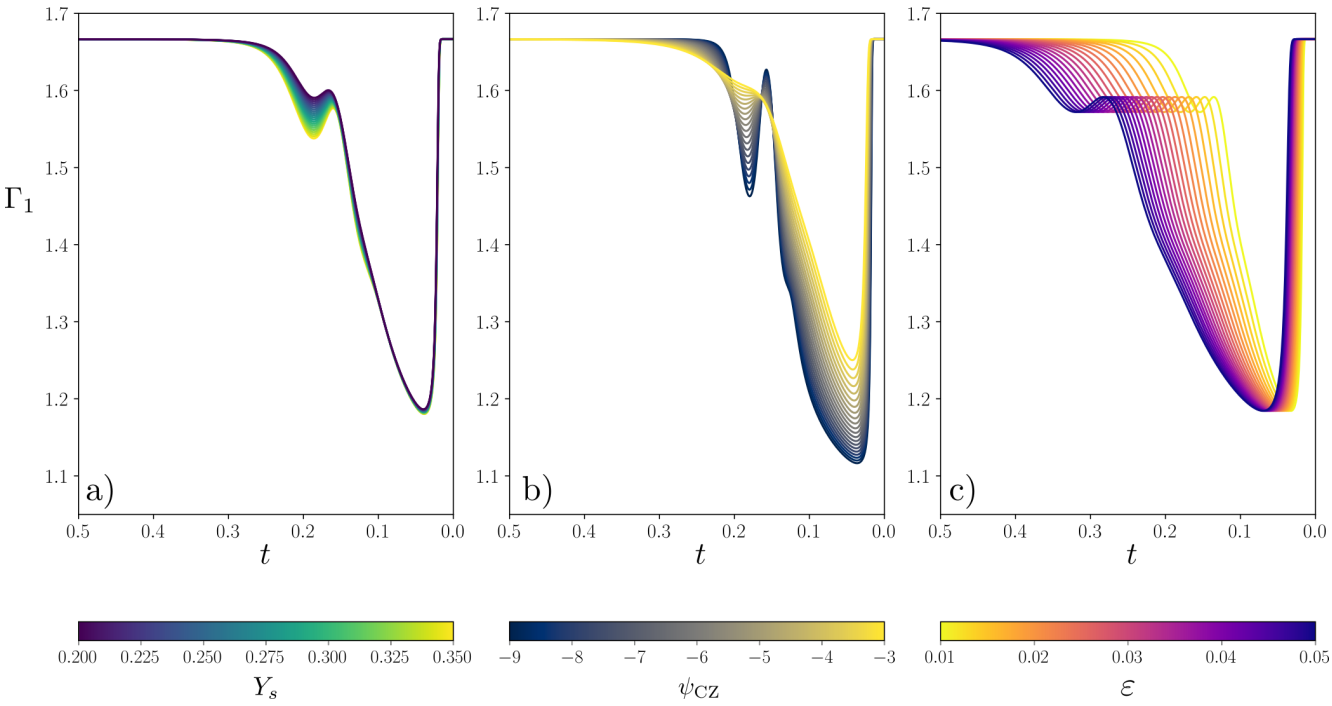

FIGURE 4.2: Γ_1 profiles as a function of the acoustic depth t relatively to the surface ($t = 0$ is the surface) by considering various sets (Y_s, ψ_{CZ}, ε_H) that cover the range of values encountered in solar-like pulsators. **(a)** Dependence of the profile on Y_s, **(b)** dependence of the profile on ψ_{CZ}, and **(c)** dependence of the profile on ε_H. Figure courtesy of Pierre Houdayer.

The surface helium abundance clearly impacts the strength of the Γ_1 variations in the helium ionisation zone, as does the electron degeneracy ψ_{CZ}. The parameter ε_H controls the location where helium ionisation takes place. As a result, these physical parameters are related to the location, the width, and the amplitude of the helium second-ionisation zone. This induces a shift in the mode frequencies that can be expressed as (Houdek and Gough, 2007; Houdayer, Reese, and Goupil, 2022)

$$\delta\omega^2 = \frac{\int_V \frac{\delta_x\Gamma_1}{\Gamma_1}\rho c_s^2(\vec{\nabla}.\vec{\xi})^2 \mathrm{d}V}{\int_V \rho\left|\vec{\xi}\right|^2 \mathrm{d}V}, \tag{4.3}$$

where V is the volume, $\vec{\xi}$ is the displacement vector, and $\delta_x\Gamma_1$ is the perturbation of Γ_1 relatively to the model without glitch at fixed normalised radius $x = r/R$. Equation 4.3 precisely quantifies the frequency shift in response to a perturbation of stellar structure caused by the helium ionisation. However, the use of this expression is not suited for the analysis of observational data because it requires the knowledge of the perturbation of Γ_1 from a reference model. This reference model is defined in the

[1] the analytical expression is $\psi_{CZ} = \ln(n_e\lambda_e^3/2)$, where n_e is the electron volume density and λ_e is the de Broglie wavelength.

absence of the helium glitch, and cannot be extracted from observations.

Instead of using these complex expressions, the perturbation in Γ_1 can be modelled by a parameterised function. Several theoretical works aimed at modelling the shape of the induced structural perturbation, as illustrated in Fig. 4.3. Assuming a model-dependent perturbation of the glitch structure significantly simplifies the problem. In this scenario, the glitch parameters cannot be directly interpreted in terms of internal structure parameters. For instance, several parameters play a role in the amplitude of the variations in the Γ_1 profile, as depicted by Fig. 4.2, so the knowledge of the glitch amplitude does not guarantee precise constraints for stellar parameter such as the helium abundance. Nevertheless, the use of these model dependent perturbations allows us to derive an expression of the signature in mode frequencies. The most commonly used model is a Gaussian perturbation (see Fig. 4.3), which reads (Houdek and Gough, 2007)

$$\frac{\delta\Gamma_1}{\Gamma_1} = -\frac{1}{\sqrt{2\pi}}\frac{\Gamma_{\rm HeII}}{\Delta_{\rm HeII}} e^{-\frac{(\tau-\tau_{\rm HeII})^2}{2\Delta^2_{\rm HeII}}}, \tag{4.4}$$

where $\Delta_{\rm HeII}$, $\Gamma_{\rm HeII}$, and $\tau_{\rm HeII}$ are the standard deviation, the area, and the acoustic depth from the surface of the distribution, respectively. This Γ_1 perturbation yields the expression of the frequency shift

$$\delta\nu = \mathcal{A}_{\rm HeII}\,\nu\, e^{-8\pi^2\Delta^2_{\rm HeII}\nu^2}\cos\left[2\left(2\pi\tau_{\rm HeII}\nu + \varepsilon_{\rm HeII}\right)\right], \tag{4.5}$$

where $\mathcal{A}_{\rm HeII} = \Gamma_{\rm HeII}\,\Delta\nu_{\rm as}$, and $\varepsilon_{\rm HeII}$ is a phase term that captures the phase changes of the seismic wave at the upper turning point of the cavity. Equation 4.5 can then be used to extract the signature of the helium second-ionisation zone in observational data, as shown in Fig. 4.1. Nevertheless, a meticulous work is needed to interpret the observed glitch signatures in terms of stellar properties because of the model dependent treatment.

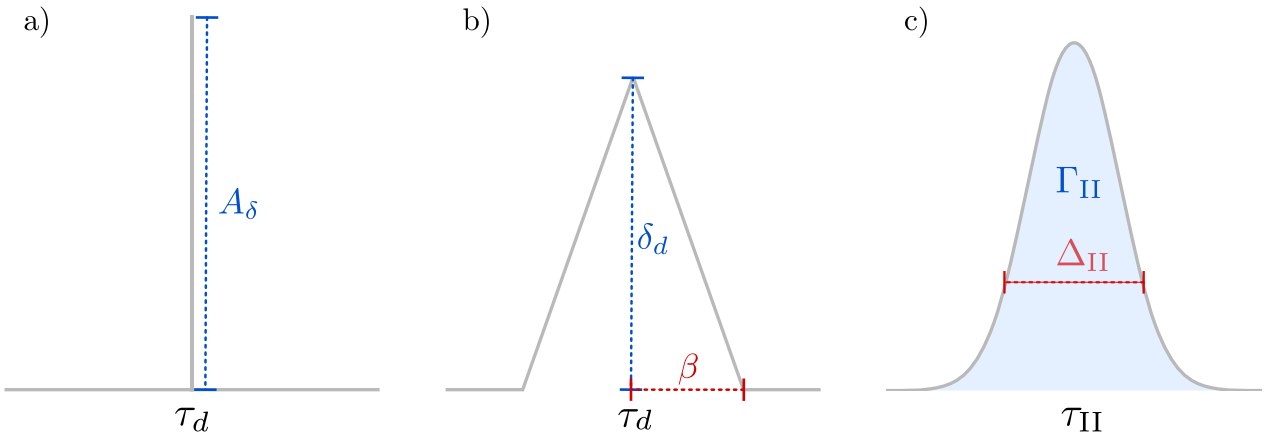

FIGURE 4.3: Shape of the parameterisations that are used to describe a structural perturbation. **(a)** Dirac function used in Monteiro, Christensen-Dalsgaard, and Thompson (1994) to model the variations in the acoustic potential (in presence of an overshooting region) passing from a radiative to a convection region. The sharp feature is modelled by a discontinuity of amplitude A_δ at the acoustic depth τ_d from the surface. **(b)** Triangular function used to reproduce the Γ_1 variations induced by the helium second-ionisation zone (Monteiro and Thompson, 2005). An additional parameter is necessary, which is the width β of the Γ_1 perturbation. **(c)** Gaussian function of the Γ_1 perturbation induced by the helium second-ionisation zone (Houdek and Gough, 2007). The parameters $\Delta_{\rm II}$ and $\Gamma_{\rm II}$ are the standard deviation and the area of the distribution, respectively. Credit: Houdayer et al. (2021)

4.3 The helium ionisation signature in low- and intermediate-luminosity red giants

4.3.1 Extracting the glitch signature

As described in the previous sections, the helium second-ionisation zone introduces a modulation term to the mode frequencies relatively to the asymptotic pattern given by Eq. 3.20. By including the glitch contribution to the universal pattern of p modes in red giants, Eq. 3.20 can be rewritten

$$\nu_{n,\ell} = \left(n + \frac{\ell}{2} + \varepsilon - d_{0\ell} + \frac{\alpha_{\rm curv}}{2} \left[n - n_{\rm max} \right]^2 + d^{\rm gl}_{n,\ell} \right) \Delta\nu, \tag{4.6}$$

where $d^{\rm gl}_{n,\ell}$ is the glitch modulation induced in mode frequencies. For example, the glitch contribution to the radial mode frequencies used by Vrard et al. (2015) has a constant amplitude, as follows

$$d^{\rm gl}_{n,0} = \frac{\mathcal{A}_{\rm HeII}\, \mathcal{G}_{\rm HeII}}{2\pi} \sin\left(2\pi \frac{n - n_{\rm max}}{\mathcal{G}_{\rm HeII}} + \Phi_{\rm HeII} \right), \tag{4.7}$$

where $\mathcal{A}_{\rm HeII}$ and $\mathcal{G}_{\rm HeII}$ are the amplitude and period of the modulation in units of $\Delta\nu$, and $\Phi_{\rm HeII}$ is the phase of the modulation centred on $n_{\rm max} = \nu_{\rm max}/\Delta\nu - \varepsilon$. However, the modulation term $d^{\rm gl}_{n,0}$ arises from a small perturbation to the reference model in the absence of the helium ionisation zone. Consequently, the modulation signal in the mode frequencies due to the sharp variations of the sound speed caused by HeII is very small relatively to the leading order terms in Eq. 3.20. To enhance the glitch signature, we can work with combinations of frequencies. For instance, Vrard et al. (2015) highlighted the glitch signature in the local large frequency separation

$$\Delta\nu_{n,\ell} = \frac{\nu_{n+1,\ell} - \nu_{n-1,\ell}}{2}. \tag{4.8}$$

computed with radial ($\ell = 0$) modes only. By assuming that the value of $\Delta\nu_{n,\ell}$ is given by the sum of two terms: one from the universal pattern of red giants Eq. 3.20 noted $\Delta\nu^{\rm RG}_{n,\ell}$ and the other from the glitch signature $\delta\Delta\nu^{\rm gl}_{n,\ell}$, we have

$$\delta\Delta\nu^{\rm gl}_{n,\ell} = \Delta\nu_{n,\ell} - \Delta\nu^{\rm RG}_{n,\ell}, \tag{4.9}$$

where

$$\Delta\nu^{\rm RG}_{n,\ell} = \left(1 + \alpha_{\rm curv} \left(n - n_{\rm max} + \frac{1}{2} \right) \right) \Delta\nu, \tag{4.10}$$

$n_{\rm max}$ is the equivalent radial order where the oscillation power is maximum, and $\alpha_{\rm curv}$ is the curvature of the radial-mode pattern. In low- and intermediate-luminosity red giants, there are typically modes with 7 different radial orders that can be observed in their oscillation spectrum. Too many free parameters are used in Eq. 4.5 , which complicates the fit of the glitch modulation as there are too few modes to reproduce the damped behaviour of the glitch modulation. Owing to the low number of measured modes, a simpler frequency-dependent amplitude is preferred. According to Eq. 4.7, the glitch signature in $d^{\rm gl}_{n,0}$ in mode frequencies has a constant amplitude. Then, Vrard et al. (2015) used a constant amplitude term for the modulation in the local large separation, which reads

$$\delta\Delta\nu^{\rm gl}_{n,\ell} = \mathcal{A}_{\rm HeII}\, \Delta\nu \cos\left(2\pi \frac{\nu - \nu_{\rm max}}{\mathcal{G}_{\rm HeII}\Delta\nu} + \Phi_{\rm HeII} \right). \tag{4.11}$$

4.3.2 Characterising the helium second-ionisation zone

The results for low- and intermediate-luminosity red giants obtained by Vrard et al. (2015) are shown in Fig. 4.4, 4.5. At a given $\Delta\nu$, the amplitude of the modulation is weaker for RGB stars than for He-core burning stars. The difference observed in the modulation amplitude $\mathcal{A}_{\rm HeII}$ between RGB and

He-burning phases is correlated with a difference of temperature at the level of the helium second-ionisation zone (Christensen-Dalsgaard et al., 2014). This difference causes a different dip in the first adiabatic exponent, which is shallower during the clump (see right panel of Fig. 4.5) then explains why the glitch amplitude is a bit larger for He-core burning stars. The mean glitch period is higher by approximately 30% for He-core burning stars relatively to RGB stars ($\mathcal{G}_{\mathrm{HeII,RGB}} = 3.08 \pm 0.65$ for RGB versus $\mathcal{G}_{\mathrm{HeII,clump}} = 3.83 \pm 0.88$ for clump stars). This difference arises from a density difference in the bulk of the convective zone, with lower density in clump stars (Christensen-Dalsgaard et al., 2014). The difference of density is related to the fact that a larger fraction of the mass is contained in the helium core in the clump phase. This produces an increase in the degree of ionisation, hence to the outward shift of the helium ionisation zone in clump stars (see Fig. 4.5).

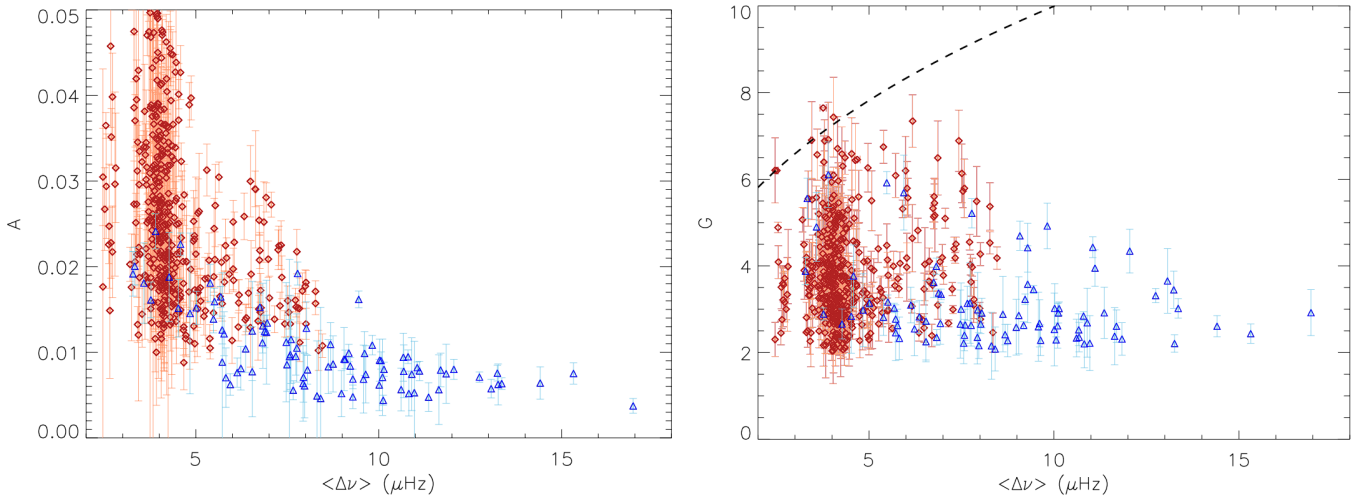

FIGURE 4.4: Dimensionless amplitude (**left**) and period (**right**) of the modulation as a function of $\Delta\nu$. RGB and He-core burning stars are shown in blue and red, respectively. The black dashed line indicates the maximum number of radial modes that can be observed at given $\Delta\nu$. Credit: Vrard et al. (2015)

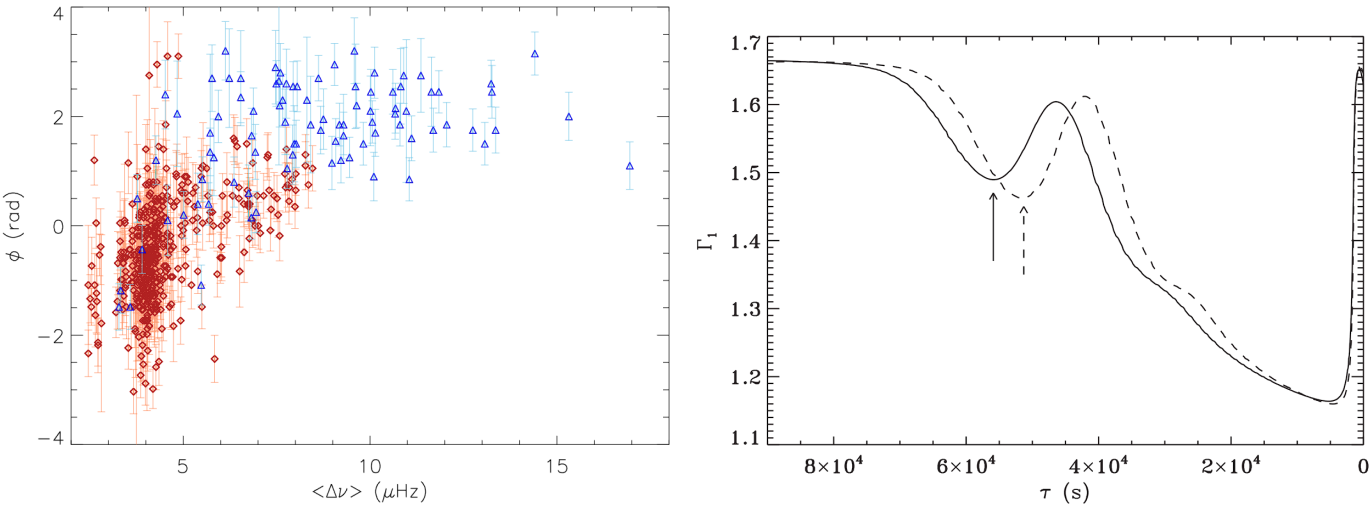

FIGURE 4.5: **Left:** Phase of the modulation as a function of $\Delta\nu$. Same label as in Fig. 4.4. Credit: Vrard et al. (2015). **Right:** First adiabatic exponent Γ_1 as a function of the acoustic depth from the surface. The solid line is for the RGB model while the dashed line is for the He-burning model. Credit: Christensen-Dalsgaard et al. (2014)

Finally, the phase of the glitch modulation is shifted between clump stars and RGB stars. While the glitch phase is included between 1 and 3 radians for RGB stars, the former takes value between -2 and 1 radians for clump stars. This phase difference is so important that the glitch modulation given by

Eq. 4.9 significantly differs between RGB and clump stars at fixed $\Delta\nu$. This phase shift can be used to measure the evolutionary status of red giants, particularly for distinguishing RGB and clump stars. This is discussed in detail in the next chapter.

Chapter 5

Classification techniques of evolved stars

Disentangling RGB and AGB stars with photometric and spectrometric global parameters is challenging. Indeed, RGB and AGB stars have close luminosities and effective temperatures, as illustrated in the colour-magnitude diagram of the globular cluster M5 (Fig. 5.1). This resemblance is not only noticeable in observations, but also in stellar models (Fig. 2.1). Despite these similarities, the internal structure of RGB and AGB stars is noticeably different. The extent of the convective envelope is smaller during the AGB phase because of the important mass loss that stars endure at the luminosity tip of the RGB. Moreover, an additional energy supply is available during the AGB, guaranteed by the He-shell burning (Fig. 1.10). Thus the crucial question arises of the enhancement of the structure differences between RGB and AGB stars, given their similar surface parameters. Hopefully, these differences can be highlighted with the seismic parameters presented in Chapter 3. These seismic parameters carry the signature of internal structures. Accordingly, asteroseismic classification methods based on seismic parameters can be established to identify those stars. In this chapter, we present the classification methods provided by asteroseismology to disentangle RGB and AGB stars.

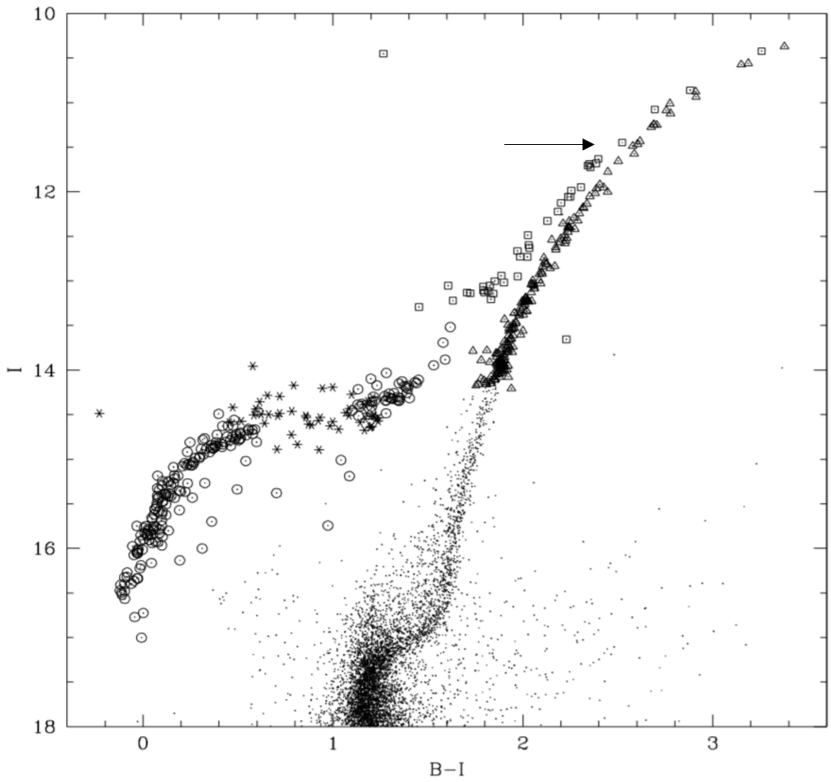

FIGURE 5.1: Colour-magnitude diagram of M5 with the CFHT data showing the intensity in the I band as a function of the colour index B−I. RGB stars are plotted with triangles while AGB or post-AGB stars are plotted with squares. Clump stars and RR Lyrae variables are plotted with circles and asterisks, respectively. Credit: Sandquist and Bolte (2004)

5.1 Distinguishing hydrogen- and helium-burning red giants with mixed modes

The stellar core undergoes significant changes from the subgiant phase up to the AGB phase. In period of quiescent core-nuclear burning, the core expands while in absence of energy supply it contracts. This core dynamic corresponds to distinct evolutionary stages, which can be evaluated with the signature of core properties in the seismic parameters. Especially, the detection of mixed modes is beneficial as they carry valuable information on the deepest layers of stars. The observed pattern of dipole mixed modes is characterised by the period spacing $\Delta\Pi_1$, which is directly related to the size of the radiative region through Eqs. 3.37−3.39, where g modes can develop. Then, measuring the period spacing of red giants helps to track the properties of the g-mode cavity along evolution. Accordingly, stars can be classified depending on their $\Delta\Pi_1$ values, as illustrated in Fig. 5.2.

Mixed modes start being visible in the oscillation spectrum when the resonant frequencies of the p- and g-mode cavities are close. This means that the coupling between the inner and outer cavities is high enough for the mixed modes to have sufficiently high amplitude in the outer cavity. This condition is first met when the star reaches the subgiant phase (Benomar et al., 2013). As the star enters the RGB, the mean core density and the large separation decrease, while the core contracts and the period spacing decreases. The properties of stellar interiors become strongly dominated by the physical conditions of the degenerate helium core and the envelope properties are related to the core mass. The transition from subgiant to red giant is marked when the core becomes degenerate, *i.e.* when the period spacing does no longer vary with the stellar mass but with the core mass (see Fig. 5.2). Accordingly, as the RGB star evolves its core contracts and the period spacing slowly decreases (Montalbán et al., 2013).
For stars that encounter the He-flash stage (*i.e.* $M \leq 2.0\,M_\odot$), the He burning in degenerate conditions makes the stars evolve rapidly on the $\Delta\Pi_1 - \Delta\nu$ diagram. Next, stars settle in a narrow region in that diagram when He gently burns in the core, around $\Delta\Pi_1 = 300\,\mathrm{s}$ and $\Delta\nu = 4\,\mu\mathrm{Hz}$. Once He burning ends in stars with mass $M \leq 2.0\,M_\odot$, the core contracts and becomes degenerate again. They follow the same trajectory regardless their mass and are located near $\Delta\nu = 3\,\mu\mathrm{Hz}$ and $\Delta\Pi_1 = 220\,\mathrm{s}$. These stars prepare to ascend the AGB (see Fig. 5.2).
For RGB stars with a mass $M \geq 2.0\,M_\odot$, He burning starts in non degenerate conditions. These stars have different luminosity and radius, so they cover a large zone in the $\Delta\Pi_1 - \Delta\nu$ diagram, where $\Delta\Pi_1 \in [150, 300]\,\mathrm{s}$ and $\Delta\nu \in [5.5, 9]\,\mu\mathrm{Hz}$. When He-shell burning starts and He-core burning ends, the high-mass stars occupy a wider range in the $\Delta\Pi_1 - \Delta\nu$ diagram compared to their low-mass counterparts, but can still be identified as AGB stars due to their high value of $\Delta\Pi_1$ with decreasing $\Delta\nu$.

As depicted by the evolution of $\Delta\Pi_1$ with $\Delta\nu$ in Fig. 5.2, stars can be efficiently classified depending on the combination of their $\Delta\Pi_1$, $\Delta\nu$, and mass M. In particular, RGB and AGB stars have distinct $\Delta\Pi_1$ at fixed $\Delta\nu$ so they can be unambiguously identified (Mosser et al., 2014). Obviously, this classification method is applicable when mixed modes are present in the oscillation spectrum, so that $\Delta\Pi_1$ can be estimated. Unluckily, the height of mixed modes decreases when $\Delta\nu$ decreases because g modes are highly damped at the outer turning point of the g-mode cavity (Dupret et al., 2009; Grosjean et al., 2014). Consequently, the mixed modes are no longer visible at low $\Delta\nu$, as shown in Sect. 3.8.2 and Fig. 3.8. The mixed-mode properties of evolved RGB and AGB stars can no longer be extracted, and the $\Delta\Pi_1 - \Delta\nu$ diagram can no longer be employed to classify these stars. Of course, the $\Delta\Pi_1$ value that reflects the radial profile of the Brunt-Väisälä frequency N_{BV} and the size of the radiative core is one of the differences between RGB and AGB stars. Other structure differences can be highlighted, specifically the helium second-ionisation zone.

5.2 The state of the helium second-ionisation zone as classifier

All along their evolution, stars carry the signature of physical processes that occur in their interiors. The presence of He burning and additional mixing between the core and envelope contributes to the

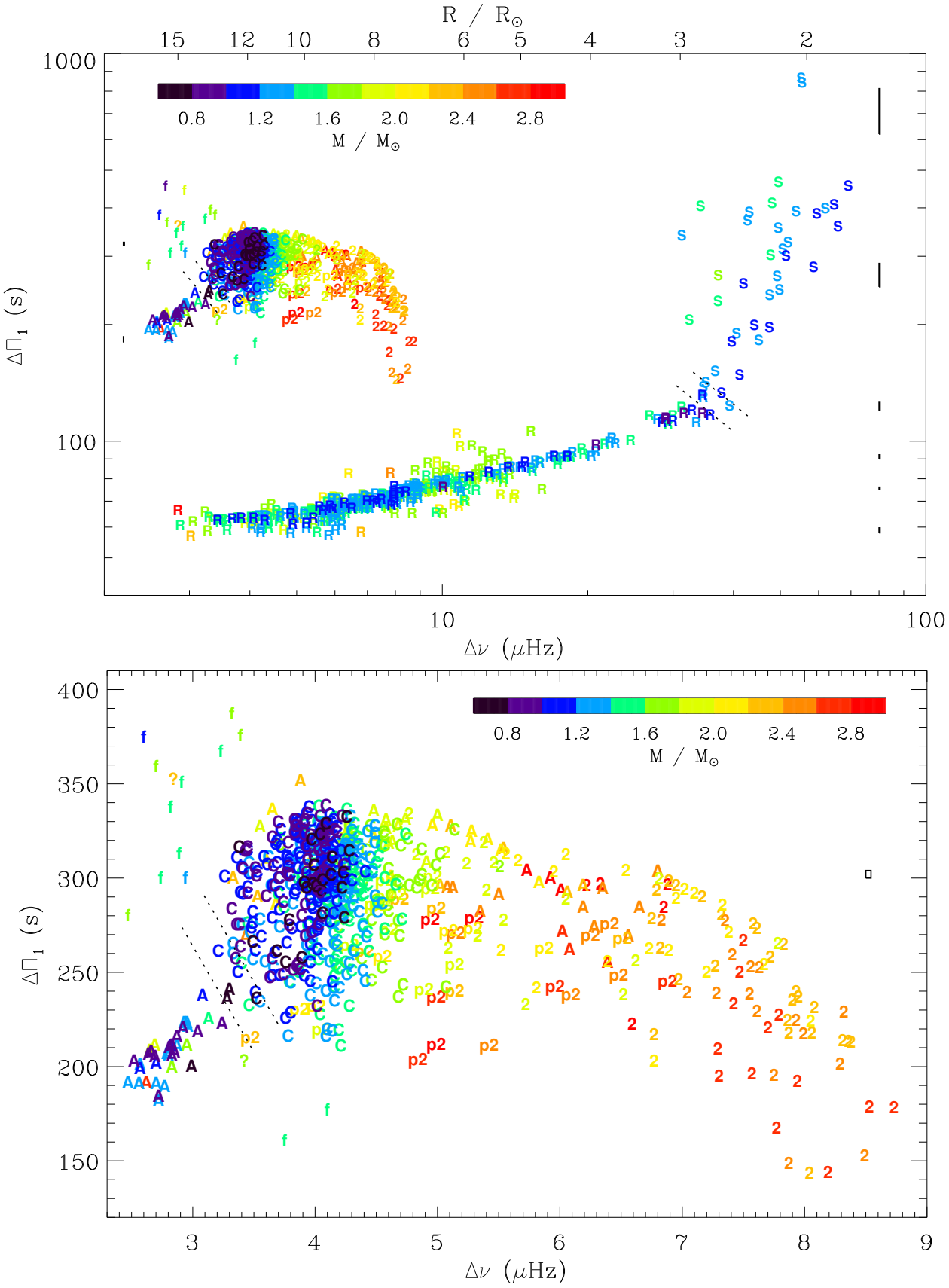

FIGURE 5.2: **Top:** Period spacing $\Delta\Pi_1$ as a function of the large frequency separation $\Delta\nu$. The stellar mass is colour-coded and symbols are associated to different evolutionary states: S for subgiant branch, R for RGB, f for suspected stars in the He subflash stage, C for red clump, p2 for pre-secondary clump, 2 for secondary clump, and A for early-AGB. The errorbars at different $\Delta\Pi_1$ values on the right side indicate the mean uncertainties for RGB stars while those on the left side show the mean uncertainties for clump stars. The dotted lines mark the limits between different evolutionary stages. **Bottom:** zoom in the He-burning region. Credit: Mosser et al. (2014)

differences between the convective envelopes of RGB and clump stars. Helium ionisation takes place in different physical conditions in the envelope of RGB and clump stars (Christensen-Dalsgaard et al., 2014). Consequently, the signature of the helium second-ionisation zone in mode frequencies differs between those stars, as presented in Sect. 4.3.2. The amplitude of the modulation introduced by the helium second-ionisation zone in mode frequencies is more intense for clump stars. Moreover, a phase difference between clump and RGB stars is noticeable in the glitch modulation. Vrard et al. (2015) have shown that the glitch modulation $\delta\Delta\nu^{\rm gl}_{n,\ell}$ given by Eq. 4.11 typically modifies the local large frequency separation with a mean relative variation of $\delta\Delta\nu_{\rm RGB} = -0.5\%$ for RGB stars and $\delta\Delta\nu_{\rm clump} = 1\%$ for clump stars at $\Delta\nu = 4\,\mu$Hz. Although this shift seems anecdotal, the relative difference between RGB and clump stars is sufficiently high for a classification of those stars to be possible (Kallinger et al., 2012). Indeed, the glitch signature in mode frequencies $d^{\rm gl}_{n,\ell}$ (Eq. 4.7) can be seen as an additional term in the acoustic offset ε, which quantifies the near-surface effects. Then, we define an effective acoustic offset $\varepsilon_{\rm eff}$ that encompasses both the near-surface effects and the glitch modulation, which reads

$$\varepsilon_{\rm eff} = \varepsilon + \delta\varepsilon = \varepsilon + d^{\rm gl}_{n,\ell}. \tag{5.1}$$

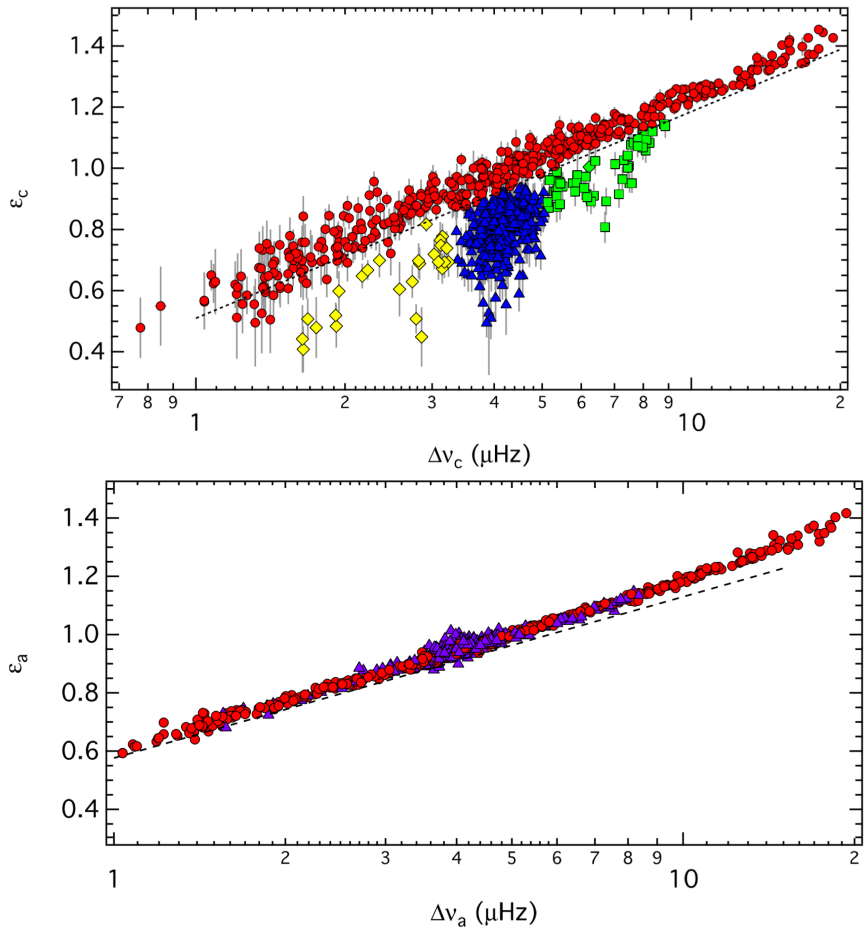

FIGURE 5.3: **Top:** The effective acoustic offset $\varepsilon_{\rm eff}$ as a function of $\Delta\nu$ for a sample of 923 *Kepler* targets. These parameters are averaged over the three central radial modes with radial orders n around $n_{\rm max}$. H-shell burning stars are shown with red circles, while red clump, secondary clump and AGB stars are indicated by blue triangles, green squares, and yellow diamonds, respectively. The dotted line divides the different groups, which expression is given by $0.532 + 0.649 \log \Delta\nu$. **Bottom:** Same figure as the top panel but parameters are averaged over all the observed modes. The label is the same, except for He-burning stars that are indistinctly represented by blue triangles. The dashed line is the scaling relation derived from Mosser et al. (2011), but shifted by -0.05 for better visibility. Credit: Kallinger et al. (2012)

The perturbation caused by the glitch in the acoustic offset $\delta\varepsilon$ and that in the local large separation $\delta\Delta\nu^{\rm gl}_{n,\ell}$ can be related by differentiating Eq. 3.20 as follows

$$\delta\varepsilon = d^{\rm gl}_{n,\ell} = -\left(n+\varepsilon\right)\frac{\delta\Delta\nu^{\rm gl}_{n,\ell}}{\Delta\nu}. \tag{5.2}$$

Accordingly, the mean relative variation in the local large frequency separation caused by the glitch is equivalent to $\delta\varepsilon_{\rm RGB} = 0.05$ for RGB stars and $\delta\varepsilon_{\rm clump} = -0.1$ for clump stars when the radial order n is about 10. The difference between RGB and clump stars in the effective acoustic offset, which is $\Delta\varepsilon = 0.15$, can be highlighted in observations with local measurements of ε as shown in Fig. 5.3.

As observed by Kallinger et al. (2012), the typical difference between clump (both red and secondary clumps) and RGB stars is similar to the difference expected from the glitch signature through Eq. 5.2. Moreover, the classification based on the acoustic offset is efficient only when local measurements of ε are performed. As illustrated in Fig. 5.3, the evolutionary effects is visible only when an average on the three central modes closest to the frequency of maximum oscillation power $\nu_{\rm max}$ is performed. When the average is computed over all the observed modes, the evolutionary effects fade and both H-shell burning stars and He-burning stars have the same seismic parameters. Therefore, the evolutionary effects are encoded in the fine structure of the p-mode pattern. This property matches with what we expect from the signature of the helium second-ionisation zone. Indeed, the average value of the modulation induced by the glitch is close to zero when the average is computed with a high number of modes (see for example Eq. 4.7). As a result, the classification method proposed by Kallinger et al. (2012) relies on the physical state of the helium second-ionisation zone. However, the classification has been justified between He-core burning stars and H-shell burning stars only. Because of the inappropriate frequency resolution, the previous study could not extract the p-mode frequencies of evolved stars at low $\Delta\nu$ with sufficient precision. Hence, the identification methods could not classify RGB and AGB stars with absolute certainty. But now, the about 1470-day time-series of *Kepler* gives access to an excellent frequency resolution reaching 7.8 nHz, which gives the opportunity to decipher the p-mode oscillation pattern of evolved giants with unprecedented precision. In my thesis, we aim at extending the conclusions raised by Vrard et al. (2015), but between RGB and AGB stars at low $\Delta\nu$. Namely, we investigate the physical basis of the identification of RGB and AGB stars, which is suspected to rely on the signature of the helium second-ionisation zone in the p-mode pattern.

5.3 The Envelope AutoCorrelation Function (EACF) signal

The autocorrelation function of observational time series is thoroughly used for estimating the large frequency separation, which gives a measure of the stellar acoustic diameter (Mosser and Appourchaux, 2009). The former simply corresponds to the Fourier spectrum of the Fourier transform of the time series. By adopting a filter $\mathcal{F}$ of width $\delta\nu_{\rm H}$ around the frequency at maximum oscillation power $\nu_{\rm max}$ in the Fourier transform of the time series $X(\nu)$, the autocorrelation function $\mathcal{C}$ reads

$$\mathcal{C}(\tau) = \int_{\nu_{\rm max}-\delta\nu_{\rm H}}^{\nu_{\rm max}+\delta\nu_{\rm H}} X(\nu)X^*(\nu)\mathcal{F}(\nu)\mathrm{e}^{2\mathrm{i}\pi\nu\tau}\mathrm{d}\nu. \tag{5.3}$$

The amplitude $\mathcal{A}_\mathcal{C}$ of the autocorrelation signal can be expressed with the dimensionless square modulus of the autocorrelation function in units of the noise level $\sigma_{\rm H}$:

$$\mathcal{A}_\mathcal{C}(\tau) = \frac{1}{\sigma_{\rm H}}\frac{\left|\mathcal{C}(\tau)^2\right|}{\left|\mathcal{C}(0)^2\right|}. \tag{5.4}$$

As a wavepacket spends a time $\tau_{\Delta\nu} = 2/\Delta\nu$ to cross the stellar diameter twice, we expect to see the signature of the seismic signal every interval of $\tau_{\Delta\nu}$ in the autocorrelation function. An example of autocorrelation peak in the profile of $\mathcal{A}_\mathcal{C}$ is shown in Fig. 5.4. The maximum amplitude of the first peak in the autocorrelation function at $\tau_{\Delta\nu}$ is noted $\mathcal{E}$. The former provides an estimate of the strength of the

seismic signal in given time series, which is useful for defining thresholds for asteroseismic detection and measurement of stellar properties (Mosser et al., 2019). In evolved stars, stellar properties dominate the signal strength in the seismic index $\mathcal{E}$. It has been shown that the seismic index $\mathcal{E}$ depends on the height-to-background ratio $\mathcal{R}$ (Mosser and Appourchaux, 2009) defined as

$$\mathcal{R} = \frac{H_{\rm max}}{B_{\rm max} + B_{\rm noise}}, \tag{5.5}$$

where $H_{\rm max}$ is the height of the oscillation power excess at $\nu_{\rm max}$, $B_{\rm max}$ is the background contribution associated to stellar granulation, and $B_{\rm noise}$ includes the photon flux noise and instrumental noises. The seismic performance index $\mathcal{E}$ also linearly depends on the observation duration $\mathcal{D}$ since the frequency resolution is inversely proportional to $\mathcal{D}$. Then the number of frequency bins linearly increases with $\mathcal{D}$, which leads to a linear increase of any relevant signal with $\mathcal{D}$ (Hekker et al., 2012). Because the number of observed modes depends on the frequency range where the oscillation power excess is observed, the signal $\mathcal{E}$ is expected to vary with $\nu_{\rm max}$. Accordingly, Mosser et al. (2019) derived a calibration of this index for the evolved stars observed by *Kepler*, which reads

$$\mathcal{E}_{\rm simu} = 0.065\, \mathcal{R}^{0.9}\, \nu_{\rm max}^{1.1}\, \mathcal{D}, \tag{5.6}$$

where $\nu_{\rm max}$ is expressed in μHz, and $\mathcal{D}$ in months. By comparing the seismic performance index $\mathcal{E}$ of a star with the predicted value $\mathcal{E}_{\rm simu}$ according to Eq. 5.6, two populations could be enhanced: H-shell burning and He-burning stars. Indeed, clump stars have lower values of $\mathcal{E}$, typically diminished by a factor 2.5 relatively to the predicted value $\mathcal{E}_{\rm simu}$ (see Fig. 5.4).

As a consequence, Mosser et al. (2019) established a classification method based on the EACF signal, evaluated by a parameter $\eta_{\mathcal{E}}$ that is the ratio between the observed EACF and the predicted value

$$\eta_{\mathcal{E}} = \frac{\mathcal{E}}{\mathcal{E}_{\rm simu}}. \tag{5.7}$$

The star is then identified as a RGB star above the threshold $\eta_{\mathcal{E},\rm lim} = 0.7$, as a red-clump star otherwise. The low value of $\eta_{\mathcal{E}}$ for clump stars is due to their low ratio $H_{\rm max}/B_{\rm max}$ as reported by Mosser et al. (2012a), which is caused by a strong mode damping in those stars (Vrard et al., 2018). Given the low values of $\eta_{\mathcal{E}}$ for AGB stars, the classification can be extended to high-luminosity red giants to identify RGB and AGB stars. This classification method is advantageous since it does not require a full seismic characterisation of the oscillation pattern to derive the classifying term $\eta_{\mathcal{E}}$. Nevertheless, this method relies on an empirical characterisation of the modes, *i.e.* the height-to-background ratio. Then, this difference cannot be easily interpreted in theoretical models to characterise the stellar structure differences between those stars.

5.4 Comparison between classification methods of RGB and AGB stars

5.4.1 Agreements and disagreements

In this section, we perform a comparison between the method based on the EACF (Mosser et al., 2019) and that based on the glitch signature (Kallinger et al., 2012). First, we visualise the distributions of agreements and disagreements in Fig. 5.5. At $\Delta\nu \geq 2.0\,\mu$Hz, it seems that both identification methods mostly agree, with a fraction below 10% of disagreements that are distributed near the cut between RGB and clump stars in ε. Nevertheless, at $\Delta\nu \leq 2.0\,\mu$Hz, this is no longer systematic and many disagreements are visible. In order to quantitatively describe the disagreements, two types of graphs are shown in Fig. 5.6:

- One graph highlights the number of agreements for the stellar evolution identification, the number of disagreements is superimposed on top of the number of agreements.
- Another graph showing the percentile of disagreements, normalised by the total number of stars in each bin.

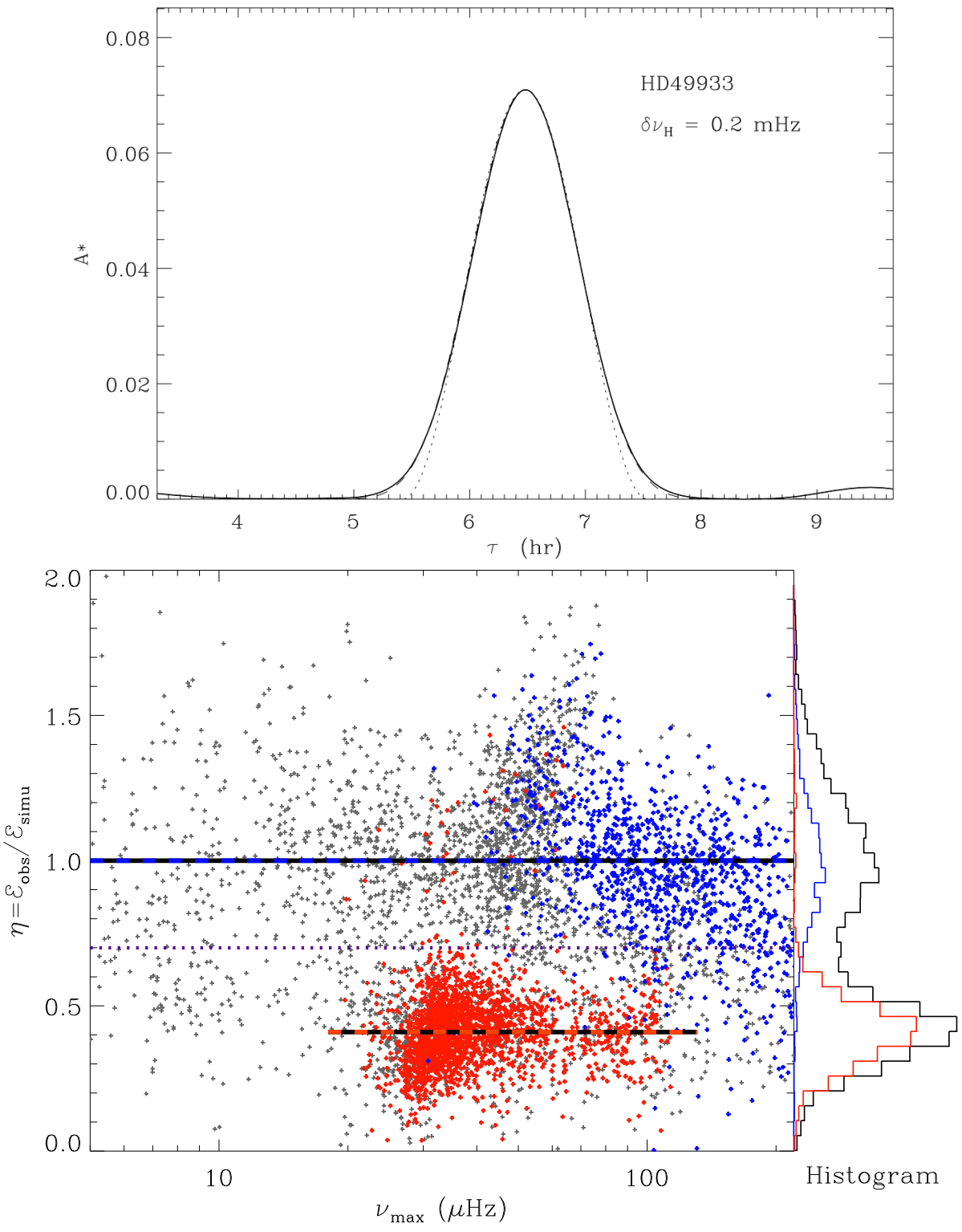

FIGURE 5.4: **Top:** Profile of the first peak in the amplitude of the autocorrelation function $\mathcal{A}_{\mathcal{C}}(\tau)$ (solid line) calculated from the power spectrum of the star HD 49933 and a filter width $\delta\nu_{\rm H} = 0.2\,$mHz. Theoretical and cosine model are shown with dashed and dotted lines, respectively. Credit: Mosser and Appourchaux (2009). **Bottom:** Ratio $\eta_{\mathcal{E}}$ defined by Eq. 5.7. Blue and red symbols indicate RGB and clump stars, respectively, identified by Vrard, Mosser, and Samadi (2016) with the method described in Sect. 5.1. Grey symbols correspond to stars with unidentified evolutionary status. The dotted line is the cut $\eta_{\mathcal{E},\rm lim} = 0.7$ between RGB and red-clump stars. The horizontal dashed lines indicate the mean value of $\eta_{\mathcal{E}}$ for both evolutionary status. Histograms of those stars with the same colour code are shown as a function of $\eta_{\mathcal{E}}$ on the right. Credit: Mosser et al. (2019)

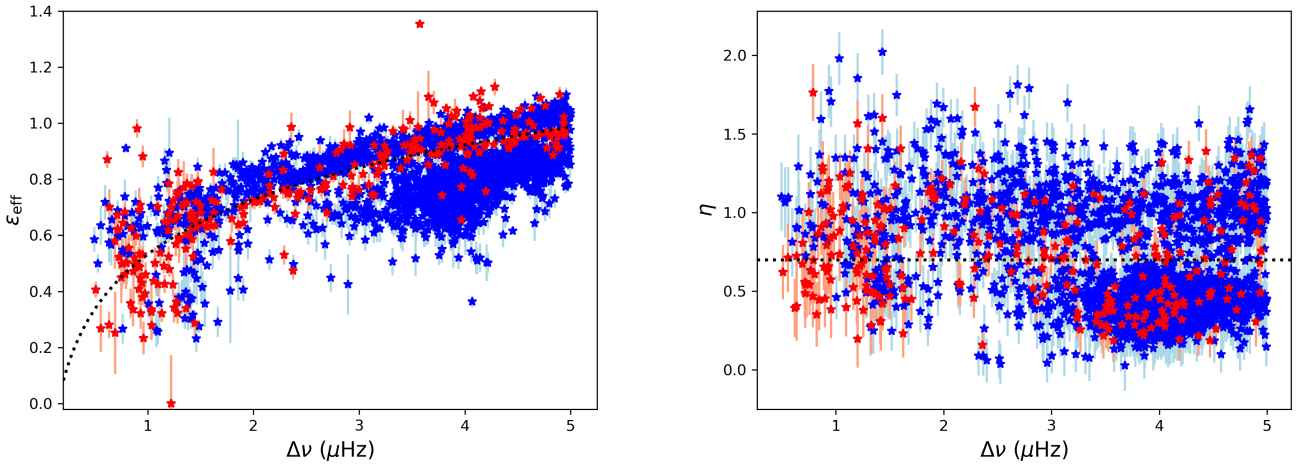

FIGURE 5.5: Identification methods used to classify stars, with an emphasis on the agreements (blue) and disagreements (red). **Left:** method based on the glitch signature, on the value of $\varepsilon_{\rm eff}$ as a function of $\Delta\nu$, $\nu_{\rm max}$, and $\eta_\mathcal{E}$. The dotted black line is the cut that separates RGB stars (above) and He-burning stars (below). **Right:** method based on the EACF, on the parameter $\eta_\mathcal{E}$. The black dotted line is the cut $\eta_{\mathcal{E},\rm lim} = 0.7$, separating RGB stars (above) from He-burning stars (below).

When looking at the agreements and the disagreements as a function of $\Delta\nu$ (resp. $\nu_{\rm max}$), it is clear that the number of disagreements sharply increases while $\Delta\nu$ (resp. $\nu_{\rm max}$) decreases. This implies that the identification methods are less efficient at low $\Delta\nu$, showing that RGB and AGB stars are more likely to be misclassified. In fact, the efficiency of these classification methods are certainly limited by the precision with which the seismic parameters ε and $\eta_\mathcal{E}$ are inferred because of the frequency resolution in observations. On the other hand, there is a peak of disagreements around $\eta_{\mathcal{E},\rm lim} = 0.7$, which corresponds to the separation criterion between H-shell burning and He-burning stars. This is expected since this limit is empirical and has been set to match as much as possible the distribution of $\eta_\mathcal{E}$ both in the H-shell burning and He burning phases in Fig. 5.4. Of course, few RGB stars with low EACF parameter $\eta_\mathcal{E}$ or He-burning stars with high EACF parameter $\eta_\mathcal{E}$ may be misidentified. Since the identification is based on an empirically calibrated cut, we need to evaluate the robustness of the classification methods.

5.4.2 Robustness of the classification methods

Previously, we did not mention any uncertainty on the identification. The uncertainties on the seismic parameters $\varepsilon_{\rm eff}$ and $\eta_\mathcal{E}$ are higher at low $\Delta\nu$. Then, we expect the identification methods to be less reliable at low $\Delta\nu$. Taking uncertainties into account is essential when evaluating the robustness of the identification methods since they are based on a hard cut in $\varepsilon_{\rm eff}$ and in $\eta_\mathcal{E}$. If a star has an $x = \{\varepsilon_{\rm eff}, \eta_\mathcal{E}\}$ close to the hard cut $x_{\rm cut}$ with large uncertainties $\sigma_x = \{\sigma_{\varepsilon_{\rm eff}}, \sigma_{\eta_\mathcal{E}}\}$, the identification may be biased. Accordingly, we need to introduce a parameter that can evaluate the robustness of the identification, for both methods. We can compute the probability p_x of how reliable the classification is. We convert the distance between the parameter $\varepsilon_{\rm eff}$ (resp. $\eta_\mathcal{E}$) and the hard cut in units of $\sigma_{\varepsilon_{\rm eff}}$ (resp. $\sigma_{\eta_\mathcal{E}}$) into a probability. We assume that the uncertainties $\sigma_{\varepsilon_{\rm eff}}$ and $\sigma_{\eta_\mathcal{E}}$ follow a normal distribution. Let x be the measured parameter ($\varepsilon_{\rm eff}$ or $\eta_\mathcal{E}$) and $x_{\rm cut}$ be the hard cut. Then, we can define the probability p_x such that the star is correctly classified with x, assuming the cut $x_{\rm cut}$ as follows

$$p_x = \int_{-\infty}^{x} \frac{1}{\sigma_x\sqrt{2\pi}} e^{-\frac{|x-x_{\rm cut}|^2}{2\sigma_x^2}} dx = 0.5\left(1 + \mathrm{erf}\left(\frac{|x - x_{\rm cut}|}{\sigma_x\sqrt{2}}\right)\right), \tag{5.8}$$

where erf is the error function. We adopt absolute value in the distance between x and $x_{\rm cut}$ in order to keep positive probabilities. According to this definition, a star has a probability p_x to be correctly

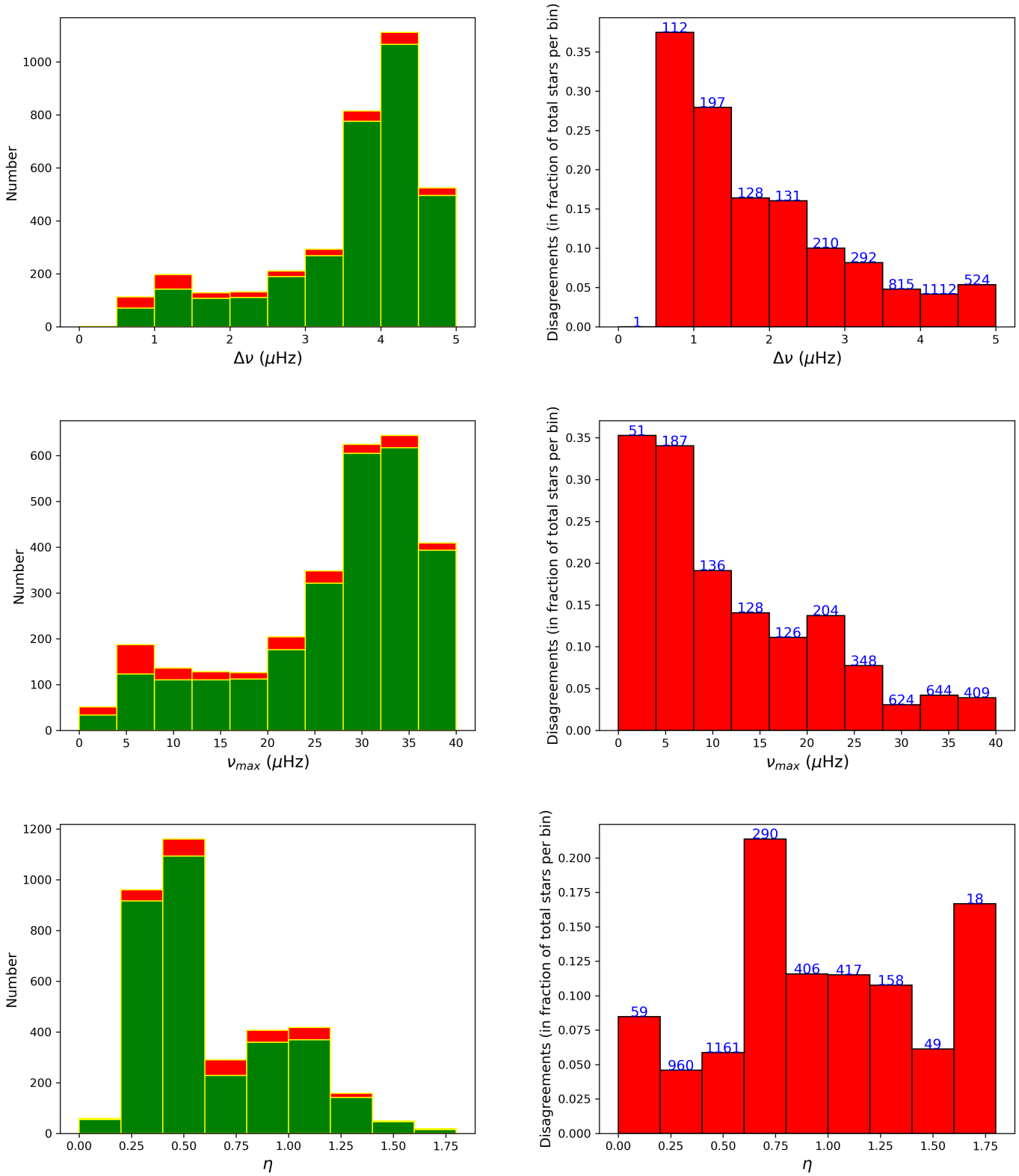

FIGURE 5.6: Agreements on the stellar evolution identification between methods based on the EACF function $\eta_{\mathcal{E}}$ and on the acoustic offset ε_{eff}. **Left:** number of agreements (green) and disagreements (red) as a function of $\Delta\nu$. **Right:** percentile of disagreements, normalised to the total number of stars in each bin. The total number of stars (agreements + disagreements) per bin is indicated in blue over each bin. The bin sizes in $\Delta\nu$, ν_{max}, and $\eta_{\mathcal{E}}$ are 0.5 μHz, 4 μHz, and 0.2, respectively.

classified and a probability $1 - p_x$ to be misclassified. In this framework, the star is either a RGB star or a He-burning star. As a guideline one can say that a $p_x > 0.97$ is very strong evidence, $p_x > 0.91$ is strong evidence, $p_x > 0.75$ is substantial evidence (Jeffreys, 1939).

5.4.3 Classification with strong evidence

The previous results took into account all stars having $\Delta\nu \leq 5.0\,\mu$Hz, whatever their probability to be correctly classified. Hereafter, we only select the stars which have been robustly classified with both identification methods. In Fig. 5.7, the disagreements are shown as a function of $\Delta\nu$, in the cases with strong evidence ($p_{\varepsilon_{\rm eff}} \geq 0.91$ and $p_{\eta_\mathcal{E}} \geq 0.91$) on the one hand and very strong evidence ($p_{\varepsilon_{\rm eff}} \geq 0.97$ and $p_{\eta_\mathcal{E}} \geq 0.97$) on the other hand. The stars that fulfil these conditions have their seismic parameters $\varepsilon_{\rm eff}$ and $\eta_\mathcal{E}$ far enough in units of the uncertainty from the cut that separate populations (see upper panels in Fig. 5.7). Both identification methods agree very well above $\Delta\nu \geq 2\,\mu$Hz. And yet, despite the fact that the seismic parameters are sufficiently far from the cut, the disagreements grow fast below $\Delta\nu \leq 2\,\mu$Hz. This means that the methods to classify RGB and AGB stars are less efficient at low $\Delta\nu$, certainly because of the frequency resolution in observations that is not adequate to extract the p-mode pattern of those stars with satisfying precision. Indeed, by selecting stars at $\Delta\nu \leq 2\,\mu$Hz, we see that the disagreements are systematically important whatever the probability levels $p_{\varepsilon_{\rm eff}}$ and $p_{\eta_\mathcal{E}}$ (see lower panels in Fig. 5.7).

5.4.4 Implications for this work

To sum up, the methods based on the EACF (Mosser et al., 2019) and that based on the glitch signature (Kallinger et al., 2012) give robust classification for stars with $\Delta\nu \geq 2\,\mu$Hz. However, when $\Delta\nu \leq 2\,\mu$Hz the frequency resolution hampers the precise characterisation of the p-mode pattern, and the classification methods are less reliable. In this work, the evolutionary status is defined only if both classification methods agree on the evolutionary status, otherwise stars are defined as unclassified. This will reduce the uncertainties on the evolutionary status and the dispersion of seismic parameters for both RGB and He-burning stars.

5.5 Spectroscopic classification of red giants

Other classification techniques are available as a complement to the asteroseismic methods described herebefore. For instance, stars can be classified according to their spectroscopic parameters such as effective temperature $T_{\rm eff}$, surface gravity $\log g$, and metallicity [M/H][1] (Holtzman et al., 2015). Indeed, at given surface gravity and metallicity red- and secondary-clump stars are hotter than RGB stars. However, the knowledge of the temperature only does not allow us to differentiate RGB from clump stars since the effective temperature is correlated to the surface gravity and metallicity. Then, these parameters can shift the RGB closer to the clump location, hampering the distinction between RGB and clump stars. Nevertheless, the metallicity and surface gravity effects can be mitigated by defining a reference effective temperature $T_{\rm eff,ref}$ expected for a typical RGB star with given surface gravity and metallicity (Holtzman et al., 2018). This identification method works if RGB and clump stars have sufficiently different effective temperature. For cool clump stars that reach a minimum distance from the RGB, the identification of the evolutionary status becomes intricate. In this case, detailed chemical abundances is required to provide a separation between RGB and red-clump stars. Indeed, the surface abundance of C and N is modified during the RGB by the first dredge-up. The latter brings to the surface the products of nuclear H-burning during the main sequence. Accordingly, the combination of the [C/N] ratio and previously defined spectroscopic parameters can be employed for evolutionary state classification (Holtzman et al., 2018). This is illustrated in Fig. 5.8, where stars are classified in the clump if the two following conditions

[1] Instead of using the ratio [Fe/H], the global metallicity ratio [M/H] is often preferred to take the enhancement in the α-elements into account. It reads $[{\rm M/H}] = [{\rm Fe/H}] + \log(0.638 f_\alpha + 0.362)$, where f_α is the average enhancement factor of the α-elements (Salaris, Chieffi, and Straniero, 1993).

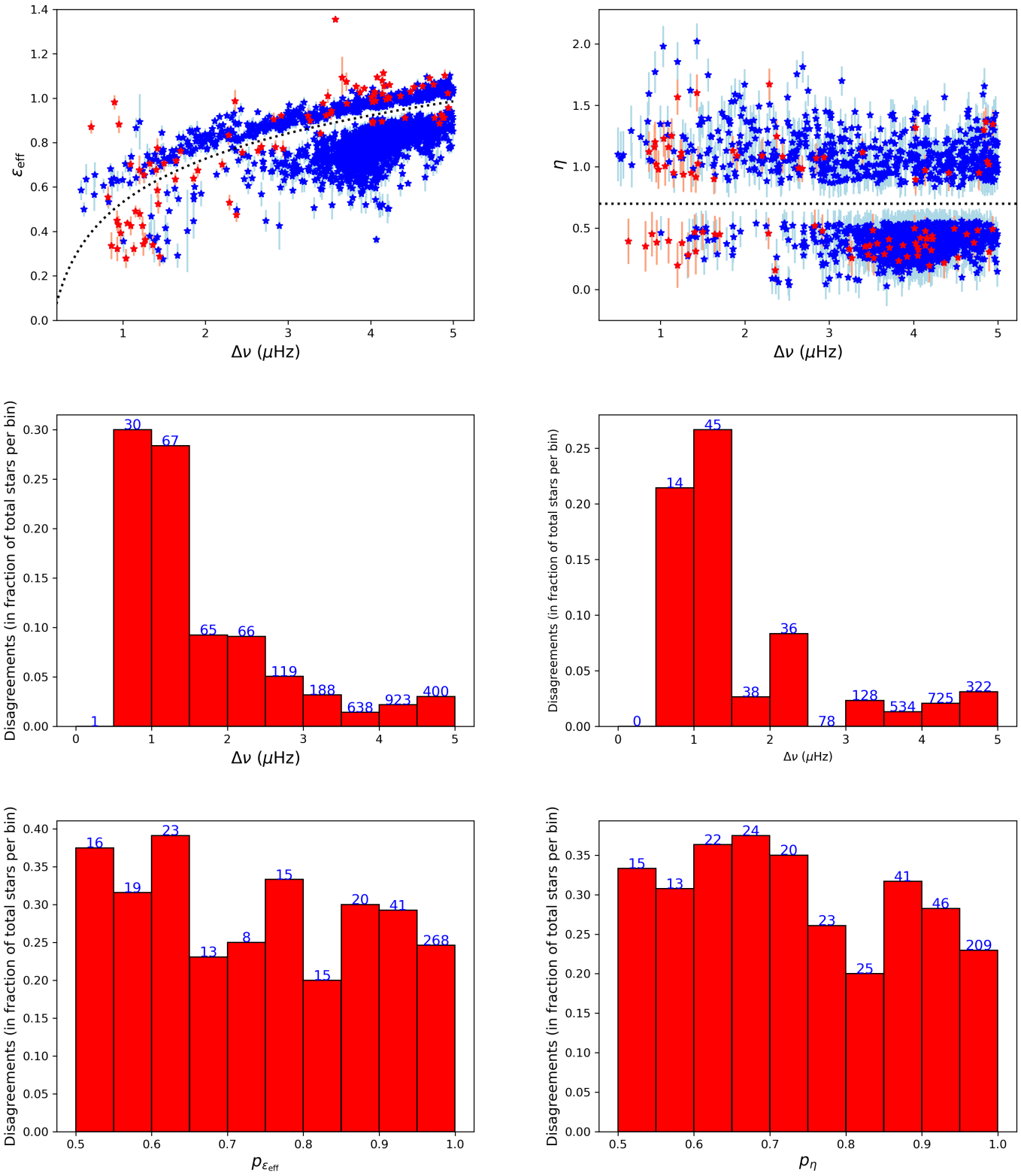

FIGURE 5.7: **Top:** Same label as in Fig. 5.5, but considering only stars that are considered as robustly classified ($p_{\varepsilon_{\rm eff}} \geq 0.91$ and $p_{EACF} \geq 0.91$.) **Middle:** Same label as the right panels in Fig. 5.6, but selecting stars with robust classification. **Middle left:** $p_{\varepsilon_{\rm eff}} \geq 0.91$ and $p_{\eta_\mathcal{E}} \geq 0.91$. **Middle right:** $p_{\varepsilon_{\rm eff}} \geq 0.97$ and $p_{\eta_\mathcal{E}} \geq 0.97$. **Bottom:** Same label as in Fig. 5.6, but representing $p_{\varepsilon_{\rm eff}}$ and $p_{\eta_\mathcal{E}}$ and only selecting stars with low $\Delta\nu \leq 2.0\,\mu$Hz.

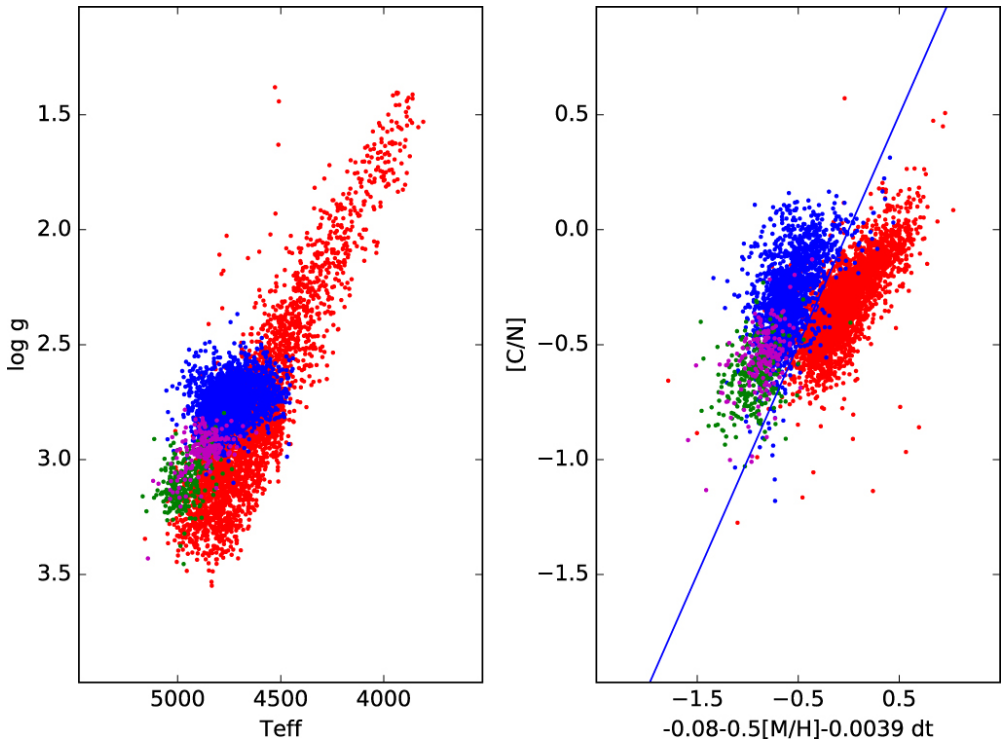

FIGURE 5.8: **Left:** Spectroscopic HR diagram for stars from the APOKASC catalog. RGB, red-clump, and secondary-clump stars are shown in red, blue, and green, respectively. Stars in between the red and secondary clumps are indicated in magenta. **Right:** Ratio [C/N] as a function of the separation criterion defined in Eq. 5.9, where the separation line between H-shell burning and He-core burning stars is indicated by the blue line. Credit: Holtzman et al. (2018)

$$\begin{cases} 2.38 < \log g < 3.5 \\ [\mathrm{C/N}] > -0.08 - 0.5[\mathrm{M/H}] - 0.0039\Delta T \end{cases} \tag{5.9}$$

are fulfilled, in the RGB otherwise. In the previous equation, $\Delta T = T_{\mathrm{eff,raw}} - T_{\mathrm{eff,ref}}$ is the difference between the uncalibrated effective temperature $T_{\mathrm{eff,raw}}$ and the reference effective temperature given by

$$T_{\mathrm{eff,ref}} = 4444.14 + 554.311\,(\log g_{\mathrm{raw}} - 2.5) - 307.962\,[\mathrm{M/H}]_{\mathrm{raw}}, \tag{5.10}$$

where the subscript 'raw' refers to the uncalibrated values. This spectroscopic classification is effective when distinguishing RGB and clump stars (Elsworth et al., 2019), but is still preliminary to distinguish RGB and AGB stars.

5.6 Summary

In this chapter, we present the asteroseismic classification methods of RGB and AGB stars. Currently, the most powerful method to classify RGB and AGB stars is based on the diagram $\Delta\Pi_1 - \Delta\nu$. Indeed, the radial profile of the Brunt-Väisälä frequency N_{BV} changes and the size of the radiative core differs between RGB and AGB stars. This impacts the mixed-mode pattern, especially the value of $\Delta\Pi_1$, making a classification of RGB and AGB stars possible. Nonetheless, this classification is no longer applicable below $\Delta\nu \leq 2.0\,\mu$Hz, *i.e.* between RGB and AGB stars, since mixed modes have too low heights in the oscillation spectrum to be detected. Accordingly, we have to turn to other methods to identify RGB and AGB stars. Currently, two options are possible. One focuses on the signature of the He second-ionisation zone in p-mode frequencies, while the other is based on the strength of the seismic signal in the time series. Basically, AGB stars have a lower envelope autocorrelation signal and a phase difference in the glitch modulation relatively to RGB stars at similar $\Delta\nu$. Unfortunately, these classification methods are

less efficient at low $\Delta\nu$ due to the insufficient frequency resolution in the oscillation spectrum that causes large uncertainties on the seismic parameters. In the following, we retain the evolutionary status only if both classification methods agree, otherwise we consider that it is undefined. Work is still in progress to improve our ability to identify RGB and AGB stars at high luminosity.

Chapter 6

Stellar evolution and oscillation codes

To bridge the gap between the observations and physical conditions in stellar interiors, we use the stellar evolution code MESA and the stellar oscillation code ADIPLS. The MESA code addresses the physical structure in stellar models from the PMS up to the AGB while the ADIPLS code determines the oscillation spectrum expected for these models. By coupling these codes, we are able to explore the evolution of the stellar structure in evolved red giants and its implications on the oscillation spectrum. This chapter is dedicated to the presentation of these codes, with an emphasis on the physical ingredients used in stellar models from the PMS up to the AGB and on the tools to extract the p-mode oscillation spectrum of high-luminosity red giants.

6.1 The stellar evolution code MESA

Modules for Experiments in Stellar Astrophysics (MESA, Paxton et al., 2011; Paxton et al., 2013; Paxton et al., 2015; Paxton et al., 2018; Paxton et al., 2019) is an ensemble of open source libraries for a wide range of applications in computational stellar astrophysics. This code is constantly improving thanks to the MESA team and the contributions of the growing MESA users community. My work has been led with the release 12778. MESA aims at modelling the structure and evolution of stars with elaborated computational methods and up-to-date input physics, opening the possibility to consistently evolve stellar models from the birth stage to the death stage of stars. This includes the modelling of challenging phases of stellar evolution, such as the He-core flash in low-mass stars where helium starts burning in unstable conditions.
In further details, MESA builds one-dimensional and spherically symmetric models, for which the structure is divided into cells. The full set of structure and composition equations is solved for all cells from the surface to the centre. In each cell, some variables are defined at the cell edges while others are mass-averaged between the edges of consecutive cells as illustrated in Fig. 6.1. Defining the internal structure parameters in this way improves the stability and efficiency of the numerical methods because of the flux conservation formulation of the equations (Sugimoto, Nomoto, and Eriguchi, 1981). The inner boundary of the innermost cell is defined as the centre of the star, at null radius, luminosity and velocity.

The number of cells depends on the complexity of nuclear burning and the gradient of internal structure parameters such as pressure, temperature and composition. The mesh may be adjusted if the structure and composition profiles abruptly change between consecutive timesteps. Remeshing is adaptive and based on allowed changes between adjacent cells. Accordingly, cells can be splitted in several subcells, or merged to form larger cells. Mesh refinement ensures that the magnitude of differences in physical parameters between any two adjacent cells are lower than the specific thresholds. Several options are available for the user to control the number of cells, especially in local regions where the gradient of physical parameters is steep, *i.e.* near the boundaries of convection zones or sharp variation regions in chemical composition. This allows the users to better resolve targeted regions in stellar interiors. By default, the mesh resolution is increased in regions of nuclear burning, where the composition gradient is important.
All the internal structure parameters are evaluated within a timestep $\delta\tau$. The timestep selection is crucial for stellar modelling. Indeed, the timestep $\delta\tau$ should be large enough to let the model evolve efficiently, but it should be small enough to ensure that the structural differences are not too important for the

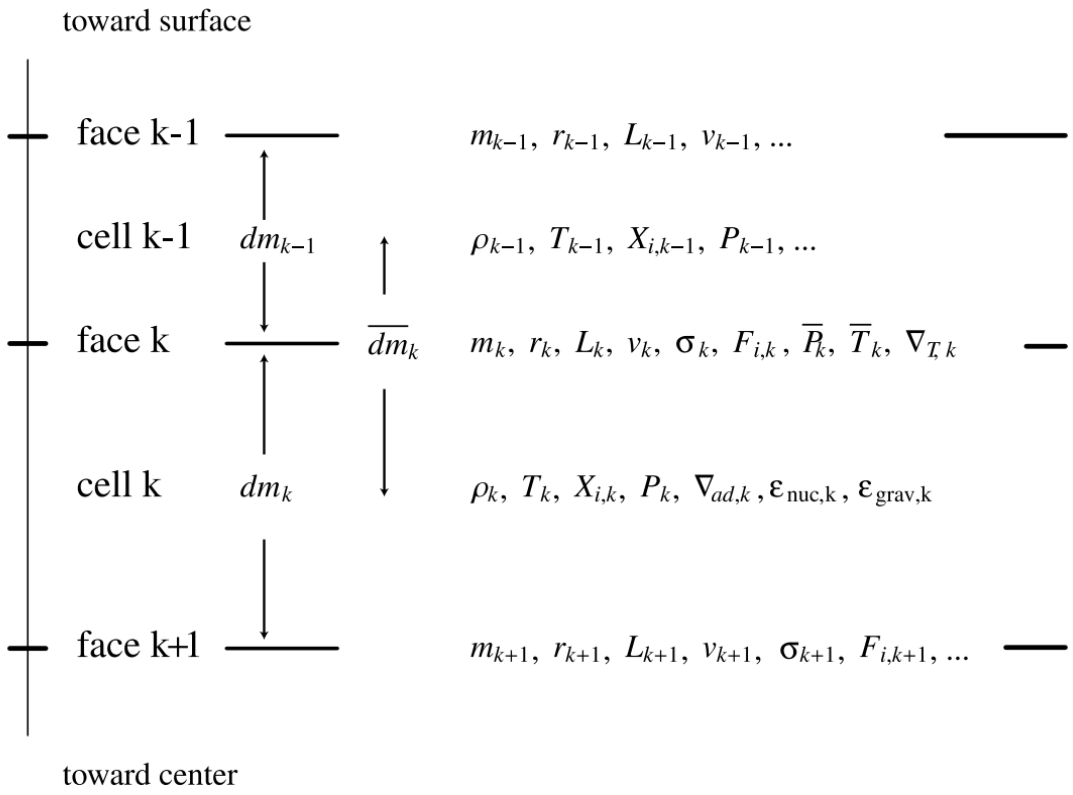

FIGURE 6.1: Schematic describing how internal structure parameters are defined in MESA. Here, the cell mass-averaged variables are the density ρ_k, temperature T_k, mass fraction vectors $X_{i,k}$, pressure P_k, ... The boundary variables are the mass interior to the face m_k, radius r_k, luminosity L_k, velocity v_k, ... Credit: Paxton et al. (2011)

numerical code to converge. In MESA, the returned solution is rejected if any physical change exceeds its specific threshold and the code is forced to retry or back up. Alternatively, the timestep can be reduced proportionally for the forthcoming models if the absolute or relative change in a physical parameter exceeds its specific threshold. This allows for studying specific events in stellar evolution, especially the AGB bump that manifests as two turning-backs of the evolutionary track in the HR diagram after the He-core burning phase.

6.2 Modelling evolution from the PMS up to the AGB

6.2.1 The test suite case *1M_pre_ms_to_wd*

In MESA package, several test cases are available to study a wide range of applications. Among them, the test suite case *1M_pre_ms_to_wd* computes the evolution of a star of mass $1M_\odot$ from the pre-main sequence to the white dwarf stage. We first use the presets of this test case to let models evolve from the PMS up to the AGB and then we consider additional physical ingredients to model the physical mechanisms that impact the evolution of low-mass stars. In this test case, five inlist files are used to control step by step the physical ingredients at specific evolutionary stages.

- The first file *'inlist_start'* initialises the global properties of the model, especially its initial mass and composition fractions. With these parameters, it creates a starting model with uniform composition and core temperature below $T_c \leq 10^6$ K so that no nuclear reaction is allowed. Then, this fully convective model evolves under the influence of a uniform contraction up to the star birthline, which is the locus in the HR diagram where the PMS star appears as a visible object, a quasi-static contraction phase begins along the Hayashi line. Typical values of luminosity at the birthline are shown for different masses in Table 6.1.

$M/M_\odot$	0.8	0.9	1.0	1.1	1.2	1.5	1.75	2.0	2.2	2.5
$\log L/L_\odot$	1.2	1.15	1.1	1.15	1.2	1.3	1.4	1.5	1.52	1.55

TABLE 6.1: Locus of the birth line in $\log L$ as a function of the initial stellar mass M. Credit: Fig. 1 of Villebrun et al. (2019)

- The second file *'inlist_to_end_core_h_burn'* lets the model evolve from the birthline up to the end of the H-core burning phase, which is marked when the central hydrogen mass fraction reaches $X_c = 10^{-4}$.
- The third file *'inlist_to_start_he_flash'* controls the evolution of the star from the subgiant phase up to the luminosity-tip of the RGB, just before the He-flash stage. The start of the He flash is marked when the total power from He-burning reactions is larger than $10\,L_\odot$.
- The He-flash and He-core burning phases are handled by the file *'inlist_to_end_core_he_burn'*. The He-core burning phase ends when the central helium mass fraction reaches $Y_c = 10^{-4}$.
- Finally, the AGB phase is taken care of by the fifth inlist file *'inlist_to_end_agb'* until the envelope mass drops below $0.01\,M_\odot$, marking the end of the AGB phase and the transition towards the white dwarf stage.

6.2.2 The physical ingredients

In each inlist file, we add physical ingredients to model internal mechanisms that affect the structure and fate of low-mass stars. All the physical processes are sorted by numerical and physics modules, for which the parameters can be initialised in inlist files. Below we describe the physical mechanisms and parameters we consider.

Mixing-Length Theory (MLT) formalism

Convective transport of energy in stellar interiors occurs through the exchange of macroscopic mass elements called "blobs". The convective velocity and flux with which the blobs are transported in our models are set following the formulation of Henyey, Vardya, and Bodenheimer (1965). The Henyey prescription lets the convective efficiency vary with the opaqueness of the convective element, which is important in regions where the opacity significantly changes, particularly near the outer stellar layers. The hotter blobs move upwards while the cooler ones descend over a characteristic distance $\ell_{\rm MLT}$ before dissolving and delivering their excess or deficiency of energy to the environment. This characteristic distance is called the mixing length and is depicted in Fig. 6.2. The latter is usually expressed in units of the pressure scale height $H_P = -(\mathrm{d}\log P/\mathrm{d}r)^{-1}$ by introducing the mixing-length parameter $\alpha_{\rm MLT}$ defined as

$$\ell_{\rm MLT} = \alpha_{\rm MLT} H_P. \tag{6.1}$$

In order to describe convection in stellar envelopes, Magic, Weiss, and Asplund (2015) studied the relation between the 1D atmosphere models that rely on the mixing length theory and atmosphere models based on full 3D radiative hydrodynamic calculations. By matching 1D and 3D models, they found that the mixing-length parameter $\alpha_{\rm MLT}$ used in 1D models depends on the evolutionary stage and stellar parameters, such as effective temperature $T_{\rm eff}$, surface gravity $\log g$, and metallicity [Fe/H]. Rigorously, the mixing-length parameter $\alpha_{\rm MLT}$ should be set as a function of these stellar parameters. To simplify, other authors assume that $\alpha_{\rm MLT}$ does not vary with stellar parameters or evolutionary status (*e.g.* Gustafsson et al., 2008; Pietrinferni et al., 2013; Choi et al., 2016). Accordingly, we keep the mixing-length parameter $\alpha_{\rm MLT}$ constant. Since its value cannot be analytically determined, a reasonable value is obtained by calibrating it with the Sun, *i.e.* to reach solar luminosity, radius and surface metallicity at solar age. In practice, $\alpha_{\rm MLT}$ depends on the treatment of the atmosphere. The value of $\alpha_{\rm MLT}$ we adopt results from the calibration of our model to the Sun, which is discussed in Sect. 6.2.3.

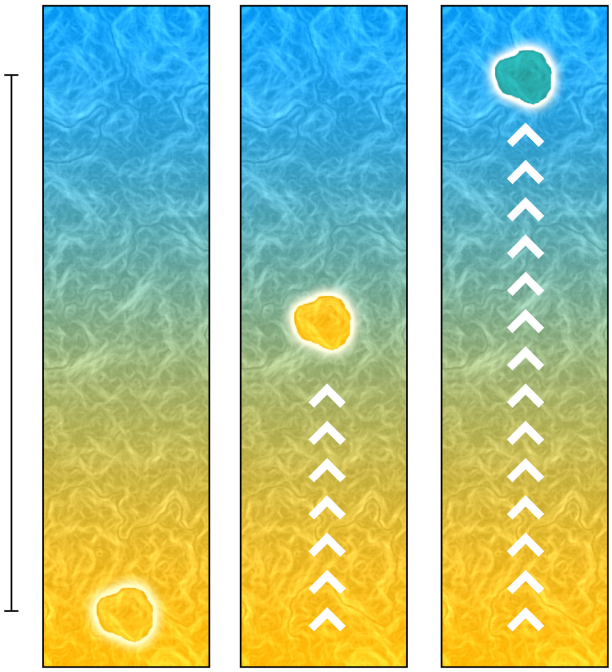

FIGURE 6.2: Timelaps of a fluid parcel that crosses a distance $\ell_{\rm MLT}$ before blending in with the surrounding fluid. The bar on the left side shows the mixing length $\ell_{\rm MLT}$. Credit: Mixing length model, Wikipedia

Nuclear-reaction network

Along evolution, the composition of stars is modified due to the complex nuclear-reaction network. As evolution proceeds, the network gets more complex due to the increase of the core temperature. It starts with the H burning on the main sequence through the PP chain and CNO cycle for stars of mass $M \leq 1.2\,M_\odot$ and $M \geq 1.2\,M_\odot$, respectively. Next, it passes through the burning of heavier elements such as the helium burning via the triple-α reaction

$$\begin{cases} {}^4_2\mathrm{He} + {}^4_2\mathrm{He} \rightarrow {}^8_4\mathrm{Be} + \gamma \\ {}^8_4\mathrm{Be} + {}^4_2\mathrm{He} \rightarrow {}^{12}_6\mathrm{C} + \gamma \end{cases} \tag{6.2}$$

and α-particle capture reactions such as ${}^{12}_6\mathrm{C} + {}^4_2\mathrm{He} \rightarrow {}^{16}_8\mathrm{O} + \gamma$ in the clump phase and on the AGB. In our model, we use a network of 32 nuclear reactions involving 23 stable or unstable species from ^{1}H to ^{24}Mg. This allows us to consistently follow the chemical changes and the production of nuclear energy up to the TP-AGB phase. The thermonuclear reaction rates are available in MESA files and are taken from NACRE (Angulo et al., 1999) and CF88 (Caughlan and Fowler, 1988), with priority on NACRE rates when available. We take into account updated rates for crucial reactions at evolved stages such as ${}^{14}_7\mathrm{N(p,}\,\gamma){}^{15}_8\mathrm{O}$ that is the bottleneck reaction for the CNO cycle (Imbriani et al., 2004) and the triple-α chain reaction for helium burning (Fynbo et al., 2005).

Opacity treatment

The opacity κ quantifies the opaqueness of a material, *i.e.* the absorption of the light as it passes through it. The opacity κ of the environment is related to the cross section $\sigma_{\rm cs}$ that is the mean area around a particle for a photon to interact with it. The former reads

$$\kappa = \sigma_{\rm cs}\,\frac{n_V}{\rho}, \tag{6.3}$$

where n_V is the number of particles per unit volume, and ρ is the density. In stellar interiors, opacities are essential to compute the energy transport in regularly stratified regions, *i.e.* radiative zones. The cross section σ_{cs} depends on the chemical composition of the environment as photons do not interact similarly with different particles. From Eq. 6.3, the opacity then varies with the chemical composition of the environment. In stellar models, opacities values are tabulated as a function of the density ρ, temperature T, and chemical composition. At low temperature ($\log T < 3.95$) we use the opacity tables from AESOPUS (Marigo and Girardi, 2007) while at high temperature ($\log T > 4.05$) we took those from OPAL1 and OPAL2 (Iglesias and Rogers, 1996). The use of the AESOPUS opacity tables at low temperature is motivated by the fact that they treat the dense chemical pattern in the photosphere of stars, particularly of AGB stars, taking into account continuum and discrete sources such as molecular absorption bands and collision-induced absorption. The AESOPUS and OPAL1 tables are for the Asplund et al. (2009) solar mixture, while the OPAL2 tables allow to account for the metal abundance changes due to the C and O enhancements that result from He burning. These tables are already generated and available in the MESA directories. In MESA, a blend (see Eq. 1 of Paxton et al. (2011)) is performed in regions where two distinct values exist for the opacity so that the derivatives smoothly vary relatively from one opacity table to the other. The delimitation of existing tables is shown in Fig. 6.3.

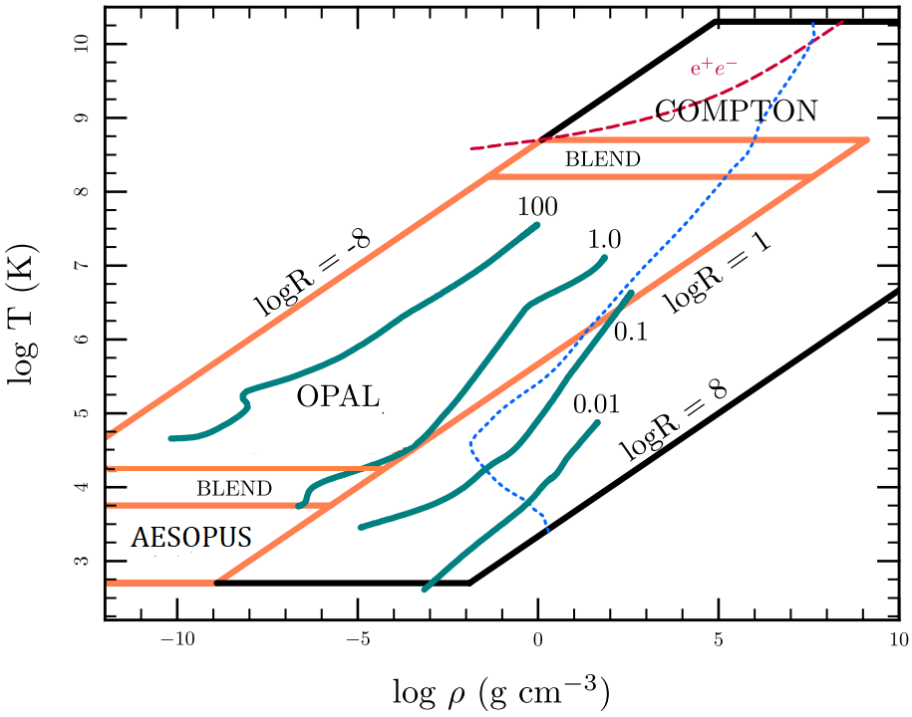

FIGURE 6.3: Sources of the MESA opacity tables depending on the temperature T and the density ρ. The sources AESOPUS (Marigo and Girardi, 2007), OPAL (Iglesias and Rogers, 1996), and COMPTON (Buchler and Yueh, 1976) are labelled in the specific regions of application. The orange solid lines delimit regions where input tables exist for radiative opacities, while the black solid lines delimit regions where algorithms are used to derive the total opacities. The opacity in the right hand side of the dashed blue lines is dominated by electron conduction. The contribution from pair production of electrons and positrons to opacity tables is accounted for and becomes noticeable when their number exceeds that of electrons from ionisation above the red dashed line. Several stellar evolutionary tracks are shown in grey solid lines (three main sequences with $M = 0.1$, 1.0, and 100 $M_\odot$ and one track of a contracting $M = 0.01\ M_\odot$ brown dwarf). Credit: Paxton et al. (2011)

Induced overshooting

In the classical bare-Schwarzschild mixing scheme, the border of the convective zone is defined according to the Schwarzschild criterion, that is where the difference $\nabla_{rad} - \nabla_{ad}$ changes sign (Schwarzschild,

1958; Straniero et al., 2003). In this case, no extra mixing is allowed beyond the convective border and a strong discontinuity in the chemical composition develops. This discontinuity grows as stellar evolution proceeds while nuclear reactions modify the core composition. Nevertheless, the bare-Schwarzschild convective border is in unstable equilibrium, meaning that a small expansion of the convective core may make $\nabla_{\rm rad}$ larger than $\nabla_{\rm ad}$ at the new border (Castellani, Giannone, and Renzini, 1971b; Gabriel et al., 2014). For this reason, an extra mixing layer must be taken into account beyond the boundary of the convective zone defined in the sense of bare-Schwarzschild, extending the mixing beyond the classical border of convective zones. This additional mixing is called induced overshooting, or equivalently convective overshooting. This process relies on the hypothesis that the convective elements that reach the classical border of the convective zone where $\nabla_{\rm rad} = \nabla_{\rm ad}$ still have a residual kinetic energy, to such an extent that they can penetrate the surrounding radiative zone and induce additional mixing by convection (Fig. 6.4). Then, two different schemes can be adopted to model this additional mixing region (Zahn, 1991).

- The classical **step function overshooting**: this scheme consists in extending the mixed region beyond the classical border of the convective zone by a fixed fraction of the pressure scale height $H_P = -(\mathrm{d}\log P/\mathrm{d}r)^{-1}$, with the temperature gradient ∇_T equal to the radiative gradient $\nabla_{\rm rad}$ in the mixed region (Maeder, 1975). The extent of this extra mixed region is parameterised by the overshooting parameter $\alpha_{\rm ov}$ such that the size of this region is $d_{\rm ov} = \alpha_{\rm ov} H_P$. In stellar evolution codes, the overshooting region is efficiently mixed by convection with respect to the characteristic timestep of the evolution. Then, in MESA we assume that the overshooting region is fully mixed. In case of a thin convective core during the H/He-core burning phases, the pressure scale height at the classical convective boundary may diverge due to its asymptotic behaviour at $r \to 0$, making the treatment tricky for small convective cores. To get around this difficulty, we use an option in MESA that sets the extent of the extra mixing region to $d_{\rm ov} = \alpha_{\rm ov} H_P$ if $H_P \leq R_{cc}$, where R_{cc} is the convective core radial thickness, and $d_{\rm ov} = \alpha_{\rm ov} R_{cc}$ otherwise.

- The **penetrative convection**: this scheme is overall similar to the step function overshooting scheme, but the thermal stratification differs. Instead of imposing $\nabla_T = \nabla_{\rm rad}$ in the extra mixed region, we require $\nabla_T = \nabla_{\rm ad}$. This change does not significantly impact the global properties of stars, such as their luminosity and effective temperature, but clearly modifies the seismic parameters that are sensitive to the inner structure near the border of the convective core.

Both mixing schemes can be used in MESA to model an additional mixed region beyond convective zones. However, these mixing schemes have different impact on the structure parameters, especially the Brunt-Väisälä frequency squared $N_{\rm BV}$. This implies that they differently affect seismic parameters, for instance the period spacing $\Delta\Pi_1$, which is expressed as an integral of the Brunt-Väisälä frequency through Eq. 3.39. Then, seismic parameters can be used to constrain the mixing scheme in the overshooting region, as performed by Bossini et al. (2017). They noticed that the period-spacing distribution of He-core burning stars observed by Vrard, Mosser, and Samadi (2016) better matches the one obtained when considering a model that includes an overshooting region with a radiative stratification.
In this work, we explore the effects of convective overshooting on the seismic parameters and the evolutionary track, especially the location of the AGBb. We consider overshooting at two different locations in stellar interiors: one from the convective core to the radiative zone, as illustrated in Fig. 6.4 during the H-core burning and He-burning phases, and the other from the convective envelope to the radiative core also called envelope undershooting (Khan et al., 2018) from the H-core burning phase to the AGB.

He-semiconvection and modified overshooting

Stellar evolution models reveal a coupling between the physical and chemical evolution of the convective core and the behaviour of the surrounding radiative layers. The quick mixing in the overshooting

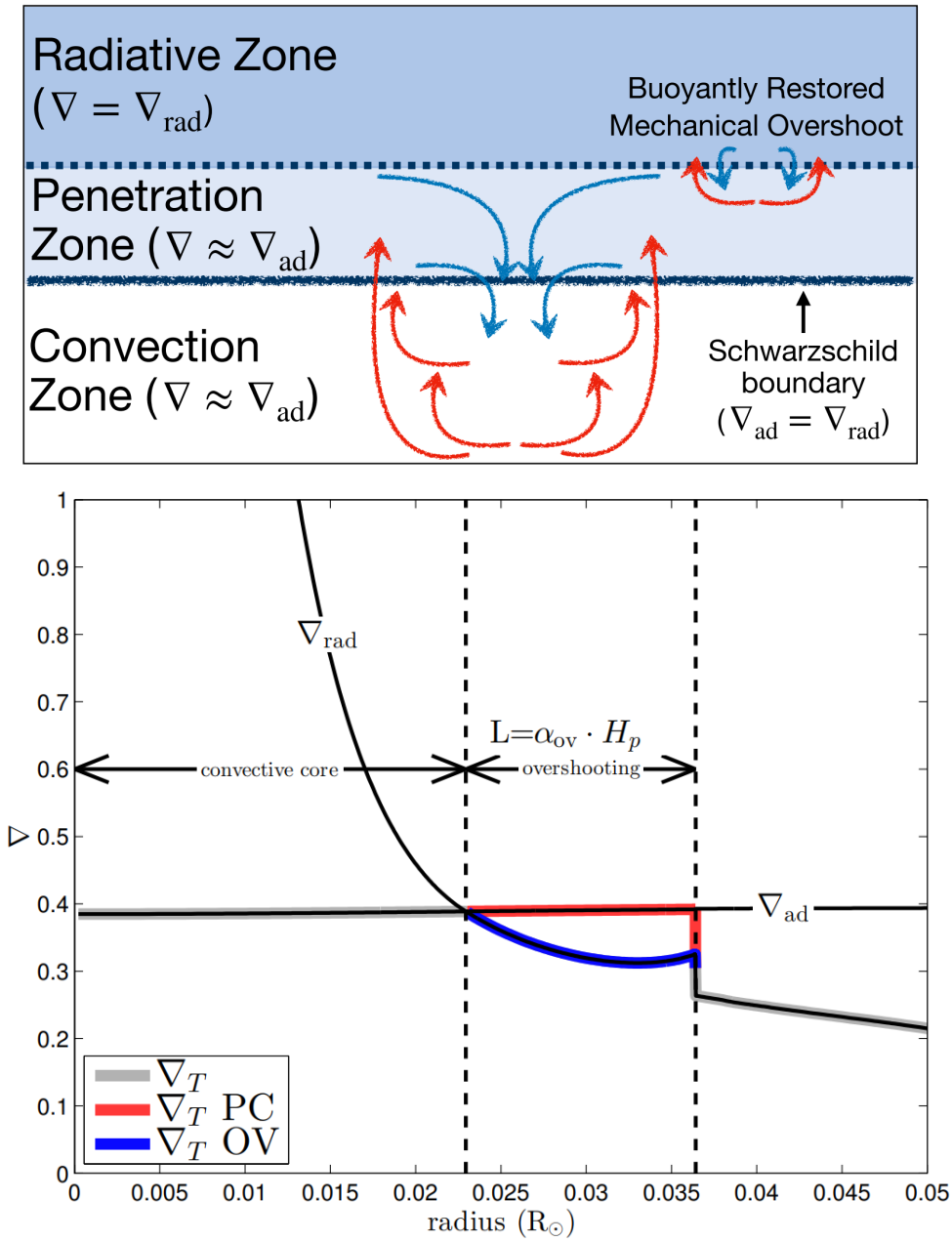

FIGURE 6.4: **Top:** Structure of a convective boundary in the convective penetration scheme as found by Anders et al. (2022). Convective elements in the penetration zone that hit the boundary of the radiative zone are braked by the buoyant restoring force, so they slightly penetrate the radiative zone. Meanwhile, motions that start in the convection zone undergo a weak restoring force when crossing the penetration zone, allowing the latter to remain thermally well mixed. Credit: Jermyn et al. (2022). **Bottom:** Schematic description of the temperature gradient in the two schemes of convective overshooting near the convective core boundary. The profile of ∇_T in the extra mixed region is shown in red for the penetrative convection scenario and in blue for the classical overshooting scenario. Figure courtesy of Diego Bossini.

region induces an overall decrease of the radiative temperature gradient in this region. This global decrease is due to the fact that the propagation of convective elements becomes more efficient and helium-rich materials are mixed in the overshooting region. On the other hand, the induced overshooting generates a local minimum in $\nabla_{\rm rad}$ within the mixed region and a local maximum at the extra-mixing border above the location of the local minimum, as illustrated in Fig. 6.4 in the classical treatment of overshooting (Bossini et al., 2017). These extrema are caused by the increasing opacity of the overshooting region due to the additional C and O elements formed in the convective core and brought by mixing processes. The overall decrease of the radiative gradient $\nabla_{\rm rad}$ brings its local minimum to values lower or equal to that of $\nabla_{\rm ad}$ in the mixed region. If the local maximum of the $\nabla_{\rm rad}$ profile exceeds the $\nabla_{\rm ad}$ value, a layer that is convectively unstable in the sense of Schwarzschild develops. In MESA, this additional convective layer induces a numerical problem since it is connected to the overshooting region, which is interpreted as part of the convective core. This leads to a non-physical injection of helium in the core (see Fig. 6.5). This problem can be lifted by considering an intermediate region called semi-convection zone between the local minimum of $\nabla_{\rm rad}$ and the outer radiative zone (Castellani, Giannone, and Renzini, 1971a). Semi-convection is related to the presence of a region that is unstable against convection, but tends to be stabilised by partial mixing. This partial mixing is induced by the convectively unstable core between the location of the minimum of $\nabla_{\rm rad}$ and the outer radiative zone. In stellar models, a smooth gradient of chemical composition is created by the partial chemical mixing in the overshooting region to satisfy $\nabla_{\rm rad} = \nabla_{\rm ad}$.

In the general case, the boundary of the convective core is set in the sense of Schwarzschild, *i.e.* where $\nabla_{\rm rad} = \nabla_{\rm ad}$. In our work, we follow the modified prescription described in Bossini et al. (2017) to avoid any artificial injection of helium in the core. This prescription consists in defining the convective border at the location of the local minimum of $\nabla_{\rm rad}$ if it has increased over $\nabla_{\rm ad}$ in the overshooting region, and at the location where $\nabla_{\rm rad} = \nabla_{\rm ad}$ otherwise (see Fig. 6.6). In parallel, we consider the He-semiconvection routine in MESA. We follow the diffusion scheme of Langer, El Eid, and Fricke (1985) that introduces the diffusion coefficient

$$D_{\rm sc} = \alpha_{\rm sc} \frac{\kappa_r}{6 c_P \rho} \frac{\nabla_T - \nabla_{\rm ad}}{\nabla_L - \nabla_T}, \tag{6.4}$$

where $\alpha_{\rm sc}$ is the efficiency for the semiconvective diffusion, c_P is the specific heat at constant pressure, ρ is the density, κ_r is the radiative conductivity, and $\nabla_L = \nabla_{\rm ad} + [\beta/(4-3\beta)]\nabla_\mu$ where β is the ratio of gas pressure to total pressure and $\nabla_\mu = {\rm d}\ln\mu/{\rm d}\ln P$. We adopt the typical value $\alpha_{\rm sc} = 0.1$ for well developed semiconvection (Langer, El Eid, and Fricke, 1985) and compute $D_{\rm sc}$ with $\nabla_T = \nabla_{\rm rad}$ in the semiconvection region. Without this treatment of semiconvection, the evolutionary track in the HR diagram and the Brunt-Väisälä frequency profile are noisy at the end of the He-core burning phase. Another effect of a unadapted semiconvection treatment is that the luminosity drop at the AGBb is less important and the star spends less time in the AGBb. Then, the treatment of He-semiconvection is crucial for our study of the AGB bump in the presence of overshooting.

Most of the 1D stellar codes make use of the diffusion scheme to cope with semiconvection during H- and He-core burning phases (*e.g.*, Noels et al., 2010; Silva Aguirre et al., 2011; Choi et al., 2016). In parallel, other treatments have been investigated to deal with the mixing in the semiconvective layer, for instance the one that consists in changing the composition until the convective neutrality (*i.e.* $\nabla_{\rm rad} = \nabla_{\rm ad}$ according to the Schwarzschild criterion) is obtained (Crowe and Matalas, 1982). In this scenario, the discontinuity in the profile of chemical elements such as hydrogen during the H-core burning phase is smoothed out. Nevertheless, these 1D schemes are incomplete as they reduce the semiconvective mixing efficiency to a free parameter ($\alpha_{\rm sc}$ in the diffusion treatment), leading to a lack of information about this mixing process in stellar interiors. In order to circumvent this difficulty, 3D hydrodynamical simulations has been released to quantify the transport of heat and composition behind semiconvection (Mirouh et al., 2012; Wood, Garaud, and Stellmach, 2013). In this case, semiconvection is often referred to as oscillatory double-diffusive (ODD) convection. In these semiconvective layers, the mean fluxes and kinetic energy vary quasi-periodically, which is caused by large-scale gravity-wave motions. These partial mixing regions are dependent of a double-diffusive instability, where two diffusion coefficients

are needed to describe the fluid motions (Stern, 1960; Walin, 1964; Veronis, 1965; Kato, 1966). Under specific conditions[1], layered convection may settle, affecting the transport of heat and composition and leading to a stair-like chemical stratification (Mirouh et al., 2012). Then, this 3D hydrodynamical treatment of semiconvective zones has been adapted to provide a 1D prescription in stellar evolution codes (Wood, Garaud, and Stellmach, 2013; Moore and Garaud, 2016).

Thermohaline convection

The thermohaline mixing has a significant role in the surface composition of red giants, as introduced in Sect. 2.3.3. After the first dredge-up, the H-burning shell advances towards the surface while the base of the convective envelope recedes toward the interior. Once the shell source reaches the homogeneous part of the envelope, an inversion of molecular weight is created by the reaction ^{3}He(^{3}He, 2p)^{4}He in the outer wing of the H-burning shell (Ulrich, 1972). At that point, thermohaline convection sets in a stably stratified region that satisfies the Ledoux criterion for convective stability, where the inversion of molecular weight occurs. Then, the conditions for thermohaline convection reads

$$\begin{cases} \nabla_{\rm ad} - \nabla_T + \left(\frac{\varphi}{\delta}\right) \nabla_\mu > 0 \\ \nabla_\mu = \frac{{\rm d}\ln\mu}{{\rm d}\ln P} < 0, \end{cases} \tag{6.5}$$

where $\varphi = (\partial \ln P / \partial \ln \mu)_{P,T}$, $\delta = -(\partial \ln \rho / \partial \ln T)_{P,\mu}$, and the subscripts P, T, and μ indicate that the partial derivatives are taken at constant pressure, temperature, and mean molecular weight, respectively. The extent of the thermohaline mixing region depends on the strength of the μ-inversion, which determines the efficiency of thermohaline mixing. For low-mass stars $M \leq 1.5\,M_\odot$, the thermohaline mixing region is large enough to connect the H-burning shell to the convective envelope (see Fig. 6.7), bringing the products of H burning in the stellar envelope then changing the stellar surface composition. In MESA, thermohaline mixing is treated as a diffusive process where the diffusion coefficient reads (Paxton et al., 2013)

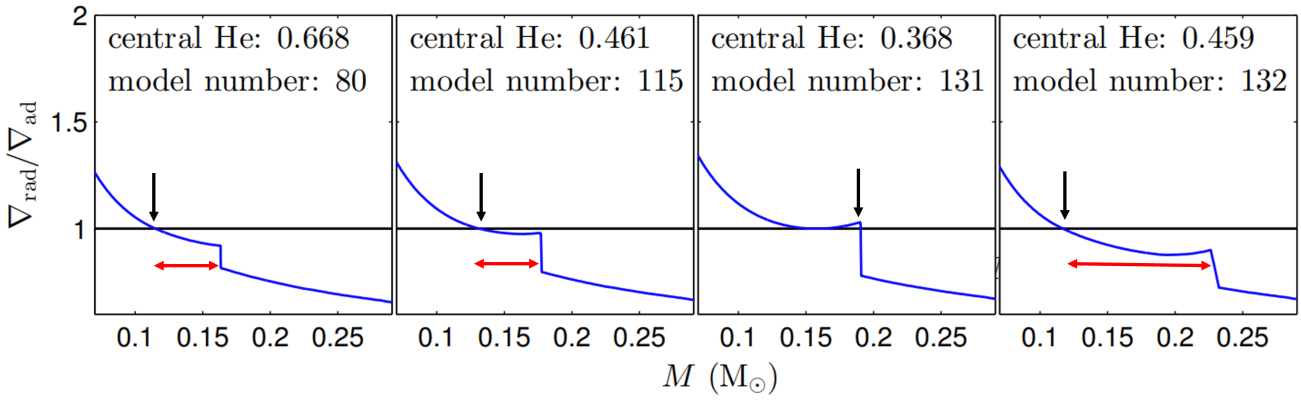

FIGURE 6.5: Ratio between the radiative gradient $\nabla_{\rm rad}$ and the adiabatic gradient $\nabla_{\rm ad}$ as a function of the mass coordinate. The profiles are computed for consecutive $1.50\,M_\odot$ models in the He-core burning phase when the standard overshooting scheme of MESA is applied ($\alpha_{\rm ov,He} = 0.3$). The consecutive panels show how the gradient profiles evolve with time from left to right. The black arrows show the position of the classical convection border while the two-sided red arrows delimit the overshooting region. In the third panel, we can see that the classical convection border is misidentified at the outer edge of the overshooting region, so in the next step (fourth panel) the overshooting region is artificially extended. This numerical problem generates an injection of helium in the core. Credit: Bossini (2016)

[1] We can define the inverse density ratio R_0^{-1} as the ratio between the destabilising thermal stratification and the stabilising compositional one by $R_0^{-1} = \frac{\nabla_\mu}{\nabla_T - \nabla_{\rm ad}}$, where ∇_μ is the molecular weight gradient defined in Eq. 6.5. If R_0^{-1} becomes lower than a specific threshold, then ODD convection is changed into layered convection

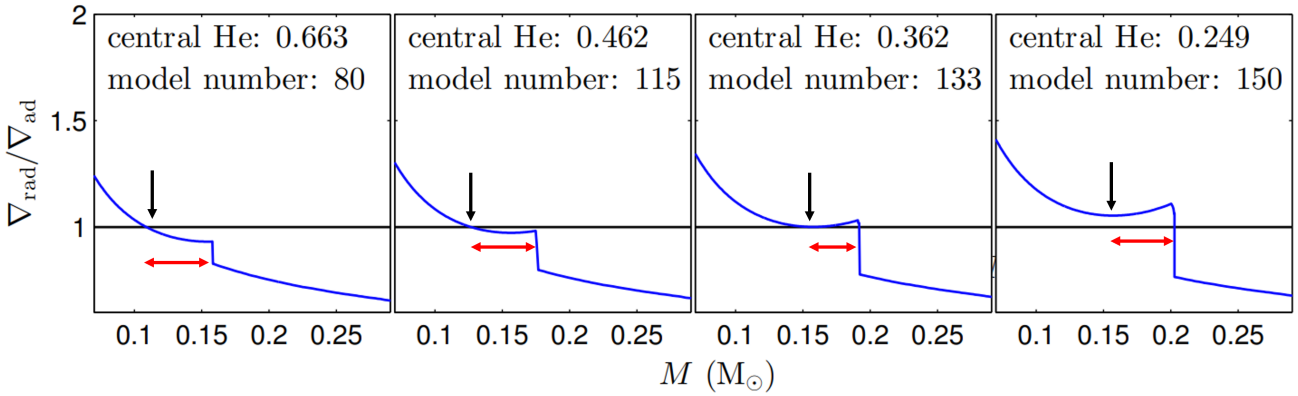

FIGURE 6.6: Same label as Fig. 6.5, but the modified overshooting scheme implemented by Bossini et al. (2017) is adopted. In this scenario, the classical convection border is taken at the point where $\nabla_{\rm rad} = \nabla_{\rm ad}$, except if the local minimum in $\nabla_{\rm rad}$ inside the convective region becomes larger than $\nabla_{\rm ad}$ (which is what we can see in the third panel). Then, the overshooting region is not extended and no artificial helium injection is noticeable. Credit: Bossini (2016)

$$D_{\rm th} = \alpha_{\rm th} \frac{3\kappa_r}{2\rho c_P} \frac{K}{\nabla_T - \nabla_{\rm ad}}. \tag{6.6}$$

In the previous equation, κ_r is the radiative conductivity, c_P is the specific heat at constant pressure, $\alpha_{\rm th}$ is the efficiency parameter for the thermohaline mixing, and

$$K = -\frac{1}{\chi_T} \sum_{i=1}^{N-1} \left(\frac{\partial \ln P}{\partial \ln X_i} \right)_{\rho,T,\{X_{j\neq i}\}} \frac{{\rm d} \ln X_i}{{\rm d} \ln P}, \tag{6.7}$$

where $\chi_T = (\partial \ln P / \partial \ln T)_\rho$, and X_i represents the mass fraction of atoms of species i in the N-component plasma. The species j is eliminated in the sum so that the constraint $\sum_{i=1}^{N-1} X_i + X_N = 1$ is fulfilled. We follow the diffusive scheme of Kippenhahn, Ruschenplatt, and Thomas (1980), which assumes that thermohaline mixing is performed with blobs of size L that diffuse while travelling over a mean free path L before dissolving, with the efficiency parameter $\alpha_{\rm th} = 2$.

Rotation

In stellar models, rotation is one of the main ingredients that affect lifetimes, surface abundances and evolutionary fates. Indeed, rotation induces mixing that brings the products of nuclear reactions to the envelope. In MESA, rotation is treated in 1D in the shellular approximation, *i.e.* the angular velocity is constant on isobars whose shapes are spherical surfaces (*e.g.*, Zahn, 1992; Meynet and Maeder, 1997). This assumption is valid because of the presence of a strong anisotropic turbulence acting along isobars, which is caused by a differential rotation and efficiently erases gradients along isobars. With the shellular rotation, MESA calculates the modification brought by the centrifugal acceleration in 1D stellar equations (Kippenhahn and Thomas, 1970; Endal and Sofia, 1976). In our work, we implement rotation from the ZAMS up to the AGB phase with a rotation rate that gradually reaches the maximum value $\Omega_{\rm ZAMS}$ at the ZAMS. The value that we use is motivated by observations of B stars (Huang, Gies, and McSwain, 2010), which is $\Omega_{\rm ZAMS}/\Omega_{\rm crit} = 0.3$, where $\Omega_{\rm crit}$ is the surface critical angular velocity for the star to be dislocated. Including rotation with this rate produces evolutionary tracks that are similar to those when adding H-core overshooting $\alpha_{\rm ov,H} \approx 0.25$, which is slightly higher than the optimal value obtained by calibration (see Fig. 2.3). Nevertheless, we do not include rotation for stars of mass $M \leq 1.5\,M_\odot$ since magnetic braking is not implemented in MESA, which is necessary to reproduce slow rotation rates of low-mass stars (Kawaler, 1988).

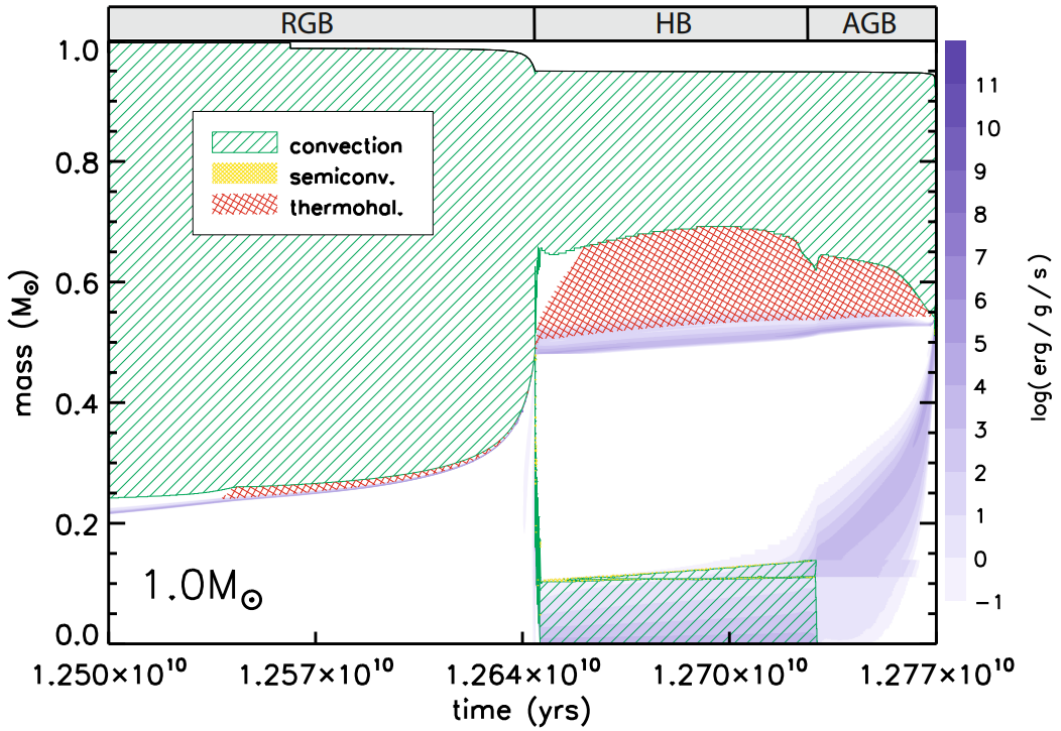

FIGURE 6.7: Evolution of the internal structure of a 1.0 $M_{\odot}$ star including thermohaline mixing and He-semiconvection, from the onset of thermohaline mixing on the RGB up to the AGB. Green, yellow and red hatched regions indicate convection, semiconvection, and thermohaline mixing, respectively. Blue shaded areas shows regions where nuclear burning proceeds. Credit: Cantiello and Langer (2010)

As mentioned herebefore, rotation induces transport of chemicals and angular momentum throughout the star. These transport mechanisms are treated in a diffusion approach through instabilities (Endal and Sofia, 1978; Pinsonneault et al., 1989; Heger, Langer, and Woosley, 2000). Six rotational instabilities are considered, which are dynamical shear, secular shear, Solberg-Høiland, Goldreich-Schubert-Fricke instabilities, Eddington-Sweet circulation, and Tayler-Spruit dynamo. The dynamical shear instability arises when the energy gained by shear flows is comparable to the work necessary for a mass element to adiabatically counterbalance the gravitational potential. If thermal adjustments of radial perturbations are allowed, then this instability is relaxed on a thermal timescale and is therefore a secular shear instability. The Solberg-Høiland instability occurs when an adiabatically displaced mass element undergoes a total force that is parallel to the direction of the displacement. The Goldreich-Schubert-Fricke instability emerges from axisymmetric perturbations, where the rotational velocity depends on the distance from the equatorial plan, creating meridional flows. In a rotating star, surfaces of constant temperature and pressure do not coincide. As a consequence, rotating stars cannot be simultaneously in thermal and hydrostatic equilibrium (Baker and Kippenhahn, 1959) and large-scale circulations develop called Eddington-Sweet circulations. Finally, the Tayler-Spruit dynamo is driven in presence of differential rotation by the Tayler instability that implies an axisymmetric toroidal magnetic field (Spruit, 1999; Spruit, 2002). The Tayler instability can generate a radial field displacement that is rewinded by differential rotation into a toroidal field, creating a dynamo loop, hence the Tayler-Spruit dynamo. These instabilities are represented by diffusion coefficients and are added to the diffusion coefficient in absence of rotation.

The atmosphere and mass loss

As presented in Chapter 3, seismic parameters are sensitive to the near-surface structures with a strong sound-speed gradient. The modelling of the stellar atmosphere is then essential as the latter directly impact the seismic parameters. Here, we take a simple grey atmosphere with an Eddington $T - \tau$ relation

$$T^4 = \frac{3}{4} T_{\rm eff}^4 \left(\tau + \frac{2}{3} \right), \tag{6.8}$$

where τ is the optical depth. The outermost meshpoint of the models is defined at the layer where the optical depth $\tau = 2/3$, which is at the limit of the photosphere. As introduced in Chapter 2, high-luminosity giants experience an important mass loss due to the radiative pressure exerced by photons that push the envelope outwards. In MESA, we used the Reimers' prescription (Eq. 2.8) from the RGB up to the He-core burning phase with a scaling factor $\eta_R = 0.3$, which is the maximum mass loss rate reported for composite populations, *i.e.* for a mixture of several stellar-cluster populations with different ages and chemical compositions (Miglio et al., 2021a). On the AGB, we use the Blöcker's prescription (Eq. 2.9) with a scaling factor equal to $\eta_B = 0.1$, which is the typical value used to reproduce the initial-final mass relation, *i.e.* the total mass loss integrated over the lifetime from the initial stage to the final stage of stellar evolution (Choi et al., 2016). In the atmosphere, we tested a varying opacity computed by numerical integration of the hydrostatic equilibrium equation, but the model could not evolve further than the He-flash stage because of convergence issues of the solution. As a consequence, we choose a uniform opacity, fixed to the opacity of the outermost cell of the interior model, which is the standard option in MESA.

6.2.3 The solar calibration

With the high-quality data available of the present-day Sun including seismic data, the global properties of the Sun such as its mass and age are well constrained (*e.g.*, Bahcall, Pinsonneault, and Wasserburg, 1995; Brown and Christensen-Dalsgaard, 1998; Fröhlich, 2006). This makes the Sun an adequate reference point for testing new input physics and comparing them with different studies. For this reason, the stellar evolutionary tracks are calibrated so that the global solar parameters are recovered for the model computed at the solar age. This procedure is called a solar calibration. The initial model used for the solar calibration is a star on the pre-main sequence with an homogeneous chemical composition at a given helium abundance Y_0, metallicity [Fe/H] and mixing length parameter $\alpha_{\rm MLT}$. In our study, we keep the mass M and H-core overshooting $\alpha_{\rm ov,H}$ fixed at the values $M = 1\,M_\odot$ and $\alpha_{\rm ov,H} = 0.2$. Then, we compute the evolution of the corresponding model up to the present solar age. If the model at the solar age fits the solar parameters within the desired accuracy then the set of parameters $\{Y_0, [{\rm Fe/H}], \alpha_{\rm MLT}\}$ is assumed to be satisfyingly calibrated to the Sun. If not, MESA computes in an iterative process the track of an other initial model with different parameters Y_0, [Fe/H], and $\alpha_{\rm MLT}$. The agreement of the computed model at the solar age is evaluated by a χ^2 method, which consists in minimising the parameter χ^2 that encompasses differences between the model and observations. This parameter is defined as

$$\chi^2 = \sum_{i=1}^{N} \frac{(y_i - y_{i,\rm obs})^2}{\sigma^2_{y_{i,\rm obs}}}, \tag{6.9}$$

where $y_{i,\rm obs}$ are the observed solar parameters, y_i are the corresponding parameters from stellar models, $\sigma_{y_{i,\rm obs}}$ are the uncertainties on $y_{i,\rm obs}$, and N is the number of total solar parameters. In MESA, the optimisation method to find the minimal χ^2 follows the Nelder-Mead simplex algorithm (Nelder and Mead, 1965), which adapts itself to local extrema and where new combinations of initial parameters $\{Y_0, [{\rm Fe/H}], \alpha_{\rm MLT}\}$ are chosen based on the previous comparison between the model at solar age and observations. Here, the observed solar parameters are the luminosity $L_\odot = 3.8418 \times 10^{26}$ W, the radius $R_\odot = 6.9598 \times 10^5$ km (Bahcall et al., 2005), and the ratio between the metal mass fraction and hydrogen mass fraction at the surface $(Z/X)_\odot = 0.0181$[2]. The latter value corresponds to the determination of the solar composition by Asplund et al. (2009). Usually, many studies use the target solar age $\tau_\odot = 4.567 \times 10^9$ yr presented in, *e.g.*, Chaussidon (2007), which corresponds to the solar age derived from the abundances and daughter products of radioactive nuclides in meteoritic material. In MESA,

[2]the metal mass fraction Z is related to the metal abundance ratio [Fe/H] by $[{\rm Fe/H}] = \log\left(\frac{(Z/X)}{(Z/X)_\odot}\right)$

the default target solar age is $\tau_\odot = 4.61 \times 10^9$ yrs, which takes into account the time spent after the ZAMS $\tau = 4.57 \times 10^9$ yrs and the time spent during the pre-main sequence $\tau_{\rm PMS} = 4 \times 10^7$ yrs. These different options for the target solar age induce insignificant differences in the calibrated parameters $\{Y_0, [{\rm Fe/H}], \alpha_{\rm MLT}\}$ (Sackmann, Boothroyd, and Fowler, 1990). With our set of physical inputs presented in Sect. 6.2 including H-core overshooting, we obtain the calibrated values $Y_0 = 0.253$, $Z = 0.0133$, and $\alpha_{\rm MLT} = 1.927$.

6.3 The stellar oscillation code ADIPLS

The Aarhus adiabatic oscillation package ADIPLS (Christensen-Dalsgaard, 2008) provides an efficient way for the computation of adiabatic oscillation frequencies and eigenfunction of stellar models. Indeed, radial and non-radial oscillations can be computed in the Cowling approximation, leading to a second-order set of equations (Eq. 3.10) or in the full case, corresponding to a fourth-order system of equations (Eq. 3.8). The code also includes a meticulous treatment of the boundary conditions. The former allows the user to consider a full model, including the core and the envelope with the regularity conditions at the boundary meshpoints, or a truncated model at a finite distance from the centre with different types of conditions that can be parameterised. In parallel, the code can adjust the treatment to different surface conditions. In vanishing surface pressure models (for example in full polytropic models), the surface is a singular point so regularity conditions are imposed. In non-vanishing surface pressure models (for instance models truncated at a suitable point in the atmosphere), various conditions can be chosen. This code is directly incorporated in MESA package and the models returned by MESA can be used as inputs to ADIPLS to compute the adiabatic frequencies corresponding to these models. ADIPLS offers multiple options to determine all frequencies of a given model in a given range of degree and frequency. The programme is controlled by various parameters, which are divided in several categories:

- The *mod* group, which is devoted to reading the stellar models returned by MESA and controlling the equilibrium model. For the computation of the adiabatic frequencies, the model can be read with a specific spacing in the stellar mesh or truncated at a specific location.
- The *osc* group, dedicated to controlling the mode degrees ℓ to be computed as well as the trial frequencies used to find the adiabatic oscillation frequencies of the models. Especially, we can choose the way trial frequencies are determined, the frequency window in which they can vary, and the way they are incremented at each step of the iteration process to reach the best solution.
- The *rot* group includes the effects of rotation.
- The *cst* group defines the fundamental constants, especially the value of the gravitational constant $G = 6.6732 \times 10^{-8}$ g^{-1}.cm^3.s^{-2}.
- The *int* group, which controls the equations, the boundary conditions and the numerical integration method of the oscillation equations. The latter can be solved by using the Cowling approximation or the full set of equations. Several boundary conditions can be adopted at the surface, either implying the pressure perturbation or the radius perturbation. The maximum number of iterations to find the solution and the precision with which the frequencies are assumed can also be initialised. The integration method can either be set following a shooting method or a relaxation technique. The shooting method assumes that for a set of two (respectively four) equations, a unique solution satisfies (respectively two linearly independent solutions satisfy) the inner boundary conditions and a unique solution satisfies (respectively two linearly independent solutions satisfy) the outer boundary conditions. The final solution can then be obtained by requiring that the solutions agree at a suitable matching point $x_f = r_f/R_*$, where r_f is the radial coordinate of the matching point and R_* is the radius of the star. In the case where one of the boundary conditions is dropped, the relaxation technique can be used to avoid ill-behaved solution where the latter is found separately for $x < x_f$ and $x \geq x_f$ by introducing a double point $x_f^- = x(k_f) = x(k_f + 1) = x_f^+$, where k_f is the $k_f^{\rm th}$ point in the mesh. Further details about the mathematical implementation of these methods can be found in Christensen-Dalsgaard (2008).

- The *out* group, which handles the outputs. The code returns the adiabatic mode frequencies, degree, the radial order, and the inertia. Parameters are available to designate the radial order and the normalisation factor for the mode energy. Finally, the frequencies are returned in a specified frequency window and the displacement eigenfunctions can be returned at provided meshpoints.

6.3.1 Computation of p-modes in evolved giants

The extraction of the pure pressure non-radial modes

To compute the adiabatic frequencies of p modes, we initialise the parameters in the control file of ADIPLS to optimise the computation of these modes in red giants. Nevertheless, computing p modes in red giants is not straightforward. In red giants, the p- and g-mode cavities are coupled, so the non-radial p modes are not directly accessible. Instead, non-radial modes are mixed modes, for which the displacement eigenfunctions is non-zero both in the envelope and in the core. The p-mode frequencies could be approximated from the mixed-mode pattern, especially with the mode of lowest inertia. But resolving the mixed modes is demanding since their displacement eigenfunctions rapidly vary in the core. For example, more than 20,000 cells are needed to resolve the displacement eigenfunctions of mixed modes in case of an intermediate red giant, and even more cells is required for a high-luminosity red giant.
Alternately, this difficulty can be circumvented by a specific treatment of non-radial modes. Mixed modes can develop because of the presence of a radiative zone where $N_{\rm BV} > 0$, which is responsible of the g-mode behaviour of mixed modes in the core. In the absence of a radiative zone, mixed modes cannot develop and non-radial modes are pure p modes. By setting the square of the Brunt-Väisälä frequency $N^2_{\rm BV}$ equal to zero in the convectively stable regions, the g modes in the core would be suppressed. Ball, Themeßl, and Hekker (2018) have shown that modifying the dimensionless square of the Brunt-Väisälä frequency in the ADIPLS files defined as

$$\mathcal{A} = \frac{r}{g} N^2_{\rm BV} = \frac{1}{\Gamma_1} \frac{{\rm d}\ln P}{{\rm d}\ln r} - \frac{{\rm d}\ln \rho}{{\rm d}\ln r}, \tag{6.10}$$

and setting it to zero wherever $\mathcal{A} > 0$ in the core allowed them to consistently extract the p-mode frequencies of dipole and quadrupole modes in RGB models. In Eq. 6.10, r is the distance to the centre, g is the local gravity, Γ_1 is the local first adiabatic exponent, P is the local pressure, and ρ is the local density. In Fig. 6.8, we can see how the frequencies of the modes of lowest inertia for non-radial modes in the unmodified model compare with those of the non-radial p modes obtained by setting $\mathcal{A} = 0$ in the core. We notice that the quadrupole modes are accurate since they do not deviate far from the modes of lowest inertia in the unmodified model. For dipole modes, a deviation of 0.1 μHz is noticeable around $\nu \sim 40\,\mu$Hz, which is equal to 2% of the value of $\Delta\nu$, which tends to confirm that the frequencies of the non-radial pure p modes are correct. These observations have been validated for several RGB models at low $\Delta\nu = 2.97, 3.15, 4.56\,\mu$Hz. As a result, setting $\mathcal{A} = 0$ allows us to extract the pure p mode frequencies of non-radial modes in evolved RGB stars with $\Delta\nu \leq 4.5\,\mu$Hz. Accordingly, we compute the frequencies of the pure p dipole and quadrupole modes by setting $\mathcal{A} = 0$ in the core for both H-shell burning and He-burning stars. In Sect. 6.3.3, we evaluate the consistency of the method for He-burning stars. This modification is not brought to the MESA models, but only achieved in the ADIPLS file, as described in Appendix A of Ball, Themeßl, and Hekker (2018). This method is efficient since we do not require a large number of cells to resolve the displacement eigenfunctions as they do not rapidly vary for pressure modes of low-radial order.

ADIPLS settings

In the *osc* group, the mode degrees that we compute are set to $\ell = 0, 1, 2$. When the MESA models are close to the luminosity tip of the RGB before undergoing the He burning, the code fails to return consistent frequencies for the non-radial modes. We reach the same conclusion for models evolving on the AGB after the AGB bump. As a consequence, we do not compute the non-radial modes near the luminosity tip of the RGB and after the AGB bump, but the radial modes only. On the other hand, trial frequencies are provided to the code to efficiently compute the p-mode frequencies. The first trial

frequency is taken very low to catch the first radial order, then the next trial frequencies are based on the mode frequencies computed at the previous radial order $n-1$. In the *int* group, we do not assume the Cowling approximation and solve the full oscillation equations. The type of integration for solving the differential equations is set following the shooting method with centred difference equations. In this scenario, the differential equations are replaced by difference equations and the numerical problem is formulated by

$$\frac{y_i(k+1)-y_i(k)}{x(k+1)-x(k)} = \frac{1}{2}\sum_{j=1}^{I}\left[a_{i,j}(k)y_j(k)+a_{i,j}(k+1)y_j(k+1)\right], \tag{6.11}$$

where $i = 1, ..., I$, I is the order of the system, $x = r/R_*$, k is the k^{th} point in the mesh, y_i are the variables in the oscillation equations to be determined, and $a_{i,j}$ are linear coefficients.

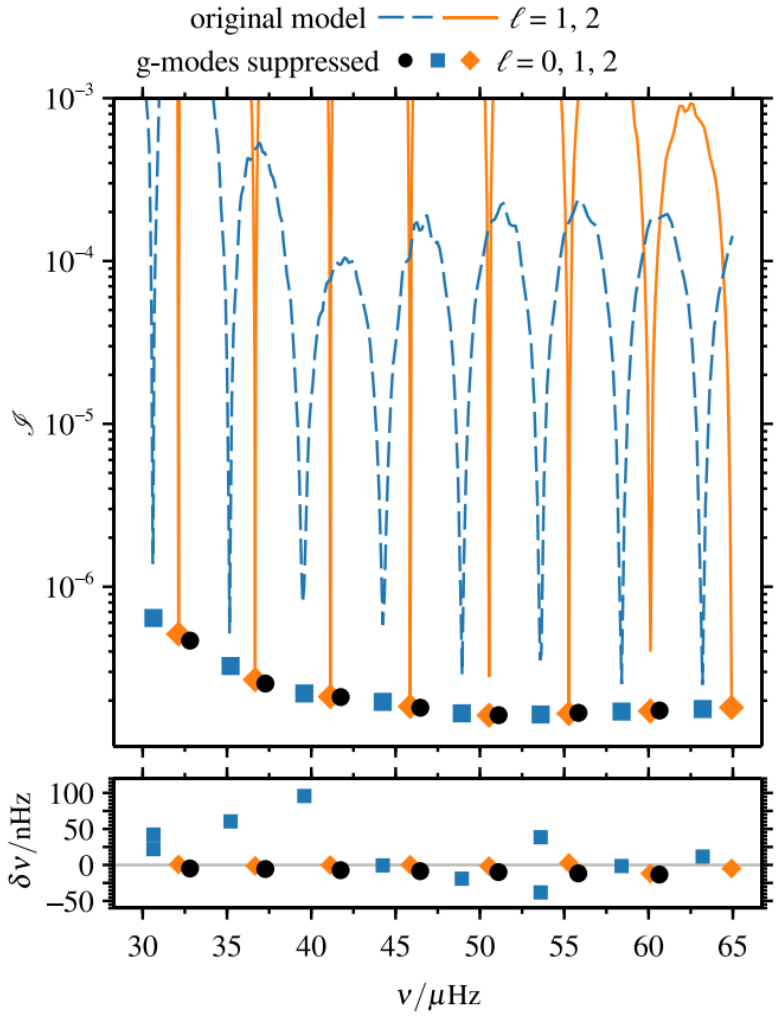

FIGURE 6.8: Demonstration of the effects of suppressing g modes in the core by setting the dimensionless square of the Brunt-Väisälä frequency $\mathcal{A} = 0$ for an RGB model of mass $M = 1.47\,M_\odot$, large separation $\Delta\nu = 4.56\,\mu$Hz, and frequency at maximum oscillation power $\nu_{\max} = 46.4\,\mu$Hz. **Upper panel**: mode inertia as a function of frequency. The dashed blue and solid orange lines refers to the $\ell = 1, 2$ modes, respectively, before the g modes are suppressed. The black circles, blue squares, and orange diamonds show the $\ell = 0, 1, 2$ modes after the g modes are suppressed. **Lower panel**: differences between the mode frequencies before and after the g mode suppression. For the non-radial modes, the differences are shown relatively to the modes of lowest inertia obtained in each $\Delta\nu$ interval in the unmodified model. For two dipole modes (at 30.6 and 53.6 μHz), two modes with low inertia are close to the expected pure p mode, they are both displayed in the figure. Credit: Ball, Themeßl, and Hekker (2018)

The numerical errors in the computed frequencies scale as N^{-2}, where N is the number of meshpoints. The computed pulsation frequencies ω are improved by using the Richardson extrapolation (Shibahashi and Osaki, 1981). If we define the dimensionless frequency σ by

$$\omega = \sqrt{\frac{GM}{R^3}}\sigma, \tag{6.12}$$

it can be shown that the eigenfrequencies obtained from models with $N/2$ and N meshpoints noted $\sigma(N/2)$ and $\sigma(N)$, respectively, can be used to improve the accuracy of the eigenfrequencies. The leading-order error term cancels when considering the frequency $\sigma_{\rm Ri}$ defined by

$$\sigma_{\rm Ri} = \frac{1}{3}\left[4\sigma(N) - \sigma(N/2)\right], \tag{6.13}$$

which is called the Richardson extrapolation. If this correction is applied, the errors on the eigenfrequencies do no longer scale as N^{-2} but as N^{-4}, which reveals to be noticeable for low-order p modes in red giants.

6.3.2 Mesh redistribution

As mentioned in Sect. 6.1, the mesh resolution in MESA depends on the local gradient of the physical parameters. Typically, the number of cells is more important in the nuclear burning regions, and more generally in regions where the composition gradient is sharp. Nevertheless, computing the evolutionary track of a star with a large number of cells is time consuming and requires a lot of disk space while not always necessary to study the internal stellar structure. In parallel, an adequate number of cells is required to compute the solution of the oscillation equations so that the displacement eigenfunctions are properly resolved, especially for evolved giants that have a large convective envelope and a small radiative core. In our case, since we aim at studying pressure modes for which the displacement eigenfunctions smoothly vary, we do not need a large number of cells in the mesh. Still, we need to redistribute the mesh to optimise the computation of the pulsation frequencies. To this end, an auxiliary program is provided in complement of ADIPLS, with a control file that includes a sample of parameters to specify how the mesh must be redistributed. Several options are available to optimise the computation of the solution depending on the outputs of ADIPLS the user seeks. The user can choose the mesh to be optimised either for the computation of p or g modes. Other parameters are dedicated to control the number of meshpoints near sharp variation regions and at the base of the convective envelope, and the fraction of points that should be kept for the near surface.

Since we aim at analysing the p-mode pattern in red giants, we perform a mesh redistribution that optimise the computation of p-modes. In this case, most of the parameters can be set to the default values of the program, except the number of meshpoints. At a given number of meshpoints, it happens that ADIPLS fails to compute some non-radial modes especially at low-radial orders. In this case, the data at the corresponding radial orders are missing. To maximise the number of non-radial modes, we run the ADIPLS code for models with several mesh redistributions with different number of points. Typically, we vary the number of meshpoints between 2,000 and 8,000 with a increment of 500 points by step. For each model, we compute the set of non-radial modes and we keep the model that includes as many modes as possible. This allows us to minimise the number of missing non-radial modes at low radial order, which is essential for evolved giants where the maximum oscillation power is located at low radial order.

6.3.3 Testing the computation of pure p modes in He burning stars

As introduced in Sect. 6.3.1, the pure pressure non-radial modes are computed by setting the squared Brunt-Väisälä frequency $N^2_{\rm BV}$ equal to zero in the core in the ADIPLS code. This trick has revealed to be powerful to assess the pure pressure dipole and quadrupole modes in H-shell burning stars (Fig. 6.8) with $\Delta\nu \leq 4.5\,\mu$Hz (Ball, Themeßl, and Hekker, 2018), but needs to be confirmed for He-burning stars.

Therefore, we verify how the pure pressure dipole and quadrupole modes inferred by setting $N^2_{\rm BV} = 0$ compare to the mixed dipole and quadrupole modes of lowest inertia, as illustrated in Fig. 6.8. To this end, we have to compute the mixed modes, which implies that we need to increase the number of meshpoints to resolve the rapid variations of their displacement eigenfunctions. Then, we redistribute the mesh and build a new mesh composed of 20,000 points. We configure the ADIPLS control file to compute mixed modes in red giants, especially the step for the trial frequencies which is not taken uniform in frequency but in period. As a result, we obtain a set of several mixed modes per radial order n, or equivalently per $\Delta\nu$ interval. The mixed modes of lowest inertia are the modes that are closest to the expected pure pressure modes. They can be taken as a reference to evaluate the potential of the mode frequencies computed with the method $N^2_{\rm BV} = 0$ to reproduce the expected pure pressure mode frequencies (Broomhall et al., 2014).

In Fig. 6.9, we compare the mode frequencies computed with the method $N^2_{\rm BV} = 0$ in the core to the frequencies of the mixed modes of lowest inertia during the He-burning phase. Globally, it seems that the frequencies of the pure pressure modes are correctly derived by setting $N^2_{\rm BV} = 0$ in the core. Most of these frequencies are extracted with a spacing lower than $0.05\,\Delta\nu$ relatively to the frequencies of the mixed modes of lowest inertia. Concerning the dipole modes, we notice a bias of $\sim 0.02\,\Delta\nu$ between those frequencies. This bias does not have important consequences for our study because the offset is present in all computed $\ell = 1$ modes. When studying the signature of glitches, we compute differences of frequencies at consecutive radial order n at the same degree ℓ so this bias is reduced. Nevertheless, the dispersion of differences is about $\sim 0.05\,\Delta\nu$, which may impact the amplitude of the glitch modulation that is typically equal to a fraction of $\Delta\nu$. In Chapter 8, we show that these differences do not prevent us from accurately reproducing the shape of the modulation. On the other hand, the quadrupole modes are accurately derived, with unbiased measurement of their frequencies. The differences that we observe between mode frequencies computed with the method $N^2_{\rm BV} = 0$ in the core and the frequencies of the mixed modes of lowest inertia can be explained by several factors:

- The method employed to compute the non-radial modes by setting $N^2_{\rm BV} = 0$ in the core introduces an error with respect to the expected pure pressure modes
- Some mixed modes are poorly estimated because the ADIPLS settings we choose are not adapted for any $\Delta\nu$. For instance, the mesh redistribution could be improved at low $\Delta\nu \leq 1\,\mu$Hz
- Although the modes of lowest inertia are the mixed modes closest to the expected pure pressure modes, they still deviate a bit from the latter

Overall, the errors that are introduced in the dipole and quadrupole mode frequencies by setting $N^2_{\rm BV} = 0$ in the core are in average the same as the largest errors reported by Ball, Themeßl, and Hekker (2018) with the same technique but applied for RGB models. Therefore, in the following we use the dipole and quadrupole mode frequencies obtained by setting $N^2_{\rm BV} = 0$ in the core as the reference frequencies for the pure pressure dipole and quadrupole modes, both for H-shell burning and He-burning stars. In parallel, we compute the radial modes with the unmodified MESA models. These radial, dipole and quadrupole modes constitute the set of modes that we use to reproduce and interpret the observations in terms of stellar structure changes.

6.4 Summary

In this work, we use the stellar evolution code MESA to compute the evolution of 1D models of initial mass $M \in [0.8, 2.5] M_\odot$ and metallicity $[{\rm Fe/H}] \in [-1.0, 0.25]$dex from the pre-main sequence up to the AGB. Several inputs physics are adopted to explore their impact on specific phases of stellar evolution. The convection efficiency is set following the mixing-length theory (Henyey, Vardya, and Bodenheimer, 1965), where blobs travel over a characteristic distance $\ell_{\rm MLT}$ before dissolving and delivering their excess or deficiency of energy to the environment. At low temperature ($\log T \leq 3.95$), the opacity tables are from AESOPUS (Marigo and Aringer, 2009) while at higher temperature ($\log T \leq 4.05$), they are from

OPAL1 and OPAL2 (Iglesias and Rogers, 1996). AESOPUS and OPAL1 tables are appropriate for the solar mixture from Asplund et al. (2009), while the OPAL2 tables are suitable when the metal mixture changes due to the enhancement of C and O elements during He-burning phases. Besides, we consider additional mixing regions beyond the boundary of convection zones (core and envelope) with the step overshooting scheme, whether in H-burning or He-burning phases. However, this extra mixing can artificially inject helium in the core during the He-burning phase, making the evolutionary track noisy at the AGBb phase. To mitigate this issue, a He-semiconvection layer connected to the overshooting region must be considered, which is unstable against convection but stabilised by partial mixing. From the RGB up to the early-AGB, we include thermohaline mixing that settles in the radiative zone in the outer wing of the H-burning shell, where an inversion of molecular weight occurs according to the scheme of Kippenhahn, Ruschenplatt, and Thomas (1980). The effects of rotation on the stellar structure are also explored in the 1D shellular approximation (Zahn, 1992; Meynet and Maeder, 1997), but only for high-mass stars ($M \geq 1.5\,M_{\odot}$). For low-mass stars ($M \leq 1.5\,M_{\odot}$), magnetic braking is an essential physical ingredient for modelling their rotation profile, but is not implemented in MESA yet. So we do not consider rotation for stars of mass $M \leq 1.5\,M_{\odot}$. Finally, the Reimers' (Reimers, 1975) and Blöcker's (Blocker, 1995) prescriptions are adopted to account for mass loss on the RGB and AGB, respectively.

In parallel, we adopt the stellar oscillation code ADIPLS, which allows us to solve the fourth-order system of oscillation equations without using the Cowling approximation (Eq. 3.8). Then, we are able to extract the adiabatic mode frequencies associated to the MESA models. In red giants, non-radial modes are mixed so the pure p-mode frequencies could be approximated by the frequencies of the p-dominated non-radial modes with lowest inertia in each $\Delta\nu$-interval. Nonetheless, this would require a mesh with a gigantic number of cells to resolve the displacement eigenfunctions of mixed modes, up to 100,000 cells for the most luminous red giants. Instead, we follow the treatment proposed by Ball, Themeßl, and Hekker (2018), which consists in suppressing the g modes in the core by setting the squared Brunt-Väisälä frequency $N^2_{\rm BV} = 0$ in the core. This trick reveals to be powerful to assess the p-mode frequencies of dipole and quadrupole modes not only in the H-shell burning phase, but also in He-burning phases. These p-mode frequencies can be used to compute the seismic parameters described in Chapter 3. In Chapter 8, we discuss how these parameters can probe the structure changes between RGB and AGB stars.

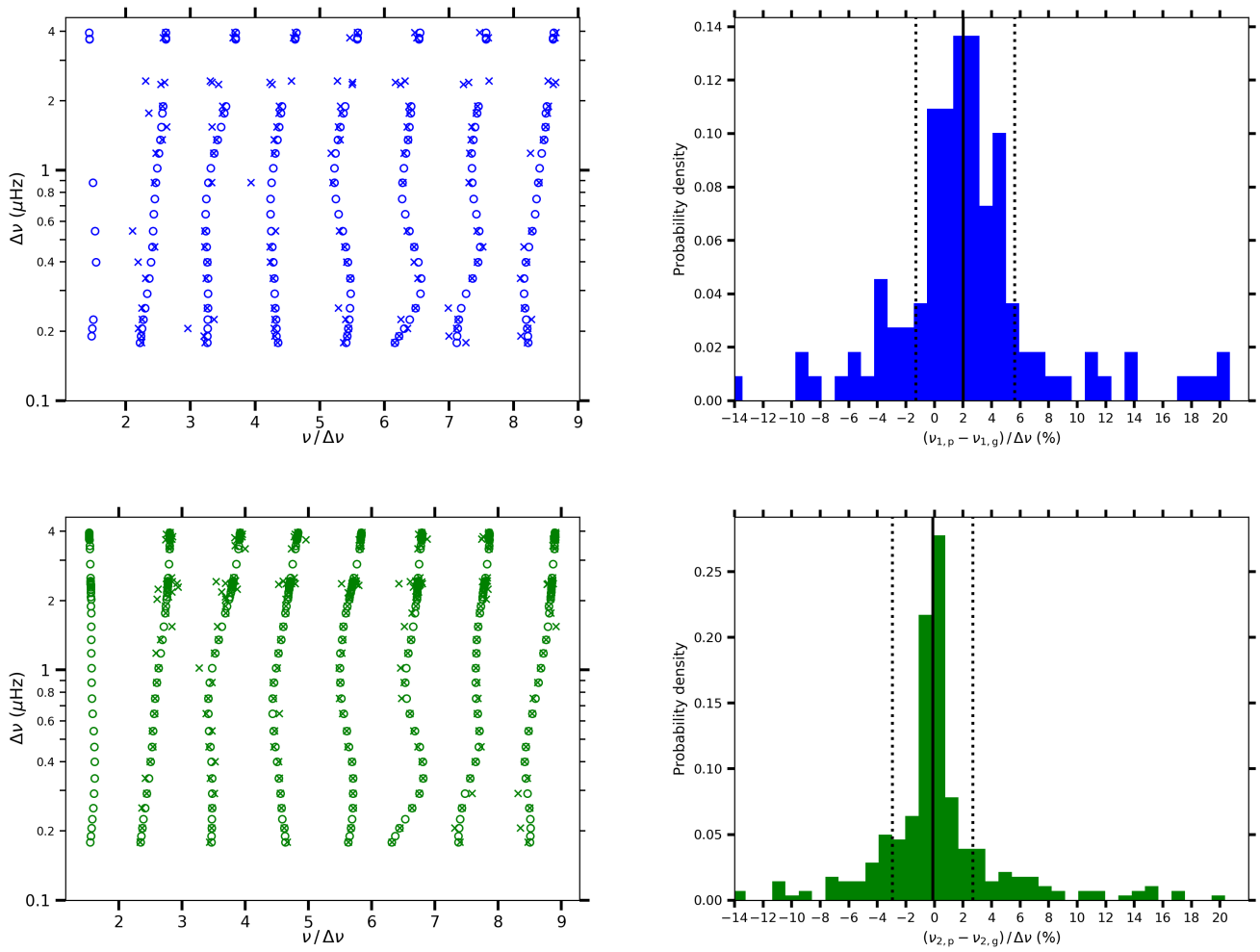

FIGURE 6.9: Comparison of the mode frequencies computed with the method $N^2_{\rm BV} = 0$ to the frequencies of the mixed modes of lowest inertia in each $\Delta\nu$ interval, without modifying the outputs of MESA. **Upper left**: Model frequencies of $\ell = 1$ modes in units of the large frequency separation $\Delta\nu$ for the 8 first radial orders and for a 1 $M_\odot$ track during the He-core burning and the early He-shell burning phase. The dipole modes computed with the method $N^2_{\rm BV} = 0$ are shown in blue circles while the mixed dipole modes of lowest inertia are exhibited in blue crosses. **Upper right**: histogram of the differences between the dipole mode frequencies $\nu_{1,\rm p}$ computed with the method $N^2_{\rm BV} = 0$ (blue circles) and the frequencies $\nu_{1,\rm g}$ of the dipole modes of lowest inertia (blue crosses). This histogram is computed for the whole He-burning phase and all radial order up to $n = 8$. These differences are expressed as a percentile of $\Delta\nu$. The black solid line localises the median of the distribution, while the dotted lines show the $16^{\rm th}$ and $84^{\rm th}$ percentiles of the distribution. **Lower left and lower right**: same label as the upper panels, but for the $\ell = 2$ modes. Some modes could not be computed because they were missing or because they were inconsistent. This explains why some symbols are missing, especially the mixed non-radial modes of lowest inertia at $n = 1$.

Chapter 7

Fitting the oscillation spectrum of evolved red giants

As depicted in Chapter 5, the oscillation spectrum of red giants is sensitive to stellar evolution. For early-RGB stars, it is marked by the presence of radial and mixed non-radial modes that result from the coupling between the p- and g-mode cavities. As stars ascend the RGB, this coupling becomes weaker and mostly p-dominated non-radial modes are visible, including dipole, quadrupole, and octupole modes potentially. These patterns are also seen in AGB stars. As a result, the oscillation spectrum of high-luminosity red giants contains considerable information on their interiors. Nonetheless, measuring the seismic parameters introduced in Chapter 3, 4 is challenging since the analysis of the oscillation spectrum is hampered by the frequency resolution. Long time series are needed so that stellar oscillation modes can be resolved and fitted with satisfactory precision. Here, we aim at extracting the seismic parameters of high-luminosity RGB and AGB stars. This set of seismic parameters will help us to constrain the physical ingredients in red-giant models.

This chapter uses the concepts presented in the article 1. The later summarises the methods used to extract the seismic parameters. Besides, we explore how physical properties of the internal structure can be inferred from the analysis of the oscillation spectrum of evolved red giants. Sect. 3.1, 3.2, 3.4 of the attached article 1 present the methods to identify the pressure modes of high-luminosity red giants. In this chapter, we focus on the techniques to analyse the oscillation spectrum of red giants, to fit their p-mode pattern, and extract their glitch signature.

7.1 Structure of the Fourier spectrum

Stellar oscillations are not the only signal that is present in the Fourier spectrum of the time series. As illustrated in Fig. 7.1, the convection currents at the stellar surface and the surface rotation induce a signal in the time series, hence a clear signature in the power spectral density (PSD). Other non-periodic signals are present such as the photon noise, instrumental effects, and non-periodic effects of the granulation signal. All the components of the PSD that are not related to stellar oscillations are treated as the background signal.

7.1.1 The full global spectrum

At very-low frequency, the PSD is dominated by the signature of the surface differential rotation through the modulation induced by the stellar spots when they cross the visible stellar surface García (2015). These rotation modulations cause series of high-amplitude peaks and their harmonics, as shown in Fig. 7.1. At higher frequencies, granulation is the main contributor to the background signal. This is the signature of surface convection taking place in the outer part of the convection zone, where bright and hot gas cells rise to the photosphere and form granules. At the granule's edges, materials cool down and descend back into the interior. These convection motions of characteristic timescale $\tau_{\rm gran}$ create a signal in the Fourier spectrum with a characteristic frequency $(2\pi\tau_{\rm gran})^{-1}$, which is closely correlated with $\nu_{\rm max}$ since it varies as $\nu_{\rm max}^{0.89}$ (Mathur et al., 2011). Finally, beyond the frequency range where stellar oscillations are observed, the spectrum is flat and is dominated by the photon noise of the source.

The full global spectrum P_0 including both the photon noise, non-periodic and periodic components can be modelled by (Harvey, 1985; Harvey et al., 1993; Vázquez Ramió, Roca Cortés, and Régulo, 2002; Lefebvre et al., 2008)

$$P_0(\nu) = N_{\rm ph} + \sum_{i=1}^{N} \frac{4\sigma_i^2 \tau_i}{1 + (2\pi\nu\tau_i)^{\beta_i}} + \sum_{j=1}^{M} H_j \left[\frac{\Gamma_j^2}{\left(\nu - \nu_{0j}\right)^2 + \Gamma_j^2} \right]^{\gamma_j}, \tag{7.1}$$

where $N_{\rm ph}$ is the photon noise that is assumed to be constant, i and j correspond to the N non-periodic and M periodic components, respectively, σ_i and τ_i are the root mean square variations and the characteristic time of the non-periodic background components i, respectively, β_i and γ_j are the decay rates of the components i and j, respectively, and H_j, ν_{0j}, and Γ_j are the height, central frequency and width of the Lorentzian profiles used to fit the periodic components, respectively. Non-periodic sources that contributes to the background signal are attributed to convection motions, which were first modelled by Harvey (1985). As for periodic sources, they are attributed to the extra power coming from the photospheric and chromospheric oscillations at high frequency (Harvey et al., 1993). In the following, the photon noise and the incoherent component are referred to as the background B and the periodic components are attributed to the stellar oscillation modes $P_{\rm osc}$

$$\begin{cases} B(\nu) = N_{\rm ph} + \sum_{i=1}^{N} \frac{4\sigma_i^2 \tau_i}{1+(2\pi\nu\tau_i)^{\beta_i}} \\ \\ P_{\rm osc}(\nu) = \sum_{j=1}^{M} H_j \left[\frac{\Gamma_j^2}{\left(\nu-\nu_{0j}\right)^2+\Gamma_j^2} \right]^{\gamma_j} \end{cases} \tag{7.2}$$

so that $P_0(\nu) = B(\nu) + P_{\rm osc}(\nu)$.

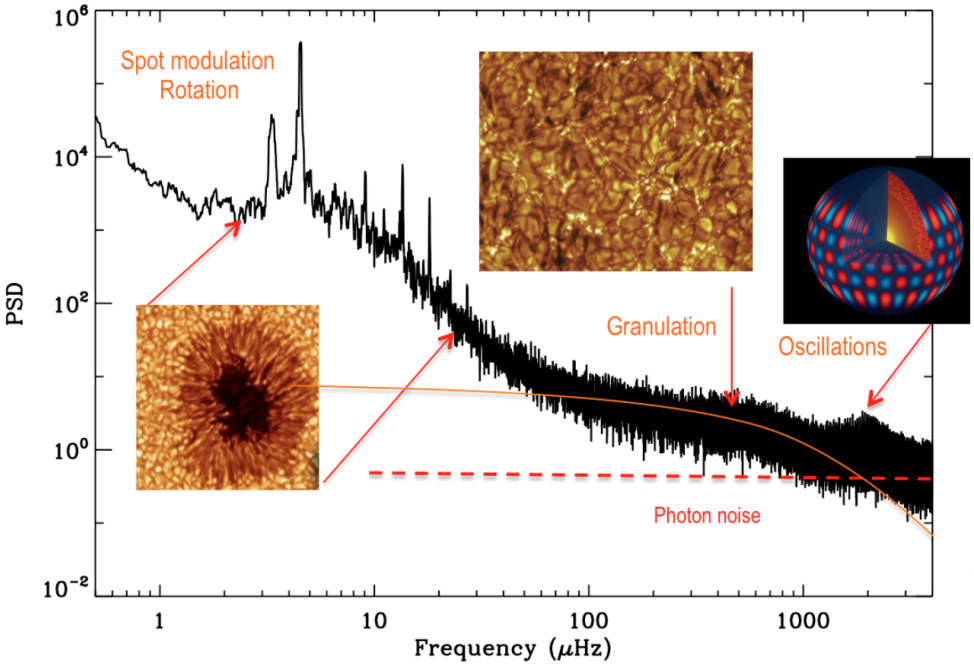

FIGURE 7.1: Power spectral density (in ppm^2.μHz^{-1}) of the *Kepler* target KIC 3733735 observed during three years. The different physical contributions to the PSD associated to each frequency range are illustrated. There are the stellar oscillations, the convection motion at the surface (granulation), the photon noise, and the rotation modulation through the spot cycles. The granulation is fitted with the orange solid line while the photon noise is shown with the red dashed line. Credit: García (2015)

7.1.2 Structure of a typical oscillation spectrum of red giants

The power excess envelope of stellar oscillations is added on top of the background components in the PSD. The general structure of an oscillation spectrum of evolved red giants is illustrated in Fig. 7.2. Given the weak coupling between the stellar envelope and core in evolved RGB and AGB stars (Dupret et al., 2009; Grosjean et al., 2014), only modes that develop in the convective envelope can be detected (see Fig. 3.8). They correspond to pressure modes that are excited by the turbulent motion of convection near the stellar surface (Goldreich and Keeley, 1977; Belkacem et al., 2006). They manifest as scattered profiles similar to speckles of width $\delta\nu_{\rm res} = 1/T_{\rm obs}$ randomly distributed in their intrinsic Lorentzian profile due to their stochastic excitation, where $T_{\rm obs}$ is the observation duration. In those evolved stars, no signature of asymmetric mechanisms such as rotation and magnetism in mode frequencies have been reported yet.

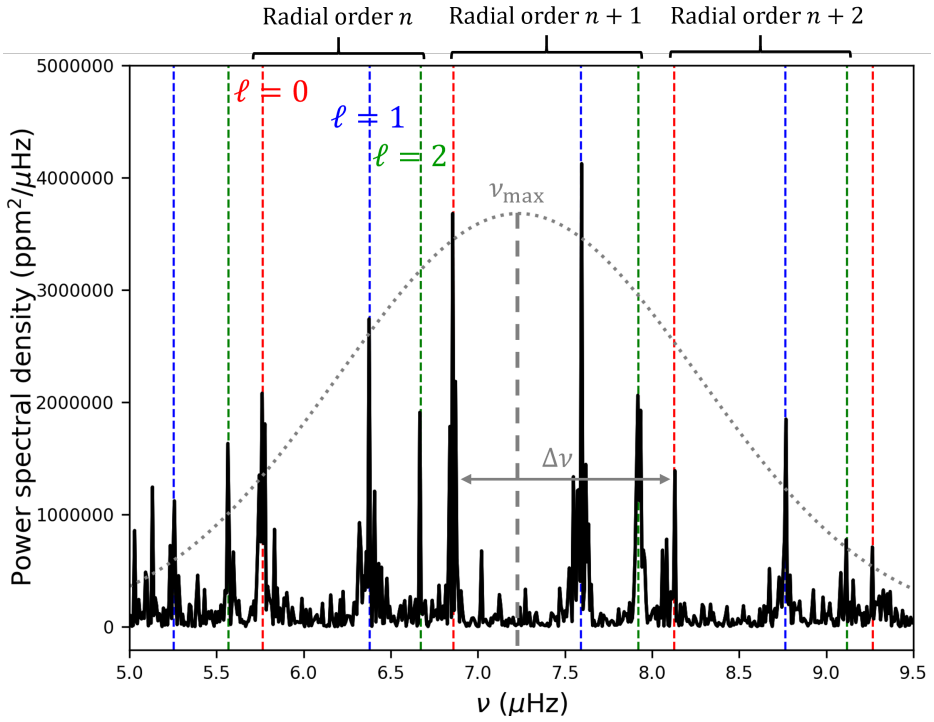

FIGURE 7.2: Oscillation spectrum of the RGB star KIC 1719297 with $\Delta\nu = 1.22$ μHz. The red dashed lines indicates the location of the radial modes ($\ell = 0$) while the blue and green dashed lines locate the non-radial modes, *i.e.* dipole ($\ell = 1$) and quadrupole modes ($\ell = 2$), respectively. The grey dotted line represents the underlying Gaussian envelope of the observable modes, where the maximum reached at $\nu_{\rm max}$ marks the maximum oscillation power.

In this case, modes are labelled with their radial order n and degree ℓ. Mainly radial ($\ell = 0$), dipole ($\ell = 1$), and quadrupole ($\ell = 2$) are observable in evolved red giants. In the best-case scenario, octupole modes ($\ell = 3$) can be observed, but sufficiently high signal-to-noise ratio and long observation duration are required. These observable modes have their frequency close to the characteristic frequency associated to the timescale of the long convective motions in the near-surface layers (Belkacem et al., 2011). The frequency at which the oscillation power is maximum is noted $\nu_{\rm max}$. The modes with a frequency far from $\nu_{\rm max}$ are not efficiently excited by the near-surface convection so they are not seen in the oscillation spectrum. Thus, the mode heights are distributed along a power distribution envelope centred on $\nu_{\rm max}$ that determines the mode observability (Mosser et al., 2012a). This envelope can be modelled by a Gaussian following

$$P_{\rm env}(\nu) = H_{\nu_{\rm max}} {\rm e}^{-\frac{(\nu-\nu_{\rm max})^2}{2\sigma^2}}, \tag{7.3}$$

where $H_{\nu_{\max}}$ is the maximum height of the power excess envelope at $\nu_{\max}$, and σ is related to the full-width at half-maximum of the Gaussian envelope $\delta\nu_{\rm env} = 2\sqrt{2\ln 2}\sigma$. As illustrated in Fig. 7.2, consecutive radial, dipole and quadrupole modes at a given radial order n form a pattern of three modes that repeats every $\Delta\nu$-intervals. The frequency spacing $\Delta\nu$ is called the large separation. Typically, the pressure modes for which the signal-to-noise ratio is sufficient to be observed lie within the range $\nu_{\max} \pm 0.75\,\delta\nu_{\rm env}$ (Broomhall et al., 2014), which corresponds to a number of ~ 6 radial orders (equivalently 6 intervals of $\Delta\nu$) at $\Delta\nu = 4\,\mu$Hz.

7.2 Enhancing the seismic signal

The light curves are optimised for the asteroseismic study of solar-like oscillating stars according to processing procedures described in García et al. (2011). By computing the Lomb-scargle periodogram of the unevenly spaced data of light curves (Scargle, 1982), we can access the signature of stellar oscillations, as reflected by Fig. 7.1. Nevertheless, several components of the background are also present in the frequency range of the observable stellar oscillations such as granulation and photon noise. To correctly characterise the oscillation spectrum, we need to reduce the effects that could bias the identification of the stellar modes.

7.2.1 Modelling the background component

In case of red giants, the background is dominated by the granulation signal near the frequency range of observable stellar oscillations. Accurately, its contribution in the Fourier spectrum can be modelled by a Lorentzian function (second term of Eq. 7.1). In fact, the background smoothly decreases with frequency in the vicinity of $\nu_{\max}$, so we can adopt a simpler model to reproduce the granulation signal. We approximate the background by a polynomial of the form

$$B(\nu) = B_{\nu_{\max}} \left(\frac{\nu}{\nu_{\max}} \right)^{\alpha_b}, \tag{7.4}$$

which provides a model of sufficient precision (Mosser et al., 2012a) and where $B_{\nu_{\max}}$ is the value of the background at $\nu_{\max}$, and α_b controls the dependence of the background with frequency. Reducing the background effects when extracting the mode characteristics is essential due to the frequency dependence of the background component. Indeed, modes at low frequency tend to have higher amplitude than at high frequency as the background component is more important at low frequency. To help the identification of the radial order n and degree ℓ performed in Sect. 7.3, we weaken the background component in the oscillation spectrum. Instead of subtracting the background model to the oscillation spectrum, we divide the latter by the background model. This allows us to reduce the background effects and keep positive values of the PSD in fraction of the background signal.

7.2.2 Mitigating the stochastic appearance of modes

As highlighted in the previous sections, the modes are stochastically excited in the star so they manifest as speckles randomly distributed in the mean predicted Lorentzian profile. Modes may not be present in the oscillation spectrum due to their stochastic nature, which makes the mode identification challenging. In order to smooth out the stochastic appearance and emphasize the distribution of the mode energy, the observed oscillation spectrum P is convolved with a Gaussian kernel G

$$P_{\rm s}(\nu) = \frac{\sum_{m=0}^{m=N_\nu} G(\nu_m) \cdot P(\nu - \nu_m)}{\sum_{m=0}^{m=N_\nu} G(\nu_m)}, \tag{7.5}$$

where P is the observed oscillation spectrum, G is the Gaussian kernel, $P_{\rm s}$ is the oscillation spectrum after convolution[1] and N_ν the number of frequencies. This convolution clearly smooths out the oscillation

[1] Note that we normalise $P_{\rm s}$ by $\sum_{m=0}^{m=N_\nu} G(\nu_m)$

spectrum leading to more accurate adjusted mode frequencies (see Fig. 7.3). However, the width at half maximum of the Gaussian kernel must be adequately chosen. It should not be too large to avoid combining two modes, especially a radial mode and a quadrupole mode because they are close one from the other. On the other hand, it should not be too small otherwise the oscillation spectrum is not sufficiently smoothed out for the stochastic nature to be diminished. As the oscillation spectrum appears to be more or less dense depending on the frequency separation $\Delta\nu$ between modes of consecutive radial order, we also need to adjust the width of the Gaussian kernel as a function of $\Delta\nu$. We found that convolving the observed oscillation spectrum with a Gaussian kernel of width

$$\Delta_G = \frac{\delta\nu_{02}}{4} \tag{7.6}$$

is an adequate response to the requirements described herebefore, where $\delta\nu_{02}$ is the small frequency separation between a radial mode and its neighbouring quadrupole mode.

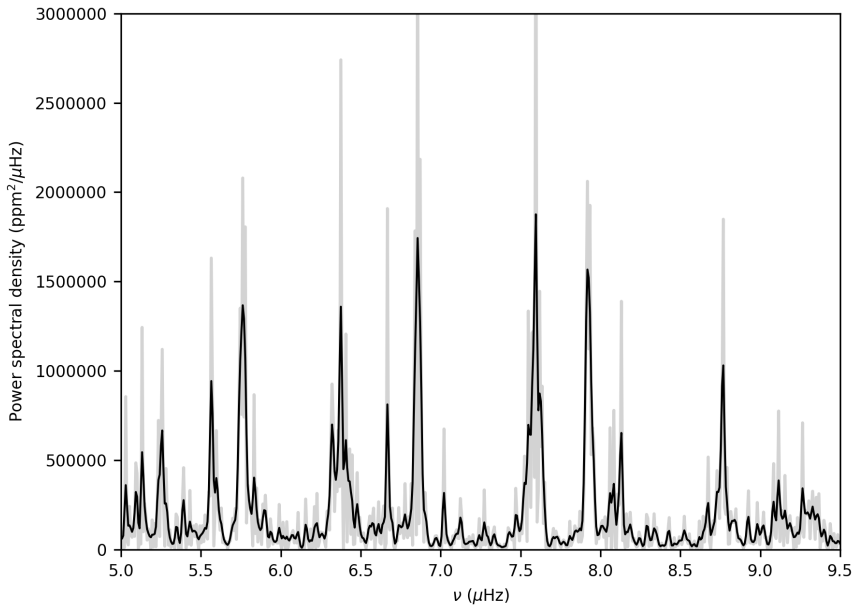

FIGURE 7.3: Oscillation spectrum of the star KIC 1719297, in grey at full resolution and in black after smoothing out the PSD with a Gaussian kernel of width Δ_G given by Eq. 7.6.

7.3 Identification of the stellar modes

7.3.1 Cross-correlation with a template spectrum

After smoothing out the PSD, the modes can be efficiently identified. To this end, we build a template spectrum based on the universal pattern of red giants (Eq. 3.20). The shape of the template oscillation spectrum is entirely controlled by $\Delta\nu$, especially the spacing between consecutive radial modes and the spacing with their neighbouring dipole and quadrupole modes. By fine-tuning the value of $\Delta\nu$, we compute the maximum cross-correlation between the template and the observed oscillation spectra. Then, the best-matching template spectrum provides the location of the modes of different degree ℓ as well as the global measurement of $\Delta\nu$ (see Fig. 7.4). Further information on the structure of the best-matching template spectrum are presented in Sect. 3.1 of the attached publication 1.

7.3.2 Detection thresholds

In Dréau et al. (2021), we also define criteria for a mode to be detected. This detection process is divided into two steps: one is dedicated to the most intense peaks and the other concerns the peaks that are less intense but are located close enough to the expected location of the pure pressure modes (Appourchaux et al., 2006). First, we select the peaks with high signal-to-noise ratio with a restrictive detection threshold. From these peaks we can extract a first set of seismic parameters that can be used to derive an estimate of the expected other mode frequencies through Eq. 3.20. Second, we apply a less restrictive detection threshold to select the peaks that are potentially present with a lower height-to-background ratio. Nevertheless, these peaks must be not too far from the expected frequency derived in the first step with Eq. 3.20. On the one hand, the larger $\Delta\nu$, the larger the spacing between modes of consecutive radial order n at fixed degree ℓ. On the other hand, radial ($\ell = 0$) and quadrupole ($\ell = 2$) modes are close to each other (see for example in Fig. 7.2). Consequently, the maximum distance between the detected and the expected mode frequencies is set according to the large separation $\Delta\nu$ and the degree ℓ (Fig. 7.5).

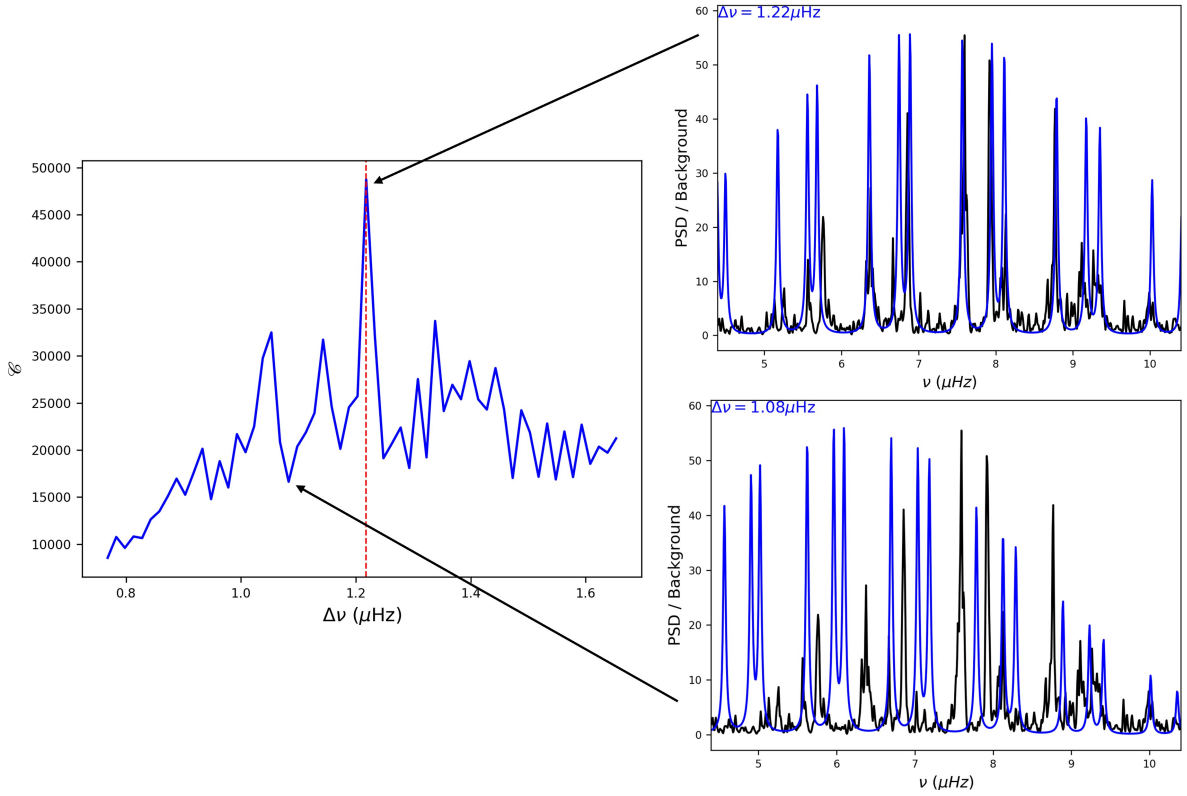

FIGURE 7.4: Correlation method to adjust the best-matching template spectrum to the observed oscillation spectrum. **Left:** Cross-correlation product $\mathcal{C}$ between the observed and the template oscillation spectra of the star KIC 1719297 as a function of $\Delta\nu$. The red dashed line shows the optimal $\Delta\nu$ that provides the best-matching template spectrum to the observed oscillation spectrum. **Right:** Two examples of template spectra with different $\Delta\nu$. One corresponds to the best-matching case at $\Delta\nu = 1.22\,\mu$Hz and the other is associated to a bad overlapping at $\Delta\nu = 1.08\,\mu$Hz between the template spectrum (blue) and the observed oscillation spectrum (black).

7.3.3 In the presence of mixed modes

The template spectrum that we use is only made of pressure modes, which implies that the cross-correlation method is therefore expected to be less effective when mixed dipole modes are present. Indeed, mixed modes are very close to each other and if their heights are high enough, some of them could be confused with radial and quadrupole modes. In case of evolved stars with $\Delta\nu \leq 4\,\mu$Hz, the

presence of mixed modes does not significantly perturb the identification process since g-dominated mixed modes have low amplitudes compared to the p-dominated mode. Accordingly, we adjust the dipole mode with the highest amplitude among the closest p-dominated dipole mode to the expected frequency of the pure p mode.

7.3.4 Limitations of the identification method

As mentioned herebefore, the mode identification is based on a template spectrum that includes pressure modes with a degree $\ell = 0, 1, 2$. The template spectrum may not be suitable if the observed spectrum does not exhibit the clear pattern made of radial, dipole and quadrupole modes. This is typically what we observe when $\Delta\nu \geq 4\,\mu$Hz since the coupling factor q between the p- and g-mode cavities is sufficiently high for the g-dominated mixed modes to be detectable. Since these mixed modes are very close to each other, they may be confused with the pattern made of radial and quadrupole modes in the template spectrum. With this respect, we do not include stars with $\Delta\nu \geq 4\,\mu$Hz in our sample as we restrict our analysis to the p-mode pattern.

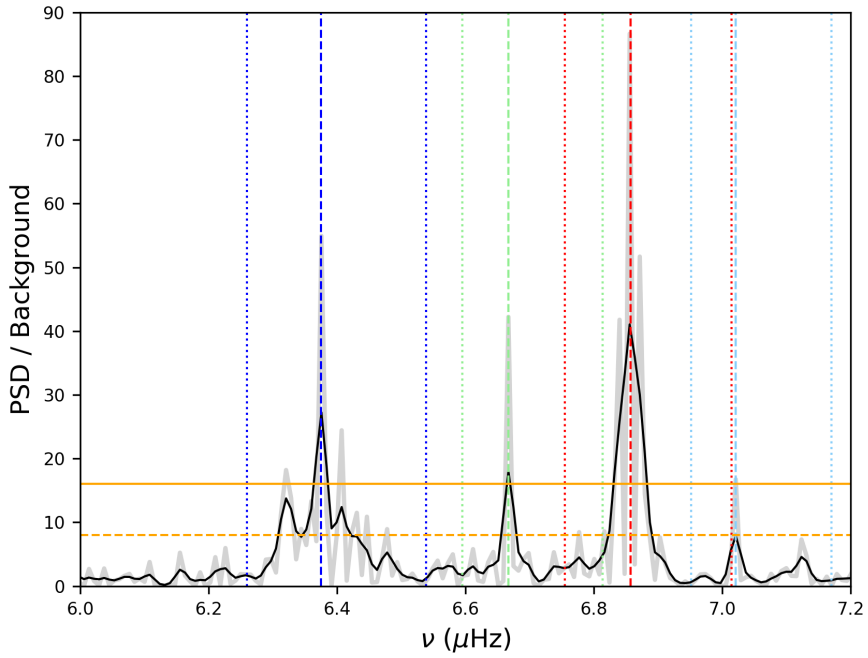

FIGURE 7.5: Example of detection thresholds for the modes to be detected. The PSD divided by the background given by Eq. 7.4 is shown as a function of ν for the star KIC 1719297 at radial order $n = 5$ for the radial mode and $n = 4$ for the non-radial modes. The raw and smoothed PSD are shown in grey and black, respectively. The vertical dashed lines indicates the expected location of the modes, in red for $\ell = 0$, in blue for $\ell = 1$, in light green for $\ell = 2$, and light blue for $\ell = 3$. The orange solid line is the restrictive height-to-background level that a peak must reach to pass the first step of the selection process. If these peaks fulfil this condition, they are considered intense enough to be identified as oscillation modes. The orange dashed line is a less restrictive detection threshold. Peaks that attain this level must not be located too far from the expected frequency given by Eq. 3.20 to be considered. The height-to-background levels are applied to the raw PSD. The vertical dotted lines delimits the region in which the peak must be located to be considered. The colour code is the same as the dashed lines.

On the other hand, at low $\Delta\nu \leq 0.5\,\mu$Hz, the seismic analysis is limited by the frequency resolution of the PSD. Indeed, the 1470-day time series of *Kepler* gives access to a frequency resolution reaching 7.8 nHz, which is close to the typical mode width at $\Delta\nu \leq 0.5\,\mu$Hz. This complicates the seismic analysis of those evolved red giants since the stellar modes are not resolved (see Fig. 7.6). Moreover, at low $\Delta\nu$,

stars oscillate at low frequency and the modes that are efficiently excited are close to the fundamental mode, *i.e.* $n = 1$ (Mosser et al., 2013b; Yu et al., 2020). In this case, the asymptotic assumption $n \ll \ell$ is invalid and the p-mode pattern is expected to significantly deviate from the asymptotic pattern shown in Eq. 3.20. The template spectrum, which is based on the universal pattern of red giants, is no longer adapted at low $\Delta\nu \leq 0.5\,\mu$Hz. Accordingly, we restrict our seismic analysis to stars with $\Delta\nu \in [0.5, 4.0]\,\mu$Hz. Our work could be extended to low $\Delta\nu \leq 0.5\,\mu$Hz in a further work with the help of ground-based observations. In fact, ground-based telescopes collected light curves of stars during a decade in the framework of the microlensing surveys MACHO (Wood et al., 1999) and OGLE (Wray, Eyer, and Paczyński, 2004). With these long time series, the frequency resolution is suitable for the study of these evolved red giants, reducing the risks of confusing radial and non-radial modes.

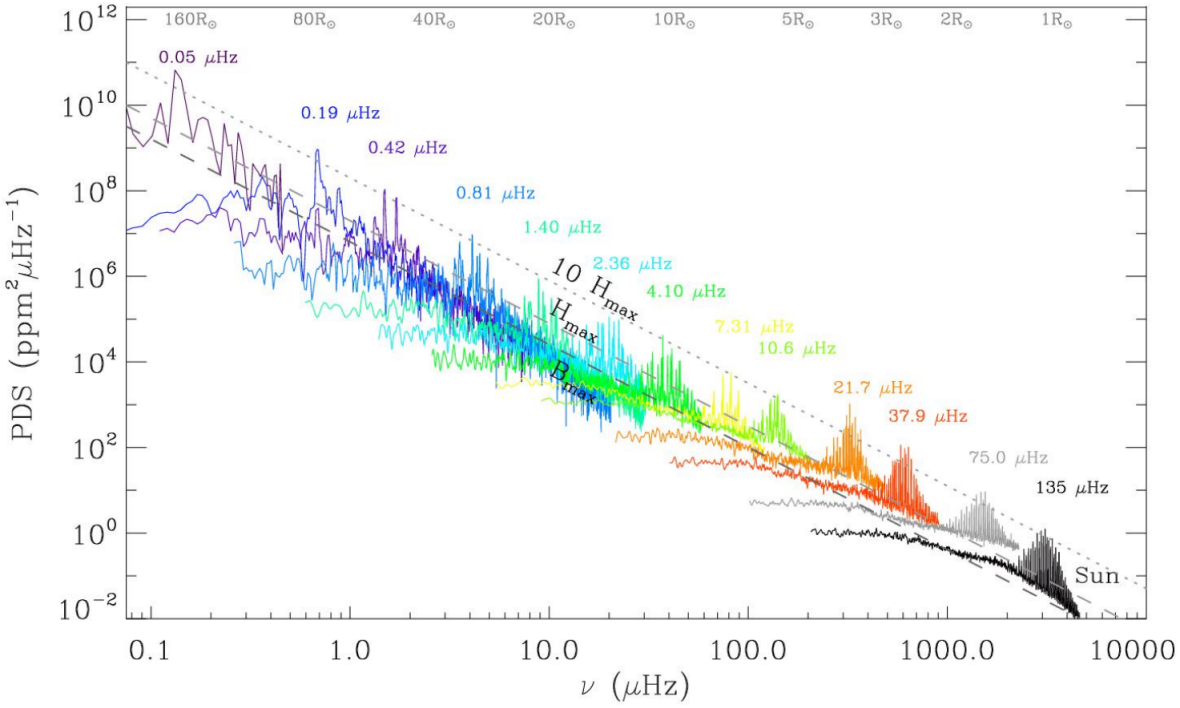

FIGURE 7.6: Superimposition of red-giant oscillation spectra indicated by different colours from the bottom to the tip of the RGB. The oscillation spectrum of the Sun in black and that of another main-sequence star in grey are added for comparison. Each oscillation spectrum is labelled by the observed large separation $\Delta\nu$, from $\Delta\nu = 0.05\,\mu$Hz to $\Delta\nu = 135\,\mu$Hz. The fit of the background $B_{\nu_{\max}}$ and mean height $H_{\nu_{\max}}$ at $\nu_{\max}$ are indicated with dashed lines. The typical radius in the observed frequency range is provided along the upper axis. Credit: Mosser, Samadi, and Belkacem (2013)

7.4 Mode fitting

7.4.1 The extraction of mode parameters

Once the modes are identified, they are fitted by Lorentzian functions following the maximum likelihood estimator technique presented in Toutain and Appourchaux (1994). This technique consists in finding the most likely values of the free parameters of the Lorentzian functions, *i.e.* the mode heights $\mathcal{H}_{n,\ell}$, widths $\Gamma_{n,\ell}$, and frequencies $\nu_{n,\ell}$. We introduce the probability density function $f(\nu)$ that describes the distribution of the observed power spectrum $P(\nu)$ around the Lorentzian profiles of the modes. This probability density function follows a χ^2 probability distribution with two degrees of freedom and is related to the expected profile of the oscillation spectrum P_0 following

$$f(\nu) = \frac{1}{P_0(\nu)} e^{-\frac{P(\nu)}{P_0(\nu)}}. \tag{7.7}$$

The modes are fitted radial order per radial order (equivalently every $\Delta\nu$-interval), meaning that 3 modes are fitted at most per iteration, *i.e.* the radial, dipole, and quadrupole modes (see Fig. 7.7). The octupole modes ($\ell = 3$) are omitted due to their low signal-to-noise ratio at low $\Delta\nu$. Then, the expected spectrum in a $\Delta\nu$-interval reads

$$P_0(\nu) = \sum_{\ell=0,1,2} \frac{\mathcal{H}_{n,\ell}}{1 + 4\left(\frac{\nu-\nu_{n,\ell}}{\Gamma_{n,\ell}}\right)^2} + B(\nu), \tag{7.8}$$

where B is the background component described by Eq. 7.4. The background is extracted separately and is kept fixed during the mode fitting. Finally, the optimal mode parameters are extracted by maximising the probability density function f with the Broyden–Fletcher–Goldfarb–Shanno (BFGS) algorithm. This algorithm makes use of the second-order derivative of the objective function $\log f$ to find the parameters of the optimal profile P_0. The former requires the calculation of the Hessian matrix composed of the partial second-order derivatives of the expected profile P_0 with respect to the mode parameters. It can be shown that the Hessian elements h_{ij} read (Toutain and Appourchaux, 1994)

$$h_{ij} \simeq \sum_{k=1}^{N} \frac{1}{P_0(\nu_k)} \frac{\partial P_0}{\partial \lambda_i} \frac{\partial P_0}{\partial \lambda_j}, \tag{7.9}$$

where the summation is performed on the frequencies and λ_i; λ_j are the mode parameters.

7.4.2 Inferring the p-mode parameters from the observation of mixed modes

This fitting technique provides a complete characterisation of the p-mode characteristics. When mixed dipole modes are present, as mentioned in Sect. 7.3 we fit the mixed dipole mode that has the highest amplitude among the p-dominated modes that are closest to the expected location of the pure p mode. For stars with $\Delta\nu \leq 4\,\mu$Hz, the frequency of the p-dominated mode does not deviate significantly from that of the pure p mode. However, the width and amplitude of the p-dominated mode are lower than those of the expected pure p mode. We can infer the amplitude and the width that the dipole mode would have if it was a pure pressure mode with the knowledge of the mode inertia fraction ζ (Benomar et al., 2014). Characterising the mixed-mode pattern is beyond the scope of this work, so we do not directly extract the mode inertia fraction ζ from the oscillation spectrum. Instead, we deduce the asymptotic value of the mode inertia fraction $\zeta_{\rm as}$ given by Eq. 3.47. To this end, we need an estimate for the coupling factor q, the period spacing $\Delta\Pi_1$, which are deduced by means of the scaling relations

$$\begin{cases} q_{\rm RGB} = -0.0034 + \frac{\Delta\Pi_{1,\rm RGB}}{597\,\rm s}; & \Delta\Pi_{1,\rm RGB} = 76\left(\frac{\Delta\nu}{10\,\mu\rm Hz}\right)^{0.26} \\ q_{\rm RC} = 0.082 + \frac{\Delta\Pi_{1,\rm RC}}{1450\,\rm s}; & \Delta\Pi_{1,\rm RC} = 297\left(\frac{\Delta\nu}{4\,\mu\rm Hz}\right)^{-0.23}, \end{cases} \tag{7.10}$$

where the dependence of q with $\Delta\Pi_1$ is presented in Mosser et al. (2017) and the scaling relations between $\Delta\Pi_1$ and $\Delta\nu$ have been calibrated with the seismic parameters reported in Vrard, Mosser, and Samadi (2016). The subscripts 'RGB' and 'RC' mean that the scaling relations are given for RGB and red clump stars, respectively. These values are then injected in Eq. 3.47 so that we can infer the asymptotic value of the mode inertia fraction $\zeta_{\rm as}$, with the expected p-mode frequency $\nu_{\rm p}$ taken from the asymptotic pattern of red giants (Eq. 3.20). With Eq. 3.75, we can deduce the width and amplitude that the mode would have if it was a pure pressure mode.

7.4.3 Correcting instrumental biases

Through Eq. 3.68, we are able to infer the mode amplitude $A_{n,\ell}$, height $\mathcal{H}_{n,\ell}$ and width $\Gamma_{n,\ell}$. However, the apparent mode amplitude deduced from the PSD is affected by the spectral response of the instrument. In order to compare the observed amplitudes from *Kepler* with those from other telescopes and theoretical predictions, we need to weaken the instrumental effects. The corrected bolometric amplitude $A_{n,\ell,\rm bol}$

can be recovered by reducing the wavelength dependence of the photometric variation integrated over the *Kepler* bandpass. This corrected bolometric amplitude can be obtained with the relation (Ballot, Barban, and van't Veer-Menneret, 2011)

$$A_{n,\ell,\mathrm{bol}} = A_{n,\ell} \left(\frac{T_{\mathrm{eff}}}{5934\,\mathrm{K}} \right)^{0.80} . \tag{7.11}$$

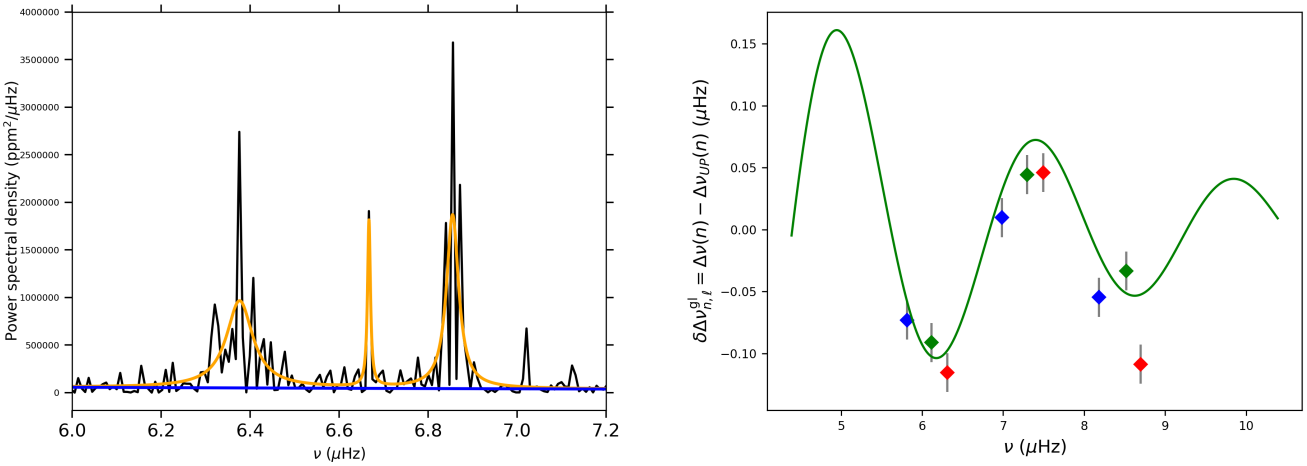

FIGURE 7.7: **Left:** fit of the detected modes with Eq. 7.8 in orange in the same frequency range as Fig. 7.5 for the star KIC 1719297. The background given by Eq. 7.4 is shown in blue. Due to their low amplitudes, octupole ($\ell = 3$) modes are not fitted. **Right:** fit of the glitch modulation with Eq. 7.13. All the detected modes of the star KIC 1719297 are used to fit the glitch modulation. The glitch contribution $\delta\Delta\nu^{\mathrm{gl}}_{n,\ell}$ in radial, dipole and quadrupole modes are shown with red, blue, and green diamonds, respectively.

7.5 Glitch inference

7.5.1 Extracting the glitch parameters

After extracting the p-mode characteristics, we study the signature of the helium second-ionisation zone. By computing the local large frequency separation $\Delta\nu_{n,\ell}$, we are able to highlight the modulation induced by the helium second-ionisation zone. The procedure is quite similar to that adopted for less evolved red giants introduced in Sect. 4.3 (Vrard et al., 2015). The method we adopt is fully described in Sect. 3.2 of the attached paper 1, here we present the main differences between our technique (adapted for high-luminosity red giants) and that from Vrard et al. (2015) (adapted for less evolved red giants).

Owing to the low number of observed modes in high-luminosity red giants, computing the local large frequency separation $\Delta\nu_{n,\ell}$ with Eq. 4.8 is restrictive since it requires the knowledge of two adjacent mode frequencies at radial orders $n-1$ and $n+1$. Instead, we prefer computing $\Delta\nu_{n,\ell}$ as

$$\Delta\nu_{n,\ell} = \nu_{n+1,\ell} - \nu_{n,\ell}. \tag{7.12}$$

As we typically observe 6 radial orders at $\Delta\nu \leq 4\,\mu$Hz, we have 5 measurements of $\Delta\nu_{n,\ell}$ at fixed degree ℓ with Eq. 7.12 instead of 4 measurements with Eq. 4.8, which is not negligible. As in the study of Vrard et al. (2015), we do not have enough data points to use an elaborate fitting function such as Eq. 4.5 for the glitch modulation in $\Delta\nu_{n,\ell}$. Instead, we use a simpler modulation model that reads

$$\delta\Delta\nu^{\mathrm{gl}}_{n,\ell} = \mathcal{A}_{\mathrm{HeII}} \left(\frac{\nu_{\mathrm{max}}}{\nu} \right)^2 \Delta\nu \cos\left(2\pi \frac{\nu - \nu_{\mathrm{max}}}{\mathcal{G}_{\mathrm{HeII}}\Delta\nu} + \Phi_{\mathrm{HeII}} \right), \tag{7.13}$$

where we consider a frequency dependence in the amplitude in contrast with Vrard et al. (2015) who adopted a constant amplitude. The fit is performed with the function *curve_fit*[2] from the *python* package *scipy.optimize*[3]. This function optimises the parameters of the model with a Levenberg–Marquardt (LM) algorithm, which is well suited for solving non-linear least squares problems. The LM algorithm adaptively varies the parameters between those obtained with the gradient descent and the Gauss-Newton methods[4]. The form of the frequency dependence in $1/\nu^2$ is chosen to reproduce the damped behaviour of the modulation (see Fig. 7.7), and motivated by the theoretical work of Monteiro, Christensen-Dalsgaard, and Thompson (1994) who studied the variations of the acoustic potential passing from a radiative to a convective zone. This frequency dependence is expected in case of a step profile of the structural perturbation.

7.5.2 The use of p-dominated mixed modes

Vrard et al. (2015) only used radial modes to fit the modulation because non-radial modes are mixed modes in their sample of stars. The modulation induced by the glitch differently affects the mode frequencies, depending on the nature of the mode (Broomhall et al., 2014). Then, adding mixed modes in the data set deteriorates the fit of the modulation and bias the glitch signature, especially for low-luminosity red giants (Dréau et al., 2020). In case of high-luminosity red giants, non-radial modes are p-dominated modes. They are more efficiently trapped in the acoustic cavity with a weak coupling between the p- and g-mode cavities Dupret et al. (2009) and Grosjean et al. (2014), so they interact with the helium second-ionisation zone in a similar way as radial modes. In particular, adding the p-dominated modes of lowest inertia in each $\Delta\nu$-interval in the data set remarkably improves the extraction of the glitch parameters (Broomhall et al., 2014). Among mixed modes, they are the closest modes to the expected pure pressure modes in terms of frequency. Then, the signature left by the helium second-ionisation zone in those modes is approximately the same as that induced in radial modes.

7.5.3 The Nyquist criterion

Considering the non-radial modes not only improves the precision but also the accuracy with which the glitch characteristics are inferred. This is particularly crucial for high-luminosity red giants since the period of the modulation induced by the glitch is short. Indeed, the period of the modulation becomes lower than $2\Delta\nu$. In this case, considering only radial modes is not sufficient to correctly reproduce the modulation. In the left panel of Fig. 7.8, we see that the spacing between consecutive frequencies of radial modes, which is of the order of $\Delta\nu$, is of the order of the period of the modulation. Then, the Nyquist criterion is not fulfilled and the glitch parameters cannot be accurately extracted. This criterion provides the minimum periodicity $\Delta_{\rm min}$ that can be robustly extracted by fitting a model given the sampling of a data set. This minimum periodicity is $\Delta_{\rm min} = \mathcal{C}_\ell \Delta\nu$, where $\mathcal{C}_\ell$ quantifies the spacing between consecutive data points in fraction of $\Delta\nu$. The factor $\mathcal{C}_\ell$ depends on the nature of the modes that are included in the data set. If only radial modes are included, the mean spacing between consecutive mode frequencies is $\Delta\nu$, so the periodicity of the modulation cannot be determined with accuracy if the former is lower than $2\Delta\nu$, then $\mathcal{C}_\ell = 2$. If both radial and dipole modes are used, the mean spacing between consecutive mode frequencies is reduced by a factor of 2 because dipole modes are nearly located halfway between two consecutive radial modes, so $\mathcal{C}_\ell = 1$. The periodicity of our fitting model defined in Eq. 7.13 is $\Delta_{\rm model} = \mathcal{G}_{\rm HeII} \Delta\nu$. Finally, the Nyquist criterion reads

$$\Delta_{\rm model} \geq \Delta_{\rm min} \qquad \Rightarrow \qquad \mathcal{G}_{\rm HeII} \geq \mathcal{C}_\ell, \tag{7.14}$$

where $\mathcal{C}_\ell = 2$ if only radial modes are included and $\mathcal{C}_\ell = 1$ if both radial and dipole modes are included. As illustrated in Fig. 7.8, the modulation profile is clearer when considering both radial and

[2] https://docs.scipy.org/doc/scipy/reference/generated/scipy.optimize.curve_fit.html

[3] https://docs.scipy.org/doc/scipy/tutorial/index.html

[4] The gradient descent method updates the parameter values in the "downhill" direction, *i.e.* the opposite direction to the gradient of the objective function. As for the Gauss-Newton method, it minimises a sum-of-squares objective function that is presumed to be approximately quadratic in the parameters near the optimal solution.

non-radial modes in the data set. This helps to provide more accurate amplitude, period, and phase of the glitch signature. In high-luminosity red giants, those non-radial modes are in fact essential because their parameter $\mathcal{G}_{\mathrm{HeII}}$ is lower than 2, which is the minimum period that can be confidently reproduced when only radial modes are used to fit the glitch modulation. Then, we use both radial, dipole, and quadrupole modes to fit the glitch signature.

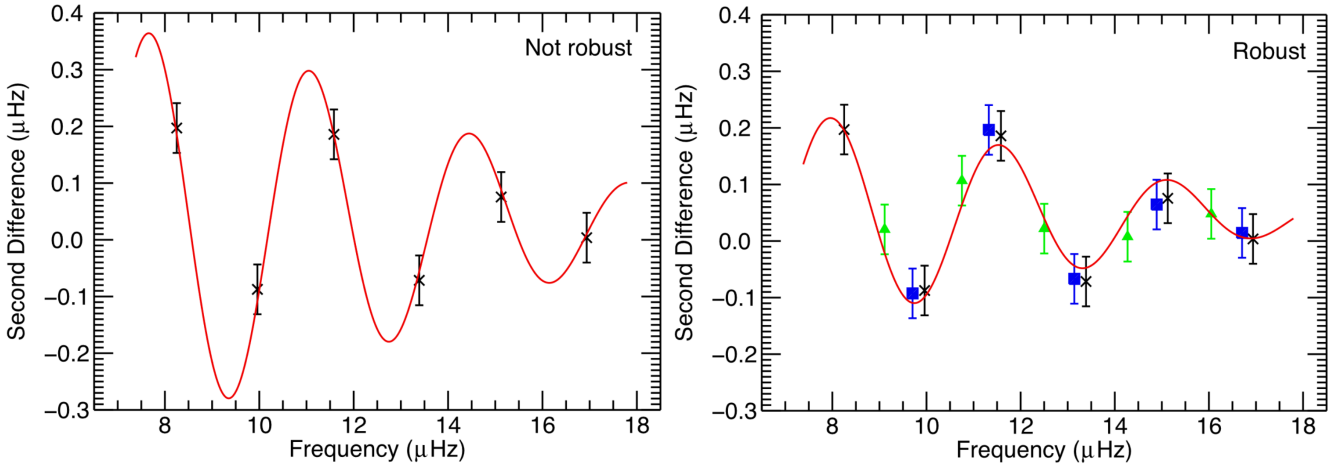

FIGURE 7.8: Fit of the glitch modulation in the second difference defined as $\Delta_2\nu_{n,\ell} = \nu_{n+1,\ell} - 2\nu_{n,\ell} + \nu_{n-1,\ell}$ from a red-giant model with $\nu_{\mathrm{max}} = 12.71\,\mu$Hz, mass $M = 1.5\,M_\odot$, initial helium mass fraction $Y = 0.278$, and initial metal mass fraction $Z = 0.020$. Radial, dipole and quadrupole modes are shown in black crosses, green triangle and blue squares, respectively. **Left:** only radial modes are used to fit the acoustic glitch modulation. **Right:** both radial, dipole and quadrupole modes are used to the acoustic glitch modulation. Credit: Broomhall et al. (2014)

7.6 Summary

In this chapter, we developped an automated method for fitting the oscillation spectrum of high-luminosity red giants. This method is suitable for stars with $\Delta\nu \in [0.5, 4.0]\mu$Hz that mainly show radial and p-dominated non-radial modes in their oscillation spectrum. First, we enhance the seismic signal by convolving the oscillation spectrum with a Gaussian kernel in order to mitigate the stochastic appearance of modes. Then, the modes are identified by matching the observed oscillation spectrum with a template spectrum made of radial, dipole, and quadrupole modes expected from the asymptotic pattern of red giants (Eq. 3.20). The peaks in the oscillation spectrum are considered as oscillation modes if the signal-to-noise ratio is high enough and if their frequency is not too far from the expected p-mode frequencies given by Eq. 3.20. The background component, made of both the photon noise and the incoherent component, is approximated by a power law around ν_{max} while the stellar oscillation modes referred to as the periodic components are fitted by Lorentzian functions with a maximum likelihood estimator technique. However, we are confronted to two complications. First, at low frequency the frequency resolution does not allow us to fit the stellar modes with Lorentzian functions below $\Delta\nu \leq 0.5\,\mu$Hz. Moreover, the template spectrum that relies on the asymptotic pattern of red giants (Eq. 3.20) may be invalid at low $\Delta\nu$. Longer time series are required to tackle these high-luminosity red giants, for instance with ground-based observations (Wood et al., 1999; Wray, Eyer, and Paczyński, 2004). Second, at high frequency mixed dipole modes are visible for $\Delta\nu \geq 3\,\mu$Hz in He-burning stars. In this case, we consider the dipole mode with the highest amplitude among the p-dominated modes that are closest to the expected pure p mode. Finally, the glitch signature is extracted in a similar way as in Vrard et al. (2015), that is we fit the glitch modulation in the local large separation $\Delta\nu_{n,\ell}$ with a damped oscillator model. In this process, we take both radial and p-dominated non-radial modes into account, which allows us to better reproduce the periodicity of the glitch signature then improves the precision of the glitch parameters.

A&A 650, A115 (2021)
https://doi.org/10.1051/0004-6361/202040240

Astronomy & Astrophysics

Seismic constraints on the internal structure of evolved stars: From high-luminosity RGB to AGB stars⋆

G. Dréau[1], B. Mosser[1], Y. Lebreton[1,2], C. Gehan[3], and T. Kallinger[4]

[1] LESIA, Observatoire de Paris, PSL Research University, CNRS, Université Pierre et Marie Curie, Université Paris Diderot, 92195 Meudon, France
e-mail: guillaume.dreau@obspm.fr
[2] Univ Rennes, CNRS, IPR (Institut de Physique de Rennes) – UMR 6251, 35000 Rennes, France
[3] Instituto de Astrofísica e Ciências do Espaço, Universidade do Porto, CAUP, Rua das Estrelas, 4150-762 Porto, Portugal
[4] Institut für Astrophysik, Universität Wien, Türkenschanzstrasse 17, 1180 Vienna, Austria

Received 24 December 2020 / Accepted 1 March 2021

ABSTRACT

Context. The space-borne missions CoRoT and *Kepler* opened up a new opportunity for better understanding stellar evolution by probing stellar interiors with unrivalled high-precision photometric data. *Kepler* has observed stellar oscillation for four years, which gave access to excellent frequency resolution that enables deciphering the oscillation spectrum of evolved red giant branch and asymptotic giant branch stars.
Aims. The internal structure of stars in the upper parts of the red and asymptotic giant branches is poorly constrained, which makes the distinction between red and asymptotic giants difficult. We perform a thorough seismic analysis to address the physical conditions inside these stars and to distinguish them.
Methods. We took advantage of what we have learnt from less evolved stars. We studied the oscillation mode properties of ∼2.000 evolved giants in a model described by the asymptotic pressure-mode pattern of red giants, which includes the signature of the helium second-ionisation zone. Mode identification was performed with a maximum cross-correlation method. Then, the modes were fitted with Lorentzian functions following a maximum likelihood estimator technique.
Results. We derive a large set of seismic parameters of evolved red and asymptotic giants. We extracted the mode properties up to the degree $\ell = 3$ and investigated their dependence on stellar mass, metallicity, and evolutionary status. We identify a clear difference in the signature of the helium second-ionisation zone between red and asymptotic giants. We also detect a clear shortage of the energy of $\ell = 1$ modes after the core-He-burning phase. Furthermore, we note that the mode damping observed on the asymptotic giant branch is similar to that observed on the red giant branch.
Conclusions. We highlight that the signature of the helium second-ionisation zone varies with stellar evolution. This provides us with a physical basis for distinguishing red giant branch stars from asymptotic giants. Here, our investigation of stellar oscillations allows us to constrain the physical processes and the key events that occur during the advanced stages of stellar evolution, with emphasis on the ascent along the asymptotic giant branch, including the asymptotic giant branch bump.

Key words. asteroseismology – stars: evolution – stars: late-type – stars: interiors – stars: AGB and post-AGB – stars: oscillations

1. Introduction

Red giant star seismology has proved to be a good tool for constraining the stellar internal structure with the ultra-high precision photometric data recorded by Convection, Rotation and planetary Transits (CoRoT, Baglin et al. 2006), *Kepler* (Borucki et al. 2010; Gilliland et al. 2010), Kepler 2 (K2, Howell et al. 2014), and now Transiting Exoplanet Survey Satellite (TESS, Ricker et al. 2015). In the case of evolved giants observed by *Kepler*, recent studies have found an equivalence between the solar-like oscillation ridges and the period-luminosity sequences (Mosser et al. 2013a; Stello et al. 2014; Yu et al. 2020) that have first been identified in the ground-based observations with the microlensing surveys Massive Compact Halo Objects (MACHO, Wood et al. 1999) and Optical Gravitational Lensing Experiment (OGLE, Wray et al. 2004; Soszyński & Wood 2013). Nevertheless, deciphering the oscillation spectrum of evolved red giant branch (RGB) and asymptotic giant branch (AGB) stars is challenging because it requires long time-series for the modes to be resolved; the lifetime of the modes is longer than one year. Fortunately, with the unrivalled four-year time series of *Kepler*, it is now possible to decipher the low-frequency oscillation spectrum of evolved red giants and asymptotic giants in detail. The pressure modes of red giants follow a clear oscillation pattern. The so-called universal pattern (UP) of red giants reads (Mosser et al. 2011)

$$\nu_{n,\ell}^{\mathrm{UP}} = \left(n + \frac{\ell}{2} + \varepsilon - d_{0\ell} + \frac{\alpha}{2}[n - n_{\max}]^2\right)\Delta\nu, \quad (1)$$

where n is the mode radial order, ℓ is the degree, ε is the acoustic offset that allows locating the radial modes, $\Delta\nu$ is the mean large frequency separation, which is the mean frequency spacing between consecutive radial modes, $d_{0\ell}$ is a reduced small separation defined as $d_{0\ell} = \delta\nu_{0\ell}/\Delta\nu$, where $\delta\nu_{0\ell}$ is the small frequency separation between a mode of degree ℓ and its neighbouring radial mode, $\alpha = (\mathrm{d}\log\Delta\nu/\mathrm{d}n)$ is the curvature term

⋆ Full Table C.1 is only available at the CDS via anonymous ftp to cdsarc.u-strasbg.fr (130.79.128.5) or via http://cdsarc.u-strasbg.fr/viz-bin/cat/J/A+A/650/A115

that accounts for the linear dependence of the large frequency separation on the radial order, and $n_{\rm max} = \nu_{\rm max}/\Delta\nu$ is the equivalent radial order corresponding to the frequency of the maximum oscillation power $\nu_{\rm max}$. The reduced small separations $d_{0\ell}$ are sensitive to any structure change that impacts the gradient of the sound speed in the deep interior (Gough 1986). These reduced small separations can be used to distinguish different stellar evolutionary stages (Christensen-Dalsgaard et al. 1988).

Firstly identified in red giants by Beck et al. (2011), mixed modes that result from the coupling between gravity waves trapped in the stellar core and pressure waves trapped in the stellar envelope carry valuable information on the physical conditions inside the stellar core. The use of mixed modes enables distinguishing core-helium-burning giants and shell-hydrogen-burning giants (Beck et al. 2011; Bedding et al. 2011; Elsworth et al. 2017). However, constraining the internal innermost structure of evolved giants is challenging because their oscillation spectrum only exhibits pure pressure modes. Mixed modes can no longer be identified because the inertia of the g modes in the core becomes too high (Grosjean et al. 2014) and the strength of the coupling between p and g modes decreases (Mosser et al. 2017a). Despite the absence of mixed modes in evolved RGB and AGB stars, some methods can still be used to distinguish shell-H-burning stars from He-burning stars[1]. On the basis of a local analysis, Kallinger et al. (2012) showed that we can distinguish stars with different evolutionary stages using the central acoustic offset $\varepsilon_{\rm c}$[2]. In addition, Mosser et al. (2019) found that He-burning stars have a lower envelope autocorrelation function than their RGB counterparts[3], making the separation between these stellar populations possible.

The stellar evolution effects reported by Kallinger et al. (2012) in the acoustic offset ε can be linked to clear stellar structure differences. The acoustic offset is expected to contain a contribution from the stellar core, hence the signature of structure changes (Roxburgh & Vorontsov 2000, 2003). However, it also contains a contribution from the stellar envelope that is dominant (Christensen-Dalsgaard et al. 2014). Then, the effects of structure changes in the stellar envelope such as acoustic glitches can be seen in the acoustic offset ε. We recall that a glitch is a sharp structural variation inside the star that causes a modulation in the frequency pattern. The existence of such regions was first predicted (Vorontsov et al. 1988; Gough 1990) and then confirmed for the Sun (Houdek & Gough 2007) for main-sequence stars (Mazumdar et al. 2012, 2014; Verma et al. 2014; Deheuvels et al. 2016) and for red giants (Miglio et al. 2010; Broomhall et al. 2014; Vrard et al. 2015; Corsaro et al. 2015a). In stellar interiors, three regions with sharp variations have been studied: the base of the convective envelope, the boundary of the convective core, and the helium second-ionisation zone (Monteiro et al. 1994; Monteiro & Thompson 2005; Houdek & Gough 2007; Deheuvels et al. 2016). In the case of red giants, it has been shown that the dominant glitch has its origin in the helium second-ionisation zone (Miglio et al. 2010). The modulation in the mode frequencies has been measured for RGB stars and clump stars (Vrard et al. 2015). Vrard et al. (2015) showed that the different modulations between these populations are linked to stellar evolution effects in the local acoustic offset ε. One of the guidelines of the present work is to perform such an analysis for stars in evolved stages on the RGB and the AGB.

Other physical processes can be constrained through the analysis of oscillation spectra, such as mode excitation and damping, especially by measuring the mode amplitudes and the widths. While the physical mechanism causing pressure mode excitation is identified as the Reynolds stresses induced by turbulent convection (Goldreich & Keeley 1977; Belkacem et al. 2006), the physical mechanisms behind the mode damping are not fully understood. Nevertheless, recent studies have been conducted to compare modelled and observed mode widths across the Hertzsprung–Russell (HR) diagram (Belkacem et al. 2012; Houdek et al. 2017; Aarslev et al. 2018). They highlighted that the perturbation of turbulent pressure is the dominant mechanism of mode damping in solar-like pulsators. Several studies have already provided mode widths for main-sequence stars (e.g., Appourchaux et al. 2012, 2014; Lund et al. 2017) and red giant stars (e.g., Baudin et al. 2011; Corsaro et al. 2012, 2015b; Handberg et al. 2017), but their samples of stars are small. With a larger sample of stars having $\Delta\nu \in [3, 15]\,\mu$Hz, Vrard et al. (2018) showed that the pressure mode widths of RGB stars and clump stars are differently distributed and have noticeable mass and temperature dependences. We performed such an analysis for stars in the most evolved stages on the RGB and the AGB.

In this framework, we analysed the oscillation spectrum of ∼2000 evolved red giants, clump stars, and asymptotic giants observed by the *Kepler* telescope in detail. We extend the analysis of Vrard et al. (2015) and Vrard et al. (2018) to the most evolved stages of stars on the RGB and on the AGB. We characterised the pressure modes of evolved stars and the modulation induced by the helium second-ionisation zone in order to obtain seismic constraints for the stellar modelling of evolved red giants and asymptotic giants.

This article is organised as follows. In Sect. 2 we describe our set of data. In Sect. 3 we describe the methods we used to extract the seismic parameters from the oscillation spectra, namely the seismic parameters involved in Eq. (1), the signature of the helium second-ionisation zone, the visibilities of the modes, the pressure mode widths, and the pressure mode amplitudes. The analysis of these quantities is performed in Sect. 4. Finally, Sects. 5 and 6 are devoted to discussion and conclusions, respectively.

2. Data set

We selected the long-cadence data from *Kepler*, including the very last data up to quarter Q17. The about 1470-day time-series gives access to a frequency resolution reaching 7.8 nHz. We focus on advanced stages of stellar evolution, including RGB, clump, and AGB giants. We selected 2103 stars from Kallinger et al. (2012) and Mosser et al. (2014, 2019) that have $\Delta\nu \leq 4.0\,\mu$Hz. We then extracted their $\Delta\nu$ and $\nu_{\rm max}$ from the database of the previous works. The distribution of their $\Delta\nu$ is shown in Fig. 1. The classical properties of these stars, such as their mass and effective temperature, were extracted from the APOKASC catalogue (Pinsonneault et al. 2014), which is a survey of *Kepler* asteroseismic targets complemented by spectroscopic data. More precisely, the stellar masses were computed according to the semi-empirical asteroseismic scaling relation presented in Kjeldsen & Bedding (1995) as corrected by Pinsonneault et al. (2018). The correcting factor was computed star by star and is a function of the stellar parameters. For some

[1] We use the expressions shell-H-burning stars and RGB stars in an equivalent manner. Core-He-burning stars and shell-He-burning stars refer to clump and AGB stars, respectively. He-burning stars indistinctly refer to core-He-burning stars and shell-He-burning stars.

[2] This central acoustic offset $\varepsilon_{\rm c}$ is a local measurement of ε that is computed with the central three radial modes that are closest to $\nu_{\rm max}$.

[3] Counterparts refer to stars that have the same $\Delta\nu$ and $\nu_{\rm max}$.

stars, the classical properties are not listed in the APOKASC catalogue either because no asteroseismic data were returned for them or because the power spectra were too noisy. This concerns roughly 5% of our sample of stars, with half of this fraction being associated with very low $\Delta\nu$-values (i.e., $\Delta\nu \leq 0.5\,\mu$Hz). In this case, we nevertheless obtained rough estimates of the stellar mass and effective temperature using semi-empirical and empirical scaling relations implying both the frequency at the maximum oscillation power $\nu_{\rm max}$ and large frequency separation $\Delta\nu$ (Kjeldsen & Bedding 1995; Kallinger et al. 2010; Mosser et al. 2010).

In order to identify the evolutionary status, we used two classification methods. The first method is based on the estimate of differences between RGB stars and He-burning stars in the pressure-mode pattern, mainly through the acoustic offset ε (Kallinger et al. 2012). The second method is based on the estimate of differences in the envelope autocorrelation function (Mosser et al. 2019). However, the disagreement between these two classification methods rapidly grows at low $\Delta\nu$. For example, we reach 35% disagreement for 112 stars having $\Delta\nu \leq 1.0\,\mu$Hz. Accordingly, we decided to only retain the evolutionary status so obtained if both classification methods agree.

3. Method

Acoustic modes dominate in the oscillation spectrum of evolved RGB and AGB stars. Gravity-dominated mixed modes start to disappear in the oscillation spectrum when $\Delta\nu \leq 3\,\mu$Hz because of their high radiative damping and inertia (Dupret et al. 2009). The oscillation pattern of evolved stars can then be described by the asymptotic expression of the frequency of acoustic modes (Eq. (1)).

3.1. Adjusting the mode frequencies $\nu_{{\rm n},\ell}$

3.1.1. Best-matching template spectrum

The first step to be performed is the identification of the modes in the oscillation spectrum, which is ensured by using Eq. (1). First, we refined the analysis of the observed spectrum as follows. The background component that is dominated by the stellar granulation (Michel et al. 2008) was parametrised in the vicinity of $\nu_{\rm max}$ by a power law of the form

$$B(\nu) = B_{\rm max}\left(\frac{\nu}{\nu_{\rm max}}\right)^{\alpha_B}, \tag{2}$$

where $B_{\rm max}$ and α_B are free parameters (Mosser et al. 2012). Then, we divided the observed spectrum by the background contribution. For the sake of visibility, we reduced the stochastic appearance of the oscillation pattern by smoothing the spectrum with a Gaussian function, for which the full width at half maximum (FWHM) is FWHM $= d_{02}\Delta\nu/4$. We estimated d_{02} following an iterative process, starting with a rough estimate extracted from the scaling relation $d_{02} = 0.162 - 0.013\log\Delta\nu$ (Mosser et al. 2013b).

Second, we built a template spectrum composed of radial, dipole, and quadrupole pressure modes located at the pressure mode frequencies derived from Eq. (1). The seismic parameters ε and $d_{0\ell}$ were set following a scaling relation of the form $A + B\,\log\Delta\nu$, where the guess values of A and B were taken from Mosser et al. (2013a). Then, the modes were modelled by Lorentzian functions. The heights of the Lorentzian functions were fixed by the underlying power excess distribution, which

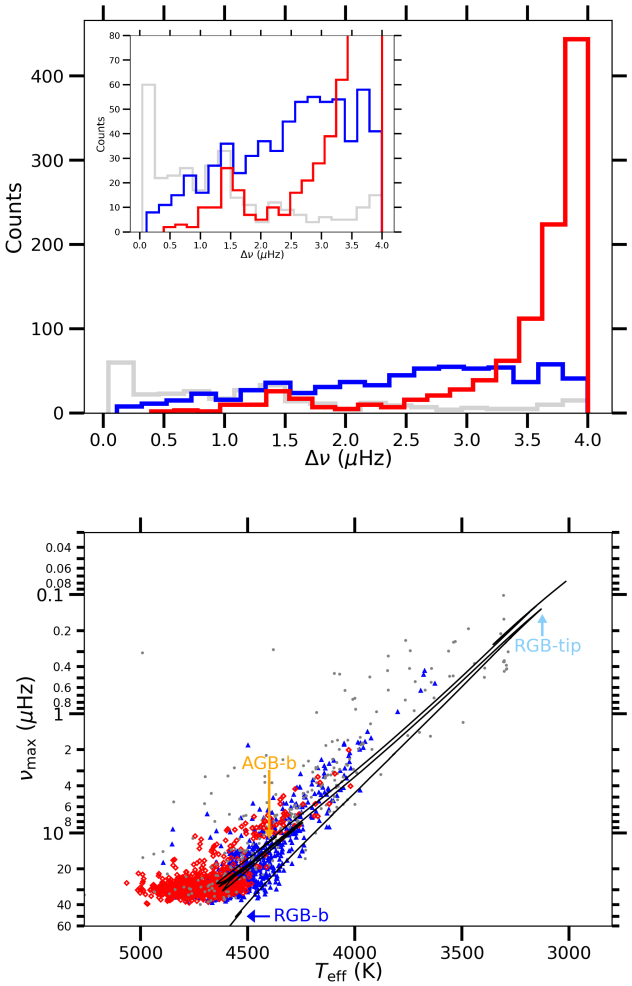

Fig. 1. *Upper panel*: distribution of our sample of stars as a function of $\Delta\nu$, with red giants in blue and He-burning stars in red. Stars with unidentified or uncertain evolutionary stage are plotted in grey. The inset is a zoom-in portion of the large panel. *Lower panel*: seismic diagram of our sample of stars with the same colour code as in the *upper panel*, where $1/\nu_{\rm max}$ is a proxy for the luminosity. The solid black line is the evolutionary track of a 1 $M_\odot$ model computed with MESA, using the 1M_pre_ms_to_wd test suite case. Some key events are highlighted: the RGB bump (RGB-b), the luminosity tip of the RGB (RGB-tip), and the AGB bump (AGB-b).

we modelled by a Gaussian function centred on the frequency of maximum oscillation power $\nu_{\rm max}$ (Mosser et al. 2012). Furthermore, the curvature term was set following the curvature of the red giant radial oscillation pattern as follows (Mosser et al. 2013b):

$$\alpha = 0.015\,\Delta\nu^{-0.32}. \tag{3}$$

We did not adjust the parameters in the expression of α since precise measurement of α is not crucial (Vrard et al. 2015). Finally, we found the best-matching template spectrum by computing the maximum cross-correlation with the smoothed spectrum. Then, the observed mode frequencies were identified at the local maxima close to the optimised frequency pattern. When mixed dipole modes were present, the most intense of the closest modes of the expected pure-pressure mode was adjusted. We report that the best-matching template spectrum is less reliable when $\Delta\nu_{\rm obs} \leq 0.4\,\mu$Hz. In this case, most spectra do not exhibit a clear and intense pattern of $\ell = 0, 1, 2$ modes, making the mode identification difficult. Nevertheless, a mode identification could be

performed for these stars by vertically stacking their power spectrum with increasing $\nu_{\max}$ (see e.g., Yu et al. 2020).

3.1.2. Detection thresholds

Because of the stochastic nature of the modes, some modes are not sufficiently intense to be detected. Once the best-matching template spectrum was found with the method described in Sect. 3.1.1, we obtained a set of candidate modes. Then, in order to reduce biases, we applied the robust detection method of Appourchaux et al. (2006) to this set. To this end, the most intense modes were selected by evaluating the $S_{\rm N}$ function, which corresponds to the most restrictive detection threshold in terms of height-to-background ratio in the power spectrum (Appourchaux et al. 2006). $S_{\rm N}$ reads

$$S_{\rm N} = -\left(\frac{s_{\rm det}}{\ln\left(P_{\rm H_1}\right)} + 1\right), \tag{4}$$

where $P_{\rm H_1}$ is the probability of accepting that the observed peak is a mode and $s_{\rm det}$ is the rejection level relative to noise. We chose $P_{\rm H_1}$ such that the height-to-background ratio $S_{\rm N}$ reached 20 when $s_{\rm det} = 8$, and the rejection level $s_{\rm det}$ was defined by

$$s_{\rm det} \approx \ln(T) + \ln(\Delta\nu) - \ln(p_{\rm det}), \tag{5}$$

where T is the observation time in units of 10^6 s, $\Delta\nu$ is given in μHz, and $p_{\rm det}$ is the rejection probability that we kept equal to 5%. Second, we retained the candidate mode frequencies that were close to the expected pressure-mode frequencies with a less restrictive height-to-background ratio, which is given by Eq. (5). Owing to the small amplitudes of the $\ell = 3$ modes due to geometric cancellation, we used a less restrictive detection threshold for the $\ell = 3$ modes. The threshold for selecting $\ell = 3$ modes is 25% lower than for the other degrees.

3.2. Glitch inference

When the best-matching template spectrum is found, we can search for the signature of glitches. To extract the signature of the helium second-ionisation zone in evolved giants, we followed the same technique as Vrard et al. (2015) for less evolved giants. As the oscillation spectrum of evolved red giants shows a limited number of radial orders, we calculated the frequency difference considering all degrees as follows:

$$\Delta\nu_{n,\ell} = \nu_{n+1,\ell} - \nu_{n,\ell}, \tag{6}$$

which is different from Eq. (4) of Vrard et al. (2015) because it is only based on radial modes. The frequency reference for these local large frequency separations was taken as the mid-point between consecutive mode frequencies. We isolated the glitch signature $\delta^{\rm g,obs}_{n,\ell}$ by computing the difference between the measured and the expected local large frequency separations according to the universal pattern (Eq. (1))

$$\delta^{\rm g,obs}_{n,\ell} = \Delta\nu_{n,\ell} - \Delta\nu^{\rm UP}_{n,\ell}, \tag{7}$$

with $\Delta\nu^{\rm UP}_{n,\ell} = \left(1 + \alpha\left(n - n_{\max} + \frac{1}{2}\right)\right)\Delta\nu$ (Mosser et al. 2013b). We then fitted a damped oscillatory component of $\delta^{\rm g,obs}_{n,\ell}$ according to

$$\delta^{\rm g,obs}_{n,\ell} = \mathcal{A}\left(\frac{\nu_{\max}}{\nu}\right)^2 \Delta\nu \cos\left(\frac{2\pi\left(\nu - \nu_{\max}\right)}{\mathcal{G}\Delta\nu} + \Phi\right), \tag{8}$$

Table 1. Boundaries for the integration of the power spectral density.

	$\nu_{\rm inf}(n,\ell)$	$\nu_{\rm sup}(n,\ell)$
$\ell = 0$	$(\nu_{n,0} + \nu_{n-1,2})/2$	$(3\,\nu_{n-1,3} + \nu_{n,0})/4$
$\ell = 3$	$(3\,\nu_{n-1,3} + \nu_{n,0})/4$	$(7\,\nu_{n-1,3} - \nu_{n,0})/6$
$\ell = 1$	$(7\,\nu_{n-1,3} - \nu_{n,0})/6$	$(4\,\nu_{n-1,2} - \nu_{n,0})/3$
$\ell = 2$	$(4\,\nu_{n-1,2} - \nu_{n,0})/3$	$(\nu_{n,0} + \nu_{n-1,2})/2$

Notes. The boundaries are equivalent to the mid-point between consecutive modes, except when $\ell = 1$ and $\ell = 3$ modes are involved. This is illustrated in Fig. 2. The boundary between the $\ell = 1$ and the $\ell = 3$ modes is chosen close to the $\ell = 3$ mode frequency. We made this choice to avoid any confusion between a $\ell = 3$ mode and the neighbouring dipole mixed-modes because the dipole mixed-modes extend up to the $\ell = 3$ modes.

where $\mathcal{A}$ and $\mathcal{G}$ are the amplitude and the period of the modulation expressed in units of $\Delta\nu$, respectively, and Φ is the phase centred on $\nu_{\max}$ (Vrard et al. 2015). Many studies have used a more complicated function for the amplitude of the modulation. As we are restricted by the low number of observed modes, we preferred to use a simple frequency-dependent amplitude as was used before in the study of the base of the solar convective zone (Monteiro et al. 1994).

In evolved giants, quadrupole modes essentially behave as pure pressure modes. The case of dipole modes is complicated: They are most often reduced to a pressure-dominated mixed mode or to a cluster of modes very close to the pressure-dominated mixed mode. Because in most cases we have no way to identify the mixed-mode pattern, in practice we also consider dipole modes as pure pressure modes. This hypothesis is discussed below. We can add them in the fit of the glitch modulation without deteriorating the fit of the modulation. Then, the Nyquist criterion, which states that the frequency of the modulation must be strictly less than half the sample rate, writes $\mathcal{G} \geq 1$ instead of $\mathcal{G} \geq 2$ when only radial modes are used. When $\Delta\nu \gtrsim 3\,\mu$Hz, dipole modes are no longer pure-pressure modes. It has been shown that adding the dipole modes of lowest inertia in each $\Delta\nu$ range could bias the fit of the modulation, especially for the least evolved red giants (Broomhall et al. 2014; Dréau et al. 2020). Nevertheless, for the range of $\Delta\nu$ we consider here, Broomhall et al. (2014) reported that the use of dipole modes of lowest inertia remarkably improves the robustness of the fit. When mixed modes are present, we then took into account the most intense dipole mode of the modes closest to the expected location of the pure-pressure mode.

3.3. Computation of mode visibilities

We investigated the energy distribution among modes of different degree ℓ in the case of evolved stars. The technique we used to compute the mode visibilities is described in Mosser et al. (2012). First, we computed the total mode energy, noted $A^2_\ell(n)$, for which the radial order n lies between the lowest and highest observed radial orders. This was done by subtracting the background component and integrating the power spectral density over the whole spectral range where the mode is expected, that is, around the p-mode frequency inferred from Eq. (1) (see Table 1 and Fig. 2). Then we computed the visibility V^2_ℓ of a mode of degree ℓ as

$$V^2_\ell = \frac{\langle A^2_\ell \rangle}{\langle A^2_0 \rangle}, \tag{9}$$

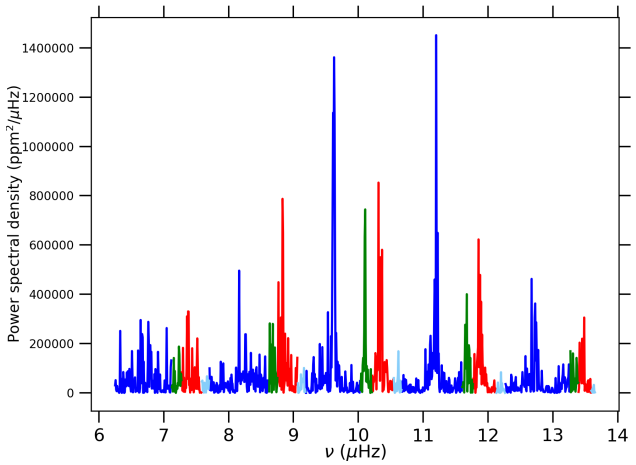

Fig. 2. Oscillation spectrum of the star KIC 2695975 ($\Delta\nu = 1.538\,\mu$Hz, and $\nu_{\max} = 10.11\,\mu$Hz), with an emphasis on the spectral range where the power spectral density is integrated for each mode. Red, blue, green, and light blue are associated with radial, dipole, quadrupole, and octupole modes, respectively. This star has been classified as an RGB star with the two identification methods adopted in this work.

where $\langle A_\ell^2 \rangle$ is the squared amplitude of the mode of degree ℓ.

When mixed modes are present, the procedure was the same: The energy $A_\ell^2(n)$ corresponds to the total energy of the mixed modes associated with the radial order n. The errors on the visibilities were computed from the errors on the boundary frequencies listed in Table 1: The energy contained in the 1σ error region of the boundary frequencies is interpreted as the error on the parameter $A_\ell^2(n)$.

3.4. Mode fitting

The mode amplitudes and widths derived from the fit of the modes provide unique constraints on the mode excitation and damping. In this context, we adopted a frequentist approach. The modes were fitted with Lorentzian profiles following the maximum likelihood estimator technique described in Toutain & Appourchaux (1994). The fit was performed radial order by radial order, so that we have three modes at most to fit per iteration. Owing to their very low amplitudes, $\ell = 3$ modes cannot be fitted. Radial, dipole, and quadrupole modes were fitted on top of the background using

$$\mathcal{L}(n) = \sum_{\ell=0,1,2} \frac{H_{n,\ell}}{1 + \left(2\frac{\nu-\nu_{n,\ell}}{\Gamma_{n,\ell}}\right)^2} + B(\nu), \tag{10}$$

where $H_{n,\ell}$, $\nu_{n,\ell}$, and $\Gamma_{n,\ell}$ are the height, frequency, and width of the mode of radial order n and degree ℓ, respectively. We point out that the background was extracted separately, and we kept it fixed when fitting the modes. The mode amplitude can be deduced from the mode height and the width by

$$A_{n,\ell} = \sqrt{H_{n,\ell}\pi\Gamma_{n,\ell}}. \tag{11}$$

Because of the low signal-to-noise ratios, the presence of mixed modes, and the stochastic excitation, some modes were not correctly fitted. The measurements were rejected when the width was too close to the frequency resolution (i.e., when $\Gamma_{n,l} \leq 1.1\delta\nu_{\rm res}$) or when the width was overestimated (i.e., when $\Gamma_{n,l} \geq \Delta\nu/7$). When mixed modes were present, we fitted the closest mixed modes to the expected pure-pressure mode. Then, following Benomar et al. (2014), Belkacem et al. (2015), and Mosser et al. (2018), we inferred the mode width and the mode amplitude that the mode would have if it were purely acoustic through

$$\Gamma^{\rm p}_{n,\ell} = \frac{\Gamma_{n,\ell}}{1-\zeta} \text{ and } A^{\rm p}_{n,\ell} = \frac{A_{n,\ell}}{\sqrt{1-\zeta}}, \tag{12}$$

where ζ depends on the inertia of the fitted mixed mode. Characterising the mixed-mode pattern is beyond the scope of this work. However, we estimated the mode inertia that is defined in Mosser et al. (2018), for example, using scaling relations (Eqs. (17) and (18) from Mosser et al. 2017a for the coupling factor q and the database from Vrard et al. 2016 for the period spacings $\Delta\Pi_1$).

We finally computed the mean mode amplitude $\langle A_\ell \rangle$ using the three p modes of degree ℓ closest to $\nu_{\max}$. We corrected the wavelength dependence of the photometric variation integrated over the *Kepler* bandpass according to

$$\langle A_{\ell,\rm bol} \rangle = \langle A_\ell \rangle \left(\frac{T_{\rm eff}}{T_K}\right)^{0.80}, \tag{13}$$

where $T_K = 5934\,$K (Ballot et al. 2011a). The average mode width $\langle \Gamma_\ell \rangle$ was computed as the weighted mean of the three p modes of degree ℓ closest to $\nu_{\max}$, where the mode amplitude was used as weight (see e.g., Vrard et al. 2018).

4. Results

In this section, we characterise the oscillation spectrum of evolved giants as precisely as possible. We compare our measurements with previous studies that focused on less evolved stages and with theoretical predictions.

4.1. Acoustic offset ε and reduced small separations $d_{0\ell}$

From the fit of the spectrum described by Eq. (1) we derived the global acoustic offset ε and the reduced small separations $d_{0\ell}$ associated with the detected modes (see Fig. 3). Scaling relations were adjusted to our sets of seismic parameters in the form $A_\ell + B_\ell \log(\Delta\nu)$, where A_ℓ and B_ℓ are free parameters that are summarised in Table 2, and $\Delta\nu$ is given in μHz.

4.1.1. Acoustic offset ε

The oscillation spectrum of radial modes is depicted by the global acoustic offset ε as shown in Fig. 3. The trend that we observe for RGB stars is similar to what has been obtained in previous studies (Mosser et al. 2013a; Yu et al. 2020). With our method, which uses a global fit of the oscillation pattern, we derive similar values of ε for RGB and He-burning stars, in contrast to Kallinger et al. (2012), who used a local approach. As they showed, the glitches have limited effect on global measurements of the seismic parameters but they affect local measurements considerably. In Sect. 4.2 we investigate the local effects on the mode frequencies by studying the modulation left by the helium second-ionisation zone in p-mode frequencies.

4.1.2. Reduced small separations $d_{0\ell}$

Theoretical models predict that the effects of stellar evolution are reflected in the reduced small separations $d_{0\ell}$. They are sensitive to any internal structure change that affects the gradient

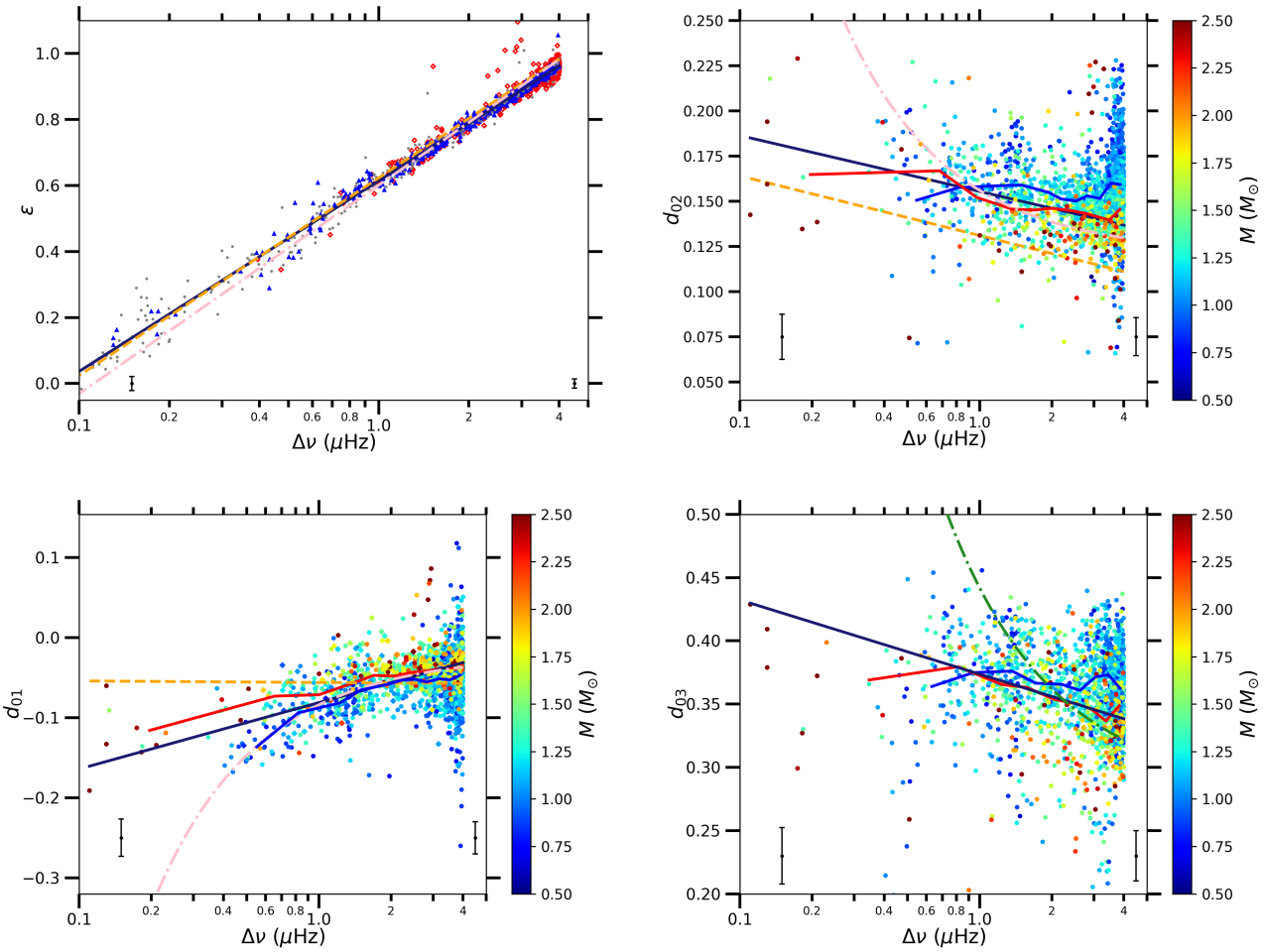

Fig. 3. Seismic parameters of the asymptotic pattern of red giants (Eq. (1)) after adjusting $\Delta\nu$ with the best-matching template following the procedure described in Sect. 3. *Upper left panel*: acoustic offset ε as a function of $\Delta\nu$, where blue triangles indicate RGB stars and red diamonds He-burning stars. Stars with either an unidentified evolutionary stage or disagreement between the two classification methods described in Sect. 2 are represented in grey. *Upper right panel*: reduced small separation d_{02} as a function of $\Delta\nu$; the stellar mass is colour-coded. *Bottom panels*: same labels as for the *upper right panel*, but for d_{01} and d_{03} as a function of $\Delta\nu$. The solid blue and red lines are the median values in 0.4 μHz $\Delta\nu$ bins for low-mass stars ($M \leq 1.2\,M_\odot$) and for high-mass stars ($M \geq 1.2\,M_\odot$), respectively. The dashed orange lines represent the scaling relations from Mosser et al. (2013a), and the solid dark blue lines are the scaling relations derived in this study (listed in Table 2). The dot-dashed pink and dark green lines correspond to the scaling relations for less evolved stars from Corsaro et al. (2012) and Huber et al. (2010), respectively. Mean error bars estimated at low $\Delta\nu$ ($\Delta\nu \leq 1.0$ μHz) and at high $\Delta\nu$ ($\Delta\nu \geq 1.0$ μHz) are represented at the bottom of each panel.

Table 2. Fit of the seismic parameters ε and $d_{0\ell}$, and the dimensionless glitch parameters.

ℓ		A_ℓ	B_ℓ
0	ε	0.614 ± 0.002	0.578 ± 0.003
1	d_{01}	−0.081 ± 0.002	0.083 ± 0.005
2	d_{02}	0.156 ± 0.001	−0.031 ± 0.003
3	d_{03}	0.374 ± 0.002	−0.059 ± 0.005
		C	D
	$\mathcal{A}$	0.072 ± 0.003	−0.411 ± 0.006
	$\mathcal{G}$	1.879 ± 0.001	0.045 ± 0.002

Notes. The fits were performed for RGB stars alone. The acoustic offset and the reduced small separations were fitted by a linear fit $A_\ell + B_\ell \log(\Delta\nu)$, while the glitch parameters were fitted by a power law $C\Delta\nu^D$.

of the sound speed (Tassoul 1980; Roxburgh & Vorontsov 2003) in the deep interiors. While a star ascends the RGB, the stellar core contracts but does not undergo important structure changes. Therefore the reduced small separations vary only slowly along the RGB.

Figure 3 shows that d_{01} decreases when $\Delta\nu$ decreases, as observed by previous observational studies on less evolved stars (Huber et al. 2010; Corsaro et al. 2012; Mosser et al. 2013a). This points out the fact that during stellar evolution, dipole p modes approach the doublet formed by $\ell = 0$ and $\ell = 2$ modes, in agreement with theoretical models (Montalbán et al. 2010; Stello et al. 2014). The variation of d_{01} during late stellar evolution can be linked to the location of the turning points of $\ell = 1$ modes. By examining the structure of low-mass red giant models, Montalbán et al. (2010) found that d_{01} takes negative values when the turning points of $\ell = 1$ modes are deep in the convective envelope. This is exactly what we observe and allows us to extend the interpretation made for RGB stars to AGB stars, which have negative d_{01}. Stellar models of Montalbán et al. (2010) also predict that core-He-burning stars have both positive and negative d_{01}, and that the turning points of $\ell = 1$ modes are located inside the radiative region. The determination of d_{01} in clump stars is more difficult because the observed large spread

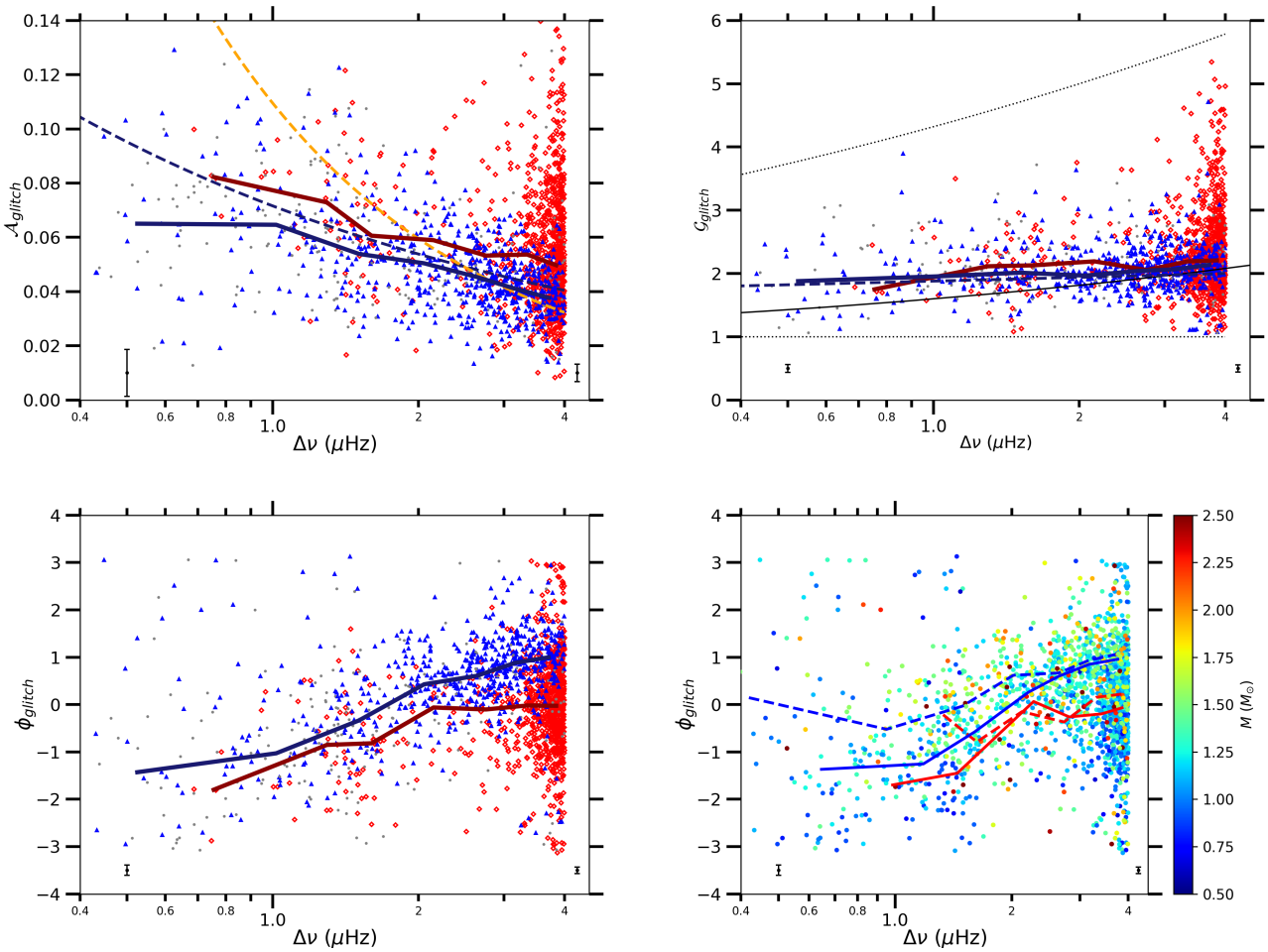

Fig. 4. Modulation amplitude $\mathcal{A}$, modulation period $\mathcal{G}$, and modulation phase Φ as a function of $\Delta\nu$, with the same labels as in Fig. 3. The thick solid lines are the median values in 0.5 µHz $\Delta\nu$ bins, shown in blue for RGB stars and in red for He-burning stars. In the *upper panels*, dashed blue lines are the fits presented in Table 2. In the *upper left panel*, the dashed orange line is the fit obtained for less evolved stars (Vrard et al. 2015), corrected with a factor that accounts for the differences between the methods we used to fit the modulation as described in Sect. 4.2. In the *upper right panel*, dotted black lines delimit the domain of reliable measurements of $\mathcal{G}$, which are described in Sect. 3, and the thin solid line is the modulation period inferred from MESA models for a 1 $M_\odot$ star and starting from the RGB up to the AGB. The error bars are computed in the same way as in Fig. 3. In the *lower right panel*, the stellar mass is colour-coded, and medians are represented by solid lines for low-mass stars ($M \leq 1.2\,M_\odot$) and by dashed lines for high-mass stars ($M \geq 1.2\,M_\odot$). Because Φ varies with stellar evolution, we calculated the medians for RGB and He-burning stars separately. We show them in blue for RGB and in red for He-burning stars.

in d_{01} mainly reflects the presence of mixed modes that perturb the adjustment of the acoustic dipole modes.

The reduced small separation d_{02} is sensitive to the structure differences between core He-burning stars and RGB stars: We report that d_{02} is larger on average for core He-burning stars than for RGB stars, as has been reported by Kallinger et al. (2012). We note a clear mass effect: the lower the mass, the larger d_{02}. The first evidence of this mass dependence in red giants has been discussed in Huber et al. (2010), in agreement with the theoretical models (Montalbán et al. 2012). We find that this mass dependence is also visible for d_{01} and d_{03}, as predicted by the theoretical models of Montalbán et al. (2010), despite the presence of mixed modes that cause the values of these parameters to become more scattered. However, Montalbán and collaborators did not discuss the origin of this mass dependence. Further work is therefore needed to physically understand this behaviour.

As for $\ell = 3$ modes (see the bottom panel of Fig. 3), we note that the reduced small separation d_{03} increases when $\Delta\nu$ decreases, as shown by the observations of *Kepler* (Huber et al. 2010) and stellar models (Montalbán et al. 2010). This expresses the fact that the $\ell = 3$ modes approach the left-hand side of $\ell = 0, 2$ modes during stellar evolution. Further theoretical work is needed to investigate and understand this behaviour.

4.2. Signature of the helium second-ionisation zone

The results obtained after fitting the modulation left by the helium second-ionisation zone in $\Delta\nu_{n,\ell}$ are shown in Fig. 4. In Table 2 we present the scaling relations found for the dimensionless amplitude $\mathcal{A}$ and period $\mathcal{G}$, computed for RGB stars alone, in the form $C\Delta\nu^D$, where C and D are free parameters and $\Delta\nu$ is given in µHz.

4.2.1. Modulation amplitude $\mathcal{A}$

When a star ascends the RGB or AGB ($\Delta\nu \lesssim 3$ µHz for the early AGB), the dimensionless amplitude of the modulation $\mathcal{A}$ notably increases. During the clump phase, it is more difficult to conclude because of the large spread of the amplitudes. We verified that most of the stars with $\mathcal{A} \geq 0.09$ also have a dim

Kepler magnitude, hence their oscillation spectrum is recorded with a low signal-to-noise ratio, so that the measurement of $\mathcal{A}$ is quite noisy. Globally, the amplitude of the modulation is larger for He-burning stars than for RGB stars. This is consistent with the results presented in Vrard et al. (2015) between clump and RGB stars having $\Delta\nu \geq 3.0\,\mu$Hz. We note that the values of the modulation amplitude are larger in our work than in Vrard et al. (2015), as expected from the different methods with which $\Delta\nu_{n,\ell}$ and $\delta_{\rm g,obs}(n,\ell)$ were computed. To compare our results with those of Vrard et al. (2015), we then estimated how different the modulation amplitudes are between the two methods. We note that our modulation amplitudes are 1.8 times larger on average than those extracted in Vrard et al. (2015). Then, we multiplied the fit reported in the latter study by 1.8 and compared it with ours, as plotted in the upper left panel of Fig. 4. Our results are also consistent with stellar evolution models that indicate that the difference observed in the modulation amplitude $\mathcal{A}$ between RGB and He-burning phases is correlated with a difference of temperature and density at the level of the helium second-ionisation zone (Christensen-Dalsgaard et al. 2014).

4.2.2. Modulation period $\mathcal{G}$

We note that the modulation period $\mathcal{G}$ slightly decreases throughout the stellar evolution (Fig. 4). This means that the helium ionisation zone slowly sinks into the stellar interior during evolution, as predicted by stellar models (Fig. 6 of Broomhall et al. 2014). The typical period does not globally differ between He-burning stars and their RGB counterparts. Our measurements were compared to the results derived with the stellar evolution code Modules for Experiments in Stellar Astrophysics (MESA) using the 1M_pre_ms_to_wd test suite case (Paxton et al. 2011, 2013, 2015, 2018, 2019). In Appendix A we describe how we extracted the modulation period $\mathcal{G}$ from stellar models. Stellar models indicate that RGB stars and He-burning stars of the same mass and same large separation should have the same modulation period $\mathcal{G}$, in agreement with observations. However, He-burning stars have more scattered $\mathcal{G}$ values than their RGB counterparts. The large spread does not appear to stem from the presence of mixed modes because Vrard et al. (2015) also reported a spread like this for clump and RGB stars, although they only used radial modes in the modulation fits. As reported for the modulation amplitude $\mathcal{A}$, the spread is rather well explained by the dim magnitudes, hence by the low signal-to-noise ratios in the oscillation spectra.

4.2.3. Modulation phase Φ

The modulation phase Φ differs depending on the evolutionary stage. By letting the phase vary in the interval $[-\pi, +\pi]$, we observe that He-burning stars globally show a negative phase difference compared to their H-burning counterparts. This difference has been reported by Vrard et al. (2015) for clump and RGB stars. The authors showed that the phase difference is related to the difference in ε reported in the study of Kallinger et al. (2012) between clump and RGB stars. The link between Φ and ε, which depends on the evolutionary stage, is discussed in Sect. 5. Similarly to the modulation amplitude $\mathcal{A}$ and the modulation period $\mathcal{G}$, the spread of the modulation phase Φ is larger for He-burning stars than for H-burning stars. We verified that the spread of Φ becomes important when the *Kepler* magnitude exceeds 11. The large spread of Φ could then be explained by low signal-to-noise ratios in the oscillation spectra.

4.2.4. Mass dependence of the glitch parameters

We also investigated the stellar mass dependence of the glitch modulation parameters. We find evidence of a mass dependence for the modulation amplitude, which varies as $\mathcal{A}_{\rm RGB} \propto \Delta\nu^{-0.41\pm0.01} M^{-0.34\pm0.02}$ on the RGB with a similar dependence during He-burning phases. Conversely, the modulation period is weakly correlated with the stellar mass on the RGB and follows $\mathcal{G}_{\rm RGB} \propto \Delta\nu^{-0.05\pm0.01} M^{-0.04\pm0.01}$, while it is practically independent of the stellar mass during the He-burning phase. The mass dependence of the modulation phase Φ is illustrated in Fig. 4. We note a negative phase difference between low-mass and high-mass RGB stars for $\Delta\nu \leq 2.0\,\mu$Hz. The lack of data for He-burning stars at low $\Delta\nu$ prevents us from drawing any conclusion. In case of less evolved stars, Vrard et al. (2015) did not find any correlation between the stellar mass and the glitch parameters, except for the modulation phase for clump stars. These mass dependences remain empirical, and further theoretical work is needed to determine their physical basis.

4.3. Mode widths

The mode widths $\langle\Gamma_\ell\rangle$ were fitted by the function

$$\langle\Gamma_\ell\rangle = a_\ell \left(\frac{T_{\rm eff}}{4800\,\mathrm{K}}\right)^{b_\ell}, \tag{14}$$

where a_ℓ and b_ℓ are free parameters. The fits are presented in Fig. 5 and summarised in Table 3.

We note that clump stars globally have larger radial mode widths with a larger spread than those observed for RGB stars, as mentioned in previous studies (Corsaro et al. 2012; Vrard et al. 2018). However, when core-He-burning ends and the star ascends the AGB ($\Delta\nu \lesssim 3\,\mu$Hz), the radial mode widths decrease and become comparable to measurements made on the RGB.

In Fig. 5 we compare the dipole mode widths $\langle\Gamma_1\rangle$ to the radial mode widths $\langle\Gamma_0\rangle$. On the RGB, we note that $\langle\Gamma_1\rangle$ values are globally 20% higher than $\langle\Gamma_0\rangle$ above $\Delta\nu \geq 3.5\,\mu$Hz, while they are globally similar below. For He-burning stars, the $\ell = 1$ modes have larger widths than the $\ell = 0$ modes above $\Delta\nu \geq 1.5\,\mu$Hz. We identified three reasons that might explain this behaviour. First, as mentioned in Sect. 3, we applied the correction expressed by Eq. (12) to $\langle\Gamma_1\rangle$ when the fitted modes are mixed modes. However, the term ζ is close to 1, therefore the correction to $\langle\Gamma_1\rangle$ introduces large uncertainties on the inferred dipole p-mode widths. Second, most of the unexpectedly high $\langle\Gamma_1\rangle$ values are in fact highly perturbed by mixed modes. Gravity-dominated mixed modes can only be observed if the condition

$$\mathcal{N} \leq \frac{1}{4q}\left(\frac{\pi}{2}\frac{\Gamma_0}{\delta\nu_{\rm res}} - 5\right) \tag{15}$$

is met (Mosser et al. 2018), where $\mathcal{N} = \Delta\nu/(\nu^2\Delta\Pi_1)$ is the number of gravity modes per radial order n, $\Delta\Pi_1$ is the period spacing, q is the coupling factor, Γ_0 is the radial mode width, and $\delta\nu_{\rm res}$ is the frequency resolution. Using typical values of q (see e.g., Mosser et al. 2017a) and $\langle\Gamma_0\rangle$, we can infer that the right-hand side term of Eq. (15) is close to 20 at $\Delta\nu \sim 3\,\mu$Hz for He-burning stars. Then, Eq. (15) is hardly verified and only p-dominated modes are mainly visible. In these cases, the mixed modes are so close that the fits rather reproduce several confused mixed modes than a unique pure pressure mode. Third, we note that all the highest values of $\langle\Gamma_1\rangle$ are systematically associated with low

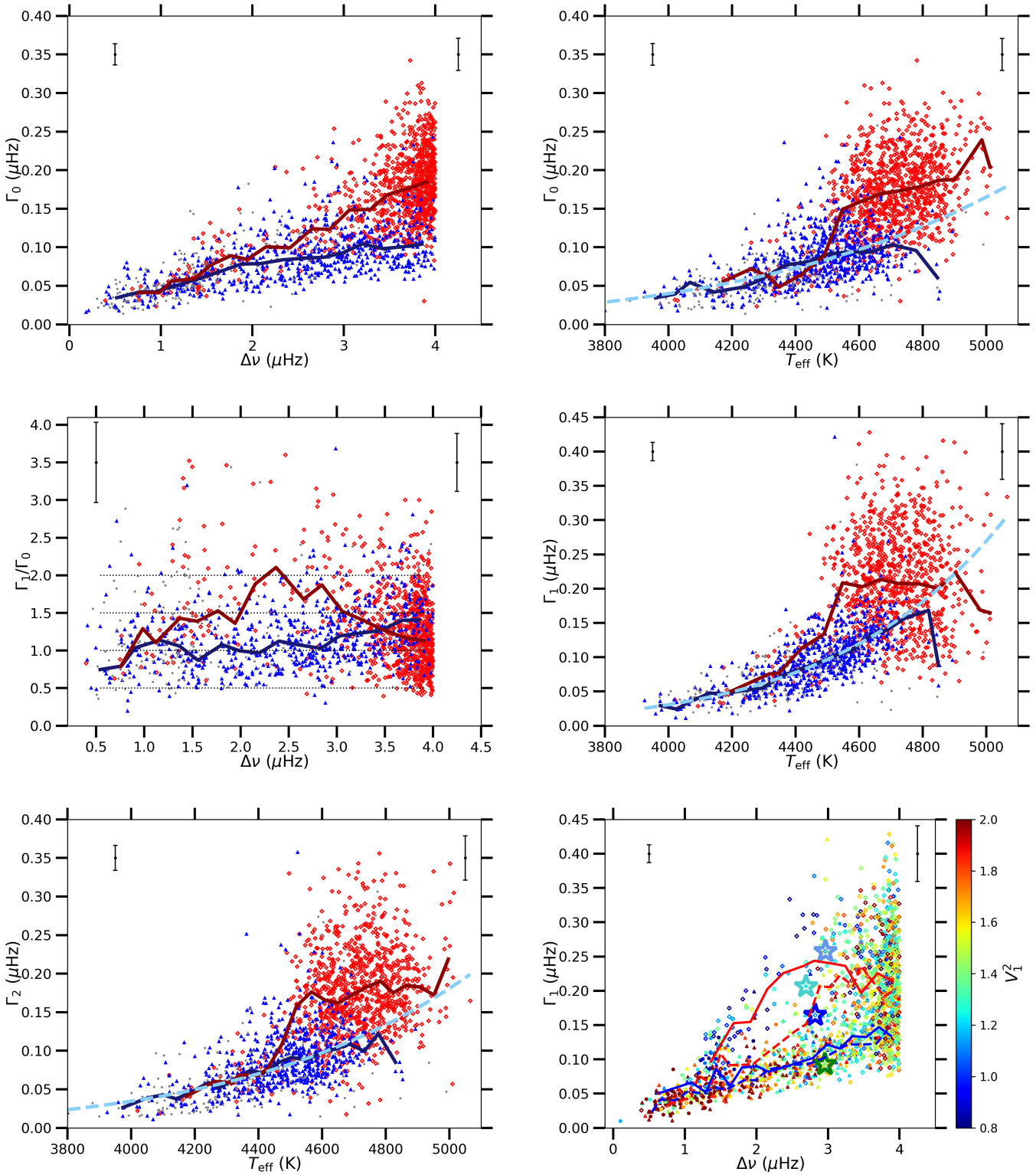

Fig. 5. *Upper panels*: $\langle\Gamma_0\rangle$ as a function of $\Delta\nu$ and $T_{\rm eff}$. *Middle panels*: ratio of $\langle\Gamma_1\rangle$ and $\langle\Gamma_0\rangle$ as a function of $\Delta\nu$ and $\langle\Gamma_1\rangle$ as a function of $T_{\rm eff}$. For convenience, horizontal dotted black lines are plotted at specific values of 0.5, 1.0, 1.5, and 2.0. *Bottom left panel*: $\langle\Gamma_2\rangle$ as a function of $T_{\rm eff}$. The colours and symbols are the same as in Fig. 4. Mean error bars on the widths have been computed both at low $T_{\rm eff}$ ($T_{\rm eff} \leq 4200$ K) and at high $T_{\rm eff}$ ($T_{\rm eff} \geq 4200$ K). These limits are equivalent to the limits in $\Delta\nu$ chosen in Fig. 3. The fits presented in Table 3 are plotted with dashed light blue lines for RGB stars. *Bottom right*: $\langle\Gamma_1\rangle$ as a function of $\Delta\nu$ with the dipole mode visibilities colour-coded. The solid and dashed lines correspond to the median values for low-visibility dipole modes ($V_1^2 \leq 1.5$) and for high-visibility dipole modes ($V_1^2 \geq 1.5$), respectively, in blue for RGB stars and in red for He-burning stars. The turquoise, dark blue, light blue and green stars are the individual stars KIC 6847371, KIC 11032660, KIC 5461447, and KIC 6768042, respectively. They are studied in Sect. 5.3 to test the reliability of the measurements of the dipole mode width. The median values are computed in 0.2 μHz wide $\Delta\nu$ bins and in 50 K wide $T_{\rm eff}$ bins.

Table 3. Scaling relations for the mode widths and for the mode amplitudes.

	Population	a_ℓ	b_ℓ
$\langle\Gamma_0\rangle$ (μHz)	RGB		10.8 (*)
	RGB	0.13 ± 0.02	6.36 ± 0.37
$\langle\Gamma_1\rangle$ (μHz)	RGB	0.18 ± 0.01	9.73 ± 0.34
$\langle\Gamma_2\rangle$ (μHz)	RGB	0.14 ± 0.02	7.41 ± 0.40
		c_ℓ	d_ℓ
$\langle A_{0,\mathrm{bol}}\rangle$ (ppm)	$M \leq 1.2\,M_\odot$	1013 ± 20	−0.64 ± 0.02
	$M \geq 1.2\,M_\odot$	902 ± 36	−0.68 ± 0.03
$\langle A_{1,\mathrm{bol}}\rangle$ (ppm)	$M \leq 1.2\,M_\odot$	928 ± 19	−0.59 ± 0.02
	$M \geq 1.2\,M_\odot$	853 ± 35	−0.64 ± 0.03
$\langle A_{2,\mathrm{bol}}\rangle$ (ppm)	$M \leq 1.2\,M_\odot$	1090 ± 31	−0.74 ± 0.02
	$M \geq 1.2\,M_\odot$	1031 ± 30	−0.75 ± 0.02

Notes. The mode widths $\langle\Gamma_\ell\rangle$ and the mode amplitudes $\langle A_{\mathrm{bol},\ell}\rangle$ are fitted by Eqs. (14) and (16), respectively. (*)The exponent $b_{\ell=0}$ indicated in the first row for $\langle\Gamma_0\rangle$ is the value expected on the RGB (Belkacem et al. 2012).

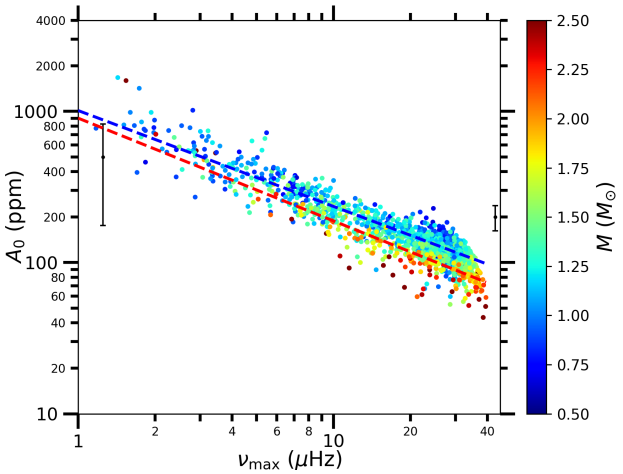

Fig. 6. Radial mode amplitude $\langle A_{0,\mathrm{bol}}\rangle$ computed from Eq. (13) as a function of $\nu_{\max}$ with the stellar mass colour-coded. The dashed lines are the fits presented in Table 3, shown in blue for low-mass stars ($M \leq 1.2\,M_\odot$) and in red for high-mass stars ($M \geq 1.2\,M_\odot$). The error bars are computed in the same way as in Fig. 5.

$\ell = 1$ mode visibilities in the interval $\Delta\nu \in [1.5, 2.5]$ μHz. These dipole modes with a low amplitude are unexpectedly large and are further discussed in Sect. 5.3. The comparison between $\langle\Gamma_2\rangle$ and $\langle\Gamma_0\rangle$ is not discussed here because $\langle\Gamma_0\rangle \sim \langle\Gamma_2\rangle$, as expected.

We also investigated the temperature dependence of $\langle\Gamma_\ell\rangle$ (Fig. 5). The fits performed on each stellar population (cf. Table 3) indicate that $\langle\Gamma_\ell\rangle$ and T_{eff} are strongly correlated, regardless of the degree ℓ. Vrard et al. (2018) also reported that $\langle\Gamma_0\rangle$ is correlated with T_{eff} for less evolved giants, but this correlation is not as pronounced as in the present study. A strong correlation like this is expected across the HR diagram according to theoretical work (Belkacem et al. 2012).

4.4. Mode amplitudes

The radial mode amplitude $\langle A_{0,\mathrm{bol}}\rangle$ defined in Eq. (13) is plotted as a function of $\nu_{\max}$ in Fig. 6 and was adjusted by the scaling relation

$$\langle A_{\ell,\mathrm{bol}}\rangle = c_\ell\, \nu_{\max}^{d_\ell}, \tag{16}$$

where c_ℓ and d_ℓ are free parameters and $\nu_{\max}$ is given in μHz. The radial mode amplitudes follow the same trend as highlighted in recent studies (e.g., Huber et al. 2011; Stello et al. 2011; Mosser et al. 2012; Vrard et al. 2018). The radial mode amplitude does not differ between RGB stars and He-burning stars. For both stellar populations, the radial mode amplitude follows a power law with an exponent roughly equal to −0.70. Furthermore, the previous studies reported a clear mass dependence regardless the evolutionary stage: the higher the mass, the lower the radial mode amplitude (see Fig. 6).

4.5. Mode visibilities

The energy distribution between modes of different degree ℓ can be studied through the mode visibilities (Eq. (9)). They are presented in Fig. 7 and were fitted by the linear function

$$V_\ell^2 = \alpha + \beta(T_{\mathrm{eff}} - 4800\,\mathrm{K}), \tag{17}$$

where α and β are free parameters and T_{eff} is given in K (see Table 4).

We verified that the high values of V_1^2 and V_2^2 can be explained by very weak radial mode amplitudes. For some He-burning stars, the dipole mixed modes extend up to the frequency range where $\ell = 3$ modes are located. When mixed modes are too close to the $\ell = 3$ modes, a fraction of the energy associated with mixed modes can be accidentally accounted for as part of the energy of $\ell = 3$ modes. Consequently, some V_1^2 values may be underestimated, and V_3^2 is inevitably overestimated. In the case of less evolved stars, Mosser et al. (2012) suggested that the scatter in V_1^2 could be related to the conditions that govern the coupling between g modes and p modes, giving rise to mixed modes. In the case of He-burning stars, this could explain the spread we obtain because these stars clearly exhibit mixed modes when $\Delta\nu \gtrsim 3.0$ μHz.

Although we note a large spread for the mode visibilities, it is clear that the non-radial mode visibilities increase when T_{eff} decreases both for RGB stars and He-burning stars, as expected from theoretical predictions (Ballot et al. 2011a). The only exception is the visibility of $\ell = 1$ modes in He-burning stars. This is due to the presence of several dipole modes with very low visibilities in the interval $T_{\mathrm{eff}} \in [4200, 4500]$ K, as reflected by the gap between the medians computed for RGB and He-burning stars. The mode visibilities in evolved stars similarly behave as in less evolved stars, except in the case of $\ell = 3$ modes, since we note that V_3^2 increases towards low T_{eff}, whereas Mosser et al. (2012) observed the opposite trend.

The visibility of dipole modes V_1^2 is represented as a function of $\nu_{\max}$ in the upper right panel of Fig. 7. We observe a clear difference between RGB stars and He-burning stars in the interval $\nu_{\max} \in [7, 20]$ μHz, with He-burning stars having weaker V_1^2 than their RGB counterparts. In parallel, we previously reported that Γ_1 is greater for He-burning stars in this interval (Fig. 5). It is certain that mixed modes perturb the extraction of the pure pressure dipole mode widths when $\Delta\nu \geq 1.5$ μHz, but the presence of low-visibility dipole modes reflects a shortage of dipole mode energy, which could be linked to a higher dipole mode damping, hence to a higher dipole mode width. We study this question in Sect. 5. Furthermore, we find that quadrupole modes have larger amplitudes in the H-burning phases than on the He-burning phases in the interval $\nu_{\max} \in [15, 35]$ μHz, as represented in the middle

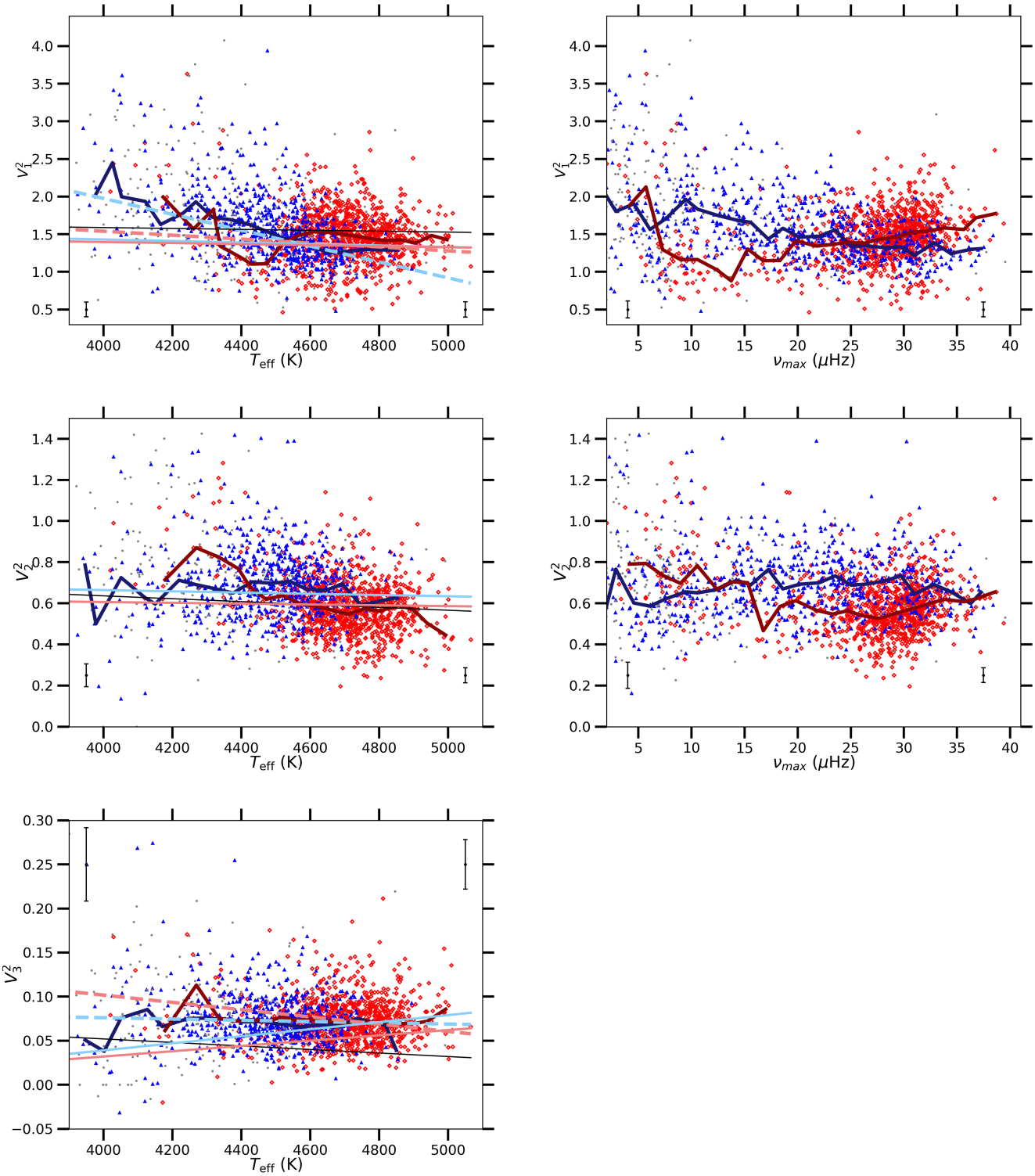

Fig. 7. *Upper panels*: visibility of the $\ell = 1$ modes as a function of $T_{\rm eff}$ in the *left panel* and of $\nu_{\rm max}$ in the *right panel*. The colours and symbols are the same as in Fig. 5. The error bars are computed in the same way as in Fig. 5. Similarly, error bars on the visibilities are given for both low $\nu_{\rm max}$ ($\nu_{\rm max} \leq 4.5\,\mu$Hz) and high $\nu_{\rm max}$ ($\nu_{\rm max} \geq 4.5\,\mu$Hz). The dashed lines are the fits presented in Table 4, in light blue for RGB stars and in light red for He-burning stars. The thin solid light blue and light red lines are the fits obtained for less evolved stars (Mosser et al. 2012) for RGB stars and for He-burning stars, respectively. The thin solid black line is the theoretical prediction (Ballot et al. 2011b). *Middle panels*: same labels as in the *upper panels*, but for the visibility of $\ell = 2$. *Lower left panel*: same labels as in the *upper left panel*, but for the visibility of $\ell = 3$ modes. The median values are computed in 50 K wide $T_{\rm eff}$ bins and in 1.5 μHz wide $\nu_{\rm max}$ bins.

right panel of Fig. 7. This difference may be linked to the mixed character of the quadrupole modes, which is more pronounced during the clump phase in the interval $\nu_{\rm max} \in [15, 35]\,\mu$Hz.

Nevertheless, we note a large spread of the dipole mode visibilities. The dipole mode visibilities of He-burning stars become comparable with those measured on the RGB at low $\Delta\nu$

Table 4. Fits of the mode visibilities presented in Fig. 7.

	Population	α	β (10^3 K^{-1})
V_1^2	Solar-like (*)	1.54	−0.06
	RGB	1.13 ± 0.02	−1.006 ± 0.012
	He-burning	1.33 ± 0.05	−0.261 ± 0.013
V_2^2	Solar-like (*)	0.58	−0.07
	RGB	0.66 ± 0.12	−0.148 ± 0.058
	He-burning	0.55 ± 0.01	−0.390 ± 0.006
V_3^2	Solar-like (*)	0.036	−0.02
	RGB	0.07 ± 0.02	−0.007 ± 0.005
	He-burning	0.07 ± 0.01	−0.041 ± 0.006

Notes. The mode visibilities are fitted by Eq. (17). (*)The expected coefficients are derived for solar-like oscillators, including RGB stars (Ballot et al. 2011a).

($\Delta\nu \leq 1.5\,\mu$Hz), when mixed modes disappear in the oscillation spectrum. The physical mechanisms that govern the coupling between the p-mode and the g-mode cavities might therefore be linked to the observation of low dipole mode visibilities. Even if the presence of depressed modes in advanced stages of stellar evolution is not clear, the simultaneous presence of low dipole mode visibilities and dipole mixed modes could help to identify the physical processes that cause the depressed modes in less evolved stages, which are still under debate (Fuller et al. 2015; Stello et al. 2016; Cantiello et al. 2016; Mosser et al. 2017b).

4.6. Comparison with other peak-bagging methods

The measurements inferred from our frequentist peak-bagging are compared with those[4] of the automated Bayesian peak-bagging algorithm AƁBA (Kallinger 2019), which uses the Bayesian nested sampling algorithm MULTINEST (Feroz et al. 2009). The average radial mode widths and bolometric amplitudes derived in the Bayesian approach were computed in the same way as in Sect. 3.4. The comparison is shown in Fig. 8.

The radial mode widths $\langle\Gamma_0\rangle$ derived with our frequentist peak-bagging are globally larger than those obtained with AƁBA by about 25%. This overestimate is frequency dependent because it increases for higher values of $\langle\Gamma_0\rangle$. Conversely, our radial bolometric mode amplitudes are weakly underestimated by about 5% with respect to the AƁBA values. Vrard et al. (2018) also reported that the radial mode width was overestimated by about 10% in the frequentist approach with respect to a Bayesian approach. Moreover, we approximated the background component by Eq. (2) around $\nu_{\rm max}$, while Kallinger (2019) modelled it with two super-Lorentzian functions (Kallinger et al. 2014). The background parametrisation has a non-negligible impact on the mode fitting, and stellar background bias is one of the main sources of frequency-dependent systematic errors in the measurements of mode widths and heights (Appourchaux et al. 2014). The way that the stellar background was modelled may therefore partly explain the differences we find between measurements.

5. Discussion

5.1. Stellar classification at advanced stages

Using a global measurement of the large separation $\Delta\nu$ and the oscillation pattern of red giants (Eq. (1)), we did not find any difference in the acoustic offset ε between RGB stars and He-burning stars. In parallel, we highlighted a difference in the signature of the helium second-ionisation zone between these stellar populations, especially in the modulation phase Φ. This phase difference locally affects the measurement of $\Delta\nu$ according to Eq. (7). A local change in $\Delta\nu$ can be linked to a local change in ε by differentiating Eq. (1), leading to

$$\delta\varepsilon = -(n+\varepsilon)\frac{\delta\Delta\nu}{\Delta\nu}\cdot \tag{18}$$

In the case of RGB and clump stars, Vrard et al. (2015) showed that the values of $\delta\varepsilon$ inferred from $\delta(\log\Delta\nu)$ that is related with the helium second-ionisation zone match the typical difference in ε between RGB and clump stars. They identified the glitch signatures as the physical basis of the stellar population identification method based on the acoustic offset ε. We extended the conclusions raised by Vrard et al. (2015) to more advanced evolutionary stages, that is, between RGB and He-burning stars, including clump and AGB stars. The difference in the local measurements of ε between RGB and AGB stars reported by Kallinger et al. (2012) is caused by the different glitch signature of the helium second-ionisation zone, especially for the modulation phase Φ.

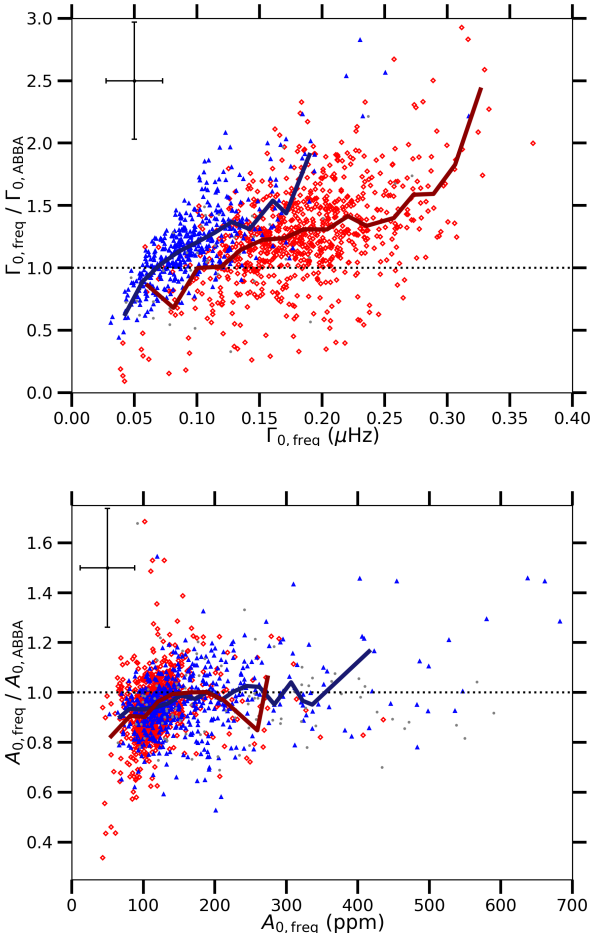

Fig. 8. *Top panel*: ratio of the average radial mode widths $\langle\Gamma_0\rangle$ obtained in this study and those obtained with a Bayesian method (Kallinger 2019). The median values are computed in 0.015 μHz wide $\Gamma_{0,\rm freq}$ bins. *Bottom panel*: same as in the *upper panel*, but for the average radial mode bolometric amplitude $\langle A_{0,\rm bol}\rangle$. The colours and symbols are the same as in Fig. 4. The median values are computed in 20 ppm $A_{0,\rm freq}$ bins. The dotted line represents the 1:1 agreement. Mean error bars are represented at the top of each panel.

[4] https://github.com/tkallinger/KeplerRGpeakbagging

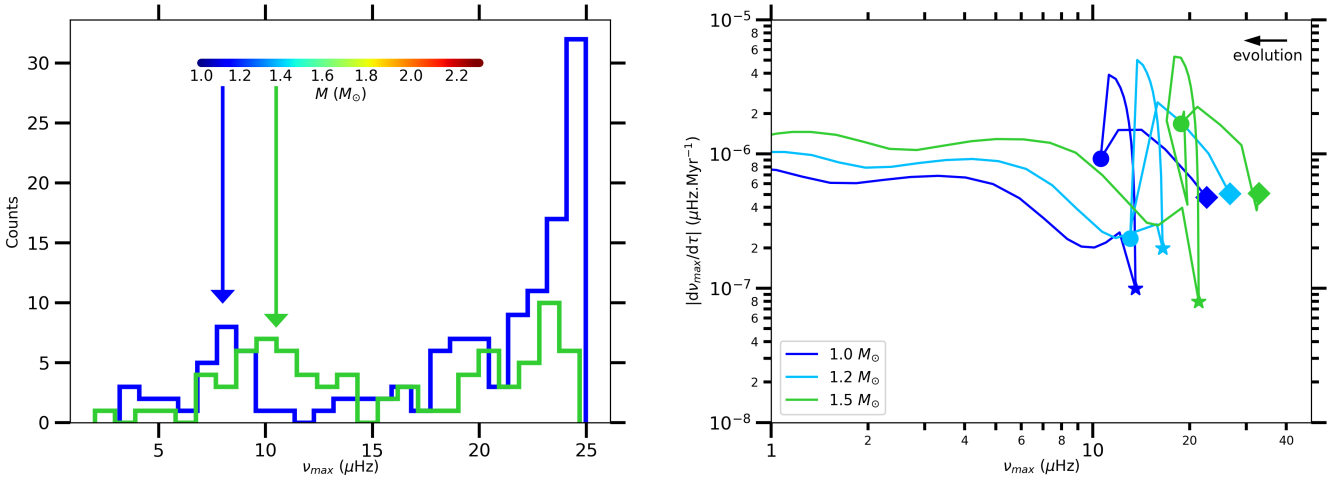

Fig. 9. *Left panel*: distribution of He-burning stars in terms of $\nu_{\max}$. In blue we show the number of low-mass He-burning stars ($M \leq 1.2\,M_\odot$), and in green we show the number of high-mass He-burning stars ($M \geq 1.2\,M_\odot$). The colour bar indicates the location in $\nu_{\max}$ where we expect the AGB bump for a given mass following Eq. (19) and adopting $T_{\rm eff} = 4800\,(\nu_{\max}/40.0)^{0.06}$ (Mosser et al. 2010). The blue and green arrows roughly indicate the location of the AGB bump for low-mass and high-mass stars, respectively, which is characterised by a local excess of stars. *Right panel*: Evolution speed $\mathrm{d}\nu_{\max}/\mathrm{d}\tau$, where τ is the stellar age, as a function of $\nu_{\max}$ for different stellar masses. The models computed with MESA start from the end of the clump phase, which is marked by a diamond. The start and the end of the AGB bump are marked by a circle and a star, respectively.

5.2. AGB bump

After leaving the clump phase where helium-burning takes place in the core, the star enters the AGB phase. During the early asymptotic giant branch (eAGB) and in the case of low-mass and intermediate-mass stars, two turning-backs of the evolutionary track can be seen in a narrow interval of luminosity, similarly to what can be seen during the RGB bump: This is the so-called AGB bump (AGBb). It is caused by the onset of the shell-He burning and was first identified in the Large Magellanic Cloud colour–magnitude diagram (Gallart 1998). The AGBb is observationally characterised by a local excess of stars in the luminosity distribution of stellar populations. Such an increment has been identified at $\log(L/L_\odot) \sim 2.2$ (Bossini et al. 2015). For a star of $M = 1.0\,M_\odot$ and $T_{\rm eff} = 4500\,\mathrm{K}$, this is equivalent to $\nu_{\max} \sim 8\,\mu\mathrm{Hz}$ according to the scaling relation (Kjeldsen & Bedding 1995)

$$\frac{\nu_{\max}}{\nu_{\max,\odot}} = \frac{M}{M_\odot}\left(\frac{L}{L_\odot}\right)^{-1}\left(\frac{T_{\rm eff}}{T_{\rm eff,\odot}}\right)^{7/2}. \tag{19}$$

Accordingly, we selected He-burning stars that left the clump phase (i.e., $\nu_{\max} \lesssim 25\,\mu\mathrm{Hz}$). Their distribution as a function of $\nu_{\max}$ is shown in Fig. 9. By tracking stellar evolution towards low $\nu_{\max}$, we note a depleted region followed by a peak for low mass-stars (at $\nu_{\max} \sim 8\,\mu\mathrm{Hz}$) and for high-mass stars (at $\nu_{\max} \sim 11\,\mu\mathrm{Hz}$). The depleted region could be explained by a difference in the evolution speed. We have computed models with the MESA code, using the 1M_pre_ms_to_wd test suite case to investigate the evolution speed between the end of the clump phase and the ascent on the AGB. The results are presented in the right panel of Fig. 9. For a given mass, we note that the evolution is faster between the end of the clump phase and the start of the AGBb than right after the AGBb since the variation of $\nu_{\max}$ with time is more important before the AGBb. The fast evolution speed before the AGBb results in a small statistical probability to meet low-mass stars in the interval $\nu_{\max} \in [8, 15]\,\mu\mathrm{Hz}$ and high-mass stars in the interval $\nu_{\max} \in [14, 18]\,\mu\mathrm{Hz}$. Investigating the AGBb in depth is part of our future work.

5.3. A strong damping during the eAGB phase?

Very low degree modes have similar eigenfunctions in the stellar outer layers, so that they are excited in similar conditions and show similar power spectral densities. However, as mentioned in Sect. 4.5, many He-burning stars have very low dipole mode visibilities below $\nu_{\max} = 20\,\mu\mathrm{Hz}$. In parallel, we found that most of the He-burning stars with low dipole mode visibilities have larger dipole mode widths. These low dipole mode visibilities reflect a lack of energy that could be linked to a strong dipole mode damping. Accordingly, we analysed the correlation between low visibility and large damping of dipole modes in detail by fitting the mixed-mode pattern during the early-AGB phase.

To this end, we considered single stars that have been identified as eAGB stars according to the classification method of Mosser et al. (2014). We selected five eAGB stars that have both low visibility dipole modes and a mixed-mode pattern clear enough to fit individual mixed modes and measure their widths (KIC 6847371, 11032660, 5461447, 10857623, and 6768042). We compared these widths to the pure-pressure dipole-mode width with Eq. (12). The results shown in Appendix B are unfortunately not unequivocal. Three of these eAGB stars present a strong dipole-mode damping, which is within the 1σ uncertainty for KIC 6847371 and KIC 5461447 and within the 2σ uncertainty for KIC 11032660. Nevertheless, this is not what we observe for KIC 10857623 and KIC 6768042. We face several constraints to reduce the uncertainties (or to fit other spectra), such as a low signal-to-noise ratio, a high ratio ζ of the mode inertia in the core and the total mode inertia (which leads to high uncertainties through Eq. (12)), limited frequency resolution, rotational splittings, and buoyancy glitch signature. We therefore tested another method to process these constraints together.

In a star in spherical equilibrium (thus non-rotating and without magnetic field), we expect the energy equipartition between modes of even and odd degrees to be satisfied. The lack of energy observed for dipole modes can be studied by comparing the energy of even-degree modes to that of odd-degree modes. To this end, we computed the ratio between the visibilities of odd

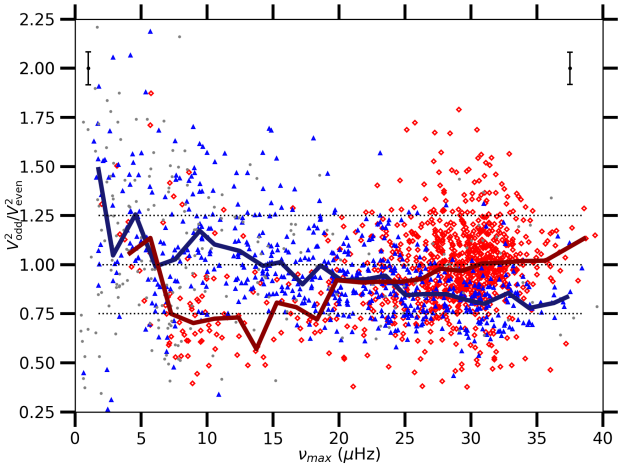

Fig. 10. Ratio of the mode visibilities of odd and even degrees as a function of $\nu_{\max}$. Same labels as in Fig. 4. For convenience, horizontal dashed black lines are plotted at specific values of 0.75, 1.00, and 1.25. The error bars are computed in the same way as in Fig. 3. The median values are computed in 1.5 μHz $\nu_{\max}$ bins.

and even degrees,

$$\frac{V_{\ell,\mathrm{odd}^2}}{V_{\ell,\mathrm{even}^2}} = \frac{V_1^2 + V_3^2}{1 + V_2^2}. \tag{20}$$

Modes that have a degree of same parity are close one to each other, as illustrated in Fig. 2. As a result, studying the global contribution of the energy then limits the impact of the energy leakage between individual degrees. We use the measurement of the odd/even visibility ratio as an indicator of the variation of the visibilities of $\ell = 1$ modes (Fig. 10). The variation is in fact dominated by the dipole modes for two reasons. On the one hand, the visibility of the octupole modes is very low for geometrical reasons. On the other hand, the quadrupole modes essentially behave as pure pressure modes for evolved giants, and always have a more pronounced pressure character than dipole modes. Below $\nu_{\max} = 20\,\mu$Hz, the energy equipartition seems to be invalid for He-burning stars. The dipole mode visibility is weaker than predicted by theory for He-burning stars. This lack of dipole mode energy is linked to a large dipole mode damping according to our study, and invalidates the energy equipartition between the different low-degree modes.

For RGB stars we can note that the visibility of $\ell = 1$ modes is globally lower at high $\nu_{\max}$ (see Fig. 7) and is especially lower than the expected value (1.54), which makes V_{ℓ,even^2} greater than V_{ℓ,odd^2} above $\nu_{\max} = 25\,\mu$Hz. This difference was first observed by Mosser et al. (2012) for less evolved red giants and can theoretically be explained by a difference of dipole mode damping (Dziembowski 2012). The radiative damping causes an energy loss at the envelope base that decreases when the star ascends the RGB (Dziembowski 2012, see Figs. 6 and 7). For a star with an initial mass $M_0 = 2\,M_\odot$, the energy loss by gravity wave emission at the envelope base is expected to cancel out when $\nu_{\max} \simeq 28\,\mu$Hz on the RGB. This is consistent with our observations because we note that V_1^2 increases with evolution below $\nu_{\max} \leq 28\,\mu$Hz (see the upper right panel of Fig. 7). On the RGB, radiative damping may explain the damping of energy of dipole modes observed at high $\nu_{\max}$. On the AGB, the dipole mode visibility evolves in the opposite direction. Given that the evanescent region between the g-mode and the p-mode cavities grows while the star ascends the AGB, mixed modes become less visible, and consequently, the only visible dipole modes are trapped in the envelope, as observed on the RGB. It might therefore be relevant to investigate the radiative damping in order to determine whether it can explain the damping of dipole modes on the AGB.

6. Conclusion

So far, we have performed the first exhaustive study of the seismic analysis of evolved giants, including ~2000 stars ascending the RGB towards the luminosity tip and He-burning stars both in the clump phase and ascending the AGB. We successfully characterised the oscillation spectrum of stars with $\Delta\nu \geq 0.5\,\mu$Hz and extracted the radial, dipole, and quadrupole mode parameters. By investigating the signature of the helium second-ionisation zone, we identified the physical origin on which the classification method based on ε and presented in Kallinger et al. (2012) relies at low $\Delta\nu$, that is, between RGB and AGB stars. We found that the amplitude and phase of the modulation introduced in the mode frequencies differ in RGB and in He-burning stars, that is, in core-He-burning and AGB stars. Work is in progress to investigate these differences with modelling. These differences affect local measurements of ε and enable classifying RGB and He-burning stars. Thus, we extended the work of Vrard et al. (2015), who drew the same conclusions, but considering RGB stars versus clump stars. As a consequence, we now have two methods relying on the same physical basis to decipher stellar evolution effects in evolved giant stars. On the one hand, we can adopt a local analysis where the signature of the helium second-ionisation zone is included in the acoustic offset ε. In this case, the possible values of ε reflect stellar evolution effects. On the other hand, we can adopt a global analysis where the values taken by ε are squeezed together and the stellar evolution effects in ε fade. However, in this case, we can still emphasise the stellar evolution effects by considering an additional term in Eq. (1) representing the signature of the helium second-ionisation zone on mode frequencies.

Having access to seismic diagnoses of evolved giants is promising for the understanding of stellar evolution, especially during the AGBb. The AGBb is expected to occur at $\log(L/L_\odot) \sim 2.2$ after the core He-burning phase. The investigation of the AGBb will be approached in a forthcoming paper. Furthermore, we highlighted that after the core He-burning phase, (i) the evolution is faster for low-mass stars, (ii) the dipole mode energy decreases, and (iii) the pressure-mode damping slowly becomes comparable to that measured on the RGB. This suggests that other physical processes need to be investigated in order to understand the mode damping and the observed visibilities as soon as core He-burning stops, that is, when the core becomes radiative again.

Acknowledgements. The authors are grateful to the anonymous referee who helped them in improving this paper with constructive suggestions. G.D. thanks P. Houdayer, R. Samadi and M. Vrard for fruitful discussions that helped improving this work. C.G. is supported by FCT – Fundação para a Ciência e a Tecnologia through national funds (PTDC/FIS-AST/30389/2017), by FEDER – Fundo Europeu de Desenvolvimento Regional through COMPETE2020 – Programa Operacional Competitividade e Internacionalização (POCI-01-0145-FEDER-030389), and by FCT/MCTES through national funds (PIDDAC) by these grants UIDB/04434/2020 and UIDP/04434/2020.

References

Aarslev, M. J., Houdek, G., Handberg, R., & Christensen-Dalsgaard, J. 2018, MNRAS, 478, 69

Appourchaux, T., Berthomieu, G., Michel, E., et al. 2006, in The CoRoT Mission Pre-Launch Status - Stellar Seismology and Planet Finding, eds. M. Fridlund, A. Baglin, J. Lochard, & L. Conroy, ESA SP, 1306, 377
Appourchaux, T., Chaplin, W. J., García, R. A., et al. 2012, A&A, 543, A54
Appourchaux, T., Antia, H. M., Benomar, O., et al. 2014, A&A, 566, A20
Baglin, A., Auvergne, M., Barge, P., et al. 2006, in The CoRoT Mission Pre-Launch Status - Stellar Seismology and Planet Finding, eds. M. Fridlund, A. Baglin, J. Lochard, & L. Conroy, ESA SP, 1306, 33
Ballot, J., Turck-Chiéze, S., & García, R. A. 2004, A&A, 423, 1051
Ballot, J., Barban, C., & van't Veer-Menneret, C. 2011a, A&A, 531, A124
Ballot, J., Gizon, L., Samadi, R., et al. 2011b, A&A, 530, A97
Baudin, F., Barban, C., Belkacem, K., et al. 2011, A&A, 529, A84
Beck, P. G., Bedding, T. R., Mosser, B., et al. 2011, Science, 332, 205
Bedding, T. R., Mosser, B., Huber, D., et al. 2011, Nature, 471, 608
Belkacem, K., Samadi, R., Goupil, M. J., Kupka, F., & Baudin, F. 2006, A&A, 460, 183
Belkacem, K., Dupret, M. A., Baudin, F., et al. 2012, A&A, 540, L7
Belkacem, K., Marques, J. P., Goupil, M. J., et al. 2015, A&A, 579, A31
Benomar, O., Belkacem, K., Bedding, T. R., et al. 2014, ApJ, 781, L29
Borucki, W. J., Koch, D., Basri, G., et al. 2010, Science, 327, 977
Bossini, D., Miglio, A., Salaris, M., et al. 2015, MNRAS, 453, 2290
Broomhall, A.-M., Miglio, A., Montalbán, J., et al. 2014, MNRAS, 440, 1828
Cantiello, M., Fuller, J., & Bildsten, L. 2016, ApJ, 824, 14
Christensen-Dalsgaard, J. 1988, in Advances in Helio- and Asteroseismology, eds. J. Christensen-Dalsgaard, & S. Frandsen, IAU Symp., 123, 295
Christensen-Dalsgaard, J., Monteiro, M. J. P. F. G., & Thompson, M. J. 1995, MNRAS, 276, 283
Christensen-Dalsgaard, J., Silva Aguirre, V., Elsworth, Y., & Hekker, S. 2014, MNRAS, 445, 3685
Corsaro, E., Stello, D., Huber, D., et al. 2012, ApJ, 757, 190
Corsaro, E., De Ridder, J., & García, R. A. 2015a, A&A, 578, A76
Corsaro, E., De Ridder, J., & García, R. A. 2015b, A&A, 579, A83
Deheuvels, S., Brandão, I., Silva Aguirre, V., et al. 2016, A&A, 589, A93
Dréau, G., Cunha, M. S., Vrard, M., & Avelino, P. P. 2020, MNRAS, 497, 1008
Dupret, M., Belkacem, K., Samadi, R., et al. 2009, A&A, 506, 57
Dziembowski, W. A. 2012, A&A, 539, A83
Elsworth, Y., Hekker, S., Basu, S., & Davies, G. R. 2017, MNRAS, 466, 3344
Feroz, F., Hobson, M. P., & Bridges, M. 2009, MNRAS, 398, 1601
Fuller, J., Cantiello, M., Stello, D., Garcia, R. A., & Bildsten, L. 2015, Science, 6259, 423
Gallart, C. 1998, ApJ, 495, L43
Gilliland, R. L., Brown, T. M., Christensen-Dalsgaard, J., et al. 2010, PASP, 122, 131
Goldreich, P., & Keeley, D. A. 1977, ApJ, 212, 243
Gough, D. O. 1986, Highlights Astron., 7, 283
Gough, D. O. 1990, in Comments on Helioseismic Inference, eds. Y. Osaki, & H. Shibahashi, 367, 283
Gough, D. O., & Thompson, M. J.1988, in Advances in Helio- and Asteroseismology, eds. J. Christensen-Dalsgaard, & S. Frandsen, IAU Symp., 123, 175
Grosjean, M., Dupret, M.-A., Belkacem, K., et al. 2014, A&A, 572, A11
Handberg, R., Brogaard, K., Miglio, A., et al. 2017, MNRAS, 472, 979
Houdek, G., & Gough, D. O. 2007, MNRAS, 375, 861
Houdek, G., Trampedach, R., Aarslev, M. J., & Christensen-Dalsgaard, J. 2017, MNRAS, 464, L124
Howell, S. B., Sobeck, C., Haas, M., et al. 2014, PASP, 126, 398
Huber, D., Bedding, T. R., Stello, D., et al. 2010, ApJ, 723, 1607
Huber, D., Bedding, T. R., Stello, D., et al. 2011, ApJ, 743, 143
Kallinger, T. 2019, ArXiv e-prints [arXiv:1906.09428]
Kallinger, T., Weiss, W. W., Barban, C., et al. 2010, A&A, 509, A77
Kallinger, T., Hekker, S., Mosser, B., et al. 2012, A&A, 541, A51
Kallinger, T., De Ridder, J., Hekker, S., et al. 2014, A&A, 570, A41
Kjeldsen, H., & Bedding, T. R. 1995, A&A, 293, 87
Lund, M. N., Silva Aguirre, V., Davies, G. R., et al. 2017, ApJ, 835, 172
Mazumdar, A., Michel, E., Antia, H. M., & Deheuvels, S. 2012, A&A, 540, A31
Mazumdar, A., Monteiro, M. J. P. F. G., Ballot, J., et al. 2014, ApJ, 782, 18
Michel, E., Baglin, A., Auvergne, M., et al. 2008, Science, 322, 558
Miglio, A., Montalbán, J., Carrier, F., et al. 2010, A&A, 520, L6
Montalbán, J., Miglio, A., Noels, A., Scuflaire, R., & Ventura, P. 2010, ApJ, 721, L182
Montalbán, J., Miglio, A., Noels, A., et al. 2012, in Red Giants as Probes of the Structure and Evolution of the Milky Way, eds. A. Miglio, J. Montalban, & A. Noels, Astrophysics and Space Science Proceedings, 23
Monteiro, M. J. P. F. G., Christensen-Dalsgaard, J., & Thompson, M. J. 1994, A&A, 283, 247
Monteiro, M. J. P. F. G., & Thompson, M. J. 2005, MNRAS, 361, 1187
Mosser, B., Belkacem, K., Goupil, M., et al. 2010, A&A, 517, A22
Mosser, B., Belkacem, K., Goupil, M., et al. 2011, A&A, 525, L9
Mosser, B., Elsworth, Y., Hekker, S., et al. 2012, A&A, 537, A30
Mosser, B., Dziembowski, W. A., Belkacem, K., et al. 2013a, A&A, 559, A137
Mosser, B., Michel, E., Belkacem, K., et al. 2013b, A&A, 550, A126
Mosser, B., Benomar, O., Belkacem, K., et al. 2014, A&A, 572, L5
Mosser, B., Pinçon, C., Belkacem, K., Takata, M., & Vrard, M. 2017a, A&A, 600, A1
Mosser, B., Belkacem, K., Pinçon, C., et al. 2017b, A&A, 598, A62
Mosser, B., Gehan, C., Belkacem, K., et al. 2018, A&A, 618, A109
Mosser, B., Michel, E., Samadi, R., et al. 2019, A&A, 622, A76
Paxton, B., Bildsten, L., Dotter, A., et al. 2011, ApJS, 192, 3
Paxton, B., Cantiello, M., Arras, P., et al. 2013, ApJS, 208, 4
Paxton, B., Marchant, P., Schwab, J., et al. 2015, ApJS, 220, 15
Paxton, B., Schwab, J., Bauer, E. B., et al. 2018, ApJS, 234, 34
Paxton, B., Smolec, R., Schwab, J., et al. 2019, ApJS, 243, 10
Pinsonneault, M. H., Elsworth, Y., Epstein, C., et al. 2014, ApJ, 215, 19
Pinsonneault, M. H., Elsworth, Y. P., Tayar, J., et al. 2018, ApJS, 239, 32
Ricker, G. R., Winn, J. N., Vanderspek, R., et al. 2015, J. Astron. Telesc. Instrum. Syst., 1
Roxburgh, I. W., & Vorontsov, S. V. 2000, MNRAS, 317, 141
Roxburgh, I. W., & Vorontsov, S. V. 2003, A&A, 411, 215
Soszyński, I., & Wood, P. R. 2013, ApJ, 763, 103
Stello, D., Huber, D., Kallinger, T., et al. 2011, ApJ, 737, L10
Stello, D., Compton, D. L., Bedding, T. R., et al. 2014, ApJ, 788, L10
Stello, D., Cantiello, M., Fuller, J., et al. 2016, Nature, 529, 364
Tassoul, M. 1980, ApJS, 43, 469
Toutain, T., & Appourchaux, T. 1994, A&A, 289, 649
Verma, K., Faria, J. P., Antia, H. M., et al. 2014, ApJ, 790, 138
Vorontsov, S. V. 1988, in Advances in Helio- and Asteroseismology, eds. J. Christensen-Dalsgaard, & S. Frandsen, IAU Symp., 123, 151
Vrard, M., Mosser, B., Barban, C., et al. 2015, A&A, 579, A84
Vrard, M., Mosser, B., & Samadi, R. 2016, A&A, 588, A87
Vrard, M., Kallinger, T., Mosser, B., et al. 2018, A&A, 616, A94
Wood, P. R., Alcock, C., Allsman, R. A., et al. 1999, in Asymptotic Giant Branch Stars, eds. T. Le Bertre, A. Lebre, & C. Waelkens, IAU Symp., 191, 151
Wray, J. J., Eyer, L., & Paczyński, B. 2004, MNRAS, 349, 1059
Yu, J., Bedding, T. R., Stello, D., et al. 2020, MNRAS, 493, 1388

Appendix A: Location of the helium second-ionisation zone

The modulation period $\mathcal{G}$ defined in Eq. (7) can be linked to the location of the helium second-ionisation zone. The structural variations caused by the helium glitch can be seen in the first adiabatic exponent profile, defined by

$$\gamma_1 = \left(\frac{\mathrm{d}\log P}{\mathrm{d}\log \rho}\right)_s, \tag{A.1}$$

where P and ρ are the pressure and the density, respectively, and the subscript s indicates that the derivative is taken at constant entropy. It is commonly assumed that the signature of the helium glitch arises from the dip in the γ_1 profile caused by the helium second-ionisation zone (Monteiro & Thompson 2005; Houdek & Gough 2007). In stellar models, we therefore took the acoustic radius at this local minimum as the location of the helium second-ionisation zone, for instance, t_{HeII}, defined by

$$t_{\mathrm{HeII}} = \int_0^{r_{\mathrm{HeII}}} \frac{\mathrm{d}r}{c_{\mathrm{s}}(r)}. \tag{A.2}$$

In this expression, r_{HeII} is the distance of the local minimum from the centre of the star, and c_{s} is the adiabatic sound speed. The helium glitch introduces an oscillatory component in the eigenfrequency pattern of the star, which is proportional to (Gough & Thompson 1988; Vorontsov et al. 1988; Gough 1990)

$$\delta\nu \propto \sin\left(4\pi\tau_{\mathrm{HeII}}\nu_{\mathrm{n},\ell} + \Phi_{\mathrm{HeII}}\right), \tag{A.3}$$

where ϕ_{HeII} is the phase of the glitch modulation and τ_{HeII} is the acoustic depth of the helium glitch relative to the surface of the star of radius R_*,

$$\tau_{\mathrm{HeII}} = \int_{r_{\mathrm{HeII}}}^{R_*} \frac{\mathrm{d}r}{c_{\mathrm{s}}(r)}. \tag{A.4}$$

The modulation introduced in the local large separation (Eq. (6)) can also be expressed in the form of Eq. (A.3) with a phase shift compared to Φ_{HeII}. Consequently, the modulation period $\mathcal{G}$ and the acoustic depth τ_{HeII} can be linked according to

$$\tau_{\mathrm{HeII}} = \frac{1}{2\mathcal{G}\Delta\nu}. \tag{A.5}$$

Furthermore, the total acoustic length of the stellar cavity is defined by

$$T_0 = \frac{1}{2\Delta\nu}, \tag{A.6}$$

so that we can convert the acoustic depth τ_{HeII} into the acoustic radius t_{HeII} with the relation $t_{\mathrm{HeII}} = T_0 - \tau_{\mathrm{HeII}}$. This transformation allows us to reduce the biases that result from the unknown exact position of the stellar surface (Christensen-Dalsgaard et al. 1995; Ballot et al. 2004). Finally, the modulation period $\mathcal{G}$ can be inferred from the location of the helium second-ionisation zone with the expression

$$\mathcal{G} = \frac{1}{1 - t_{\mathrm{HeII}}/T_0}. \tag{A.7}$$

Appendix B: Mixed-mode measurements in the eAGB phase

We selected individual stars identified as eAGB stars according to the classification method of Mosser et al. (2014) and fitted their mixed dipole modes near ν_{max} to extract an estimate of the mode widths. The mixed dipole mode widths were then used to infer the pure-pressure dipole mode widths according to Eq. (12).

Results are shown in Figs. B.1 and B.2, and in the fifth column of Table B.2. Their average values are presented in Table B.1.

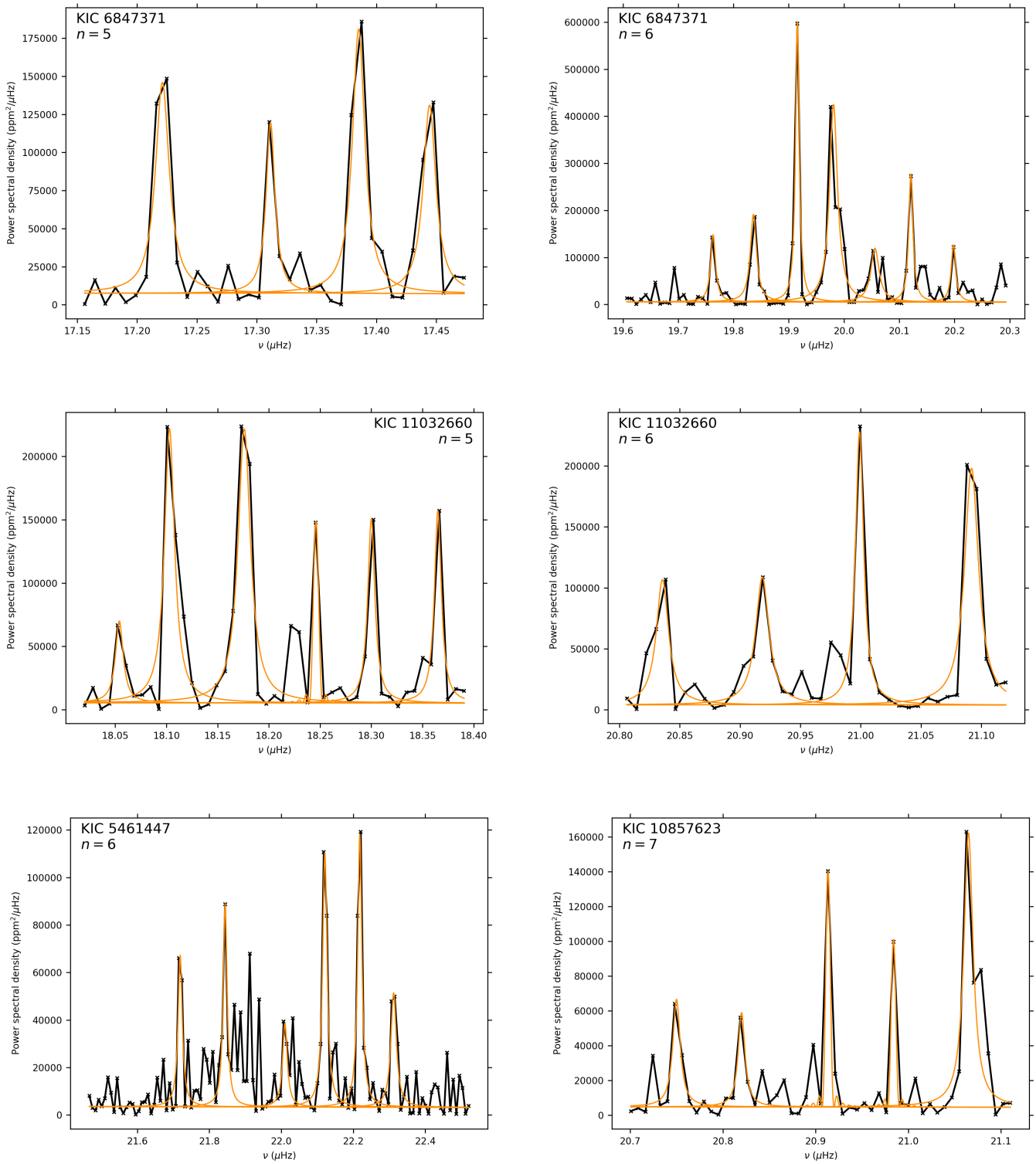

Fig. B.1. Mixed-mode pattern for KIC 6847371 ($V_1^2 = 1.23 \pm 0.10$) at radial order $n = 5$ (*top left*) and at $n = 6$ (*top right*), for KIC 11032660 ($V_1^2 = 1.14 \pm 0.10$) at $n = 5$ (*middle left*) and at $n = 6$ (*middle right*), for KIC 5461447 ($V_1^2 = 1.15 \pm 0.15$) at $n = 6$ (*bottom left*), and for KIC 10857623 ($V_1^2 = 1.01 \pm 0.12$) at $n = 7$ (*bottom right*). The stars are marked by stars in the lower right panel of Fig. 5 except for KIC 10857623 because we were unable to reliably extract its dipole mode widths following the method described in Sect. 3.4. Resolved modes are plotted by individual Lorentzians in blue, with the parameters given in Table B.2, while the unresolved modes at $\nu = 18.246\,\mu$Hz (KIC 11032660), $\nu = 20.913\,\mu$Hz, and $\nu = 20.984\,\mu$Hz (KIC 10857623) are plotted by sinc^2 functions.

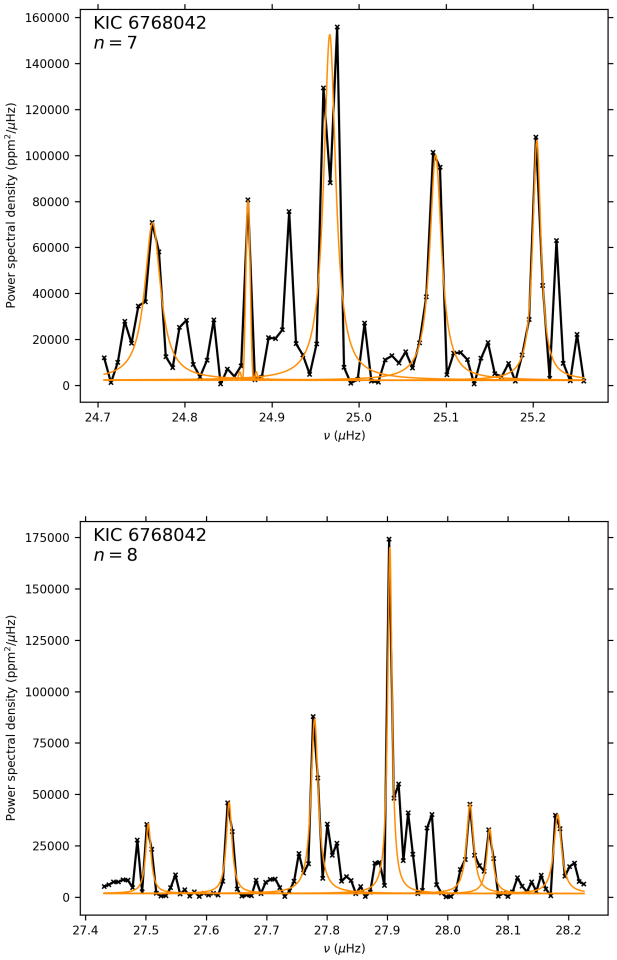

Fig. B.2. Same labels as in Fig. B.1 for KIC 6768042 ($V_1^2 = 1.38 \pm 0.13$) at radial order $n = 7$ (*top*) and at $n = 8$ (*bottom*). The mode located at $\nu = 24.873\,\mu$Hz is unresolved and has been fitted by a sinc^2 function.

Table B.1. Pressure dipole mode widths compared to the radial mode widths.

KIC	$\Delta\nu$ (μHz)	$\nu_{\max}$ (μHz)	$\langle\Gamma^{\rm p}_{n,1}\rangle$ (μHz)	$\langle\Gamma_0\rangle$ (μHz)
6847371	2.69	19.84	0.189 ± 0.070	0.128 ± 0.032
11032660	2.83	19.66	0.142 ± 0.051	0.121 ± 0.026
5461447	2.97	21.76	0.163 ± 0.051	0.088 ± 0.017
10857623	2.49	16.11	0.083 ± 0.029	0.121 ± 0.023
6768042	2.96	23.37	0.138 ± 0.069	0.150 ± 0.024

Notes. The average value of the dipole mode widths is computed as the arithmetic mean of the pressure mode widths $\Gamma^{\rm p}_{n,1}$ presented in Table B.2.

Table B.2. Estimates of the ratio ζ between the mode inertia in the core and the total mode inertia, the mixed dipole mode widths $\Gamma_{n,1}$, heights $H_{n,1}$ and the pressure dipole mode widths $\Gamma^{\rm p}_{n,1}$ for the stars KIC 6847371 at radial order $n = 5$ and 6, KIC 11032660 at $n = 5$ and 6, KIC 5461447 at $n = 6$, KIC 10857623 at $n = 7$, and KIC 6768042 at $n = 7$ and 8.

KIC	ν (μHz)	ζ	$\Gamma_{n,1}$ (nHz)	$\Gamma^{\rm p}_{n,1}$ (μHz)	$H_{n,1}$ (ppm$^2\,\mu$Hz^{-1})
6847371					
	17.221	0.912	14.0	0.173	148 042
	17.312	0.933	8.9	0.134	119 977
	17.385	0.951	12.6	0.256	185 682
	17.444	0.961	12.8	0.330	132 426
	19.763	0.917	10.8	0.130	142 715
	19.836	0.900	13.5	0.135	185 918
	19.916	0.895	8.1	0.077	595 653
	19.981	0.908	17.5	0.190	419 721
	20.056	0.929	18.0	0.254	114 214
	20.121	0.944	9.1	0.163	272 377
	20.198	0.958	9.8	0.233	121 588
11032660					
	18.054	0.901	9.1	0.092	66 802
	18.103	0.906	11.9	0.126	223 603
	18.176	0.922	14.7	0.189	223 744
	18.246	0.940	8.1 (*)	0.135	147 870
	18.300	0.956	8.5	0.191	149 941
	18.365	0.967	8.2	0.246	156 975
	20.836	0.892	12.3	0.113	106 265
	20.918	0.872	13.5	0.105	108 367
	20.999	0.881	8.2	0.069	231 565
	21.092	0.911	14.1	0.158	200 770
5461447					
	21.715	0.947	13.9	0.263	65 961
	21.844	0.902	12.9	0.131	88 352
	22.007	0.835	15.5	0.094	39 418
	22.121	0.879	14.9	0.123	110 662
	22.218	0.925	13.7	0.183	118 859
	22.315	0.954	18.4	0.398	49 835
10857623					
	20.745	0.924	9.7	0.127	63 988
	20.820	0.891	8.8	0.081	56 137
	20.913	0.848	7.8 (*)	0.051	140 292
	20.984	0.851	7.8 (*)	0.052	99 708
	21.065	0.882	12.1	0.103	163 003
6768042					
	24.763	0.839	22.1	0.138	70 787
	24.873	0.832	7.9 (*)	0.047	80 691
	24.967	0.878	16.6	0.136	155 491
	25.088	0.928	16.3	0.225	101 482
	25.204	0.953	11.5	0.243	107 916
	27.504	0.927	10.5	0.143	35 161
	27.639	0.863	11.3	0.082	45 895
	27.780	0.790	14.5	0.069	87 860
	27.904	0.820	8.7	0.048	174 133
	28.037	0.899	14.0	0.138	45 005
	28.070	0.909	11.7	0.129	32 445
	28.182	0.940	15.3	0.254	39 866

Notes. The different estimates of $\Gamma^{\rm p}_{6,1}$ are inferred from Eq. (12). For these particular stars, the term ζ is not derived from scaling relations as described in Sect. 3, but is extracted from the database of Mosser et al. (2018). (*)The measurement of the modes located at $\nu = 18.246\,\mu$Hz (KIC 11032660), $\nu = 20.913\,\mu$Hz and $\nu = 20.984\,\mu$Hz (KIC 10857623), and $\nu = 24.873\,\mu$Hz (KIC 6768042) are limited by the resolution.

Appendix C: Table available at the CDS with results of pressure mode-fitting

The approach described in Sect. 3 allowed us to thoroughly characterise the pressure modes of 2103 evolved red giants observed by *Kepler* with $\Delta\nu \leq 4.0\,\mu$Hz. A selection of the seismic parameters, obtained in Sect. 4, is shown in Table C for 25 stars. The complete set of global seismic parameters of the whole sample of stars is available at the CDS. The stellar mass and effective temperature were extracted from the APOKASC catalogue (Pinsonneault et al. 2014). For some stars, the stellar mass and the effective temperature are not listed in the APOKASC catalogue. It concerns roughly 5% of our sample, with half of this fraction being associated with very low $\Delta\nu$-values (i.e., $\Delta\nu \leq 0.5\,\mu$Hz). For these stars, we nevertheless obtained rough estimates of the stellar mass and effective temperature using semi-empirical and empirical scaling relations implying both the frequency at the maximum oscillation power $\nu_{\rm max}$ and large frequency separation $\Delta\nu$ (Kjeldsen & Bedding 1995; Kallinger et al. 2010; Mosser et al. 2010).

Table C.1. Seismic parameters.

KIC	$\Delta\nu$ (μHz)	M ($M_\odot$)	$T_{\rm eff}$ (K)	ε	$\delta\varepsilon$	d_{01}	δd_{01}	d_{02}	δd_{02}	d_{03}	δd_{03}
01026309	1.944	2.58	4514	0.795	0.011	−0.043	0.017	0.126	0.007	0.391	0.016
01160789	3.524	0.86	4724	0.950	0.014	−0.053	0.021	0.144	0.011	0.389	0.022
01162746	3.804	0.85	4762	0.956	0.016	−0.093	0.023	0.173	0.012	0.343	0.026
01163359	2.644	1.67	4560	0.855	0.012	−0.013	0.017	0.143	0.008	0.342	0.017
01432587	1.082	0.85	4295	0.635	0.011	−0.042	0.017	0.171	0.009	0.378	0.017
01435573	3.587	0.90	4698	0.945	0.017	−0.091	0.023	0.181	0.013	0.358	0.022
01572780	2.693	0.97	4738	0.854	0.013	−0.054	0.022	0.171	0.012	0.392	0.023
01719297	1.215	1.29	4255	0.664	0.010	−0.083	0.016	0.157	0.009	0.362	0.017
01720425	3.667	1.09	4798	0.945	0.015	−0.044	0.021	0.169	0.011	0.382	0.022
01725552	1.221	1.53	4344	0.654	0.010	−0.090	0.020	0.146	0.010	0.362	0.018
01725732	0.707	0.87	4100	0.565	0.010	−0.148	0.014	0.182	0.008	0.396	0.014
01726211	3.720	1.32	4862	0.963	0.016	−0.010	0.024	0.162	0.014	0.338	0.022
01865595	1.815	1.34	4386	0.755	0.011	−0.044	0.018	0.128	0.009	0.406	0.019
01868101	3.785	1.28	4633	0.966	0.015	−0.030	0.017	0.149	0.009	0.376	0.021
01872517	3.299	1.14	4543	0.915	0.015	−0.043	0.019	0.148	0.011	0.356	0.020
01995358	3.238	1.17	4824	0.930	0.015	−0.029	0.020	0.155	0.011	0.429	0.020
02011582	3.863	2.15	4684	0.943	0.015	−0.060	0.020	0.130	0.010	0.328	0.020
02017541	1.457	1.33	4242	0.690	0.011	−0.055	0.018	0.155	0.009	0.364	0.018
02018392	3.789	1.52	4669	0.943	0.015	−0.035	0.021	0.136	0.009	0.316	0.019
02141932	3.013	1.37	4429	0.894	0.014	−0.017	0.019	0.146	0.009	0.426	0.021
02142095	3.694	1.17	4839	0.932	0.015	−0.046	0.019	0.151	0.009	0.391	0.019
02156178	3.824	0.95	4853	0.932	0.018	−0.047	0.030	0.188	0.016	0.391	0.031
02157059	3.002	1.27	4424	0.874	0.013	−0.056	0.017	0.161	0.009	0.353	0.017
02157901	3.795	1.05	4760	0.933	0.017	−0.049	0.027	0.205	0.017	0.374	0.031
02164874	1.779	1.45	4447	0.765	0.011	−0.029	0.019	0.142	0.009	0.359	0.018

Notes. The columns correspond to, from left to right, the KIC number, the large separation $\Delta\nu$, the stellar mass M, the effective temperature $T_{\rm eff}$, the acoustic offset ε, the uncertainty on ε, the reduced small separations $d_{0\ell}$ and the uncertainties on $d_{0\ell}$. The list of the full data set, including the glitch parameters, the mean mode widths, amplitudes, visibilities and the evolutionary stages, is available at the CDS.

Chapter 8

Analysis of the seismic parameters at evolved stages on the RGB and AGB

The seismic parameters derived from the oscillation spectrum allow a fruitful diagnostic of the stellar interiors. They offer unique information on the stellar core and envelope properties, which is complementary to that carried by photometric and spectrometric parameters that probe the superficial layers of stars. With the 1470-day time series of *Kepler*, we are able to accurately extract the seismic parameters of stars with $\Delta\nu$ down to 0.5 μHz. Tracking the structure changes between RGB and AGB stars is now within reach by studying the global behaviour of the seismic parameters in a large sample of stars. In the attached paper 1, we analyse the seismic parameters that are obtained with the data fitting technique presented in Chapter 7. With a set of thousands of high-luminosity red giants observed by *Kepler* including RGB, clump and AGB stars, we follow the dependence of the stellar parameters on stellar evolution. This in turn helps us to identify the physical basis on which the classification of RGB and AGB stars relies on. Hereafter, we mainly exploit the p-mode frequencies obtained with ADIPLS by applying the method described in Sect. 6.3.1. This gives us the opportunity to compare the seismic parameters derived from observations to those from stellar models as well as to extend the analysis up to the luminosity-tip of the RGB ($\Delta\nu = 0.06\,\mu$Hz).

The dependence of the observed seismic parameters on the mass and evolution stage is analysed in Sect. 4.1, 4.2 and 5.1 of the attached article 1. We suggest the reader to refer to them for a detailed discussion. Here, we focus on stellar models, studying the implications of these observations on the evolution of the stellar structure, including on the structure differences between RGB and AGB stars.

8.1 Seismic inference with the asymptotic pattern of red giants

8.1.1 Evolution of the structure of the oscillation spectrum

The pressure-mode frequencies computed with ADIPLS can be used to follow the evolution of the structure of the oscillation spectrum. This concerns the frequency spacing $\Delta\nu$ between modes of consecutive radial order n and same degree ℓ, but also the dimensionless small frequency spacing $d_{0\ell}$ between non-radial modes and their neighbouring radial mode. In stellar models, we compute the large frequency separation as the gradient of the radial-mode frequencies with respect to the radial order n

$$\Delta\nu = \frac{\mathrm{d}\nu_{n,0}}{\mathrm{d}n}. \tag{8.1}$$

The local acoustic offset $\varepsilon(n)$, which corresponds to the frequency spacing at radial order n between the radial mode at frequency $\nu_{n,0}$ and $n\Delta\nu$, is computed as

$$\varepsilon(n) = \frac{\nu_{n,0} - n\Delta\nu}{\Delta\nu}. \tag{8.2}$$

The local small frequency separations in fraction of $\Delta\nu$ are obtained by combining Eq. 3.30 with Eq. 3.32. Then, the global seismic parameters ε and $d_{0\ell}$ are taken as the average local value of the 7 modes for which the frequencies are closest to the maximum oscillation power, which is representative of the

number of observed modes per degree ℓ around $\Delta\nu \sim 4\,\mu$Hz. The dependence of these seismic parameters on stellar evolution is shown in Fig. 8.1. Overall, we see that the acoustic offset ε decreases as the star evolves on its respective branch, meaning that the frequency of the radial mode of order n comes closer to $n\Delta\nu$. In absolute value, the dimensionless small separations d_{01} and d_{02} increase as $\Delta\nu$ decreases, implying that the non-radial modes get closer to the neighbouring radial mode as the star gradually evolves. This behaviour coincides with the observations of evolved stars presented in Sect. 4.1 of the publication 1. Moreover, the evolutionary effects can easily be highlighted when the seismic parameters are averaged over few radial orders. Indeed, we notice that the difference between RGB and clump/AGB in the ε values is more important when the three central radial modes closest to the maximum oscillation power are selected. This point is discussed in further details in Sect. 8.1.2.

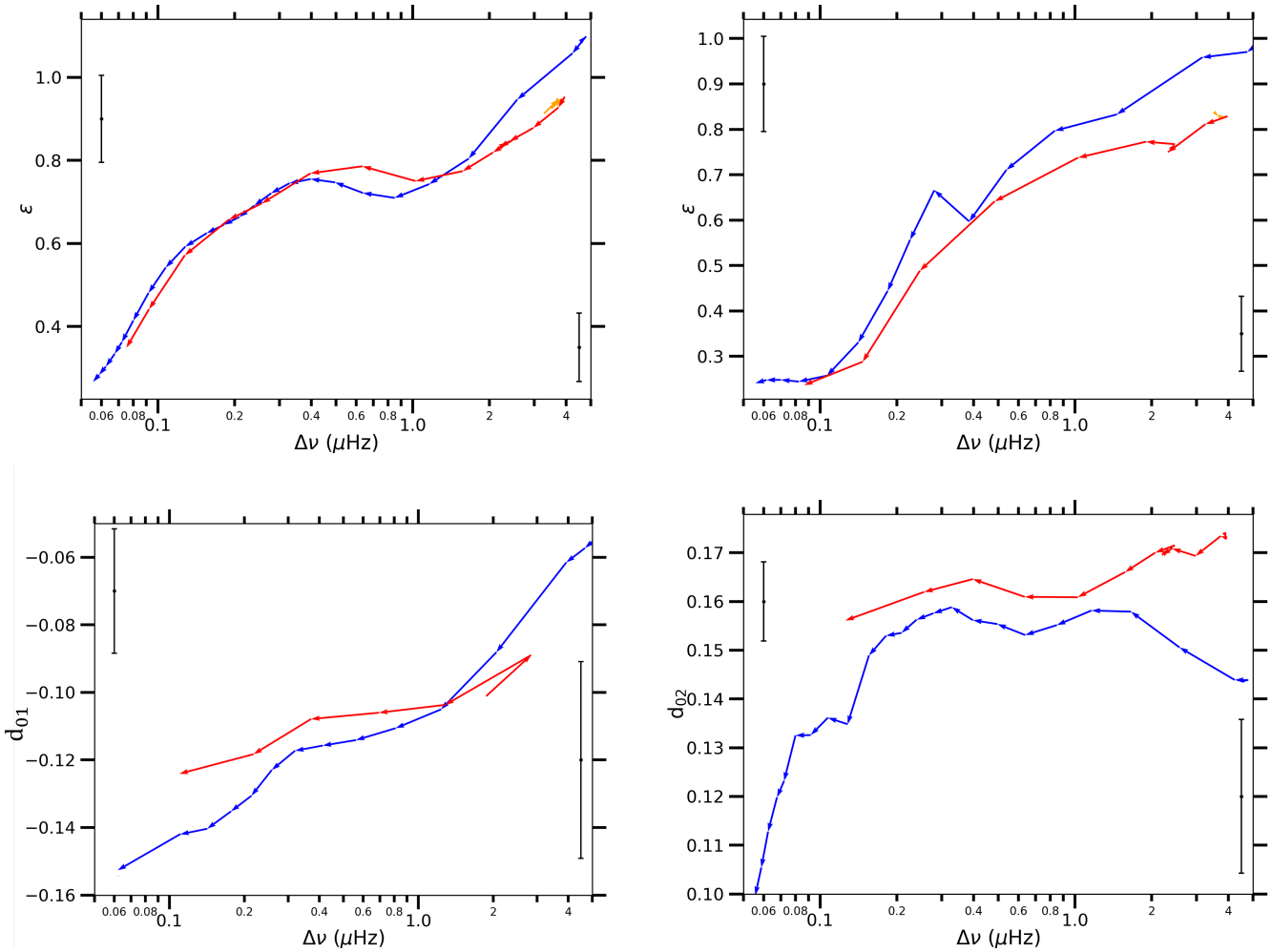

FIGURE 8.1: Synthetic seismic parameters extracted from the p-mode frequencies computed with ADIPLS, as described in Chapter 6. The MESA models are computed with the reference input physics listed in Table 10.1. **Upper left:** variation of the acoustic offset ε as a function of $\Delta\nu$, with an emphasis on the evolutionary stage. RGB, clump and AGB are colour-coded in blue, orange and red, respectively. The arrows indicate the direction of evolution between two consecutive models. We have used the seven $\ell = 0$ modes closest to the maximum oscillation power to compute ε. **Upper right:** same as upper left, but the acoustic offset ε has been computed with the average of the three $\ell = 0$ modes closest to the maximum oscillation power. **Lower panel:** the dimensionless small separations $d_{0\ell}$ as a function of $\Delta\nu$, computed with the seven radial order n closest to $n_{\max}$. Mean error bars estimated for $\Delta\nu$ below or above 1 μHz are represented on each panel.

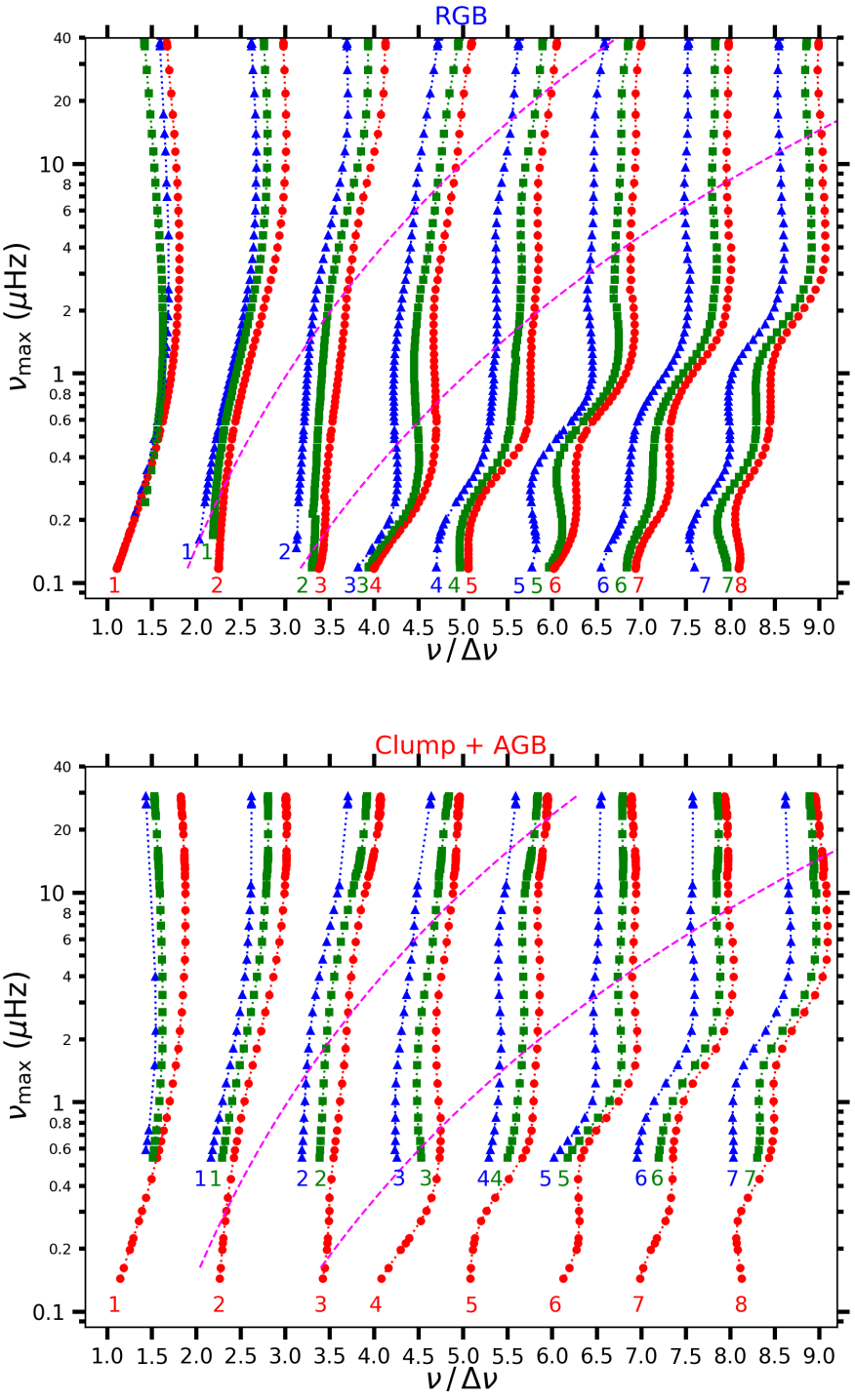

FIGURE 8.2: Model frequencies from radial order $n = 1$ up to $n = 8$ computed with ADIPLS for a $1\,M_\odot$ track at solar metallicity. The MESA models are computed with the reference input physics listed in Table 10.1. Radial, dipole and quadrupole modes are shown in red circles, blue triangles and green squares, respectively. The non-radial modes ($\ell = 1, 2$) are computed by setting the squared Brunt-Väisälä frequency $N^2_{BV} = 0$ in the core, as described in Sect. 6.3.1. Modes of the same degree ℓ and same radial order n are connected by dotted lines, in red for $\ell = 0$, in blue for $\ell = 1$, and in green for $\ell = 2$. The radial orders are indicated at the lower edge of each branch, with the same colour code as the mode degree ℓ. The magenta dashed lines delimit the typical frequency range that can be observed on the oscillation spectrum. They correspond to the location of 75% and 125% of ν_{max}. **Top**: on the RGB. **Bottom**: during the He-burning phase. Note that with the method "$N^2_{BV} = 0$ in the core", the code could not find out the $\ell = 1$ modes during the clump phase and the early-AGB ($\nu_{max} \in [10, 25]\,\mu$Hz). Because the code had troubles to return the non-radial modes for high-luminosity AGB models, we stopped the computation of non-radial modes below $\nu_{max} \leq 0.5\,\mu$Hz after the He-core burning phase.

As presented in the models performed by Stello et al. (2014), the evolution of these frequency separations can also be observed in the radial and non-radial ridges (Fig. 8.2). Along a specific ridge at fixed radial order n, we can see that as the star evolves (equivalently, $\nu_{\max}$ decreases), the $\ell = 1$ and $\ell = 2$ ridges get closer to the neighbouring $\ell = 0$ ridge. Moreover, non-radial ridges are even closer to the neighbouring radial ridge at low radial order n. Since the frequency range of the maximum oscillation power changes with $\nu_{\max}$, low radial orders are more easily observable at low $\nu_{\max}$. These ridge behaviours explain why the observed frequency spacings between non-radial modes and the neighbouring radial mode shrink while stars gradually evolve.

The small frequency separations are sensitive to the distance between the inner turning point of the cavity and the base of the convective zone (Montalbán et al., 2010). Indeed, the convective envelope represents a large fraction of the stellar radius during the RGB, so the turning point of the dipole mode cavity falls in the convective envelope. When He-core burning starts, the radiative core grows and the extent of the convective envelope shrinks. In this case, the inner turning point of dipole modes falls in the radiative zone. We can define the acoustic radius as

$$t(r') = \int_0^{r'} \frac{\mathrm{d}r}{c}, \tag{8.3}$$

which corresponds to the time a sound wave spends to travel from the centre up to a distance r' from the centre, where c is the sound speed. By noting the acoustic radius of the inner turning point of the $\ell = 1$ mode cavity t_{tp1} and that of the base of the convective zone t_{BCZ}, t_{tp1} is larger than t_{BCZ} in the H-shell burning phase, and lower than t_{BCZ} in the He-core burning phase. This leads to different values of the dimensionless frequency spacing d_{01}, as illustrated in Fig. 8.3. The scatter of d_{01} is small on the RGB but becomes more important once the inner turning point of the $\ell = 1$ modes reaches the base of the convective zone during the He-core burning phase. This explains the dispersion of the dimensionless small separations $d_{0\ell}$ that are presented in Fig. 3 of the article 1.

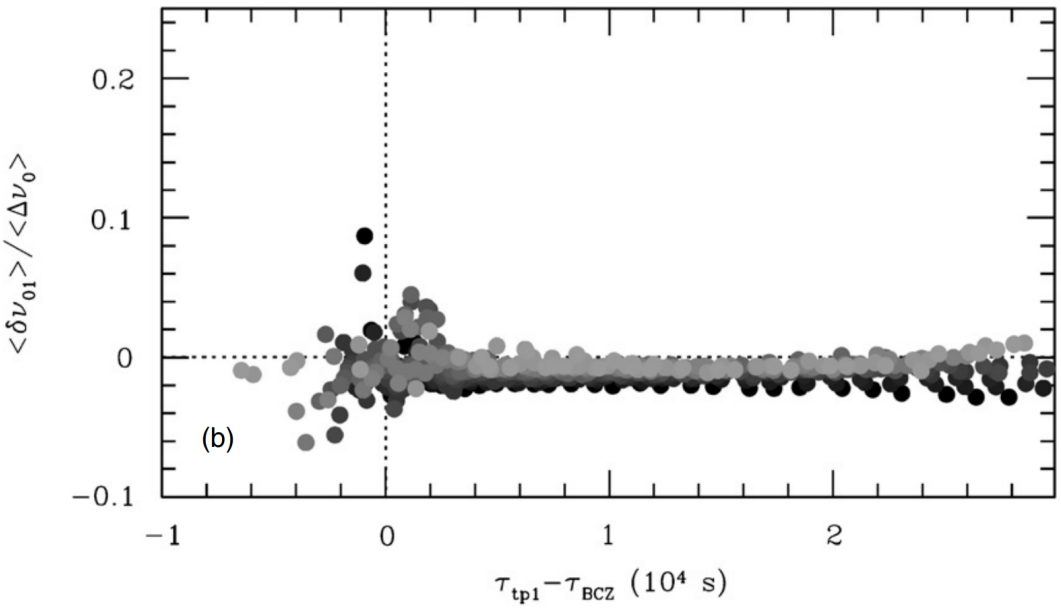

FIGURE 8.3: Dimensionless small frequency separation d_{01} as a function of the distance in acoustic radius between the inner turning point of the $\ell = 1$ cavity t_{tp1} and the base of the convective zone t_{BCZ}. Negative values of $t_{\mathrm{tp1}} - t_{\mathrm{BCZ}}$ mean that the inner turning point is located in the radiative zone while positive values indicate that the inner turning point is in the convective envelope. Several low-mass RGB and He-core burning models with $Z = 0.02$, $Y = 0.278$, $\alpha_{\mathrm{MLT}} = 1.9$, between 0.7 and 2.3 $M_\odot$, are shown with colour-coded points. The lighter the colour, the higher the mass. Credit: Montalbán et al. (2010)

8.1.2 Global analysis versus local analysis

In Fig. 3 of the paper 1, we see that the seismic parameters follow a clear trend with $\Delta\nu$, especially the acoustic offset ε. The ε estimates distribute closely around the scaling relation, without strong differences between RGB and He-burning stars. In parallel, Kallinger et al. (2012) found clear differences in the ε estimates of RGB and He-burning stars as depicted by Fig. 5.3, allowing a classification between those stars. Nevertheless, the way Kallinger et al. (2012) extract these seismic parameters is based on a different approach. In their work, they individually fit the observed stellar modes and compute the seismic parameters with the individual frequencies near the maximum oscillation power. Their approach is based on local measurements of the seismic parameters, which contain the signature of sharp variations regions of the sound speed. As discussed in Sect. 5.2, this signature substantially shifts the seismic parameters, which differs between H-shell burning and He-core burning stars, making a classification method possible (Vrard et al., 2015).
Conversely, the technique presented in Sect. 7.3 that we use to identify the degree ℓ and radial order n of all observed modes is based on a global analysis of the oscillation spectrum. In that sense, the whole template oscillation spectrum is parameterised by a global $\Delta\nu$ and is adjusted to reach the maximum cross-correlation with the observed oscillation spectrum. Then, the seismic parameters describing the asymptotic pattern of red giants Eq. 3.20 are inferred by taking the optimised global measurement of $\Delta\nu$ as the reference large frequency separation. In this global analysis, since these seismic parameters are averaged over the whole frequency range of observable modes, the signature of localised regions with sharp variations in the sound speed (see Chapter 4) is smoothed out. Indeed, the signature of those regions is a frequency-dependent modulation, for which the average over a large frequency range is close to zero (see Eq. 7.13). In this case, the evolutionary effects fade and both RGB and clump stars have the same seismic parameters. As a result, this reduces the spread of the seismic parameters around the asymptotic values. For instance, the difference between RGB and clump/AGB stars computed with ADIPLS is more significant when the acoustic offset ε is averaged over three radial orders instead of seven radial orders (top panels of Fig. 8.1). In this scenario, the signature of those sharp variation regions is not included in the seismic parameters and an additional term must be accounted for in the asymptotic pattern of red giants, as described in Eq. 4.6.

To sum up, there are two ways of analysing the oscillation spectrum (Vrard et al., 2015):

- On the one hand, a local analysis can be adopted, where seismic parameters are inferred from a few number of individual frequencies. In this scenario, the seismic parameters deviate a bit from the asymptotic pattern as they contain signatures of sharp variation regions, which differ depending on the evolutionary stage.
- On the other hand, a global analysis can be followed, where seismic parameters are inferred from the whole set of observable modes. In this scenario, the signature of sharp variation regions fades and seismic parameters closely follow the asymptotic pattern of red giants. However, an additional term (see Eq. 4.6) reflecting the glitch signature must be accounted for in the asymptotic pattern so that the oscillation spectrum of red giants is accurately characterised.

8.2 The signature of the helium second-ionisation zone in high-luminosity red giants

8.2.1 Characterising the helium second-ionisation zone

As presented in Chapter 4, sharp variation regions of sound speed, such as the HeII zone, leave a signature in the stellar modes that probe these regions. This signature depends on the characteristics of the HeII zone and is expected to be more important as the sound speed profile gets steeper. In our work, we fit the variation caused by He second ionisation in the first adiabatic exponent Γ_1 profile (related with the sound speed profile following Eq. 4.1) by a Gaussian, as represented in case **(c)** of Fig. 4.3. Then, we characterise the HeII zone by three parameters, which are the amplitude $H_{\rm HeII}$ of the Γ_1 variation,

its acoustic radius $t_{\rm HeII}$, and the width $\Delta_{\rm HeII}$ over which the Γ_1 variation caused by HeII extends. We extract these parameters by fitting the Γ_1 profile all around the HeII zone with

$$\mathcal{L}_{\rm HeII}(t) = -H_{\rm HeII}\, e^{-\frac{(t-t_{\rm HeII})^2}{2\Delta^2_{\rm HeII}}} + a_0 + a_1 t, \tag{8.4}$$

where t is the acoustic radius, a_0 and a_1 are the coefficients of the polynomial that reproduces the baseline of the Γ_1 profile (see Fig. 8.4). In the previous equation, we keep the parameter $H_{\rm HeII}$ positive, so we consider a negative Gaussian function. We notify that both $t_{\rm HeII}$ and $\Delta_{\rm HeII}$ are dimensionless parameters, they are normalised by the total acoustic length of the stellar cavity $T_0 = 1/(2\Delta\nu)$. In the fitting process, both $H_{\rm HeII}$, $t_{\rm HeII}$, and $\Delta_{\rm HeII}$ are left as free parameters, but the polynomial coefficients a_0 and a_1 are fixed by connecting the local maximum after the dip caused by HeII with the Γ_1 profile before the dip. By fitting the Γ_1 dip, we are able to track the evolution of the HeII characteristics from the RGB up to the AGB, especially to investigate how they relate to the parameters of the glitch modulation introduced in mode frequencies.

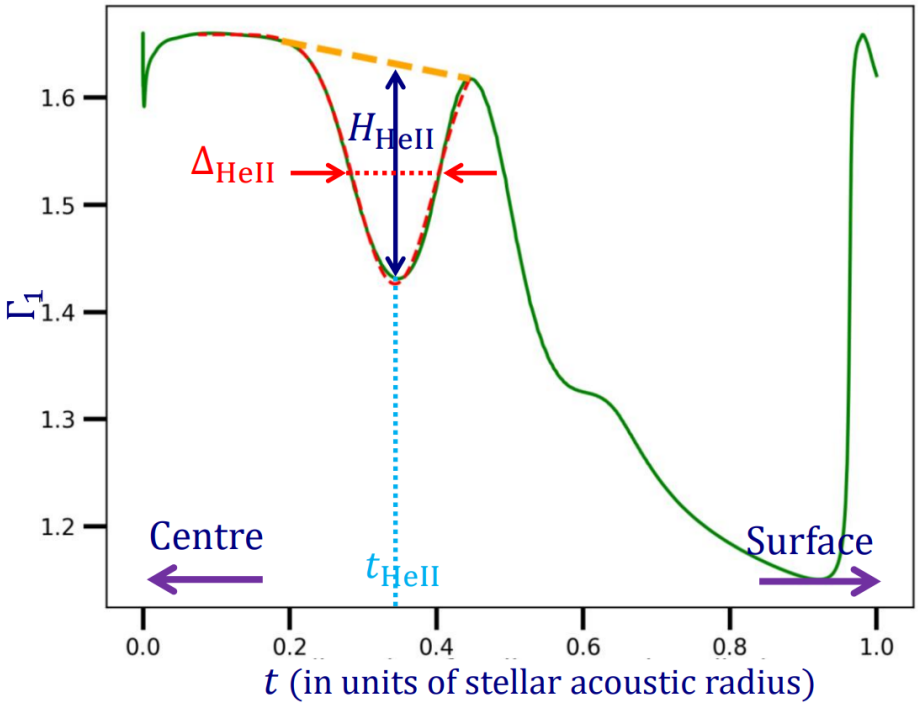

FIGURE 8.4: Γ_1 profile of a $1\,M_\odot$ model computed with MESA. The parameters of the Γ_1 variations ($H_{\rm HeII}$, $t_{\rm HeII}$, and $\Delta_{\rm HeII}$), are directly shown in the figure. The green solid line is the Γ_1 profile throughout the star. The thick orange dashed line indicates the baseline that connects the local maximum after the dip caused by HeII with the Γ_1 profile before the dip. The thin red dashed line gives the fit of the Γ_1 profile with Eq. 8.4 around the dip.

8.2.2 Inferring the glitch parameters from stellar models

After computing the mode frequencies with the oscillation code ADIPLS, we are able to extract the parameters of the modulation induced by the HeII zone in mode frequencies. The procedure we follow to derive the glitch parameters with the ADIPLS mode frequencies is similar to that used with the observed mode frequencies presented in Sect. 7.5. Nevertheless, there are two main differences in the fitting method:

- The set of the ADIPLS mode frequencies is not based on the range of frequencies over which modes are intense enough to be detected (*i.e.* $\nu \in [\nu_{\rm max} - 0.75\,\delta\nu_{\rm env}, \nu_{\rm max} + 0.75\,\delta\nu_{\rm env}]$, where $\delta\nu_{\rm env}$ is the full-width at half maximum of the power excess envelope, see Sect. 7.1.2). Instead, we directly select a fixed number of modes during the whole evolutionary track from RGB to

AGB. We select the 7 radial orders that are the closest to the maximum oscillation power, *i.e.* 7 modes per degree $\ell = 0$, 1, 2 for which the frequencies are closest to $\nu_{\max}$. This number of modes is obviously representative of the number of observed modes for the least evolved stars in our sample (near $\Delta\nu \sim 4\,\mu$Hz) but overestimated for the most evolved RGB and AGB stars, for which the number of observed modes can drop to 3. We choose to select a fixed number of modes to keep the oscillatory component of the glitch signature clear, then optimise the extraction of the glitch modulation, regardless the evolutionary status.

- The most difficult parameter to converge is the glitch period because the optimisation function that we need to minimise have several local extrema as a function of the modulation period. So the fitting process largely depends on the initial values given to the glitch parameters. In parallel, the range of all possible values taken by the glitch parameters is large throughout the evolution from the RGB up to the AGB. In order to mitigate the bias induced by the choice of initial conditions, the optimised glitch parameters at step $N-1$ are given as initial guesses for the glitch parameters at step N. This allows us to extract glitch parameters that smoothly evolve between consecutive stellar models.

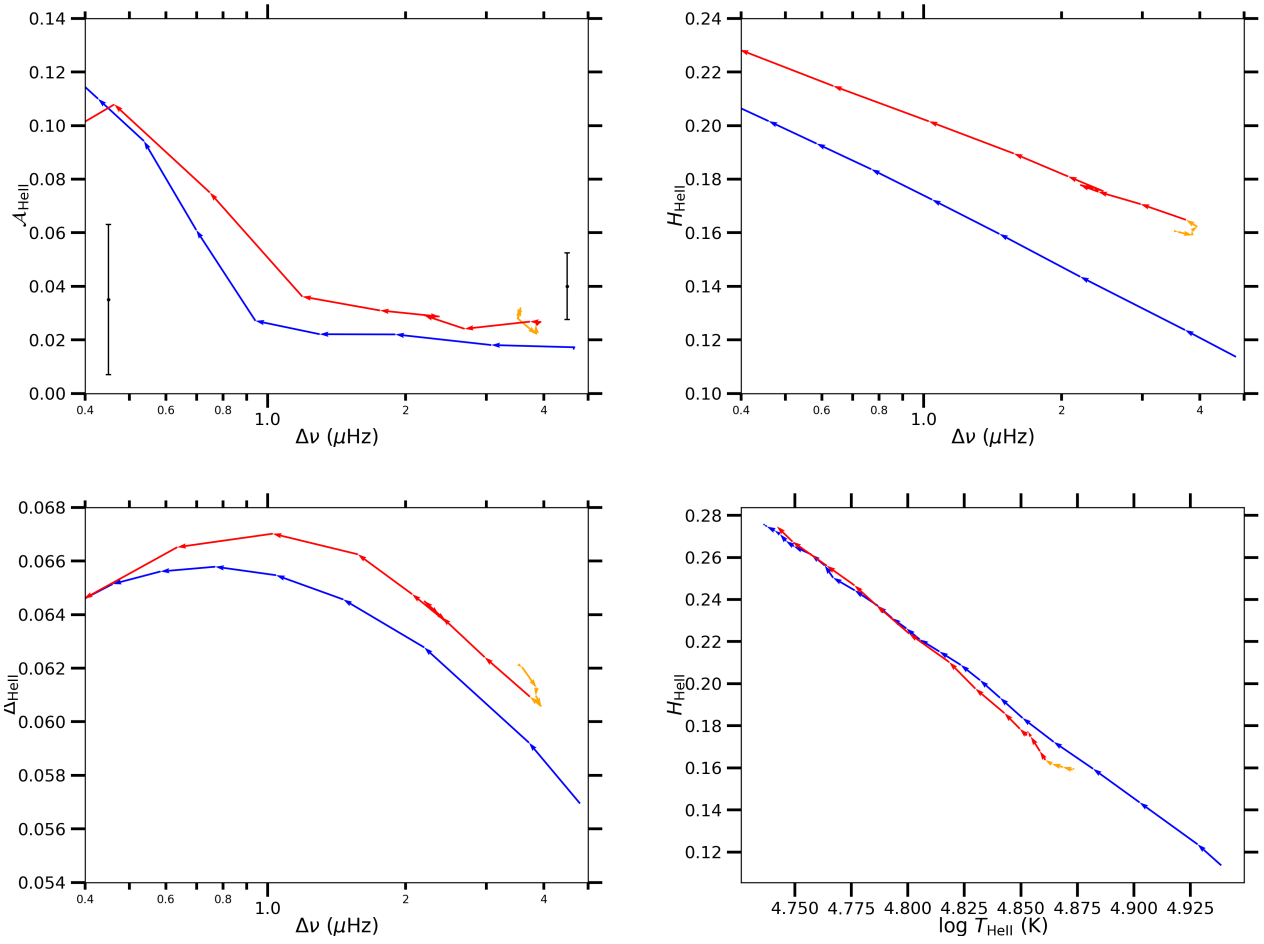

FIGURE 8.5: Synthetic glitch and structure parameters computed with MESA and ADIPLS. The MESA models are computed with the reference input physics listed in Table 10.1. **Top left**: dependence of the glitch amplitude $\mathcal{A}_{\rm HeII}$ on stellar evolution. Mean error bars estimated for $\Delta\nu$ below or above 1 μHz are represented. **Top right**: same as top left but for the amplitude $H_{\rm HeII}$ of the Γ_1 variation. **Bottom left**: same as top left but for the width $\Delta_{\rm HeII}$ of the HeII zone. **Bottom right**: dependence of the amplitude $H_{\rm HeII}$ on the average temperature $\log T_{\rm HeII}$ in the HeII zone. The arrows indicate the direction of the evolution, while blue, orange and red solid lines refer to the H-shell, He-core and He-shell burning phases, respectively. The evolution has been computed with a mass 1 $M_\odot$ and solar metallicity.

This way, we can investigate the dependence of the glitch parameters on stellar parameters, in order to evaluate their potential to provide structure changes with stellar evolution. Particularly, we study the correlation between glitch parameters and the HeII zone characteristics.

8.2.3 Understanding the strength of the glitch signature

The evolution of the modulation amplitude of the glitch signature is shown in Fig. 8.5. We notice that the amplitude of the modulation is higher during the He-burning phase than on the RGB, by an average factor of 40%. These ADIPLS results support the analysis of the modulation amplitude measured in high-luminosity red giants (see Fig. 4 of paper 1). This difference between RGB and clump/AGB can be attributed to the strength of the Γ_1 variation at the HeII zone. Indeed, the depth $H_{\rm HeII}$ and the width of the Γ_1 dip are larger on the clump/AGB than on the RGB, which demonstrates that the signature of the HeII zone in mode frequencies is stronger once He burning occurs. In parallel, we identify a clear correlation between the amplitude of the Γ_1 variation and the average temperature at the HeII zone. As depicted in Fig. 8.5, we highlight an unequivocal relation between those two parameters, where the depth $H_{\rm HeII}$ linearly depends on $\log T_{\rm HeII}$ whatever the evolutionary stage. The difference of glitch amplitude reported between He-burning and H-shell burning phases is related to a difference of temperature at the HeII zone, reflecting a difference of physical conditions and degree of ionisation in the envelope. This confirms and expands the conclusions raised for less evolved red giants presented in Sect. 4.3.

8.2.4 Deciphering the glitch period

The link between the location of the HeII zone $t_{\rm HeII}$ and the modulation period $\mathcal{G}_{\rm HeII}$

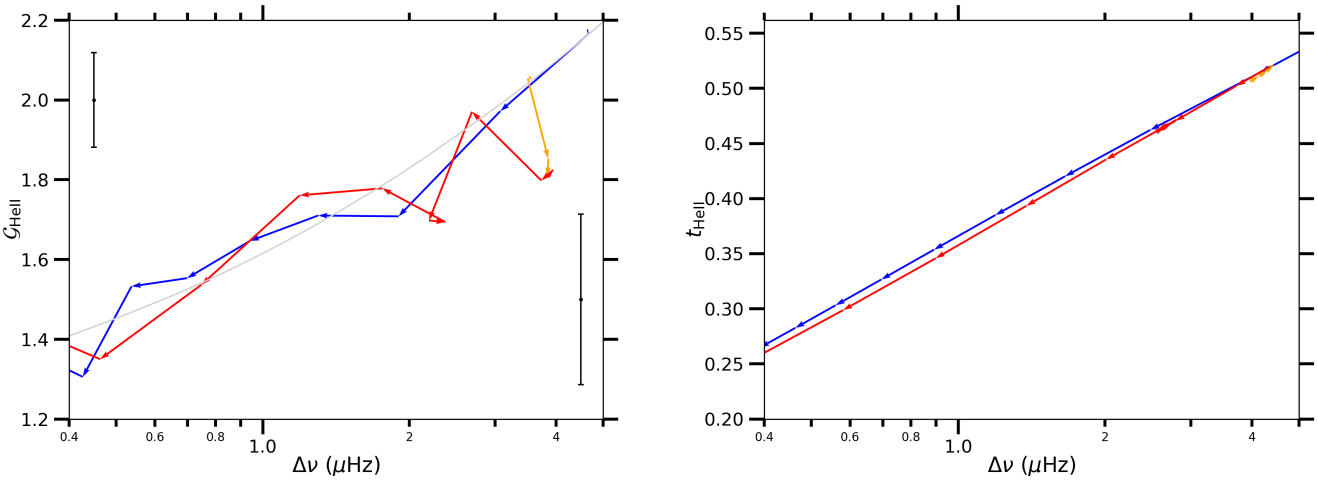

FIGURE 8.6: Synthetic glitch period and acoustic radius of HeII computed with the stellar codes MESA and ADIPLS for the same evolutionary sequences as in Fig. 8.5. **Left**: dependence of the modulation period $\mathcal{G}_{\rm HeII}$ on stellar evolution. Mean error bars estimated for $\Delta\nu$ below or above 1 μHz are exhibited. The additional light grey solid line is the modulation period expected from the location of the HeII zone $t_{\rm HeII}$, which is computed according to Eq. 8.7. **Right**: same as left panel, but for the acoustic radius $t_{\rm HeII}$ of the HeII zone.

The modulation period of the glitch signature computed with ADIPLS decreases when stars evolve on their branches (equivalently when $\Delta\nu$ decreases, see Fig. 8.6). Moreover, the modulation period does not depend on the evolutionary stage. This reproduces the evolution of the glitch period that is measured with the *Kepler* high-luminosity stars, as reported in Sect. 4.2 of the article 1, but with a stronger dependence on $\Delta\nu$. In parallel, the HeII zone sinks into the interior as $\Delta\nu$ decreases both on the RGB and AGB, meaning that the temperature required to ionise helium is reached deeper in the interior. This is not mere coincidence, since the glitch period is directly related to the HeII location. Indeed, the

oscillatory component in the mode frequency is given by (Gough and Thompson, 1988; Vorontsov, 1988; Gough, 1990)

$$\delta\nu^{\rm gl} \propto \sin\left(4\pi\tau_{\rm HeII}\nu_{n,\ell} + \Phi_{\rm HeII}\right), \tag{8.5}$$

where $\tau_{\rm HeII}$ is the acoustic depth of the HeII zone. The glitch modulation introduced in the local large separation $\delta\Delta\nu^{\rm gl}_{n,\ell}$ can be expressed in the form of Eq. 8.5, but with a phase shift relatively to $\Phi_{\rm HeII}$. Then, the modulation period $\mathcal{G}_{\rm HeII}$ can be related to $\tau_{\rm HeII}$ according to (see Eqs. 4.7, 4.11)

$$\tau_{\rm HeII} = \frac{1}{2\mathcal{G}_{\rm HeII}\Delta\nu}. \tag{8.6}$$

By definition, the acoustic radius can be inferred from the acoustic depth with $t_{\rm HeII} = T_0 - \tau_{\rm HeII}$, where $T_0 = 1/(2\Delta\nu)$ is the total acoustic length of the stellar cavity. Then, the modulation period $\mathcal{G}_{\rm HeII}$ can be inferred from the acoustic radius $t_{\rm HeII}$ of the HeII zone by

$$\mathcal{G}_{\rm HeII} = \frac{1}{1 - t_{\rm HeII}/T_0}. \tag{8.7}$$

In this way, we can derive an estimate of the modulation period with an independent method that does not make use of the mode frequencies. In Fig. 8.6, we superimpose the modulation period inferred from Eq. 8.7 with that inferred from fitting the glitch modulation induced in the local large separation $\delta\Delta\nu^{\rm gl}_{n,\ell}$ by Eq. 7.13. We obtain identical values with both methods, which confirms that the glitch signature is properly extracted. This similarity supports that the mode frequencies computed by ADIPLS are sufficiently accurate to study the glitch signature.

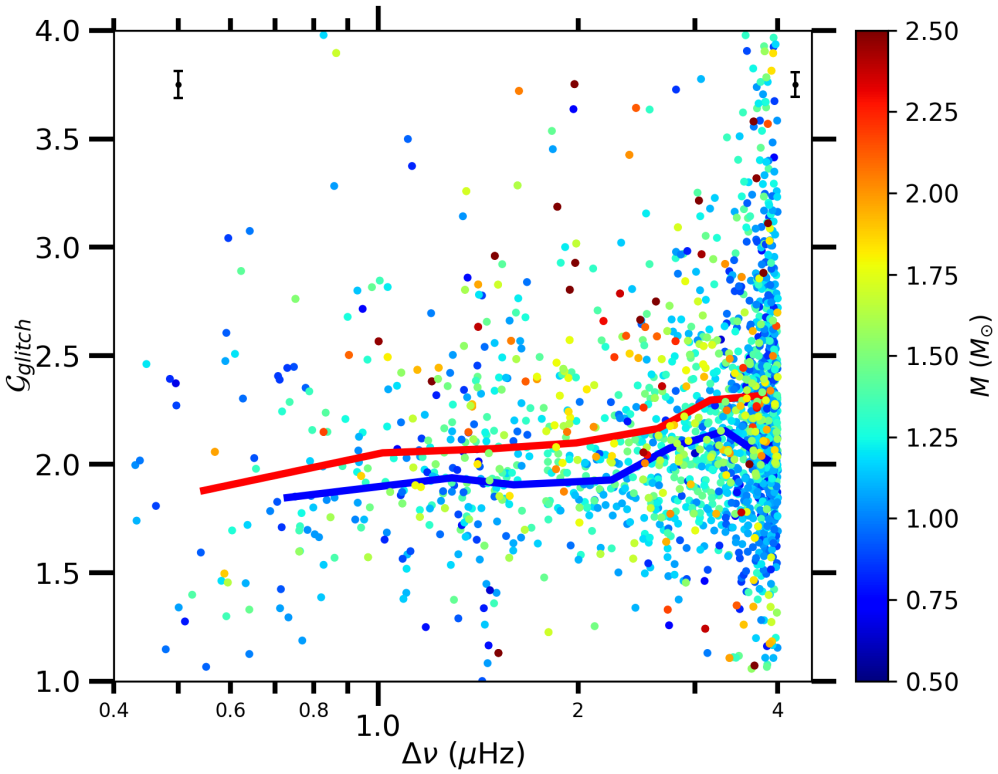

FIGURE 8.7: Period of the glitch modulation from *Kepler* data as a function of $\Delta\nu$, where the stellar mass is colour-coded. Mean error bars estimated for $\Delta\nu$ below or above 1 μHz are represented on each panel. The thick solid lines are the median values in 0.5 μHz $\Delta\nu$ bins, shown in blue for low-mass stars ($M \leq 1.2\,M_\odot$) and in red for high-mass stars ($M \geq 1.2\,M_\odot$).

The dependence of the glitch period on stellar parameters

As reported in Sect. 4.2 of the publication 1, the glitch parameters are sensitive to stellar parameters, especially the mass. In Fig. 8.7, we present in more details the dependence of the modulation period on the stellar mass obtained with the sample of *Kepler* evolved stars. We notice that low-mass stars preferably have a lower modulation period than their high-mass counterparts, implying that the HeII zone is located deeper in the interior for low-mass stars. This behaviour is accentuated by stellar models (top panels of Fig. 8.8), where we see that both $\mathcal{G}_{\rm HeII}$ and $t_{\rm HeII}$ are larger at fixed $\Delta\nu$ for high-mass stars. The medians presented in Fig. 8.7 are computed regardless the evolutionary stage since in Sect. 4.2 of the article 1, we did not find any correlation between the modulation period and the evolutionary stage.

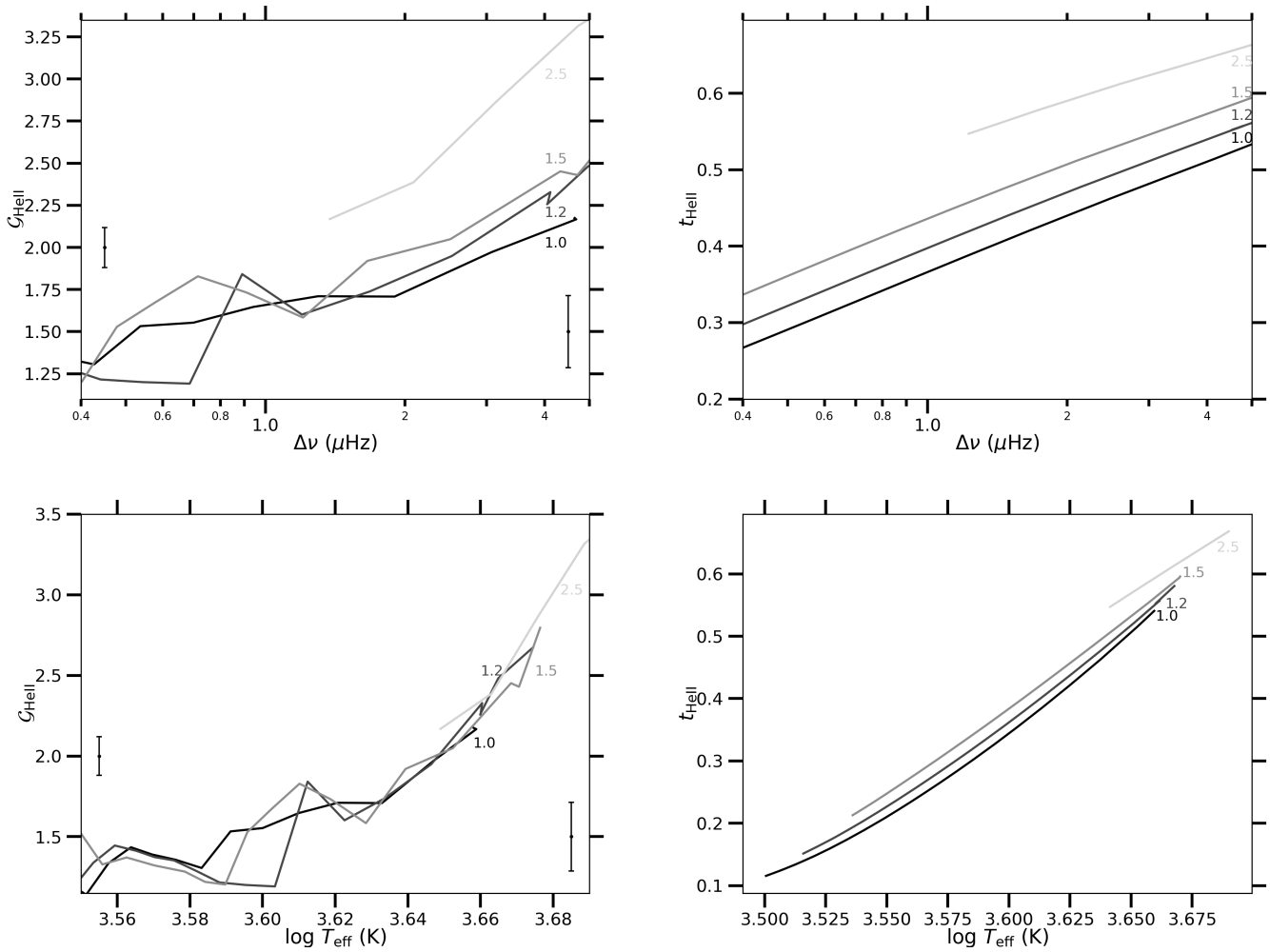

FIGURE 8.8: Synthetic glitch period and acoustic radius of HeII computed with the stellar codes MESA and ADIPLS during the RGB. The MESA models are computed with the reference input physics listed in Table 10.1. **Top left**: dependence of the modulation period $\mathcal{G}_{\rm HeII}$ on the stellar mass as a function of $\Delta\nu$. The mass is shown with different shades of grey. Mean error bars estimated for $\Delta\nu$ below or above 1 μHz are shown. **Top right**: same as the upper left panel but for the acoustic radius $t_{\rm HeII}$. **Bottom left**: same as the upper left panel but for $\mathcal{G}_{\rm HeII}$ as a function of log $T_{\rm eff}$. **Bottom right**: same as the upper left panel but for $t_{\rm HeII}$ as a function of log $T_{\rm eff}$.

The difference in the modulation period, hence in the acoustic radius of the HeII zone between low-mass and high-mass stars can be explained by a difference of effective temperature $T_{\rm eff}$. Indeed, in the bottom panels of Fig. 8.8, we see that there is an almost unequivocal relation between the modulation period and the effective temperature for any stellar mass M. Such behaviour is also visible in the acoustic radius of the HeII zone. In parallel, we know that high-mass stars have higher effective temperature than their low-mass counterparts at fixed $\Delta\nu$. Therefore, the higher the mass, the higher the effective temperature, the higher the modulation period hence the more superficial the HeII zone. In fact, the HeII zone is located in the region where the physical conditions for helium ionisation are fulfilled, which means that helium ionisation is expected to occur close to the surface if the effective temperature is high. Low-mass stars have low effective temperature, so the internal temperature reaches the threshold for helium ionisation deep in the interior.

8.2.5 Stellar classification by evaluating the modulation phase

In Sect. 4.2 of the paper 1, we highlight a clear difference in the modulation phase of the glitch signature between H-shell burning and He-burning stars, including clump and AGB stars observed by *Kepler*. There is a negative phase difference between He-burning and H-shell burning stars of about -1 radians during the clump phase, which becomes -0.5 radians during the AGB. Through Eq. 5.2, this difference in $\Phi_{\rm HeII}$ translates into a difference in the acoustic offset ε. By defining a cut that depends on the acoustic offset ε and the large separation $\Delta\nu$, we are able to draw up a classification method of H-shell burning and He-burning stars, as illustrated in Fig. 5.3. By measuring the glitch signature in evolved stars, we therefore extend the conclusions raised by Vrard et al. (2015), not only between RGB and clump stars but more generally between RGB and He-burning stars, including clump and AGB stars.

In order to understand the modulation phase difference in terms of physical parameters, we analyse the glitch signature computed with ADIPLS mode frequencies. The dependence of the modulation phase on stellar evolution is shown in Fig. 8.9. For the $0.9\,M_\odot$ evolutionary track, we clearly recover the negative modulation phase difference observed between H-shell burning and He-burning stars. Nevertheless, with the same input physics in stellar models we do not meet the same phase difference when the mass increases (see right panel of Fig. 8.9). When $M \geq 1.5\,M_\odot$, we do not find any phase difference between H-shell burning and He-burning stars. Concurrently, we report a clear modulation phase difference between those stars observed by *Kepler*, not only at low-mass $M \leq 1.2\,M_\odot$, but also at high-mass $M \geq 1.5\,M_\odot$ (see lower right panel of Fig. 4 in paper 1). In this regard, additional input physics are needed at high mass to reproduce the phase difference between RGB and clump/AGB stars. To reproduce this phase difference at high mass, we would need input physics that affect the stellar structure on the RGB/clump phase. For instance, low-mass stars experience an important mass loss at the luminosity tip of the RGB, while that of high-mass stars is less significant. The difference $\Delta M = M_{\rm RGB} - M_{\rm He}$ between the mass on the RGB, $M_{\rm RGB}$, and the final mass reached on the clump phase, $M_{\rm He}$, may be a possible explanation to the phase difference $\Phi_{\rm HeII,RGB} - \Phi_{\rm HeII,He}$. At this stage, understanding the phase difference between H-shell burning and He-burning stars in terms of stellar parameters is still in progress.

8.3 Validity of the asymptotic approach at low $\Delta\nu$

Until now, we restricted our analysis to stars with $\Delta\nu \geq 0.5\,\mu$Hz, for which we could successfully extract the glitch signature in the asymptotic assumption. In stellar models, we could infer the frequencies of the pressure radial, dipole, and quadrupole modes in an efficient way down to $\Delta\nu \sim 0.06\,\mu$Hz (equivalently $\nu_{\rm max} \sim 0.1\,\mu$Hz) with the code ADIPLS (see Fig. 8.2). This offers the opportunity to test the relevance of the asymptotic expansion at low $\Delta\nu$, which is based on the assumption $n \gg \ell$. In this approach, the ionisation-induced dip of the first adiabatic exponent Γ_1 is treated as a structural perturbation to a reference model in absence of the effects of helium ionisation on the stellar structure. The glitch signature, that is a decaying periodic function in frequency given by Eq. 4.5, is then obtained as a perturbation to the asymptotic expansion. Accordingly, we expect the amplitude of the glitch signature

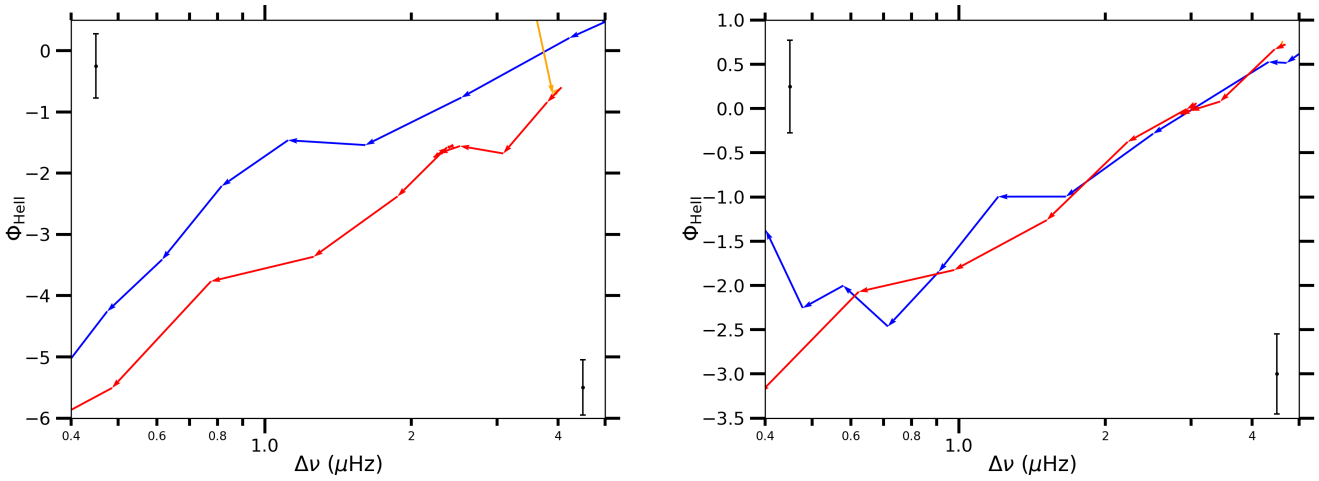

FIGURE 8.9: Synthetic modulation phase computed with the code ADIPLS for the same evolutionary sequences as in Fig. 8.5. **Left**: evolution of the modulation phase $\Phi_{\rm HeII}$ with $\Delta\nu$ for models of initial mass 0.9 $M_\odot$ at solar metallicity, with an emphasis on the evolutionary stage. The RGB, clump, and AGB phase are shown in blue, orange, and red solid lines, respectively. The arrows indicate the direction of the evolution between consecutive models. **Right**: same as left, but for models of initial mass 1.5 $M_\odot$. Mean error bars estimated for $\Delta\nu$ below or above 1 μHz are represented on each panel.

to be small relatively to the large separation $\Delta\nu$. In Fig. 8.10, we show the trend of the modulation amplitude $\mathcal{A}_{\rm HeII}$ with stellar evolution at very low $\Delta\nu$. We remind that $\mathcal{A}_{\rm HeII}$ is a dimensionless parameter expressed in fraction of $\Delta\nu$, as depicted by Eq. 7.13. Below $\Delta\nu \leq 0.5\,\mu$Hz, we note that the amplitude $\mathcal{A}_{\rm HeII}$ of the glitch modulation becomes larger than 0.1, and eventually reaches 0.5 at the luminosity-tip of the RGB, corresponding to a modulation amplitude in μHz equal to half the value of $\Delta\nu$. This means that the large separation $\Delta\nu$ is perturbed by 50% of its global value. So, the glitch modulation $\delta\Delta\nu^{\rm gl}_{n,\ell}$ given by Eq. 7.13 is no longer a small perturbation to $\Delta\nu$. We identified two reasons for this intense glitch modulation:

- The asymptotic expansion of the mode frequencies must not be valid below $\Delta\nu \leq 0.5\,\mu$Hz (equivalently $\nu_{\rm max} \leq 2\,\mu$Hz) because modes at low-radial orders are used to fit the glitch signature (see Fig. 8.2), and the assumption $n \gg \ell$ is not met. If so, then the usual decaying periodic functions in frequency to fit the glitch signature are no longer relevant since they are derived in the asymptotic approach.

- The perturbative approach must not be adapted at low $\Delta\nu$. By checking the evolution of the HeII zone characteristics at low $\Delta\nu$, we notice that the amplitude $H_{\rm HeII}$ of the dip in the Γ_1 profile is larger and the extent $\Delta_{\rm HeII}$ of the dip is narrower when $\Delta\nu \leq 0.5\,\mu$Hz (see Fig. 8.10). The variation in the Γ_1 profile caused by helium ionisation is stronger and located deeper in the interior. Then, the HeII zone may leave a stronger imprint in mode frequencies, and the approach to derive the glitch signature must be revisited.

It is likely that both the asymptotic expansion and the perturbation approach of the signature of HeII in mode frequencies are not adapted at low $\Delta\nu$. Surely, the accuracy on the mode parameters is affected by the frequency resolution of *Kepler* observations that is insufficient for a comprehensive seismic study of these red giants. In particular, we cannot robustly extract the width and amplitude of the modes, but still their frequency can be correctly inferred.
On the one hand, we clearly detect modes with low-radial orders $n \leq 5$ at low $\Delta\nu \leq 0.5\,\mu$Hz (Mosser et al., 2013b; Yu et al., 2020; Dréau et al., 2021). In our work, we encounter difficulties to match the observed and the template oscillation spectra when identifying the oscillation modes according to Sect. 7.3 when $\Delta\nu \leq 0.5\,\mu$Hz. At the optimal $\Delta\nu$ that maximises the cross correlation between the observed and

template oscillation spectrum, the modes from observations and models do not overlap for all radial orders n. This is because the template spectrum is based on the asymptotic p-mode frequencies of red giants (Eq. 3.20), which is not suitable at low $\Delta\nu$. Therefore, we have some observational evidence that the asymptotic expansion is not appropriate to describe the oscillation spectrum of evolved red giants with $\Delta\nu \leq 0.5\,\mu$Hz.

On the other hand, the glitch amplitude in *Kepler* observations becomes significant at low $\Delta\nu$, as described in Sect. 4.2 of Dréau et al. (2021) (see Appendix 1). Indeed, the amplitude of the glitch modulation introduced in the local large separation $\delta\Delta\nu^{\rm gl}_{n,\ell}$ at $\Delta\nu = 1.0\,\mu$Hz is $\sim 0.07\,\Delta\nu$ on the RGB and $\sim 0.08\,\Delta\nu$ on the AGB. This means that the HeII zone induces an additional term $\delta\Delta\nu^{\rm gl}_{n,\ell}$ in the local large separation $\Delta\nu_{n,\ell}$ that becomes significant relatively to the mean value $\Delta\nu$. This tends to confirm that the perturbation approach to the asymptotic pattern is not appropriate to account for the signature of the HeII zone in mode frequencies at low $\Delta\nu \leq 0.5\,\mu$Hz. As a result, the efficiency of the classification method based on the signature of the HeII zone (Sect. 5.2) may not be only affected by the insufficient frequency resolution at low $\Delta\nu$, but also by the inadequate scheme to derive p-mode frequencies. Accordingly, we need a more adapted framework to interpret the oscillation spectrum of high-luminosity red giants with $\Delta\nu \leq 0.5\,\mu$Hz. Investigating the limits of our method to characterise the HeII zone and extract its signature in mode frequencies at low $\Delta\nu$ is in progress.

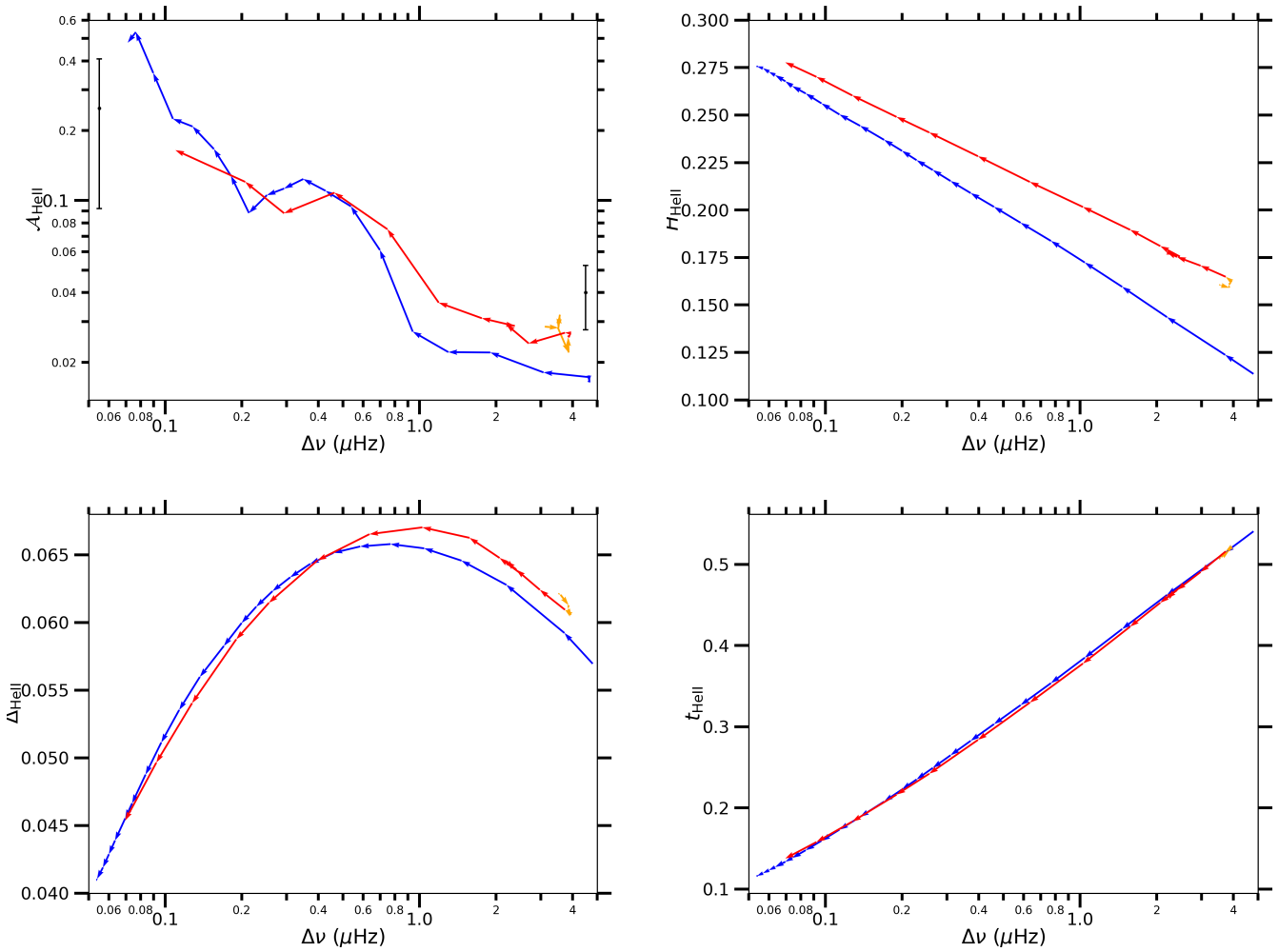

FIGURE 8.10: Same models as Fig. 8.5, but the $\mathcal{A}_{\rm HeII}$ axis is logarithmic and the $\Delta\nu$ axis is extended at very low values attained near the luminosity-tip of the RGB. The MESA models are computed with the reference input physics listed in Table 10.1. **Bottom right**: acoustic radius $t_{\rm HeII}$ of the HeII zone as a function of $\Delta\nu$.

8.4 Summary

In this chapter, we present a complete analysis of the p-mode oscillation spectrum of high-luminos- ity red giants, including stars ascending the RGB towards the luminosity tip and He-burning stars both in the clump phase and ascending the AGB. We compare the p-mode frequencies computed with stellar models with those detected in thousands of evolved stars observed by *Kepler*. The structure of the oscillation spectrum of these red giant changes with stellar evolution. This can be connected with the underlying structure changes of the core and envelope, which impacts the distance between the inner turning point of the p-mode cavity and the base of the convective zone. The $\ell = 1$ and $\ell = 2$ modes get closer to the neighbouring $\ell = 0$ modes as stars ascend their branch, forming a triplet with the $\ell = 2$ mode in between the $\ell = 0$ mode on the right and $\ell = 1$ on the left, as described in Stello et al. (2014).
We successfully extract the glitch signature induced in the large frequency separation $\Delta\nu$ by the helium second-ionisation zone. We find differences in the glitch signature between RGB and clump/AGB stars with the *Kepler* observations. Then, by jointly computing the internal structure with MESA and the associated stellar pressure modes with ADIPLS, we can understand the cause of these differences in terms of structure changes. First, the amplitude of the glitch signature is larger during He-burning phase. This difference of glitch amplitude between H-shell burning and He-burning phase is related to a stronger dip in the Γ_1 profile during the He-burning phase, which is correlated with a lower temperature at the HeII zone. The amplitude of the glitch signature then reflects the physical conditions in the envelope that are different between RGB and clump/AGB stars.
Second, the period of the glitch signature, which is related to the acoustic radius of the HeII zone, does not differ between the H-shell burning and He-burning phase. Nevertheless, we identify a clear difference between low-mass and high-mass stars. The physical conditions for helium ionisation are fulfilled closer to the surface when the effective temperature $T_{\rm eff}$ is high, typically in high-mass stars.
Third, a classification of RGB/AGB stars is possible by analysing the glitch signature. Indeed, we identify a clear negative phase difference between the glitch signature of He-burning and H-shell burning stars. This difference can be highlighted either in a global analysis by considering an additional term reflecting the glitch signature in the asymptotic pattern of red giants, or in a local analysis by including the glitch signature in the local acoustic offset ε. Then, we extend the work of Vrard et al. (2015), who drew the same conclusions but considering RGB versus clump stars.
Finally, we notice that the asymptotic pattern of red giants established for low- and intermediate-luminosity red giants does not match the p-mode pattern of red giants with $\Delta\nu \leq 0.5\,\mu$Hz. Furthermore, the amplitude of the glitch modulation is too intense to be treated in a perturbative approach when $\Delta\nu \leq 0.5\,\mu$Hz. In this case, we suspect the asymptotic pattern to be irrelevant to characterise the p-mode oscillation spectrum of these evolved red giants at low $\Delta\nu$, where the assumption $n \gg \ell$ is invalid.

Chapter 9

Mode energetics in high-luminosity red giants

Fitting the oscillation spectrum of red giants allows us to extract the width and amplitude of the pressure modes that develop in their interiors. These seismic parameters provide valuable information on the excitation and damping mechanisms of stellar modes, as described in Chapter 3. This offers the opportunity to follow the mode lifetime across the HR diagram, and examine the main physical mechanisms that play a part in the mode energy, hence in the mode visibility. Hereafter, we study the dependence of the mode width and mode energy on stellar evolution with the same sample of red giants studied in Chapter 8. Then, we investigate potential supplementary damping, especially during the ascent on the AGB.

Sect. 3.3, 3.4, 4.3−4.6 and 5.3 of the attached article 1 present the dependence of the mode energy and width on stellar parameters as well as the damping of modes at different degrees ℓ. In this chapter, we focus on the implications of our observations on the damping mechanisms from RGB to AGB.

9.1 Deriving the seismic parameters

9.1.1 The mode visibilities

Studying the mode visibilities in red giants provides fruitful information on how the energy is distributed among modes of different degrees ℓ. By definition, the visibility of a mode of degree ℓ is equal to its squared amplitude in fraction of the squared amplitude of $\ell = 0$ modes as given by Eq. 3.69. In order to compute the energy of a mode, we first need to locate the modes in the oscillation spectrum, which is done by the identification technique described in Sect. 7.3. Then, we are able to bracket the frequency range where $\ell = 0$, 1, 2, 3 modes are expected. This precise delimitation of the spectral range where modes are expected is detailed in Table 1 of the paper 1 and illustrated in Fig. 9.1.
The individual squared amplitude $A^2_{n,\ell}$ of a mode of radial order n and degree ℓ is estimated by integrating the power spectral density P across the frequency range where the energy of this mode is distributed, with the integral being corrected from the background contribution B defined in Eq. 7.4. This yields

$$A^2_{n,\ell} = \int_{\nu_{\rm inf}}^{\nu_{\rm sup}} \left(P(\nu) - B(\nu)\right) \mathrm{d}\nu, \tag{9.1}$$

where $\nu_{\rm inf}$ and $\nu_{\rm sup}$ delimit the frequency range where the modes are expected. The mean squared amplitude of a mode of degree ℓ is obtained by averaging the individual squared amplitudes $A^2_{n,\ell}$ over all observed radial orders n, weighted by the Gaussian power excess envelope as follows

$$A^2_\ell = \frac{\sum_{n_{\rm inf}}^{n_{\rm sup}} A^2_{n,\ell}}{\sum_{n_{\rm inf}}^{n_{\rm sup}} \exp\left[-\frac{(\nu_{n,\ell}-\nu_{\rm max})^2}{2\sigma^2}\right]}, \tag{9.2}$$

where σ is related to the full-width at half-maximum of the Gaussian envelope $\delta\nu_{\rm env} = 2\sqrt{2\ln 2}\sigma$ (Eq. 7.3), $n_{\rm inf}$ and $n_{\rm sup}$ are the minimum and maximum radial orders that are detected, respectively. We notify that the weighting is not performed before the summation in order to reduce the dispersion of the average squared amplitudes caused by the stochastic excitation of modes. Moreover, we consider all the modes for which the radial order is included between $n_{\rm inf}$ and $n_{\rm sup}$, whether they are detected or not. Accounting for the undetected modes in the mean squared amplitude A^2_ℓ is necessary because some of these modes can have an unexpected low amplitude due to additional damping. Particularly, the depressed modes, which are modes with very-low amplitudes certainly due to the presence of a magnetic field in the core of red giants (Loi and Papaloizou, 2018; Loi and Papaloizou, 2020), can be left undetected with our detection thresholds (Sect. 7.3.2). Finally, the mode visibility V^2_ℓ are inferred from A^2_ℓ through Eq. 3.69. The analysis of the mode visibilities is presented in Sect. 4.5 of the publication 1.

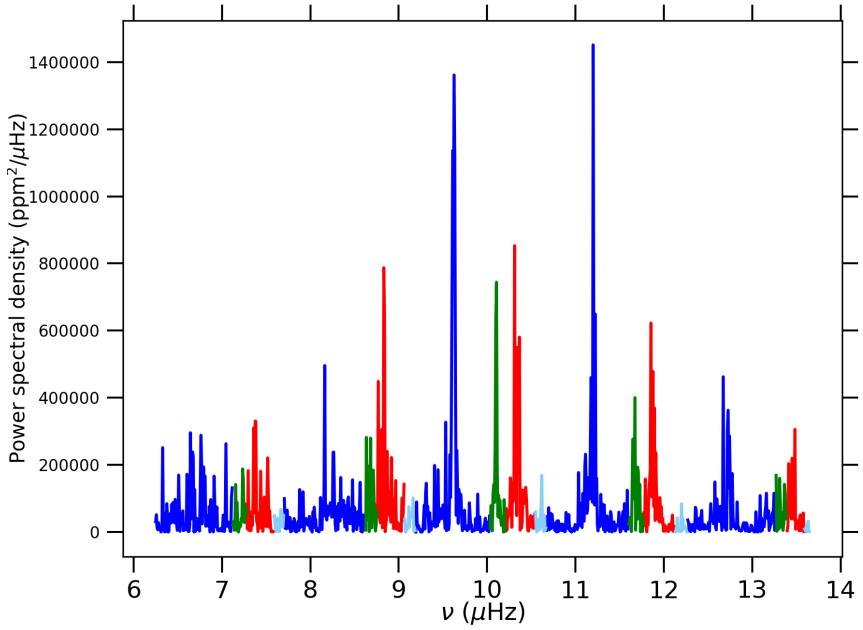

FIGURE 9.1: Oscillation spectrum of the red-giant star KIC 2695975 ($\Delta\nu = 1.538\,\mu$Hz, $\nu_{\rm max} = 10.11\,\mu$Hz), with an emphasis on the spectral range where modes are expected to be located and where the power spectral density is integrated for each mode. Red, blue, green, and light blue are associated with radial, dipole, quadrupole and octupole modes, respectively.

When mixed modes are present, we follow the same procedure *i.e.* we define the boundaries between which we expect the mixed modes to be detected, and we integrate the total power spectral density P in this range of frequency. Accordingly, $A^2_{n,\ell}$ is the sum of the individual squared amplitude of all mixed modes of pressure radial order n at degree ℓ. Thus, we can infer the average squared amplitude A^2_ℓ and the mode visibility V^2_ℓ by averaging $A^2_{n,\ell}$ over all pressure radial orders n according to Eq. 9.2. These quantities are comparable to the squared amplitude and visibility that the mode would have if it was a single pure pressure mode.

Modes for which the degrees have the same parity have their frequencies close one to the other, as illustrated in Fig. 9.1. For instance, $\ell = 2$ modes are close to their neighbouring $\ell = 0$ modes and some mixed $\ell = 1$ modes spread near the $\ell = 3$ modes and can be misidentified subsequently. As we sum the power spectral density between boundaries that delimit the energy distribution of modes, a fraction of the energy of a mode of degree ℓ can be mistakenly considered as part of the energy of the neighbouring mode near the boundaries. In order to limit the impact of the energy leakage between individual degrees, we can study the ratio between the visibility of odd and even degrees

$$\frac{V^2_{\ell,\text{odd}}}{V^2_{\ell,\text{even}}} = \frac{V_1^2 + V_3^2}{1 + V_2^2}, \tag{9.3}$$

where the visibility of $\ell = 0$ modes is taken equal to 1 by definition. In a star in spherical equilibrium (thus non-rotating and without magnetic field), this ratio is useful when studying the energy distribution between modes of different degrees since for symmetry reasons we expect the energy equipartition between modes of even and odd degrees to be satisfied ($V^2_{\ell,\text{odd}} = V^2_{\ell,\text{even}}$).

9.1.2 Sensitivity of the mode width estimation to the stellar background

The technique we use to fit the modes and extract their width and height is a maximum likelihood estimator as described in Sect. 7.4. As depicted by Eq. 7.8, the power spectral density is reproduced by a pattern of three modes at different degrees ℓ on top of the background signal. With the polynomial term Eq. 7.4, we are able to satisfyingly reproduce the stellar background signal. Nevertheless, this polynomial form only approximates the background component around $\nu_{\max}$, and may not be as precise as the full expression Eq. 7.1 at the edges of the observation window. Especially, Appourchaux et al. (2014) highlighted that the expression chosen for modelling the background has a non-negligible impact on the mode width and height. As illustrated in Sect. 4.6 of the article 1, our method provides measurements that are larger by about 25% compared to those derived in Kallinger (2019), who used a different model to fit the background component. This is the typical difference that can be found between different stellar background models, which is of the order of 30% in the worst-case scenario and 10% in the best-case scenario (Appourchaux et al., 2014). Moreover, this difference is frequency-dependent since the deviations between our measurements and those from Kallinger (2019) depends on the radial mode width Γ_0, which varies with $\Delta\nu$. Such effects produced by different estimated stellar backgrounds must be kept in mind when comparing theoretical mode width and height with the observed values in order to understand the physical nature of these parameters.

9.2 Mode damping from the RGB up to the AGB

9.2.1 Dependence of the mode width Γ_0 on the effective temperature T_{eff}

Theoretical models predict that the main contributions to the mode damping in red giants is determined by four main contributors presented in Eq. 3.60, which can be rewritten (Grigahcène et al., 2005)

$$\eta = \frac{1}{2\omega\mathcal{I}} \int_0^M \text{Im}\left[\left(\frac{\partial T_0}{\partial \rho_0}\right)_s \frac{\delta\rho^*}{\rho_0} T_0 \delta S + \frac{\delta\rho^*}{\rho_0}\frac{\delta P_{\text{turb}}}{\rho_0}\right] \text{d}m, \tag{9.4}$$

where Im denotes the imaginary part, the exponent '*' refers to the complex conjugate, P_0, ρ_0, T_0 are the pressure, density, and temperature at equilibrium, respectively, ω is the pulsation frequency, $\mathcal{I}$ is the mode inertia, δS is the Lagrangian perturbation of the entropy, and δP_{turb} is the perturbation of turbulent pressure. In the previous equation, the first term, which is found to be negative, is thus a driving contribution and includes the perturbations of the radiative and convective fluxes, as well as that of the dissipation rate of turbulent kinetic energy into heat. The second term is associated to the perturbation of the turbulent pressure already presented in Eq. 3.60. Both contributions approximately have the same order of magnitude and the contribution of the perturbation of turbulent pressure is partly compensated by that of entropy. The maximum compensation between the two contributions leads to the characteristic depression in the profile of the damping rate η as a function of the frequency ν (Belkacem et al., 2012) as seen in Fig. 9.2 around $\nu = 32.5\,\mu$Hz. This behaviour of the damping rate η with frequency is clearly visible for stars with $\Delta\nu \geq 3.0\,\mu$Hz, where at least 6 radial modes have sufficiently high amplitudes to be detected. Nevertheless, this tendency is hardly visible in evolved red giants with $\Delta\nu \leq 3.0\,\mu$Hz since too few modes are observable.

Next, we can directly compare the predicted mode width with those observed for the sample of stars we consider in the paper 1 (see right panel of Fig 9.3). We notice that the mode widths predicted by the

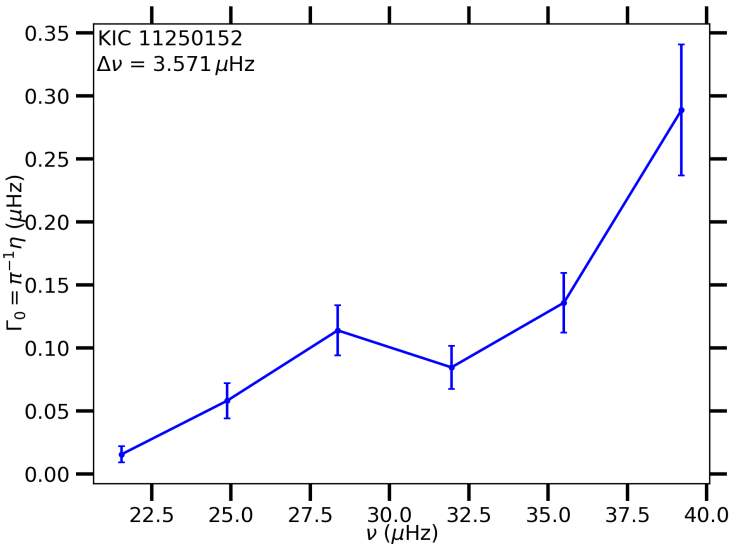

FIGURE 9.2: Variation of the radial mode width $\Gamma_{n,0}$ (or equivalently $\pi^{-1}\eta$) as a function of the frequency ν. The mode frequencies and widths have been computed with the fitting technique described in Sect. 7.4 for KIC 11250152 identified as a RGB star.

theoretical models of Belkacem et al. (2012) satisfyingly reproduce the radial mode widths measured in H-shell burning and He-burning stars. However, the mode widths measured in cool red giants ($T_{\rm eff} \leq$ 4200 K) are a bit smaller by about $\sim$ 30% than predicted by theory. In this case, we may be limited by the frequency resolution, the modes may not be fully resolved, which could provide underestimated widths. This could also be linked to the choice of the background model that distinctly affects the measurement of mode characteristics, as described in Sect. 9.1.2. Finally, as discussed in Sect. 4.3 of the publication 1, the mode widths Γ_ℓ are strongly correlated with the effective temperature following the scaling relation $\Gamma_\ell \propto T_{\rm eff}^{b_\ell}$, with $b_\ell \geq 6-10$ depending on the mode degree ℓ. This agrees with the theoretical predictions of Belkacem et al. (2012), who report a correlation of

$$\eta \propto T_{\rm eff}^{10.8} g^{-0.3}, \tag{9.5}$$

where g is the surface gravity. Altogether, the mode damping profile with frequency and effective temperature predicted by the theoretical models of Belkacem et al. (2012) are in agreement with the observations of evolved red giants, which suggests that the contributions to mode damping described in Eq. 9.4 are likely to explain mode damping in evolved red giants. This finding is valid for radial and quadrupole modes, but additional contributions to mode damping are necessary to address the $\ell = 1$ modes, as we will see in Sect. 9.3.

9.2.2 Mode damping and stellar evolution

As reported in the previous section, the main sources of damping for pressure modes are the action of turbulent pressure and those of the convective and radiative fluxes, which are partly compensated by that of the dissipation rate of turbulent kinetic energy into heat. As depicted by Fig. 9.3, the total mode damping in RGB star decreases as the star gradually evolves on its branch (equivalently as $T_{\rm eff}$ decreases). This means that the driving term, *i.e.* the action of entropy, is more important in absolute value. The former becomes closer to the action of turbulent pressure, which makes them compensate even more and the total damping η decreases. When the star reaches the stage of He-core burning, the effective temperature increases, the mode damping increases and becomes larger than that observed on the RGB. Vrard et al. (2018) also reported a clear difference between the radial mode width of less

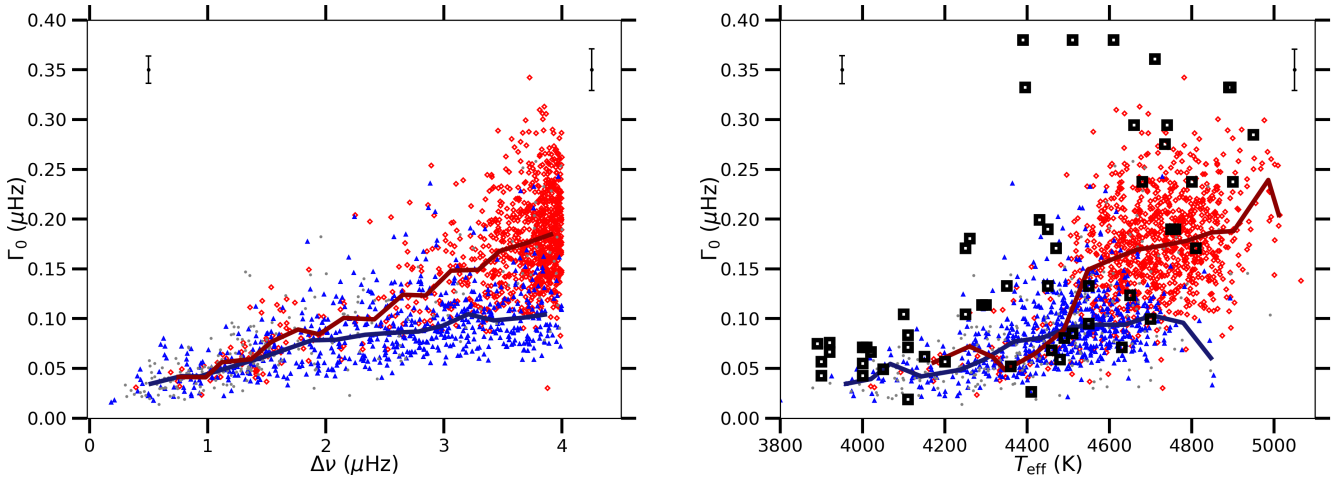

FIGURE 9.3: **Left**: radial mode width Γ_0 computed as the weighted mean of the three modes of degree $\ell = 0$ closest to $\nu_{\rm max}$ with the mode amplitude A_0 used as a weight, as a function of $\Delta\nu$. Mean error bars on the mode widths have been computed both at low $\Delta\nu$ ($\Delta\nu \leq 1.0\,\mu$Hz) and at high $\Delta\nu$ ($\Delta\nu \geq 1.0\,\mu$Hz). **Right**: same as left panel but the radial mode width Γ_0 is plotted as a function of the effective temperature $T_{\rm eff}$. Mean error bars on the mode widths have been computed both at low $T_{\rm eff}$ ($T_{\rm eff} \leq 4200\,$K) and at high $T_{\rm eff}$ ($T_{\rm eff} \geq 4200\,$K). Blue triangles and red diamonds indicate indicate RGB stars and clump/AGB stars, respectively. The thick solid lines are the median values in $0.2\,\mu$Hz wide $\Delta\nu$ bins and 50 K wide $T_{\rm eff}$ bins, in dark blue for RGB stars and dark red for clump/AGB stars. Theoretical predictions for RGB stars from Belkacem et al. (2012) are indicated by black squares. Credit: Dréau et al. (2021)

evolved RGB and clump stars at similar effective temperature. In a way, this difference could be explained by the theoretical models of Belkacem et al. (2012). Indeed, Eq. 9.5 tells us that the mode damping not only depends on the effective temperature $T_{\rm eff}$, but also on the surface gravity g to a lesser extent ($\eta \propto g^{-0.3}$). At fixed $T_{\rm eff}$, clump stars have a lower surface gravity than RGB stars. Then, the mode damping η is expected to be larger during the clump phase, as the former is inversely proportional to g. Still, given the significant structure changes between H-shell and He-core burning phases, further work would be desirable to investigate potential additional contributors to mode damping during the clump phase. For example, this could be a radiative damping, as described in the next subsection.
After the He-core burning phase, the He-shell burning phase starts and the mode damping gradually becomes similar to that observed on the RGB as $\Delta\nu$ decreases (Fig. 9.3). RGB and AGB stars have similar $T_{\rm eff}$ and g at high luminosity, which could explain why RGB and AGB stars have a similar mode damping at low $\Delta\nu$. As a conclusion, the theoretical models of Belkacem et al. (2012) allow us to understand the evolution of the mode damping across the HR diagram from the RGB up to the AGB.

9.2.3 Radiative damping for non-radial modes

In red giants, non-radial modes are mixed modes, which means that they are sensitive to the interaction between p- and g-mode cavities. This introduces additional contributions to the mode damping. Particularly, the radiative damping corresponds to the energy loss caused by gravity wave emission especially around the bottom of the H-burning shell (Dupret et al., 2009). On the one hand, the modes that could develop in the g-mode cavity would have low amplitude because of their large inertia and significant radiative damping at the bottom of the H-burning shell. On the other hand, non-radial modes trapped in the envelope experience weak radiative damping. As a result, the oscillation spectrum of non-radial modes is composed of p-dominated modes with similar widths and heights as radial modes, and low-height g-dominated modes. When the star reaches high-luminosity stages on the RGB, the modes trapped in the core experience an increasing radiative damping. Meanwhile, the energy loss by

gravity wave emission near the base of the convective envelope for modes trapped in the envelope is negligible (Dziembowski, 2012). As a consequence, g-dominated modes cannot be detected and only p-dominated modes trapped in the envelope can be observed. When He-core burning starts, the radiative damping is small enough for the mixed modes to be detectable again (Dupret et al., 2009; Grosjean et al., 2014). Then, the structure of the oscillation spectrum in the He-core burning phase is similar to that of an intermediate-luminosity red giant, but with different seismic parameters at a given $T_{\rm eff}$ (mode frequencies, widths, heights) due to structure changes.

9.3 A strong non-radial mode damping during the early-AGB

In spherical equilibrium in absence of rotation and magnetic field, we expect the mode energy to be equally distributed between odd and even degrees, since they are excited and damped in the same physical conditions. That being said, in red giants we observe modes that are excited by the turbulent motions near the surface and are strongly trapped in the envelope. In this situation, we expect the conditions

$$\begin{cases} 1 + V_2^2 = V_1^2 + V_3^2 \\ \Gamma_0 = \Gamma_1 = \Gamma_2 = \Gamma_3 \end{cases} \tag{9.6}$$

to be fulfilled. In order to identify potential contributions to non-radial mode damping that may invalidate the energy equipartition, we study the behaviour of the non-radial mode visibilities and widths with stellar evolution.

9.3.1 Dipole modes

In Fig. 9.4, we examine the ratio between dipole and radial mode widths from the RGB up to the AGB. We note that the widths of dipole modes are larger than those of radial modes by a factor of $1.5 - 2.0$ on the early-AGB in the interval $\Delta\nu \in [1.5, 3.0]\mu$Hz. As discussed in the article 1, several reasons could explain these large dipole mode widths Γ_1. First, additional contributions to dipole mode damping may be at work, which would make dipole mode widths larger than those of radial modes. Second, most of the detected dipole modes are mixed for He-burning stars with $\Delta\nu \geq 2.5\mu$Hz. In this case, we fit the mixed mode with the highest amplitude among the other mixed modes closest to the expected pure pressure mode (see Sect. 7.4). Then, we infer the width Γ_1 that would have the dipole mode if it was a pure pressure mode through Eq. 3.75. Nevertheless, the factor $\zeta_{\rm as}$ introduced in this equation is close to 1, which means that the correction (Eq. 3.75) used to infer the width of the pure pressure dipole mode introduces large uncertainties on Γ_1. Third, the observability of mixed modes is limited by the frequency resolution around $\Delta\nu \sim 3.0\,\mu$Hz (see Sect. 3.6.2). The criterion given by Eq. 3.50 to determine the observability of gravity-dominated modes may not be fulfilled and most of the g-dominated modes may overlap. In this case, the mixed modes are so close that the fits rather reproduce several confused mixed modes than a unique pure pressure mode. To be properly reproduced, these mixed modes need to be fitted with a different function made of several Lorentzian functions. In Appendix 2 of the paper 1, we carefully fit all the observed mixed modes of five stars that have been identified on the early-AGB following the method of Mosser et al. (2014). Then, we deduce the width Γ_1 that the modes would have if they were pure pressure modes following Eq. 3.75. Nonetheless, our measurements of Γ_1 are affected by large uncertainties due to the use[1] of Eq. 3.75, to low signal-to-noise ratio, to the insufficient frequency resolution, to the presence of rotational splittings and to buoyancy glitch signatures. As a result, measuring the widths of dipole mixed modes does not allow us to certify the presence of a strong dipole mode damping on the early-AGB. In order to check if the additional dipole mode damping that we measure is not caused by large uncertainties, we investigate the energy distribution between modes of different degrees.

[1] because $\zeta_{\rm as}$ introduced in this equation is close to 1, as discussed herebefore

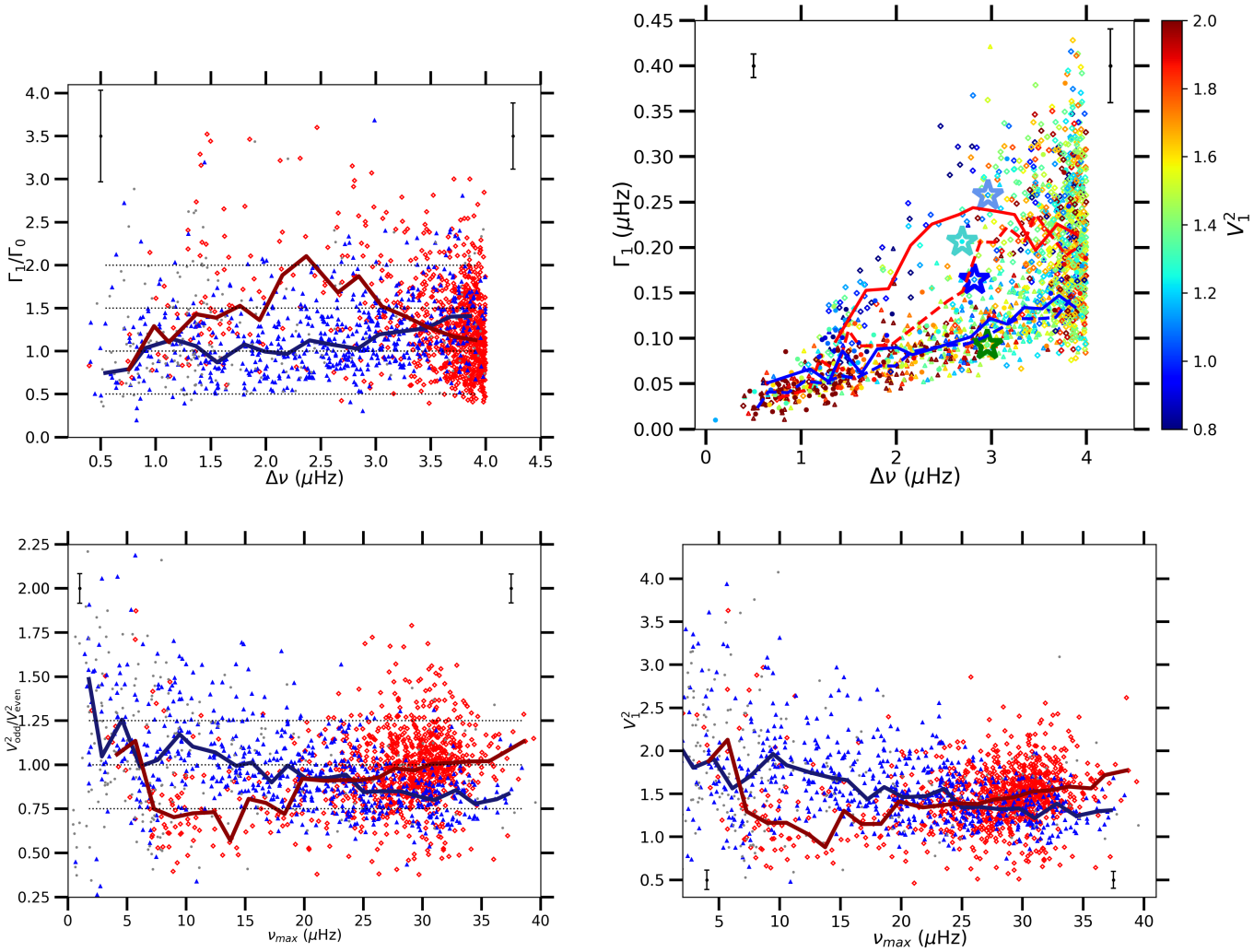

FIGURE 9.4: **Top left**: ratio between the dipole and radial mode widths. Blue triangles, red diamonds, and grey dots correspond to RGB stars, clump/AGB stars, and stars with unidentified evolutionary stages with the methods of Mosser et al. (2019) and Kallinger et al. (2012), respectively. The mode widths are computed as the weighted mean of the three modes closest to $\nu_{\rm max}$ with the mode amplitudes used as weights. Mean error bars have been computed both at low $\Delta\nu$ ($\Delta\nu \leq 1.0\,\mu$Hz) and at high $\Delta\nu$ ($\Delta\nu \geq 1.0\,\mu$Hz). The thick solid lines are the median values in $0.4\,\mu$Hz wide $\Delta\nu$ bins, in dark blue for RGB stars and dark red for clump/AGB stars. For convenience, horizontal dotted black lines are plotted at specific values of 0.5, 1.0, 1.5, and 2.0. **Top right**: dipole mode width as a function of $\Delta\nu$, where the dipole mode visibility V_1^2 is colour-coded. The solid and dashed lines correspond to the median values for low-visibility dipole modes ($V_1^2 \leq 1.5$) and for high-visibility dipole modes ($V_1^2 \geq 1.5$), respectively, in blue for RGB stars and in red for He-burning stars. In fact, we separate low-visibility and high-visibility dipole modes since they are likely to experience a different damping rate. The turquoise, dark blue, light blue and green stars are the individual stars KIC 6847371, KIC 11032660, KIC 5461447, and KIC 6768042, respectively, which are studied in Appendix 2 of the paper 1. **Bottom left**: ratio between the visibilities of odd and even degrees as a function of $\nu_{\rm max}$. **Bottom right**: dipole mode visibility V_1^2 as a function of $\nu_{\rm max}$. The median values are computed in $1.5\,\mu$Hz wide $\nu_{\rm max}$ bins. Error bars on the visibilities are given for both low $\nu_{\rm max}$ ($\nu_{\rm max} \leq 4.5\,\mu$Hz) and high $\nu_{\rm max}$ ($\nu_{\rm max} \geq 4.5\,\mu$Hz).

If the additional dipole mode damping is real, we expect the first condition of Eq. 9.6 to be invalid. In the bottom left panel of Fig. 9.4, we remark that the energy equipartition between even and odd degrees is invalid during the early-AGB when $\nu_{\rm max} \in [7, 20]\,\mu$Hz, which coincides with the interval where we report a strong dipole mode damping in He-burning stars. This implies that the modes of odd degrees ($\ell = 1, 3$) carry less energy than the modes of even degrees. Given that the $\ell = 3$ modes have weak visibilities ($V_3^2 \sim 0.05 - 0.10$), the low visibilities of odd degree modes is caused by a lack of energy in dipole modes. Indeed, in the bottom right panel of Fig. 9.4 we note a similar difference between the dipole mode visibility of RGB and clump/AGB stars. He-burning stars have smaller V_1^2 than their RGB counterparts at fixed $\nu_{\rm max}$, which justifies the difference between the visibilities of odd and even degrees. To sum up, we observe both large dipole mode widths and low dipole mode visibilities on the early-AGB, which implies a strong mode damping in the regions that are probed by dipole modes. In the next section, we see that the damping of quadrupole modes is not as pronounced as that of dipole modes. This implies that the extra damping observed in dipole modes is mainly caused near the inner turning point of the dipole mode cavity, which is not probed by quadrupole modes. Then, it may be relevant to investigate the radiative damping as a possible additional damping to non-radial modes after the He-core burning phase. For instance, the radiative damping causes an energy loss near the H-burning shell on the RGB. This damping experienced by dipole modes trapped in the envelope decreases as the RGB star ascends its branch, and for a RGB star of mass $M = 2\,M_\odot$ the energy loss by gravity wave emission near the H-burning shell cancels out when $\nu_{\rm max} = 28\,\mu$Hz (Dziembowski, 2012). This explains why the dipole mode visibilities increase as $\nu_{\rm max}$ decreases on the RGB (see right panel of Fig. 9.4). At the end of the He-core burning phase, dipole modes that can be observed are those that are mainly trapped in the envelope, similarly as on the RGB when $\Delta\nu \leq 4\,\mu$Hz. The physical conditions in which dipole modes develop on the AGB are similar to those on the RGB, which justifies that the radiative damping may be at work on the early-AGB.

9.3.2 Quadrupole modes

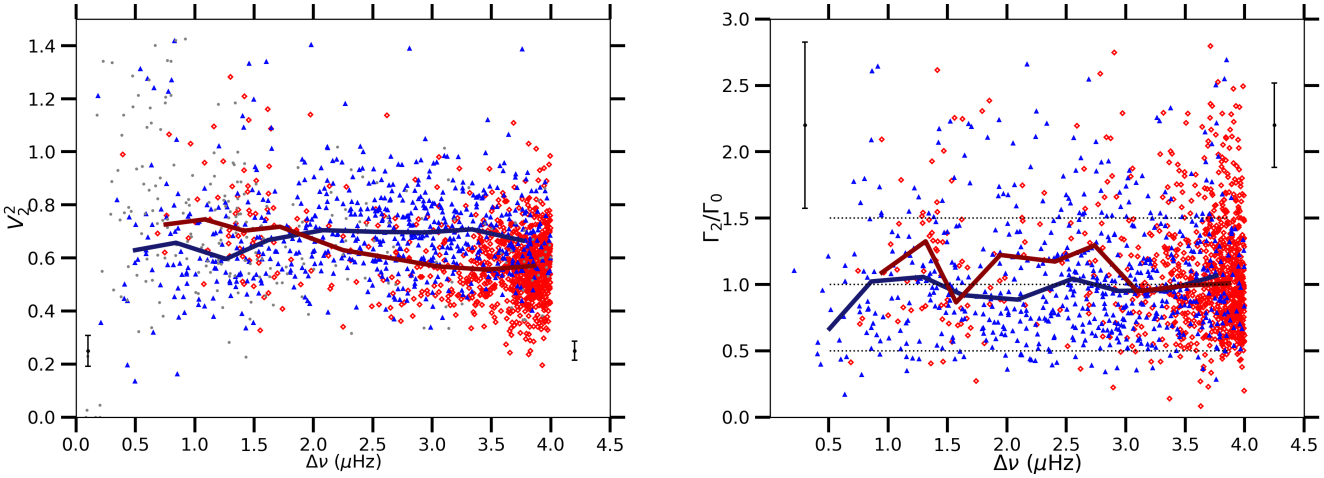

FIGURE 9.5: **Left**: Visibility of $\ell = 2$ modes as a function of $\Delta\nu$. **Right**: Ratio of the quadrupole and radial mode widths as a function of $\Delta\nu$. The mode widths are computed as the weighted mean of the three modes closest to $\nu_{\rm max}$ with the mode amplitudes used as weights. For convenience, horizontal dotted black lines are plotted at specific values of 0.5, 1.0, 1.5, and 2.0. Blue triangles, red diamonds, and grey dots correspond to RGB stars, clump/AGB stars, and stars with unidentified evolutionary stages with the methods of Mosser et al. (2019) and Kallinger et al. (2012), respectively. Mean error bars have been computed both at low $\Delta\nu$ ($\Delta\nu \leq 1.0\,\mu$Hz) and at high $\Delta\nu$ ($\Delta\nu \geq 1.0\,\mu$Hz). The thick solid lines are the median values in $0.4\,\mu$Hz wide $\Delta\nu$ bins, in dark blue for RGB stars and dark red for clump/AGB stars.

Similarly as for dipole modes, we investigate potential additional damping in quadrupole modes. In Fig. 9.5, we note that the visibility of $\ell = 2$ modes is a bit lower during the He-burning phase than during the H-shell burning phase, but remains close to the theoretical expected value $V_2^2 \sim 0.6$ (Ballot, Barban, and van't Veer-Menneret, 2011). Moreover, quadrupole modes have approximately the same width as radial modes, except for He-burning stars in the interval $\Delta\nu = [1.5, 3.0]\,\mu$Hz where quadrupole are slightly larger by an average factor of 1.25. This corresponds to the same $\Delta\nu$ interval where we report a strong dipole mode damping, but the difference between quadrupole and radial mode is not as strong as that between dipole and radial modes. The inner turning point of the $\ell = 2$ outer cavity is located closer to the surface than that of the $\ell = 1$ outer cavity. Then, $\ell = 2$ modes do not experience the damping coming from the inner layers that $\ell = 1$ modes probe. Accordingly, quadrupole modes experience a damping close to that of radial modes, both during the H-shell burning and He-burning phases.

9.4 Summary

In this chapter, we extend the seismic analysis of the p-mode oscillation spectrum led in Chapter 8 in order to understand the evolution of mode energetics in high-luminosity red giants. We measure the width, amplitude and visibility of radial and non-radial modes and study their dependence on the effective temperature $T_{\rm eff}$ and the large frequency separation $\Delta\nu$. First, we notice that the theoretical predictions of Belkacem et al. (2012) aimed at understanding the mode damping across the HR diagram totally reproduce the radial mode widths observed for RGB and clump/AGB stars. We observe the typical depression in the profile of Γ_0 as a function of the mode frequency caused by the competition between the driving and damping terms. Moreover, we also remark the strong dependence on effective temperature $\Gamma_\ell \propto T_{\rm eff}^{6-10}$ expected from theoretical predictions. These results tend to confirm that the main sources of mode damping from RGB to AGB are the action of turbulent pressure and those of the convective and radiative fluxes, which are partly compensated by the action of the dissipation rate of turbulent kinetic energy into heat.

Besides, the mode damping depends on stellar evolution. The former decreases as the star gradually evolves on its respective branch, either on the RGB or AGB. This implies that the role of turbulent pressure to mode damping is more compensated by that of the dissipation rate of turbulent kinetic energy into heat. On top of that, the structure changes between RGB and clump stars induce different surface gravities g at fixed effective temperature $T_{\rm eff}$. This difference combined with potential additional contribution to mode damping, which needs further investigation, makes the mode damping more important during the He-core burning phase compared to the H-shell burning phase. Despite the structure differences between RGB and AGB stars, the mode damping remains similar at high-luminosity stages ($\Delta\nu \leq 1.5\,\mu$Hz).

The previous paragraph is valid for modes that are strongly trapped in the envelope. This concerns radial modes regardless the evolutionary stage, and also non-radial modes when the coupling between the p- and g-mode cavity is weak, *i.e.* in high-luminosity RGB and AGB stars. In the clump and early-RGB/AGB, dipole modes are mixed so they are sensitive to the interaction between the inner and outer cavities, which adds a damping contribution. Indeed, we highlight a clear additional damping to non-radial modes, in particular for dipole modes. Dipole modes have larger widths than radial modes and low visibilities on the early-AGB. This additional damping is not as pronounced in quadrupole modes as in dipole modes, which means that the former is introduced in the innermost layers mostly probed by dipole modes. Then, the energy equipartition between modes of odd and even degrees is not fulfilled on the early-AGB. Further work is needed to identify this additional mode damping, but the similarities in the p-mode cavities of RGB and AGB stars tend to point out the radiative damping as potential candidate for this extra damping, *i.e.* energy loss by gravity waves emission near the H-burning shell.

Chapter 10

Seismic study of the AGBb

As introduced in Chapter 1, the AGBb manifests as a drop of luminosity along the AGB, causing a local excess of stars in the luminosity distribution of stellar population. Recently, such an overdensity of stars has been detected in a sample of *Kepler* stars of mass $M \in [1.3, 1.7]M_{\odot}$ and metallicity $[\mathrm{M/H}] \in [-0.4, 0.4]$dex, which allowed for a precise location of the AGBb in terms of surface luminosity L (Bossini et al., 2015). Because of the clear identification of the AGBb overdensity in the *Kepler* data, these authors could replicate the AGBb position in stellar models with a specific combination of physical ingredients. They showed that the AGBb has a strong potential to constrain stellar models, especially the mixing processes during the He-core burning phase. Nevertheless, the previous study focuses on a single bin of mass and metallicity because the number of stars observed by *Kepler* at that very moment was insufficient for a proper determination of the mass and metallicity dependence of the AGBb occurrence. Presently, on top of the about 1470-day time-series by *Kepler*, we have access to the recent observations of TESS. By combining *Kepler* and TESS data, we are able to study a sample of $\sim 4,100$ RGB and AGB stars, which allows us to investigate the mass and metallicity dependence of the AGBb location. Hereafter, we extract the AGBb spot among *Kepler* and TESS targets in several bins of mass and metallicity. We also compute models with different input physics in order to identify the combination of physical ingredients that are needed to reproduce the observed AGBb spot for all range of mass and metallicity.

The organisation of this chapter is based on the article 2. The later describes the approach to derive the AGBb position in the HR diagram and illustrates how the AGBb position can be used to constrain mixing processes in stellar interiors. Sect. 4, 5, and 6 of the attached article 2 present the dependence of the AGBb location on the stellar mass and metallicity. We investigate how the calibration of stellar models to observations changes with mass and metallicity.

10.1 Theoretical predictions of the AGBb

10.1.1 The potential of AGBb stars to be standard candles

Standard candles are astronomical sources that have a well-known luminosity due to some characteristics of a specific class of objects. The specificity of standard candles is that their apparent magnitude m_b in a given bandpass b, which can be measured in photometry, only depends on the distance d between the object and Earth through

$$m_b - \mathrm{M}_b = 5 \log \frac{d}{10\,\mathrm{pc}}, \tag{10.1}$$

where absorption is omitted, M_b is the absolute magnitude of the source in the photometric bandpass b, and d is given in parsec (pc). Here, we would like to assess the potential of the AGBb to be a suitable standard candle. To this end, we need to characterise the AGBb as a function of stellar parameters such as mass and metallicity. Since the AGBb is marked by a turning-back in the evolutionary track, the former is easily identifiable in stellar models. Therefore, the AGBb position can be extracted from tracks at different masses and metallicities. The dependence of the AGBb location on mass M and metallicity

[Fe/H] can then be predicted using stellar models. The theoretical results of Alves and Sarajedini (1999) lead to the relation

$$\log\left(\frac{L_{\rm AGBb}}{L_\odot}\right) = 1.90 + 0.215\left(\frac{M}{M_\odot}\right) - 0.155\left(\frac{M}{M_\odot}\right)\left(\frac{[{\rm Fe/H}]}{1\,{\rm dex}}\right) - 0.047\left(\frac{[{\rm Fe/H}]}{1\,{\rm dex}}\right)^2, \qquad (10.2)$$

where $\log L_{\rm AGBb}$ is the surface luminosity at the AGBb. The dependence of $\log L_{\rm AGBb}$ on M and [Fe/H] is shown in Fig. 10.1. From these theoretical results, we expect the AGBb to occur at higher luminosity for high-mass stars. Moreover, the lower the metallicity, the higher the luminosity at the AGBb. Nevertheless, the luminosity at the AGBb approximately remains constant below $[{\rm Fe/H}] \leq -1.5\,{\rm dex}$ at fixed stellar mass M. Accordingly, the luminosity of metal-poor stars at the AGBb is expected to be independent of the metallicity ($[{\rm Fe/H}] \leq -1.5\,{\rm dex}$) at fixed mass. Then, theoretical work suggests that metal-poor AGBb stars could be used as standard candles (Ferraro, 1992; Pulone, 1992). By being potential standard candles, metal-poor AGBb stars could be suitable distance indicators and asteroseismology of those stars could bring valuable constraints for astrometry.

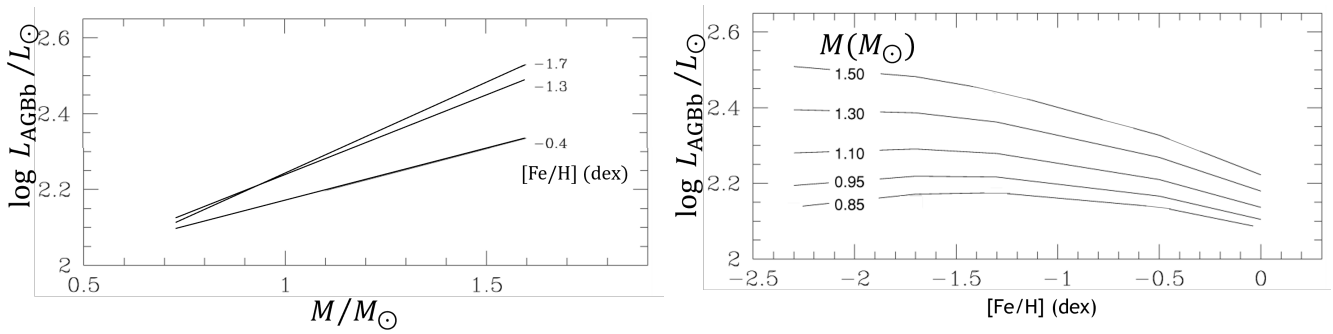

FIGURE 10.1: Theoretical models for the AGBb luminosity as a function of the mass (left) and metallicity (right). The solid lines are extracted from the analytic fit given by Eq. 10.2 to theoretical data. Credit: Alves and Sarajedini (1999)

10.1.2 The evolution speed after the He-core burning phase

The synthetic colour-magnitude diagrams computed with the models of Pulone (1992) revealed that the evolution speed is fast from the end of the He-core burning phase to the beginning of the AGBb. After inspection of the left panel of Fig. 10.2, we note that the evolution rate $|{\rm d}\nu_{\rm max}/{\rm d}\tau|$ is larger before the AGBb than after the AGBb, where τ is the stellar age, regardless the stellar mass M. This means that for the same timestep ${\rm d}\tau$, the change $|{\rm d}\nu_{\rm max}|$ is larger after the AGBb than before, hence the evolution is faster after the clump phase. This induces two effects in the observational data:

- Very few stars are observed between the end of the clump phase and the beginning of the AGBb. There is a low statistical probability to find a He-burning star between the end of the clump phase and the AGBb, and a gap is visible.
- Due to the turning-back of the evolutionary track at the AGBb and the lower evolution speed rate ${\rm d}\nu_{\rm max}/{\rm d}\tau$ at the end of the AGBb, an excess of stars is detectable at the AGBb

In their work, Bossini et al. (2015) have located the AGBb at $\log(L_{\rm AGBb}/L_\odot) = 2.2$ in the bin of mass $M \in [1.3, 1.7]M_\odot$ and metallicity $[{\rm M/H}] \in [-0.4, 0.4]$dex. In the right panel of Fig. 10.2, we assume that the AGBb spot $\log(L_{\rm AGBb}/L_\odot) = 2.2$ is the same at low mass $M \leq 1.2\ M_\odot$ and high mass $M \geq 1.2\ M_\odot$ and infer the position of the AGBb in $\nu_{\rm max}$ through [1] (Kjeldsen and Bedding, 1995)

[1] This only serves as a crude estimate of the AGBb spot in $\nu_{\rm max}$. As described in Sect. 10.1.1, we expect the AGBb location to vary with the mass, and this will be shown in the next sections.

$$\frac{\nu_{\max}}{\nu_{\max,\odot}} = \frac{M}{M_\odot}\left(\frac{L}{L_\odot}\right)^{-1}\left(\frac{T_{\rm eff}}{T_{\rm eff,\odot}}\right)^{7/2}. \tag{10.3}$$

The depletion of stars between the end of the clump phase and the AGBb can be highlighted in our sample of stars. In the right panel of Fig. 10.2, a depleted region followed by a peak is noticeable both for low-mass stars (at $\nu_{\max} \sim 8\,\mu$Hz) and for high-mass stars (at $\nu_{\max} \sim 11\,\mu$Hz). Nevertheless, the sample used in Fig. 10.2 is made of He-burning stars that have been classified by the methods of Mosser et al. (2019) and Kallinger et al. (2012). Since both identification methods are inefficient at low $\nu_{\max}$ (see Sect. 5.4), we do not have a lot of stars identified in the He-burning phase with $\nu_{\max} \leq 8\,\mu$Hz. Then, we must keep in mind that the maximum of these peaks may provide biased estimates for the AGBb location.

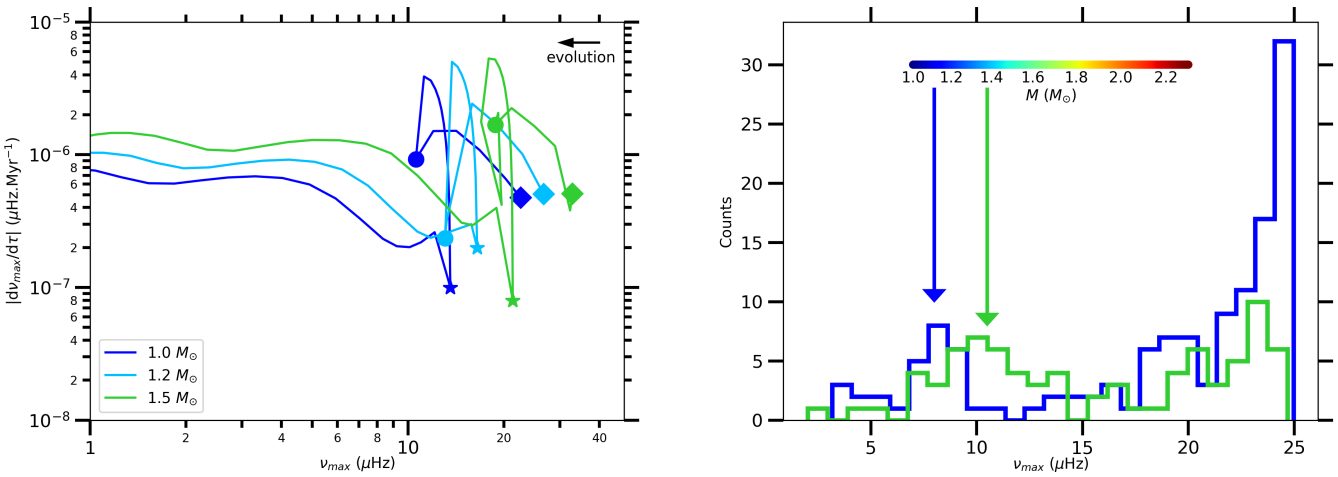

FIGURE 10.2: **Left**: absolute value of the evolution speed $|d\nu_{\max}/\tau|$ as a function of $\nu_{\max}$ after the He-core burning phase, for models that have been computed with the test suite case *1M_pre_ms_to_wd* of MESA. The end of the clump phase, the start and the end of the AGBb are marked by a diamond, a circle and a star, respectively. **Right**: histogram of the sample of He-burning stars used in the paper 1 that leave the clump phase and begin their ascent on the AGB. We show in blue the number of low-mass He-burning stars ($M \leq 1.2\,M_\odot$) and green the number of high-mass He-burning stars ($M \geq 1.2\,M_\odot$). The colour bar indicates the location of the AGBb in $\nu_{\max}$ according to Eq. 10.3 by considering $\log(L_{\rm AGBb}/L_\odot) = 2.2$ and $T_{\rm eff} = 4800\,(\nu_{\max}/40.0)^{0.06}$ (Mosser et al., 2010). The blue and green arrows roughly indicate the spot of the AGB bump respectively for low-mass stars and high-mass stars, which is characterised by a local excess of stars. From Dréau et al. (2021)

10.2 Detecting the AGBb in *Kepler* and TESS data

10.2.1 Determining the sample of stars

In order to study the AGBb, the sample of stars must be carefully selected. Indeed, the overdensity of stars caused by the turning-backs in the evolutionary tracks is small compared to the number of clump stars. According to the stellar models with initial mass $M = 1\,M_\odot$ computed with MESA, stars spend ~ 100 Myrs in the He-core burning phase compared to ~ 5 Myrs in the AGBb phase. This results in a small statistical probability to meet AGBb stars in a sample of He-burning stars. In Fig. 10.3, we can see that the He-burning *Kepler* targets are mainly dominated by clump stars around $\Delta\nu \sim 4\,\mu$Hz (equivalently $\nu_{\max} \sim 30\,\mu$Hz). However, since the overdensity of stars associated to the AGBb is well separated from the peak associated to He-core burning stars, the latter can be rejected in our final sample so that the AGBb overdensity unambiguously appears. Accordingly, we reject stars with $\Delta\nu \geq 2.7\,\mu$Hz

(equivalently $\nu_{max} \geq 22\,\mu$Hz) so that our fitting method is not impacted by the clump peak. Furthermore, we note an increasing number of stars with unidentified or uncertain identification of the evolutionary stage at $\Delta\nu \leq 2.0\,\mu$Hz. As discussed in Sect. 5.4; 8.3, this is due to the classification methods that are less efficient at low $\Delta\nu$ because they rely on stellar parameters, for example the acoustic offset ε, that are affected by large uncertainties and on the asymptotic approach that may be invalid for these stars. This inevitably reduces the number of AGB stars that we could classify. In order to avoid these complications, we decide not to reject RGB stars and keep stars regardless their evolutionary stages. Despite the presence of RGB and unclassified stars, the local excess of AGBb stars is still visible on top of the background made of RGB and He-burning stars that do not belong to the AGBb overdensity (Bossini et al., 2015). This allows us to include as many AGB stars as possible, whether they have been successfully classified or not. Classifying RGB/AGB stars is demanding because long time-series are required to extract precise seismic parameters for the stars to be confidently classified. Since our sample is no longer based on the evolutionary stage but only on ν_{max}, we can include additional RGB/AGB stars that have been recently observed by TESS, but not classified yet. Therefore, we combine the *Kepler* targets analysed in Dréau et al. (2021) with the TESS targets investigated in Mackereth et al. (2021), for which ν_{max} estimates are available.

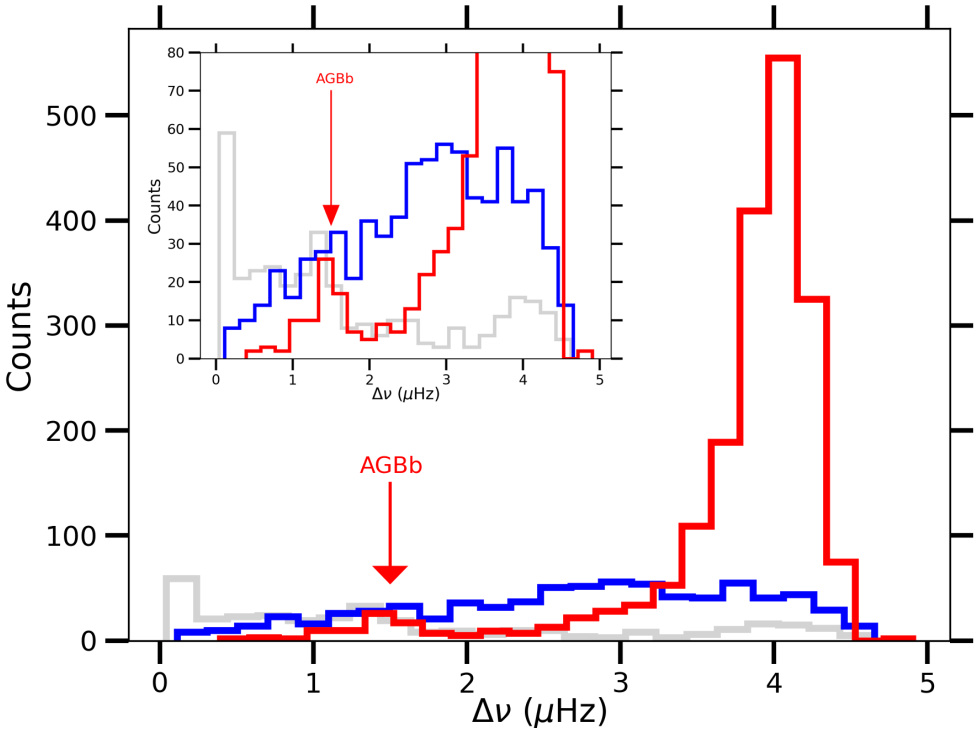

FIGURE 10.3: Distribution of the sample of stars as a function of $\Delta\nu$ used in Dréau et al. (2021), classified with the identification methods of Mosser et al. (2019) and Kallinger et al. (2012) with RGB stars in blue and clump/AGB stars in red. Stars with unidentified or uncertain evolutionary stage are shown in grey. The inset is a zoom-in portion of the large panel.

All in all, our final sample of stars is composed of $\sim 4,100$ *Kepler* and TESS targets, for which $\nu_{max} \leq 22\,\mu$Hz, regardless their evolutionary stage. As depicted by Table 1 in the publication 2, this final sample allows us to have hundreds of stars in sixteen bins of mass and metallicity, which is sufficient to detect the AGBb and study its dependence with stellar parameters.

10.2.2 Detecting the AGBb

We aim at characterising the AGBb with seismic parameters inferred from the *Kepler* and TESS oscillation spectra to bring new asteroseismic constraints on the AGBb phase. In this context, we opt for locating the AGBb with the frequency at maximum oscillation power $\nu_{\rm max}$. This choice is motivated by the close connection between the surface luminosity L and $\nu_{\rm max}$ through the scaling relation (Kjeldsen and Bedding, 1995)

$$\frac{\nu_{\rm max}}{\nu_{\rm max,\odot}} = \frac{M}{M_\odot}\left(\frac{L}{L_\odot}\right)^{-1}\left(\frac{T_{\rm eff}}{T_{\rm eff,\odot}}\right)^{7/2}. \tag{10.4}$$

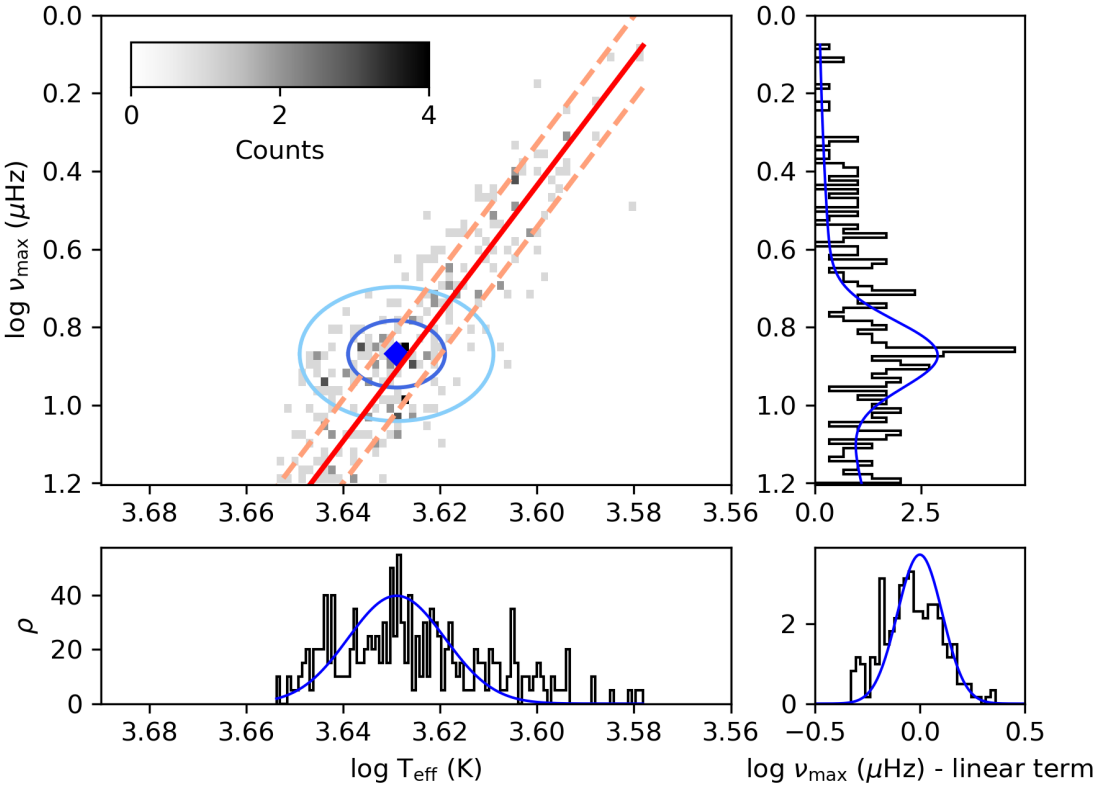

FIGURE 10.4: Probability distribution functions of our data set in the $\log T_{\rm eff} - \log \nu_{\rm max}$ plane, in the bins $M \in [0.9, 1.2] M_\odot$ and $[{\rm Fe/H}] \in [-0.25, 0.0]$ dex. **Upper left panel**: 2D histogram where the AGBb is located by a blue diamond. Dark blue and light blue ellipses correspond to the 1σ and 2σ regions of the bivariate Gaussian, respectively. The red solid line reproduces the linear term belonging to the RGB/AGB background and the pink dashed lines correspond to the normal scatter around the linear term. **Upper right panel**: the normalised 1D histogram in $\log \nu_{\rm max}$ is shown in black. The ordinate axis is the same as in the upper left panel. The blue line corresponds to the probability distribution function associated to the overdensity in $\log \nu_{\rm max}$ (see Sect. 4.1 of the article 2 for further information). **Lower left panel**: same label as in the upper right panel but in terms of $\log T_{\rm eff}$. The abscissa axis is the same as in the upper left panel. **Lower right panel**: difference between $\log \nu_{\rm max}$ and the linear term in the 2D histogram (shown by the red solid line). The blue line illustrates the normal distribution around the same linear term.

Then, we expect to characterise the overdensity of stars associated to the AGBb in $\nu_{\rm max}$, similarly as Khan et al. (2018) who could locate the RGBb with the seismic parameters $\nu_{\rm max}$ and $\Delta\nu$. To this end, we adopt the statistical mixture model presented in Hogg, Bovy, and Lang (2010). This approach is a statistical framework where the data set is assumed to be multimodal, *i.e.* with several regions of high

probability separated by regions of low probability. In this situation, we modelled the data with a mixture of several components, where each data point belongs to one of these components. We distinguish two categories, which are the foreground and background data points. The background component referred to as the RGB/AGB background sample contains stars that are ascending the RGB/AGB while the foreground component quoted AGBb sample includes AGBb stars, which are localised in the overdensity stage caused by the luminosity drop. Given these two different categories, the mixture statistical model aims at fitting the whole data set with two different models at once, one associated to the foreground and the other to the background. For illustration, the 2D histogram of our sample of RGB/AGB stars with $M \in [0.9, 1.2] M_{\odot}$ and $[\mathrm{Fe/H}] \in [-0.25, 0.0]$ dex is shown in Fig. 10.4, where the foreground is modelled by a bivariate Gaussian and the background is fitted by a normal scatter around a linear term in $\nu_{\max}$ (see Sect. 4.1 of paper 2 for the exact expression of the foreground and background components). Then, both models are weighted by a parameter, say P_{bg} for the background model and $1 - P_{\mathrm{bg}}$ for the foreground model, where P_{bg} represents the probability of a data point to belong to the RGB/AGB background. The full fitting function to reproduce the 1D and 2D histograms in $\log \nu_{\max}$ and $\log T_{\mathrm{eff}}$ is detailed in Sect. 4.1 of the paper 2. The free parameters of the model are extracted in a Bayesian approach, where the posterior probability distribution function f_{post} is generated by the prior probability f_{prior} times the mixture probability distribution function f_{mix}

$$f_{\mathrm{post}} \propto f_{\mathrm{prior}} \times f_{\mathrm{mix}}, \tag{10.5}$$

within a normalisation factor. The prior probabilities f_{prior} are chosen to be uniform for all free parameters while the mixture probability distribution is defined as

$$f_{\mathrm{mix}} = (1 - P_{\mathrm{bg}}) f_{\mathrm{biv}} + P_{\mathrm{bg}} f_{\mathrm{bg}}, \tag{10.6}$$

where f_{biv} and f_{bg} are the probability distribution functions of the foreground and background models, respectively. Then, the posterior probability distribution function is marginalised with a Markov Chain Monte-Carlo (MCMC) sampler. The MCMC algorithm generates random walkers in the parameter space that draw a representative set of samples from the posterior probability distribution function. Once the samples are computed, the marginal probability distribution of a given parameter X can be approximated by the histogram of the samples projected into the parameter subspace of all possible X. The average value of X as well as its dispersion can then be extracted from these histograms, assuming that the posterior probability distribution function f_{post} correctly describes the distribution of the data set. Before accepting the outputs of the fitting process, we check that the walkers that explore the parameter space converge for all free parameters. We make sure that the outputs are consistent with the 1D and 2D histograms, as depicted by Fig. 10.4. Among the sixteen bins of mass and metallicity, we could not extract the AGBb parameters for $M \in [0.6, 0.9] M_{\odot}$ and $[\mathrm{Fe/H}] \in [0.0, 0.25]$dex because we lack some stars to properly fit the AGBb overdensity and the RGB/AGB background.

10.3 Can AGBb stars be standard candles?

In Sect. 5.1 of the article 2, we analyse in detail the dependence of the AGBb location on stellar mass and metallicity. They are depicted in Fig. 10.5. To summarise, the higher the mass, the lower the frequency $\nu_{\max}$ (equivalently, the higher the luminosity), and the lower the effective temperature. This dependence in $\log \nu_{\max}$ is clear since the variation of the AGBb location with the mass is larger than the typical uncertainty with which we extract the AGBb spot. Moreover, the dependence of the AGBb position on mass is less important at high metallicity $[\mathrm{Fe/H}] \geq 0.0$ dex. Thus, these observations confirm the theoretical results of Alves and Sarajedini (1999) shown in Fig. 10.1. In $\log T_{\mathrm{eff}}$, a larger sample of stars is desirable to confirm or infirm the dependence of the AGBb location on stellar mass because of large uncertainties. Since the frequency at maximum oscillation power $\nu_{\max}$ during the clump phase is higher for high-mass stars (Bedding et al., 2011; Stello et al., 2013; Mosser et al., 2014), our observations show that the $\nu_{\max}$ difference between clump and AGBb stars increases with the mass.

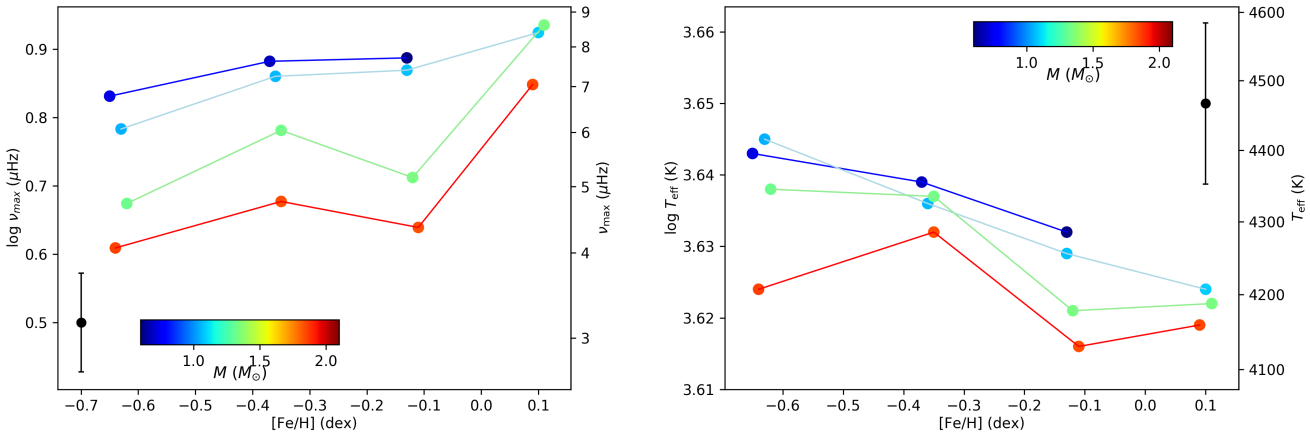

FIGURE 10.5: Location of the AGBb in $\log \nu_{max}$ (**left**) and in $\log T_{eff}$ (**right**) from observations, as a function of the metallicity [Fe/H]. The AGBb occurrence is marked by dots and the stellar mass is colour-coded. AGBb spots obtained in the same bin of mass $M \in [0.6, 0.9]$, $[0.9, 1.2]$, $[1.2, 1.5]$, $[1.5, 2.5] M_\odot$ are connected by dark blue, light blue, light green, and red lines, respectively. Mean error bars on the position of the AGBb in $\log \nu_{max}$ and in $\log T_{eff}$ are shown in black. Data in the bin ($M \in [0.6, 0.9] M_\odot$, [Fe/H]$\in [0, 0.25]$ dex) are not shown because there are not enough stars to perform the statistical mixture analysis. From Dréau et al. (2022)

In parallel, we observe some variations of the AGBb spot with [Fe/H] for metal-rich stars ([Fe/H] ≥ -0.5 dex), which is especially remarkable for stars of mass $M \geq 1.2\, M_\odot$. The higher the metallicity, the higher the frequency ν_{max} (equivalently, the lower the luminosity). Although we observe a smooth increase of $\log \nu_{max}$ with [Fe/H] for stars of mass $M \leq 1.2\, M_\odot$, this behaviour seems weaker for low-mass stars. These observations are in agreement with the theoretical results of Alves and Sarajedini (1999) shown in Fig. 10.1. This tends to show that the luminosity of metal-rich stars ([Fe/H] ≥ -0.5 dex) varies with metallicity, hence the apparent magnitude m_b may not only depend on the distance d between the star and Earth as depicted by Eq. 10.1, but also on metallicity at fixed stellar mass. Using metal-rich stars in the AGBb phase as standard candles may be questionnable since Eq. 10.1 is subject to metallicity biases. However, our work is essentially based on stars with [Fe/H] ≥ -1.0 dex since too few metal-poor stars with [Fe/H] ≤ -1.0 dex have been subject to an asteroseismic study with the *Kepler* and TESS missions. Initially, the potential of AGBb stars as standard candles was highlighted for metal-poor stars with [Fe/H] $\in [-2.0, -0.65]$ dex (Ferraro, 1992; Pulone, 1992). In the right panel of Fig. 10.1, we indeed notice that the luminosity at the AGBb remains approximately constant when [Fe/H] ≤ -1.0 dex (respectively [Fe/H] ≤ -1.5 dex) for stars of mass $M \leq 1.1\, M_\odot$ (respectively $M \geq 1.3\, M_\odot$). Further asteroseismic observations of metal-poor AGB stars are needed to expand the seismic characterisation of the AGBb at low metallicity. Meanwhile, Yu et al. (2022) derived the stellar radius R and luminosity L of about 1.5 million stars for which spectroscopic estimates of the effective temperature T_{eff} are available. Many low-metallicity AGB stars are expected to be present in this sample, as illustrated by Fig. 10.6. Then, the next step is to extract the position of the AGBb in $\log L$ or $\log R$ at low metallicity [Fe/H] ≤ -0.5 dex and conclude about the potential of metal-poor AGBb stars as standard candles.

10.4 Constraining the physical ingredients with the AGBb

10.4.1 Method

Since the AGBb is identified at a specific position in $\log \nu_{max}$ and $\log T_{eff}$, the AGBb event can be used as a constraint for stellar models. Indeed, the AGBb is easily identifiable since it manifests as a turning-back of the evolutionary track in stellar models after the He-core burning phase. By choosing a specific set of physical ingredients, we can replicate the observed AGBb location with models. Accordingly, we

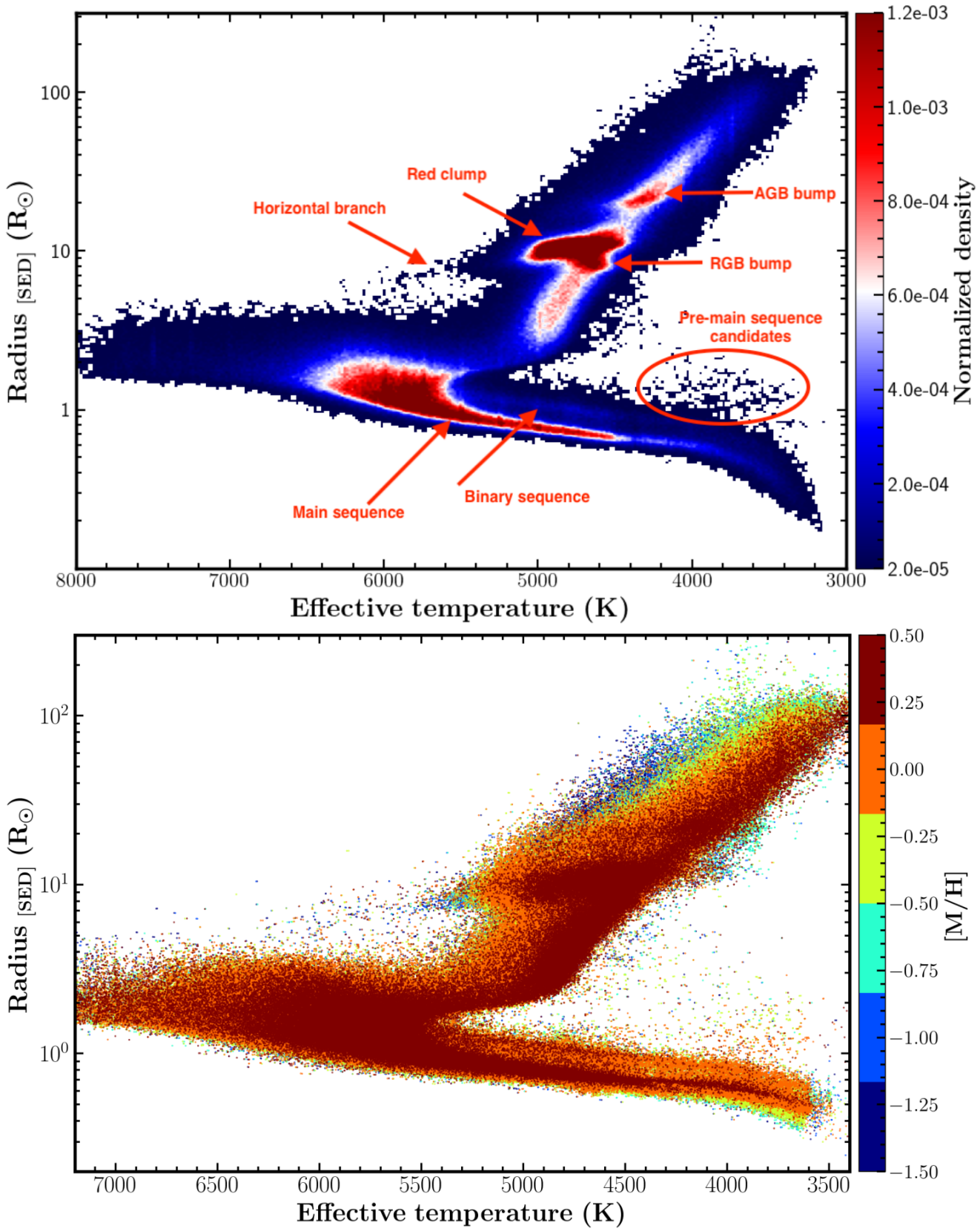

FIGURE 10.6: Radius estimates derived from spectral energy distribution (SED) fitting as a function of the effective temperature. **Top:** the normalised number density is colour-coded. Some key events of stellar evolution are highlighted. **Bottom:** the metallicity is colour-coded. Credit: Yu et al. (2022)

aim at identifying the physical ingredients that would allow us to reproduce the observed AGBb spot.

In Fig. 10.4, the most obvious signature of the AGBb is the overdensity of stars in the 1D histograms. With a large sample of stars, these histograms give us an approximation of the probability of finding a star at a given $\log \nu_{\max}$ or $\log T_{\rm eff}$. In order to evaluate how far the models are able to replicate observations, we compute the probability density function $\mathrm{PDF}_{M,[\mathrm{Fe/H}]}(x)$ of finding a model of mass M and metallicity [Fe/H] at a given $x = \log \nu_{\max}$ or $\log T_{\rm eff}$. Actually, the additional time spent by a star in the AGBb phase due to the turning-back in the evolutionary track leads to an increased probability to find a star in the AGBb phase. So the AGBb is identifiable by the increased time spent in the evolutionary track after the He-core burning phase. The probability density function $\mathrm{PDF}_{M,[\mathrm{Fe/H}]}(x)$ can be inferred by computing the fractional time $\delta\tau_{M,[\mathrm{Fe/H}]}(x)$ that is spent in a given bin of $x = \log \nu_{\max}$ or $\log T_{\rm eff}$. To this end, we cut the evolutionary track from the RGB up to the AGB in several bins of $\log \nu_{\max}$ or $\log T_{\rm eff}$ (see Fig. 10.7).

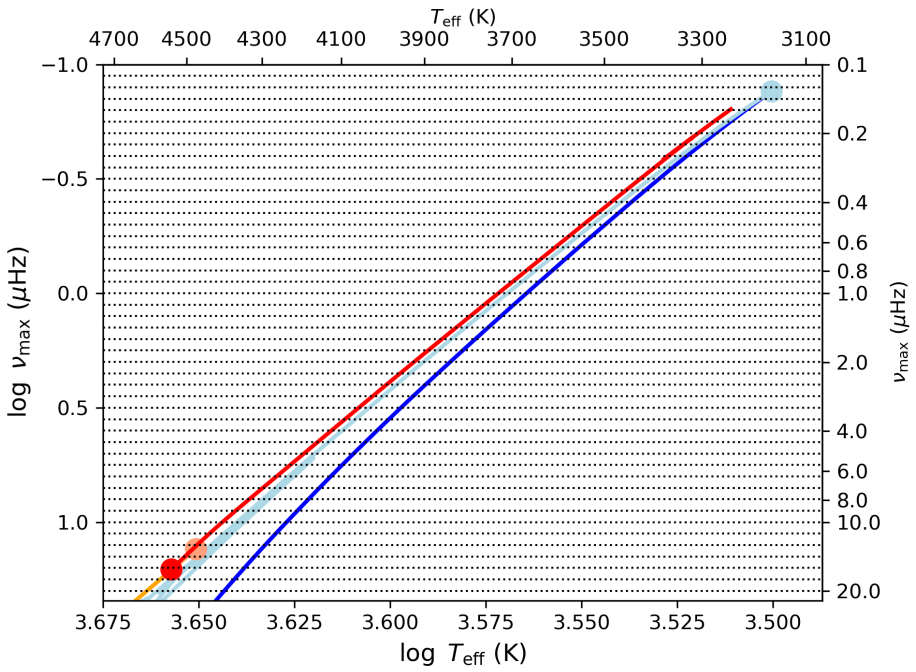

FIGURE 10.7: Evolutionary track of the reference model defined in Table 10.1 at mass $M = 1\,M_\odot$ and solar metallicity in the plane $\log T_{\rm eff} - \log \nu_{\max}$. The blue and red solid lines are the RGB and AGB, respectively. The light blue solid line is the evolutionary track between the luminosity tip of the RGB (light blue dot) and the He-core burning phase. The AGBb is delimited by the pink dot (start) and dark red dot (end). The horizontal dotted lines delimit the bins of $\log \nu_{\max}$ that are used to compute the fractional time $\delta\tau_{M,[\mathrm{Fe/H}]}(\log \nu_{\max})$ spent in those bins. We omit the binning in $\log T_{\rm eff}$ for clarity, but the procedure is similar as for $\log \nu_{\max}$.

Then, the fractional time $\delta\tau_{M,[\mathrm{Fe/H}]}(x)$ is simply taken as the sum of the timesteps between consecutive models, for which x is contained in a specific bin. The probability density function $\mathrm{PDF}_{M,[\mathrm{Fe/H}]}$ is obtained by normalising this fractional time by the total time spent by the star on its evolutionary track

$$\mathrm{PDF}_{M,[\mathrm{Fe/H}]}(x) = \frac{\delta\tau_{M,[\mathrm{Fe/H}]}(x)}{\sum_{x'=x_{\min}}^{x_{\max}} \delta\tau_{M,[\mathrm{Fe/H}]}(x')}, \tag{10.7}$$

where x can be $\log \nu_{\max}$ or $\log T_{\rm eff}$. Since Eq. 10.7 is defined for one combination of mass M and metallicity [Fe/H], $\mathrm{PDF}_{M,[\mathrm{Fe/H}]}$ is not directly comparable to observations. The 1D histograms are observed for stars with different masses and metallicity in a given bin, so the probability distribution function must be averaged with several evolutionary tracks obtained at different masses and metallicities. Then, the average probability distribution function PDF to be compared with observations is computed as the

sum of all individual $\mathrm{PDF}_{M,[\mathrm{Fe/H}]}(x)$, for which the mass M and metallicity [Fe/H] are contained in the considered bin. We have

$$\mathrm{PDF}(x) = \frac{1}{A_{\mathrm{norm}}} \sum_{M,[\mathrm{Fe/H}]} \mathrm{PDF}_{M,[\mathrm{Fe/H}]}, \tag{10.8}$$

where A_{norm} is a normalisation factor. In the sample of *Kepler* and TESS stars, the mass is not uniformly distributed between 0.8 $M_\odot$ and 2.5 $M_\odot$, *i.e.* we do not have as many low-mass stars as high-mass stars. When computing the probability distribution function PDF, we do not take the observed mass and metallicity distributions into account and we assume that they are uniformly distributed. This treatment could be improved, but we checked that the inferred AGBb peak in $\log \nu_{\mathrm{max}}$ and $\log T_{\mathrm{eff}}$ are consistent with the location of the turning-back in the evolutionary tracks. An example of PDF computed for the reference model (defined in Sect. 10.4.2) in the bin $M \in [0.9, 1.2]M_\odot$ and [Fe/H] $\in [-0.25, 0.0]$dex is shown in Fig. 10.8. In the left panel, we see that the local maximum of PDF associated to the AGBb does not match the observed AGBb overdensity. Our goal is to make the observations and models overlap by changing the physical parameters of the model, as illustrated in the right panel of Fig. 10.8. This procedure allows us to study the impact of the physical parameters on the AGBb location.

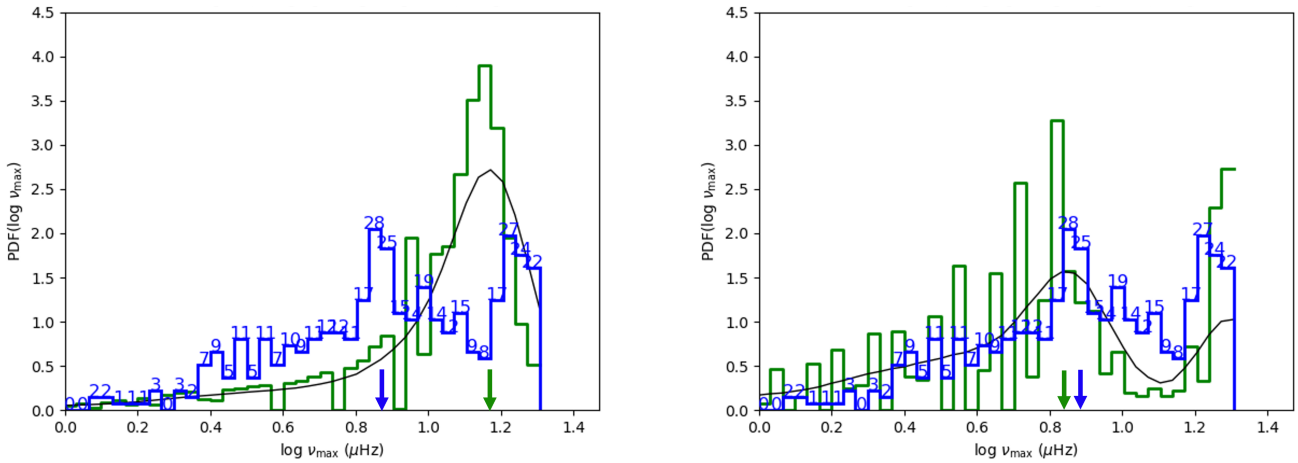

FIGURE 10.8: Distribution of $\log \nu_{\mathrm{max}}$ in the bins of mass $M \in [0.9, 1.2]M_\odot$ and metallicity [Fe/H] $\in [-0.25, 0.0]$dex. The 1D histograms extracted from observations are indicated in blue, while the probability density functions extracted from models are shown in green. The number of stars per bin from observations is written in blue on top of the histogram while the black thin line is the convolution between PDF from Eq. 10.8 and a Gaussian function. The arrows show the AGBb location in $\log \nu_{\mathrm{max}}$ from observations in blue and stellar models in green. **Left:** The model 1D histogram is obtained with the reference model defined in Table 10.1 and associated to the evolutionary track in Fig. 10.7. **Right:** Same as left figure but the model 1D histogram is obtained by adding He-core overshooting. The overshooting parameter is $\alpha_{\mathrm{ov,He}} = 0.5$.

10.4.2 Reproducing the AGBb overdensity with stellar models

In the following, we define a reference model with a specific set of physical parameters (see Table 10.1). Individual changes are brought to the reference model to inspect how physical parameters affect the AGBb position. A thorough analysis of the sensitivity of the AGBb location to physical parameters is presented in Sect. 5 and 6 of the publication 2. To sum up, we highlight that the reference model in absence of mixing processes is not able to recreate the AGBb spot both in $\log \nu_{\mathrm{max}}$ and $\log T_{\mathrm{eff}}$, whatever the stellar mass and metallicity considered. As examined by Bossini et al. (2015), an additional mixing region above the convective core of He-core burning stars is required to reproduce the observed AGBb luminosity. These authors calibrated the extent of the He-core overshooting region in fraction of the pressure scale height H_P and found 0.5 H_P for the specific mass and metallicity domain, defined by $M \in [1.3, 1.7]M_\odot$ and [M/H] $\in [-0.4, 0.4]$dex. Here, we extend their work to a broader range of

masses and metallicities in order to explore how the calibration of those mixing processes varies with these stellar parameters.

TABLE 10.1: Specifications of the MESA reference model

Y_0	$\alpha_{\rm MLT}$	η_R	$\alpha_{\rm ov,H}$	$\alpha_{\rm ov,He}$	$\alpha_{\rm ov,env}$	$\alpha_{\rm th}$	$\Omega_{\rm ZAMS}/\Omega_{\rm crit}$
0.253	1.92	0.3	0.2	0	0	0	0

Notes: Y_0 is the initial helium mass fraction; $\alpha_{\rm MLT}$ is the mixing length parameter; η_R is the Reimers' scaling factor for the mass loss prescription on the RGB in Eq. 2.8; $\alpha_{\rm ov,H}$, $\alpha_{\rm ov,He}$, and $\alpha_{\rm ov,env}$ are the H-core overshooting, He-core overshooting, and envelope undershooting parameters, respectively, in units of H_P; $\alpha_{\rm th}$ is the efficiency of thermohaline convection following Eq. 6.6; $\Omega_{\rm ZAMS}/\Omega_{\rm crit}$ is the ratio between the angular velocity at the ZAMS and the surface critical angular velocity for the star to be dislocated. These physical ingredients are described in details in Chapter 6.

Stars of mass $M \leq 1.5\,M_\odot$

Adding He-core overshooting to the reference model is sufficient to recreate observations of low-mass stars. Different He-core overshooting parameters are needed depending on the mass. For instance, $\alpha_{\rm ov,He} \in [0.25, 0.50]$ satisfyingly reproduces the AGBb position in $\log \nu_{\rm max}$ in the mass bin $M \in [0.6, 1.2]\,M_\odot$ while $\alpha_{\rm ov,He} \in [0.5, 1.0]$ is more appropriate for $M \in [1.2, 1.5]M_\odot$. Then, the AGBb can be used to constrain mixing processes taking place in the He-core burning phase, as presented in Bossini et al. (2015). However, we do not exactly replicate the observed AGBb position simultaneously in $\log \nu_{\rm max}$ and $\log T_{\rm eff}$ with He-core overshooting only. We find that modifying the mixing length parameter $\alpha_{\rm MLT}$ mainly shifts the AGBb position along the $\log T_{\rm eff}$ axis. Indeed, by decreasing $\alpha_{\rm MLT}$ the energy transport via convection in the envelope is less efficient, then the stellar radius increases and the effective temperature decreases. According to the scaling relation

$$\frac{\nu_{\rm max}}{\nu_{\rm max,\odot}} = \frac{M}{M_\odot}\left(\frac{R}{R_\odot}\right)^{-2}\left(\frac{T_{\rm eff}}{T_{\rm eff,\odot}}\right)^{-1/2}, \tag{10.9}$$

increasing the radius R and decreasing the effective temperature $T_{\rm eff}$ simultaneously has limited effect on $\nu_{\rm max}$. Then, adjusting $\alpha_{\rm MLT}$ mainly shifts the evolutionary track in $\log T_{\rm eff}$, which can help to match the effective temperature at the AGBb in stellar models with the observed value.

Stars of mass $M \geq 1.5\,M_\odot$

Adding He-core overshooting to the reference model alone does not allow us to match observations with models for stellar masses above $1.5\,M_\odot$. In fact, a large overshooting parameter $\alpha_{\rm ov,He} = 2.0$ could help us to diminish the differences in $\log \nu_{\rm max}$, but such value would induce an extra mixing region that is clearly larger than the convective core. Currently, we do not have theoretical arguments to justify such strong He-core overshooting. Accordingly, we investigate other sources of mixing. We find that the mixing processes taking place in the envelope (envelope undershooting and thermohaline mixing as described in Chapter 6) insignificantly impact the AGBb location. Then, we focus on the mixing produced near the core.

In stars of mass $M \geq 1.2\,M_\odot$, the convective core is sufficiently developed to enable H-core overshooting during the main sequence. By combining high He-core overshooting $\alpha_{\rm ov,He} = 1.0$ and H-core overshooting $\alpha_{\rm ov,H} = 0.6$, we could match observations with models. However, this H-core overshooting appears to be too large considering that $0.2\,H_P$ is the maximum extent of the extra mixing region when $M \leq 2.5\,M_\odot$ according to the observed properties of eclipsing binaries (*e.g.* Claret and Torres,

2016; Claret and Torres, 2017; Claret and Torres, 2018; Claret and Torres, 2019) and the seismic constraints provided by $\ell = 1$ modes of main-sequence stars (Deheuvels et al., 2016). Such a maximum extent is also supported by recent theoretical predictions based on 3D numerical hydrodynamics simulations of penetrative convection (Anders et al., 2022; Jermyn et al., 2022).

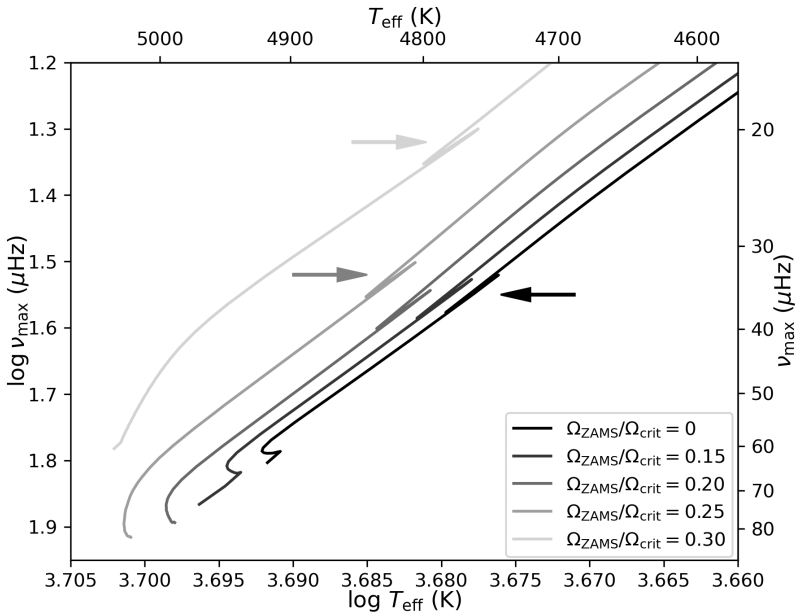

FIGURE 10.9: Evolutionary tracks from the clump phase up to the AGB for 2 $M_\odot$ models at solar metallicity with different rotation rates during the main sequence. The input physics is that indicated in Table 10.1, but we disable H-core overshooting and add rotation rate as indicated on the figure. The lighter the colour, the larger the rotation rate. The arrows indicate the AGBb turning-backs.

Finally, we study the influence of rotation, which creates transport of chemicals and angular momentum throughout the star. The rotational mechanisms responsible for mixing and the prescription adopted in MESA for rotation are presented in Chapter 6. Initially, we tested the rotation rate $\Omega_{\rm ZAMS}/\Omega_{\rm crit} = 0.3$ from the ZAMS up to the AGB, which is motivated by observations of B stars (Huang, Gies, and McSwain, 2010). This value is equivalent to having a surface rotational velocity of $v_{\rm eq,ZAMS} = 145\,{\rm km.s^{-1}}$ for a ZAMS star of mass $M = 2.0\,M_\odot$ at solar metallicity. However, we noticed that the turning-back shape of the AGBb in the evolutionary track is then noisy. We also remarked that the position of the AGBb turning-back does not change if rotation is included during main sequence only. Therefore, we apply rotation during the main sequence only. In that case, the surface rotational velocity at the TAMS is $v_{\rm eq,TAMS} = 140\,{\rm km.s^{-1}}$ for a 2 $M_\odot$ star at solar metallicity, which corresponds to a rotation rate[2] $\Omega_{\rm TAMS}/\Omega_{\rm crit} = 0.45$. These rotation rates are consistent with those obtained in the stellar grids of Ekström et al. (2012). By considering rotation during the main sequence with a rate $\Omega_{\rm ZAMS}/\Omega_{\rm crit} = 0.3$ at the ZAMS, we note that rotationally-induced mixing has similar effects as He-core overshooting on the AGBb value of $\nu_{\rm max}$. By combining rotation with a high He-core overshooting $\alpha_{\rm ov,He} = 1.0$ we are able to replicate the AGBb location in $\nu_{\rm max}$. This suggests that several mixing processes must be simultaneously considered in order to reproduce the observed AGBb spot when $M \geq 1.5\,M_\odot$. Nonetheless, we point out that the shift of the AGBb location induced by rotation is visible only with a rotation rate $\Omega_{\rm ZAMS}/\Omega_{\rm crit} \geq 0.25$. Indeed, the AGBb location is not impacted when considering a rotation rate $\Omega_{\rm ZAMS}/\Omega_{\rm crit} = 0.2$. In parallel, we note that the envelope abundance mass fractions of H and He are not modified from the ZAMS up to the TAMS when setting $\Omega_{\rm ZAMS}/\Omega_{\rm crit} = 0.2$,

[2] the surface critical angular velocity decreases as the star reaches the TAMS, which explains why $\Omega/\Omega_{\rm crit}$ is higher at the TAMS than at the ZAMS

but they significantly change with $\Omega_{\rm ZAMS}/\Omega_{\rm crit} = 0.3$ (Fig. 10.10). Consequently, the capability of rotation to affect the AGBb location can be attributed to the potential of the rotationally-induced mixing to bring additional chemicals from the core to the envelope.

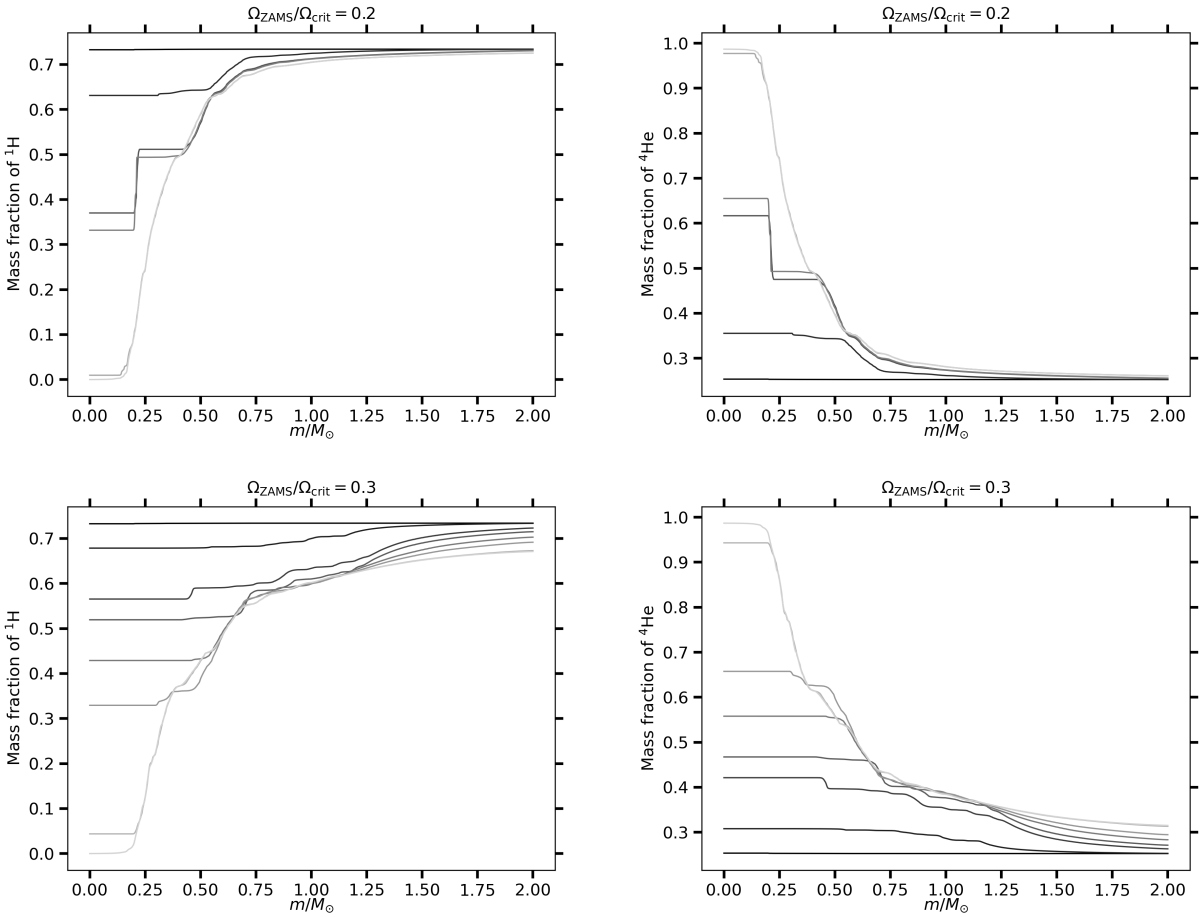

FIGURE 10.10: Profiles of the abundance mass fractions of ^{1}H and ^{4}He as a function of the mass coordinate in the interior ($m/M_\odot = 0$ is the centre). The solid lines are associated to distinct stages in the H-core burning process. The darker the colour, the closer to the ZAMS the star is. Conversely, the lighter the colour, the closer to the TAMS the star is. **Top**: we consider the reference MESA model defined in Table 10.1, we disable H-core overshooting and we adopt a rotation rate $\Omega_{\rm ZAMS}/\Omega_{\rm crit} = 0.2$. **Bottom**: same as the top panels but we take the rotation rate $\Omega_{\rm ZAMS}/\Omega_{\rm crit} = 0.3$.

It is noteworthy that this work remains exploratory since we mainly identify the physical parameters needed to recreate the observed AGBb in $\log \nu_{\rm max}$ with stellar models. In fact, we do not precisely quantify the weights of these physical parameters required to reproduce the AGBb position in $\log \nu_{\rm max}$ and $\log T_{\rm eff}$ for all bins of mass and metallicity. We only provide rough estimates of these physical parameters depending on the stellar mass. In stars of mass $M \leq 1.2\,M_\odot$, the convective core is either absent or very small, which explains why H-core overshooting has small impact at low mass. Moreover, magnetic braking is not implemented in MESA, which would be necessary to reproduce slow rotation rates of low-mass stars (Kawaler, 1988). Then, we could not explore the effects of rotationally-induced mixing in stars of mass $M \leq 1.5\,M_\odot$.

All the physical ingredients considered here not only influence the AGBb position but also other key events of stellar evolution. Several observational parameters could be employed simultaneously to constrain physical parameters with better precision. Theoretical models report a weak dependence of the luminosity ratio between the AGBb and red clump phase on metallicity and initial helium abundance

(Castellani, Chieffi, and Pulone, 1991; Bono et al., 1995). Then, combining the position of the clump phase in $\log \nu_{\rm max}$ and $\log T_{\rm eff}$ with that of the AGBb could help to improve the calibration of physical ingredients. In Appendix B inserted in article 2, we explore how physical parameters impact the $\nu_{\rm max}$ ratio between the AGBb and clump phase. We remark that mainly He-core overshooting modifies this $\nu_{\rm max}$ ratio, which suggests that the $\nu_{\rm max}$ difference between the AGBb and clump phase is affected. For stars of mass $M \geq 1.5\,M_{\odot}$, we saw that mixing processes such as H-core overshooting and rotationally-induced mixing impact the $\nu_{\rm max}$ and $T_{\rm eff}$ at the AGBb. In parallel, we report that the $\nu_{\rm max}$ ratio between AGBb and clump phase do not change after adding these mixing processes. This implies that these input physics not only impacts the AGBb position but also that of the clump phase. This illustrates the potential of using several observational features to accurately quantify the relevance of physical ingredients in stellar models, which have crucial impact on the evolution of stars up to the white dwarf stage as introduced in Sect. 2.6.

10.5 Summary

The observations of *Kepler* can be handled to extract the seismic characteristics of AGBb stars. In particular, the AGBb luminosity (equivalently $\nu_{\rm max}$) could be extracted from these observations (Bossini et al., 2015). Nevertheless, the sample of *Kepler* stars was not sufficient to infer the AGBb position in $\nu_{\rm max}$ in several bins of mass and metallicity, preventing us from following the dependence of the AGBb value of $\nu_{\rm max}$ on stellar parameters. Now, studying the mass and metallicity dependence of the AGBb luminosity is possible with the additional seismic observations of TESS. Here, we combine *Kepler* and TESS observations, which allows us to gather more than 4,100 RGB and AGB stars where the AGBb can be detected. We highlight a fast evolution between the end of the He-core burning phase and the AGBb, leading to a weakly populated region between these events. Similarly as in the work done for studying the RGBb (Khan et al., 2018), we characterise the AGBb in the plane $\log T_{\rm eff} - \log \nu_{\rm max}$ in fifteen distinct bins of mass and metallicity with the statistical model of Hogg, Bovy, and Lang (2010).

First, we notice that the AGBb occurs at lower $\nu_{\rm max}$ (equivalently higher luminosity) and lower $T_{\rm eff}$ for high-mass stars, in agreement with theoretical results (Alves and Sarajedini, 1999). This suggests that the $\nu_{\rm max}$ difference between clump and AGBb stars increases with mass. Second, we report metallicity effects on the AGBb spot in $\log \nu_{\rm max}$ for stars of metallicity $[{\rm Fe/H}] \in [-1.0, 0.25]$dex, which are particularly notable at high mass $M \geq 1.2\,M_{\odot}$. The higher the metallicity, the higher the $\nu_{\rm max}$ (equivalently the lower the luminosity) at the AGBb. This implies that the luminosity of AGBb stars with $[{\rm Fe/H}] \in [-1.0, 0.25]$dex varies with stellar parameters, so does their apparent magnitude. Accordingly, using AGBb stars as standard candles may be questionable if $[{\rm Fe/H}] \geq -1.0$ dex. Nevertheless, the AGBb luminosity is expected to be independent of the metallicity for metal-poor stars with $[{\rm Fe/H}] \leq -1.0$ dex (Ferraro, 1992; Pulone, 1992). To address this concern, further work is dedicated to detect the AGBb in the luminosity distribution of metal-poor stars derived from spectral energy distribution fitting (Yu et al., 2022).

Finally, we show that He-core overshooting is needed to reproduce the AGBb location in $\log \nu_{\rm max}$ for any mass $M \in [0.6, 2.5]M_{\odot}$ and metallicity $[{\rm Fe/H}] \in [-1.0, 0.25]$dex, as initially highlighted by Bossini et al. (2015) in stars of mass $M \in [1.3,\ 1.7]M_{\odot}$ and metallicity $[{\rm M/H}] \in [-0.4,\ 0.4]$dex. Precisely, $\alpha_{\rm ov,He} \in [0.25, 0.50]$ is adapted to reproduce the AGBb position in $\log \nu_{\rm max}$ in the mass bin $M \in [0.6, 1.2]M_{\odot}$ while $\alpha_{\rm ov,He} \in [0.5, 1.0]$ is more appropriate for $M \in [1.2, 1.5]M_{\odot}$. Yet, He-core overshooting alone cannot recreate the AGBb location in $\log \nu_{\rm max}$ for stars of mass $M \in [1.5, 2.5]M_{\odot}$. Additional mixing processes are needed to match models with observations. For instance, we identify that rotationally-induced mixing during the main sequence combined with He-core overshooting is able to replicate the $\log \nu_{\rm max}$ at the AGBb. This work remains exploratory and additional work is required to quantify the weight of those mixing processes in stellar models, for example by considering other observational constraints such as the clump stage position.

Astronomy & Astrophysics manuscript no. output
July 27, 2022

Characterising the AGB bump and its potential to constrain mixing processes in stellar interiors

G. Dréau[1], Y. Lebreton[1,2], B. Mosser[1], D. Bossini[3], J. Yu[4]

[1] LESIA, Observatoire de Paris, PSL Research University, CNRS, Université Pierre et Marie Curie, Université Paris Diderot, F-92195 Meudon, France
email: Guillaume.Dreau@obspm.fr
[2] Univ Rennes, CNRS, IPR (Institut de Physique de Rennes) - UMR 6251, F-35000 Rennes, France
[3] Instituto de Astrofísica e Ciências do Espaço, Universidade do Porto, CAUP, Rua das Estrelas, PT4150-762 Porto, Portugal
[4] Max Planck Institute for Solar System Research, Justus-von-Liebig-Weg 3, D-37077 Göttingen, Germany

Preprint online version: July 27, 2022

ABSTRACT

Context. In the 90's, theoretical studies motivated the use of the asymptotic-giant branch bump (AGBb) as a standard candle given the weak dependence between its luminosity and stellar metallicity. Because of the small size of observed asymptotic-giant branch (AGB) samples, detecting the AGBb is not an easy task. However, this is now possible thanks to the wealth of data collected by the CoRoT, *Kepler*, and TESS space-borne missions.
Aims. It is well-known that the AGB bump provides valuable information on the internal structure of low-mass stars, particularly on mixing processes such as core overshooting during the core He-burning phase. Here, we investigate the dependence with stellar mass and metallicity of the calibration of stellar models to observations.
Methods. In this context, we analysed $\sim$ 4,000 evolved giants observed by *Kepler* and TESS, including red-giant branch (RGB) stars and AGB stars, for which asteroseismic and spectrometric data are available. By using statistical mixture models, we detected the AGBb both in frequency at maximum oscillation power $\nu_{\rm max}$ and in effective temperature $T_{\rm eff}$. Then, we used the Modules for Experiments in Stellar Astrophysics (MESA) stellar evolution code to model AGB stars and match the AGBb occurrence with observations.
Results. From observations, we could derive the AGBb location in 15 bins of mass and metallicity. We noted that the higher the mass, the later the AGBb occurs in the evolutionary track, which agrees with theoretical works. Moreover, we found a slight increase of the luminosity at the AGBb when the metallicity increases. By fitting those observations with stellar models, we noticed that low-mass stars ($M \leq 1.0 M_{\odot}$) require a small core overshooting region during the core He-burning phase. This core overshooting extent increases toward high mass, but above $M \geq 1.5 M_{\odot}$ we found that the AGBb location cannot be reproduced with a realistic He-core overshooting alone, and instead additional mixing processes have to be invoked.
Conclusions. The observed dependence on metallicity complicates the use of the AGBb as a standard candle. Moreover, different mixing processes may occur according to the stellar mass. At low mass ($M \leq 1.5 M_{\odot}$), the AGBb location can be used to constrain the He-core overshooting. At high mass ($M \geq 1.5 M_{\odot}$), an additional mixing induced for instance by rotation is needed to reproduce observations.

Key words. asteroseismology – stars: oscillations – stars: interiors – stars: evolution – stars: late-type – stars: AGB and post-AGB

1. Introduction

The asymptotic-giant branch (AGB) is a key stage of stellar evolution that can be used to constrain both the stellar structure and environment. On the one hand, observations of circumstellar CO line emission and stellar light scattered by dust in circumstellar envelopes allow us to estimate the mass-loss rate on the AGB, which is crucial to understand the final stages of stellar evolution and the metal enrichment in the interstellar medium, hence the chemical enrichment of galaxies (e.g. Knapp et al. 1998; Mauron & Huggins 2006; Ramstedt et al. 2008; McDonald et al. 2018; McDonald & Trabucchi 2019). On the other hand, the AGB provides valuable constraints for stellar interiors with the help of stellar models (Bossini et al. 2015). Current stellar models suffer from systematic uncertainties due to our limited understanding of physical processes in stellar interiors. Particularly, constraining mixing processes in advanced burning stages is demanding because it requires to implement helium semiconvection to take into account the additional helium captured by the growing He-core (e.g. Castellani et al. 1971a; Robertson & Faulkner 1972; Sweigart & Gross 1973; Salaris & Cassisi 2017). Then, the use of observational constraints linked to stellar interiors is crucial to test the reliability of stellar models. With this in mind, several studies aimed at constraining stellar parameters of red giants with asteroseismic observables (di Mauro et al. 2011; Baudin et al. 2012; Lagarde et al. 2015). Using the global seismic parameters, i.e. the large frequency separation $\Delta\nu$ and the frequency of the maximum oscillation power $\nu_{\rm max}$,

these authors could infer the mass and radius of red giants and reduce their uncertainties by a factor of more than 3 compared with those based on spectroscopic constraints only. On top of these asteroseismic observables, the use of both the mode inertias and coupling factor between the g- and p- mode cavities in red giants provides unique constraints on the mode trapping, hence on the innermost stellar structure (Benomar et al. 2014; Pinçon et al. 2020). However, all the studies mentioned herebefore focus on the early stages of red giants, so that additional work needs to be done to constrain stellar structure during the helium burning stages.

One of the key events happening in the helium burning phase that still needs to be constrained is the AGBb. This is now possible with the recent seismic constraints obtained for high-luminosity RGB and AGB stars with $\Delta\nu \leq 4.0$ μHz (Dréau et al. 2021). The AGBb manifests through a luminosity drop as a star evolves on the AGB and is associated with the ignition of the He-burning shell source. The AGBb is then characterised by a local excess of stars in the luminosity distribution of stellar populations. While the AGBb has been first predicted by stellar evolutionary models (Caputo et al. 1978), it has then been identified in the colour-magnitude diagram of a few Galactic globular clusters (Ferraro 1992). Bossini et al. (2015) have shown that the AGBb can be used to constrain the core mixing scheme during the core He-burning phase. They could reproduce both the seismic constraints and the AGBb luminosity of observed *Kepler* red clump stars by considering core overshooting of the mixed He core with a moderate value of core overshooting ($\alpha_{\rm ov,He} = 0.5$ where $\alpha_{\rm ov,He}$ is the ratio of the overshooting length to the pressure scale height). Using the AGBb luminosity as a stellar model constraint allows to reduce the systematic uncertainties on the mixing processes beyond the boundary of the convective envelope, which are essential to predict stellar lifetime in the core He-burning phase (e.g., Castellani et al. 1971b; Chiosi 2007).

The characterisation of the luminosity bump on the RGB with seismic data has already been achieved (Khan et al. 2018). By combining *Kepler* and APOGEE data of thousands of red giants, these authors highlighted that the location of the red-giant branch bump (RGBb) is sensitive to the stellar mass and metallicity. Moreover, they showed that significant overshooting from the base of the convective envelope during the main sequence must be considered to reproduce the location of the RGBb, with an efficiency that increases with decreasing metallicity. A similar description of mixing beyond the convective envelope during He-burning phases would help to predict the third dredge-up efficiency on the thermally pulsing AGB (TP-AGB) phase (Herwig et al. 2000; Marigo & Girardi 2007; Wagstaff et al. 2020). Moreover, a precise characterisation of the AGBb would confirm or disprove the potential of the AGBb to be a suitable candidate for standard candles (Pulone 1992; Ferraro 1992).

In this study, we aim at detecting and characterising the AGBb. First, we investigate its dependence with the stellar mass and metallicity by using *Kepler* and TESS asteroseismic targets. Then, we use the AGBb as a calibrator for mixing processes, particularly for core overshooting during the He-burning phase. The article is organised as follows. The data set is described in Sect. 2. In Sect. 3, we define the macrophysics and microphysics implemented to model stellar evolution up to the AGB phase. Methods used to locate and characterise the AGBb in models and observations are presented in Sect. 4. The results are analysed in Sect. 5. They illustrate the needs to take He-core overshooting into account in stellar models to reproduce the observed location of the AGBb. We discuss our results and explore the impact of other parameters on the AGBb location in Sect. 6. Eventually, Sect. 7 is devoted to conclusions.

2. Data set

In order to detect the AGBb, we selected evolved stars that have been observed by the *Kepler* and TESS telescopes, including RGB and AGB stars. In order to reject red clump stars from the sample, we only kept stars with $\nu_{\rm max} \leq 22$ μHz (or equivalently $\Delta\nu \lesssim 2.7$ μHz) because no AGBb is expected to occur above this limit (Dréau et al. 2021, their Fig. 9). It has been shown that at low $\nu_{\rm max} \leq 10$ μHz (or equivalently $\Delta\nu \lesssim 1.5\mu$Hz), it is difficult to safely distinguish AGB stars from RGB ones (Kallinger et al. 2012; Mosser et al. 2019). On the other hand, the local excess associated to the AGBb is well visible on top of the background composed of RGB and He-burning stars (Bossini et al. 2015). Therefore, since we wished to work on a sample containing as many AGB stars as possible, we decided not to reject any (suspected) RGB star from the initial sample. Considering more stars, even unclassified, allowed us to include more AGB stars in our sample. The evolved *Kepler* targets around this evolutionary stage have been the subject of an exhaustive seismic analysis (Mosser et al. 2013, 2014, 2019; Stello et al. 2014; Yu et al. 2020, 2021; Dréau et al. 2021), providing estimates of $\nu_{\rm max}$. Then, we used the $\nu_{\rm max}$ estimates from Mosser et al. (2014, 2019) while we selected their mass M from the APOKASC catalogue (Pinsonneault et al. 2014, 2018). The later is a survey of *Kepler* targets complemented by spectroscopic data. The effective temperatures $T_{\rm eff}$ and stellar metallicities are taken from the catalogues of APOGEE DR17 (Abdurro'uf et al. 2021), GALAH DR3 (Buder et al. 2021), and RAVE DR6 (Steinmetz et al. 2020). We took the stellar masses derived from the semi-empirical asteroseismic scaling relation presented in Kjeldsen & Bedding (1995), and corrected by a factor that is adjusted star by star when available[1] (Pinsonneault et al. 2018). When stellar masses are not available, which concerns about 10% of our *Kepler* targets, we estimated them with the semi-empirical relation without any correction factor. As for the TESS targets, they have been studied in Mackereth et al. (2021). We picked $\nu_{\rm max}$ as the mean value between three pipelines (Mosser & Appourchaux 2009; Mathur et al. 2010; Elsworth et al. 2020). We extracted the mass M, effective temperature $T_{\rm eff}$, and metallicity [Fe/H] in the same way as for the *Kepler* targets. To sum up, roughly 70% of the spectroscopic estimates are from the APOGEE DR17 catalogue, 2% are from GALAH DR3, and 28% are from RAVE DR6. The typical uncertainties on so obtained global parameters are

[1] This correction is applied to capture the deviations from the asteroseismic scaling relations between the stellar mass M, radius R, large frequency separation $\Delta\nu$, and frequency at maximum oscillation power $\nu_{\rm max}$.

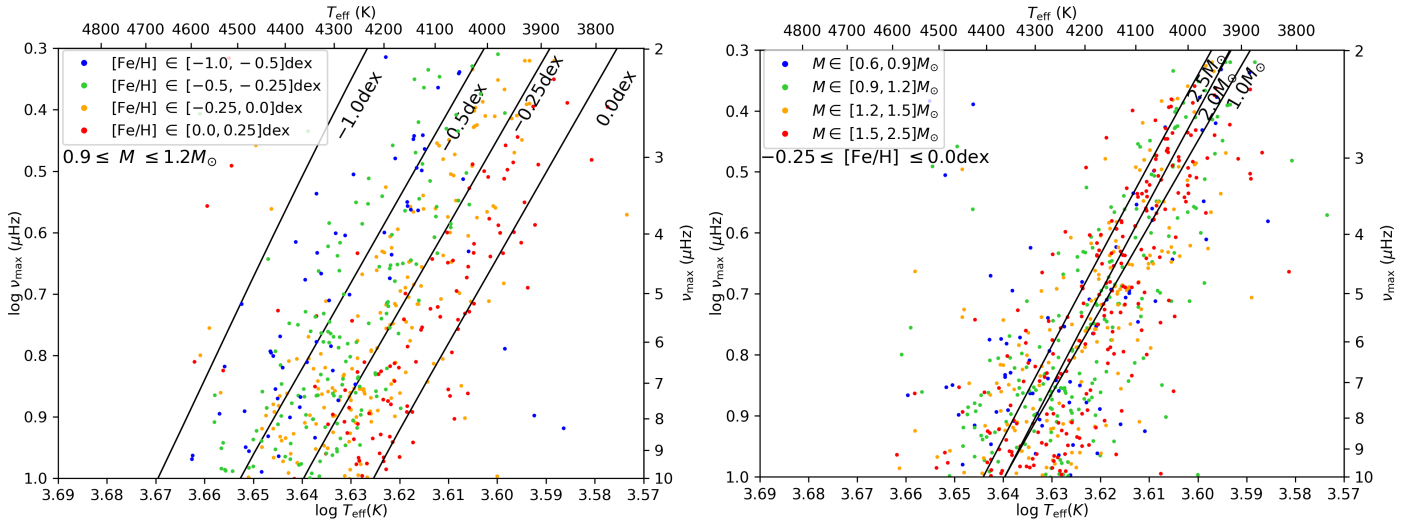

Fig. 1: Seismic HR diagram of our sample of stars in the bin of mass $M \in [0.9, 1.2]M_\odot$ (left) and in the bin of metallicity [Fe/H] $\in [-0.25, 0.0]$ dex (right). In both panels, stars with different metallicities (left) and masses (right) are represented with different colours. On top of those observations, stellar evolutionary tracks along the AGB are represented with black lines at different metallicities at $1\,M_\odot$ (left) and masses at [Fe/H] $= -0.25$ dex (right).

$\sigma_M = 12\%$, $\sigma_{\rm [Fe/H]} = 0.06$ dex, $\sigma_{T_{\rm eff}} = 64$K, $\sigma_{\nu_{\rm max}} = 9\%$. Our final sample is composed of 4099 stars, including RGB and AGB stars, as well as stars leaving the clump phase. Some of them are shown in given bins of mass and metallicity in Fig. 1.

3. Stellar models

Evolutionary tracks and stellar models are derived with the release 12778 of the stellar evolution code Modules for Experiments in Stellar Astrophysics (MESA, Paxton et al. 2011, 2013, 2015, 2018, 2019). We computed a grid of stellar models with initial mass $M = [0.8, 0.9, 1.0, 1.1, 1.2, 1.5, 1.75, 2.0, 2.5]M_\odot$ and initial metallicity [Fe/H] $= [-1.0, -0.5, -0.25, 0.0, 0.25]$ dex. The initial fractional abundance of metals in mass was set following the solar chemical composition described in Asplund et al. (2009). The treatment of convection is based on the mixing-length formalism presented in Henyey et al. (1965), which takes the opacity of the convective eddies into account. The initial helium abundance Y_0, the metallicity [Fe/H] and the mixing-length parameter $\alpha_{\rm MLT}$ were calibrated to reproduce the present solar luminosity, radius, and surface metal abundance. To this end, we adapted the MESA test suite case *simplex_solar_calibration* and took the $\log L$, $\log R$ and Z/X terms[2] into account in the χ^2 value. We performed the solar calibration without microscopic diffusion. This gave us the solar-calibrated values $Y_0 = 0.253$, [Fe/H] $= 0$ (equivalently $Z_0 = 0.0133$), and $\alpha_{\rm MLT} = 1.92$ at a solar age of 4.61 Gyrs [3]. We do not assume any coupling of Y and Z through the $\Delta Y/\Delta Z$ helium-to-metal Galactic enrichment ratio, but rather explore different values of the couple (Y, Z).

We started from the *1M_pre_ms_to_wd* test suite case and customised the physical ingredients to model stellar evolution up to the AGB. To follow chemical changes and the production of nuclear energy, we used a network of 32 nuclear reactions involving 23 stable or unstable species from ^{1}H to ^{24}Mg. The thermonuclear reaction rates are taken from NACRE (Angulo et al. 1999) and CF88 (Caughlan & Fowler 1988), with priority on NACRE rates when available. We took into account some updates to crucial reaction rates at evolved stages, such as $^{14}{\rm N}(p,\gamma)^{15}{\rm O}$ (Imbriani et al. 2004) and triple-α (Fynbo et al. 2005).

Opacities are needed to compute the energy transport in regularly stratified regions, that is in radiative zones. At low temperatures ($\log T < 3.95$), we used the opacity tables from AESOPUS (Marigo & Aringer 2009) while at high temperatures ($\log T > 4.05$), we took either the OPAL1 or OPAL2 opacity tables (Iglesias & Rogers 1996). The AESOPUS and OPAL1 tables are for the Asplund et al. (2009) solar mixture, while the OPAL2 tables allow to account for the metal mixture changes due to the C and O enhancements that result from He burning. In the region around $\log T = 4.00 \pm 0.05$, we performed a blend as described by Paxton et al. (2011) (see their Eq. (1)) between AESOPUS and OPAL1 tables. Furthermore, in the regions with C and O enhancements where the initial metallicity Z_0 is increased by an amount dZ we used the OPAL2 opacity tables. A blend between OPAL1 and OPAL2 is made in the region where d$Z \in [0.001, 0.01]$. Finally, the resulting opacity is combined with the electron conduction opacity, as prescribed in Cassisi et al. (2007).

We considered convective core overshooting during the main sequence following a step scheme (e.g. Maeder 1975).

[2] $Z/X = (Z/X)_\odot\ 10^{\rm [Fe/H]}$, where the solar value $(Z/X)_\odot = 0.0181$ is taken from Asplund et al. (2009)

[3] This value corresponds to the default solar age in MESA, taken as the sum of the time spent on the MS starting on the ZAMS (4.57×10^9 yrs) and that spent on the PMS (0.04×10^9 yrs). It is larger than the value commonly adopted $\tau_\odot = 4.57 \times 10^9$ yrs (see, e.g., Chaussidon 2007). However, we do not account for the PMS in the calibration and it has been shown that adopting those two target solar ages does not impact the solar calibration significantly (see Table 2 of Sackmann et al. 1990).

It means that the mixing region extends over a distance $d_{\rm ov}$ toward the surface from the boundary of convective instability in the core where the Schwarzschild condition $\nabla_{\rm rad} > \nabla_{\rm ad}$ is fulfilled. If $H_P \leq R_{cc}$, where H_P is the pressure scale height at the boundary of the convective core and R_{cc} is the convective core radial thickness, then we keep $d_{\rm ov} = \alpha_{\rm ov,H} H_P$, otherwise $d_{\rm ov} = \alpha_{\rm ov,H} R_{cc}$. We adopted the overshooting parameter $\alpha_{\rm ov,H} = 0.2$ in the reference model. Similarly, we computed evolutionary tracks with and without convective core overshooting during core He-burning phase following two scenarii. Either the temperature gradient ∇_T is kept equal to the radiative gradient $\nabla_{\rm rad}$ (usual overshooting scenario) or it is kept equal to the adiabatic temperature gradient $\nabla_{\rm ad}$ (penetrative convection scenario) in the overshooting region (Zahn 1991). The Schwarzschild convective border is in an unstable equilibrium in the sense that a small expansion of the convective core may make $\nabla_{\rm rad}$ larger than $\nabla_{\rm ad}$ at the new border (Castellani et al. 1971b). Adding core overshooting during the core He-burning phase induces a possible local minimum and maximum in $\nabla_{\rm rad}$ in the extra-mixing region due to the increasing opacity that results from the transport of C and O elements in that region. Should this maximum increase above $\nabla_{\rm ad}$, a separate convective instability would occur in the overshooting region in absence of an appropriate treatment of semi convection. To address this issue, we allowed a partially mixed He-semiconvection region between the minimum of $\nabla_{\rm rad}$ and the outer radiative zone (Castellani et al. 1971a) following the diffusion scheme of Langer et al. (1985) with the efficiency factor $\alpha_{\rm sc} = 0.1$. In parallel, we followed the treatment proposed by Bossini et al. (2017) to consider a stable convective border and suppress such spurious convective instabilities. This treatment consists in defining the convective border at the point where $\nabla_{\rm rad}$ has reached its local minimum if the local maximum of $\nabla_{\rm rad}$ created by adding He-core overshooting has increased over $\nabla_{\rm ad}$ in the extra-mixing region, otherwise the convective boundary is set at the point where $\nabla_{\rm rad} = \nabla_{\rm ad}$.

We also explored the effect of envelope undershooting, which induces an extra-mixing region of extent $\alpha_{\rm ov,env} H_P$ below the convective envelope into the radiative core. Similarly as convective core overshooting, we adopted a step scheme and applied envelope undershooting from the main sequence up to the AGB, with $\nabla_T = \nabla_{\rm rad}$ in the extra-mixing region. The typical value for low-mass red giants ($M \leq 1.6 M_\odot$) at solar metallicity recommended by Khan et al. (2018), i.e. $\alpha_{\rm ov,env} = 0.3$ is considered.

Other transport processes arise in stellar interiors, such as thermohaline mixing and rotation-induced mixing. Thermohaline convection starts along the RGB in regions that are stable against convection (according to the Ledoux criterion) and where the molecular weight gradient becomes negative (i.e. $\nabla_\mu = {\rm d}\ln\mu/{\rm d}\ln P < 0$) between the H-burning shell surrounding the degenerate core and the convective envelope. This composition gradient inversion is induced by the ^{3}He(^{3}He, $2p$)^{4}He reactions that take place around the H-burning shell (Ulrich 1972; Eggleton et al. 2006, 2008; Charbonnel & Zahn 2007). Here, thermohaline mixing is treated in a diffusion approximation based on the work of Kippenhahn et al. (1980), where the corresponding diffusion coefficient reads (Paxton et al. 2013)

$$D_{\rm th} = \alpha_{\rm th} \frac{3K}{2\rho c_P} \frac{B}{\nabla_T - \nabla_{\rm ad}}. \quad (1)$$

In the previous equation, K is the radiative conductivity, c_P is the specific heat at constant pressure, $\alpha_{\rm th}$ is the efficiency parameter for the thermohaline mixing, and

$$B = -\frac{1}{\chi_T} \sum_{i=1}^{N-1} \left(\frac{\partial \ln P}{\partial \ln X_i} \right)_{\rho,T,\{X_{j\neq i}\}} \frac{{\rm d}\ln X_i}{{\rm d}\ln P}, \quad (2)$$

where $\chi_T = (\partial \ln P/\partial \ln T)_\rho$, and X_i represents the mass fraction of atoms of species i in the N-component plasma. The species j is eliminated in the sum so that the constraint $\sum_{i=1}^{N-1} X_i + X_N = 1$ is fulfilled. We adopted $\alpha_{\rm th} = 2$, which corresponds to the prescription of Kippenhahn et al. (1980) where blobs of size L diffuse while travelling over a mean free path L before dissolving. We checked that the extent of the extra mixing regions caused by thermohaline convection is in agreement with the one obtained by Cantiello & Langer (2010). Especially, we verified that the extra mixing region is large enough to connect the H-burning shell and the convective envelope during the core He-burning phase for stars with a mass below $1.5 M_\odot$.

We investigated the effects of rotation on the AGBb location since rotation is known to impact lifetimes, surface abundances and evolutionary fates. Rotation is treated in 1D in the shellular approximation (e.g. Meynet & Maeder 1997). Further information can be found in Paxton et al. (2013) to learn more about how rotation is implemented in MESA where it is treated as a diffusive process. We took rotation into account from the zero-age main sequence (ZAMS), as often done in stellar evolution codes (e.g. Pinsonneault et al. 1989), up to the terminal-age main sequence (TAMS). First, we implemented rotation up to the early AGB phase, but it made the evolutionary track noisy at the AGBb without modifying its position. Therein, we only kept rotation during the main sequence. The rotation rate gradually reaches the maximum value $\Omega_{\rm ZAMS}/\Omega_{\rm crit} = 0.3$, where $\Omega_{\rm crit}$ is the surface critical angular velocity for the star to be dislocated, which is the typical rotation rate motivated by observations of B stars (Huang et al. 2010). For a $2 M_\odot$ star, the evolutionary track that includes the rotation rate $\Omega_{\rm ZAMS}/\Omega_{\rm crit} = 0.3$ during the main sequence is equivalent to that including a H-core overshooting $\alpha_{\rm ov,H} \approx 0.25$. We checked that the evolution of the surface rotation rate so obtained along the main sequence is similar to that obtained in Ekström et al. (2012). We only studied rotating models with $M \geq 1.5 M_\odot$ since magnetic braking is not included in MESA, which does not allow to reproduce slow rotation rates of low-mass stars (Kawaler 1988).

Rotation induces both chemical and angular momentum transports through instabilities that are treated in a diffusion approximation (Endal & Sofia 1978; Pinsonneault et al. 1989; Heger et al. 2000). In our models, we included six equally weighted instabilities induced by rotation which are dynamical shear, Solberg-Høiland, secular shear, Goldreich-Schubert-Fricke instabilities, Eddington-Sweet circulation, and Tayler-Spruit dynamo. Then, each diffusion coefficient associated to those rotationally induced

Table 1: Number of stars per mass and metallicity bins

$M/M_\odot \in$	[Fe/H] (dex) $\in [-1.0, -0.5]$	$[-0.5, -0.25]$	$[-0.25, 0.0]$	$[0.0, 0.25]$
$[0.6, 0.9]$	122	174	204	$107^{(*)}$
$[0.9, 1.2]$	130	344	432	213
$[1.2, 1.5]$	108	322	426	244
$[1.5, 2.5]$	143	346	518	266

Notes: $^{(*)}$ refers to mass and metallicity bins for which the fit could not converge

instabilities is added to the diffusion coefficient in absence of rotation. On top of this resulting diffusion coefficient, two free parameters need to be fixed in diffusion equations: the factor f_c that scales the efficiency of composition mixing relatively to that of the angular momentum transport, and the factor f_μ that encodes the sensitivity of rotational mixing to the mean molecular weight gradient. Typical values from Heger et al. (2000) such as $f_c = 1/30$ and $f_\mu = 0.05$ are adopted.

We took a grey atmosphere with an Eddington $T(\tau)$ relation. We defined the outermost meshpoint of the models as the layer where the optical depth τ verifies $\tau = 2/3$, which is at the limit of the photosphere. Another important parameter that impacts the fate of stars is the mass-loss rate. We used Reimers' prescription (Reimers 1975)

$$\dot{M}_R = -4 \times 10^{-13}\ \eta_R \frac{L}{L_\odot}\frac{R}{R_\odot}\left(\frac{M}{M_\odot}\right)^{-1} M_\odot.\mathrm{yr}^{-1} \quad (3)$$

from the RGB up to the core He-burning phase, where η_R is the Reimers' scaling factor that we take equal to $\eta_R = 0.3$ (Miglio et al. 2021). On the AGB, we use the Blöcker's prescription (Blocker 1995)

$$\dot{M}_B = -1.93\times10^{-21}\eta_B \left(\frac{M}{M_\odot}\right)^{-3.1}\frac{R}{R_\odot}\left(\frac{L}{L_\odot}\right)^{3.7} M_\odot.\mathrm{yr}^{-1}, \quad (4)$$

where η_B is the Blöcker's scaling factor taken equal to $\eta_B = 0.1$. In both Reimers' and Blöcker's prescriptions, L, R and M are expressed in solar units.
The screening factors were computed with the implementation of Chugunov et al. (2007) for weak and strong screening conditions. We kept the default coverage of the equation of state in the $\log\rho - \log T$ plane, they are summarised in Fig. 50 of Paxton et al. (2019).

4. Characterisation of the AGBb

4.1. Observations

Herebefore we found that the AGBb manifests as a local excess of stars on top of a background composed of RGB and AGB stars. In order to infer the AGBb location in $\nu_{\max}$ and $T_{\rm eff}$, in the way Khan et al. (2018) proceeded to characterise the RGBb, we adopted the statistical mixture model presented in Hogg et al. (2010). This approach is a statistical framework where the data set is assumed to be multimodal, i.e. with several regions of high probability separated by regions of low probability. In this situation, we modelled the data with a mixture of several components, where each data point belongs to one of these components. This allowed us to use multiple models to fit our data set. We distinguished the inliers, which are stars belonging to the AGBb overdensity and the outliers, which are stars that belong to the RGB/AGB background and do not lie in the AGBb phase. The fit was performed using the *Python* module *Emcee*, which is an affine invariant Markov Chain Monte Carlo (MCMC) ensemble sampler (Foreman-Mackey et al. 2013). The likelihood function is defined as

$$\mathcal{L} = (1-P_{\rm bg})f_{\rm biv}(\log T_{\rm eff}, \log\nu_{\max}) + P_{\rm bg} f_{\rm bg}(\log T_{\rm eff}, \log\nu_{\max}), \quad (5)$$

where $f_{\rm biv}$ describes the AGBb foreground with a bivariate normal distribution function, $f_{\rm bg}$ describes the RGB/AGB background with the product of a normalised rising exponential in $\log\nu_{\max}$ and a linear term with a normally distributed scatter, and $P_{\rm bg}$ is the mixture model weighting factor that gives the probability for a star to belong to the RGB/AGB background. The foreground and background probability distribution functions are

$$f_{\rm biv}(x_1, x_2) = \frac{1}{2\pi\sigma_1\sigma_2\sqrt{1-\rho_{12}^2}} \mathrm{e}^{-\frac{z}{2(1-\rho_{12}^2)}}, \quad (6)$$

$$\text{with } z = \frac{(x_1-\mu_1)^2}{\sigma_1^2} + \frac{(x_2-\mu_2)^2}{\sigma_2^2} - \frac{2\rho_{12}(x_1-\mu_1)(x_2-\mu_2)}{\sigma_1\sigma_2}$$

and

$$f_{\rm bg}(x_1, x_2) = \frac{1}{\sqrt{2\pi}\sigma_{\rm bg}} \mathrm{e}^{-\frac{(x_2-(a_{\rm bg}x_1+b_{\rm bg}))^2}{2\sigma_{\rm bg}^2}} \times A_{\rm exp}\ \mathrm{e}^{c_{\rm bg}\nu_{\max}}, \quad (7)$$

respectively. In the previous equations, $x_1 = \log T_{\rm eff}$ and $x_2 = \log\nu_{\max}$, μ_1 and μ_2 are the AGBb locations in $\log T_{\rm eff}$ and $\log\nu_{\max}$, respectively, σ_1 and σ_2 are the AGBb standard deviations in $\log T_{\rm eff}$ and $\log\nu_{\max}$, respectively, ρ_{12} is the correlation of the bivariate Gaussian, $a_{\rm bg}$ and $b_{\rm bg}$ are the linear coefficients, $\sigma_{\rm bg}$ is the standard deviation of the normal distribution of the linear term, $c_{\rm bg}$ and $A_{\rm exp}$ are the coefficient and the normalisation factor of the exponential term, respectively.
Given the small amplitude of the AGBb overdensity in $\log\nu_{\max}$ (see Fig. 2), σ_2 failed to converge when we used the fitting method described above. Consequently, we estimated σ_2 separately by fitting the AGBb overdensity with a normal distribution function in the 1D histogram of $\log\nu_{\max}$. We took this estimate and kept it fixed during the MCMC process. Then, the posterior probability distributions of our set of 9 free parameters, which are μ_1,

μ_2, σ_1, ρ_{12}, $a_{\rm bg}$, $b_{\rm bg}$, $\sigma_{\rm bg}$, $c_{\rm bg}$, and $P_{\rm bg}$, were visualised with the *Python* module *Corner* (Foreman-Mackey 2016). First, the guess values of the bivariate Gaussian and the exponential term were extracted from the 1D histograms in $\log \nu_{\rm max}$ and $\log T_{\rm eff}$ and those of the linear term were obtained from the 2D histogram, as seen in Fig. 2. Then, parameters were left free to vary according to a uniform prior probability distribution.

We performed this fitting method in the $\log T_{\rm eff} - \log \nu_{\rm max}$ plane, in restricted bins of mass and metallicity, which are $M \in [0.6, 0.9]$, $[0.9, 1.2]$, $[1.2, 1.5]$, $[1.5, 2.5]\,M_\odot$ and [Fe/H] $\in [-1.0, -0.5]$, $[-0.5, -0.25]$, $[-0.25, 0.0]$, $[0.0, 0.25]$ dex. The bins are wider at high mass and low metallicity to include enough stars and hence ensure the free parameters to converge. The number of stars per bin is shown in Table 1. We show in Fig. 2 the results for the bin $M \in [0.9, 1.2] M_\odot$ and [Fe/H] $\in [-0.25, 0.0]$ dex.

4.2. Models

To extract the probability for a star to lie in a given bin of $\nu_{\rm max}$ and $T_{\rm eff}$ along its evolutionary track, we computed the inverse of the evolution speeds $\mathrm{d}\tau/\mathrm{d}\nu_{\rm max}$ and $\mathrm{d}\tau/\mathrm{d}T_{\rm eff}$, where τ is the stellar age. Then, we integrated $\mathrm{d}\tau/\mathrm{d}\nu_{\rm max}$ and $\mathrm{d}\tau/\mathrm{d}T_{\rm eff}$ over $\nu_{\rm max}$ and $T_{\rm eff}$, respectively. This gives us the fractional time that is spent in a given bin of $\nu_{\rm max}$ and $T_{\rm eff}$, respectively. We used this fractional time as a proxy of the probability distribution for a star to lie in a given bin of $\nu_{\rm max}$ and $T_{\rm eff}$. The procedure was repeated for each pair of mass and metallicity in our grid of stellar models presented in Sect. 3. We summed the probability distributions of all pairs of mass and metallicity lying in the considered bin of mass and metallicity, and we normalised the resulting probability distribution. Because the grid of stellar models is discontinuous compared to observations and because the probability distributions are narrow at the turning-backs of the AGBb (i.e. where the quantities $\mathrm{d}\tau/\mathrm{d}\nu_{\rm max}$ and $\mathrm{d}\tau/\mathrm{d}T_{\rm eff}$ change sign), we convolved the resulting probability distribution by a normal one. Eventually, the maximum of the convolved probability distribution was interpreted as the AGBb location.

With the aim to investigate the potential of the AGBb to constrain physical processes in stellar interiors, we attempted to make the observed AGBb location match the expected AGBb one as well as possible by comparing the 1D histograms of $\log \nu_{\rm max}$ and $\log T_{\rm eff}$ from observations with the corresponding probability distributions derived from stellar models. To this end, we defined a reference model and varied the stellar parameters to explore their impact on the expected AGBb location in $\log \nu_{\rm max}$ and $\log T_{\rm eff}$. The results are presented in the following section.

5. Results

We applied the procedure described in Sect. 4 both to the data set and the stellar models and examined the AGBb location for all the bins of mass and metallicity previously introduced. The results are presented in Fig. 3−7 and Tables A.1−A.4 in Appendix A.

5.1. The AGBb seen from observations

From observations, we can highlight a clear mass dependence in the AGBb location: the higher the mass, the lower the $\nu_{\rm max}$ associated to the AGBb, whatever the range of metallicity (see left panel of Fig. 3). Namely, the higher the mass, the farther the distance between the AGBb and the clump phase along the evolutionary track. We find the AGBb to occur around $\log \nu_{\rm max} \sim 0.84$ ($\nu_{\rm max} \sim 6.9$ μHz) at $M \sim 1 M_\odot$ and $\log \nu_{\rm max} \sim 0.52$ ($\nu_{\rm max} \sim 3.3$ μHz) at $M \sim 2 M_\odot$, with a typical standard deviation of $\sigma_2 = 0.06$ and uncertainty on the $\log \nu_{\rm max}$ measurements of $\sigma_{\log \nu_{\rm max}} = 0.02$. According to seismic scaling relations, the luminosity L depends on $\nu_{\rm max}$ following

$$\frac{L}{L_\odot} = \frac{M}{M_\odot} \left(\frac{\nu_{\rm max}}{\nu_{\rm max,\odot}} \right)^{-1} \left(\frac{T_{\rm eff}}{T_{\rm eff,\odot}} \right)^{7/2} . \quad (8)$$

Then, the higher the mass, the higher the luminosity, which totally agrees with theoretical predictions since the AGBb luminosity has been found to increase with mass at fixed metallicity (Alves & Sarajedini 1999, their Fig. 3). This behaviour has also been found by Yu et al. 2022 (in prep), who observed that the overdensity of stars associated to the AGBb is shifted between *Kepler*, APOGEE and GALAH stars. This overdensity shift is correlated with a shift of the stellar mass distribution, resulting in a different mean stellar mass in those samples. Besides, we notice in the right panel of Fig. 3 that the AGBb occurs at lower temperature for high-mass stars (around $\log T_{\rm eff} \sim 3.630$ at $M \sim 1 M_\odot$ and $\log T_{\rm eff} \sim 3.610$ at $M \sim 2 M_\odot$). Although this temperature dependence is clear in Fig. 3, it may be subject to the uncertainty on the $\log T_{\rm eff}$ measurements of $\sigma_{\log T_{\rm eff}} = 0.01 - 0.02$ and our ability to precisely delimit the overdensity, with a standard deviation $\sigma_2 = 0.01 - 0.02$.

Beyond that mass dependence, we can see in Fig. 3 a weak metallicity effect on the AGBb location in $\nu_{\rm max}$. At fixed mass, the AGBb location in $\nu_{\rm max}$ slowly increases with metallicity at low mass ($M \leq 1.2 M_\odot$) and noticeably increases at high mass ($M \geq 1.2 M_\odot$). This observational trend is consistent with the theoretical results of Alves & Sarajedini (1999). Indeed, for low-mass stars ($M \leq 1.2 M_\odot$), these authors showed that a change of metallicity does not highly impact the luminosity of the AGBb whereas for high-mass stars ($M \geq 1.2 M_\odot$) metallicity effects are more important, which is what we observe. Nevertheless, these trends are mainly valid for high-metallicity stars since our sample only contains a small number of metal-poor stars (with [Fe/H] ≤ -0.5 dex, see Table 1). Besides, we can see in Fig. 3 that the AGBb tends to occur at lower $\log T_{\rm eff}$ when the metallicity increases. However, the $\log T_{\rm eff}$ variations with metallicity are close to the typical uncertainty on $\log T_{\rm eff}$, so this behaviour needs to be confirmed. Overall, our results tend to confirm that the AGBb occurrence slightly depends on the metallicity which would make the use of AGBb as standard candle questionable (Pulone 1992; Ferraro 1992), at least at high metallicity. This is discussed in Sect. 6.
To sum up, we find a clear mass dependence of the AGBb location, the higher the mass, the lower $\nu_{\rm max}$ and $T_{\rm eff}$ at which the AGBb occurs, i.e. the later the AGBb occurrence. Moreover, the AGBb tends to occur at slightly higher $\nu_{\rm max}$ and lower $T_{\rm eff}$ for metal-rich stars.

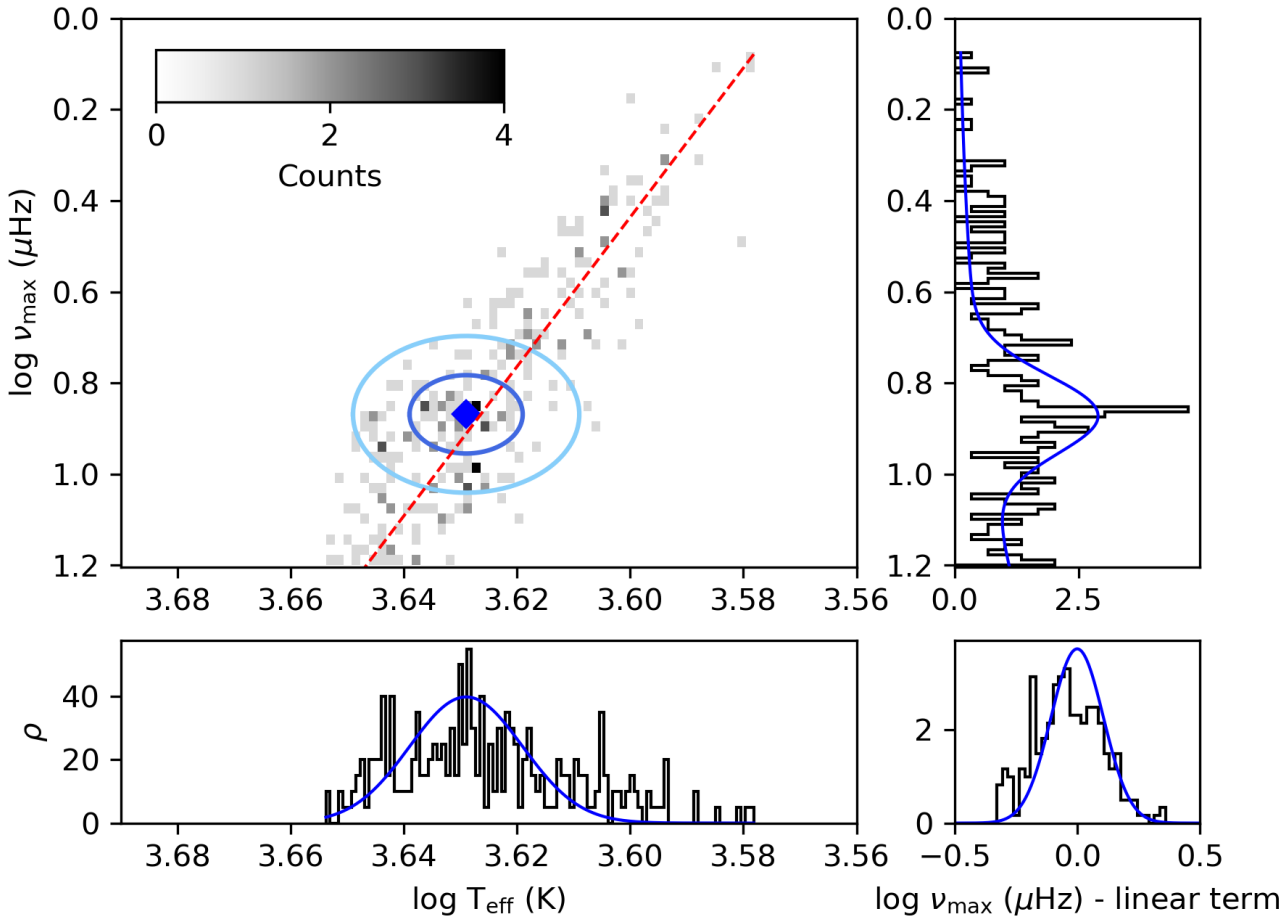

Fig. 2: Probability distribution functions of our data set in the $\log T_{\rm eff} - \log \nu_{\rm max}$ plane, in the bins $M \in [0.9, 1.2] M_{\odot}$ and [Fe/H] $\in [-0.25, 0.0]$ dex. Upper left panel: 2D histogram where the AGBb is located by a blue diamond. Dark blue and light blue ellipses correspond to the 1σ and 2σ regions of the bivariate Gaussian, respectively. The red dashed line reproduces the linear term belonging to the RGB/AGB background. Upper right panel: the normalised 1D histogram in $\log \nu_{\rm max}$ is shown in black. The ordinate axis is the same as in the upper left panel. The blue line corresponds to the probability distribution function made of the Gaussian associated to the overdensity in $\log \nu_{\rm max}$, multiplied by the rising exponential in $\log \nu_{\rm max}$. Lower left panel: same label as in the upper right panel but in terms of $\log T_{\rm eff}$. The abscissa axis is the same as in the upper left panel. The blue line shows the Gaussian associated to the overdensity in $\log T_{\rm eff}$. Lower right panel: difference between $\log \nu_{\rm max}$ and $a_{\rm bg} \log T_{\rm eff} + b_{\rm bg}$. The blue line illustrates the normal distribution around the linear term.

5.2. The necessity to calibrate the core overshooting parameter

In order to estimate the amount of core overshooting $\alpha_{\rm ov,He}$ needed to reproduce the observations, we computed evolutionary tracks without core overshooting ($\alpha_{\rm ov,He} = 0$). In Fig. 4–7, we can see that the AGBb locations in observations and models without core overshooting during the clump phase do not overlap at all, neither in the $M - [{\rm Fe/H}] - \log \nu_{\rm max}$ nor in the $M - [{\rm Fe/H}] - \log T_{\rm eff}$ plane. However, we notice that for a given set of stellar parameters, the larger the mass, the larger the differences between observations and models in $\nu_{\rm max}$ and $T_{\rm eff}$ at the AGBb. This is also what we observe toward low metallicity, but only in $T_{\rm eff}$. As highlighted in Sect. 5.1 and in theoretical works (Alves & Sarajedini 1999, their Fig. 3), the metallicity effects are small but still impacts the frequency $\nu_{\rm max}$ at which the AGBb occurs. Consequently, we can conclude that models with different masses and metallicities have to be differently calibrated.

Then, we adopted a moderate and high core overshooting parameter $\alpha_{\rm ov,He} = 0.5$ and 1.0, which are the values that provide the best matching of the period-spacing and luminosity distributions between observations and stellar models during He-burning phases in the range $M \in [1.3, 1.7] M_{\odot}$ (Bossini et al. 2015). From Fig. 4–7, we can conclude that core overshooting has to take place during the core He-burning phase to reproduce observations. Adding core overshooting during the clump phase increases the distance between the latter and the AGBb location

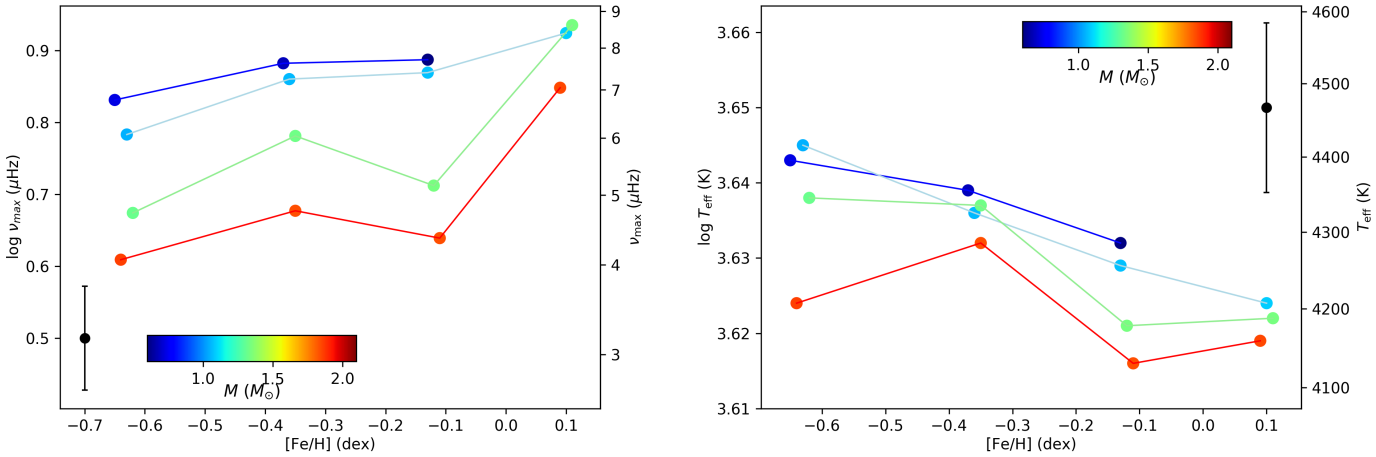

Fig. 3: Location of the AGBb in $\log \nu_{\rm max}$ (left) and in $\log T_{\rm eff}$ (right) from observations, as a function of the metallicity [Fe/H]. The AGBb occurrence is marked by dots and the stellar mass is colour-coded. AGBb locations obtained in the same bin of mass $M \in [0.6, 0.9]$, $[0.9, 1.2]$, $[1.2, 1.5]$, $[1.5, 2.5] M_\odot$ are connected by dark blue, light blue, light green, and red lines, respectively. Mean error bars on the location of the AGBb in $\log \nu_{\rm max}$ and in $\log T_{\rm eff}$ are shown in black. Data in the bin ($M \in [0.6, 0.9] M_\odot$, [Fe/H]$\in [0, 0.25]$ dex) are not shown because there are not enough stars to perform the statistical mixture model.

along the evolutionary track, which makes the AGBb occur at lower $\nu_{\rm max}$ and lower $T_{\rm eff}$. We note that $\alpha_{\rm ov,He} = 0.5$ (respectively $\alpha_{\rm ov,He} = 1.0$) gives a nice agreement between models and observations for stellar mass $M \in [0.9, 1.2] M_\odot$ (respectively $M \in [1.2, 1.5] M_\odot$) for all metallicities. This tends to confirm that the higher the mass, the higher the core overshooting $\alpha_{\rm ov,He}$ must be for the models to agree with observations. Nevertheless, for high-mass stars adding He-core overshooting seems inadequate to reproduce observations. The value $\alpha_{\rm ov,He} = 1.0$ in units of H_P, which quantifies the extent of the mixing region beyond the boundary of convective instability, may be unrealistic since the overshooting region then becomes larger than the convective core. Consequently, the inclusion of additional physical processes may be necessary to make models and observations match at high mass.

In $\log T_{\rm eff}$, the AGBb location varies with metallicity at fixed mass in stellar models, see Fig. 4−7 and Tables A.1−A.4. Therefore, other model parameters have to be fine-tuned in order to make observations and models agree both in $\log \nu_{\rm max}$ and $\log T_{\rm eff}$ for all bins of metallicity. This raises the question of degeneracies and uncertainties on stellar parameters. In Sect. 6, we explore the effects of model input physics that could influence the AGBb location.

6. Discussion

6.1. Calibration of physical parameters at low mass

In Sect. 6, we explore the effects of model input physics that could influence the AGBb. Up to this point, we investigated the impact of He-core overshooting on the AGBb by taking $\nabla_T = \nabla_{\rm rad}$ in the overshooting region. Following Bossini et al. (2015), we also investigated the penetrative convection scenario defined as $\nabla_T = \nabla_{\rm ad}$ in the overshooting region. According to Fig. 4−6 there is no difference in the location of the AGBb between those two scenarios. Bossini et al. (2015) reached the same conclusion, nevertheless Bossini et al. (2017) noticed that the period-spacing distribution of He-burning stars observed by Vrard et al. (2016) better matches the one obtained with a radiative transport in the overshooting region. Therefore, seismic constraints support the use of overshooting with radiative transport during core He-burning phase, without any impact on the calibration of the AGBb.

6.1.1. Efficiency of convection

Besides, by changing the mixing length parameter $\alpha_{\rm MLT}$, we noted that the convection efficiency considerably impacts the AGBb location in $T_{\rm eff}$. In Fig. 4−6, we can see that a $\Delta\alpha_{\rm MLT}$ decrease of 0.3 induces a shift of the AGBb toward low $T_{\rm eff}$, but marginally modifies its luminosity. In fact, when the mixing length parameter decreases, the energy transport in the envelope is less efficient, the stellar radius R increases and the effective temperature $T_{\rm eff}$ decreases. Then, the evolutionary track is shifted toward low $T_{\rm eff}$, including the AGBb location. On the other hand, by considering the scaling relation

$$\frac{\nu_{\rm max}}{\nu_{\rm max,\odot}} \simeq \frac{M}{M_\odot} \left(\frac{R}{R_\odot}\right)^{-2} \left(\frac{T_{\rm eff}}{T_{\rm eff,\odot}}\right)^{-1/2}, \quad (9)$$

we see that at fixed mass, increasing the radius R and decreasing the effective temperature $T_{\rm eff}$ simultaneously has limited effect on $\nu_{\rm max}$, which justifies the minor impact of $\Delta\alpha_{\rm MLT}$ on the AGBb location in $\nu_{\rm max}$.

6.1.2. Other model inputs

We checked that some physical mechanisms do not modify the AGBb location. They are summarised below:

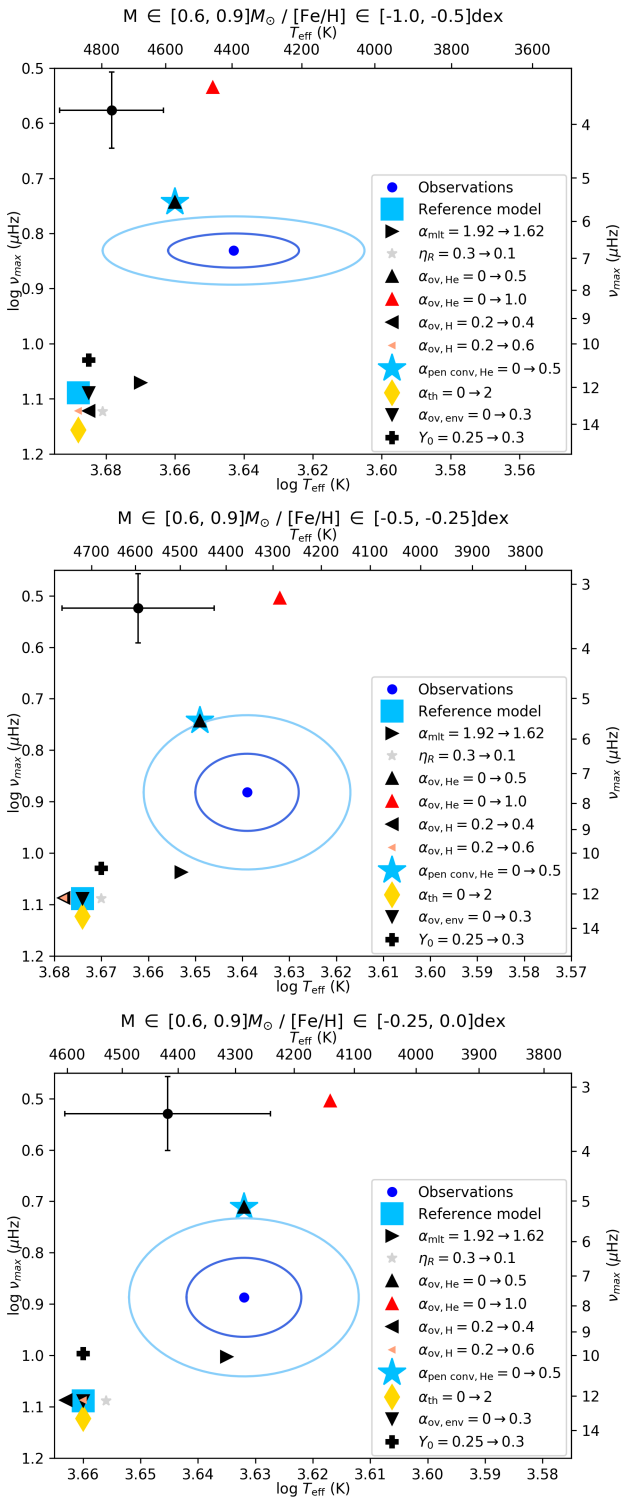

Fig. 4: Location of the AGBb in the plane $\log T_{\rm eff} - \log \nu_{\rm max}$ in the mass bin $M \in [0.6, 0.9] M_\odot$ and metallicity bins [Fe/H] $\in [-1.0, -0.5]$, $[-0.5, -0.25]$, $[-0.25, 0.0]$ dex. The metallicity bin [Fe/H]$\in [0.0, 0.25]$ dex is missing because we have not enough stars to perform a statistical study. Observations are marked by blue dots, the dark blue and light blue ellipses correspond to the 1σ and 2σ regions, respectively. The reference model presented is shown by a light blue square. Other models are shown with different symbols listed in the labels, they have been obtained by individually changing the parameters of the reference model. The changes are indicated in the label of each panel. The black dot with errorbars indicates the mean uncertainty we have for all models. The uncertainty on the AGBb location in $\log \nu_{\rm max}$ and $\log T_{\rm eff}$ for each model is taken as the standard deviation of the Gaussian function that reproduces the overdensity caused by the AGBb in the 1D histograms. The numerical values are listed in Table A.1 in Appendix A. Ranges of the axes vary in the different panels.

- Modifying the H-core overshooting $\alpha_{\rm ov,H}$ during the MS does not shift the AGBb location for low-mass stars ($M \leq 1.5 M_\odot$) since their convective core is either not developed yet or very small.
- Interestingly, adding an amount of envelope undershooting of $\alpha_{\rm ov,env} = 0.3 H_P$ (i.e. overshooting from the convective envelope into the radiative core) from the main sequence up to the AGB does not impact the AGBb location, while it does impact the RGBb location (Khan et al. 2018). This implies that the calibrations of mixing processes brought by the RGBb (envelope undershooting) and AGBb (He-core overshooting) are independent.
- On the other hand, adding thermohaline convection from the main sequence up to the early AGB with $\alpha_{\rm th} = 2$ marginally modifies the AGBb location. Mixing processes between the convective envelope and the radiative core do not seem to significantly impact the AGBb.
- Changing the mass loss rate on the RGB from $\eta_R = 0.3$ to $\eta_R = 0.1$ slightly shifts the AGBb location. This suggests that the changes the star experienced due to mass loss do not impact the AGBb occurrence. Only the final mass reached at the AGBb matters for determining the AGBb location.
- By varying the initial helium mass fraction from $Y_0 = 0.253$ to $Y_0 = 0.303$, the AGBb occurs at slightly lower $\nu_{\rm max}$, i.e. at higher luminosity. This is consistent with expectations since an increased initial helium mass fraction enlarges the lifetime of the core He-burning phase. More thermonuclear energy is released, then the luminosity is higher at this evolutionary stage.

As a conclusion, we are able to reproduce the AGBb location of low-mass stars with stellar models, particularly by including He-core overshooting $\alpha_{\rm ov,He}$ as investigated by Bossini et al. (2015). We find that a helium core overshooting parameter $\alpha_{\rm ov,He} \in [0.25, 0.50]$ is needed to make observations and models match in the mass bins $M \in [0.6, 0.9], [0.9, 1.2] M_\odot$ while $\alpha_{\rm ov,He} \in [0.50, 1.0]$ is more appropriate in the mass bin $M \in [1.2, 1.5] M_\odot$. Deviations of models from observations in $T_{\rm eff}$ can be captured by adjusting the mixing length parameter $\alpha_{\rm MLT}$. The main sources of uncertainty on the calibration of He-core overshooting come from the initial helium mass fraction and potential other mixing processes such as rotational mixing. Additional observational constraints could be used to reduce these uncertainties, in particular the location of the red clump phase. The physical parameter changes we explored also have an impact on the location of the red clump phase, so combining the observed AGBb location with that of the red clump phase would lead to a more precise calibration. In Appendix B, we explore how physical ingredients impact the ratio of location in $\log \nu_{\rm max}$ and $\log T_{\rm eff}$ between the AGBb and the red clump phase. We note that only the adding of He-core overshooting modifies the distance between the AGBb and the red clump locations along the evolutionary track, while the other parameters leave this distance unchanged. Some parameters not only have an effect on the AGBb location but also on the red clump location, such as the initial helium abundance. Additional work is required to improve the calibration of the simultaneous investigations of the red clump and AGBb locations. On the other hand, we did not explore rotation-induced mixing in low-mass stars since physical ingredients such as

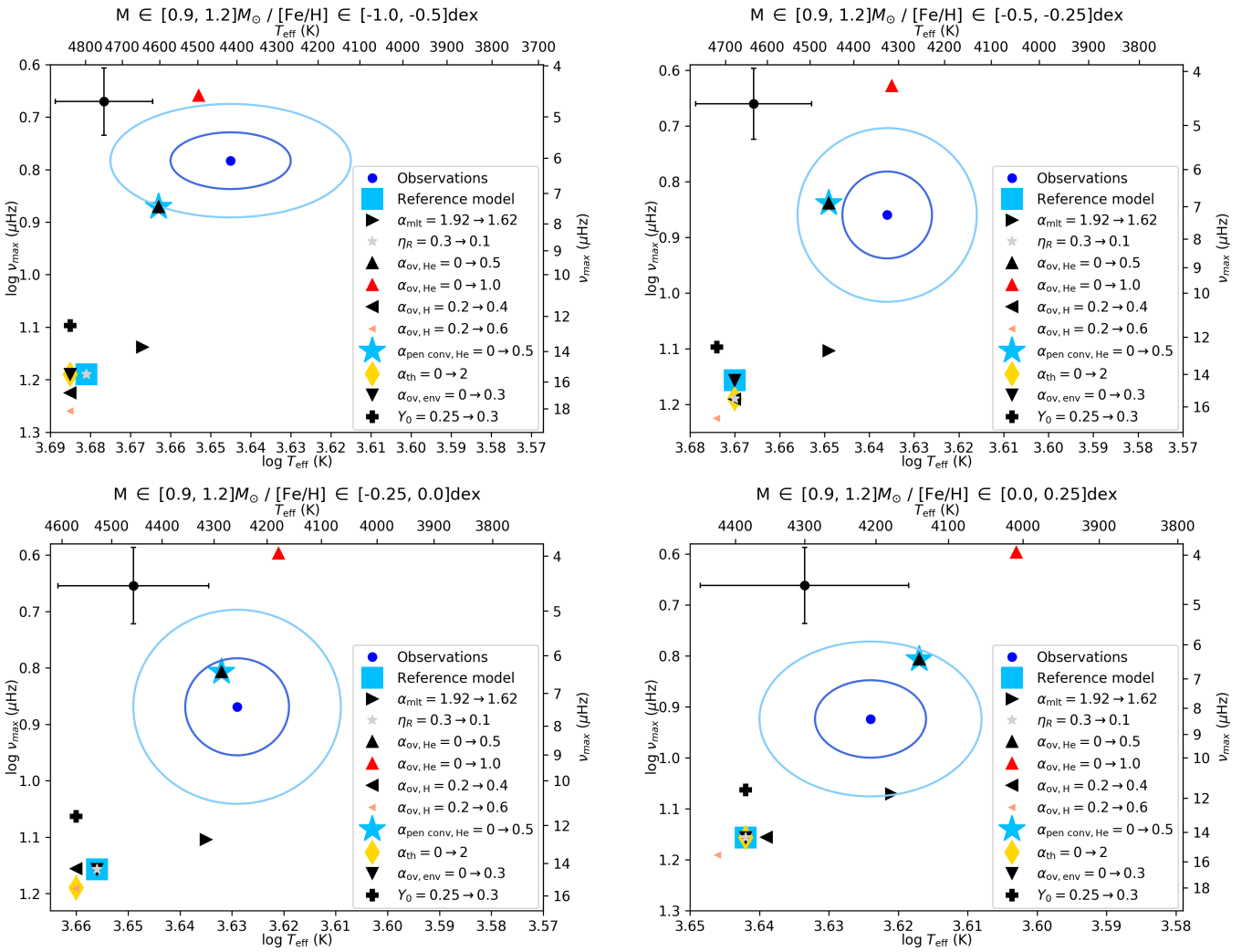

Fig. 5: Same label as in Fig. 4, but for the bins of mass $M \in [0.9, 1.2] M_\odot$ and metallicity [Fe/H] $\in [-1.0, -0.5]$, $[-0.5, -0.25]$, $[-0.25, 0.0]$, $[0.0, 0.25]$ dex. The numerical values are listed in Table A.2 in Appendix A. Ranges of the axes vary in the different panels.

surface magnetic braking (Ekström et al. 2012) are missing to correctly model rotational mixing in low-mass stars ($M \leq 1.5 M_\odot$) in the default MESA files.

6.2. Calibration of physical parameters at high mass

The location of the AGBb derived from observations and stellar models are represented in Fig. 7 for high-mass stars. Modifying the reference model in a similar way as for low-mass stars leads to the same effects highlighted in Sec. 5.2. Adding He-core overshooting increases the distance between the AGBb occurrence and the core He-burning phase along the evolutionary track, decreasing the mixing length parameter $\alpha_{\rm MLT}$ makes the AGBb occur at lower $T_{\rm eff}$, and modifying the other parameters does not highly impact the AGBb location except for the H-core overshooting parameter. Indeed, for stellar masses above $1.5 M_\odot$ the convective core during the main sequence is sufficiently developed so that H-core overshooting can occur. In Fig. 7, it can be seen that increasing $\alpha_{\rm ov,H}$ from 0.2 to 0.6 has roughly the same effect on the AGBb location as adding He-core overshooting $\alpha_{\rm ov,He} = 0.5$. Nevertheless, a high efficiency of H-core overshooting appears to be unrealistic considering the latest values calibrated with observational constraints in eclipsing binaries (e.g. Claret & Torres 2016, 2017, 2018, 2019) which do not exceed $\alpha_{\rm ov,H} \sim 0.2$. Similarly, values of $\alpha_{\rm ov,H}$ lower than 0.2 have been derived from the calibration of dipole modes in low-mass stars by Deheuvels et al. (2016). Finally, recent theoretical predictions based on 3D numerical hydrodynamics simulations of penetrative convection also give $\alpha_{\rm ov,H} < 0.2$ for masses $M < 3\ M_\odot$ (Anders et al. 2022; Jermyn et al. 2022). The additional effects of this unrealistic H-core overshooting can be mimicked by taking into account additional mixing processes at work between the convective core and the radiative core. For instance, we found that adding rotational mixing during the main sequence with a rotation rate $\Omega_{\rm ZAMS}/\Omega_{\rm crit} = 0.3$ roughly produces the same changes in the AGBb location (see Fig. 7, for the metallicity bins [Fe/H] $\in [-0.25, 0.0], [0.0, 0.25]$ dex).

None of the physical mechanisms added to the reference model is enough to reproduce observations. Even the model closest to observations that is obtained by adding a high

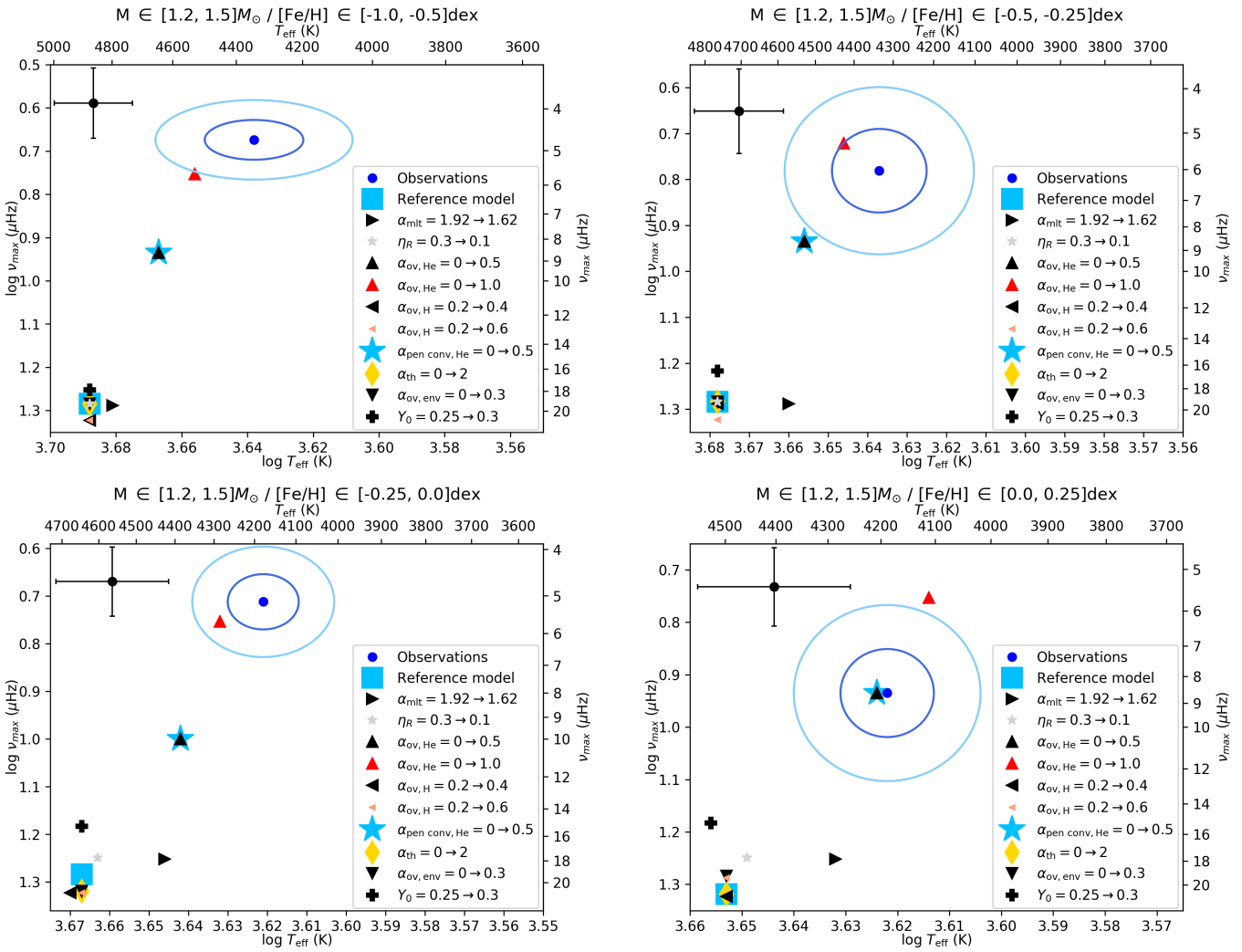

Fig. 6: Same label as in Fig. 5, but for the bins of mass $M \in [1.2, 1.5]M_\odot$ and metallicity [Fe/H] $\in [-1.0, -0.5]$, $[-0.5, -0.25]$, $[-0.25, 0.0]$, $[0.0, 0.25]$ dex. The numerical values are listed in Table A.3 in Appendix A. Ranges of the axes vary in the different panels.

He-core overshooting cannot reproduce the observed AGBb location. Choosing a higher efficiency of He-core overshooting may be unrealistic since the extent of the extra mixing region would be even higher than that of the convective core, but it suggests that additional mixing processes are needed to match models and observations. To investigate those effects a bit further, we combined the two mixing processes that mostly impact the AGBb location, i.e. core overshooting during the core He-burning phase and rotational mixing during the main sequence, and added them to the reference model. As illustrated in Fig. 7, by adding rotational mixing with a rotation rate $\Omega_{\rm ZAMS}/\Omega_{\rm crit} = 0.3$, He-core overshooting $\alpha_{\rm ov,He} = 1.0$, by taking H-core overshooting away $\alpha_{\rm ov,He} = 0$ and decreasing the mixing length parameter of $\Delta\alpha_{\rm MLT} = 0.3$, we are able to reproduce the observed AGBb location.

To sum up, several mixing processes such as rotational mixing and He-core overshooting need to be simultaneously taken into account and calibrated to reproduce observations of high-mass stars. However, rotational mixing during the main sequence remains exploratory and further work is required to quantify its significance relatively to other mixing processes such as He-core overshooting.

6.3. The AGBb as a distance indicator

In Sect. 5.1, we noticed that the AGBb location in $\nu_{\rm max}$ slightly changes with metallicity at fixed mass, especially for high-mass stars, which implies that the luminosity at the AGBb varies with metallicity. This agrees with the theoretical results of Alves & Sarajedini (1999), where the AGBb luminosity is expected to significantly vary with metallicity, especially for high-mass stars with $M \geq 1.2M_\odot$. At first glance, our conclusions seem to be in disagreement with the results of the models of Pulone (1992) and Ferraro (1992) as they justified the use of the AGBb as standard candle by its independence from metallicity. However, these studies are based on a sample of low-metallicity stars in Galactic globular clusters with [Fe/H] $\lesssim -0.5$ dex while ours is mainly composed of high-metallicity stars with [Fe/H] $\gtrsim -0.5$ dex (see Table 1). This tends to confirm that the AGBb location changes at high metallicity. Therefore, metal-rich AGBb stars cannot be used as standard candles. However, this behaviour needs further inspections at low metallicity. We do not have a large enough number of metal-poor AGB stars with [Fe/H] < -0.75 dex to create additional metallicity bins, which limits the analysis of the metallicity

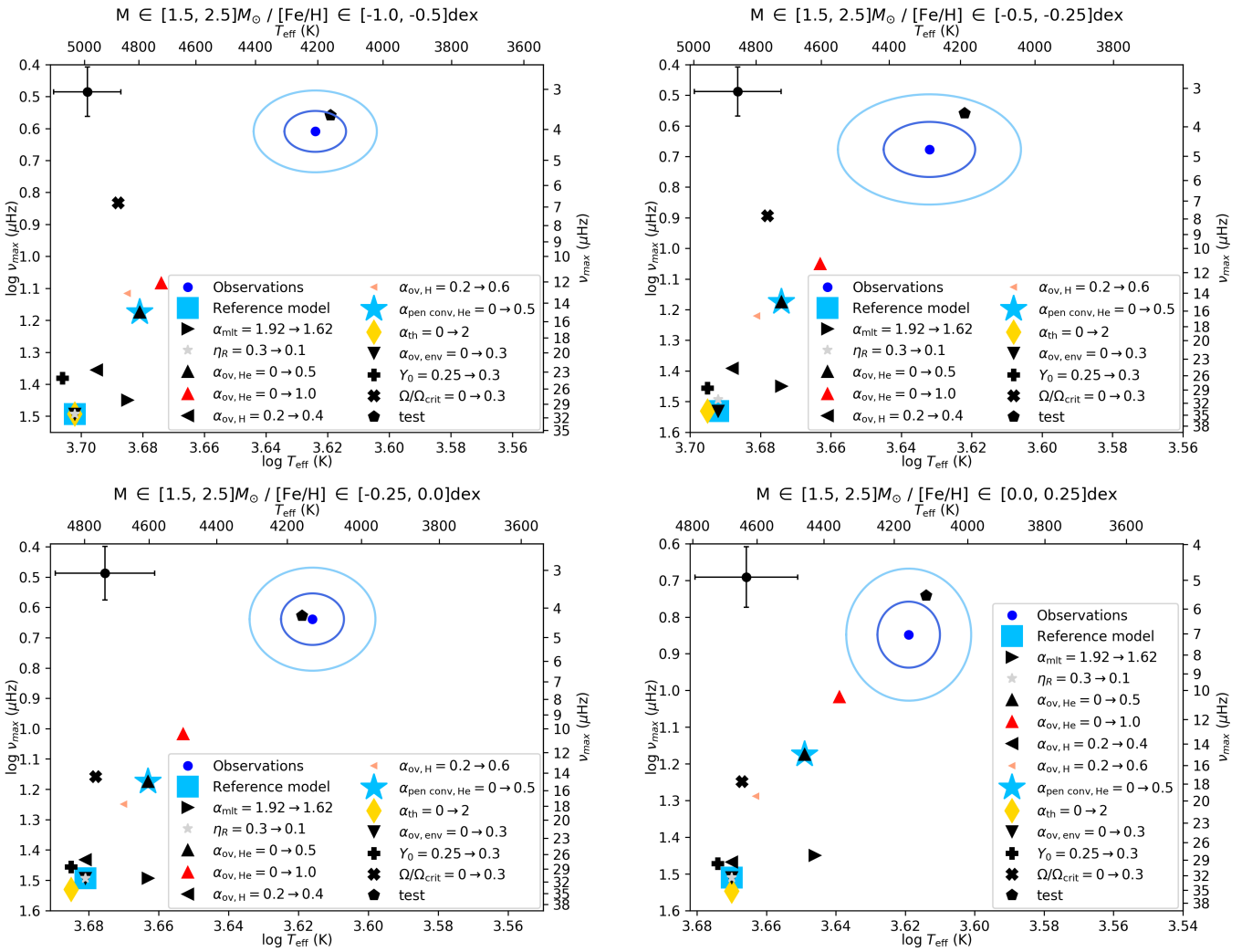

Fig. 7: Same label as in Fig. 5, but for the bins of mass $M \in [1.5, 2.5] M_\odot$ and metallicity [Fe/H] $\in [-1.0, -0.5]$, $[-0.5, -0.25]$, $[-0.25, 0.0]$, $[0.0, 0.25]$ dex. An additional model represented by a black cross has been computed to explore the effects of rotation by taking the rotation rate $\Omega_{\rm ZAMS}/\Omega_{\rm crit} = 0.3$ during the main sequence, relatively to the reference model, where $\Omega_{\rm crit}$ is the surface critical angular velocity for the star to be dislocated. Another model labelled 'test' and represented by a black pentagon has been computed to check if combining several changes could allow us to reproduce observations. Relatively to the reference model, these changes are the adding of rotation $\Omega_{\rm ZAMS}/\Omega_{\rm crit} = 0.3$, He-core overshooting $\alpha_{\rm ov,He} = 1.0$, the removal of H-core overshooting $\alpha_{\rm ov,H} = 0.2 \rightarrow 0$, and the decrease of $\alpha_{\rm MLT} = 1.92 \rightarrow 1.62$. The numerical values are listed in Table A.4 in Appendix A. We warn that the range of the axes are not the same between panels.

dependence of the AGBb. A larger sample of stars would be desirable to confirm or infirm this metallicity dependence at low metallicity. In parallel, it could be interesting to evaluate the potential of the AGBb as a distance indicator, and test if any metallicity bias is identifiable.

7. Conclusion

With the excellent precision of photometric data collected by *Kepler* and TESS, we are now able to perform asteroseismic studies of high-luminosity red giants. This gives access to oscillation mode properties of those stars, which can be used to constrain stellar interiors. In this work, we took advantage of the $\nu_{\rm max}$ estimates from *Kepler* and TESS targets and combined them with spectroscopic data to characterise the AGBb in the widest range and most resolved bins of mass and metallicity explored so far. This would not have been possible without combining targets from several catalogs given the small number of evolved giants subject to a seismic study and the uncertainties on the classification methods between RGB and AGB stars. We detected and accurately located the AGBb in the $\log T_{\rm eff} - \log \nu_{\rm max}$ plane, using a statistical method to distinguish stars belonging to the AGBb and to the AGB background. We highlighted that the occurrence of the AGBb depends on the stellar mass: it clearly takes place at lower $\nu_{\rm max}$ (i.e. at higher luminosity) and occurs within uncertainty at cooler temperature for high-mass stars, in agreement with theoretical models. In parallel, the dependence of the AGBb location on metallicity implies that using it as a standard candle requires some care.

Then, we were able to use the AGBb location in the $\log T_{\rm eff} - \log \nu_{\rm max}$ plane as a constraint for parameters in stellar models in limited bins of mass and metallicity. Mainly the mixing-length parameter and mixing processes

such as He-core overshooting affect the location of the AGBb. Some stellar parameters do not affect the AGBb location, or slightly only, such as the initial helium abundance Y_0, the mass-loss rate on the RGB η_R, the envelope undershooting $\alpha_{\rm ov,env}$ and the thermohaline convection $\alpha_{\rm th}$. Those stellar parameters contribute to the uncertainty of the calibration of mixing processes to match observations. We confirmed that models without core overshooting during the core He-burning phase cannot reproduce observations, as already shown in Bossini et al. (2015). Moreover, we reported that the amount of He-core overshooting needed to match observations and models depends on the stellar mass, and increases with it. Indicatively, the core overshooting value $\alpha_{\rm ov,He} \in [0.25, 0.50]$ nicely suits observations for stars with $M \in [0.6, 1.2]M_\odot$ while $\alpha_{\rm ov,He} \in [0.5, 1.0]$ better suits those for stars with $M \in [1.2, 1.5]M_\odot$. However, for high-mass stars $M \geq 1.5M_\odot$, modifying the He-core overshooting only does not allow us to reproduce observations. In this case, we explored additional mixing processes, especially rotational mixing during the main sequence, and we found that we could match models and observations by combining rotation-induced mixing and He-core overshooting. Further work is needed to investigate the possible degeneracy between those mixing processes at high mass, and quantify their weight.
The core overshooting calibration does also depend on the metallicity, but not as strongly as the mass in terms of $\log \nu_{\rm max}$, which makes the values previously cited well suited to all bins of metallicity studied. However, because the AGBb location in $\log T_{\rm eff}$ varies with metallicity in models, we need to calibrate other parameters such as the mixing-length parameter $\alpha_{\rm MLT}$ in stellar models so that observations and stellar models match in $\log T_{\rm eff}$ and $\log \nu_{\rm max}$ in the same time.

In the future, new space-borne missions will be helpful to fill the sample of evolved red giants targets, hence to take into account more low-metallicity stars ([Fe/H]≤ -0.5 dex) and high-mass stars ($M \geq 1.5M_\odot$). This will give the opportunity to improve the precision on the observed AGBb location for those bins of mass and metallicity where we lack asteroseismic and spectroscopic data. Besides, it will confirm or disprove the potential of the AGBb to be a suitable standard candle.

Acknowledgements

The authors are grateful to the anonymous referee who helped them in improving this paper with constructive suggestions. G.D. thanks S. Khan and O. Hall for their valuable suggestions that helped improving this work. D.B. acknowledges supported by FCT through the research grants UIDB/04434/2020, UIDP/04434/2020 and PTDC/FIS-AST/30389/2017, and by FEDER-Fundo Europeu de Desenvolvimento Regional through COMPETE2020-Programa Operacional Competitividade e Internacionalização (grant: POCI-01-0145-FEDER-030389).

References

Abdurro'uf, Accetta, K., Aerts, C., et al. 2021, arXiv e-prints, arXiv:2112.02026
Alves, D. R. & Sarajedini, A. 1999, ApJ, 511, 225
Anders, E. H., Jermyn, A. S., Lecoanet, D., & Brown, B. P. 2022, ApJ, 926, 169
Angulo, C., Arnould, M., Rayet, M., et al. 1999, Nucl. Phys. A, 656, 3
Asplund, M., Grevesse, N., Sauval, A. J., & Scott, P. 2009, ARA&A, 47, 481
Baudin, F., Barban, C., Goupil, M. J., et al. 2012, A&A, 538, A73
Benomar, O., Belkacem, K., Bedding, T. R., et al. 2014, ApJ, 781, L29
Blocker, T. 1995, A&A, 297, 727
Bono, G., Castellani, V., degl'Innocenti, S., & Pulone, L. 1995, A&A, 297, 115
Bossini, D., Miglio, A., Salaris, M., et al. 2015, MNRAS, 453, 2290
Bossini, D., Miglio, A., Salaris, M., et al. 2017, MNRAS, 469, 4718
Buder, S., Sharma, S., Kos, J., et al. 2021, MNRAS, 506, 150
Cantiello, M. & Langer, N. 2010, A&A, 521, A9
Caputo, F., Castellani, V., & Wood, P. R. 1978, MNRAS, 184, 377
Cassisi, S., Potekhin, A. Y., Pietrinferni, A., Catelan, M., & Salaris, M. 2007, ApJ, 661, 1094
Castellani, V., Chieffi, A., & Pulone, L. 1991, ApJS, 76, 911
Castellani, V., Giannone, P., & Renzini, A. 1971a, Ap&SS, 10, 355
Castellani, V., Giannone, P., & Renzini, A. 1971b, Ap&SS, 10, 340
Caughlan, G. R. & Fowler, W. A. 1988, Atomic Data and Nuclear Data Tables, 40, 283
Charbonnel, C. & Zahn, J. P. 2007, A&A, 467, L15
Chaussidon, M. 2007, in Lectures in Astrobiology, ed. M. Gargaud, H. Martin, & P. Claeys, 45
Chiosi, C. 2007, in Convection in Astrophysics, ed. F. Kupka, I. Roxburgh, & K. L. Chan, Vol. 239, 235–246
Chugunov, A. I., Dewitt, H. E., & Yakovlev, D. G. 2007, Phys. Rev. D, 76, 025028
Claret, A. & Torres, G. 2016, A&A, 592, A15
Claret, A. & Torres, G. 2017, ApJ, 849, 18
Claret, A. & Torres, G. 2018, ApJ, 859, 100
Claret, A. & Torres, G. 2019, ApJ, 876, 134
Deheuvels, S., Brandão, I., Silva Aguirre, V., et al. 2016, A&A, 589, A93
di Mauro, M. P., Cardini, D., Catanzaro, G., et al. 2011, MNRAS, 415, 3783
Dréau, G., Mosser, B., Lebreton, Y., Gehan, C., & Kallinger, T. 2021, A&A, 650, A115
Eggleton, P. P., Dearborn, D. S. P., & Lattanzio, J. C. 2006, Science, 314, 1580
Eggleton, P. P., Dearborn, D. S. P., & Lattanzio, J. C. 2008, ApJ, 677, 581
Ekström, S., Georgy, C., Eggenberger, P., et al. 2012, A&A, 537, A146
Elsworth, Y., Themeßl, N., Hekker, S., & Chaplin, W. 2020, Research Notes of the American Astronomical Society, 4, 177
Endal, A. S. & Sofia, S. 1978, ApJ, 220, 279
Ferraro, F. R. 1992, Mem. Soc. Astron. Italiana, 63, 491
Foreman-Mackey, D. 2016, The Journal of Open Source Software, 1, 24
Foreman-Mackey, D., Hogg, D. W., Lang, D., & Goodman, J. 2013, PASP, 125, 306
Fynbo, H. O. U., Diget, C. A., Bergmann, U. C., et al. 2005, Nature, 433, 136
Heger, A., Langer, N., & Woosley, S. E. 2000, ApJ, 528, 368
Henyey, L., Vardya, M. S., & Bodenheimer, P. 1965, ApJ, 142, 841
Herwig, F., Blöcker, T., & Driebe, T. 2000, Mem. Soc. Astron. Italiana, 71, 745
Hogg, D. W., Bovy, J., & Lang, D. 2010, arXiv e-prints, arXiv:1008.4686
Huang, W., Gies, D. R., & McSwain, M. V. 2010, ApJ, 722, 605
Iglesias, C. A. & Rogers, F. J. 1996, ApJ, 464, 943
Imbriani, G., Costantini, H., Formicola, A., et al. 2004, A&A, 420, 625
Jermyn, A. S., Anders, E. H., Lecoanet, D., & Cantiello, M. 2022, arXiv e-prints, arXiv:2203.09525
Kallinger, T., Hekker, S., Mosser, B., et al. 2012, A&A, 541, A51
Kawaler, S. D. 1988, ApJ, 333, 236
Khan, S., Hall, O. J., Miglio, A., et al. 2018, ApJ, 859, 156
Kippenhahn, R., Ruschenplatt, G., & Thomas, H. C. 1980, A&A, 91, 175
Kjeldsen, H. & Bedding, T. R. 1995, A&A, 293, 87
Knapp, G. R., Young, K., Lee, E., & Jorissen, A. 1998, ApJS, 117, 209
Lagarde, N., Miglio, A., Eggenberger, P., et al. 2015, A&A, 580, A141

Langer, N., El Eid, M. F., & Fricke, K. J. 1985, A&A, 145, 179
Mackereth, J. T., Miglio, A., Elsworth, Y., et al. 2021, MNRAS, 502, 1947
Maeder, A. 1975, A&A, 40, 303
Marigo, P. & Aringer, B. 2009, A&A, 508, 1539
Marigo, P. & Girardi, L. 2007, A&A, 469, 239
Mathur, S., García, R. A., Régulo, C., et al. 2010, A&A, 511, A46
Mauron, N. & Huggins, P. J. 2006, A&A, 452, 257
McDonald, I., De Beck, E., Zijlstra, A. A., & Lagadec, E. 2018, MNRAS, 481, 4984
McDonald, I. & Trabucchi, M. 2019, MNRAS, 484, 4678
Meynet, G. & Maeder, A. 1997, A&A, 321, 465
Miglio, A., Chiappini, C., Mackereth, J. T., et al. 2021, A&A, 645, A85
Mosser, B. & Appourchaux, T. 2009, A&A, 508, 877
Mosser, B., Benomar, O., Belkacem, K., et al. 2014, A&A, 572, L5
Mosser, B., Dziembowski, W. A., Belkacem, K., et al. 2013, A&A, 559, A137
Mosser, B., Michel, E., Samadi, R., et al. 2019, A&A, 622, A76
Paxton, B., Bildsten, L., Dotter, A., et al. 2011, ApJS, 192, 3
Paxton, B., Cantiello, M., Arras, P., et al. 2013, ApJS, 208, 4
Paxton, B., Marchant, P., Schwab, J., et al. 2015, ApJS, 220, 15
Paxton, B., Schwab, J., Bauer, E. B., et al. 2018, ApJS, 234, 34
Paxton, B., Smolec, R., Schwab, J., et al. 2019, ApJS, 243, 10
Pinçon, C., Goupil, M. J., & Belkacem, K. 2020, A&A, 634, A68
Pinsonneault, M. H., Elsworth, Y., Epstein, C., et al. 2014, ApJS, 215, 19
Pinsonneault, M. H., Elsworth, Y. P., Tayar, J., et al. 2018, ApJS, 239, 32
Pinsonneault, M. H., Kawaler, S. D., Sofia, S., & Demarque, P. 1989, ApJ, 338, 424
Pulone, L. 1992, Mem. Soc. Astron. Italiana, 63, 485
Ramstedt, S., Schöier, F. L., Olofsson, H., & Lundgren, A. A. 2008, A&A, 487, 645
Reimers, D. 1975, Memoires of the Societe Royale des Sciences de Liege, 8, 369
Robertson, J. W. & Faulkner, D. J. 1972, ApJ, 171, 309
Sackmann, I. J., Boothroyd, A. I., & Fowler, W. A. 1990, ApJ, 360, 727
Salaris, M. & Cassisi, S. 2017, Royal Society Open Science, 4, 170192
Steinmetz, M., Guiglion, G., McMillan, P. J., et al. 2020, AJ, 160, 83
Stello, D., Compton, D. L., Bedding, T. R., et al. 2014, ApJ, 788, L10
Sweigart, A. V. & Gross, P. G. 1973, in Bulletin of the American Astronomical Society, Vol. 5, 314
Ulrich, R. K. 1972, ApJ, 172, 165
Vrard, M., Mosser, B., & Samadi, R. 2016, A&A, 588, A87
Wagstaff, G., Miller Bertolami, M. M., & Weiss, A. 2020, MNRAS, 493, 4748
Yu, J., Bedding, T. R., Stello, D., et al. 2020, MNRAS, 493, 1388
Yu, J., Hekker, S., Bedding, T. R., et al. 2021, MNRAS, 501, 5135
Zahn, J. P. 1991, A&A, 252, 179

Appendix A: Effects of stellar parameters on the AGBb occurrence

The AGBb locations in $\log T_{\rm eff}$ and $\log \nu_{\rm max}$ presented in Fig. 4, 5, 6, 7 in the mass bins $M \in [0.6, 0.9]$, $[0.9, 1.2]$, $[1.2, 1.5]$, $[1.5, 2.5] M_\odot$ and metallicity bins [Fe/H] $\in [-1.0, -0.5]$, $[-0.5, -0.25]$, $[-0.25, 0.0]$, $[0.0, 0.25]$ dex are summarised in Table A.1, A.2, A.3, A.4.

Appendix B: Distance between the AGBb and clump phase

Another relevant property of the AGBb to investigate is the distance in $\log \nu_{\rm max}$ and $\log T_{\rm eff}$ between its location and that of the core He-burning phase. Indeed, theoretical models report a weak dependence of the luminosity ratio between the AGBb and red clump locations on the metallicity and initial helium abundance (Castellani et al. 1991; Bono et al. 1995). Accordingly, we inspected how the ratio of $\log \nu_{\rm max}$ and $\log T_{\rm eff}$ between the AGBb and red clump phase varies with a change in physical parameters. To this end, we needed to extract the location of the red clump. We proceeded in the same way as that described in Sect. 4.2, but we adapted it for the overdensity of stars in the clump phase. We only included stellar models for which the core helium abundance lies in the interval $Y_{\rm c} \in [0.01, 0.95]$ in the histogram. Then, we extracted the clump location independently from that of the AGBb. The ratios in $\log \nu_{\rm max}$ and $\log T_{\rm eff}$ between the AGBb and the red clump phase for our set of stellar models are shown in Table B.1, B.2, B.3, B.4.

Overall, the ratio in $\log T_{\rm eff}$ is almost constant and the ratio in $\log \nu_{\rm max}$ weakly decreases (equivalently the ratio in $\log L$ weakly increases) when the metallicity increases with a given set of physical ingredients. This agrees with the typical difference between metal-poor and metal-rich models obtained with the theoretical models of Castellani et al. (1991) (their Fig. 7). These ratios do not significantly change within uncertainties when a specific change in physical parameter is performed, except when adding He-core overshooting. Indeed, both ratios in $\log \nu_{\rm max}$ and $\log T_{\rm eff}$ substantially decrease (namely the ratio in $\log L$ increases) when adding He-core overshooting. This implies that the adding of He-core overshooting causes an increase of the distance between the AGBb and the red clump locations along the evolutionary track, but a change in other physical parameters leave this distance constant.
Given that some physical ingredients have an effect on the AGBb location but leave the ratio of location between the AGBb and the red clump unchanged, it means that some of those physical ingredients also impact the red clump location. This is not surprising for physical parameters such as the initial helium abundance, as it determines how much helium burning contributes to the stellar luminosity during the red clump phase. Consequently, this ratio in $\log \nu_{\rm max}$ could also be used in combination with the AGBb location in $\log \nu_{\rm max}$ as calibrators for mixing processes to reproduce both the AGBb and the red clump locations in the same time.

Table A.1: AGBb location for observations and models with $M \in [0.6, 0.9] M_\odot$

M ($M_\odot$)			[0.6, 0.9]		
[Fe/H] (dex)		$[-1.0, -0.5]$	$[-0.5, -0.25]$	$[-0.25, 0.0]$	$[0.0, 0.25]$
Observations	$\log T_{\rm eff}$	3.643 ± 0.019	3.639 ± 0.011	3.632 ± 0.010	-
	$\log \nu_{\rm max}$	0.831 ± 0.031	0.882 ± 0.075	0.887 ± 0.077	-
Reference model	$\log T_{\rm eff}$	3.688 ± 0.011	3.674 ± 0.014	3.660 ± 0.018	3.642 ± 0.014
	$\log \nu_{\rm max}$	1.089 ± 0.060	1.089 ± 0.037	1.089 ± 0.065	1.055 ± 0.064
$\alpha_{\rm MLT} = 1.92 \rightarrow 1.62$	$\log T_{\rm eff}$	3.670 ± 0.018	3.653 ± 0.019	3.635 ± 0.015	3.628 ± 0.012
	$\log \nu_{\rm max}$	1.071 ± 0.060	1.037 ± 0.076	1.003 ± 0.057	1.003 ± 0.040
$\eta_R = 0.3 \rightarrow 0.1$	$\log T_{\rm eff}$	3.681 ± 0.011	3.670 ± 0.011	3.656 ± 0.015	3.642 ± 0.015
	$\log \nu_{\rm max}$	1.123 ± 0.045	1.089 ± 0.038	1.089 ± 0.069	1.089 ± 0.067
$\alpha_{\rm ov,He} = 0 \rightarrow 0.5$	$\log T_{\rm eff}$	3.660 ± 0.019	3.649 ± 0.022	3.632 ± 0.023	3.617 ± 0.021
	$\log \nu_{\rm max}$	0.743 ± 0.099	0.743 ± 0.099	0.711 ± 0.090	0.743 ± 0.184
$\alpha_{\rm ov,He} = 0 \rightarrow 1.0$	$\log T_{\rm eff}$	3.649 ± 0.020	3.632 ± 0.020	3.617 ± 0.021	3.603 ± 0.018
	$\log \nu_{\rm max}$	0.535 ± 0.108	0.504 ± 0.116	0.504 ± 0.124	0.504 ± 0.120
$\alpha_{\rm ov,H} = 0.2 \rightarrow 0.4$	$\log T_{\rm eff}$	3.685 ± 0.014	3.678 ± 0.015	3.663 ± 0.019	3.646 ± 0.017
	$\log \nu_{\rm max}$	1.122 ± 0.053	1.087 ± 0.062	1.087 ± 0.063	1.087 ± 0.044
$\alpha_{\rm ov,H} = 0.2 \rightarrow 0.6$	$\log T_{\rm eff}$	3.688 ± 0.013	3.678 ± 0.015	3.660 ± 0.020	3.642 ± 0.016
	$\log \nu_{\rm max}$	1.122 ± 0.050	1.087 ± 0.034	1.087 ± 0.061	1.087 ± 0.071
$\alpha_{\rm pen\ conv,He} = 0 \rightarrow 0.5$	$\log T_{\rm eff}$	3.660 ± 0.019	3.649 ± 0.022	3.632 ± 0.023	3.617 ± 0.021
	$\log \nu_{\rm max}$	0.743 ± 0.099	0.743 ± 0.099	0.711 ± 0.090	0.743 ± 0.184
$\alpha_{\rm th} = 0 \rightarrow 2$	$\log T_{\rm eff}$	3.688 ± 0.013	3.674 ± 0.014	3.660 ± 0.013	3.646 ± 0.014
	$\log \nu_{\rm max}$	1.157 ± 0.062	1.123 ± 0.073	1.123 ± 0.072	1.089 ± 0.072
$\alpha_{\rm ov,env} = 0 \rightarrow 0.3$	$\log T_{\rm eff}$	3.685 ± 0.014	3.674 ± 0.014	3.660 ± 0.017	3.642 ± 0.015
	$\log \nu_{\rm max}$	1.089 ± 0.065	1.089 ± 0.044	1.089 ± 0.040	1.055 ± 0.080
$Y_0 = 0.253 \rightarrow 0.303$	$\log T_{\rm eff}$	3.685 ± 0.014	3.670 ± 0.012	3.660 ± 0.013	3.642 ± 0.015
	$\log \nu_{\rm max}$	1.030 ± 0.061	1.030 ± 0.062	0.997 ± 0.059	0.997 ± 0.077

Notes: The AGBb locations are plotted in Fig. 4. Models have been obtained by individually changing the parameters of the reference model. These changes are indicated by the arrow.

Table A.2: AGBb location for observations and models with $M \in [0.9, 1.2] M_\odot$

M ($M_\odot$)			[0.9, 1.2]		
[Fe/H] (dex)		$[-1.0, -0.5]$	$[-0.5, -0.25]$	$[-0.25, 0.0]$	$[0.0, 0.25]$
Observations	$\log T_{\rm eff}$	3.645 ± 0.015	3.636 ± 0.010	3.629 ± 0.010	3.624 ± 0.008
	$\log \nu_{\rm max}$	0.783 ± 0.054	0.860 ± 0.078	0.869 ± 0.086	0.924 ± 0.076
Reference model	$\log T_{\rm eff}$	3.681 ± 0.010	3.670 ± 0.011	3.656 ± 0.013	3.642 ± 0.014
	$\log \nu_{\rm max}$	1.190 ± 0.048	1.157 ± 0.066	1.157 ± 0.071	1.157 ± 0.063
$\alpha_{\rm MLT} = 1.92 \rightarrow 1.62$	$\log T_{\rm eff}$	3.667 ± 0.016	3.649 ± 0.013	3.635 ± 0.014	3.621 ± 0.013
	$\log \nu_{\rm max}$	1.138 ± 0.062	1.104 ± 0.058	1.104 ± 0.051	1.071 ± 0.048
$\eta_R = 0.3 \rightarrow 0.1$	$\log T_{\rm eff}$	3.681 ± 0.010	3.670 ± 0.010	3.656 ± 0.013	3.642 ± 0.013
	$\log \nu_{\rm max}$	1.190 ± 0.050	1.190 ± 0.057	1.157 ± 0.070	1.157 ± 0.063
$\alpha_{\rm ov,He} = 0 \rightarrow 0.5$	$\log T_{\rm eff}$	3.663 ± 0.016	3.649 ± 0.017	3.632 ± 0.019	3.617 ± 0.019
	$\log \nu_{\rm max}$	0.871 ± 0.055	0.839 ± 0.042	0.807 ± 0.062	0.807 ± 0.082
$\alpha_{\rm ov,He} = 0 \rightarrow 1.0$	$\log T_{\rm eff}$	3.653 ± 0.018	3.635 ± 0.019	3.621 ± 0.018	3.603 ± 0.018
	$\log \nu_{\rm max}$	0.659 ± 0.112	0.628 ± 0.114	0.597 ± 0.110	0.597 ± 0.110
$\alpha_{\rm ov,H} = 0.2 \rightarrow 0.4$	$\log T_{\rm eff}$	3.685 ± 0.011	3.670 ± 0.011	3.660 ± 0.013	3.639 ± 0.014
	$\log \nu_{\rm max}$	1.225 ± 0.076	1.191 ± 0.073	1.156 ± 0.065	1.156 ± 0.068
$\alpha_{\rm ov,H} = 0.2 \rightarrow 0.6$	$\log T_{\rm eff}$	3.685 ± 0.009	3.674 ± 0.012	3.660 ± 0.013	3.646 ± 0.015
	$\log \nu_{\rm max}$	1.260 ± 0.058	1.225 ± 0.071	1.191 ± 0.073	1.191 ± 0.084
$\alpha_{\rm pen\ conv,He} = 0 \rightarrow 0.5$	$\log T_{\rm eff}$	3.663 ± 0.016	3.649 ± 0.017	3.632 ± 0.019	3.617 ± 0.019
	$\log \nu_{\rm max}$	0.871 ± 0.055	0.839 ± 0.042	0.807 ± 0.062	0.807 ± 0.082
$\alpha_{\rm th} = 0 \rightarrow 2$	$\log T_{\rm eff}$	3.685 ± 0.009	3.670 ± 0.011	3.660 ± 0.012	3.642 ± 0.014
	$\log \nu_{\rm max}$	1.190 ± 0.065	1.190 ± 0.068	1.190 ± 0.065	1.157 ± 0.069
$\alpha_{\rm ov,env} = 0 \rightarrow 0.3$	$\log T_{\rm eff}$	3.685 ± 0.010	3.670 ± 0.011	3.656 ± 0.013	3.642 ± 0.013
	$\log \nu_{\rm max}$	1.190 ± 0.057	1.157 ± 0.043	1.157 ± 0.043	1.157 ± 0.073
$Y_0 = 0.253 \rightarrow 0.3$	$\log T_{\rm eff}$	3.685 ± 0.009	3.674 ± 0.010	3.660 ± 0.013	3.642 ± 0.013
	$\log \nu_{\rm max}$	1.097 ± 0.066	1.097 ± 0.067	1.063 ± 0.073	1.063 ± 0.077

Notes: The AGBb locations are plotted in Fig. 5. Models have been obtained by individually changing the parameters of the reference model. These changes are indicated in the first column.

Table A.3: AGBb location for observations and models with $M \in [1.2, 1.5] M_\odot$

M ($M_\odot$)		[1.2, 1.5]			
[Fe/H] (dex)		$[-1.0, -0.5]$	$[-0.5, -0.25]$	$[-0.25, 0.0]$	$[0.0, 0.25]$
Observations	$\log T_{\rm eff}$	3.638 ± 0.015	3.637 ± 0.012	3.621 ± 0.009	3.622 ± 0.009
	$\log \nu_{\rm max}$	0.674 ± 0.046	0.781 ± 0.091	0.712 ± 0.058	0.935 ± 0.084
Reference model	$\log T_{\rm eff}$	3.688 ± 0.011	3.678 ± 0.010	3.667 ± 0.012	3.653 ± 0.011
	$\log \nu_{\rm max}$	1.284 ± 0.033	1.284 ± 0.078	1.284 ± 0.078	1.319 ± 0.074
$\alpha_{\rm MLT} = 1.92 \rightarrow 1.62$	$\log T_{\rm eff}$	3.681 ± 0.014	3.660 ± 0.013	3.646 ± 0.014	3.632 ± 0.016
	$\log \nu_{\rm max}$	1.288 ± 0.066	1.288 ± 0.066	1.252 ± 0.060	1.252 ± 0.063
$\eta_R = 0.3 \rightarrow 0.1$	$\log T_{\rm eff}$	3.688 ± 0.010	3.678 ± 0.011	3.663 ± 0.014	3.649 ± 0.013
	$\log \nu_{\rm max}$	1.284 ± 0.066	1.284 ± 0.072	1.249 ± 0.079	1.249 ± 0.071
$\alpha_{\rm ov,He} = 0 \rightarrow 0.5$	$\log T_{\rm eff}$	3.667 ± 0.015	3.656 ± 0.011	3.642 ± 0.019	3.624 ± 0.019
	$\log \nu_{\rm max}$	0.935 ± 0.078	0.935 ± 0.081	1.000 ± 0.071	0.935 ± 0.057
$\alpha_{\rm ov,He} = 0 \rightarrow 1.0$	$\log T_{\rm eff}$	3.656 ± 0.016	3.646 ± 0.015	3.632 ± 0.019	3.614 ± 0.017
	$\log \nu_{\rm max}$	0.753 ± 0.108	0.721 ± 0.112	0.753 ± 0.089	0.753 ± 0.092
$\alpha_{\rm ov,H} = 0.2 \rightarrow 0.4$	$\log T_{\rm eff}$	3.688 ± 0.010	3.678 ± 0.011	3.670 ± 0.012	3.653 ± 0.013
	$\log \nu_{\rm max}$	1.323 ± 0.051	1.288 ± 0.053	1.323 ± 0.052	1.323 ± 0.095
$\alpha_{\rm ov,H} = 0.2 \rightarrow 0.6$	$\log T_{\rm eff}$	3.688 ± 0.009	3.678 ± 0.010	3.667 ± 0.013	3.653 ± 0.014
	$\log \nu_{\rm max}$	1.323 ± 0.074	1.323 ± 0.088	1.323 ± 0.097	1.288 ± 0.089
$\alpha_{\rm pen\ conv,He} = 0 \rightarrow 0.5$	$\log T_{\rm eff}$	3.667 ± 0.015	3.656 ± 0.011	3.642 ± 0.019	3.624 ± 0.019
	$\log \nu_{\rm max}$	0.935 ± 0.078	0.935 ± 0.081	1.000 ± 0.071	0.935 ± 0.057
$\alpha_{\rm th} = 0 \rightarrow 2$	$\log T_{\rm eff}$	3.688 ± 0.010	3.678 ± 0.010	3.667 ± 0.010	3.653 ± 0.014
	$\log \nu_{\rm max}$	1.284 ± 0.023	1.284 ± 0.060	1.319 ± 0.076	1.319 ± 0.083
$\alpha_{\rm ov,env} = 0 \rightarrow 0.3$	$\log T_{\rm eff}$	3.688 ± 0.011	3.678 ± 0.010	3.667 ± 0.011	3.653 ± 0.015
	$\log \nu_{\rm max}$	1.284 ± 0.066	1.284 ± 0.063	1.319 ± 0.050	1.284 ± 0.049
$Y_0 = 0.253 \rightarrow 0.303$	$\log T_{\rm eff}$	3.688 ± 0.010	3.678 ± 0.012	3.667 ± 0.014	3.656 ± 0.011
	$\log \nu_{\rm max}$	1.252 ± 0.105	1.217 ± 0.133	1.183 ± 0.073	1.183 ± 0.095

Notes: The AGBb locations are plotted in Fig. 6. Models have been obtained by individually changing the parameters of the reference model. These changes are indicated in the first column.

Table A.4: AGBb location for observations and models with $M \in [1.5, 2.5] M_\odot$

M ($M_\odot$)		$[1.5, 2.5]$			
[Fe/H] (dex)		$[-1.0, -0.5]$	$[-0.5, -0.25]$	$[-0.25, 0.0]$	$[0.0, 0.25]$
Observations	$\log T_{\rm eff}$	3.624 ± 0.010	3.632 ± 0.013	3.616 ± 0.009	3.619 ± 0.009
	$\log \nu_{\rm max}$	0.609 ± 0.064	0.677 ± 0.090	0.639 ± 0.085	0.848 ± 0.090
Reference model	$\log T_{\rm eff}$	3.702 ± 0.009	3.692 ± 0.009	3.681 ± 0.013	3.670 ± 0.014
	$\log \nu_{\rm max}$	1.493 ± 0.065	1.531 ± 0.065	1.493 ± 0.062	1.510 ± 0.088
$\alpha_{\rm MLT} = 1.92 \rightarrow 1.62$	$\log T_{\rm eff}$	3.685 ± 0.012	3.674 ± 0.012	3.663 ± 0.013	3.646 ± 0.015
	$\log \nu_{\rm max}$	1.450 ± 0.037	1.450 ± 0.078	1.493 ± 0.089	1.450 ± 0.071
$\eta_R = 0.3 \rightarrow 0.1$	$\log T_{\rm eff}$	3.702 ± 0.009	3.692 ± 0.009	3.681 ± 0.012	3.670 ± 0.014
	$\log \nu_{\rm max}$	1.493 ± 0.027	1.493 ± 0.086	1.493 ± 0.085	1.510 ± 0.080
$\alpha_{\rm ov,He} = 0 \rightarrow 0.5$	$\log T_{\rm eff}$	3.681 ± 0.011	3.674 ± 0.011	3.663 ± 0.015	3.649 ± 0.016
	$\log \nu_{\rm max}$	1.175 ± 0.042	1.175 ± 0.062	1.175 ± 0.070	1.175 ± 0.075
$\alpha_{\rm ov,He} = 0 \rightarrow 1.0$	$\log T_{\rm eff}$	3.674 ± 0.013	3.663 ± 0.013	3.653 ± 0.017	3.639 ± 0.017
	$\log \nu_{\rm max}$	1.084 ± 0.082	1.051 ± 0.073	1.018 ± 0.084	1.018 ± 0.112
$\alpha_{\rm ov,H} = 0.2 \rightarrow 0.4$	$\log T_{\rm eff}$	3.695 ± 0.010	3.688 ± 0.010	3.681 ± 0.012	3.670 ± 0.014
	$\log \nu_{\rm max}$	1.355 ± 0.067	1.392 ± 0.087	1.432 ± 0.069	1.468 ± 0.095
$\alpha_{\rm ov,H} = 0.2 \rightarrow 0.6$	$\log T_{\rm eff}$	3.685 ± 0.013	3.681 ± 0.012	3.670 ± 0.011	3.663 ± 0.012
	$\log \nu_{\rm max}$	1.116 ± 0.155	1.221 ± 0.110	1.249 ± 0.060	1.288 ± 0.088
$\alpha_{\rm pen\ conv,He} = 0 \rightarrow 0.5$	$\log T_{\rm eff}$	3.681 ± 0.011	3.674 ± 0.011	3.663 ± 0.015	3.649 ± 0.016
	$\log \nu_{\rm max}$	1.175 ± 0.042	1.175 ± 0.062	1.175 ± 0.070	1.175 ± 0.075
$\alpha_{\rm th} = 0 \rightarrow 2$	$\log T_{\rm eff}$	3.702 ± 0.008	3.695 ± 0.007	3.685 ± 0.011	3.670 ± 0.014
	$\log \nu_{\rm max}$	1.493 ± 0.090	1.531 ± 0.080	1.531 ± 0.082	1.547 ± 0.090
$\alpha_{\rm ov,env} = 0 \rightarrow 0.3$	$\log T_{\rm eff}$	3.702 ± 0.010	3.692 ± 0.010	3.681 ± 0.011	3.670 ± 0.014
	$\log \nu_{\rm max}$	1.493 ± 0.079	1.531 ± 0.077	1.493 ± 0.085	1.510 ± 0.057
$Y_0 = 0.253 \rightarrow 0.303$	$\log T_{\rm eff}$	3.706 ± 0.013	3.695 ± 0.012	3.685 ± 0.014	3.674 ± 0.014
	$\log \nu_{\rm max}$	1.381 ± 0.129	1.456 ± 0.102	1.456 ± 0.108	1.472 ± 0.086
$\Omega_{\rm ZAMS}/\Omega_{\rm crit} = 0 \rightarrow 0.3$	$\log T_{\rm eff}$	3.688 ± 0.006	3.678 ± 0.009	3.678 ± 0.011	3.667 ± 0.013
	$\log \nu_{\rm max}$	0.833 ± 0.061	0.894 ± 0.017	1.159 ± 0.091	1.249 ± 0.081
test	$\log T_{\rm eff}$	3.619 ± 0.017	3.622 ± 0.035	3.619 ± 0.030	3.614 ± 0.019
	$\log \nu_{\rm max}$	0.559 ± 0.066	0.559 ± 0.059	0.628 ± 0.167	0.742 ± 0.077

Notes: The AGBb locations are plotted in Fig. 7. Models have been obtained by individually changing the parameters of the reference model. These changes are indicated in the first column. The model labelled 'test' is obtained with the following changes: $\Omega_{\rm ZAMS}/\Omega_{\rm crit} = 0 \rightarrow 0.3$, $\alpha_{\rm ov,H} = 0.2 \rightarrow 0$, $\alpha_{\rm ov,He} = 0 \rightarrow 1.0$, and $\alpha_{\rm MLT} = 1.92 \rightarrow 1.62$.

Table B.1: Ratio between the AGBb location and the clump location for models with $M \in [0.6, 0.9] M_\odot$

M ($M_\odot$)		$[0.6, 0.9]$			
[Fe/H] (dex)		$[-1.0, -0.5]$	$[-0.5, -0.25]$	$[-0.25, 0.0]$	$[0.0, 0.25]$
Reference model	$\log T_{\rm eff,AGBb}/\log T_{\rm eff,clump}$	0.993 ± 0.006	0.993 ± 0.008	0.993 ± 0.008	0.992 ± 0.007
	$\log \nu_{\rm max,AGBb}/\log \nu_{\rm max,clump}$	0.757 ± 0.058	0.757 ± 0.042	0.757 ± 0.061	0.734 ± 0.060
$\alpha_{\rm MLT} = 1.92 \rightarrow 1.62$	$\log T_{\rm eff,AGBb}/\log T_{\rm eff,clump}$	0.994 ± 0.009	0.993 ± 0.008	0.993 ± 0.007	0.993 ± 0.005
	$\log \nu_{\rm max,AGBb}/\log \nu_{\rm max,clump}$	0.767 ± 0.061	0.743 ± 0.074	0.741 ± 0.057	0.741 ± 0.043
$\eta_R = 0.3 \rightarrow 0.1$	$\log T_{\rm eff,AGBb}/\log T_{\rm eff,clump}$	0.994 ± 0.005	0.994 ± 0.005	0.993 ± 0.007	0.993 ± 0.007
	$\log \nu_{\rm max,AGBb}/\log \nu_{\rm max,clump}$	0.781 ± 0.041	0.757 ± 0.036	0.757 ± 0.059	0.757 ± 0.061
$\alpha_{\rm ov,He} = 0 \rightarrow 0.5$	$\log T_{\rm eff,AGBb}/\log T_{\rm eff,clump}$	0.986 ± 0.009	0.986 ± 0.009	0.985 ± 0.009	0.985 ± 0.008
	$\log \nu_{\rm max,AGBb}/\log \nu_{\rm max,clump}$	0.502 ± 0.076	0.502 ± 0.080	0.480 ± 0.073	0.502 ± 0.133
$\alpha_{\rm ov,He} = 0 \rightarrow 1.0$	$\log T_{\rm eff,AGBb}/\log T_{\rm eff,clump}$	0.985 ± 0.007	0.982 ± 0.007	0.980 ± 0.008	0.981 ± 0.008
	$\log \nu_{\rm max,AGBb}/\log \nu_{\rm max,clump}$	0.372 ± 0.081	0.350 ± 0.086	0.350 ± 0.093	0.350 ± 0.091
$\alpha_{\rm ov,H} = 0.2 \rightarrow 0.4$	$\log T_{\rm eff,AGBb}/\log T_{\rm eff,clump}$	0.994 ± 0.007	0.995 ± 0.007	0.994 ± 0.008	0.994 ± 0.007
	$\log \nu_{\rm max,AGBb}/\log \nu_{\rm max,clump}$	0.780 ± 0.054	0.756 ± 0.058	0.756 ± 0.057	0.756 ± 0.045
$\alpha_{\rm ov,H} = 0.2 \rightarrow 0.6$	$\log T_{\rm eff,AGBb}/\log T_{\rm eff,clump}$	0.994 ± 0.006	0.994 ± 0.007	0.993 ± 0.006	0.993 ± 0.007
	$\log \nu_{\rm max,AGBb}/\log \nu_{\rm max,clump}$	0.780 ± 0.049	0.756 ± 0.038	0.756 ± 0.058	0.756 ± 0.066
$\alpha_{\rm pen\ conv,He} = 0 \rightarrow 0.5$	$\log T_{\rm eff,AGBb}/\log T_{\rm eff,clump}$	0.986 ± 0.009	0.986 ± 0.009	0.985 ± 0.009	0.985 ± 0.008
	$\log \nu_{\rm max,AGBb}/\log \nu_{\rm max,clump}$	0.502 ± 0.076	0.502 ± 0.080	0.480 ± 0.073	0.502 ± 0.133
$\alpha_{\rm th} = 0 \rightarrow 2$	$\log T_{\rm eff,AGBb}/\log T_{\rm eff,clump}$	0.995 ± 0.007	0.995 ± 0.006	0.994 ± 0.006	0.994 ± 0.007
	$\log \nu_{\rm max,AGBb}/\log \nu_{\rm max,clump}$	0.805 ± 0.059	0.781 ± 0.064	0.781 ± 0.063	0.757 ± 0.064
$\alpha_{\rm ov,env} = 0 \rightarrow 0.3$	$\log T_{\rm eff,AGBb}/\log T_{\rm eff,clump}$	0.994 ± 0.007	0.994 ± 0.007	0.993 ± 0.007	0.993 ± 0.007
	$\log \nu_{\rm max,AGBb}/\log \nu_{\rm max,clump}$	0.757 ± 0.060	0.757 ± 0.045	0.757 ± 0.043	0.734 ± 0.068
$Y_0 = 0.253 \rightarrow 0.303$	$\log T_{\rm eff,AGBb}/\log T_{\rm eff,clump}$	0.995 ± 0.006	0.994 ± 0.005	0.994 ± 0.006	0.993 ± 0.007
	$\log \nu_{\rm max,AGBb}/\log \nu_{\rm max,clump}$	0.761 ± 0.061	0.761 ± 0.062	0.736 ± 0.059	0.736 ± 0.074

Notes: Models have been obtained by individually changing the parameters of the reference model. These changes are indicated in the first column.

Table B.2: Ratio between the AGBb location and the clump location for models with $M \in [0.9, 1.2] M_\odot$

M ($M_\odot$)		$[0.9, 1.2]$			
[Fe/H] (dex)		$[-1.0, -0.5]$	$[-0.5, -0.25]$	$[-0.25, 0.0]$	$[0.0, 0.25]$
Reference model	$\log T_{\rm eff,AGBb}/\log T_{\rm eff,clump}$	0.995 ± 0.004	0.994 ± 0.005	0.993 ± 0.006	0.993 ± 0.007
	$\log \nu_{\rm max,AGBb}/\log \nu_{\rm max,clump}$	0.804 ± 0.053	0.782 ± 0.061	0.782 ± 0.064	0.782 ± 0.057
$\alpha_{\rm MLT} = 1.92 \rightarrow 1.62$	$\log T_{\rm eff,AGBb}/\log T_{\rm eff,clump}$	0.995 ± 0.007	0.993 ± 0.006	0.994 ± 0.007	0.993 ± 0.006
	$\log \nu_{\rm max,AGBb}/\log \nu_{\rm max,clump}$	0.791 ± 0.054	0.768 ± 0.052	0.768 ± 0.049	0.745 ± 0.049
$\eta_R = 0.3 \rightarrow 0.1$	$\log T_{\rm eff,AGBb}/\log T_{\rm eff,clump}$	0.995 ± 0.005	0.994 ± 0.005	0.993 ± 0.006	0.993 ± 0.006
	$\log \nu_{\rm max,AGBb}/\log \nu_{\rm max,clump}$	0.804 ± 0.055	0.804 ± 0.056	0.760 ± 0.063	0.760 ± 0.061
$\alpha_{\rm ov,He} = 0 \rightarrow 0.5$	$\log T_{\rm eff,AGBb}/\log T_{\rm eff,clump}$	0.990 ± 0.006	0.988 ± 0.006	0.987 ± 0.008	0.986 ± 0.008
	$\log \nu_{\rm max,AGBb}/\log \nu_{\rm max,clump}$	0.589 ± 0.052	0.567 ± 0.039	0.530 ± 0.049	0.530 ± 0.064
$\alpha_{\rm ov,He} = 0 \rightarrow 1.0$	$\log T_{\rm eff,AGBb}/\log T_{\rm eff,clump}$	0.987 ± 0.006	0.984 ± 0.007	0.984 ± 0.007	0.982 ± 0.008
	$\log \nu_{\rm max,AGBb}/\log \nu_{\rm max,clump}$	0.445 ± 0.086	0.424 ± 0.082	0.403 ± 0.081	0.392 ± 0.080
$\alpha_{\rm ov,H} = 0.2 \rightarrow 0.4$	$\log T_{\rm eff,AGBb}/\log T_{\rm eff,clump}$	0.996 ± 0.005	0.994 ± 0.005	0.994 ± 0.006	0.993 ± 0.004
	$\log \nu_{\rm max,AGBb}/\log \nu_{\rm max,clump}$	0.805 ± 0.086	0.783 ± 0.075	0.781 ± 0.057	0.781 ± 0.061
$\alpha_{\rm ov,H} = 0.2 \rightarrow 0.6$	$\log T_{\rm eff,AGBb}/\log T_{\rm eff,clump}$	0.995 ± 0.004	0.995 ± 0.005	0.993 ± 0.006	0.994 ± 0.007
	$\log \nu_{\rm max,AGBb}/\log \nu_{\rm max,clump}$	0.764 ± 0.093	0.762 ± 0.113	0.762 ± 0.089	0.762 ± 0.087
$\alpha_{\rm pen\ conv,He} = 0 \rightarrow 0.5$	$\log T_{\rm eff,AGBb}/\log T_{\rm eff,clump}$	0.990 ± 0.006	0.988 ± 0.006	0.987 ± 0.008	0.986 ± 0.008
	$\log \nu_{\rm max,AGBb}/\log \nu_{\rm max,clump}$	0.589 ± 0.052	0.567 ± 0.039	0.530 ± 0.049	0.530 ± 0.064
$\alpha_{\rm th} = 0 \rightarrow 2$	$\log T_{\rm eff,AGBb}/\log T_{\rm eff,clump}$	0.996 ± 0.004	0.995 ± 0.005	0.994 ± 0.006	0.994 ± 0.007
	$\log \nu_{\rm max,AGBb}/\log \nu_{\rm max,clump}$	0.804 ± 0.065	0.804 ± 0.066	0.804 ± 0.063	0.782 ± 0.065
$\alpha_{\rm ov,env} = 0 \rightarrow 0.3$	$\log T_{\rm eff,AGBb}/\log T_{\rm eff,clump}$	0.996 ± 0.005	0.994 ± 0.005	0.993 ± 0.006	0.993 ± 0.006
	$\log \nu_{\rm max,AGBb}/\log \nu_{\rm max,clump}$	0.804 ± 0.059	0.782 ± 0.045	0.782 ± 0.044	0.782 ± 0.064
$Y_0 = 0.253 \rightarrow 0.303$	$\log T_{\rm eff,AGBb}/\log T_{\rm eff,clump}$	0.996 ± 0.004	0.995 ± 0.004	0.994 ± 0.006	0.993 ± 0.006
	$\log \nu_{\rm max,AGBb}/\log \nu_{\rm max,clump}$	0.786 ± 0.069	0.786 ± 0.065	0.761 ± 0.068	0.739 ± 0.068

Notes: Models have been obtained by individually changing the parameters of the reference model. These changes are indicated in the first column.

Table B.3: Ratio between the AGBb location and the clump location for models with $M \in [1.2, 1.5] M_\odot$

M ($M_\odot$)		$[1.2, 1.5]$			
[Fe/H] (dex)		$[-1.0, -0.5]$	$[-0.5, -0.25]$	$[-0.25, 0.0]$	$[0.0, 0.25]$
Reference model	$\log T_{\rm eff,AGBb}/\log T_{\rm eff,clump}$	0.995 ± 0.005	0.995 ± 0.004	0.994 ± 0.006	0.995 ± 0.006
	$\log \nu_{\rm max,AGBb}/\log \nu_{\rm max,clump}$	0.821 ± 0.067	0.799 ± 0.091	0.779 ± 0.057	0.800 ± 0.055
$\alpha_{\rm MLT} = 1.92 \rightarrow 1.62$	$\log T_{\rm eff,AGBb}/\log T_{\rm eff,clump}$	0.997 ± 0.006	0.994 ± 0.006	0.995 ± 0.007	0.994 ± 0.007
	$\log \nu_{\rm max,AGBb}/\log \nu_{\rm max,clump}$	0.846 ± 0.088	0.824 ± 0.054	0.801 ± 0.049	0.801 ± 0.049
$\eta_R = 0.3 \rightarrow 0.1$	$\log T_{\rm eff,AGBb}/\log T_{\rm eff,clump}$	0.995 ± 0.004	0.995 ± 0.005	0.994 ± 0.006	0.993 ± 0.006
	$\log \nu_{\rm max,AGBb}/\log \nu_{\rm max,clump}$	0.821 ± 0.086	0.821 ± 0.093	0.799 ± 0.095	0.777 ± 0.081
$\alpha_{\rm ov,He} = 0 \rightarrow 0.5$	$\log T_{\rm eff,AGBb}/\log T_{\rm eff,clump}$	0.990 ± 0.006	0.989 ± 0.004	0.987 ± 0.008	0.986 ± 0.008
	$\log \nu_{\rm max,AGBb}/\log \nu_{\rm max,clump}$	0.614 ± 0.083	0.598 ± 0.079	0.622 ± 0.053	0.567 ± 0.041
$\alpha_{\rm ov,He} = 0 \rightarrow 1.0$	$\log T_{\rm eff,AGBb}/\log T_{\rm eff,clump}$	0.987 ± 0.006	0.986 ± 0.005	0.985 ± 0.008	0.983 ± 0.007
	$\log \nu_{\rm max,AGBb}/\log \nu_{\rm max,clump}$	0.495 ± 0.096	0.461 ± 0.095	0.469 ± 0.061	0.469 ± 0.064
$\alpha_{\rm ov,H} = 0.2 \rightarrow 0.4$	$\log T_{\rm eff,AGBb}/\log T_{\rm eff,clump}$	0.995 ± 0.005	0.994 ± 0.005	0.994 ± 0.004	0.993 ± 0.006
	$\log \nu_{\rm max,AGBb}/\log \nu_{\rm max,clump}$	0.802 ± 0.105	0.762 ± 0.080	0.763 ± 0.105	0.782 ± 0.070
$\alpha_{\rm ov,H} = 0.2 \rightarrow 0.6$	$\log T_{\rm eff,AGBb}/\log T_{\rm eff,clump}$	0.995 ± 0.004	0.994 ± 0.004	0.994 ± 0.005	0.993 ± 0.007
	$\log \nu_{\rm max,AGBb}/\log \nu_{\rm max,clump}$	0.782 ± 0.106	0.763 ± 0.085	0.763 ± 0.092	0.762 ± 0.113
$\alpha_{\rm pen\ conv,He} = 0 \rightarrow 0.5$	$\log T_{\rm eff,AGBb}/\log T_{\rm eff,clump}$	0.990 ± 0.006	0.989 ± 0.004	0.987 ± 0.008	0.986 ± 0.008
	$\log \nu_{\rm max,AGBb}/\log \nu_{\rm max,clump}$	0.614 ± 0.083	0.598 ± 0.079	0.622 ± 0.053	0.567 ± 0.041
$\alpha_{\rm th} = 0 \rightarrow 2$	$\log T_{\rm eff,AGBb}/\log T_{\rm eff,clump}$	0.996 ± 0.005	0.995 ± 0.004	0.995 ± 0.005	0.995 ± 0.007
	$\log \nu_{\rm max,AGBb}/\log \nu_{\rm max,clump}$	0.821 ± 0.065	0.799 ± 0.085	0.821 ± 0.058	0.821 ± 0.063
$\alpha_{\rm ov,env} = 0 \rightarrow 0.3$	$\log T_{\rm eff,AGBb}/\log T_{\rm eff,clump}$	0.995 ± 0.005	0.995 ± 0.004	0.994 ± 0.005	0.995 ± 0.007
	$\log \nu_{\rm max,AGBb}/\log \nu_{\rm max,clump}$	0.821 ± 0.087	0.821 ± 0.078	0.821 ± 0.047	0.799 ± 0.043
$Y_0 = 0.253 \rightarrow 0.303$	$\log T_{\rm eff,AGBb}/\log T_{\rm eff,clump}$	0.995 ± 0.005	0.995 ± 0.005	0.994 ± 0.006	0.994 ± 0.005
	$\log \nu_{\rm max,AGBb}/\log \nu_{\rm max,clump}$	0.823 ± 0.135	0.800 ± 0.144	0.777 ± 0.099	0.777 ± 0.108

Notes: Models have been obtained by individually changing the parameters of the reference model. These changes are indicated in the first column.

Table B.4: Ratio between the AGBb location and the clump location for models with $M \in [1.5, 2.5] M_\odot$

M ($M_\odot$)		[1.5, 2.5]			
[Fe/H] (dex)		$[-1.0, -0.5]$	$[-0.5, -0.25]$	$[-0.25, 0.0]$	$[0.0, 0.25]$
Reference model	$\log T_{\rm eff,AGBb}/\log T_{\rm eff,clump}$	0.996 ± 0.004	0.995 ± 0.004	0.995 ± 0.006	0.994 ± 0.007
	$\log \nu_{\rm max,AGBb}/\log \nu_{\rm max,clump}$	0.841 ± 0.109	0.823 ± 0.083	0.803 ± 0.075	0.812 ± 0.099
$\alpha_{\rm MLT} = 1.92 \rightarrow 1.62$	$\log T_{\rm eff,AGBb}/\log T_{\rm eff,clump}$	0.996 ± 0.005	0.995 ± 0.005	0.994 ± 0.006	0.994 ± 0.008
	$\log \nu_{\rm max,AGBb}/\log \nu_{\rm max,clump}$	0.837 ± 0.105	0.817 ± 0.099	0.821 ± 0.099	0.798 ± 0.094
$\eta_R = 0.3 \rightarrow 0.1$	$\log T_{\rm eff,AGBb}/\log T_{\rm eff,clump}$	0.996 ± 0.004	0.995 ± 0.003	0.995 ± 0.005	0.994 ± 0.007
	$\log \nu_{\rm max,AGBb}/\log \nu_{\rm max,clump}$	0.841 ± 0.090	0.803 ± 0.092	0.803 ± 0.085	0.812 ± 0.093
$\alpha_{\rm ov,He} = 0 \rightarrow 0.5$	$\log T_{\rm eff,AGBb}/\log T_{\rm eff,clump}$	0.990 ± 0.005	0.991 ± 0.004	0.990 ± 0.006	0.988 ± 0.007
	$\log \nu_{\rm max,AGBb}/\log \nu_{\rm max,clump}$	0.695 ± 0.110	0.646 ± 0.075	0.646 ± 0.070	0.632 ± 0.076
$\alpha_{\rm ov,He} = 0 \rightarrow 1.0$	$\log T_{\rm eff,AGBb}/\log T_{\rm eff,clump}$	0.989 ± 0.005	0.988 ± 0.004	0.987 ± 0.006	0.985 ± 0.007
	$\log \nu_{\rm max,AGBb}/\log \nu_{\rm max,clump}$	0.641 ± 0.128	0.592 ± 0.080	0.560 ± 0.074	0.547 ± 0.091
$\alpha_{\rm ov,H} = 0.2 \rightarrow 0.4$	$\log T_{\rm eff,AGBb}/\log T_{\rm eff,clump}$	0.997 ± 0.005	0.996 ± 0.004	0.996 ± 0.005	0.995 ± 0.006
	$\log \nu_{\rm max,AGBb}/\log \nu_{\rm max,clump}$	0.890 ± 0.159	0.823 ± 0.105	0.807 ± 0.101	0.807 ± 0.101
$\alpha_{\rm ov,H} = 0.2 \rightarrow 0.6$	$\log T_{\rm eff,AGBb}/\log T_{\rm eff,clump}$	0.999 ± 0.007	0.998 ± 0.006	0.996 ± 0.006	0.996 ± 0.006
	$\log \nu_{\rm max,AGBb}/\log \nu_{\rm max,clump}$	0.865 ± 0.221	0.875 ± 0.178	0.844 ± 0.131	0.801 ± 0.118
$\alpha_{\rm pen\ conv,He} = 0 \rightarrow 0.5$	$\log T_{\rm eff,AGBb}/\log T_{\rm eff,clump}$	0.990 ± 0.005	0.991 ± 0.004	0.990 ± 0.006	0.988 ± 0.007
	$\log \nu_{\rm max,AGBb}/\log \nu_{\rm max,clump}$	0.695 ± 0.110	0.646 ± 0.075	0.646 ± 0.070	0.632 ± 0.076
$\alpha_{\rm th} = 0 \rightarrow 2$	$\log T_{\rm eff,AGBb}/\log T_{\rm eff,clump}$	0.997 ± 0.004	0.995 ± 0.003	0.995 ± 0.005	0.994 ± 0.008
	$\log \nu_{\rm max,AGBb}/\log \nu_{\rm max,clump}$	0.841 ± 0.127	0.823 ± 0.101	0.805 ± 0.086	0.813 ± 0.089
$\alpha_{\rm ov,env} = 0 \rightarrow 0.3$	$\log T_{\rm eff,AGBb}/\log T_{\rm eff,clump}$	0.996 ± 0.005	0.995 ± 0.004	0.995 ± 0.005	0.994 ± 0.007
	$\log \nu_{\rm max,AGBb}/\log \nu_{\rm max,clump}$	0.841 ± 0.101	0.842 ± 0.085	0.803 ± 0.095	0.812 ± 0.087
$Y_0 = 0.253 \rightarrow 0.303$	$\log T_{\rm eff,AGBb}/\log T_{\rm eff,clump}$	0.998 ± 0.005	0.996 ± 0.005	0.995 ± 0.005	0.995 ± 0.006
	$\log \nu_{\rm max,AGBb}/\log \nu_{\rm max,clump}$	0.859 ± 0.197	0.840 ± 0.124	0.820 ± 0.103	0.810 ± 0.081
$\Omega_{\rm ZAMS}/\Omega_{\rm crit} = 0 \rightarrow 0.3$	$\log T_{\rm eff,AGBb}/\log T_{\rm eff,clump}$	0.999 ± 0.004	0.995 ± 0.005	0.995 ± 0.005	0.994 ± 0.006
	$\log \nu_{\rm max,AGBb}/\log \nu_{\rm max,clump}$	0.820 ± 0.200	0.754 ± 0.150	0.783 ± 0.174	0.777 ± 0.118
test	$\log T_{\rm eff,AGBb}/\log T_{\rm eff,clump}$	0.985 ± 0.007	0.985 ± 0.012	0.984 ± 0.010	0.985 ± 0.007
	$\log \nu_{\rm max,AGBb}/\log \nu_{\rm max,clump}$	0.733 ± 0.275	0.508 ± 0.136	0.464 ± 0.183	0.474 ± 0.096

Notes: Models have been obtained by individually changing the parameters of the reference model. These changes are indicated in the first column. The model labelled 'test' is obtained with the following changes: $\Omega_{\rm ZAMS}/\Omega_{\rm crit} = 0 \rightarrow 0.3$, $\alpha_{\rm ov,H} = 0.2 \rightarrow 0$, $\alpha_{\rm ov,He} = 0 \rightarrow 1.0$, and $\alpha_{\rm MLT} = 1.92 \rightarrow 1.62$.

Chapter 11

Conclusions and prospects

The main concern of this thesis was to investigate the signature of structure differences between Red-Giant Branch (RGB) and Asymptotic-Giant Branch (AGB) stars. This is made possible with asteroseismology, which consists in studying the stellar oscillations caused by the propagation of internal waves. These stellar oscillations induce variations of the surface luminosity that can be detected with high-precision photometry. The recent space-borne telescopes CoRoT by CNES (Baglin et al., 2006), *Kepler* (Borucki et al., 2010; Gilliland et al., 2010) and TESS (Ricker et al., 2015) by NASA have collected tens of thousands of lightcurves of red giants with unprecedented quality, which paved the way for the understanding of the structure of these stars. Indeed, the stellar oscillations of red giants manifest as a power excess in the power spectral density referred to as the oscillation spectrum, in which a repetitive structure of peaks is visible. These peaks correspond to the stellar modes, which result from the constructive interferences of the internal waves. The fine structure of the oscillation spectrum, particularly the mode frequencies, widths, and amplitudes carry the imprints of the stellar structure probed by the internal waves. Accordingly, we are able to study the physical mechanisms that govern the stellar interior of red giants.

High-luminosity RGB and AGB stars are targets of interest since they are the site of an important mass loss that not only impacts their structure and evolution but also contributes to the chemical enrichment of the Galaxy. In spite of the difference of mass due to substantial mass loss at the luminosity-tip of the RGB and the additional He-burning shell in AGB stars, disentangling RGB and AGB stars is challenging since their luminosity and effective temperature are close. Hopefully, the structural differences between those stars can be probed by analysing the properties of their oscillation spectra. The latter are marked by the presence of pressure modes that are excited by the turbulent motion of convective cells at the near surface. The fine structure of the p-mode pattern contains the signature of the helium second-ionisation (HeII) zone (Kallinger et al., 2012; Vrard et al., 2015), which can be used to distinguish H-shell and He-core burning stars. This signature varies with the evolutionary stage since the physical conditions in the envelope of those stars are different (Christensen-Dalsgaard et al., 2014). These works suggest that RGB and AGB stars could still be identified from their different seismic signatures of the HeII zone. However, they lacked a comprehensive seismic study of AGB stars, they did not confirm how the differences observed between RGB and AGB stars are related to their structure differences. The lack of seismic constraints on the AGB is adverse not only for the classification of RGB and AGB stars, but also for the understanding of the physical processes that govern their interiors. In particular, the AGB bump (AGBb) is poorly constrained due to the limited number of AGB stars subject to a seismic study. Yet, AGBb stars reveal to provide valuable constrain on the mixing processes in the He-core burning phase (Bossini et al., 2015). Moreover, theoretical models suggest that AGBb stars could be suitable standard candles, allowing for consistent estimates of distances. All in all, the study of AGB stars provides keys to understand the final stages of stellar evolution, before the formation of compact objects, as well as the chemical evolution of the Galaxy.

11.1 What did we learn?

In this thesis, I performed a thorough analysis of the oscillation spectra of high-luminosity RGB and AGB targets observed by *Kepler* with a cumulative duration of four years. I developed an automated code to decipher the p-mode spectrum of these stars, which is suitable for $\Delta\nu \in [0.5, 4.0]\,\mu$Hz. This code is dedicated to measuring the p-mode frequencies, widths, amplitudes and signature of the HeII zone in these stars. This allowed us to extract the signature of structure differences between RGB and AGB stars, and investigate the physical mechanisms behind mode damping in these stars. In order to interpret the differences between RGB and AGB stars highlighted in the p-mode pattern, I computed a grid of stellar models with MESA, including a large set of physical ingredients from the main sequence up to the AGB. Among these physical processes, we followed the prescription of Bossini et al. (2017) to consider He-core overshooting. Their routine addresses the incomplete treatment of He-semiconvection in MESA, to mitigate artificial injections of helium in the core. In conjunction with MESA models, I computed the adiabatic oscillation frequencies with ADIPLS. We extracted the adiabatic p-mode frequencies following the prescription of Ball, Themeßl, and Hekker (2018). It consists in suppressing the g modes in the core by setting the squared Brunt-Väisälä frequency $N^2_{\rm BV} = 0$ in the core. The extracted p-mode frequencies reveal to be accurate for RGB stars with $\Delta\nu \leq 4.5\,\mu$Hz (Ball, Themeßl, and Hekker, 2018), we checked that they are valid for He-burning stars as well. Last but not least, I characterised the AGBb with a sample of *Kepler* and TESS targets as a function of the stellar mass and metallicity in a statistical framework. Hereafter, I summarise the main conclusions of this thesis.

11.1.1 Classification of RGB and AGB stars

A classification of RGB and AGB stars is possible with the seismic parameters inferred from their oscillation spectra. Initially, Kallinger et al. (2012) proposed a method to classify cold giants in RGB, clump and AGB stages based on the acoustic offset ε that defines the frequency of radial modes according to the asymptotic pattern of red giants (Mosser et al., 2011). However, this seismic parameter is predominantly determined by the envelope properties, including the upper layers of the surface that are poorly understood. This hampers the identification of the physical mechanism behind this classification method. In fact, the asymptotic pattern of red giants relies on the assumption that the gradients of the physical parameters such as sound speed, density, temperature, are not important on a scale of the order of the wavelength of the oscillations. In the asymptotic approach, any strong gradient inevitably introduces a deviation from the asymptotic pattern. Vrard et al. (2015) examined the deviation of the observed radial-mode frequencies with the expected asymptotic frequencies of RGB and clump stars. They highlighted that the magnitude of the frequency shift induced by the HeII zone was equivalent to the typical acoustic offset ε shift reported by Kallinger et al. (2012). Therefore, they identified the HeII imprint on the mode frequencies as the physical basis to distinguish RGB and clump stars with $\Delta\nu \geq 3\,\mu$Hz. In this work, we broaden the conclusions raised by Vrard et al. (2015) at lower $\Delta\nu \leq 3\,\mu$Hz, showing that RGB and AGB stars can be disentangled on the basis of the signature of the HeII zone in the p-mode frequencies.

In parallel, by comparing this identification method to that based on the strength of the seismic signal in time series (Mosser et al., 2019), we could see that they agree when classifying H-shell and He-burning stars with $\Delta\nu \geq 2.5\,\mu$Hz ($\leq 10\%$ of disagreements). Nevertheless, the number of disagreements substantially increases at low $\Delta\nu$, reaching $\sim 30\%$ when $\Delta\nu \leq 1.0\,\mu$Hz. This implies that these classification methods are less efficient at low $\Delta\nu$, making the disentanglement of RGB and AGB stars complicated. Actually, we identified two arguments that could explain this low efficiency rate at low $\Delta\nu$. First, the seismic parameters on which the classification techniques rely are affected by large uncertainties due to the limited frequency resolution. Second, the classification method based on the signature of the HeII zone rests on the asymptotic expansion, which may be unsuitable at low $\Delta\nu \leq 1.0\,\mu$Hz.

11.1.2 Is the asymptotic expansion valid for evolved red giants?

In the asymptotic expansion, regions with strong gradients of physical parameters cannot be addressed. In low- and intermediate-luminosity red giants, the deviations induced by such sharp variations structures are small relatively to the leading terms of the asymptotic expansion, to the extent that they are commonly treated as a small perturbation to the asymptotic expansion. Notwithstanding, we found that the amplitude of the HeII signature in the local large separation $\delta\Delta\nu^{\rm gl}_{n,\ell}$ represents a large fraction of the mean value $\Delta\nu$ for evolved red giants observed by *Kepler*, reaching $\sim 0.08\,\Delta\nu$ when $\Delta\nu \leq 1.0\,\mu$Hz. This finding is reinforced by stellar model analysis since we reached the same conclusion when fitting the glitch signature with the p-mode frequencies returned by ADIPLS. This shows that the perturbation approach to take the glitch signature into account in the mode frequencies cannot apply at low $\Delta\nu$.
When identifying the modes, the template we use to match the observed oscillation spectrum is based on the asymptotic p-mode frequencies of red giants, where the radial order n is assumed to be large relatively to the degree ℓ. Although the assumption $n \gg \ell$ is not valid for low- and intermediate-luminosity red giants, the asymptotic expansion is still appropriate to decipher their oscillation spectrum. Though, we encountered complications to identify the stellar modes by cross correlating the template with the observed oscillation spectrum of high-luminosity red giants when $\Delta\nu \leq 0.5\,\mu$Hz (equivalently when the radial order at maximum oscillation power $n_{\rm max} \leq 4$). In fact, the dipole ($\ell = 1$) and quadrupole ($\ell = 2$) modes get closer to the neighbouring radial ($\ell = 0$) mode as $\Delta\nu$ decreases, forming a triplet structure (Stello et al., 2014). On top of that, as the triplet structure shrinks, the amplitude of the modes is affected and the relative difference of mode heights between different degree ℓ differs when red giants reach high-luminosity stages (Yu et al., 2020). Therefore, the template spectrum based on the asymptotic pattern of low- and intermediate-luminosity red giants is no longer adequate for high-luminosity red giants. In order to extract the mode characteristics, we need to define several template oscillation spectra with different patterns and find the best-matching model, which is work in progress.
As a conclusion, the asymptotic expansion must be inaccurate when interpreting the oscillation spectrum of red giants at low $\Delta\nu \leq 0.5\,\mu$Hz. We need a more appropriate framework for a comprehensive physical understanding of their oscillation spectrum.

11.1.3 Structure differences between RGB and AGB stars

By studying the HeII signature in the local large separation $\delta\Delta\nu^{\rm gl}_{n,\ell}$, we were not only able to confirm the physical basis of the classification method proposed by Kallinger et al. (2012), but also to probe the different physical conditions in RGB and AGB stars. Indeed, the amplitude of the glitch signature is more important during the He-burning phase than during the H-shell burning phase, at fixed $\Delta\nu$. Through stellar models computed with MESA, we could show that this difference is related to a stronger variation of the first adiabatic exponent Γ_1 in the HeII zone during the He-burning phase. This strong variation is correlated with the fact that the helium second ionisation occurs at lower temperature in the He-burning phase, while the acoustic radius of the HeII zone is left unchanged.
Moreover, the period of the glitch modulation is slightly lower for low-mass stars than for high-mass stars at fixed $\Delta\nu$ according to *Kepler* observations and MESA models. Because glitch modulations with short periods are associated to deep structures in the interior, this means that the helium second ionisation occurs deeper in low-mass red giants. Actually, the physical conditions for helium ionisation are reached closer to the surface for high-mass stars with higher effective temperature, which explains our observations.

11.1.4 Additional damping on the early-AGB

By measuring the radial mode widths in *Kepler* observations, I collected evidence that the p-mode damping in high-luminosity red giants is ruled by the action of turbulent pressure, partly compensated by that of entropy. Indeed, these measurements reproduce the values expected from theoretical models, in particular the strong dependence on the effective temperature during the H-shell burning stage (Belkacem

et al., 2012). The radial mode damping increases once the He burning in the core sets in, as highlighted by Vrard et al. (2018). When stars leave the He-core burning phase and gradually ascend the AGB, the radial mode damping becomes similar to that measured on the RGB. This can be explained by the fact that RGB and AGB stars have close effective temperature and surface gravity.

The previous remarks are also valid when considering non-radial modes. Nonetheless, we detected a larger damping for dipole modes when stars leave the clump and begin their ascent on the AGB. When $\Delta\nu \leq 1.25\,\mu$Hz, the dipole mode widths become similar on the RGB and AGB. This suggests that an additional contribution to the mode damping must be taken into account on the early-AGB for non-radial modes, especially for dipole modes. Some mixed dipole modes are still visible in the oscillation spectrum of He-burning stars around $\Delta\nu \sim 2.5\,\mu$Hz, meaning that dipole modes probe deep layers. Then, this additional contribution could be a radiative damping near the H-burning shell, as proposed in Dziembowski (2012) who explained the evolution of dipole mode damping on the RGB.

11.1.5 The need for mixing processes to reproduce the observed AGBb

By combining the seismic observations of *Kepler* and TESS, we could study the dependence of the AGBb location in $\nu_{\rm max}$ and $T_{\rm eff}$ on stellar parameters such as mass and metallicity. On the one hand, the AGBb occurs at higher luminosity L and lower effective temperature $T_{\rm eff}$ when the mass increases. Since the He-core burning takes place at lower luminosity when the mass increases, this means that the luminosity difference between the clump and AGBb phases is more important at high mass. On the other hand, we emphasised that the AGBb occurs at lower luminosity when the metallicity increases, which is mostly visible for stars of mass $M \geq 1.2\,M_\odot$ in our metallicity sample $[{\rm Fe/H}] \in [-1.0, 0.25]$dex.

This dependence on stellar parameters has implications on the calibration of physical ingredients in stellar models. Indeed, the observed position of the AGBb can be used to calibrate mixing processes in stellar interiors. Specifically, Bossini et al. (2015) demonstrated that an extra mixing region above the core is necessary to reproduce the AGBb luminosity in the range of mass $M \in [1.3, 1.7]M_\odot$ and metallicity $[{\rm M/H}] \in [-0.4, 0.4]$dex. Here, we explored how the calibration changes with respect to the mass and metallicity. For stars of mass $M \leq 1.5\,\mu$Hz, we found that He-core overshooting is needed to recreate the observed AGBb location in $\nu_{\rm max}$. Precisely, we showed that the overshooting region should extend over a distance $\alpha_{\rm ov,He}$ in fraction of the pressure scale height H_P from the boundary of the convective core, with $\alpha_{\rm ov,He} \in [0.25, 0.5]$ if $M \in [0.6, 1.2]M_\odot$ and $\alpha_{\rm ov,He} \in [0.5, 1.0]$ if $M \in [1.2, 1.5]M_\odot$. For higher masses ($M \geq 1.5\,M_\odot$), the He-core overshooting alone is not sufficient to justify the AGBb position in $\nu_{\rm max}$. Additional physical ingredients are needed to reproduce observational constraints, such as rotationally-induced mixing. This calibration of stellar models at high mass remains exploratory and more comprehensive work is needed to quantify the weights of physical processes that come into play, for instance by considering additional observational constraints such as the clump position.

11.2 Paving the way for future projects

11.2.1 Near the luminosity-tip of red-giant stars

The seismic analysis of red giants near the luminosity tip is essential not only to understand the physical mechanisms behind the variability of the different red-giant categories, but also to characterise the mass-loss rate that substantially sets in at pulsation periods above $\sim$ 60 days, *i.e.* when the dominant mode is of radial order $n \leq 2$ (Yu et al., 2021). With *Kepler* observations, RGB and AGB stars classified as semi-regular variables based on the regularity and amplitudes of their light curves could be interpreted as solar-like oscillators, with a small number of observed stochastically excited oscillation modes (Mosser et al., 2013b; Yu et al., 2020). Such semi-regular variables are present in our sample of *Kepler* red giants with $\Delta\nu \leq 0.5\,\mu$Hz. Unfortunately, we highlighted that we could not robustly extract the mode characteristics of red giants with $\Delta\nu \leq 0.5\,\mu$Hz. Two main restricting factors make the seismic analysis of red giants complicated in this $\Delta\nu$ domain. First, the modes are not resolved because the

Kepler telescope did not monitor these stars long enough. Second, addressing their oscillation spectrum with the asymptotic p-mode pattern of low- and intermediate-luminosity red giants does not seem to be an adequate method. Nevertheless, a global analysis of the oscillation spectrum could still be performed. Especially, the mode identification can be led and the large frequency separation $\Delta\nu$ as well as the frequency at maximum oscillation power $\nu_{\rm max}$ can be extracted. In my code, I would need to build template spectra that are no longer based on the asymptotic p-mode pattern of low- and intermediate-luminosity red giants, but on the modelled p-mode frequencies returned by ADIPLS (Stello et al., 2014). In order to help the interpretation of the oscillation spectrum of red giants near the luminosity tip, the analysis of *Kepler* observations could also be complemented with ground-based observations. For example, the OGLE-III Catalog of Variable Stars contains about 80,000 low-amplitude red-giant variables (called OGLE Small Amplitude Red Giants, OSARG), which have been continuously observed during eight years (Soszyński et al., 2009). This would offer a better frequency resolution, but at the cost of a complex processing of observational data due to atmospheric effects and day/night aliases.

11.2.2 On detecting He-flash stars

The physical conditions in which He ignites in degenerate conditions in the central layers at the He-subflash stage are still poorly understood. Due to the rapid evolution (tenth of a megayear) between the tip of the RGB and the RC, we have too little information to constrain the structure evolution in the He-subflash stage. However, theoretical studies have highlighted a clear signature of the innermost layers of He-subflash stars in their oscillation spectrum (Deheuvels and Belkacem, 2018). The He burning in unstable conditions creates a convective shell in the core, leading to two g-mode cavities separated by an evanescent zone in the core, referred to as g_1- and g_2-mode cavities. Consequently, a three-cavity mixed-mode pattern is expected, carrying valuable information on the cavities in which mixed modes develop. Of course, detecting the mixed modes that develop in the innermost cavity is challenging because they have very low amplitudes at the surface. On the one hand, the g-dominated mixed modes have large inertias in the core so their heights in the power spectrum are weaker than those of p-dominated modes. On the other hand, the coupling factor between the g_1- and g_2-mode cavities must be high enough for the mixed modes to have non-negligible contribution from the g_1-mode cavity. Nevertheless, with the time-series of about 1470 days collected by *Kepler*, the mixed modes that have a significant contribution from the g_1-mode cavity are expected to have high enough heights in the power spectrum to be detected (Deheuvels and Belkacem, 2018).
By fitting the mixed-modes pattern of red giants, few *Kepler* targets have been suspected to undergo He subflashes as they have different period spacings $\Delta\Pi_1$ relatively to clump stars near $\Delta\nu \sim 3.0\,\mu$Hz (Mosser et al., 2014). Yet, we currently lack a seismic characterisation of these stars, which is crucial to understand the evolution of the structure and the physical conditions in which the ignition of He takes place. At the moment, the fitting technique I use is limited to p modes, but could be properly extended to mixed modes. After extracting the mixed-mode parameters, I could look for two distinct mixed-mode patterns with different period spacings $\Delta\Pi_1$. This could be done by means of period échelle diagrams[1] based on the stretched periods of modes (Mosser et al., 2015). For a specific parameterisation of the stretching, the periods exhibit a nearly vertical ridge in the échelle diagram if the mixed modes follow the same pattern. If two distinct vertical ridges can be enhanced, then they would reflect the presence of two g-mode cavities in the interior. In this scenario, the links between seismic parameters and internal structure, especially between the observed mixed-mode pattern and the size of the two inner g-mode cavities, could be investigated with the grid of stellar models presented in the Appendix 2.

[1]These diagrams exhibit the mode frequencies as a function of the mode periods modulo $\Delta\Pi_1$. They are useful to enhance evenly spaced periods, to visualise regular patterns or departures to regularity (attributed to signatures of rotation or core structural discontinuities) in the oscillation spectrum.

11.2.3 On determining the helium abundance

Precise and accurate masses of stars are crucial for estimating their evolutionary stage (Eggenberger, Carrier, and Bouchy, 2005; Provost et al., 2006) and inferring the mass of orbiting companions in exoplanetary systems (Perryman, 2011). Mass can be inferred from stellar models but even with precise asteroseismic constraints, a strong anticorrelation between mass and the initial helium abundance of the star limits the power of modelling (Lebreton and Goupil, 2014; Noll, Deheuvels, and Ballot, 2021). Therefore, accurate stellar helium abundance is essential to reduce the uncertainties on stellar masses. Notwithstanding, assessing the helium abundance in cool stars is challenging since helium lines do not form in the spectra of cool stars, preventing the surface helium abundance to be inferred. In this context, the asset of asteroseismology is to provide unique contraints on the helium abundance of these stars. Specifically, estimates of the envelope helium abundance can be extracted from the signature of the helium second-ionisation zone in mode frequencies (Verma et al., 2014; Verma et al., 2019; Verma et al., 2022). Since the amplitude of the glitch signature depends on the helium abundance in the stellar envelope, the helium mass fraction can be calibrated to reproduce the glitch amplitude with stellar model grids. Yet, theoretical work uncovered the dependence of the glitch signature on stellar parameters, showing that the glitch amplitude not only depends on the helium mass fraction but also on the electron degeneracy from the centre up to the helium-ionisation region (Houdayer et al., 2021; Houdayer, Reese, and Goupil, 2022). Consequently, a direct connection between the glitch amplitude and the helium abundance may not be straightforward. In this regard, I will be part of a future project, with Pierre Houdayer, aimed at assessing our ability to extract the helium abundance from the glitch amplitude and at investigating potential biases caused by electron degeneracy. We will explore how the electron degeneracy near the helium-ionisation region varies as stellar evolution proceeds. Specifically, we would like to check whether the glitch signature changes can be linked to variations of the electron degeneracy or helium abundance in the envelope. Then, I will make use of stellar models to study the possible impact of physical processes on the mode frequencies and glitch signature. This way, I intend to identify the physical parameters that can play a role in the electron degeneracy near the helium-ionisation zone.

11.2.4 On using AGBb as standard candle

Standard candles are astronomical sources that have a well-known luminosity as being part of a specific category of objects. They are of major importance since they can be used as distance indicators. As a matter of fact, their apparent magnitude mainly depends on their distance[2] from Earth as their surface luminosity is independent of a given set of parameters. Particularly, theoretical models motivated the use of metal-poor AGBb stars as standard candles since their luminosity is expected to be independent of the metallicity at a given mass (Ferraro, 1992; Pulone, 1992). In case of stars with metallicity $[\mathrm{Fe/H}] \in [-1.0, 0.25]$dex, we obtained that the AGBb location in $\nu_{\max}$ varies with metallicity, which is mostly noticeable for stars with mass $M \geq 1.2\,M_{\odot}$. This confirms the theoretical results of Alves and Sarajedini (1999), who enhanced a pronounced metallicity dependence of the AGBb luminosity for stars of mass $M \in [0.9, 1.5]M_{\odot}$ in the metallicity range $[\mathrm{Fe/H}] \in [-1.0, 0.25]$dex. Then, the apparent magnitude of these stars must not only depend on the distance, but also on the metallicity, so that AGBb stars with $[\mathrm{Fe/H}] \in [-1.0, 0.25]$dex are not suitable standard candles.
However, these observations only concern stars of metallicity $[\mathrm{Fe/H}] \in [-1.0, 0.25]$dex. The use of the AGBb as standard candle was initially proposed for metal-poor stars with $[\mathrm{Fe/H}] \in [-2.0, -0.65]$dex at low mass $M \leq 1.0\,M_{\odot}$ (Ferraro, 1992; Pulone, 1992), which is in line with the theoretical predictions of Alves and Sarajedini (1999). Unfortunately, we cannot investigate the dependence of the AGBb location on metallicity with seismic data since too few metal-poor *Kepler* and TESS targets with $[\mathrm{Fe/H}] \leq -1.0$ dex have been subject to an asteroseismic study. Hopefully, the effects of metallicity on the AGBb position could still be examined with the global parameters extracted from spectral energy distributions. Indeed, Yu et al. (2022) derived the radius R and luminosity L of more than 1.5 millions stars observed by APOGEE (Abdurro'uf et al., 2021), GALAH (Buder et al., 2021), and RAVE (Steinmetz et al., 2020), for which spectroscopic estimates of the effective temperature T_{eff} are available. Among

[2] assuming that there is no absorption in the line of sight

them, many AGB stars with metallicity down to -1.5 dex are expected to be present. The next step of this work is to spot the AGBb location in $\log L$ in a wider range of metallicity, which would in turn allow us to conclude about the potential of the AGBb as standard candle.

11.2.5 Chemical enrichment of the Galaxy

In the last decade, the *Kepler*, CoRoT and TESS space-photometry missions have revealed the potential of asteroseismology not only to constrain stellar structure and evolution, but also to derive precise and accurate stellar parameters that impact Galactic astrophysics. The seismic parameters of ensembles of stars provides mass and age estimates of tens of thousands of stars across the Galaxy (*e.g.*, Miglio et al., 2013; Casagrande et al., 2016; Anders et al., 2017). By complementing asteroseismic constraints with astrometric and spectroscopic data, it is possible to follow the chemical and dynamical evolution of the Milky Way, open and globular clusters (Silva Aguirre et al., 2018; Mackereth et al., 2021).
In the same way as Bossini et al. (2015), we could calibrate He-core overshooting in stellar models by reproducing the AGBb position in $\nu_{\rm max}$. In particular, the He-core overshooting efficiency depends on the mass, additional mixing processes are needed to explain the observed AGBb position at mass $M \geq 1.5\,M_{\odot}$. These physical mechanisms directly impact the chemical abundances in the core, bringing additional chemicals in the radiative zone. In parallel, Khan et al. (2018) have shown that the luminosity bump on the RGB can be used to calibrate overshooting below the convective envelope. On top of that, the dredge-up events on the RGB and AGB bring materials produced by nuclear reactions to the surface as the base of the convective zone progresses deeper in the interior. Altogether, these mixing mechanisms affect the composition of the stellar surface. Finally, the chemical composition of the stellar environment is enriched through mass-loss mechanisms. This illustrates how mixing processes in stellar interiors are essential to understand the chemodynamics of the Galaxy. Additional work would be desirable to quantify the chemical enrichment of the Galaxy induced by stellar mixing processes. This is one of the science objectives of the small/medium class space mission High-precision AsteroseismologY in DeNse stellar fields (HAYDN, Miglio et al., 2021b), which will observe stars in dense environments that are hardly observed by previous and current photometric missions.

Bibliography

Abdurro'uf et al. (Dec. 2021). "The Seventeenth Data Release of the Sloan Digital Sky Surveys: Complete Release of MaNGA, MaStar and APOGEE-2 Data". In: *arXiv e-prints*, arXiv:2112.02026, arXiv:2112.02026. arXiv: 2112.02026 [astro-ph.GA].

Aerts, Conny, Jørgen Christensen-Dalsgaard, and Donald W. Kurtz (2010). *Asteroseismology*.

Althaus, Leandro G. et al. (Apr. 2015). "White dwarf evolutionary sequences for low-metallicity progenitors: The impact of third dredge-up". In: *A&A* 576, A9, A9. DOI: 10.1051/0004-6361/201424922. arXiv: 1502.03882 [astro-ph.SR].

Althaus, Leandro G. et al. (Jan. 2017). "The evolution of white dwarfs resulting from helium-enhanced, low-metallicity progenitor stars". In: *A&A* 597, A67, A67. DOI: 10.1051/0004-6361/201629909. arXiv: 1611.06191 [astro-ph.SR].

Alves, David R. and Ata Sarajedini (Jan. 1999). "The Age-dependent Luminosities of the Red Giant Branch Bump, Asymptotic Giant Branch Bump, and Horizontal Branch Red Clump". In: *ApJ* 511.1, pp. 225–234. DOI: 10.1086/306655. arXiv: astro-ph/9808253 [astro-ph].

Anders, Evan H. et al. (Feb. 2022). "Stellar Convective Penetration: Parameterized Theory and Dynamical Simulations". In: *ApJ* 926.2, 169, p. 169. DOI: 10.3847/1538-4357/ac408d. arXiv: 2110.11356 [astro-ph.SR].

Anders, F. et al. (Jan. 2017). "Galactic archaeology with asteroseismology and spectroscopy: Red giants observed by CoRoT and APOGEE". In: *A&A* 597, A30, A30. DOI: 10.1051/0004-6361/201527204. arXiv: 1604.07763 [astro-ph.GA].

Angulo, C. et al. (Aug. 1999). "A compilation of charged-particle induced thermonuclear reaction rates". In: *Nucl. Phys. A* 656.1, pp. 3–183. DOI: 10.1016/S0375-9474(99)00030-5.

Appourchaux, T. et al. (Nov. 2006). "Data Analysis Tools for the Seismology Programme". In: *The CoRoT Mission Pre-Launch Status - Stellar Seismology and Planet Finding*. Ed. by M. Fridlund et al. Vol. 1306. ESA Special Publication, p. 377.

Appourchaux, T. et al. (June 2014). "Oscillation mode linewidths and heights of 23 main-sequence stars observed by Kepler". In: *A&A* 566, A20. DOI: 10.1051/0004-6361/201323317. arXiv: 1403.7046 [astro-ph.SR].

Arentoft, T. et al. (Oct. 2001). "Irregular amplitude variations and another abrupt period change in the δ Scuti star V 1162 Ori". In: *A&A* 378, pp. L33–L36. DOI: 10.1051/0004-6361:20011248.

Asplund, Martin et al. (Sept. 2009). "The Chemical Composition of the Sun". In: *ARA&A* 47.1, pp. 481–522. DOI: 10.1146/annurev.astro.46.060407.145222. arXiv: 0909.0948 [astro-ph.SR].

Baglin, A. et al. (Nov. 2006). "Scientific Objectives for a Minisat: CoRoT". In: *The CoRoT Mission Pre-Launch Status - Stellar Seismology and Planet Finding*. Ed. by M. Fridlund et al. Vol. 1306. ESA Special Publication, p. 33.

Bahcall, John N., M. H. Pinsonneault, and G. J. Wasserburg (Oct. 1995). "Solar models with helium and heavy-element diffusion". In: *Reviews of Modern Physics* 67.4, pp. 781–808. DOI: 10.1103/RevModPhys.67.781. arXiv: hep-ph/9505425 [hep-ph].

Bahcall, John N. et al. (Jan. 2005). "Helioseismological Implications of Recent Solar Abundance Determinations". In: *ApJ* 618.2, pp. 1049–1056. DOI: 10.1086/426070. arXiv: astro-ph/0407060 [astro-ph].

Baker, N. and R. Kippenhahn (Jan. 1959). "Untersuchungen über rotierende Sterne. III. Meridionale Zirkulation bei nichtstarrer Rotation". In: *ZAp* 48, p. 140.

Ball, W. H., N. Themeßl, and S. Hekker (Aug. 2018). "Surface effects on the red giant branch". In: *MNRAS* 478.4, pp. 4697–4709. DOI: 10.1093/mnras/sty1141. arXiv: 1804.11153 [astro-ph.SR].

Ballot, J., C. Barban, and C. van't Veer-Menneret (July 2011). "Visibilities and bolometric corrections for stellar oscillation modes observed by Kepler". In: *A&A* 531, A124, A124. DOI: 10.1051/0004-6361/201016230. arXiv: 1105.4557 [astro-ph.SR].

Ballot, J., S. Turck-Chièze, and R. A. García (Sept. 2004). "Seismic extraction of the convective extent in solar-like stars. The observational point of view". In: *A&A* 423, pp. 1051–1061. DOI: 10.1051/0004-6361:20035898.

Balmforth, N. J. (Apr. 1992). "Solar pulsational stability - I. Pulsation-mode thermodynamics". In: *MNRAS* 255, pp. 603–649. DOI: 10.1093/mnras/255.4.603.

Barban, C. et al. (Oct. 1999). "Solar-like oscillations of Procyon A: stellar models and time series simulations versus observations". In: *A&A* 350, pp. 617–625.

Barban, C. et al. (Oct. 2004). "Detection of Solar-Like Oscillations in Two Red Giant Stars". In: *SOHO 14 Helio- and Asteroseismology: Towards a Golden Future*. Ed. by D. Danesy. Vol. 559. ESA Special Publication, p. 113.

Basu, Sarbani et al. (May 2004). "Asteroseismic determination of helium abundance in stellar envelopes". In: *MNRAS* 350.1, pp. 277–286. DOI: 10.1111/j.1365-2966.2004.07644.x. arXiv: astro-ph/0402360 [astro-ph].

Beck, P. G. et al. (Jan. 2012). "Fast core rotation in red-giant stars as revealed by gravity-dominated mixed modes". In: *Nature* 481, pp. 55–57. DOI: 10.1038/nature10612. arXiv: 1112.2825 [astro-ph.SR].

Bedding, T. R. et al. (Mar. 2011). "Gravity modes as a way to distinguish between hydrogen- and helium-burning red giant stars". In: *Nature* 471, pp. 608–611. DOI: 10.1038/nature09935. arXiv: 1103.5805 [astro-ph.SR].

Belkacem, K. et al. (Dec. 2006). "A closure model with plumes. II. Application to the stochastic excitation of solar p modes". In: *A&A* 460, pp. 183–190. DOI: 10.1051/0004-6361:20065370. arXiv: 0607570 [astro-ph.SR].

Belkacem, K. et al. (June 2011). "The underlying physical meaning of the ν_{max} - ν_c relation". In: *A&A* 530, A142, A142. DOI: 10.1051/0004-6361/201116490. arXiv: 1104.0630 [astro-ph.SR].

Belkacem, K. et al. (Apr. 2012). "Damping rates of solar-like oscillations across the HR diagram. Theoretical calculations confronted to CoRoT and Kepler observations". In: *A&A* 540, L7, p. L7. DOI: 10.1051/0004-6361/201218890. arXiv: 1203.1737 [astro-ph.SR].

Benomar, O. et al. (Apr. 2013). "Properties of Oscillation Modes in Subgiant Stars Observed by Kepler". In: *ApJ* 767, 158, p. 158. DOI: 10.1088/0004-637X/767/2/158. arXiv: 1302.4143 [astro-ph.SR].

Benomar, O. et al. (Feb. 2014). "Asteroseismology of Evolved Stars with Kepler: A New Way to Constrain Stellar Interiors Using Mode Inertias". In: *ApJ* 781, L29, p. L29. DOI: 10.1088/2041-8205/781/2/L29. arXiv: 1401.5152 [astro-ph.SR].

Blocker, T. (May 1995). "Stellar evolution of low and intermediate-mass stars. I. Mass loss on the AGB and its consequences for stellar evolution." In: *A&A* 297, p. 727.

Bono, G. et al. (May 1995). "Advanced evolutionary phases of low-mass stars: the role of the original helium." In: *A&A* 297, pp. 115–126.

Borre, Camilla C. et al. (Aug. 2022). "Age determination of galaxy merger remnant stars using asteroseismology". In: *MNRAS* 514.2, pp. 2527–2544. DOI: 10.1093/mnras/stac1498. arXiv: 2111.01669 [astro-ph.GA].

Borucki, W. J. et al. (Feb. 2010). "Kepler Planet-Detection Mission: Introduction and First Results". In: *Science* 327, pp. 977–. DOI: 10.1126/science.1185402.

Bossini, D. et al. (Nov. 2015). "Uncertainties on near-core mixing in red-clump stars: effects on the period spacing and on the luminosity of the AGB bump". In: *MNRAS* 453, pp. 2290–2301. DOI: 10.1093/mnras/stv1738. arXiv: 1507.07797 [astro-ph.SR].

Bossini, D. et al. (Aug. 2017). "Kepler red-clump stars in the field and in open clusters: constraints on core mixing". In: *MNRAS* 469, pp. 4718–4725. DOI: 10.1093/mnras/stx1135. arXiv: 1705.03077.

Bossini, Diego (Jan. 2016). "Asteroseismology of red giant stars : a tool for constraining stellar models". PhD thesis. University of Birmingham, UK.

Bowen, G. H. (June 1988). "Dynamical Modeling of Long-Period Variable Star Atmospheres". In: *ApJ* 329, p. 299. DOI: 10.1086/166378.

Breger, M. and A. A. Pamyatnykh (May 2006). "Amplitude variability or close frequencies in pulsating stars - the δ Scuti star FG Vir". In: *MNRAS* 368.2, pp. 571–578. DOI: 10.1111/j.1365-2966.2006.10119.x. arXiv: astro-ph/0602037 [astro-ph].

Breger, M. et al. (Sept. 1999). "30+ frequencies for the delta Scuti variable 4 Canum Venaticorum: results of the 1996 multisite campaign". In: *A&A* 349, pp. 225–235.

Brocato, E. et al. (Feb. 1990). "Synthetic Colors and the Chemical Evolution of Elliptical Galaxies". In: *ApJ* 349, p. 458. DOI: 10.1086/168330.

Broomhall, A.-M. et al. (May 2014). "Prospects for asteroseismic inference on the envelope helium abundance in red giant stars". In: *MNRAS* 440, pp. 1828–1843. DOI: 10.1093/mnras/stu393. arXiv: 1403.7045 [astro-ph.SR].

Brown, T. M. and J. Christensen-Dalsgaard (June 1998). "Accurate Determination of the Solar Photospheric Radius". In: *ApJ* 500.2, pp. L195–L198. DOI: 10.1086/311416. arXiv: astro-ph/9803131 [astro-ph].

Brown, Timothy M. et al. (Feb. 1991). "Detection of Possible p-Mode Oscillations on Procyon". In: *ApJ* 368, p. 599. DOI: 10.1086/169725.

Buchler, J. R. and W. R. Yueh (Dec. 1976). "Compton scattering opacities in a partially degenerate electron plasma at high temperatures." In: *ApJ* 210, pp. 440–446. DOI: 10.1086/154847.

Buder, Sven et al. (Sept. 2021). "The GALAH+ survey: Third data release". In: *MNRAS* 506.1, pp. 150–201. DOI: 10.1093/mnras/stab1242. arXiv: 2011.02505 [astro-ph.GA].

Bugnet, L. et al. (June 2021). "Magnetic signatures on mixed-mode frequencies. I. An axisymmetric fossil field inside the core of red giants". In: *A&A* 650, A53, A53. DOI: 10.1051/0004-6361/202039159. arXiv: 2102.01216 [astro-ph.SR].

Cantiello, M. and N. Langer (Oct. 2010). "Thermohaline mixing in evolved low-mass stars". In: *A&A* 521, A9, A9. DOI: 10.1051/0004-6361/201014305. arXiv: 1006.1354 [astro-ph.SR].

Cantiello, Matteo, Jim Fuller, and Lars Bildsten (June 2016). "Asteroseismic Signatures of Evolving Internal Stellar Magnetic Fields". In: *ApJ* 824, 14, p. 14. DOI: 10.3847/0004-637X/824/1/14. arXiv: 1602.03056 [astro-ph.SR].

Caputo, F., V. Castellani, and P. R. Wood (Aug. 1978). "Evolutionary parameters in observed horizontal and asymptotic branches." In: *MNRAS* 184, pp. 377–386. DOI: 10.1093/mnras/184.3.377.

Casagrande, L. et al. (Jan. 2016). "Measuring the vertical age structure of the Galactic disc using asteroseismology and SAGA". In: *MNRAS* 455.1, pp. 987–1007. DOI: 10.1093/mnras/stv2320. arXiv: 1510.01376 [astro-ph.GA].

Cassisi, Santi, Maurizio Salaris, and Giuseppe Bono (Feb. 2002). "The Shape of the Red Giant Branch Bump as a Diagnostic of Partial Mixing Processes in Low-Mass Stars". In: *ApJ* 565.2, pp. 1231–1238. DOI: 10.1086/324695. arXiv: astro-ph/0110247 [astro-ph].

Castellani, V., A. Chieffi, and L. Pulone (July 1991). "The Evolution of He-burning Stars: Horizontal and Asymptotic Branches in Galactic Globulars". In: *ApJS* 76, p. 911. DOI: 10.1086/191584.

Castellani, V., P. Giannone, and A. Renzini (Mar. 1971a). "Induced Semi-Convection in Helium-Burning Horizontal-Branch Stars II". In: *Ap&SS* 10.3, pp. 355–362. DOI: 10.1007/BF00649680.

— (Feb. 1971b). "Overshooting of Convective Cores in Helium-Burning Horizontal-Branch Stars". In: *Ap&SS* 10.2, pp. 340–349. DOI: 10.1007/BF00704092.

Catelan, Márcio (Sept. 2007). "Structure and Evolution of Low-Mass Stars: An Overview and Some Open Problems". In: *Graduate School in Astronomy: XI Special Courses at the National Observatory of Rio de Janeiro (XI CCE)*. Ed. by Fernando Roig and Dalton Lopes. Vol. 930. American Institute of Physics Conference Series, pp. 39–90. DOI: 10.1063/1.2790333. arXiv: astro-ph/0703724 [astro-ph].

Caughlan, Georgeann R. and William A. Fowler (Jan. 1988). "Thermonuclear Reaction Rates V". In: *Atomic Data and Nuclear Data Tables* 40, p. 283. DOI: 10.1016/0092-640X(88)90009-5.

Chaplin, William J. et al. (Sept. 1996). "BiSON Performance". In: *Sol. Phys.* 168.1, pp. 1–18. DOI: 10.1007/BF00145821.

Charbonnel, C. and N. Lagarde (Nov. 2010). "Thermohaline instability and rotation-induced mixing. I. Low- and intermediate-mass solar metallicity stars up to the end of the AGB". In: *A&A* 522, A10, A10. DOI: 10.1051/0004-6361/201014432. arXiv: 1006.5359 [astro-ph.SR].

Charbonnel, C. and J. P. Zahn (May 2007). "Thermohaline mixing: a physical mechanism governing the photospheric composition of low-mass giants". In: *A&A* 467.1, pp. L15–L18. DOI: 10.1051/0004-6361:20077274. arXiv: astro-ph/0703302 [astro-ph].

Charpinet, S. et al. (July 2021). "Toward a systematic cartography of the chemical stratification inside white dwarfs from deep asteroseismic probing of ZZ Ceti stars". In: *arXiv e-prints*, arXiv:2107.03797, arXiv:2107.03797. arXiv: 2107.03797 [astro-ph.SR].

Chaussidon, Marc (2007). "Formation of the Solar System: a Chronology Based on Meteorites". In: *Lectures in Astrobiology*. Ed. by Muriel Gargaud, Hervé Martin, and Philippe Claeys, p. 45. DOI: 10.1007/978-3-540-33693-8_2.

Choi, Jieun et al. (June 2016). "Mesa Isochrones and Stellar Tracks (MIST). I. Solar-scaled Models". In: *ApJ* 823.2, 102, p. 102. DOI: 10.3847/0004-637X/823/2/102. arXiv: 1604.08592 [astro-ph.SR].

Christensen-Dalsgaard, J. (Jan. 1982). "Seismological studies of the sun and other stars". In: *Advances in Space Research* 2.9, pp. 11–19. DOI: 10.1016/0273-1177(82)90250-2.

— (Jan. 1988). "A Hertzsprung-Russell Diagram for Stellar Oscillations". In: *Advances in Helio- and Asteroseismology*. Ed. by Jorgen Christensen-Dalsgaard and Soren Frandsen. Vol. 123. IAU Symposium, p. 295.

Christensen-Dalsgaard, J., D. O. Gough, and M. J. Thompson (Sept. 1991). "The Depth of the Solar Convection Zone". In: *ApJ* 378, p. 413. DOI: 10.1086/170441.

Christensen-Dalsgaard, J., H. Kjeldsen, and J. A. Mattei (Dec. 2001). "Solar-like Oscillations of Semiregular Variables". In: *ApJ* 562.2, pp. L141–L144. DOI: 10.1086/338194. arXiv: astro-ph/0110475 [astro-ph].

Christensen-Dalsgaard, J. et al. (Dec. 2014). "On the asymptotic acoustic-mode phase in red giant stars and its dependence on evolutionary state". In: *MNRAS* 445, pp. 3685–3693. DOI: 10.1093/mnras/stu2007. arXiv: 1409.7949 [astro-ph.SR].

Christensen-Dalsgaard, Jørgen (Apr. 2004). "Physics of solar-like oscillations". In: *Sol. Phys.* 220.2, pp. 137–168. DOI: 10.1023/B:SOLA.0000031392.43227.7d.

— (Aug. 2008). "ADIPLS—the Aarhus adiabatic oscillation package". In: *Ap&SS* 316.1-4, pp. 113–120. DOI: 10.1007/s10509-007-9689-z. arXiv: 0710.3106 [astro-ph].

Claret, A. and G. Torres (July 2016). "The dependence of convective core overshooting on stellar mass". In: *A&A* 592, A15, A15. DOI: 10.1051/0004-6361/201628779.

Claret, Antonio and Guillermo Torres (Nov. 2017). "The Dependence of Convective Core Overshooting on Stellar Mass: A Semi-empirical Determination Using the Diffusive Approach with Two Different Element Mixtures". In: *ApJ* 849.1, 18, p. 18. DOI: 10.3847/1538-4357/aa8770. arXiv: 1710.08417 [astro-ph.SR].

— (June 2018). "The Dependence of Convective Core Overshooting on Stellar Mass: Additional Binary Systems and Improved Calibration". In: *ApJ* 859.2, 100, p. 100. DOI: 10.3847/1538-4357/aabd35. arXiv: 1804.03148 [astro-ph.SR].

— (May 2019). "The Dependence of Convective Core Overshooting on Stellar Mass: Reality Check and Additional Evidence". In: *ApJ* 876.2, 134, p. 134. DOI: 10.3847/1538-4357/ab1589. arXiv: 1904.02714 [astro-ph.SR].

Coelho, H. R. et al. (Aug. 2015). "A test of the asteroseismic ν_{max} scaling relation for solar-like oscillations in main-sequence and subgiant stars". In: *MNRAS* 451.3, pp. 3011–3020. DOI: 10.1093/mnras/stv1175. arXiv: 1505.06087 [astro-ph.SR].

Corsaro, E., J. De Ridder, and R. A. García (June 2015). "High-precision acoustic helium signatures in 18 low-mass low-luminosity red giants. Analysis from more than four years of Kepler observations". In: *A&A* 578, A76, A76. DOI: 10.1051/0004-6361/201525922. arXiv: 1504.04674 [astro-ph.SR].

Córsico, A. H. and L. G. Althaus (Sept. 2005). "Can pulsating PG 1159 stars place constraints on the occurrence of core overshooting?" In: *A&A* 439.3, pp. L31–L34. DOI: 10.1051/0004-6361:200500154. arXiv: astro-ph/0507255 [astro-ph].

Córsico, A. H. et al. (May 2002). "The mode trapping properties of full DA white dwarf evolutionary models". In: *A&A* 387, pp. 531–549. DOI: 10.1051/0004-6361:20020384. arXiv: astro-ph/0203453 [astro-ph].

Cowling, T. G. (Jan. 1941). "The non-radial oscillations of polytropic stars". In: *MNRAS* 101, p. 367. DOI: 10.1093/mnras/101.8.367.

Crowe, R. A. and R. Matalas (Apr. 1982). "Semiconvection in Low-Mass Main Sequence Stars". In: *A&A* 108, p. 55.

Cunha, M. S. et al. (June 2015). "Structural Glitches near the Cores of Red Giants Revealed by Oscillations in g-mode Period Spacings from Stellar Models". In: *ApJ* 805, 127, p. 127. DOI: 10.1088/0004-637X/805/2/127. arXiv: 1503.09085 [astro-ph.SR].

Cunha, M. S. et al. (Nov. 2019). "Analytical modelling of period spacings across the HR diagram". In: *MNRAS* 490.1, pp. 909–926. DOI: 10.1093/mnras/stz2582. arXiv: 1909.04966 [astro-ph.SR].

Cunha, Margarida S. (Jan. 2018). "Theory of Stellar Oscillations". In: *Asteroseismology and Exoplanets: Listening to the Stars and Searching for New Worlds*. Ed. by Tiago L. Campante, Nuno C. Santos, and Mário J. P. F. G. Monteiro. Vol. 49. Astrophysics and Space Science Proceedings, p. 27. DOI: 10.1007/978-3-319-59315-9_2. arXiv: 1711.01236 [astro-ph.SR].

Deepak and David L. Lambert (July 2021). "Lithium abundances and asteroseismology of red giants: understanding the evolution of lithium in giants based on asteroseismic parameters". In: *MNRAS* 505.1, pp. 642–648. DOI: 10.1093/mnras/stab1195. arXiv: 2104.11741 [astro-ph.SR].

Deheuvels, S. and K. Belkacem (Dec. 2018). "Seismic characterization of red giants going through the helium-core flash". In: *A&A* 620, A43, A43. DOI: 10.1051/0004-6361/201833409. arXiv: 1808.09458 [astro-ph.SR].

Deheuvels, S. et al. (Apr. 2014). "Seismic constraints on the radial dependence of the internal rotation profiles of six Kepler subgiants and young red giants". In: *A&A* 564, A27, A27. DOI: 10.1051/0004-6361/201322779. arXiv: 1401.3096 [astro-ph.SR].

Deheuvels, S. et al. (Aug. 2015). "Seismic evidence for a weak radial differential rotation in intermediate-mass core helium burning stars". In: *A&A* 580, A96, A96. DOI: 10.1051/0004-6361/201526449. arXiv: 1506.02704 [astro-ph.SR].

Deheuvels, S. et al. (May 2016). "Measuring the extent of convective cores in low-mass stars using Kepler data: toward a calibration of core overshooting". In: *A&A* 589, A93, A93. DOI: 10.1051/0004-6361/201527967. arXiv: 1603.02332 [astro-ph.SR].

Deheuvels, S. et al. (Aug. 2021). "Seismic signature of electron degeneracy in the core of red giants: hints for mass transfer between close red-giant companions". In: *arXiv e-prints*, arXiv:2108.11848, arXiv:2108.11848. arXiv: 2108.11848 [astro-ph.SR].

Di Mauro, M. P. and W. A. Dziembowski (Jan. 1998). "Differential rotation of the solar interior: new helioseismic results by inversion of the SOI-MDI/SOHO data". In: *Mem. Soc. Astron. Italiana* 69, p. 559.

Dréau, G. et al. (July 2020). "On using dipolar modes to constrain the helium glitch in red giant stars". In: *MNRAS* 497.1, pp. 1008–1014. DOI: 10.1093/mnras/staa1981. arXiv: 2007.01976 [astro-ph.SR].

Dréau, G. et al. (June 2021). "Seismic constraints on the internal structure of evolved stars: From high-luminosity RGB to AGB stars". In: *A&A* 650, A115, A115. DOI: 10.1051/0004-6361/202040240. arXiv: 2103.16718 [astro-ph.SR].

Dréau, G. et al. (July 2022). "Characterising the AGB bump and its potential to constrain mixing processes in stellar interiors". In: *arXiv e-prints*, arXiv:2207.00571, arXiv:2207.00571. arXiv: 2207.00571 [astro-ph.SR].

Dupret, M. A. et al. (Oct. 2006). "Theoretical damping rates and phase-lags for solar-like oscillations". In: *Proceedings of SOHO 18/GONG 2006/HELAS I, Beyond the spherical Sun*. Ed. by Karen Fletcher and Michael Thompson. Vol. 624. ESA Special Publication, 97, p. 97.

Dupret, M.-A. et al. (Oct. 2009). "Theoretical amplitudes and lifetimes of non-radial solar-like oscillations in red giants". In: *A&A* 506, pp. 57–67. DOI: 10.1051/0004-6361/200911713. arXiv: 0906.3951.

Dziembowski, W. A. (Mar. 2012). "Dipolar modes in luminous red giants". In: *A&A* 539, A83, A83. DOI: 10.1051/0004-6361/201117733. arXiv: 1201.3762 [astro-ph.SR].

Dziembowski, W. A., A. A. Pamiatnykh, and R. . Sienkiewicz (Apr. 1991). "Helium content in the solar convective envelope from helioseismology". In: *MNRAS* 249, pp. 602–605. DOI: 10.1093/mnras/249.4.602.

Dziembowski, W. A. and I. Soszyński (Dec. 2010). "Acoustic oscillations in stars near the tip of the red giant branch". In: *A&A* 524, A88, A88. DOI: 10.1051/0004-6361/201015205.

Dziembowski, W. A. et al. (Dec. 2001). "Oscillations of α UMa and other red giants". In: *MNRAS* 328.2, pp. 601–610. DOI: 10.1046/j.1365-8711.2001.04894.x. arXiv: astro-ph/0108337 [astro-ph].

Eggenberger, P., F. Carrier, and F. Bouchy (Jan. 2005). "Models of Procyon A including seismic constraints". In: *New A* 10.3, pp. 195–208. DOI: 10.1016/j.newast.2004.10.002. arXiv: astro-ph/0501270 [astro-ph].

Ekström, S. et al. (Jan. 2012). "Grids of stellar models with rotation. I. Models from 0.8 to 120 $M_\odot$ at solar metallicity (Z = 0.014)". In: *A&A* 537, A146, A146. DOI: 10.1051/0004-6361/201117751. arXiv: 1110.5049 [astro-ph.SR].

Elsworth, Yvonne et al. (Dec. 2015). "The Importance of Long-Term Synoptic Observations and Data Sets for Solar Physics and Helioseismology". In: *Space Sci. Rev.* 196.1-4, pp. 137–166. DOI: 10.1007/s11214-015-0212-5.

Elsworth, Yvonne et al. (Nov. 2019). "Insights from the APOKASC determination of the evolutionary state of red-giant stars by consolidation of different methods". In: *MNRAS* 489.4, pp. 4641–4657. DOI: 10.1093/mnras/stz2356. arXiv: 1909.06266 [astro-ph.SR].

Endal, A. S. and S. Sofia (Nov. 1976). "The evolution of rotating stars. I. Method and exploratory calculations for a 7 M sun star." In: *ApJ* 210, pp. 184–198. DOI: 10.1086/154817.

— (Feb. 1978). "The evolution of rotating stars. II. Calculations with time-dependent redistribution of angular momentum for 7 and 10 M sun stars." In: *ApJ* 220, pp. 279–290. DOI: 10.1086/155904.

Evans, J. W. and R. Michard (Sept. 1962). "Observational Study of Macroscopic Inhomogeneities in the Solar Atmosphere. III. Vertical Oscillatory Motions in the Solar Photosphere." In: *ApJ* 136, p. 493. DOI: 10.1086/147403.

Ferraro, Francesco R. (Jan. 1992). "The AGB and RGB clump as standard candles." In: *Mem. Soc. Astron. Italiana* 63, pp. 491–503.

Fossat, Eric (May 1991). "The IRIS Network for Full Disk Helioseismology - Present Status of the Programme". In: *Sol. Phys.* 133.1, pp. 1–12. DOI: 10.1007/BF00149818.

Frandsen, S. et al. (Oct. 2002). "Detection of Solar-like oscillations in the G7 giant star xi Hya". In: *A&A* 394, pp. L5–L8. DOI: 10.1051/0004-6361:20021281. eprint: arXiv:astro-ph/0209325.

Fröhlich, C. (Aug. 2006). "Solar Irradiance Variability Since 1978. Revision of the PMOD Composite during Solar Cycle 21". In: *Space Sci. Rev.* 125.1-4, pp. 53–65. DOI: 10.1007/s11214-006-9046-5.

Fuller, Jim et al. (Oct. 2015). "Asteroseismology can reveal strong internal magnetic fields in red giant stars". In: *Science* 6259, pp. 423–426. DOI: 10.1126/science.aac6933. eprint: arXiv:astro-ph/1510.06960.

Fynbo, Hans O. U. et al. (Jan. 2005). "Revised rates for the stellar triple-α process from measurement of ^{12}C nuclear resonances". In: *Nature* 433.7022, pp. 136–139.

Gabriel, A. H. et al. (Dec. 1995). "Global Oscillations at Low Frequency from the SOHO Mission (GOLF)". In: *Sol. Phys.* 162.1-2, pp. 61–99. DOI: 10.1007/BF00733427.

Gabriel, M. et al. (Sept. 2014). "Proper use of Schwarzschild Ledoux criteria in stellar evolution computations". In: *A&A* 569, A63, A63. DOI: 10.1051/0004-6361/201423442. arXiv: 1405.0128 [astro-ph.SR].

Gallart, Carme (Mar. 1998). "Observational Discovery of the Asymptotic Giant Branch Bump in Densely Populated Color-Magnitude Diagrams of Galaxies and Star Clusters". In: *ApJ* 495.1, pp. L43–L46. DOI: 10.1086/311218. arXiv: astro-ph/9712283 [astro-ph].

García, R. A. (Feb. 2015). "Observational techniques to measure solar and stellar oscillations". In: *EAS Publications Series*. Vol. 73-74. EAS Publications Series, pp. 193–259. DOI: 10.1051/eas/1573004. arXiv: 1510.02651 [astro-ph.SR].

García, R. A. et al. (June 2011). "Preparation of Kepler light curves for asteroseismic analyses". In: *MNRAS* 414, pp. L6–L10. DOI: 10.1111/j.1745-3933.2011.01042.x. arXiv: 1103.0382 [astro-ph.SR].

Gehan, C. et al. (Aug. 2018). "Core rotation braking on the red giant branch for various mass ranges". In: *A&A* 616, A24, A24. DOI: 10.1051/0004-6361/201832822. arXiv: 1802.04558 [astro-ph.SR].

Giammichele, N. et al. (Feb. 2017). "The potential of asteroseismology for probing the core chemical stratification in white dwarf stars". In: *A&A* 598, A109, A109. DOI: 10.1051/0004-6361/201629935. arXiv: 1611.05071 [astro-ph.SR].

Gilliland, R. L. et al. (Feb. 2010). "Kepler Asteroseismology Program: Introduction and First Results". In: *PASP* 122, pp. 131–143. DOI: 10.1086/650399. arXiv: 1001.0139.

Girardi, L. (Sept. 1999). "A secondary clump of red giant stars: why and where". In: *MNRAS* 308, pp. 818–832. DOI: 10.1046/j.1365-8711.1999.02746.x. eprint: arXiv:astro-ph/9901319.

Gizon, L. and S. K. Solanki (June 2003). "Determining the Inclination of the Rotation Axis of a Sun-like Star". In: *ApJ* 589.2, pp. 1009–1019. DOI: 10.1086/374715.

Goldreich, P. and D. A. Keeley (Feb. 1977). "Solar seismology. II. The stochastic excitation of the solar p-modes by turbulent convection." In: *ApJ* 212, 158, pp. 243–251. DOI: 10.1086/155043.

Goldreich, Peter and Pawan Kumar (June 1991). "Thermal and Mechanical Damping of Solar p-Modes". In: *ApJ* 374, p. 366. DOI: 10.1086/170126.

Gough, D. (1980). "Some theoretical remarks on solar oscillations". In: *Nonradial and Nonlinear Stellar Pulsation*. Ed. by H. A. Hill and W. A. Dziembowski. Vol. 125, pp. 273–299. DOI: 10.1007/3-540-09994-8_27.

Gough, D. O. (Jan. 1986). "Solar and solar-like oscillations: theory." In: *Highlights of Astronomy* 7, pp. 283–293.

— (1990). "Comments on Helioseismic Inference". In: *Progress of Seismology of the Sun and Stars*. Ed. by Yoji Osaki and Hiromoto Shibahashi. Vol. 367, p. 283. DOI: 10.1007/3-540-53091-6.

— (Jan. 2002). "Helioseismology: some current issues concerning model calibration". In: *Stellar Structure and Habitable Planet Finding*. Ed. by B. Battrick et al. Vol. 485. ESA Special Publication, pp. 65–73.

Gough, D. O. and M. J. Thompson (Jan. 1988). "On the Implications of the Symmetric Component of the Frequency Splitting". In: *Advances in Helio- and Asteroseismology*. Ed. by Jorgen Christensen-Dalsgaard and Soren Frandsen. Vol. 123. IAU Symposium, p. 175.

Goupil, M. J. et al. (Jan. 2013). "Seismic diagnostics for transport of angular momentum in stars. II. Interpreting observed rotational splittings of slowly rotating red giant stars". In: *A&A* 549, A75, A75. DOI: 10.1051/0004-6361/201220266. arXiv: 1211.1546 [astro-ph.SR].

Greggio, Laura and Alvio Renzini (Nov. 1990). "Clues on the Hot Star Content and the Ultraviolet Output of Elliptical Galaxies". In: *ApJ* 364, p. 35. DOI: 10.1086/169384.

Grigahcène, A. et al. (May 2005). "Convection-pulsation coupling. I. A mixing-length perturbative theory". In: *A&A* 434.3, pp. 1055–1062. DOI: 10.1051/0004-6361:20041816.

Grosjean, M. et al. (Dec. 2014). "Theoretical power spectra of mixed modes in low-mass red giant stars". In: *A&A* 572, A11, A11. DOI: 10.1051/0004-6361/201423827. arXiv: 1409.6121 [astro-ph.SR].

Gustafsson, B. et al. (Aug. 2008). "A grid of MARCS model atmospheres for late-type stars. I. Methods and general properties". In: *A&A* 486.3, pp. 951–970. DOI: 10.1051/0004-6361:200809724. arXiv: 0805.0554 [astro-ph].

Handberg, R. et al. (Nov. 2017). "NGC 6819: testing the asteroseismic mass scale, mass loss and evidence for products of non-standard evolution". In: *MNRAS* 472, pp. 979–997. DOI: 10.1093/mnras/stx1929. arXiv: 1707.08223 [astro-ph.SR].

Handler, Gerald (2013). "Asteroseismology". In: *Planets, Stars and Stellar Systems. Volume 4: Stellar Structure and Evolution*. Ed. by Terry D. Oswalt and Martin A. Barstow. Vol. 4, p. 207. DOI: 10.1007/978-94-007-5615-1_4.

Harvey, J. (June 1985). "High-resolution helioseismology". In: *Future Missions in Solar, Heliospheric & Space Plasma Physics*. Ed. by E. Rolfe & B. Battrick. Vol. 235. ESA Special Publication, pp. 199–208.

Harvey, J. W. et al. (Jan. 1993). "Chromospheric Oscillations and the Background Spectrum". In: *GONG 1992. Seismic Investigation of the Sun and Stars*. Ed. by Timothy M. Brown. Vol. 42. Astronomical Society of the Pacific Conference Series, p. 111.

Havel, M. et al. (July 2011). "The multiple planets transiting Kepler-9. I. Inferring stellar properties and planetary compositions". In: *A&A* 531, A3, A3. DOI: 10.1051/0004-6361/201116779. arXiv: 1103.6020 [astro-ph.EP].

Heger, A., N. Langer, and S. E. Woosley (Jan. 2000). "Presupernova Evolution of Rotating Massive Stars. I. Numerical Method and Evolution of the Internal Stellar Structure". In: *ApJ* 528.1, pp. 368–396. DOI: 10.1086/308158. arXiv: astro-ph/9904132 [astro-ph].

Hekker, S. and J. Christensen-Dalsgaard (June 2017). "Giant star seismology". In: *A&A Rev.* 25. DOI: 10.1007/s00159-017-0101-x. arXiv: 1609.07487 [astro-ph.SR].

Hekker, S. et al. (Aug. 2012). "Solar-like oscillations in red giants observed with Kepler: influence of increased timespan on global oscillation parameters". In: *A&A* 544, A90, A90. DOI: 10.1051/0004-6361/201219328. arXiv: 1207.0615 [astro-ph.SR].

Hekker, S. et al. (Mar. 2020). "Mirror principle and the red-giant bump: the battle of entropy in low-mass stars". In: *MNRAS* 492.4, pp. 5940–5948. DOI: 10.1093/mnras/staa176. arXiv: 2001.06064 [astro-ph.SR].

Henyey, Louis, M. S. Vardya, and Peter Bodenheimer (Oct. 1965). "Studies in Stellar Evolution. III. The Calculation of Model Envelopes." In: *ApJ* 142, p. 841. DOI: 10.1086/148357.

Hill, Frank et al. (July 1994a). "The Global Oscillation Network Group Site Survey - Part One". In: *Sol. Phys.* 152.2, pp. 321–349. DOI: 10.1007/BF00680443.

Hill, Frank et al. (July 1994b). "The Global Oscillation Network Group Site Survey - Part Two". In: *Sol. Phys.* 152.2, pp. 351–379. DOI: 10.1007/BF00680444.

Hogg, David W., Jo Bovy, and Dustin Lang (Aug. 2010). "Data analysis recipes: Fitting a model to data". In: *arXiv e-prints*, arXiv:1008.4686, arXiv:1008.4686. arXiv: 1008.4686 [astro-ph.IM].

Holtzman, Jon A. et al. (Nov. 2015). "Abundances, Stellar Parameters, and Spectra from the SDSS-III/APOGEE Survey". In: *AJ* 150.5, 148, p. 148. DOI: 10.1088/0004-6256/150/5/148. arXiv: 1501.04110 [astro-ph.GA].

Holtzman, Jon A. et al. (Sept. 2018). "APOGEE Data Releases 13 and 14: Data and Analysis". In: *AJ* 156.3, 125, p. 125. DOI: 10.3847/1538-3881/aad4f9. arXiv: 1807.09773 [astro-ph.GA].

Houdayer, Pierre S., Daniel R. Reese, and Marie-Jo Goupil (July 2022). "Properties of the ionisation glitch. II. Seismic signature of the structural perturbation". In: *A&A* 663, A60, A60. DOI: 10.1051/0004-6361/202243298. arXiv: 2202.04638 [astro-ph.SR].

Houdayer, Pierre S. et al. (Nov. 2021). "Properties of the ionisation glitch. I. Modelling the ionisation region". In: *A&A* 655, A85, A85. DOI: 10.1051/0004-6361/202141711. arXiv: 2110.00246 [astro-ph.SR].

Houdek, G. and D. O. Gough (Mar. 2007). "An asteroseismic signature of helium ionization". In: *MNRAS* 375, pp. 861–880. DOI: 10.1111/j.1365-2966.2006.11325.x. eprint: arXiv:astro-ph/0612030.

Houdek, G. et al. (Nov. 1999). "Amplitudes of stochastically excited oscillations in main-sequence stars". In: *A&A* 351, pp. 582–596. eprint: arXiv:astro-ph/9909107.

Huang, Wenjin, D. R. Gies, and M. V. McSwain (Oct. 2010). "A Stellar Rotation Census of B Stars: From ZAMS to TAMS". In: *ApJ* 722.1, pp. 605–619. DOI: 10.1088/0004-637X/722/1/605. arXiv: 1008.1761 [astro-ph.SR].

Huber, D. et al. (Nov. 2012). "Fundamental Properties of Stars Using Asteroseismology from Kepler and CoRoT and Interferometry from the CHARA Array". In: *ApJ* 760, 32, p. 32. DOI: 10.1088/0004-637X/760/1/32. arXiv: 1210.0012 [astro-ph.SR].

Iben I., Jr. and A. Renzini (Jan. 1983). "Asymptotic giant branch evolution and beyond." In: *ARA&A* 21, pp. 271–342. DOI: 10.1146/annurev.aa.21.090183.001415.

Iben Icko, Jr. (Nov. 1968). "Low-Mass Red Giants". In: *ApJ* 154, p. 581. DOI: 10.1086/149782.

Iglesias, Carlos A. and Forrest J. Rogers (June 1996). "Updated Opal Opacities". In: *ApJ* 464, p. 943. DOI: 10.1086/177381.

Imbriani, G. et al. (June 2004). "The bottleneck of CNO burning and the age of Globular Clusters". In: *A&A* 420, pp. 625–629. DOI: 10.1051/0004-6361:20040981. arXiv: astro-ph/0403071 [astro-ph].

Jeffreys, Harold (1939). *The Theory of Probability*.

Jermyn, Adam S. et al. (Apr. 2022). "Convective Penetration in Early-type Stars". In: *ApJ* 929.2, 182, p. 182. DOI: 10.3847/1538-4357/ac5f08. arXiv: 2203.09525 [astro-ph.SR].

Kallinger, T. (June 2019). "Release note: Massive peak bagging of red giants in the Kepler field". In: *arXiv e-prints*, arXiv:1906.09428, arXiv:1906.09428. arXiv: 1906.09428 [astro-ph.SR].

Kallinger, T. et al. (Jan. 2010). "Oscillating red giants in the CoRoT exofield: asteroseismic mass and radius determination". In: *A&A* 509, A77, A77. DOI: 10.1051/0004-6361/200811437.

Kallinger, T. et al. (May 2012). "Evolutionary influences on the structure of red-giant acoustic oscillation spectra from 600d of Kepler observations". In: *A&A* 541, A51, A51. DOI: 10.1051/0004-6361/201218854. arXiv: 1203.3134 [astro-ph.SR].

Kato, S. (Jan. 1966). "Overstable Convection in a Medium Stratified in Mean Molecular Weight". In: *PASJ* 18, p. 374.

Kawaler, Steven D. (Oct. 1988). "Angular Momentum Loss in Low-Mass Stars". In: *ApJ* 333, p. 236. DOI: 10.1086/166740.

Khan, S. et al. (June 2018). "The Red-giant Branch Bump Revisited: Constraints on Envelope Overshooting in a Wide Range of Masses and Metallicities". In: *ApJ* 859, 156, p. 156. DOI: 10.3847/1538-4357/aabf90. arXiv: 1804.06669 [astro-ph.SR].

King, C. R., G. S. Da Costa, and P. Demarque (Dec. 1985). "The luminosity function on the subgiant branch of 47 Tucanae : a comparison of observation and theory." In: *ApJ* 299, pp. 674–682. DOI: 10.1086/163733.

Kippenhahn, R., G. Ruschenplatt, and H. C. Thomas (Nov. 1980). "The time scale of thermohaline mixing in stars". In: *A&A* 91.1-2, pp. 175–180.

Kippenhahn, R. and H. C. Thomas (Jan. 1970). "A Simple Method for the Solution of the Stellar Structure Equations Including Rotation and Tidal Forces". In: *IAU Colloq. 4: Stellar Rotation*. Ed. by Arne Slettebak, p. 20.

Kippenhahn, R., A. Weigert, and A. Weiss (2012). *Stellar Structure and Evolution*. DOI: 10.1007/978-3-642-30304-3.

Kjeldsen, H. and T. R. Bedding (Jan. 1995). "Amplitudes of stellar oscillations: the implications for asteroseismology." In: *A&A* 293, pp. 87–106. eprint: arXiv:astro-ph/9403015.

Knapp, G. R. et al. (July 1998). "Multiple Molecular Winds in Evolved Stars. I. A Survey of CO(2-1) and CO(3-2) Emission from 45 Nearby Asymptotic Giant Branch Stars". In: *ApJS* 117.1, pp. 209–231. DOI: 10.1086/313111. arXiv: astro-ph/9711125 [astro-ph].

Lagarde, N. et al. (May 2017). "Population synthesis to constrain Galactic and stellar physics. I. Determining age and mass of thin-disc red-giant stars". In: *A&A* 601, A27, A27. DOI: 10.1051/0004-6361/201630253. arXiv: 1702.01769 [astro-ph.SR].

Lamers, Henny J. G. L. M. and Emily M. Levesque (2017). *Understanding Stellar Evolution*. DOI: 10.1088/978-0-7503-1278-3.

Langer, N., M. F. El Eid, and K. J. Fricke (Apr. 1985). "Evolution of massive stars with semiconvective diffusion". In: *A&A* 145.1, pp. 179–191.

Leavitt, Henrietta S. and Edward C. Pickering (Mar. 1912). "Periods of 25 Variable Stars in the Small Magellanic Cloud." In: *Harvard College Observatory Circular* 173, pp. 1–3.

Lebreton, Y. and M. J. Goupil (Aug. 2012). "Seismic signature of envelope penetrative convection: the CoRoT star HD 52265". In: *A&A* 544, L13, p. L13. DOI: 10.1051/0004-6361/201220000. arXiv: 1207.6957 [astro-ph.SR].

— (Sept. 2014). "Asteroseismology for "à la carte" stellar age-dating and weighing. Age and mass of the CoRoT exoplanet host HD 52265". In: *A&A* 569, A21, A21. DOI: 10.1051/0004-6361/201423797. arXiv: 1406.0652 [astro-ph.SR].

Lebreton, Yveline and Josefina Montalbán (June 2009). "Stellar ages from asteroseismology". In: *The Ages of Stars*. Ed. by Eric E. Mamajek, David R. Soderblom, and Rosemary F. G. Wyse. Vol. 258, pp. 419–430. DOI: 10.1017/S1743921309032074. arXiv: 0811.2908 [astro-ph].

Lefebvre, S. et al. (Nov. 2008). "Variations of the solar granulation motions with height using the GOLF/SoHO experiment". In: *A&A* 490.3, pp. 1143–1149. DOI: 10.1051/0004-6361:200810344. arXiv: 0808.0422 [astro-ph].

Leibacher, J. W. and R. F. Stein (Jan. 1971). "A New Description of the Solar Five-Minute Oscillation". In: *Astrophys. Lett.* 7, pp. 191–192.

Leighton, Robert B., Robert W. Noyes, and George W. Simon (Mar. 1962). "Velocity Fields in the Solar Atmosphere. I. Preliminary Report." In: *ApJ* 135, p. 474. DOI: 10.1086/147285.

Lighthill, M. J. (May 1962). "The Bakerian Lecture, 1961. Sound Generated Aerodynamically". In: *Proceedings of the Royal Society of London Series A* 267.1329, pp. 147–182. DOI: 10.1098/rspa.1962.0090.

Loi, Shyeh Tjing and John C. B. Papaloizou (July 2018). "Effects of a strong magnetic field on internal gravity waves: trapping, phase mixing, reflection, and dynamical chaos". In: *MNRAS* 477.4, pp. 5338–5357. DOI: 10.1093/mnras/sty917. arXiv: 1804.03664 [astro-ph.SR].

— (Jan. 2020). "Low-degree mixed modes in red giant stars with moderate core magnetic fields". In: *MNRAS* 491.1, pp. 708–724. DOI: 10.1093/mnras/stz2987. arXiv: 1910.09940 [astro-ph.SR].

Mackereth, J. Ted et al. (Apr. 2021). "Prospects for Galactic and stellar astrophysics with asteroseismology of giant stars in the TESS continuous viewing zones and beyond". In: *MNRAS* 502.2, pp. 1947–1966. DOI: 10.1093/mnras/stab098. arXiv: 2012.00140 [astro-ph.GA].

Maeder, A. (May 1975). "Stellar evolution III: the overshooting from convective cores." In: *A&A* 40.3, pp. 303–310.

Maeder, André (2009). *Physics, Formation and Evolution of Rotating Stars*. DOI: 10.1007/978-3-540-76949-1.

Magic, Z., A. Weiss, and M. Asplund (Jan. 2015). "The Stagger-grid: A grid of 3D stellar atmosphere models. III. The relation to mixing length convection theory". In: *A&A* 573, A89, A89. DOI: 10.1051/0004-6361/201423760. arXiv: 1403.1062 [astro-ph.SR].

Marigo, P. and B. Aringer (Dec. 2009). "Low-temperature gas opacity. ÆSOPUS: a versatile and quick computational tool". In: *A&A* 508.3, pp. 1539–1569. DOI: 10.1051/0004-6361/200912598. arXiv: 0907.3248 [astro-ph.SR].

Marigo, P. and L. Girardi (July 2007). "Evolution of asymptotic giant branch stars. I. Updated synthetic TP-AGB models and their basic calibration". In: *A&A* 469.1, pp. 239–263. DOI: 10.1051/0004-6361:20066772. arXiv: astro-ph/0703139 [astro-ph].

Martić, M. et al. (Nov. 1999). "Evidence for global pressure oscillations on Procyon". In: *A&A* 351, pp. 993–1002.

Mathur, S. et al. (Nov. 2011). "Granulation in Red Giants: Observations by the Kepler Mission and Three-dimensional Convection Simulations". In: *ApJ* 741, 119, p. 119. DOI: 10.1088/0004-637X/741/2/119. arXiv: 1109.1194 [astro-ph.SR].

Mauron, N. and P. J. Huggins (June 2006). "Imaging the circumstellar envelopes of AGB stars". In: *A&A* 452.1, pp. 257–268. DOI: 10.1051/0004-6361:20054739. arXiv: astro-ph/0602623 [astro-ph].

Mayor, Michel and Didier Queloz (Nov. 1995). "A Jupiter-mass companion to a solar-type star". In: *Nature* 378.6555, pp. 355–359. DOI: 10.1038/378355a0.

Mazumdar, A. et al. (Apr. 2012). "Seismic detection of acoustic sharp features in the CoRoT target <ASTROBJ>HD 49933</ASTROBJ>". In: *A&A* 540, A31, A31. DOI: 10.1051/0004-6361/201118495. arXiv: 1202.2692 [astro-ph.SR].

Mazumdar, A. et al. (Feb. 2014). "Measurement of Acoustic Glitches in Solar-type Stars from Oscillation Frequencies Observed by Kepler". In: *ApJ* 782, 18, p. 18. DOI: 10.1088/0004-637X/782/1/18. arXiv: 1312.4907 [astro-ph.SR].

Meynet, G. and A. Maeder (May 1997). "Stellar evolution with rotation. I. The computational method and the inhibiting effect of the μ-gradient." In: *A&A* 321, pp. 465–476.

Miglio, A. et al. (Sept. 2010). "Evidence for a sharp structure variation inside a red-giant star". In: *A&A* 520, L6, p. L6. DOI: 10.1051/0004-6361/201015442. arXiv: 1009.1024 [astro-ph.SR].

Miglio, A. et al. (Jan. 2012). "Asteroseismology of old open clusters with Kepler: direct estimate of the integrated red giant branch mass-loss in NGC 6791 and 6819". In: *MNRAS* 419, pp. 2077–2088. DOI: 10.1111/j.1365-2966.2011.19859.x. arXiv: 1109.4376 [astro-ph.SR].

Miglio, A. et al. (Feb. 2013). "Galactic archaeology: mapping and dating stellar populations with asteroseismology of red-giant stars". In: *MNRAS* 429.1, pp. 423–428. DOI: 10.1093/mnras/sts345. arXiv: 1211.0146 [astro-ph.GA].

Miglio, A. et al. (Jan. 2021a). "Age dissection of the Milky Way discs: Red giants in the Kepler field". In: *A&A* 645, A85, A85. DOI: 10.1051/0004-6361/202038307. arXiv: 2004.14806 [astro-ph.GA].

Miglio, Andrea et al. (June 2021b). "Haydn". In: *Experimental Astronomy* 51.3, pp. 963–1001. DOI: 10.1007/s10686-021-09711-1. arXiv: 1908.05129 [astro-ph.SR].

Miller Bertolami, Marcelo Miguel (Apr. 2016). "New models for the evolution of post-asymptotic giant branch stars and central stars of planetary nebulae". In: *A&A* 588, A25, A25. DOI: 10.1051/0004-6361/201526577. arXiv: 1410.1679 [astro-ph.SR].

Mirouh, G. M. et al. (May 2012). "A New Model for Mixing by Double-diffusive Convection (Semi-convection). I. The Conditions for Layer Formation". In: *ApJ* 750.1, 61, p. 61. DOI: 10.1088/0004-637X/750/1/61. arXiv: 1112.4819 [astro-ph.SR].

Montalbán, J. et al. (Oct. 2010). "Seismic Diagnostics of Red Giants: First Comparison with Stellar Models". In: *ApJ* 721.2, pp. L182–L188. DOI: 10.1088/2041-8205/721/2/L182. arXiv: 1009.1754 [astro-ph.SR].

Montalbán, J. et al. (2012). "Adiabatic Solar-Like Oscillations in Red Giant Stars". In: *Red Giants as Probes of the Structure and Evolution of the Milky Way*. Ed. by A. Miglio, J. Montalban, and A. Noels. Astrophysics and Space Science Proceedings, p. 23. DOI: 10.1007/978-3-642-18418-5_3.

Montalbán, J. et al. (Apr. 2013). "Testing Convective-core Overshooting Using Period Spacings of Dipole Modes in Red Giants". In: *ApJ* 766, 118, p. 118. DOI: 10.1088/0004-637X/766/2/118. arXiv: 1302.3173 [astro-ph.SR].

Monteiro, M. J. P. F. G., J. Christensen-Dalsgaard, and M. J. Thompson (Mar. 1994). "Seismic study of overshoot at the base of the solar convective envelope". In: *A&A* 283, pp. 247–262.

Monteiro, M. J. P. F. G. and M. J. Thompson (Aug. 2005). "Seismic analysis of the second ionization region of helium in the Sun - I. Sensitivity study and methodology". In: *MNRAS* 361, pp. 1187–1196. DOI: 10.1111/j.1365-2966.2005.09246.x. eprint: arXiv:astro-ph/0506286.

Moore, Kevin and Pascale Garaud (Jan. 2016). "Main Sequence Evolution with Layered Semiconvection". In: *ApJ* 817.1, 54, p. 54. DOI: 10.3847/0004-637X/817/1/54. arXiv: 1506.01034 [astro-ph.SR].

Mosser, B. (Feb. 2015). "Stellar oscillations - I - The adiabatic case". In: *EAS Publications Series*. Vol. 73-74. EAS Publications Series, pp. 3–110. DOI: 10.1051/eas/1573002. arXiv: 1509.08077 [astro-ph.SR].

Mosser, B. and T. Appourchaux (Dec. 2009). "On detecting the large separation in the autocorrelation of stellar oscillation times series". In: *A&A* 508, pp. 877–887. DOI: 10.1051/0004-6361/200912944. arXiv: 0909.0782.

Mosser, B., K. Belkacem, and M. Vrard (Dec. 2013). "Sounding stellar cores with mixed modes". In: *EAS Publications Series*. Ed. by G. Alecian et al. Vol. 63. EAS Publications Series, pp. 137–150. DOI: 10.1051/eas/1363016. arXiv: 1310.4752 [astro-ph.SR].

Mosser, B., A. Miglio, and CoRot Team (2016). "IV.2 Pulsating red giant stars". In: *The CoRoT Legacy Book: The Adventure of the Ultra High Precision Photometry from Space*, p. 197. DOI: 10.1051/978-2-7598-1876-1.c042.

Mosser, B., R. Samadi, and K. Belkacem (Nov. 2013). "Red giants seismology". In: *SF2A-2013: Proceedings of the Annual meeting of the French Society of Astronomy and Astrophysics*. Ed. by L. Cambresy et al., pp. 25–36. arXiv: 1310.4748 [astro-ph.SR].

Mosser, B. et al. (July 2010). "Red-giant seismic properties analyzed with CoRoT". In: *A&A* 517, A22. DOI: 10.1051/0004-6361/201014036. arXiv: 1004.0449 [astro-ph.SR].

Mosser, B. et al. (Jan. 2011). "The universal red-giant oscillation pattern. An automated determination with CoRoT data". In: *A&A* 525, p. L9. DOI: 10.1051/0004-6361/201015440. arXiv: 1011.1928 [astro-ph.SR].

Mosser, B. et al. (Jan. 2012a). "Characterization of the power excess of solar-like oscillations in red giants with Kepler". In: *A&A* 537, A30, A30. DOI: 10.1051/0004-6361/201117352. arXiv: 1110.0980 [astro-ph.SR].

Mosser, B. et al. (Apr. 2012b). "Probing the core structure and evolution of red giants using gravity-dominated mixed modes observed with Kepler". In: *A&A* 540, A143, A143. DOI: 10.1051/0004-6361/201118519. arXiv: 1203.0689 [astro-ph.SR].

Mosser, B. et al. (Dec. 2012c). "Spin down of the core rotation in red giants". In: *A&A* 548, A10, A10. DOI: 10.1051/0004-6361/201220106. arXiv: 1209.3336 [astro-ph.SR].

Mosser, B. et al. (Feb. 2013a). "Asymptotic and measured large frequency separations". In: *A&A* 550, A126, A126. DOI: 10.1051/0004-6361/201220435. arXiv: 1212.1687 [astro-ph.SR].

Mosser, B. et al. (Nov. 2013b). "Period-luminosity relations in evolved red giants explained by solar-like oscillations". In: *A&A* 559, A137, A137. DOI: 10.1051/0004-6361/201322243. arXiv: 1310.0839 [astro-ph.SR].

Mosser, B. et al. (Dec. 2014). "Mixed modes in red giants: a window on stellar evolution". In: *A&A* 572, L5, p. L5. DOI: 10.1051/0004-6361/201425039. arXiv: 1411.1082 [astro-ph.SR].

Mosser, B. et al. (Dec. 2015). "Period spacings in red giants. I. Disentangling rotation and revealing core structure discontinuities". In: *A&A* 584, A50, A50. DOI: 10.1051/0004-6361/201527075. arXiv: 1509.06193 [astro-ph.SR].

Mosser, B. et al. (Apr. 2017). "Period spacings in red giants. III. Coupling factors of mixed modes". In: *A&A* 600, A1, A1. DOI: 10.1051/0004-6361/201630053. arXiv: 1612.08453 [astro-ph.SR].

Mosser, B. et al. (Oct. 2018). "Period spacings in red giants IV. Toward a complete description of the mixed-mode pattern". In: *A&A* 618, A109, A109. DOI: 10.1051/0004-6361/201832777. arXiv: 1612.08453 [astro-ph.SR].

Mosser, B. et al. (Feb. 2019). "Seismic performance". In: *A&A* 622, A76, A76. DOI: 10.1051/0004-6361/201834607. arXiv: 1812.11906 [astro-ph.SR].

Nelder, J. A. and R. Mead (Jan. 1965). "A Simplex Method for Function Minimization". In: *The Computer Journal* 7.4, pp. 308–313. ISSN: 0010-4620. DOI: 10.1093/comjnl/7.4.308. eprint: https://academic.oup.com/comjnl/article-pdf/7/4/308/1013182/7-4-308.pdf. URL: https://doi.org/10.1093/comjnl/7.4.308.

Noels, A. et al. (July 2010). "Overshooting and semiconvection: structural changes and asteroseismic signatures". In: *Ap&SS* 328.1-2, pp. 227–236. DOI: 10.1007/s10509-009-0203-7.

Noll, A., S. Deheuvels, and J. Ballot (Mar. 2021). "Probing core overshooting using subgiant asteroseismology: The case of KIC10273246". In: *A&A* 647, A187, A187. DOI: 10.1051/0004-6361/202040055. arXiv: 2101.11025 [astro-ph.SR].

Paxton, Bill et al. (Jan. 2011). "Modules for Experiments in Stellar Astrophysics (MESA)". In: *ApJS* 192.1, 3, p. 3. DOI: 10.1088/0067-0049/192/1/3. arXiv: 1009.1622 [astro-ph.SR].

Paxton, Bill et al. (Sept. 2013). "Modules for Experiments in Stellar Astrophysics (MESA): Planets, Oscillations, Rotation, and Massive Stars". In: *ApJS* 208.1, 4, p. 4. DOI: 10.1088/0067-0049/208/1/4. arXiv: 1301.0319 [astro-ph.SR].

Paxton, Bill et al. (Sept. 2015). "Modules for Experiments in Stellar Astrophysics (MESA): Binaries, Pulsations, and Explosions". In: *ApJS* 220.1, 15, p. 15. DOI: 10.1088/0067-0049/220/1/15. arXiv: 1506.03146 [astro-ph.SR].

Paxton, Bill et al. (Feb. 2018). "Modules for Experiments in Stellar Astrophysics (MESA): Convective Boundaries, Element Diffusion, and Massive Star Explosions". In: *ApJS* 234.2, 34, p. 34. DOI: 10.3847/1538-4365/aaa5a8. arXiv: 1710.08424 [astro-ph.SR].

Paxton, Bill et al. (July 2019). "Modules for Experiments in Stellar Astrophysics (MESA): Pulsating Variable Stars, Rotation, Convective Boundaries, and Energy Conservation". In: *ApJS* 243.1, 10, p. 10. DOI: 10.3847/1538-4365/ab2241. arXiv: 1903.01426 [astro-ph.SR].

Pekeris, C. L. (Sept. 1938). "Nonradial Oscillations of Stars." In: *ApJ* 88, p. 189. DOI: 10.1086/143971.

Perez Hernandez, F. and J. Christensen-Dalsgaard (July 1994). "The phase function for stellar acoustic oscillations - III. The solar case". In: *MNRAS* 269, p. 475. DOI: 10.1093/mnras/269.2.475.

Perryman, Michael (2011). *The Exoplanet Handbook*.

Pietrinferni, Adriano et al. (Oct. 2013). "The BaSTI Stellar Evolution Database: models for extremely metal-poor and super-metal-rich stellar populations". In: *A&A* 558, A46, A46. DOI: 10.1051/0004-6361/201321950. arXiv: 1308.3850 [astro-ph.SR].

Pinçon, C., M. Takata, and B. Mosser (June 2019). "Evolution of the gravity offset of mixed modes in RGB stars". In: *A&A* 626, A125, A125. DOI: 10.1051/0004-6361/201935327. arXiv: 1905.05691 [astro-ph.SR].

Pinsonneault, M. H. et al. (Mar. 1989). "Evolutionary Models of the Rotating Sun". In: *ApJ* 338, p. 424. DOI: 10.1086/167210.

Provost, J. and G. Berthomieu (Sept. 1986). "Asymptotic properties of low degree solar gravity modes". In: *A&A* 165, pp. 218–226.

Provost, J. et al. (Dec. 2006). "Asteroseismology and evolutionary status of Procyon A". In: *A&A* 460.3, pp. 759–767. DOI: 10.1051/0004-6361:20065251.

Pulone, L. (Jan. 1992). "AGB clump as standard candle". In: *Mem. Soc. Astron. Italiana* 63.2, pp. 485–490.

Ramstedt, S. et al. (Aug. 2008). "On the reliability of mass-loss-rate estimates for AGB stars". In: *A&A* 487.2, pp. 645–657. DOI: 10.1051/0004-6361:20078876. arXiv: 0806.0517 [astro-ph].

Refsdal, S. and A. Weigert (July 1970). "Shell Source Burning Stars with Highly Condensed Cores". In: *A&A* 6, p. 426.

Reimers, D. (Jan. 1975). "Circumstellar absorption lines and mass loss from red giants." In: *Memoires of the Societe Royale des Sciences de Liege* 8, pp. 369–382.

Ricker, George R. et al. (Jan. 2015). "Transiting Exoplanet Survey Satellite (TESS)". In: *Journal of Astronomical Telescopes, Instruments, and Systems* 1, 014003, p. 014003. DOI: 10.1117/1.JATIS.1.1.014003.

Robertson, J. W. and D. J. Faulkner (Feb. 1972). "Semiconvection in the Core-Helium Phase of Stellar Evolution". In: *ApJ* 171, p. 309. DOI: 10.1086/151283.

Roxburgh, I. W. and S. V. Vorontsov (Sept. 2000). "Semiclassical approximation for low-degree stellar p modes - I. The classical eigenfrequency equation". In: *MNRAS* 317.1, pp. 141–150. DOI: 10.1046/j.1365-8711.2000.03623.x.

— (Nov. 2003). "The ratio of small to large separations of acoustic oscillations as a diagnostic of the interior of solar-like stars". In: *A&A* 411, pp. 215–220. DOI: 10.1051/0004-6361:20031318.

Rui, Nicholas Z. and Jim Fuller (Dec. 2021). "Asteroseismic fingerprints of stellar mergers". In: *MNRAS* 508.2, pp. 1618–1631. DOI: 10.1093/mnras/stab2528. arXiv: 2108.10322 [astro-ph.SR].

Sackmann, I. Juliana, Arnold I. Boothroyd, and William A. Fowler (Sept. 1990). "Our Sun. I. The Standard Model: Successes and Failures". In: *ApJ* 360, p. 727. DOI: 10.1086/169158.

Salaris, Maurizio and Santi Cassisi (2005). *Evolution of Stars and Stellar Populations*.

— (Aug. 2017). "Chemical element transport in stellar evolution models". In: *Royal Society Open Science* 4.8, 170192, p. 170192. DOI: 10.1098/rsos.170192. arXiv: 1707.07454 [astro-ph.SR].

Salaris, Maurizio, Alessandro Chieffi, and Oscar Straniero (Sept. 1993). "The alpha -enhanced Isochrones and Their Impact on the FITS to the Galactic Globular Cluster System". In: *ApJ* 414, p. 580. DOI: 10.1086/173105.

Salaris, Maurizio et al. (Nov. 2015). "Post first dredge-up [C/N] ratio as age indicator. Theoretical calibration". In: *A&A* 583, A87, A87. DOI: 10.1051/0004-6361/201526951. arXiv: 1509.06904 [astro-ph.SR].

Samadi, R., K. Belkacem, and T. Sonoi (Feb. 2015). "Stellar oscillations - II - The non-adiabatic case". In: *EAS Publications Series*. Vol. 73-74. EAS Publications Series, pp. 111–191. DOI: 10.1051/eas/1573003. arXiv: 1510.01151 [astro-ph.SR].

Sandquist, Eric L. and Michael Bolte (Aug. 2004). "Exploring the Upper Red Giant and Asymptotic Giant Branches: The Globular Cluster M5". In: *ApJ* 611.1, pp. 323–337. DOI: 10.1086/422134. arXiv: astro-ph/0404447 [astro-ph].

Scargle, J. D. (Dec. 1982). "Studies in astronomical time series analysis. II. Statistical aspects of spectral analysis of unevenly spaced data." In: *ApJ* 263, pp. 835–853. DOI: 10.1086/160554.

Scherrer, P. H. et al. (Jan. 1983). "Detection of solar five-minute oscillations of low degree". In: *Sol. Phys.* 82, pp. 75–87. DOI: 10.1007/BF00145547.

Schönberg, M. and S. Chandrasekhar (Sept. 1942). "On the Evolution of the Main-Sequence Stars." In: *ApJ* 96, p. 161. DOI: 10.1086/144444.

Schou, J. et al. (Sept. 1998). "Helioseismic Studies of Differential Rotation in the Solar Envelope by the Solar Oscillations Investigation Using the Michelson Doppler Imager". In: *ApJ* 505.1, pp. 390–417. DOI: 10.1086/306146.

Schwarzschild, Martin (1958). *Structure and evolution of the stars.*

Shapley, Harlow (Dec. 1914). "On the Nature and Cause of Cepheid Variation". In: *ApJ* 40, p. 448. DOI: 10.1086/142137.

Sharma, Sanjib et al. (May 2016). "Stellar Population Synthesis Based Modeling of the Milky Way Using Asteroseismology of 13,000 Kepler Red Giants". In: *ApJ* 822.1, 15, p. 15. DOI: 10.3847/0004-637X/822/1/15. arXiv: 1603.05661 [astro-ph.GA].

Shibahashi, H. (1979). "Modal Analysis of Stellar Nonradial Oscillations by an Asymptotic Method". In: *PASJ* 31, pp. 87–104.

Shibahashi, H. and Y. Osaki (Jan. 1981). "Theoretical Eigenfrequencies of Solar Oscillations of Low Harmonic Degree L in 5-MINUTE Range". In: *PASJ* 33, p. 713.

Silva Aguirre, V. et al. (May 2011). "Constraining mixing processes in stellar cores using asteroseismology. Impact of semiconvection in low-mass stars". In: *A&A* 529, A63, A63. DOI: 10.1051/0004-6361/201015847. arXiv: 1102.0779 [astro-ph.SR].

Silva Aguirre, V. et al. (Apr. 2018). "Confirming chemical clocks: asteroseismic age dissection of the Milky Way disc(s)". In: *MNRAS* 475.4, pp. 5487–5500. DOI: 10.1093/mnras/sty150. arXiv: 1710.09847 [astro-ph.GA].

Soszyński, I. et al. (Sept. 2009). "The Optical Gravitational Lensing Experiment. The OGLE-III Catalog of Variable Stars. IV. Long-Period Variables in the Large Magellanic Cloud". In: *Acta Astron.* 59.3, pp. 239–253. arXiv: 0910.1354 [astro-ph.SR].

Soszyński, I. and P. R. Wood (Feb. 2013). "Semiregular Variables with Periods Lying between the Period-Luminosity Sequences C', C, and D". In: *ApJ* 763, 103, p. 103. DOI: 10.1088/0004-637X/763/2/103.

Spruit, H. C. (Sept. 1999). "Differential rotation and magnetic fields in stellar interiors". In: *A&A* 349, pp. 189–202. arXiv: astro-ph/9907138 [astro-ph].

— (Jan. 2002). "Dynamo action by differential rotation in a stably stratified stellar interior". In: *A&A* 381, pp. 923–932. DOI: 10.1051/0004-6361:20011465. arXiv: astro-ph/0108207 [astro-ph].

Steinmetz, Matthias et al. (Aug. 2020). "The Sixth Data Release of the Radial Velocity Experiment (RAVE). II. Stellar Atmospheric Parameters, Chemical Abundances, and Distances". In: *AJ* 160.2, 83, p. 83. DOI: 10.3847/1538-3881/ab9ab8. arXiv: 2002.04512 [astro-ph.SR].

Stello, D. et al. (Mar. 2013). "Asteroseismic Classification of Stellar Populations among 13,000 Red Giants Observed by Kepler". In: *ApJ* 765, L41, p. L41. DOI: 10.1088/2041-8205/765/2/L41. arXiv: 1302.0858 [astro-ph.SR].

Stello, D. et al. (June 2014). "Non-radial Oscillations in M-giant Semi-regular Variables: Stellar Models and Kepler Observations". In: *ApJ* 788, L10, p. L10. DOI: 10.1088/2041-8205/788/1/L10. arXiv: 1406.0003 [astro-ph.SR].

Stello, Dennis et al. (Jan. 2016a). "A prevalence of dynamo-generated magnetic fields in the cores of intermediate-mass stars". In: *Nature* 529, pp. 364–367. DOI: 10.1038/nature16171. arXiv: 1601.00004 [astro-ph.SR].

Stello, Dennis et al. (Dec. 2016b). "The K2 M67 Study: Revisiting Old Friends with K2 Reveals Oscillating Red Giants in the Open Cluster M67". In: *ApJ* 832.2, 133, p. 133. DOI: 10.3847/0004-637X/832/2/133. arXiv: 1610.03060 [astro-ph.SR].

Stern, Melvin E. (Jan. 1960). "The "Salt-Fountain" and Thermohaline Convection". In: *Tellus* 12.2, pp. 172–175. DOI: 10.3402/tellusa.v12i2.9378.

Straniero, Oscar et al. (Feb. 2003). "The Chemical Composition of White Dwarfs as a Test of Convective Efficiency during Core Helium Burning". In: *ApJ* 583.2, pp. 878–884. DOI: 10.1086/345427. arXiv: astro-ph/0210191 [astro-ph].

Sugimoto, D., K. Nomoto, and Y. Eriguchi (Jan. 1981). "Stable Numerical Method in Computation of Stellar Evolution". In: *Progress of Theoretical Physics Supplement* 70, pp. 115–131. DOI: 10.1143/PTPS.70.115.

Sweigart, A. V. and P. G. Gross (June 1973). "Horizontal Branch Tracks with Semiconvection." In: *Bulletin of the American Astronomical Society*. Vol. 5, p. 314.

— (Mar. 1978). "Evolutionary sequences for red giant stars." In: *ApJS* 36, pp. 405–437. DOI: 10.1086/190506.

Takata, M. (Oct. 2006). "Analysis of Adiabatic Dipolar Oscillations of Stars". In: *PASJ* 58, pp. 893–908. DOI: 10.1093/pasj/58.5.893.

Tassoul, M. (Aug. 1980). "Asymptotic approximations for stellar nonradial pulsations". In: *ApJS* 43, pp. 469–490. DOI: 10.1086/190678.

Toutain, T. and T. Appourchaux (Sept. 1994). "Maximum likelihood estimators: an application to the estimation of the precision of helioseismic measurements". In: *A&A* 289, 649-658, pp. 649–658.

Trabucchi, Michele et al. (Oct. 2017). "A New Interpretation of the Period-Luminosity Sequences of Long-period Variables". In: *ApJ* 847.2, 139, p. 139. DOI: 10.3847/1538-4357/aa8998. arXiv: 1708.09350 [astro-ph.SR].

Ulrich, R. K. (July 1986). "Determination of Stellar Ages from Asteroseismology". In: *ApJ* 306, L37, p. L37. DOI: 10.1086/184700.

Ulrich, Roger K. (Dec. 1970). "The Five-Minute Oscillations on the Solar Surface". In: *ApJ* 162, p. 993. DOI: 10.1086/150731.

— (Feb. 1972). "Thermohaline Convection in Stellar Interiors." In: *ApJ* 172, p. 165. DOI: 10.1086/151336.

Unno, W. et al. (1989). *Nonradial oscillations of stars*. Ed. by Unno, W., Osaki, Y., Ando, H., Saio, H., & Shibahashi, H.

Vázquez Ramió, H., T. Roca Cortés, and C. Régulo (Dec. 2002). "Background solar irradiance spectrum at high and low phases of the solar activity cycle". In: *Solar Variability: From Core to Outer Frontiers*. Ed. by A. Wilson. Vol. 2. ESA Special Publication, pp. 897–900.

Verma, K. et al. (Aug. 2014). "Asteroseismic Estimate of Helium Abundance of a Solar Analog Binary System". In: *ApJ* 790, 138, p. 138. DOI: 10.1088/0004-637X/790/2/138. arXiv: 1405.7512 [astro-ph.SR].

Verma, Kuldeep et al. (Mar. 2019). "Helium abundance in a sample of cool stars: measurements from asteroseismology". In: *MNRAS* 483.4, pp. 4678–4694. DOI: 10.1093/mnras/sty3374. arXiv: 1812.02751 [astro-ph.SR].

Verma, Kuldeep et al. (July 2022). "Advanced asteroseismic modelling: breaking the degeneracy between stellar mass and initial helium abundance". In: *MNRAS*. DOI: 10.1093/mnras/stac1860. arXiv: 2207.00235 [astro-ph.SR].

Veronis, G. (Jan. 1965). "On parametric values and types of representation in wind-driven ocean circulation studies". In: *Tellus* 17.1, pp. 77–84. DOI: 10.3402/tellusa.v17i1.9005.

Villebrun, F. et al. (Feb. 2019). "Magnetic fields of intermediate-mass T Tauri stars. I. Magnetic detections and fundamental stellar parameters". In: *A&A* 622, A72, A72. DOI: 10.1051/0004-6361/201833545. arXiv: 1810.12803 [astro-ph.SR].

Vorontsov, S. V. (Jan. 1988). "A Search of the Effects of Magnetic Field in the Solar 5-Minute Oscillations". In: *Advances in Helio- and Asteroseismology*. Ed. by Jorgen Christensen-Dalsgaard and Soren Frandsen. Vol. 123. IAU Symposium, p. 151.

Vrard, M., B. Mosser, and R. Samadi (Apr. 2016). "Period spacings in red giants. II. Automated measurement". In: *A&A* 588, A87, A87. DOI: 10.1051/0004-6361/201527259. arXiv: 1602.04940 [astro-ph.SR].

Vrard, M. et al. (July 2015). "Helium signature in red giant oscillation patterns observed by Kepler". In: *A&A* 579, A84, A84. DOI: 10.1051/0004-6361/201425064. arXiv: 1505.07280 [astro-ph.SR].

Vrard, M. et al. (Aug. 2018). "Amplitude and lifetime of radial modes in red giant star spectra observed by Kepler". In: *A&A* 616, A94, A94. DOI: 10.1051/0004-6361/201732477. arXiv: 1805.03690 [astro-ph.SR].

Vrard, Mathieu and Margarida S. Cunha (Nov. 2019). "Influence of structural discontinuities present in the core of red-giant stars on the observed mixed-mode pattern and characterization of their properties". In: *arXiv e-prints*, arXiv:1911.05175, arXiv:1911.05175. arXiv: 1911.05175 [astro-ph.SR].

Walin, Gösta (Jan. 1964). "Note on the stability of water stratified by both salt and heat". In: *Tellus* 16.3, pp. 389–393. DOI: 10.3402/tellusa.v16i3.8930.

Wood, P. R. et al. (1999). "MACHO observations of LMC red giants: Mira and semi-regular pulsators, and contact and semi-detached binaries". In: *Asymptotic Giant Branch Stars*. Ed. by T. Le Bertre, A. Lebre, and C. Waelkens. Vol. 191. IAU Symposium, p. 151.

Wood, T. S., P. Garaud, and S. Stellmach (May 2013). "A New Model for Mixing by Double-diffusive Convection (Semi-convection). II. The Transport of Heat and Composition through Layers". In: *ApJ* 768.2, 157, p. 157. DOI: 10.1088/0004-637X/768/2/157. arXiv: 1212.1218 [astro-ph.SR].

Wray, J. J., L. Eyer, and B. Paczyński (Apr. 2004). "OGLE small-amplitude variables in the Galactic bar". In: *MNRAS* 349, pp. 1059–1068. DOI: 10.1111/j.1365-2966.2004.07587.x.

Yu, Jie et al. (Mar. 2020). "Asteroseismology of luminous red giants with Kepler I: long-period variables with radial and non-radial modes". In: *MNRAS* 493, pp. 1388–1403. DOI: 10.1093/mnras/staa300.

Yu, Jie et al. (Mar. 2021). "Asteroseismology of luminous red giants with Kepler - II. Dependence of mass-loss on pulsations and radiation". In: *MNRAS* 501.4, pp. 5135–5148. DOI: 10.1093/mnras/staa3970. arXiv: 2012.12414 [astro-ph.SR].

Yu, Jie et al. (May 2022). "Revised extinctions and radii for 1.5 million stars observed by APOGEE, GALAH, and RAVE". In: *arXiv e-prints*, arXiv:2206.00046, arXiv:2206.00046. arXiv: 2206.00046 [astro-ph.SR].

Zahn, J. P. (Dec. 1991). "Convective penetration in stellar interiors." In: *A&A* 252, pp. 179–188.

— (Nov. 1992). "Circulation and turbulence in rotating stars". In: *A&A* 265, pp. 115–132.

Zinn, Joel C. et al. (Nov. 2019). "Testing the Radius Scaling Relation with Gaia DR2 in the Kepler Field". In: *ApJ* 885.2, 166, p. 166. DOI: 10.3847/1538-4357/ab44a9. arXiv: 1910.00719 [astro-ph.SR].

RÉSUMÉ

L'astérosismologie fournit des informations uniques sur les étoiles qui sont non seulement essentielles pour sonder leur intérieur et leur évolution, mais aussi pour suivre l'évolution de la Galaxie et pour estimer les propriétés physiques des exoplanètes qu'elles abritent. Pour cela, l'étude des paramètres sismiques globaux d'un ensemble d'étoiles donne accès aux variations de leurs propriétés internes au fil de leur évolution. Les séries temporelles collectées par *Kepler* pendant quatre ans nous permettent de déchiffrer en détail le signal sismique des étoiles de la branche des géantes asymptotiques (AGB). De plus, les données de *Kepler* montrent nettement la présence d'une accumulation d'étoiles AGB assimilable au bump de l'AGB. L'un des objectifs principaux de ma thèse concerne l'analyse complète du spectre d'oscillation des géantes évoluées. J'investigue les principales différences de structure entre les étoiles de la branche des géantes rouges (RGB) et de l'AGB en couplant cette analyse sismique avec des modèles stellaires et leurs fréquences d'oscillation associées calculées à partir des codes MESA et ADIPLS, respectivement. La seconde facette importante de ma thèse consiste à évaluer la pertinence d'utiliser le bump de l'AGB comme chandelle standard ainsi que comme contrainte pour les processus de mélange dans les intérieurs stellaires. Enfin, je passe en revue les implications de ce travail sur les domaines de l'astrométrie et de l'archéologie Galactique.

MOTS CLÉS

astérosismologie – étoiles : oscillations – étoiles : intérieurs – étoiles : évolution – étoiles : phases évoluées − étoiles: AGB et post-AGB

ABSTRACT

Asteroseismology provides unique information on stars, which is crucial for probing their structure and evolution, but also for understanding the Galaxy evolution and for assessing the physical properties of the exoplanets they host. To this end, studying the global seismic parameters of an ensemble of stars gives us the opportunity to analyse the variation of stellar internal properties along stellar evolution. The four-year time series of *Kepler* allow us to decipher in detail the oscillation spectrum of Asymptotic-Giant Branch (AGB) stars. Moreover, *Kepler* data clearly exhibit an excess of AGB stars that can be identified as the AGB bump. First, this thesis focuses on a thorough analysis of the oscillation spectrum of evolved red giants. I investigate the main structural differences between Red-Giant Branch (RGB) and AGB stars by complementing this seismic study with stellar models and their oscillation frequencies calculated with the codes MESA and ADIPLS, respectively. Second, this thesis is dedicated to assessing the potential of the AGB bump to be a suitable standard candle as well as to constraining mixing processes in stellar interiors. At last, I discuss the implications of this work on astrometry and Galactic archaeology.

KEYWORDS

asteroseismology − stars: oscillations − stars: interiors − stars: evolution − stars: late-type − stars: AGB and post-AGB